

Lecture Notes on Data Engineering  
and Communications Technologies 92

Hari Vasudevan  
Zoran Gajic  
Amit A. Deshmukh *Editors*



# Proceedings of International Conference on Wireless Communication

ICWiCom 2021

 Springer

# **Lecture Notes on Data Engineering and Communications Technologies**

Volume 92

## **Series Editor**

Fatos Xhafa, Technical University of Catalonia, Barcelona, Spain

The aim of the book series is to present cutting edge engineering approaches to data technologies and communications. It will publish latest advances on the engineering task of building and deploying distributed, scalable and reliable data infrastructures and communication systems.

The series will have a prominent applied focus on data technologies and communications with aim to promote the bridging from fundamental research on data science and networking to data engineering and communications that lead to industry products, business knowledge and standardisation.

Indexed by SCOPUS, INSPEC, EI Compendex.

All books published in the series are submitted for consideration in Web of Science.

More information about this series at <https://link.springer.com/bookseries/15362>

Hari Vasudevan · Zoran Gajic · Amit A. Deshmukh  
Editors

# Proceedings of International Conference on Wireless Communication

ICWiCom 2021

 Springer

*Editors*

Hari Vasudevan  
Dwarkadas J. Sanghvi College  
of Engineering  
Mumbai, Maharashtra, India

Amit A. Deshmukh  
Dwarkadas J. Sanghvi College  
of Engineering  
Mumbai, Maharashtra, India

Zoran Gajic  
Department of Electrical and Computer  
Engineering  
Rutgers, The State University of New Jersey  
New Brunswick, NJ, USA

ISSN 2367-4512

ISSN 2367-4520 (electronic)

Lecture Notes on Data Engineering and Communications Technologies

ISBN 978-981-16-6600-1

ISBN 978-981-16-6601-8 (eBook)

<https://doi.org/10.1007/978-981-16-6601-8>

© The Editor(s) (if applicable) and The Author(s), under exclusive license to Springer Nature Singapore Pte Ltd. 2022

This work is subject to copyright. All rights are solely and exclusively licensed by the Publisher, whether the whole or part of the material is concerned, specifically the rights of translation, reprinting, reuse of illustrations, recitation, broadcasting, reproduction on microfilms or in any other physical way, and transmission or information storage and retrieval, electronic adaptation, computer software, or by similar or dissimilar methodology now known or hereafter developed.

The use of general descriptive names, registered names, trademarks, service marks, etc. in this publication does not imply, even in the absence of a specific statement, that such names are exempt from the relevant protective laws and regulations and therefore free for general use.

The publisher, the authors and the editors are safe to assume that the advice and information in this book are believed to be true and accurate at the date of publication. Neither the publisher nor the authors or the editors give a warranty, expressed or implied, with respect to the material contained herein or for any errors or omissions that may have been made. The publisher remains neutral with regard to jurisdictional claims in published maps and institutional affiliations.

This Springer imprint is published by the registered company Springer Nature Singapore Pte Ltd.

The registered company address is: 152 Beach Road, #21-01/04 Gateway East, Singapore 189721, Singapore

# **ICWiCOM 2021 Committee**

Shri Amrish R. Patel, Chief Patron, President, SVKM  
Shri Bhupesh R. Patel, Patron, Hon. Joint President and Trustee, SVKM  
Shri Bharat M. Sanghvi, Patron, Hon. Vice President and Trustee, SVKM and I/C,  
DJSCE  
Shri Chintan A. Patel, Patron, Hon. Vice President and Trustee, SVKM  
Shri Sunandan R. Divatia, Patron, Hon. Secretary, SVKM  
Shri Harshad H. Shah, Patron, Hon. Treasurer, SVKM  
Shri Jayant P. Gandhi, Patron, Hon. Joint Secretary, SVKM  
Shri Shalin S. Divatia, Patron, Hon. Joint Secretary, SVKM  
Shri Harit H. Chitalia, Patron, Hon. Joint Treasurer, SVKM  
Shri Jagdish B. Parikh, Patron, Hon. Joint Treasurer, SVKM

## **International Advisory Committee**

Dr. W. Ross Stone, Ph.D., LFIEEE, FURSI, FCIE, Stoneware Ltd., San Diego,  
California, USA  
Dr. Zoran Gajic, Rutgers University, USA  
Dr. Banmali Rawat, University of Nevada, Reno, USA  
Dr. Sheel Aditya, Former Professor, IIT Delhi and Former Associate Professor, NTU,  
Singapore  
Dr. Alexander B. Yakovlev, University of Mississippi, USA  
Dr. Manoj Patankar, Purdue University, USA

## **National Advisory Committee**

Mr. Asoke Basak, CEO, SVKM  
Prof. R. K. Shevgaonkar, Emeritus Professor, IIT Bombay

Dr. Nageshwar Rao, Vice Chancellor, IGNOU, India  
Dr. S. N. Merchant, IIT Bombay  
Dr. Girish Kumar, IIT Bombay  
Dr. D. Manjunath, IIT Bombay  
Dr. K. P. Ray, DIAT, Pune  
Dr. Debatosh Guha, Institute of Radio Physics and Electronics, University of Calcutta  
Dr. Pravin Bhagwat, Arista Networks Inc., India  
Dr. Asha E. Daniel, CUSAT, Kochi, India  
Dr. Suresh Ukarande, Principal, KJSIEIT and Associate Dean, Faculty of Science and Technology, UoM  
Dr. U. D. Kolekar, Principal, APSIT

## **Committee**

Dr. Hari Vasudevan, General Chair, Principal, DJSCE  
Dr. A. C. Daptardar, General Co-Chair, Vice-Principal (Administration), DJSCE  
Dr. Manali J. Godse, General Co-Chair, Vice-Principal (Academics), DJSCE  
Dr. Amit A. Deshmukh, Conference Chair, Professor and Head, EXTC Dept., DJSCE  
Prof. T. D. Biradar, Finance Chair  
Prof. S. B. Deshmukh, Finance Chair  
Prof. R. S. Taware, Finance Chair  
Prof. A. A. Odhekar, Technical Program Chair  
Prof. A. G. Ambekar, Technical Program Chair  
Prof. V. V. Kelkar, Organizing Chair  
Prof. P. A. Kadam, Organizing Chair  
Prof. A. A. Chaudhary, Organizing Chair  
Prof. S. S. Bhattacharjee, Publication Chair  
Prof. V. A. P. Chavali, Publication Chair  
Prof. Revathi A. S., Publication Chair  
Dr. S. H. Karamchandani, Publicity Chair  
Prof. A. A. Kadam, Publicity Chair  
Prof. R. Pal, Publicity Chair  
Prof. M. S. Pimpale, Sponsorship Chair  
Prof. Y. S. Bandi, Sponsorship Chair

# Preface

In modern communication technology, Wireless Communication has a major role to play and thus has a profound influence on the lives of the people. In continuation with Institute's earlier National (NCCT 2011) and International conferences 'ICCT 2013 and ICCT 2015' and 'ICWiCOM 2017' and 'ICWiCOM 2019', this International Conference on Wireless Communication 'ICWiCOM 2021' is being organized. The ICWiCOM 2021 includes papers with high quality and depth, which focus on the advances in various aspects of Wireless Communication domains like RF, Microwave and Antennas and Networking. The aim of 'ICWiCOM 2021' has been to unite Academic scientists, Engineers and Industry researchers for exchanging their experiences and research results and for the discussion of the current practical challenges.

The proceedings contain the papers presented at the conference and are divided into topics which are related to **Antenna Design, Networking and Signal Processing, Embedded Systems and Internet of Things (IoT)**. The future for wireless networking is very bright indeed, especially when the advances continue to support more sophisticated applications.

Mumbai, India  
Rutgers, USA  
Mumbai, India

Hari Vasudevan  
Zoran Gajic  
Amit A. Deshmukh



# Contents

## Antenna Design

<b>Resonant Length Formulations and Redesigning Methodology for Wideband Dual Polarized Y-Shape Microstrip Antenna</b> .....	3
Aarti Gajanan Ambekar, Amit A. Deshmukh, and Venkata A. P. Chavali	
<b>A Single Port Dual-Polarized Microstrip-Slot Antenna System for 5G Mid-Band Frequencies</b> .....	13
B. M. S. Sreenivasa Rao and B. Rajasekar	
<b>Gap-Coupled Microstrip Antenna Backed by Rectangular Slots Cut Ground Plane for Enhanced Bandwidth</b> .....	21
Poonam A. Kadam and Amit A. Deshmukh	
<b>Wideband and Circularly Polarized Variations of Sectoral Microstrip Antennas</b> .....	29
Amit A. Deshmukh, Tushar Sawant, and Aarti G. Ambekar	
<b>Coplanar Waveguide Fed Modified Helicopter Fan-Shaped Microstrip Antenna for Circularly Polarized Response</b> .....	39
Anuja Odhekar and Amit A. Deshmukh	
<b>Space-Fed Variations of Compact Microstrip Antennas Using Modified Feed Elements</b> .....	49
Adil Parvez, Kshitij Lele, Amit A. Deshmukh, and Venkata APC	
<b>Rectangular Slot Cut Sectoral Microstrip Antenna for Broadband Response</b> .....	65
Venkata A. P. Chavali, Amit A. Deshmukh, and Aarti G. Ambekar	
<b>Analysis and Design of Variations of Planar Inverted F-shape Microstrip Antennas for Wider Bandwidth</b> .....	75
Mohil Gala, Amit A. Deshmukh, and Aarti G. Ambekar	

<b>Analysis and Design of Variations of Compact U-Slot Cut Microstrip Antennas for Wider Bandwidth</b> .....	91
Mohil Gala, Amit A. Deshmukh, and A. P. C. Venkata	
<b>Microstrip-Line Resonator-Fed Rectangular Microstrip Antenna Using Gap-Coupled Parasitic Semi-circular Shape Patches</b> .....	109
Sanjay B. Deshmukh and Amit A. Deshmukh	
<b>Microstrip-Line Resonator-Fed Equilateral Triangular Antenna Using Gap-Coupled Parasitic Triangular Shape Patches</b> .....	119
Sanjay B. Deshmukh and Amit A. Deshmukh	
<b>Designs of Letter Shape Microstrip Antennas for Wideband, Dual-Band, and Circularly Polarized Response</b> .....	129
Shefali Pawar, Amit A. Deshmukh, and Aarti G. Ambekar	
<b>Analysis of Broadband Circularly Polarized Half E-Shape Microstrip Antenna</b> .....	139
Venkata A. P. Chavali, Amit A. Deshmukh, and Aarti G. Ambekar	
<b>Modal Analysis of Penta Band-Notched Elliptical Planar UWB Antenna</b> .....	147
Ameya A. Kadam and Amit A. Deshmukh	
<b>Sectoral Microstrip Antenna for Dual-Polarized Broadband Response</b> .....	157
Aarti G. Ambekar, Amit A. Deshmukh, and Venkata A. P. Chavali	
<b>Stub Loaded A-Shape Microstrip Antenna for Dual Polarized Multiband Response</b> .....	167
Aarti Gajanan Ambekar, Amit A. Deshmukh, and Venkata A. P. Chavali	
<b>Space Fed Rectangular Microstrip Antenna Arrays</b> .....	177
Adil Parvez, Amit A. Deshmukh, A. P. C. Venkata, and Tushar Sawant	
<b>Space-Fed Variations of Circularly Polarized Microstrip Antennas Using Modified Feed Elements</b> .....	193
Kshitij Lele, Adil Parvez, Amit A. Deshmukh, and A. G. Ambekar	
<b>Analysis of Multiple Shorting Posts Loaded Square Microstrip Antenna for Circular Polarized Response</b> .....	207
Amit A. Deshmukh, A. P. C. Venkata, Aarti G. Ambekar, and Tushar Sawant	
<b>Design of UWB Rectangular Microstrip Antenna with Defected Ground Structure to Detect Breast Cancer</b> .....	215
A. Sudhakar, M. V. Nageswara Rao, and Telagarapu Prabhakar	

**Networking & Signal Processing**

**Mode Selection Criterion Using Statistics for Direct Link Communication in Next Generation** ..... 225

Pallavi Sapkale and Uttam Kolekar

**Impact of 5G Technology on Indian Industries** ..... 235

C. A. Sathiyamoorthy, V. Sivasankaran, V. Venkataramanan, Mohd Faisal Mohd Sadique, and Soumyaprabakash Dashmohapatra

**Remote ECG Monitoring System Using IoT and Machine Learning** .... 249

Bhavya Sekhani, Dishay Shah, and Vishaka Kelkar

**Cognitive Radio Networks: Path Toward Advanced Spectrum Sensing—A Survey** ..... 259

Pradnya Kamble and Alam N. Shaikh

**Pattern Classification for Remote Sensing Images Using Back Propagation Network** ..... 271

Telagarapu Prabhakar, S. Sri Durga Kameswari, and A. Sudhakar

**Design of Spectral and Energy Efficient Network in Massive MIMO System** ..... 281

Suresh Dannana and Gottapu Sasibhushana Rao

**Autonomous Pesticide Spraying Robot Using SVM** ..... 293

S. Sri Durga Kameswari, Telagarapu Prabhakar, and K. Krishna Kishore

**Applications of AI Techniques like Machine Learning Methods and Deep Learning Models (ANNs) in Emerging Areas: A Review** ..... 303

Pranav H. Panicker, Amit A. Deshmukh, and Sunil H. Karamchandani

**Embedded Systems and Internet of Things (IoT)**

**Detection and Monitoring of Harmful Gases in Air Using a Microcontroller and Android App** ..... 315

Nidhi Patel, Yuti Bhavsar, Sakshi Mundra, Vraj Dharia, and Rahul Taware

**Telecom Customer Churn Prediction** ..... 325

Mehul Bhargava, Shruti Singh, Jaya Sharma, and D. Franklin Vinod

**Delve into the Realms with 3D Forms: Visualization System Aid Design in an IOT-Driven World** ..... 335

Aamir Khambaty, Drumil Joshi, Fawzan Sayed, Keagan Pinto, and Sunil Karamchandani

**Autonomous Parking System Perception and Control Simulations on ROS-Gazebo** ..... 345

Sunil Karamchandani, Saurabh Pednekar, Atharva Pusalkar, Shivani Bhattacharjee, and Disha Issrani

**Bus Monitoring System Using Raspberry Pi** ..... 355  
Tushar Sawant and Krupansh Shah

**Author Index** ..... 367

# About the Editors



**Dr. Hari Vasudevan** has obtained his Masters in Production Engineering as well as a Post Graduate Diploma in Industrial Engineering from VJTI, Mumbai, and Ph.D. from IIT Bombay. He has also done a 3 months full time certificate program (ERP-BaaN) under the University Synergy Programme of BaaN Institute, Netherlands from S. P. Jain Institute of Management & Research, Mumbai. His area of interest include manufacturing engineering, manufacturing systems and strategy, market orientation of manufacturing firms and world-class manufacturing. He is an approved Ph.D guide at the University of Mumbai and NMIMS (Deemed to be university) and has so far guided 8 Ph.D. students. He is President of Indian Society of Manufacturing Engineering (ISME), Life member of ISTE, New Delhi, Fellow of the Institution of Engineers India, Fellow of ISME, and a Senior Member of IEDRC. He has over 28 years of teaching experience and 2 years of experience in industry. Presently he is working as Principal of D J Sanghvi College of Engineering. He has published over 134 papers in International conferences and Journals as well as in National conferences, Journals and has authored a couple of books and contributed book chapters in various publications.



**Dr. Zoran Gajic** is Professor of Electrical and Computer Engineering at Rutgers University. He has been teaching linear systems and signals, controls, communication networks, optical networks, and electrical circuit courses at the same school since 1984. Dr. Gajic's research interests are in controls systems, energy systems (fuel and solar cells, wind, smart grids), wireless communications, and networking. He is Author/Coauthor of close to 100 journal papers, primarily published in IEEE Transactions on Automatic Control and IFAC Automatica journals, and eight books on linear systems and linear and bilinear control systems published by Academic Press, Prentice Hall, Marcel Dekker, Taylor and Francis, and Springer Verlag. His Prentice Hall book *Linear Dynamic Systems and Signals* was translated into the Chinese Simplified Language by Jiaotong University Press in 2004. His 1995 Academic Press book *Lyapunov Matrix Equation in Systems Stability and Control* was republished in 2008 by Dover Publications. Professor Gajic has delivered four plenary lectures at international conferences and presented more than one hundred forty conference papers. He has served on editorial boards for nine journals and as Guest Editor for five journal special issues. Professor Gajic supervised 18 doctoral dissertations and 25 master theses. Fourteen of his former doctoral students hold faculty positions at respected world universities. Zoran Gajic received Dipl. Ing. (5 year program) and Mgr. Sci. (2 year program) degrees in Electrical Engineering from the University of Belgrade, M.S. degree in Applied Mathematics, and Ph.D. in Systems Science Engineering under direction of Professor Hassan Khalil from Michigan State University in 1984. His research was supported by US National Science Foundation and AT&T Bell Laboratories. Dr. Gajic was Visiting Professor at Princeton University in 2003, and the American University of Sharjah (UAE) in 2011. He is Life Master of the U.S. Chess Federation and Master of the World Chess Federation. From September 2003 to June 2020, Dr. Gajic has served as Graduate Program Director for the Rutgers University Electrical and Computer Engineering Department.



**Dr. Amit A. Deshmukh** obtained B.E. (Electronics) from V.I.T., Pune University in 1997. He obtained M.Tech. Degree in 2000 and Ph. D. in 2004 from Department of Electrical Engineering, IIT Bombay. His thesis work during masters and doctoral was on compact broadband and dual-band microstrip antennas. He worked as Research Assistant in Department of Electrical Engineering, IIT Bombay. Further, He worked as Assistant Professor in Sardar Patel Institute of Technology, Mukesh Patel School of Technology and Management (NMIMS – DU), and D. J. Sanghvi College of Engineering. He also worked as Member of Technical staff in R&D division of Air Tight Network Pvt. Ltd., Pune. Currently, he is working as Professor & Head of the Department of Electronics and Telecommunication Engineering at D. J. Sanghvi College of Engineering, Vile – Parle (W), Mumbai, India. He has together (Teaching, Industry, and Research) more than 18 years of experience. He is an approved Ph.D. guide at University of Mumbai. He has published more than 300 research papers in various International, National Journals and Conferences. He is on reviewer list of many International Journals like, IEEE Magazine on Antennas and Propagation, IEEE Transaction of Antennas and Propagation, IEEE Antennas and Wireless Propagation Letters, IET Microwave Antennas and Propagation, PIERS journals, International Journal of Electronics, IETE Journal of Research, Elsevier Electronics and Communication Journal, and International Journal of RF and Microwave Computer-Aided Engineering. He has delivered many lecture talks in National/International conferences and workshops in the areas of patch antennas.

# Antenna Design



# Resonant Length Formulations and Redesigning Methodology for Wideband Dual Polarized Y-Shape Microstrip Antenna



Aarti Gajanan Ambekar, Amit A. Deshmukh, and Venkata A. P. Chavali

**Abstract** A Y-shape microstrip antenna derived from an L-shape microstrip antenna is a compact version of basic rectangular microstrip antenna. The Y-shape microstrip antenna is reported for wideband response with dual polarization. Owing to the fine-tuning of  $TM_{20}$  mode with the basic mode  $TM_{10}$ . In this paper the surface current variations of the respective modes are studied and based on that resonant length formulations for the Y-shape patch modes are proposed. Further, redesigning methodology is proposed for the designing of similar Y-shape antennas at different frequencies. The redesigned antennas yield the similar characteristics with appreciable impedance bandwidth and gain.

**Keywords** Y-shape antenna · Wideband response · Dual polarization · Resonant length formulation

## 1 Introduction

Dual polarized (DP) antennas play a very vital role in modern communication system, for avoiding multipath propagation. Due to low profile and ease of fabrication, microstrip antennas (MSAs) are suitable for realization of DP response. Many applications require a compact antenna structure with dual polarization and wider bandwidth (BW). Geometrical modifications can be done in regular shape MSAs like rectangular MSA (RMSA), circular MSA (CMSA) or triangular MSA (TMSA) for realizing compact structures [1–4]. These geometrical modifications are done in terms of embedded slots, slits, connected stubs or modified feeds for realization of wideband response with dual polarization [5–9]. But in most of the modified geometries, explanation about effect of geometrical modifications done in patch on realization of dual-polarized wideband response is not provided. A Y-shape MSA is derived from an L-shape MSA, which is a compact version of basic rectangular MSA (RMSA) [10]. The stub positioned on edges of basic L-shape patch adjusts the

---

A. G. Ambekar · A. A. Deshmukh (✉) · V. A. P. Chavali  
Department of EXTC, SVKM's DJSCE, UOM, Mumbai, India

spacing between  $TM_{20}$  mode with respect to the fundamental mode  $TM_{10}$ , which produces wideband response with  $BW > 200$  MHz ( $>25\%$ ). Orthogonal orientations of surface currents for  $TM_{10}$  and  $TM_{20}$  yields dual polarized response. Parametric study reinforced by resonance curves and surface current variations in terms of stub length variations were also carried out in the reported work. Surface current distributions for the basic patch modes were also studied but resonant length formulations based on those surface current distributions were not present in the reported work [10]. Also, the reported work does not provide any re-design guidelines for designing of alike Y-shape antennas for various frequencies of operation.

In the current paper first Y-shape MSA fabricated of air suspended FR4 substrate is discussed ( $h = 0.16$  cm,  $\epsilon_r = 4.3$ ), for the frequency range of 900 MHz [10]. Dual polarized wideband response in Y-shape MSA is the outcome of coupling among  $TM_{10}$  and  $TM_{20}$  modes. Further by learning the modal current plots at the two modes, their resonant length formulation is projected. Frequencies intended using those formulae match closely with the simulated values. Using these formulations, redesigning methodology is proposed for designing of same type of antenna for different frequencies depending on the applications. The antenna designed by means of the proposed formulation, produces the same dual polarized wideband response with  $BW$  375 MHz (23%) and broadside gain  $>5$  dBi. The re-designed configurations are first analyzed using CST Microwave Studio [11]. Proximity feeding technique using SMA type connector is selected for exciting the antenna. High frequency instruments namely ZVH 8, FSC 6, and SMB-100A are used for testing. A decent matching is observed among the simulated and measured results.

## 2 Resonant Length Formulation and Designing Methodology for Y-Shape MSA

An optimized design of Y-shape MSA evolved from the L-shape MSA is as revealed in Fig. 1a–c [10]. The patch is fabricated on suspended FR4 substrate ( $\epsilon_r = 4.3$ ,  $h = 0.16$  cm,  $\tan \delta = 0.02$ ) which is suspended above ground plane using air gap ‘ $h_a$ ’. Y-shape patch is derived from equivalent rectangular and L-shape patch as shown in the figure. For realization of wideband response with dual polarization tuning between  $TM_{10}$  and  $TM_{20}$  mode of basic L-shape MSA is achieved by connecting a L-shape stub of length ‘ $L_1$ ’ and ‘ $L_2$ ’ at the middle point edge of L-shape patch as publicized in Fig. 1b.

Parametric is carried with respect to stub lengths variations in [10], corresponding resonance plots as per reported work are as shown in Fig. 2a–c. The  $TM_{20}$  mode frequency is decrementing with respect to incrementing stub length. The configuration yields, simulated dual polarized wideband response with  $BW$  269 MHz (26.5%), whereas measured is 280 MHz (28%). Across the  $BW$  at lower frequencies E-plane is directed along  $\Phi = 90^\circ$  due to  $TM_{10}$  mode while at higher frequencies it is directed along  $\Phi = 0^\circ$  because of  $TM_{20}$  mode.

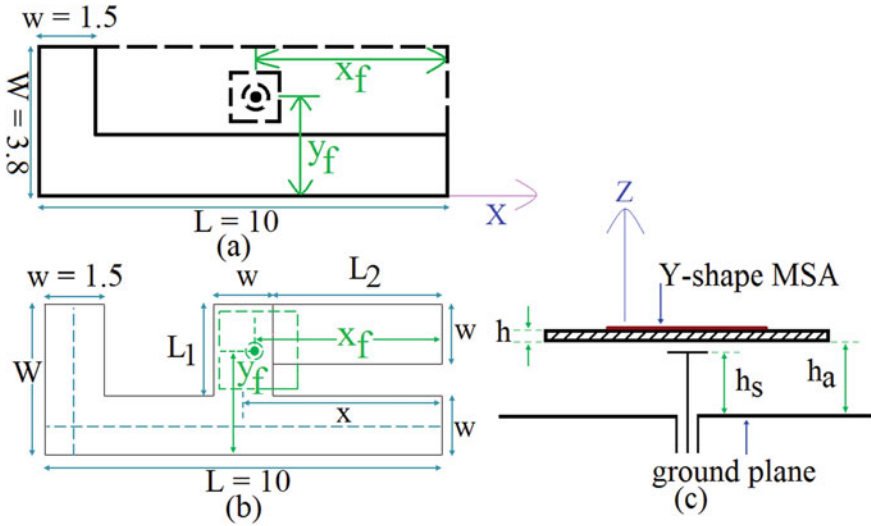


Fig. 1 a–c Geometry of the proximity fed L-shape and Y-shape MSA [10]

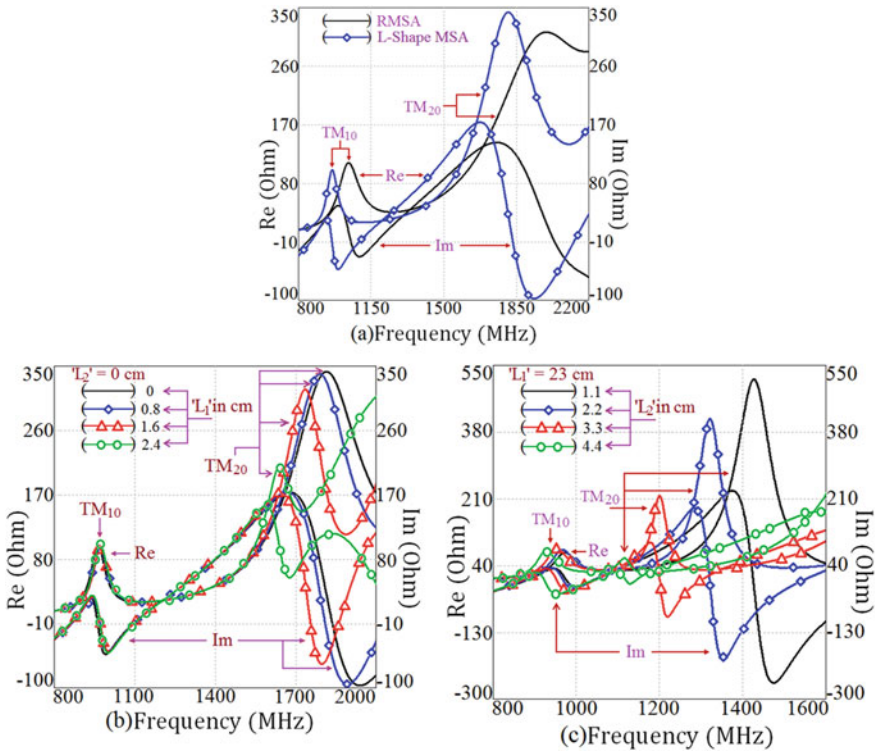
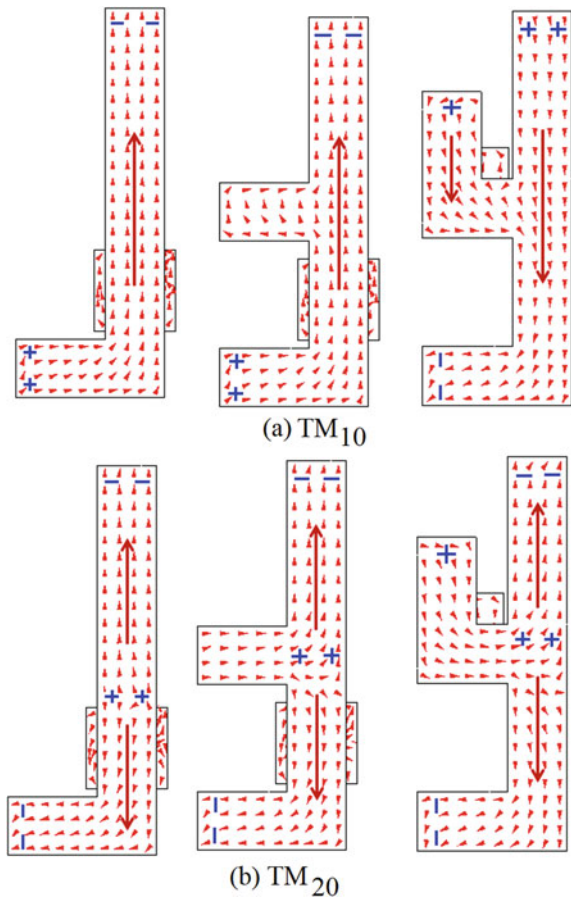
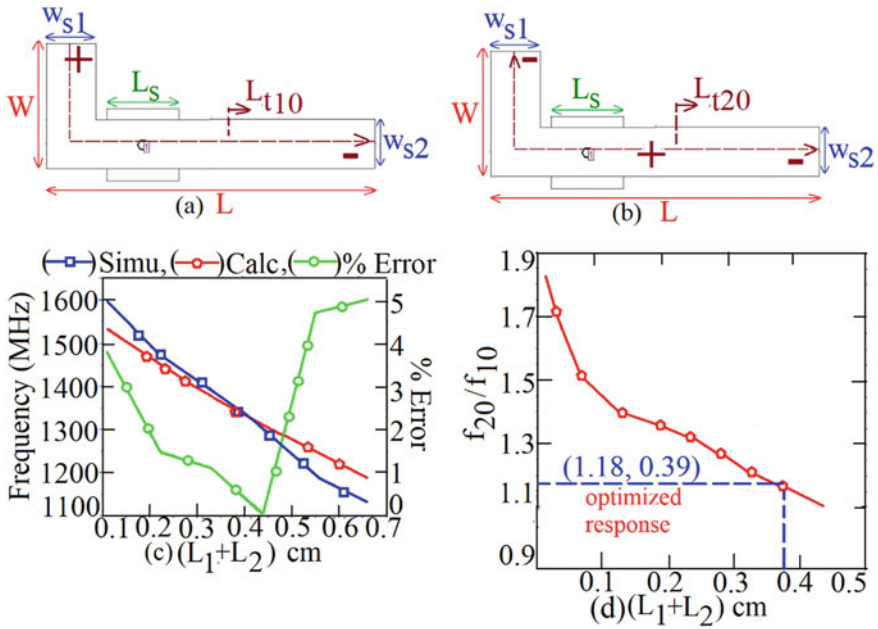


Fig. 2 a–c Resonance plots for stub length variations of Y-shape MSA [10]

Although the respective modes  $TM_{10}$  and  $TM_{20}$ , are mentioned but the surface current paths are not given in the [10], for the respective modes. Based on its formulations in the resonant length followed by redesigning methodology for the  $TM_{10}$  and  $TM_{20}$  mode is also not provided in [10]. Now here for proposing the resonant length formulations for the  $TM_{10}$  and  $TM_{20}$  mode surface currents are studied first. As the structure is evolved step by step from the basic L-shape patch and then a stub connected to it hence the corresponding surface currents are as revealed in Fig. 3a, b. For the first peak of the resonant mode, half wavelength variation is observed along the horizontal direction as shown in Fig. 3a, which resembles to  $TM_{10}$  mode. Whereas for the second peak two half wavelength variations are observed along the length, that corresponds to  $TM_{20}$  mode as shown in Fig. 3b. Now using these current distribution resonant length formulations for the corresponding modes can be derived. Now by studying these current distributions shown, the actual resonant length is marked for the respective modes with respect to the basic L-shape MSA

**Fig. 3 a, b** Surface current distributions for the Y-shape MSA





**Fig. 4** a, b Effective resonant lengths at TM<sub>10</sub> and TM<sub>20</sub> mode, c frequency and % error plots at TM<sub>20</sub> mode against varying total stub length, and d frequency ratio plots for  $f_{20}/f_{10}$  for varying stub lengths of redesigned configuration at 1500 MHz of the Y-shape MSA

as shown in Fig. 4a, b. For the simplifications, the stub width along patch width is renamed as ‘ $w_{s1}$ ’ while along patch length is renamed as ‘ $w_{s2}$ ’.

Since for the TM<sub>10</sub> mode half wavelength variation is observed in the horizontal direction along the patch length, its resonant length formula is defined as given in Eq. (1) below. The total length calculated for TM<sub>10</sub> is then equated to half the wavelength. Similarly, as TM<sub>20</sub> shows two half wavelength variations along the same patch, the resonant length equation for TM<sub>20</sub> mode is then equated to the wavelength equation. Effective length for TM<sub>10</sub> and TM<sub>20</sub> mode are then calculated using Eqs. (3) and (4). ‘ $\Delta L$ ’ indicates the fringing field, given by Eq. (2). As the MSA is fabricated on air-suspended FR4 substrate, its effective ‘ $\epsilon_{re}$ ’ is calculated using Eq. (5) while from the fundamental mode frequency ‘ $\lambda_g$ ’ is calculated using Eq. (6). These two values are used for calculating frequencies of the respective modes.

$$L_t = \left[ W - \frac{w_{s2}}{2} \right] + [L - w_{s1}/2] \quad (1)$$

$$\Delta L = (h_a + h) / \sqrt{\epsilon_{re}} \quad (2)$$

$$L_{eff10} = L_t + 2(0.6\Delta L) \quad (3)$$

$$L_{\text{eff}20} = L_t + 2(0.35\Delta L) \quad (4)$$

$$\epsilon_{\text{re}} = \epsilon_r(h + h_a) / \epsilon_r h_a + h \quad (5)$$

$$\lambda_g = 30 / f_{\text{TM}} \sqrt{\epsilon_{\text{re}}} \quad (6)$$

$$f_{10} = \frac{c}{[(2 \times L_{\text{eff}10}) \times (\sqrt{\epsilon_{\text{re}}})]} \quad (7)$$

$$f_{20} = \frac{c}{[(L_{\text{eff}20}) \times (\sqrt{\epsilon_{\text{re}}})]} \quad (8)$$

$$\% \text{error} = \left| \frac{f_{\text{simu}} - f_{\text{calc}}}{f_{\text{simu}}} \right| \quad (9)$$

Frequencies for TM<sub>10</sub> and TM<sub>20</sub> mode are then calculated using Eqs. (7) and (8) respectively while % error is calculated using Eq. (9). Now for the basic Y-shape MSA without stub simulated TM<sub>10</sub> mode frequency is 957 MHz while the calculated one is 955 MHz there by yielding ‘% Error’ equal to 0.2%. While for the TM<sub>20</sub> mode simulated frequency is 1724 MHz and calculated one is 1711 MHz, yielding ‘% Error’ equal to 0.75%. ‘% Error’ below 1% indicates close prediction between simulated and calculated frequency values.

Now tuning of TM<sub>20</sub> mode with respect to the TM<sub>10</sub> mode is achieved using L-shape stub, and from the parametric done as per the reported work [10], this stub is affecting the TM<sub>20</sub> mode frequency. Hence formulation of this mode is revised by adding the vertical and horizontal stub length as given in Eqs. (10) and (11) its effect needs to be added in the resonant length equation of TM<sub>20</sub> mode, the same is reflected from Eq. (10). The frequencies calculated for the increasing stub length using Eq. (11) shows close prediction with the simulated result with increasing total stub lengths, as shown in Fig. 4c.

$$L_{\text{eff}20\text{stub}} = L_t + 2(\Delta L) + L_1 + L_2 \quad (10)$$

$$f_{20} = \frac{c}{[(L_{\text{eff}20\text{stub}}) \times (\sqrt{\epsilon_{\text{re}}})]} \quad (11)$$

Now based on these resonant length formulations, redesigning methodology is proposed. As the Y-shape configuration usages air suspended substrate, the ‘ $\epsilon_{\text{re}}$ ’ wants to be considered. Now value of air gap ‘ $h_a$ ’ is not known, hence for preliminary calculation, ‘ $\epsilon_{\text{re}}$ ’ is presumed to be 1.06. For redesigning band start frequency is considered as frequency at which the configuration is to be designed. From the reported optimized configuration [10] fundamental frequency TM<sub>10</sub> is expressed as  $f_{10} = 1.02$  band start frequency. For the specified fundamental TM<sub>10</sub> mode frequency, the ‘ $\lambda_g$ ’ is considered by means of Eq. (6). With regard to the optimized design

given in [10], the total substrate thickness ' $h_t$ ' = ( $h_a$  +  $h$ ) for redesigning is taken as  $0.09\lambda_g$ . Next, the actual attainable value of ' $h_a$ ' is selected, and via this value, ' $\epsilon_{re}$ ' and ' $\lambda_g$ ' are again re-calculated using Eqs. (5) and (6). Via the new value of ' $\epsilon_{re}$ ', ' $h_t$ ', ' $h_a$ ' is re-calculated. It is clear that value of practically realizable ' $h_a$ ', slightly varies concerning the previous calculated value. Henceforth the preliminary calculated value of the ' $h_a$ ' is maintained. Then, a new value of ' $\epsilon_{re}$ ' is used for frequency calculations of the respective modes, using Eqs. (7) and (8). For calculating the dimensions of the redesigned Y-shape MSA, the physical length ' $L_p$ ' is calculated for  $TM_{10}$  mode using Eq. (12). As per the resonant length shown in Fig. 4a, length ' $L_p$ ' is stated in terms of the basic Y-shape patch dimensions as per Eq. (13). Now from the reported configuration patch width ' $W$ ' =  $W = 0.380L$ ,  $w_{s2}/W = 0.394$ ,  $w_{s1}/L = 0.15$  are consider. By substituting this in ' $L_p$ ' equation, patch length is expressed as  $L = 0.812L_p$ . These dimensions complete the Y-shape structure. Now the stub is connected at the middle of patch, while its stub width is expressed as  $w = 0.394 W$  from the optimized reported configuration [10].

$$L_p = \frac{c}{[(2 \times f_{10}) \times (\sqrt{\epsilon_{re}})]} - 2(0.6\Delta L) \quad (12)$$

$$L_p = \left[ W - \frac{w_{s2}}{2} \right] + [L - w_{s1}/2] \quad (13)$$

Now from the given parametric in [10], stub length variation ' $L_1$ ' and ' $L_2$ ' is affecting  $TM_{20}$  mode. For the specified stub length, optimum wideband response with dual polarization is realized for ' $TM_{20}/TM_{10}$ ' of 1.18 and aspect ratio ' $w_s/L_1 + L_2$ ' of 0.230, Using the Eqs. (1)–(11), the  $f_{10}$  and  $f_{20}$ , mode frequencies against changing stub lengths are calculated and the ratio plots for the same are as revealed in Fig. 4d. The 'stub' length is noted that realizes the desired frequency and aspect ratio. Now from reported optimized configuration vertical stub length ' $L_1$ ' =  $0.353(L_1 + L_2)$  and horizontal stub length ' $L_2$ ' =  $0.656(L_1 + L_2)$ , using this relation then total stub length is divided into vertical and horizontal length respectively. For the antenna feeding, a proximity strip of length ' $L_s$ ' =  $0.07\lambda_g$ , is kept at the substrate thickness ' $h_s$ '. The position of this strip for optimized configuration is at ' $x_f, y_f$ ' =  $0.013 \lambda_g, 0.058 \lambda_g$ . Using this methodology, the Y-shape configuration is redesigned for 1500 MHz frequency. This is simulated and tested in antenna lab. Various calculated parameters are as given in Table 1. The  $S_{11}$  and gain plots for the redesigned configuration are as revealed in Fig. 5a. Fabricated MSA for the same is as revealed in Fig. 5b

### 3 Conclusions

A compact design of a reported Y-shape MSA for wideband response with dual polarization is discussed. By observing surface current variations of the mode  $TM_{10}$  and  $TM_{20}$  respectively resonant length formulations are derived. The frequencies

**Table 1** Different parameters for the re-designed Y-shape MSA

Antenna parameters	$f_{\text{band start}} = 1500 \text{ MHz}$	
$f_{10}$	1530 MHz	
$(h_a + h)$	1.76 cm	
$(L, W)$	(6.0, 2.3) cm	
$w_{s1} = w_{s2} = w$	0.9 cm	
Stub position	3.0 cm	
$L_s$	1.3 cm	
$(x_f, y_f)$	(0.24, 1.1) cm	
$(L_1, L_2)$	(1.45, 2.45) cm	
	<b>Simu</b>	<b>Meas</b>
BW (MHz, %)	398 (24)	400 (25)
Gain (dBi)	5.5	5.0

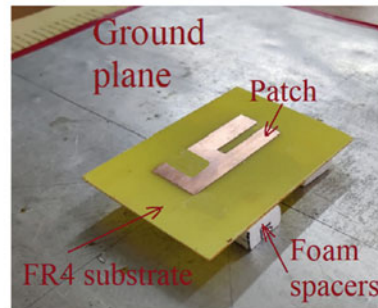
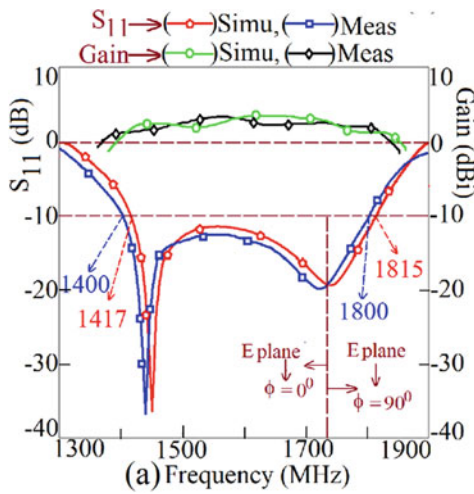


**Fig. 5** **a**  $S_{11}$  and gain plots, and **b** fabricated prototype for Y-shape MSA redesigned at 1500 MHz

calculated using those formulations shows marginal variations with respect to the simulated values. Based on the formulation, redesigned methodology is proposed. The similar Y-shape MSAs designed at different frequencies using those methodology shows similar dual polarized wideband characteristics yielding impedance BW more than 300 MHz (>20%) and broadside gain more than 4.5 dBi.



## References

1. Garg R, Bhartia P et al (2001) *Microstrip antenna design handbook*, 1st edn. Artech House
2. Bahal IJ, Bhatia B (1980) *Microstrip antenna*, 1st edn. Artec House
3. Kumar G, Ray KP (2003) *Broadband microstrip antennas*, 1st edn. Artech House, USA
4. Wong KL (2002) *Compact and broadband microstrip antennas*. Wiley, New York
5. Row J-S, Yeh SH, Wong KL (2004) Compact dual-polarized microstrip antennas. *Microw Opt Technol Lett* 27(4):284–287
6. Lam KY, Luk KM, Lee KF, Wong H, Ng KB (2011) Small circularly polarized u-slot wideband patch antenna. *IEEE Antennas Wireless Propagat Lett* 10:87–90
7. Wong K-L, Hao CT, Tzung WC (2002) Broadband dual-polarized aperture-coupled patch antennas with modified H-shaped coupling slots. *IEEE Trans Antennas Propagat* 50:188–191
8. Wong K-L, Chiou TW (2002) Broadband dual-polarized patch antennas fed by capacitively coupled feed and slot-coupled feed. *IEEE Trans Antennas Propagat* 50(3):346–351
9. Deshmukh AA, Pawar S, Ray KP (2017) Multi-band configurations of L-shape and F-shape microstrip antennas. In: *Proceedings of ICCUBE—2017, 17th–18th December, 2017*
10. Deshmukh AA, Pawar S, Ambekar AG, Kamble P, Ray KP (2017) Compact Y-shape antenna for dual polarized wideband response. In: *IEEE applied electromagnetics conference (AEMC), Aurangabad*, pp 1–2
11. CST Microwave Studio, Version 2019

# A Single Port Dual-Polarized Microstrip-Slot Antenna System for 5G Mid-Band Frequencies



B. M. S. Sreenivasa Rao and B. Rajasekar

**Abstract** This study investigates a single port dual-polarized slot antenna used for 5G indoor wireless access points. It is described as one element or one port dual-polarized circular ring slot radiators fed by microstrip line architectures. These are the radiation elements that are meant to operate at 5G mobile phone frequencies ranging from 2.6 to 9.0 GHz. Each circular ring slot radiator is mounted with a pair of parasite ring/open-ended structures to improve the isolation and minimize the mutual interconnection between the additional ports of the dual-polarized. Despite being built on a high-loss FR-4 dielectric, this single port dual-polarized slot antenna has acceptable S-parameters, high-gain radiation patterns, and adequate overall efficiencies. This antenna has strong characteristics and can be used in 5G mid-band frequencies.

**Keywords** Dual-polarized · MIMO system · Circular ring slot antenna

## 1 Introduction

Wireless communication system has experienced a dramatic development over the recent years, with expanding users and higher data rates. Antennas, as a critical part of any wireless communication system, have also undergone tremendous evolvement. Compared with the base station antennas, antennas in the mobile terminals experienced more evolution, from external antennas to internal antennas, from single-band antennas to multiband antennas, from single antennas to MIMO antennas from

---

B. M. S. Sreenivasa Rao (✉)

Sathyabama Institute of Science and Technology, Chennai, India

Department of Electronics and Communication Engineering, GMR Institute of Technology, Rajam, Srikakulam Dist., Andhra Pradesh, India

B. Rajasekar

Department of Electronics & Communication Engineering, Sathyabama Institute of Science and Technology, Chennai, Tamil Nadu, India

low frequencies to millimeter-wave frequencies [1]. In addition, some related technologies emerged recently such as MIMO, massive MIMO, and millimeter wave antennas. An antenna is necessary in a wireless system to transmit or receive EMW (electromagnetic wave) [2]. The antenna is a critical component of it. In wireless communication, the antenna is a device that connects the transmitter and reception sections. At the transmitter part, the antenna takes electric power and transforms it into a radio wave, that it finally emits into free space. Nowadays, wireless gadgets must be compact, modest in size, easy to install, and lightweight [3–5]. We require a low-profile antenna for this reason.

Multiple-input-multiple-output (MIMO) systems are one of the key technologies that can improve data throughput in 5G networks. Multiple-input multiple-output (MIMO) technology has remained a topic of attention over the last two decades due to its capacity to cope with increased wireless data traffic and enhance wireless system reliability [6–10]. MIMO wireless technology may greatly improve the data rate, capacity, and connection dependability of wireless systems by using multi-path data transmission and reception. MIMO is a method that is presently utilized in 4G user equipment and might be employed in future 5G mobile terminals [11, 12].

## 2 Methodology

Microwave antennas are often single polarized or dual-polarized. We constructed a dual-polarized MIMO antenna in this article. A single polarized antenna reacts to only one polarization orientation, either horizontal or vertical. Thus, either a horizontal or a vertical polarized radio wave is received or sent by a single polarized antenna. Whereas a dual-polarized antenna may concurrently react to radio waves both vertically and horizontally polarized. This enhances the traffic handling capability of the system through the utilization of both polarizations. One transmitter/receiver pair, for example, can be set to vertical polarization, while a second independent transmitter/receiver pair can be set to horizontal polarization.

Slot antennas got evolved into particularly fascinating wireless systems candidates. It has many interesting properties such as simple construction, broad bandwidth impedance, excellent isolation, easy integration in active systems, and so on. While cutting a lot in the bottom layer of the antenna allows it to radiate on both sides of the substrate, the slot antenna is an excellent choice for developing dual-polarized antennas for use in wireless communication platforms. In addition, it is far easier than other conventional antennas to achieve a dual-polarized feature for the microstrip-line feeding slot-antenna (such as Dipole, Monopole, Yagi, and so on). A compact square-ring slot antenna is fed by rectangular microstrip lines in the dual-polarized slot antenna element's design. Moreover, a couple of parasites in the circular ring/open end were used throughout the ring slot to decrease the typical mutual coupling between two ports for microstrip feeding. The ring-slot radiators for

**Table 1** MIMO slot antenna tables

The outer circle	Radius-3.75 mm	$R_1$
The inner circle	Radius-3 mm	$R_2$
Outer circle	Radius-7 mm	$r_1$
Inner circle	Radius-6 mm	$r_2$
Length	11 mm	L
Width	3 mm	W

the planned 5G antenna are located at four edges of the PCB to offer complete radiation coverage via various polarizations. For MIMO applications the single element and antenna array suggested have good feature.

### 3 Analysis of Single Port Parameters

The low profile antenna of the  $WS \times WS$  is built with a FR4 dielectric with 4.4 relative permittivity, 0.025 loss tangent and 1.6 mm thickness. The single-element antenna's parameter are specified in Table 1 below and the proposed circular ring antenna top view, bottom view, HFSS top view and HFSS bottom view are shown in Fig. 1a–d.

### 4 Simulation Results for Proposed Antenna

HFSS software is used to calculate the results of the conventional and modified antennas. The frequency range for conventional antennas is configured at 3–10 GHz. The antenna's parameters include return loss ( $S_{11}$ ), VSWR, and gain. The fabricated antenna top view and bottom view are shown in Fig. 2a, b.

#### 4.1 $S_{11}$ Parameter Characteristics for Modified Circular Slot Antenna (40 mm \* 40 mm)

The S-parameter plot in Fig. 3 depicts the change of return loss (in dB) over a frequency range. Because the antenna has the optimum impedance matching at resonance, the return loss is low. The antenna's peak frequencies are 3.78, 5.38, and 8.8 GHz.

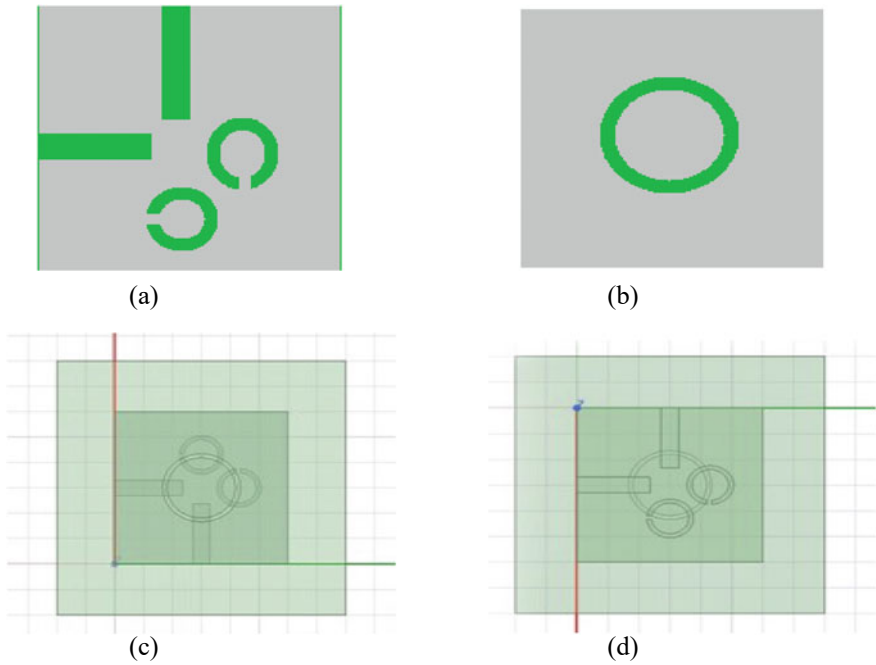


**Fig. 1** The proposed circular ring antenna **a** the top view and **b** the bottom view **c** HFSS top view and **d** HFSS bottom view



**Fig. 2** Fabricated antenna **a** top view and **b** bottom view

#### **4.2** *VSWR for Modified MIMO Slot Antenna (40 mm \* 40 mm)*

The VSWR describes the power reflected from the antenna. The better the antenna's match to the feedline and the more power delivered to the antenna, the lower the VSWR. The VSWR describes the power reflected from the antenna. The better the

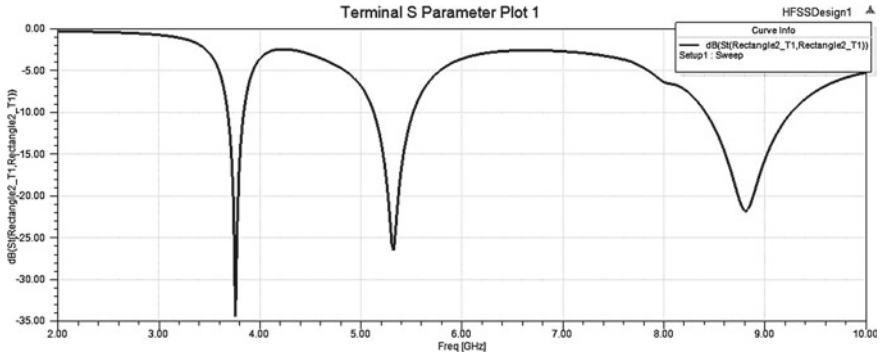


Fig. 3 S-parameter result of circular slot antenna

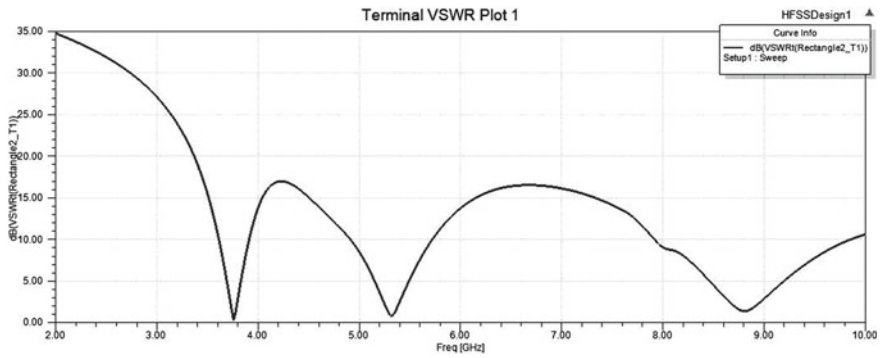


Fig. 4 VSWR of a circular antenna result

antenna’s match to the feedline and the more power delivered to the antenna, the lower the VSWR (Fig. 4).

### 4.3 Gain for Modified Circular Slot Antenna (40 mm \* 40 mm)

The gain of an antenna defines how efficiently it converts input power to radio waves in a certain direction. The gain of the modified antenna is shown at different frequencies. The gain is found  $-10$  dB at a frequency of 1.11 GHz (Fig. 5).

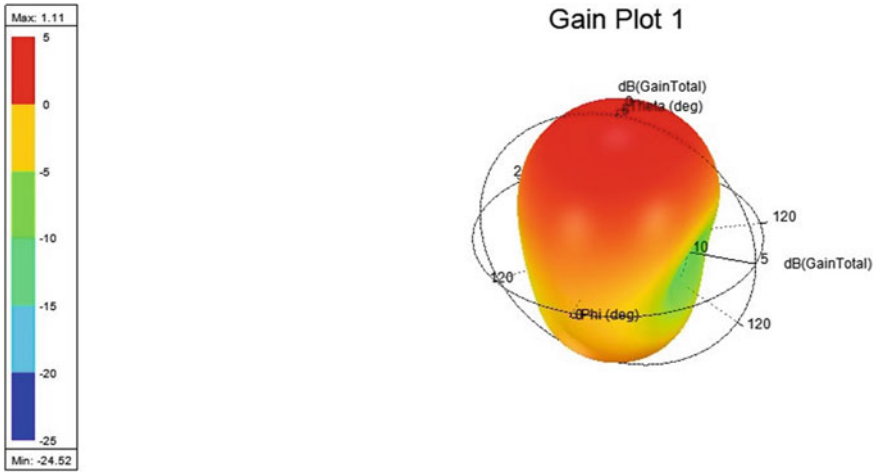


Fig. 5 Gain of modified circular slot antenna

#### 4.4 Directivity for Modified Circular Slot Antenna (40 mm \* 40 mm)

The gain of an antenna refers to how efficiently it transforms input power into radio waves in a certain direction. The gain of the modified antenna is shown at different frequencies. The gain is found  $-10$  dB at a frequency of 2.68 GHz (Fig. 6).

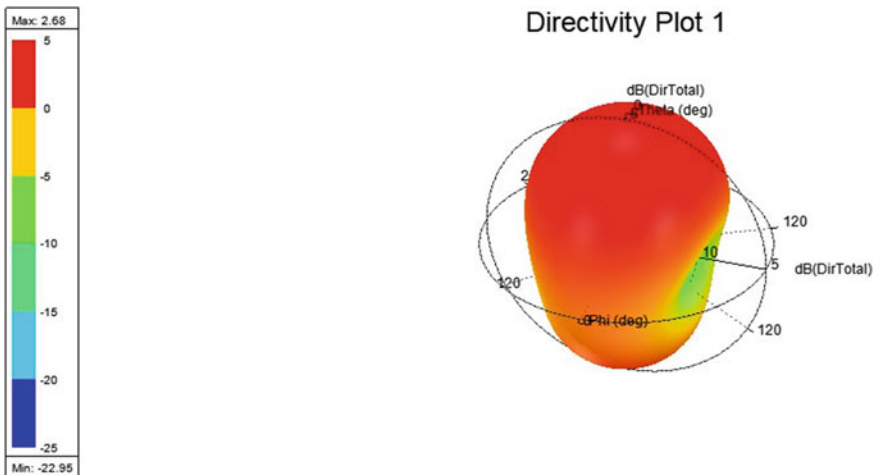


Fig. 6 Directivity of modified MIMO circular slot antenna

## 5 Conclusion

For 5G MIMO mobile terminals, a new low-coupling slot antenna array design has been proposed. The proposed MIMO antenna structure is as follows: a dual-polarizing circular ring slot antenna placed on the smartphone's edge. A pair of circular ring constructions nearby was utilized to link the antenna components. The center frequency of the circular ring slot antenna can be seen as 3.78, 5.38, 8.8 GHz.

## References

1. Kammoun A, Debbah M, Alouini MS (2017) Design of 5G full dimension massive MIMO systems. *IEEE Trans Commun* 66(2):726–740
2. Osseiran A, Boccardi F, Braun V, Kusume K, Marsch P, Maternia M, Fallgren M (2014) Scenarios for 5G mobile and wireless communications. In: The vision of the METIS project. *IEEE Commun Mag* 52(5):26–35
3. Statement: Improving consumer access to mobile services at 3.6 GHz to 3.8 GHz. [Online]. <https://www.ofcom.org.uk/consultations-and-statements/category1/future-use-at-3.6-3.8-GHz>. Accessed 21 Oct 2018
4. Yang HH, Quek TQ (2017) Massive MIMO meets small cell. In: Backhaul and cooperation. Springer International Publishing
5. Qin Z, Geyi W, Zhang M, Wang J (2016) Printed eight-element MIMO system for compact and thin 5G mobile handset. *Electron Lett* 52(6):416–418
6. Li Y, Zou H, Wang M, Peng M, Yang G (2018) Eight-element MIMO antenna array for 5G/Sub-6GHz indoor micro wireless access points. In: 2018 International workshop on antenna technology (iWAT). IEEE, pp 1–4
7. Hussain R, Alreshaid AT, Podilchak SK, Sharawi MS (2017) Compact 4G MIMO antenna integrated with a 5G array for current and future mobile handsets. *IET Microw Antennas Propag* 11(2):271–279
8. Al-Hadi AA, Ilvonen J, Valkonen R, Viikari V (2014) Eight-element antenna array for diversity and MIMO mobile terminal in LTE 3500 MHz band. *Microw Opt Technol Lett* 56(6):1323–1327
9. Wong KL, Lu JY, Chen LY, Li WY, Ban YL, Li C (2015) 16-antenna array in the smartphone for the 3.5-GHz MIMO operation. In: 2015 Asia-Pacific microwave conference (APMC), vol 1. IEEE, pp 1–3
10. Sun L, Feng H, Li Y, Zhang Z (2018) Compact 5G MIMO mobile phone antennas with tightly arranged orthogonal-mode pairs. *IEEE Trans Antennas Propag* 66(11):6364–6369
11. Li Y, Luo Y, Yang G (2018) Multiband 10-antenna array for sub-6 GHz MIMO applications in 5-G smartphones. *IEEE Access* 6:28041–28053
12. Wong KL, Tsai CY, Lu JY (2017) Two asymmetrically mirrored gap-coupled loop antennas as a compact building block for eight-antenna MIMO array in the future smartphone. *IEEE Trans Antennas Propag* 65(4):1765–1778



# Gap-Coupled Microstrip Antenna Backed by Rectangular Slots Cut Ground Plane for Enhanced Bandwidth



Poonam A. Kadam and Amit A. Deshmukh

**Abstract** A novel gap-coupled rectangular microstrip antenna backed by rectangular slots cut ground plane is proposed. The slots are placed on the ground plane below each of the fed and parasitic patches such that the  $TM_{30}$  ground mode frequency of the antenna is altered, thereby giving a wideband response. The proposed antenna yields larger bandwidth and comparable gain value with reference to the conventional un-slotted gap-coupled antenna operating at the same frequency. The impedance bandwidth of 365 MHz (12.84%), the peak gain of 6 dBi, is achieved. Thus, the proposed gap-coupled design offers 47% bandwidth improvement as compared to the gap-coupled design with the normal ground plane.

**Keywords** Broadband microstrip antenna · Defected ground plane · Ground plane mode · Multi-resonator structure

## 1 Introduction

Numerous methods have been devised to enhance the impedance bandwidth (BW) of a conventional microstrip antenna (MSA). The use of thicker substrate having low dielectric constant being the most traditional way to improve the impedance BW and gain of MSA [1–4]. This can also be achieved by employing suspended MSA structures, where the overall thickness of the antenna is increased [5, 6]. However, it is difficult to achieve impedance matching over wide frequency range due to thicker substrate. By etching the slots on the radiating patch impedance BW can be increased [7–11]. Also, by etching slots on both the patch and the ground plane [12–15], the antenna BW can be enhanced significantly. Although reasonable BW enhancement is observed, the achievable gains for these designs are low. An improvement in the BW and gain in MSA can be obtained by employing multi-resonator concept. Here, the parasitic patches are laterally gap-coupled with the fed patch [16–20]. This simple well-known multi-resonator technique can yield impedance BW as large as

---

P. A. Kadam · A. A. Deshmukh (✉)  
SVKM's EXTC Department, DJSCE, Mumbai, India

five times that of a single patch with an improved gain. Further improvement in the BW is achieved by employing slot cuts on the ground plane of the gap-coupled MSA as proposed in the present paper. The ground slot optimally places the higher order ground mode frequency closer to the fundamental mode frequency of the MSA to realize a wider BW response.

In this paper, a rectangular gap-coupled MSA (RMSA) backed by rectangular slot cut ground plane is proposed on thinner Taconic substrate ( $\epsilon_r = 3$ ,  $\tan \delta = 0.002$ ,  $h = 1.6$ ). The gap-coupled configuration yields 192 MHz (6.2%) impedance BW. To further enhance the BW thin rectangular slots are present under each resonator in the offset position. The slot perturbs the surface current distribution on the patch and yields impedance matching at higher order  $TM_{30}$  ground mode frequency. The slots introduced in the ground plane tune the fundamental mode resonance frequency of the fed and parasitic patches along with  $TM_{30}$  mode together and optimal spacing between thereby yields the BW enhancement. The proposed defected ground gap-coupled MSA yields BW of 365 MHz (12.84%) with a peak gain of 6 dBi. Across the wider BW, the antenna yields a broadside radiation pattern. The proposed antenna is studied initially using CST software [21]. The MSA is fed using an SMA connector of an inner probe radius 0.6 mm. In the measurement, R & S high-frequency instruments namely, ZVH 8, FSC 6, and SMB 100A were used. A reference horn antenna is used in the pattern and gain measurement which is carried out inside the Antenna lab. The broadside gain is measured using the three antenna method. A good agreement is obtained between the simulated and measured results. All the patch dimensions and frequencies referred in this paper are in ‘mm’ and MHz, respectively.

## 2 Gap-Coupled RMSA Backed by Slot Cut Ground Plane

The gap-coupled RMSA coupled along the radiating edges backed by the rectangular slot cut ground plane is shown in Fig. 1a. The conventional radiating edge coupled RMSA is designed to operate at a  $TM_{10}$  mode frequency of 3000 MHz. The antenna is optimized for the BW, by means of parametric optimization. Various antenna dimensions in the optimized gap-coupled RMSA are, ‘L’ = 30, ‘W’ = 40, ‘L<sub>1</sub>’ = 29, ‘s’ = 0.5, ‘L<sub>g</sub>’ = 110, ‘W<sub>g</sub>’ = 60 and ‘x<sub>f</sub>’ = 10 mm. The gap-coupled antenna yields a simulated BW of 192 MHz (6.7%) as against 66 MHz (2.3%) of BW in the single patch designed at the same operating frequency. Due to the symmetrical parasitic patches placed along both the radiating edges of the fed RMSA, the symmetrical broadside radiation pattern is obtained. Further, modifications are made in the antenna structure by incorporating the slots on the ground plane, to realize broader impedance BW. A thin vertically aligned open-ended rectangular slots of dimension ‘t’ × ‘w<sub>s</sub>’ are introduced on the ground plane under the center position of each resonator. The slots are aligned along the width of the patch in an orthogonal direction to the current path at  $TM_{10}$  mode frequency of both the fed and parasitic RMSAs. Thus, because of the slot, the current path length at the fundamental mode frequency is elongated as shown in Fig. 1b, resulting in the reduction in the center frequency of all the patches.

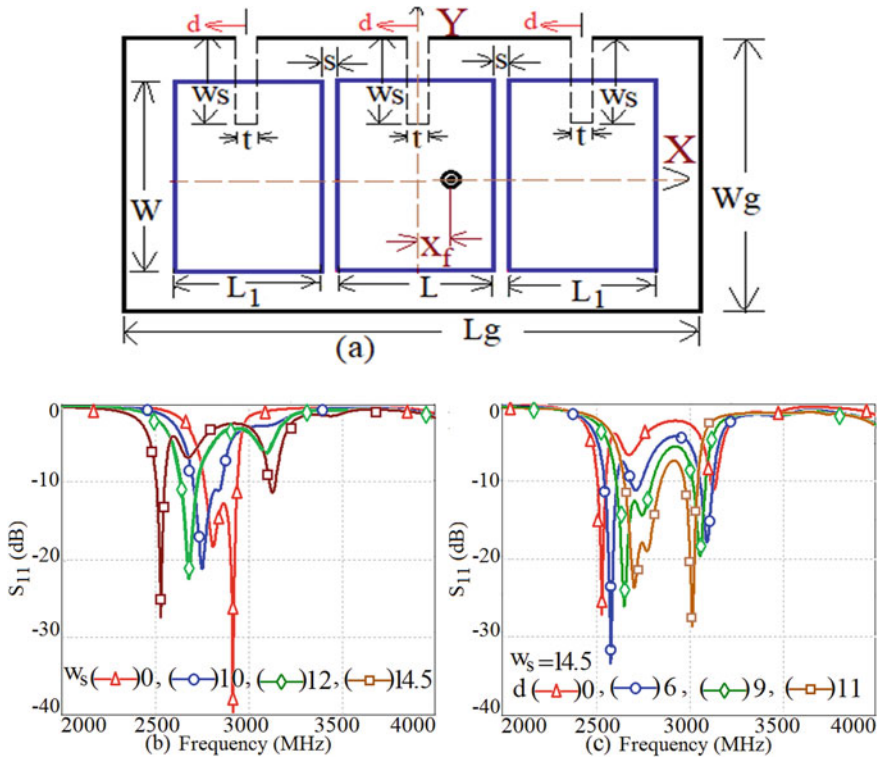


**Fig. 1** a Gap-coupled design of RMSAs along radiating edges backed by slot cut ground plane, its b reflection coefficient ( $S_{11}$ ) plot against slot length ' $w_s$ ' c reflection coefficient ( $S_{11}$ ) plot against slot offset position ' $d$ '

For each slot width ' $w_s$ ' increment, input impedance variation over all the patches alters that requires optimization of the feed point location ' $x_f$ ' nearer to the slot. For ' $t = 2$  mm and for each slot width increment, gap-coupled MSA is optimized for the BW as shown in Fig. 1c. With an increase in slot length ' $w_s$ ', as the  $TM_{10}$  mode frequency on the fed and parasitic patch decreases, the center frequency of the realized BW reduces as shown in Fig. 1c. At  $w_s = 10$  mm a new mode is observed. The resonance for  $w_s = 10$  mm is shown in Fig. 2a. Three resonant peaks can be viewed in the resonance plot at 2714 MHz, 2853 MHz and 3150 MHz frequency. The surface current distribution on the patch at these frequencies is shown in Fig. 2b–d. The surface current distribution at the first two modes shows one half-wavelength variation along the patch and no variation along the patch width. Thus, first and the second mode corresponds to  $TM_{10}$  fed patch mode ( $TM_{10fp}$ ) and  $TM_{10}$  parasitic patch mode ( $TM_{10pp}$ ), respectively. The current distribution at 3150 MHz frequency on the patch and the ground plane is depicted in Fig. 2d, e.

The current distribution at this mode shows one half wave variation along the patch length and three half wavelength variation along the ground plane. In order

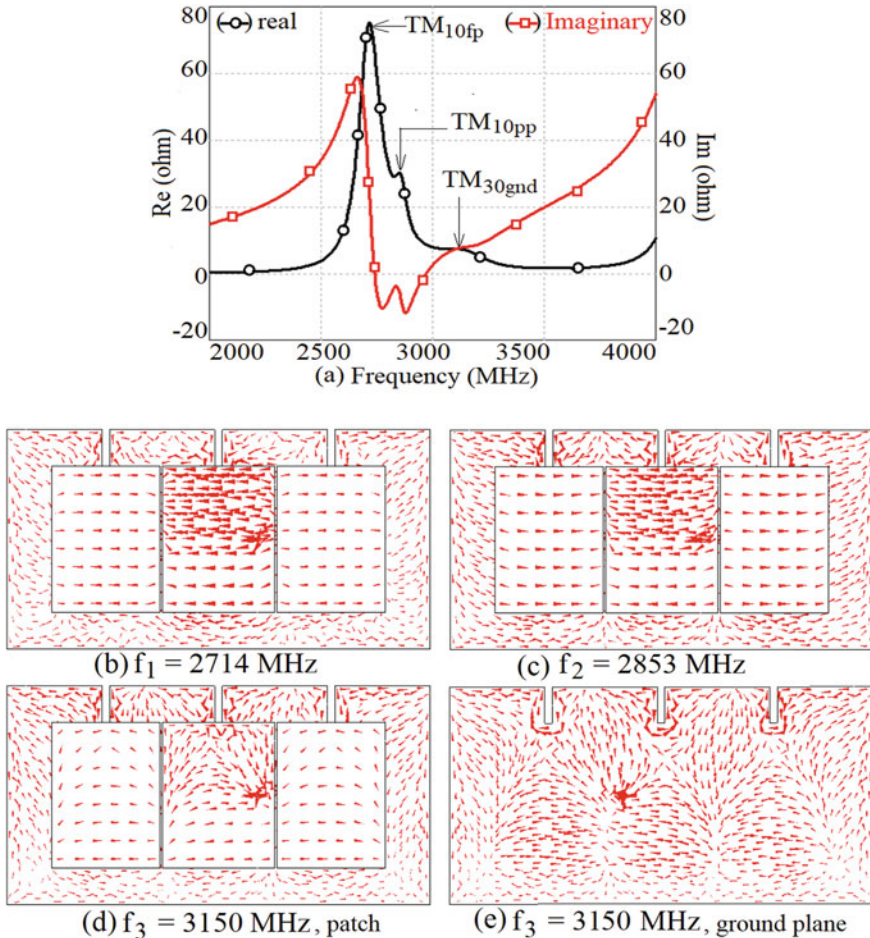


**Fig. 2** Resonance plot of gap-coupled MSA for  $w_s = 10$  mm and its **a** current distribution seen on **b** patch at  $f_1 = 2714$  MHz, **c** patch at  $f_2 = 2853$  MHz, **d** patch at  $f_3 = 3150$  MHz, **e** ground plane at  $f_3 = 3150$  MHz

to understand the third mode, ground plane is simulated as patch and vice versa in presence of ground slots of length  $w_s = 10$  mm. The current distribution observed at the three peaks are shown in Fig. 3a–c. As seen in Fig. 3c current distribution at 3150 MHz frequency shows three half wavelength current variation along patch length and no variation along patch width. When current distribution at this mode (Fig. 3c) is compared with newly excited mode in proposed configuration (Fig. 2e), both current distribution resembled completely with complimentary current directions. Thus, it ensures that newly excited mode in proposed DGS MSA configuration is ground mode and its current distribution indicates  $TM_{30}$  ground mode ( $TM_{30g}$ ). So, the three resonant modes responsible for achieving wide band response are  $TM_{10}$

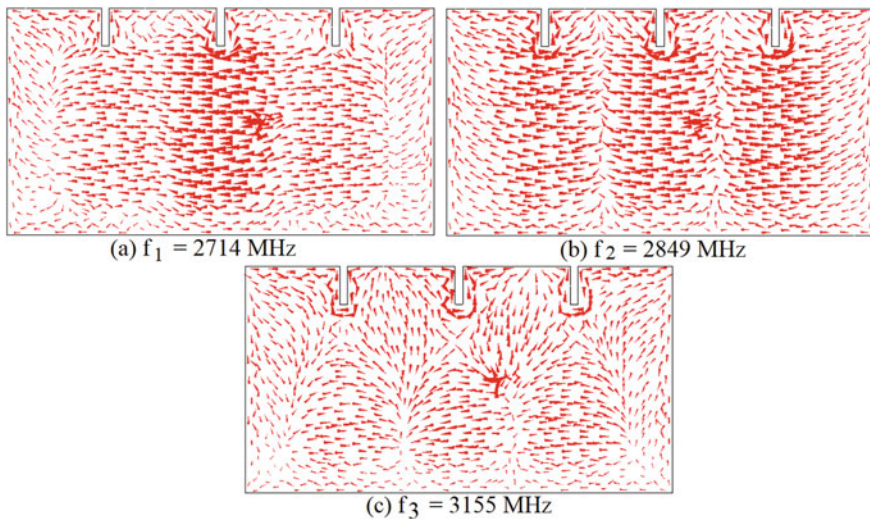


**Fig. 3** a Current distribution of gap-coupled MSA with ground dimension taken as patch size and vice versa at **a**  $f_1 = 2714$  MHz, **b**  $f_2 = 2849$  MHz, **c**  $f_3 = 3155$  MHz

fed and parasitic patch mode,  $TM_{30}$  ground mode frequencies. The slots are further shifted away from the center position, which results in altering the current distribution and impedance at  $TM_{30}$  ground mode frequency of the antenna. The parametric study of variation in the slot position with respect to the center position is depicted in Fig. 1c. With increase shift in the slot position, the resonance frequency at  $TM_{10}$  mode increases, while the  $TM_{30}$  ground mode frequency reduces. The increase in  $TM_{10}$  mode frequency is because the slot is shifted to minimum current position. Whereas, with respect to  $TM_{30}$  ground mode, the slots are shifted to maximum current position.

The optimum spacing between the  $TM_{10}$  mode and  $TM_{30}$  ground mode frequencies results in broader BW. The feed point is shifted at ' $x_f$ ' = 13 mm to match 50  $\Omega$  impedance. Thus, for RMSAs gap-coupled along the radiating edges, optimum result is obtained for ' $w_s$ ' = 14 mm and antenna parameters in the optimum configuration are, ' $L$ ' = 30, ' $W$ ' = 40, ' $L_1$ ' = 29, ' $w_s$ ' = 14.5, ' $t$ ' = 2, ' $s$ ' = 1.5, ' $d$ ' = 11, ' $x_f$ ' = 13 mm. The simulated and measured impedance BW is 336 MHz (11.8%) and 365 MHz (12.84%), respectively as shown in Fig. 4a. The simulated and measured peak broadside gain over the BW is above 6 dBi. The radiation pattern at the center frequency as shown in Fig. 4b, is in broadside direction with E and H planes aligned along  $\Phi = 0^\circ$  and  $90^\circ$ , respectively.

Further, the performance of the optimum design is compared against the reported wideband variations as presented in Table 1. In Table 1, ' $\lambda_c$ ' is the wavelength at the center frequency of the realized BW. In [7–11], BW enhancement using the resonant slots on the radiating patches has been reported. However, the slot cut technique is a complex technique to design as compared to simpler gap-coupled designs. The configurations reported in [12–15], have slots on both the patch and

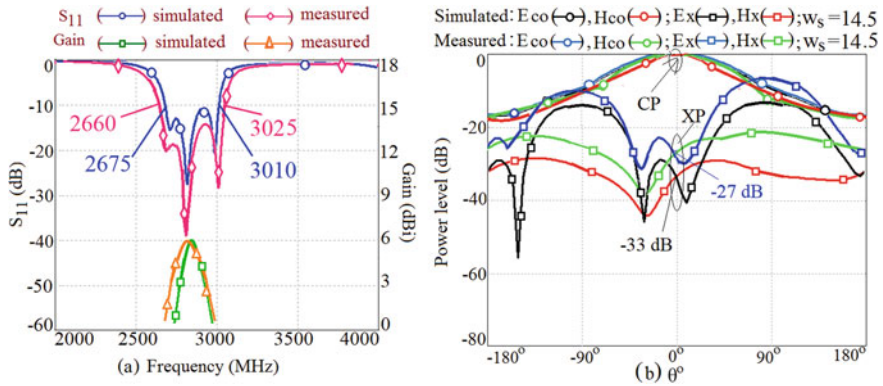


**Fig. 4** **a** Simulated and measured  $S_{11}$  plots, **b** radiation pattern at the center frequency of the BW of the fabricated prototype, for ' $w_s$ ' = 14.5 mm, ' $d$ ' = 11 mm, ' $s$ ' = 1.5 mm, ' $x_f$ ' = 14 mm (optimum design)

**Table 1** Comparison of proposed gap-coupled MSAs against reported wideband MSAs

Antenna structure Shown in	Meas. BW, % (MHz, %)	Gain (dBi)	$h/\lambda_c$
Figure 1a	365, 12.84	6.0	0.013
Ref. [5]	247, 12.1	8.9	0.06
Ref. [6]	260, 13	7	0.03
Ref. [7]	730, 30	7	0.08
Ref. [8]	3150, 55	10	0.12
Ref. [9]	874,23	–	0.2
Ref. [10]	3600, 44	4.7	0.13
Ref. [11]	860, 47	2.5	0.01
Ref. [12]	5760, 99	3.6	0.038
Ref. [13]	6500, 84.96	4.1	0.06
Ref. [14]	7700, 110	5.1	0.07
Ref. [15]	2470, 39	4.5	0.06
Ref. [16]	52, 5	–	0.006
Ref. [17]	225, 6.9	–	0.028
Ref. [18]	225, 7.2	–	0.026
Ref. [20]	350, 6.8	7	0.043

the ground plane which yields wider BW but the achievable gain in those designs is not higher. Moreover, none of the work provides any explanation for the resonant modes involved in the modified ground plane design that yield wider BW. For the gap-coupled designs as reported in [16–20], the BW and gain obtained is smaller than the proposed gap-coupled RMSA.

Thus, the present paper attempts to improve the BW further with respect to simple gap-coupled structure. By employing the DGS structure, the BW of gap-coupled antennas is substantially increased.

### 3 Conclusions

Novel gap-coupled RMSA employing a modified ground plane is proposed. The slot cut on the ground plane reduces  $TM_{30}$  ground mode frequency and brings it closer to the fundamental mode frequencies of the fed and parasitic patches and thus, yields broader BW. The proposed gap-coupled RMSA offers optimum BW of 12.84% and 6 dBi gain. The above results are obtained on thinner Taconic substrate ( $h < 0.02 \lambda_c$ ). Thus, the proposed work discusses a simpler gap-coupled technique on defected ground plane for BW enhancement.

### References

1. Kumar G, Ray KP (2003) Broadband microstrip antenna. Artech House, USA
2. Wong K (2002) Compact and broadband microstrip antenna. Wiley
3. Garg R, Bhartia P, Bahl I, Ittipiboon A (2001) Microstrip antenna design handbook. Artech House, USA
4. Guha D, Antar YM (2011) Microstrip and printed antennas-new trends, techniques and applications. Wiley
5. Wong K, Tang C, Chiou J (2002) Broadband probe-fed patch antenna with a W-shaped ground plane. *IEEE Trans Antenna Propag* 50:827–829
6. Liu N, Zhu L, Choi W (2017) A differential-fed microstrip patch antenna with bandwidth enhancement under operation of  $TM_{10}$  and  $TM_{30}$  modes. *IEEE Trans Antennas Propag* 65:1607–1614
7. Khodaei GF, Nourinia J, Ghobadi C (2008) A practical miniaturized U-slot patch antenna with enhanced bandwidth. *Progress Electromagn Res B* 3:47–62
8. Sharma SK, Shafai L (2009) Performance of a novel  $\Psi$ -shaped microstrip patch antenna with wide bandwidth. *IEEE Antennas Wireless Propag Lett* 8:468–471
9. Khan M, Chatterjee D (2016) Characteristic mode analysis of a class of empirical design techniques for probe-fed, U-slot microstrip patch antennas. *IEEE Trans Antennas Propag* 64:2758–2770
10. Ghosh J, Roy J (2008) Design of wideband microstrip antenna. *J Electromagn Waves Appl* 22:2379–2389
11. Sze J (2000) Slotted rectangular microstrip antenna for bandwidth enhancement. *IEEE Trans Antennas Wave Propag* 48:1149–1152
12. Mondal K, Sarkar P (2015) M-shaped broadband microstrip patch antenna with modified ground plane. *Microwave Opt Technol Lett* 57:1308–1312
13. Mandal K, Sarkar P (2013) High gain wide-band U-shaped patch antennas with modified ground planes. *IEEE Trans Antennas Propag* 61:2279–2282
14. Baudha S, Yadav MV (2019) A novel design of a planar antenna with modified patch and defective ground plane for ultra-wideband applications. *Microwave Opt Technol Lett* 61:1320–1327

15. Anil KG, Aditi B, Binod KK (2016) A wideband antenna with defected ground plane for WLAN/WiMAX applications. *AEÜ-Int J Electron Commun Elsevier* 70:354–358
16. Anandan C, Mohanan K, Nair KG (1990) Broadband gap-coupled microstrip antenna. *IEEE Trans Antennas Propag* 38:1581–1586
17. Kumar G, Gupta KC (1984) Broadband Microstrip antenna using additional resonators gap-coupled to the radiating edges. *IEEE Trans Antenna Propag* 32:1375–1379
18. Kumar G, Gupta KC (1985) Non-radiating edges and Four edges gap-coupled multiple resonator broadband Microstrip antennas. *IEEE Trans Antennas Propag* 33:173–178
19. Kumar P, Singh G, Bhooshan S, Chakravarty T (2007) Gap-coupled microstrip antennas. International conference on computational intelligence and multimedia applications (ICCIMA 2007), Sivakasi, Tamil Nadu, pp 434–437
20. Yoo J, Son H (2020) A simple compact wideband microstrip antenna consisting of three staggered patches. *IEEE Antennas Wirel Propag Lett* 19:2038–2042
21. CST Microwave Studio, Version 2019



# Wideband and Circularly Polarized Variations of Sectoral Microstrip Antennas



Amit A. Deshmukh, Tushar Sawant, and Aarti G. Ambekar

**Abstract** Sectoral microstrip antenna is a variation of circular microstrip antenna and in the literature, various configurations of the same offering wideband, multi-band, and circular polarized response are reported. However, in many of those configurations, which are supposed to be functional at higher-order modes of the patch, the detailed explanation for the resonant modes present in the patch to achieve reported frequency characteristics is not discussed. This paper proposes a detailed study for the two of such Sectoral microstrip antenna designs. In the first design, stub-loaded variation of  $270^\circ$  Sectoral microstrip antenna is presented whereas in the second variation, shorted and slot cut variation of  $330^\circ$  Sectoral microstrip antenna is discussed. Using thinner substrate, in the stub loaded variation, wideband response due to the tuning of  $TM_{20}$  and  $TM_{02}$  modes is achieved thereby giving impedance bandwidth of 60 MHz (4.18%). In the shorted and slot cut design, circular polarized response due to the tuning in between  $TM_{1/2,0}$  and  $TM_{1/2,1}$  modes, thereby giving an axial ratio bandwidth of 11 MHz (1.8%) is achieved. The proposed designs are compact and low-profile ones since they are realized on a thinner and lossy substrate. The equivalents of the proposed Sectoral variations can find applications in WiFi and personal communication applications within a short distance range.

**Keywords** Sectoral microstrip antenna · Wideband microstrip antenna · Compact microstrip antenna · Circular Polarization · Rectangular stub · Shorting post · Rectangular Slot

## 1 Introduction

The microstrip antenna (MSA) finds many applications in modern-day wireless communication systems due to its many advantages [1]. With suitable modifications in the patch parameters like dielectric constant and substrate thickness and by employing parasitic patches or resonant slots, bandwidth (BW) of the MSA has been

---

A. A. Deshmukh (✉) · T. Sawant · A. G. Ambekar  
Department of EXTC, SVKM's DJSCE, Mumbai, India

increased [2–4]. Of these, the slot cut technique is widely used since it maintains the low-profile nature of the antenna. The wideband response in this slot cut or parasitic patch loaded MSAs is obtained around the fundamental patch mode frequency. The circular polarized (CP) response in MSA is obtained due to the close proximity of dual orthogonal resonant modes which satisfy the equal amplitude and phase orthogonality condition or realized due to the modified surface current distribution at given resonant mode that yields equal contribution of bi-directional current components. Thus, CP response in MSA has been realized using techniques like dual feeds, single feed designs employing narrow slots, unequal length resonant slots, or using modified patch shapes [2, 3, 5, 6]. Designs of shorted compact MSAs giving CP response are not widely reported. In the recent literature, various designs of Sectoral MSA employing additional stub or slot, for realizing wideband or CP response are reported [7–10]. The modal description for the resonant modes presented on the Sectoral patch is reported, however, that is complex in understanding as the boundary condition of the Sectoral patch for the resonant field distribution is not highlighted. Also, none of those reported papers for Sectoral MSA variations provide any design methodology.

In this paper, two variations of Sectoral MSA for wideband and CP response are proposed. In the first design, two stub loaded variation of  $270^\circ$  Sectoral MSA is presented. The placement of stub here tunes the spacing between  $TM_{20}$  and  $TM_{02}$  resonant modes of the modified patch that yields 60 MHz (4.18%) of impedance BW. The antenna yields a broadside pattern across the BW but shows lower gain, as the patches were fabricated on FR4 substrate ( $\epsilon_r = 4.3$ ,  $h = 0.16$  cm,  $\tan \delta = 0.02$ ). Thus, in this case wideband response is realized around the higher-order  $TM_{20}$  mode frequency of the Sectoral patch. Due to the modified surface current distribution as present on the Sectoral patch, the patch shows a broadside pattern despite operating around the second-order patch mode. Further compact shorted design of  $330^\circ$  Sectoral MSA is presented. The slot employed in this shorted patch tunes the spacing between first and second-order resonant modes of a shorted patch (i.e.  $TM_{1/2,0}$  and  $TM_{1/2,1}$ ) which yields axial ratio (AR) BW of 11 MHz (1.8%). The antenna yields a nearly omnidirectional pattern across the short and offers lower gain. This is attributed to the lossy substrate. For improving the gain, air-suspended variation of Sectoral MSAs can be designed, which will increase the gain as well as respective impedance and AR BW. Thus, as against the reported designs of Sectoral MSA, in this paper, a detailed discussion for the resonant modes of Sectoral patch is presented. The effects of selecting stub and slot with reference to the modal current distribution on each of the patches are discussed. The compact design of shorted Sectoral patch for CP response is presented. These are all the new technical contributions in the proposed study.

## 2 Sectoral MSA Loaded with Pair of Rectangular Stub

The design of stub-loaded  $270^\circ$  Sectoral MSA is shown in Fig. 1a. The patch is loaded with pair of the rectangular stub on its perimeter. The radius of  $270^\circ$  Sectoral MSA is

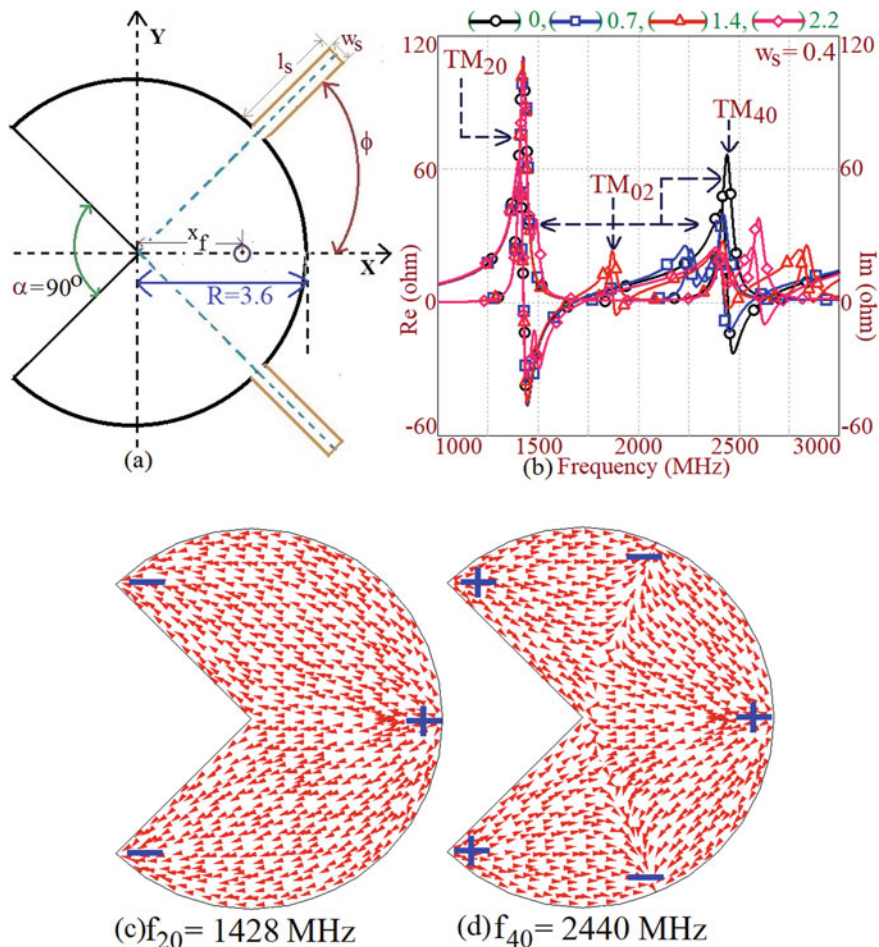


**Fig. 1** a Pair of stub loaded  $270^\circ$  Sectoral MSA, its b resonance curve plots for varying ' $l_s$ ', and its c, d surface current distribution at observed resonant modes for ' $l_s$ ' = 0 cm

selected such that it resonates in its second-order  $TM_{20}$  mode around the frequency of 1500 MHz. For calculating the radius for this frequency, the patch perimeter is equated to the wavelength variation. The Sectoral patch is simulated using CST software [11] and its resonance curve plot is shown in Fig. 1b. The plot shows two peaks and the current distribution at them is shown in Fig. 1c, d. As mentioned above, the first mode corresponds to  $TM_{20}$  mode showing two half-wavelength variations along the patch perimeter, whereas the second peak corresponds to  $TM_{40}$  mode. Here in a Sectoral patch, modal identification is done by observing the surface current distributions along the patch perimeter and radius. Thus, for  $TM_{mn}$  mode, 'm' is for several

half-wavelength variations along patch perimeter and ‘ $n$ ’ is for the number half-wavelength variation along patch radius. The modes corresponding to radial variations are observed at a higher frequency due to their smaller dimension in comparison with respect to patch perimeter. Here the fundamental  $TM_{10}$  mode, wherein perimeter equals half wave in length is not observed as feed position coincides with minimum field location at  $TM_{10}$  mode. To obtain a wideband response, higher-order modes on the patch are tuned with respect to lower-order modes. Thus, here for given feed excitation,  $TM_{40}$  mode can be tuned with reference to  $TM_{20}$  mode. To achieve this, a pair of stubs are placed at the maximum field location of  $TM_{40}$  mode at an angle as shown in Fig. 1a, c, d. The resonance curve and current distribution against an increase in stub length ‘ $l_s$ ’ are shown in Fig. 1b and 2a–f. Here, ‘ $w_s$ ’ = 0.4 cm. The units for patch dimension and frequency are in cm and MHz, respectively.

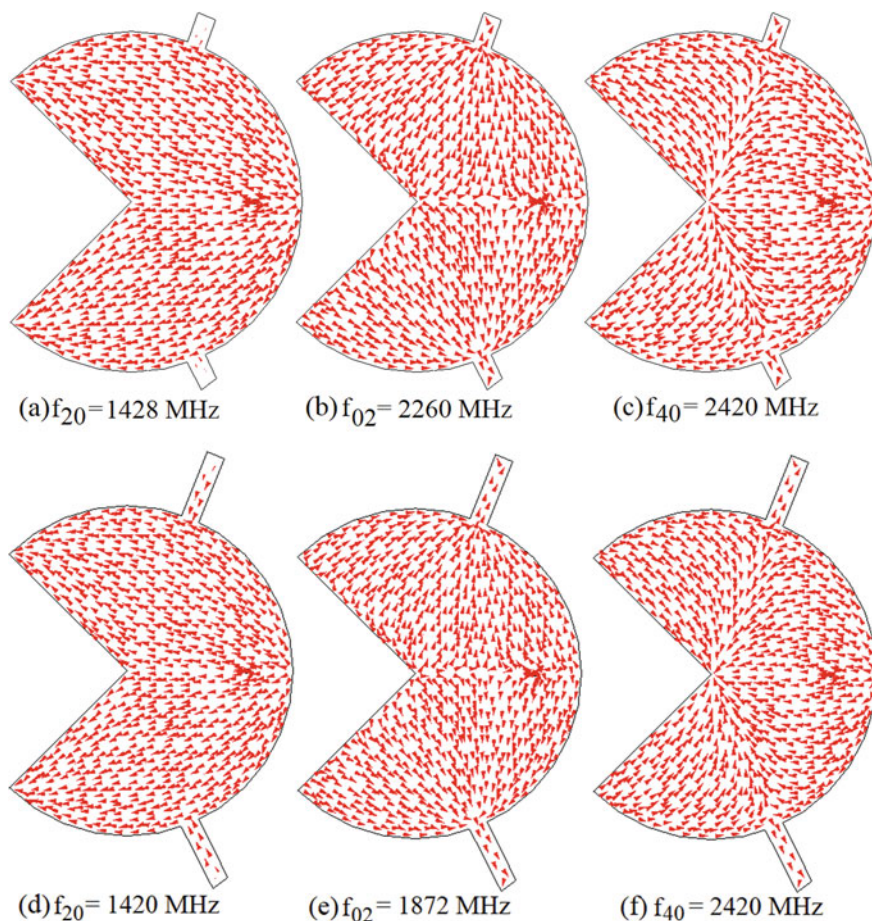


**Fig. 2** Surface current distribution at first three observed resonant modes for ‘ $l_s$ ’ = **a–c** 0.7 and **d–f** 1.4 cm

With an increase in stub length, frequencies of higher-order resonant modes reduce. Against increase in 'l<sub>s</sub>', an additional peak nearer to the TM<sub>40</sub> mode frequency is noticed. At this peak, currents show two half-wavelength variations along patch width, hence this mode is referred to as TM<sub>02</sub>. As observed from the resonance curve plots that frequency of this resonant mode reduces with stub length whereas that of TM<sub>20</sub> mode remains constant. The optimum tuning of TM<sub>02</sub> mode frequency with reference to TM<sub>20</sub> mode is obtained for 'l<sub>s</sub>' = 2.2 cm and optimum results for the stub-loaded antenna are shown in Fig. 3. The impedance BW using simulation is 60 MHz (4.18%) whereas that using measurement is 70 MHz (4.84%). The pattern

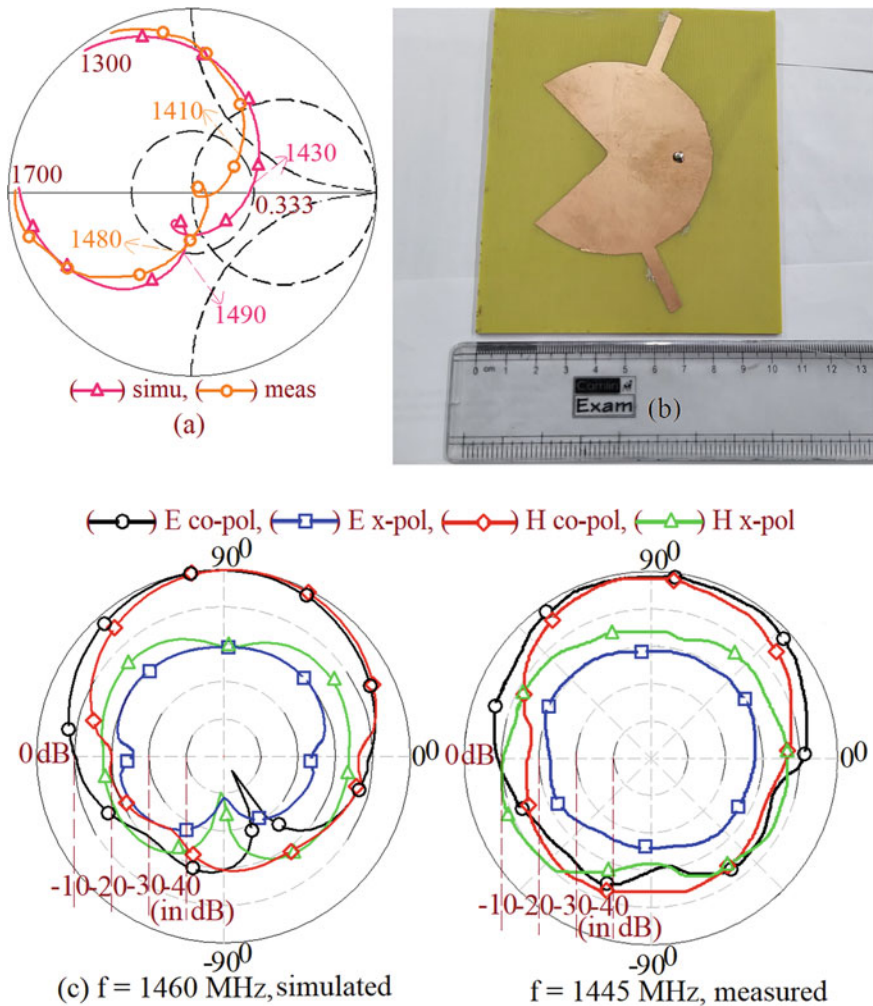


**Fig. 3** a Smith chart, b fabricated prototype and c, d radiation pattern at the center frequency of impedance BW for 270° Sectoral MSA loaded with pair of stubs

at the center frequency of the impedance BW shows radiation in the broadside direction. The E and H-planes are aligned along  $\Phi = 0^\circ$  and  $90^\circ$ , respectively. Due to the finite contribution of vertically directed surface currents at modified  $TM_{02}$  mode, the cross-polarization level increases toward the band edge frequencies. The antenna gain is lower as it is fabricated on a low-cost lossy FR4 substrate. The proposed antenna is fabricated on FR4 to prove the concept and working of the antenna. For gain improvement, the air suspended design of stub-loaded antenna can be realized.

Thus, for BW improvement, coupling between  $TM_{20}$  and  $TM_{02}$  mode is responsible. For MSA without stub  $TM_{02}$  mode is not present. The same get excited due to the loading of two stubs. The frequency of  $TM_{40}$  mode shows marginal reduction. This explanation for the wideband response with an insight into the resonant modes present is not given in the Sectoral MSAs designs as reported in [7–10], which is being provided here. Further, a simple explanation and identification for the patch modes are also provided for the Sectoral patch.

### 3 Shorted Sectoral MSA Loaded with Rectangular Slot

The design of shorted slot cut  $330^\circ$  Sectoral MSA on thinner FR4 substrate is shown in Fig. 4a. One edge of the patch is shorted to the ground plane using five shorting posts of diameter 0.08 cm. The patch is simulated for ' $x_f = 2.0$ ' and ' $y_f = 1.8$ ' cm, and surface current distribution at observed resonant modes is shown in Fig. 4b, c.

At the first mode, the current shows quarter wavelength variation along perimeter length with zero fields nearer to the shorted edge. Due to this distribution, this mode is referred to as  $TM_{1/2,0}$ . Here '1/2' refers to half of the half-wavelength variation, i.e. a quarter wavelength variation. The second index is zero since the variation along the radius is absent. At second mode, currents are showing quarter wavelength variation along shorted perimeter length and half-wavelength variation along the radius, and hence this mode is referred to as  $TM_{1/2,1}$  mode. As can be seen from the current distribution, the maximum of surface currents is orthogonal to each other and thus tuning and close spacing between them will give CP response. Therefore, rectangular slot at a given position is cut to tune these two frequencies. This slot position is selected so as it only reduces  $TM_{1/2,1}$  mode frequency as shown in Fig. 5a. The optimum separation between  $TM_{1/2,0}$  and  $TM_{1/2,1}$  resonant mode leads to the formation of a loop inside  $VSWR = 2$  circles as shown in Fig. 5b.

Here the impedance BW observed in simulation is 34 MHz (5.6%) whereas as obtained in the measurement is 32 MHz (5.37%). Due to the shorted patch and lossy substrate, this impedance BW is substantial on a thinner substrate. Due to optimum separation between orthogonal modes, CP response is realized. The AR BW as observed in the simulation and measurement is 11 MHz (1.83%) and 12 MHz (2%), respectively. The antenna exhibits a nearly omnidirectional pattern across the impedance and AR BW. Due to thinner lossy FR4 substrate, proposed slot cut and shorted design offers lower gain, which can be improved by using suspended design.

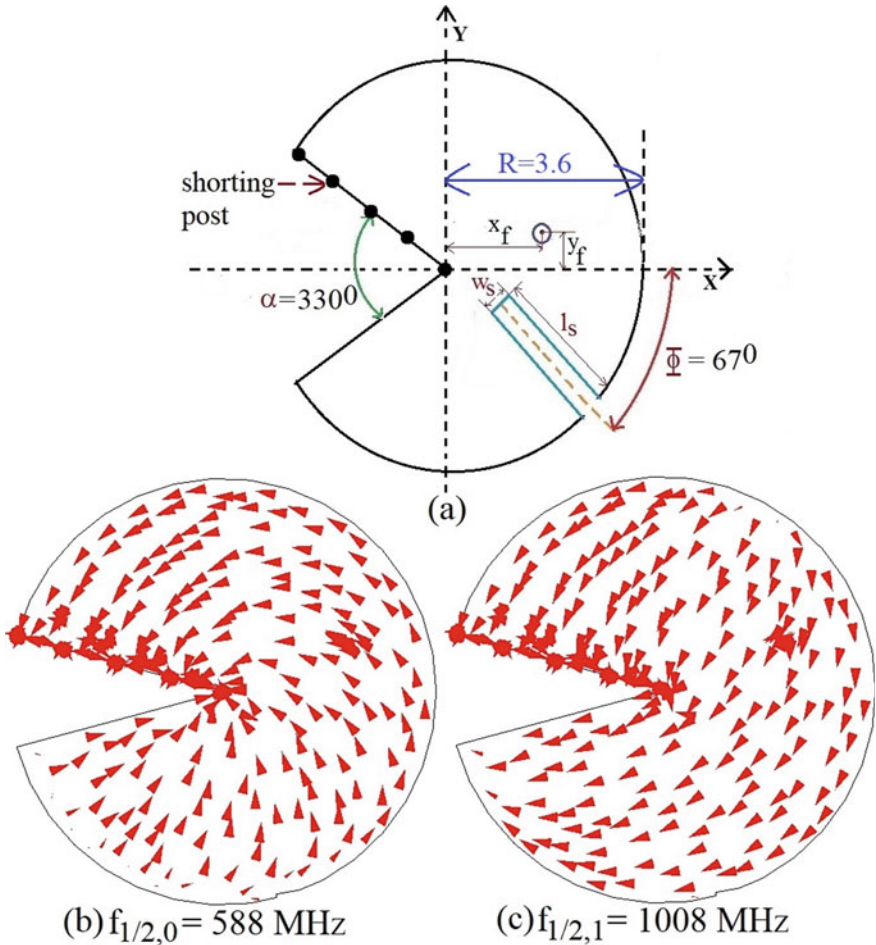


**Fig. 4** a Shorted 330° Sectoral MSA embedded with rectangular slot, its b surface current distribution at first two resonant modes

Since the shorted patch is used, with respect to the center frequency of the AR BW, the antenna size is  $1.65\lambda_{AR}$ , thereby proving to be a compact CP design.

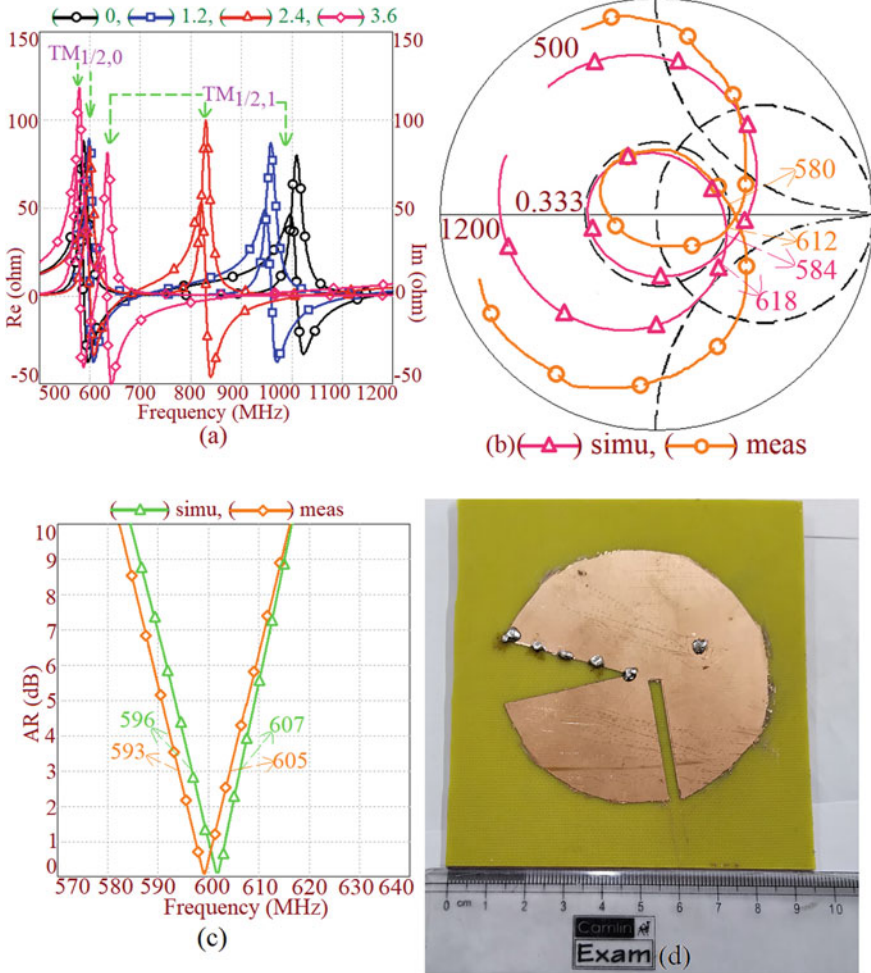


**Fig. 5** **a** Resonance curve plots for variation in ‘l<sub>s</sub>’ for ‘w<sub>s</sub>’ = 0.4 cm, **b** smith chart for optimum design, ‘l<sub>s</sub>’ = 3.6 cm, **c** AR BW plots and **d** fabricated prototype for shorted slot cut 330<sup>0</sup> Sectoral MSA

### 4 Conclusions

Variations of Sectoral MSA for wideband and CP response are proposed. A detailed explanation for the modes present in individual patches is presented. In 270<sup>0</sup> Sectoral MSA loaded with stubs, due to the optimum spacing between TM<sub>20</sub> and TM<sub>02</sub> resonant modes, a wider BW of nearly 5% on a thinner substrate is achieved. In shorted 330<sup>0</sup> Sectoral MSA, because of the optimum separation between TM<sub>1/2,1</sub> and TM<sub>1/2,0</sub> resonant modes, CP AR BW of nearly 2% is achieved. Here the shorted antenna size is 1.65λ<sub>AR</sub>, thereby realizing a compact CP configuration.



## References

1. James JR, Hall PS (1989) Handbook of microstrip antennas, vol I. London Peter Peregrinus
2. Kumar G, Ray KP (2003) Broadband microstrip antennas. Artech House
3. Wong KL (2002) Compact and broadband microstrip antennas. Wiley, New York
4. Islam MT, Shakib MN et al (2009) Multi-slotted microstrip patch antenna for wireless communication. Progress Electromagn Res Lett 10:11–18
5. Kovitz JM, Rajagopalan H, Rahmat SY (2016) Circularly polarised half E-shaped patch antenna: a compact and fabrication-friendly design. IET Microwaves Antennas Propag 10(9):932–938
6. Ding K, Gao C, Qu D, Yin Q (2017) Compact broadband circularly polarized antenna with parasitic patches. IEEE Trans Antennas Propag 65(9):4854–4857
7. Lu W-J, Li X-Q, Li Q, Zhu L (2018) Generalized design approach to compact wideband multiresonant patch antennas. RF Microwave Comput Aided Eng 28(8):1–13
8. Lu W-J, Li Q, Wang S-G, Zhu L (2017) Design approach to a novel dual-mode wideband circular sector patch antenna. IEEE Trans Antennas Propag 65(10):4980–4990
9. Yu J, Lu W-J, Cheng Y, Zhu L (2020) Tilted circularly polarized beam microstrip antenna with miniaturized circular sector patch under wideband dual-mode resonance. IEEE Trans Antennas Propag 68(9):6580–6590
10. Wu Z-F, Lu W-J, Yu J, Zhu L (2020) Wideband null frequency scanning circular sector patch antenna under triple resonance. IEEE Trans Antennas Propag 68(11):7266–7274
11. CST Microwave Studio, Version 2019

# Coplanar Waveguide Fed Modified Helicopter Fan-Shaped Microstrip Antenna for Circularly Polarized Response



Anuja Odhekar and Amit A. Deshmukh

**Abstract** Modal analysis based on magnetic dipole theory and thorough parametric study for various geometrical dimensions brings out detailed explanation of coplanar waveguide fed modified helicopter fan-shaped microstrip antenna for wideband circular polarization response. Two slots perpendicular to feed induce two electric field vectors of  $180^\circ$  with each other ( ${}^{+y}\text{TM}_{10}$  and  ${}^{-y}\text{TM}_{10}$ ). The slot length decides separation between mode frequencies. Third slot, perpendicular these two slots forming shape like helicopter fan is inserted. This slot induces magnetic field ( ${}^h\text{TM}_{01}$ ) perpendicular to both induced electric fields yielding circular polarization response. With increase in length of the third slot, magnetic current path length reduces. This increases electric current path length of three orthogonal modes. Thus, length of third slot tunes resonance frequencies corresponding to these three orthogonal modes yielding wideband CP response. Antenna configuration exhibits axial ratio bandwidth of 1.062 GHz (31.1%) superimposed on VSWR bandwidth of 2.215 GHz. Simulated broadside gain over axial ratio bandwidth is 4 dBi. The radiation pattern exhibits right hand and left hand circular polarization responses along the  $+z$ -axis and  $-z$ -axis respectively. The cross-polarization amplitude for both circular polarization is 19 dB down.

**Keywords** Circularly polarized slot microstrip Antenna · Coplanar waveguide fed · Magnetic dipole

## 1 Introduction

With advancements in wireless communication systems, numerous advantages like low profile design which can be easily integrated with microwave integrated circuits using coplanar waveguide (CPW) fed, microstrip antenna (MSA) finds many applications [1, 2]. Major characteristic of MSA is its polarization. The circularly polarized (CP) MSA became famous in today's wireless communication systems due to its

---

A. Odhekar · A. A. Deshmukh (✉)

Department of EXTC Engineering, SVKM's DJSCE, UOM, Mumbai, India

freedom from antenna orientation between transmitter and receiver. To minimize the signal loss, CP MSAs are preferred since they receive signals from any direction with equal strength [3]. Main characteristics of CP MSA are orientation of CP response, axial ratio (AR) bandwidth (BW) superimposed on the desired VSWR BW and antenna gain. Using single radiating patch, CP response in MSA is obtained by using appropriate perturbation either in form of slit, slot or stubs [4–8]. These techniques are easy to implement and fabricate resulting in narrow AR BW. Various techniques such as stacked antenna configurations [9, 10], modified shapes of MSA [11–14], fractal geometries [15, 16] are used to widen the AR BW. The complicated technique suggested in [17] uses thin single layer double-sided partially reflected surface (PRS) with complementary structure. Though these techniques result in wide AR BW, it is difficult to integrate them with monolithic microwave integrated circuits (MMIC). The CPW fed MSAs result in wideband CP response and can be easily integrated with MMIC. The proposed technique in [18, 19] proposes CPW CP MSA yielding wideband CP response. The proposed technique in [20, 21], uses CPW fed or microstrip line fed CP multiple input and multiple output (MIMO) MSA. Four semicircular patches printed on each side of double-sided PCB in pair fed with complicated feed network yields ultra wideband CP response [22]. Triple band CP response is proposed in [23] is fed with microstrip line. The article [24] proposes low profile, high directivity CP MSA. Here, modified  $TM_{12/21}$  modes with reshaped  $TM_{10/01}$  modes enhance directivity along broadside. Also, article proposes characteristics mode theory to analyze the differential fed patch. The letter [25] presents simple microstrip line fed CP MSA at 28 GHz. The configuration yields small size, wideband and high gain MSA. The novel multimode resonance technique proposed in [26] results in wideband CP MSA response. Though the proposed MSA is low profile, it is difficult to fabricate. The proposed various shaped slot MSA [27–32], utilizes perturbations in form of slots to realize wideband CP response. The stair [27] and arc-shaped [28] slots generates orthogonal mode to realize the CP response. The CPW fed slot MSAs discussed in [29–32], are complicated structure to implement though yielding wideband CP response at the cost of broadside gain of 4 dBi only. The reported antenna configurations in literature are very complicated to implement and fabricate. Though they are yielding wideband CP response, broadside gain is low. In many reported papers, AR BW is not part of the VSWR BW. The major limitation of the reported work is that they don't give insight on the realization CP response based on the antenna modes. How an embedded perturbation for CPW fed MSA, generates orthogonal modes to yield CP response is not mentioned in the literature. Also, contribution of dimensions and positions of the perturbations for widening of the CP response are not explained.

This paper presents the detailed study carried out for the modal analysis of CPW fed helicopter fan-shaped MSA yielding wideband CP response based on the magnetic dipole theory. The helicopter fan-shaped slot embedded on the MSA is considered as complimentary structure of MSA. The helicopter fan-shaped slot is a combination of three slots. Out of these three slots, two slots are aligned along +y-axis and -y-axis respectively. As these two slots are perpendicular to the CPW fed, they induce two electric field vectors which are  $180^\circ$  out of phase. The slot-1 of

dimensions ' $L_1$ ' and ' $W_1$ ' are optimized to match impedance of electric field vector. With increase in length ' $L_1$ ' and ' $L_2$ ' of slot-1 and slot-2, respectively, corresponding path length of magnetic current reduces. This increases current path length of electric field vector. Thus, reduction in the corresponding resonance frequencies is observed. These two anti-parallel electric field vectors yield CP response. To widen the AR BW one more slot perpendicular to these two slots is inserted. The slot-3 length is ' $L_3$ ' and is aligned along x-axis. This slot induces magnetic field and is aligned along x-axis. Two anti-parallel electric field vectors and magnetic field vector perpendicular to them yields CP response. To widen the AR BW, length ' $L_3$ ' is tuned. When ' $L_3$ ' increases, corresponding magnetic current path decreases yielding decrease in corresponding mode frequency. Also, increase in ' $L_3$ ', increases current path length of both electric field vectors. Thus, these three orthogonal modes are tuned to widen the CP response. The antenna configuration yields axial ratio bandwidth of 1.062 GHz (31.1%) and is superimposed on the VSWR bandwidth of 2.215 GHz. The simulated broadside gain over the axial ratio bandwidth is 4 dBi. The simulated radiation pattern exhibits right hand and left hand circular polarization response along the +z-axis and -z-axis, respectively. The cross-polarization amplitude for right and left circular polarization is 19 dB down. The antenna analyzed in this paper was simulated using CST software [33]. All dimensions are given in 'mm'.

## 2 CPW Fed Wideband CP Stair-Shaped Slot MSA

The wideband CP CPW fed MSA reported in [27] is shown in Fig. 1a. In this paper, the slot antenna and feeding structure are fabricated on the same plane. This helps to simplify the process of circuit process and position alignment. The proposed geometry in [27] is fabricated on the FR4 substrate of dielectric constant 4.4 and thickness of 0.8 mm. The stair-shaped slot is etched on the ground plane of the substrate. The geometrical parameters and position of the slot with respect to the feed are adjusted to tune the AR BW. The dimensions of the stair-shaped slot tune VSWR BW and AR BW. The optimized geometrical dimensions are reported in [27]. The antenna attains a measured matching bandwidth of 55.0% (2.24–3.94 GHz). Moreover, the antenna attains a measured AR bandwidth of 31.2% (2.30–3.15 GHz). The results are shown in Fig. 1b, c. The antenna supports right hand (RH) CP response. Though the proposed antenna in [27] is simple to implement and yielding wideband CP response, the systematic evolution of antenna configuration with the help of modal analysis is not given. The role of both vertical slots and role of dimensions of all three slots to widen the AR BW is not explained. The reported work in [27] does not have sufficient parametric study leading to the tuning of the orthogonal modes responsible for the wideband CP response. Even the design guidelines are not found in [27].

In this paper, initially stair-shaped CPW fed slot MSA is simulated as per the dimensions given in [27]. To understand the excitation of orthogonal modes to yield CP response for the reported antenna configuration in [27], step by step simulation

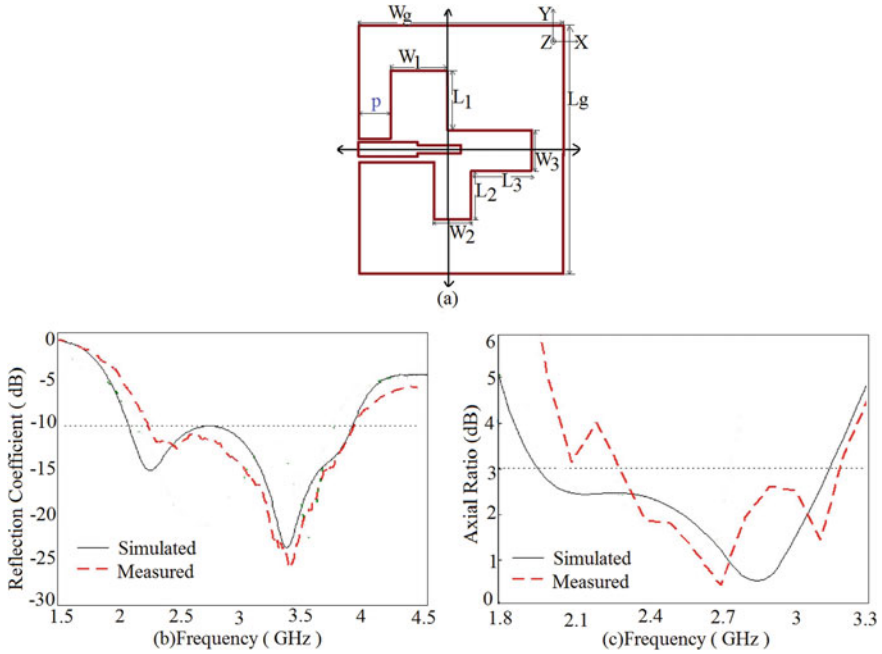


**Fig. 1** a CPW fed slot MSA [27], its b, c simulated and measured VSWR BW AR BW for optimized designed geometrical dimensions

is carried out. Evolution of the antenna configuration is shown in Fig. 2a–c. Also, paper discusses step by step evolution of the proposed geometry with the help of

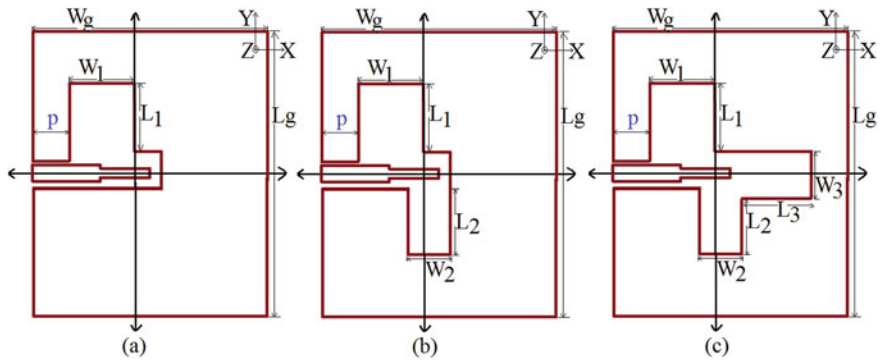


**Fig. 2** Evolution of the proposed antenna configuration. a, b Two vertical slot of dimensions ‘ $L_1$ ’ and ‘ $L_2$ ’ inducing electric field vectors along +y and –y axis. c Horizontal slot of dimensions ‘ $L_3$ ’ and ‘ $W_3$ ’ inducing magnetic field in horizontal direction showing CPW fed staircase-shaped slot antenna [27] yielding CP response

impedance curve and mode analysis. The reported detailed parametric study in this paper explains effects of various geometrical parameters on the CP response.

### 3 Analysis of the CPW Fed Modified Helicopter Fan-Shaped MSA for Wideband CP Response

Initially, only slot-1 of dimensions ' $L_1$ ' and ' $W_1$ ' is inserted. This is shown in Fig. 2a. This slot induces an electric field along y-axis. The resonance curve sketched in Fig. 3a, b interprets that electric field vector along y-axis is function of geometrical parameters ' $L_1$ ', ' $W_1$ '. The resonance frequency of this electric field vector reduces with increase in slot length ' $L_1$ ' enhancing magnitude of field vector. Increase in slot width ' $W_1$ ' lengthens the current path resulting in reduction of corresponding

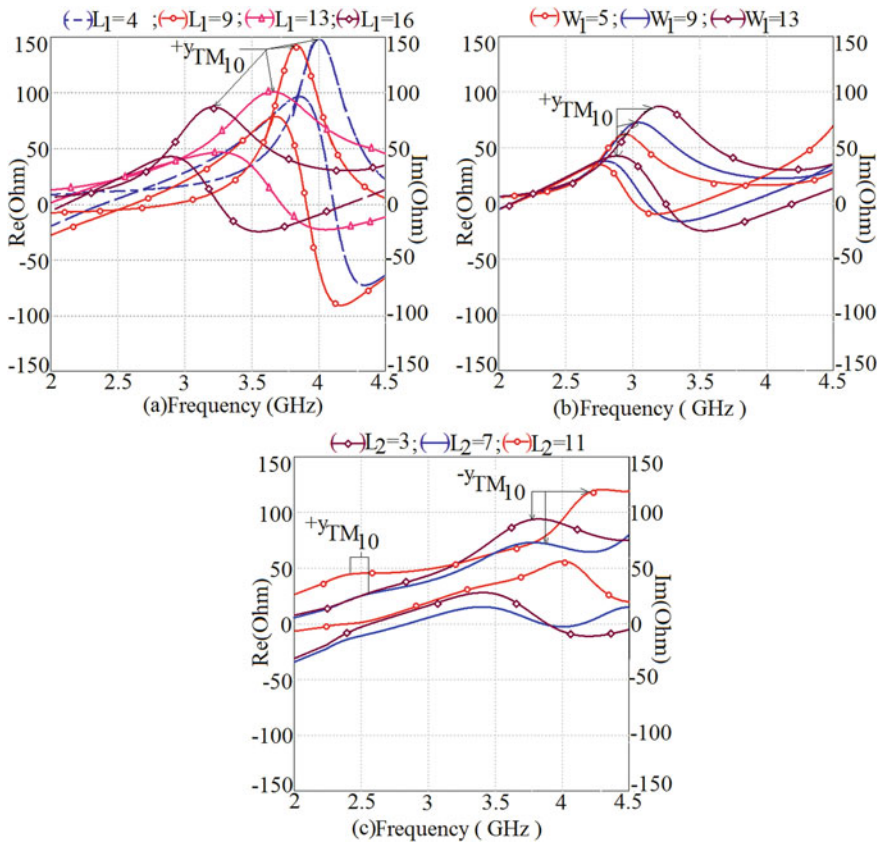
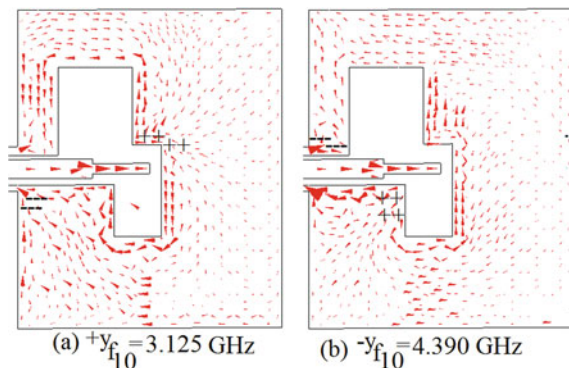


**Fig. 3** Resonance curves for variation in **a** slot length ' $L_1$ ' when slot width ' $W_1$ ' is constant and **b** slot width ' $W_1$ ' for constant length of ' $L_1$ ' **c** slot length ' $L_2$ '

**Fig. 4** Surface current distribution for the induced electric field due to slots inserted at  $90^\circ$  with respect to the CPW feed **a** induced electric field vector along  $+y$ -axis ( $^{+y}TM_{10}$ ) **b** induced electric field vector along  $-y$ -axis ( $^{-y}TM_{10}$ )



resonance frequency and also tunes this resonance frequency. This is shown in Fig. 3b. Further, second slot of dimensions ' $L_2$ ', ' $W_2$ ' is inserted. The slot is positioned at  $180^\circ$  with respect to first slot at some offset as shown in Fig. 2b. Insertion of the slot-2 induces electric field vector which is  $180^\circ$  out of phase with respect to electric field vector induced by slot-1. These results are interpreted from the resonance curve shown in Fig. 3c and also supported with the help of current distribution shown in Fig. 4a, b. The detailed parametric study is carried out for position of the slot-2 along with its geometrical dimensions. Study showed that symmetrical placement of slot-1 and slot-2 with respect to the CPW feed is unable to create phase difference of  $180^\circ$  between the two electric field vectors.

Thus, role of position of slot-1 with respect to the CPW feed is tune impedance at the resonance frequency ( $^{+y}f_{10}$ ) corresponding to the induced electric field. Whereas, role of position and dimensions of the slot-2 is to tune impedance at the resonance frequency ( $^{-y}f_{10}$ ) corresponding to the induced electric field and adjust the phase difference of exact  $180^\circ$  between both electric field vectors. Dimensions and position of slot-1 and slot-2 optimize spacing between resonance frequencies and phase difference. As slot-1 and slot-2 are attached to each other, extension of the connection induces magnetic field and is aligned along the x-axis. This magnetic field vector is perpendicular to both electric field vectors.

The geometrical dimension of slot-3 decides resonance frequency of the magnetic field vector. Thus, the final geometry to yield CP response which is proposed in [27] is sketched in Fig. 2c. Here, three orthogonal modes out of which two orthogonal modes are resultant of two electric field vectors and one is due magnetic field vector, yields CP response. As the separation between these three orthogonal modes tunes CP response, detailed parametric study is carried out for dimension ' $L_3$ '. The detailed parametric study is shown in Fig. 5a–f. With an increase in ' $L_3$ ', increase in current path length corresponding to the modes ' $^{+y}TM_{10}$ ' and ' $^{-y}TM_{10}$ ' is observed. This reduces corresponding mode frequencies. Along with this slot-3 introduces one more mode which is perpendicular to both modes. Thus, slot length ' $L_3$ ' not only introduces one more orthogonal mode to tune the CP response but also tunes lower orthogonal modes in order to increase AR BW. The current path length reduction corresponding

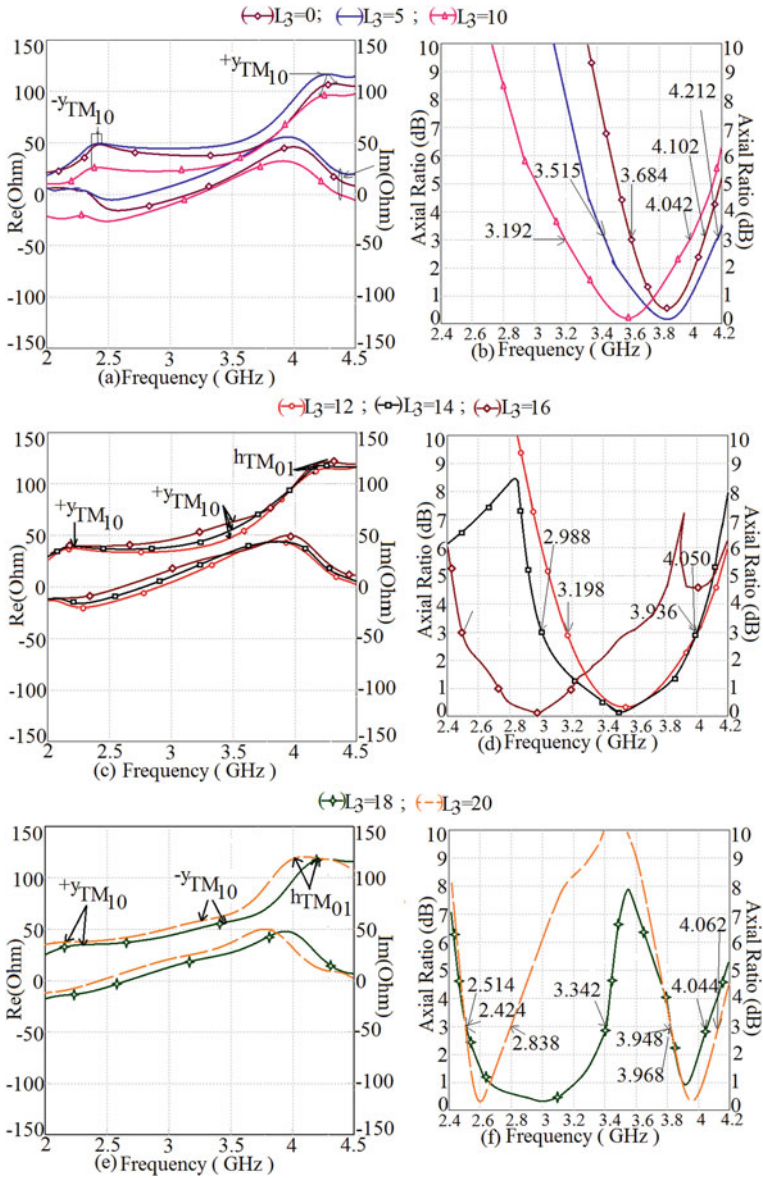


**Fig. 5** a-f Resonance curve and AR BW showing tuning of three orthogonal modes by varying ' $L_3$ ' for CPW fed modified helicopter fan-shaped MSA



to the modes ‘ $+yTM_{10}$ ’ and ‘ $-yTM_{10}$ ’ and insertion of the new orthogonal mode ‘ $^hTM_{01}$ ’ is observed from surface current distribution and is sketched in Fig. 6a–c.

Further, length of the all three slots is tuned simultaneously to optimize the spacing between these three orthogonal modes. Further, increment in ‘ $L_3$ ’ increases current path length corresponding to all three orthogonal modes and decreases corresponding frequencies. This results in decrease in spacing between orthogonal modes and yields dual-band CP response. This is sketched in Fig. 5e, f. The optimized design has the geometrical dimensions as ‘ $L_1$ ’ = 16 mm, ‘ $L_2$ ’ = 12, and ‘ $L_3$ ’ = 14 mm. The corresponding optimized results are shown in Fig. 7. The result shows that an AR BW of 1.062 GHz (31.1%) is superimposed on the VSWR BW of 2.215 GHz. The

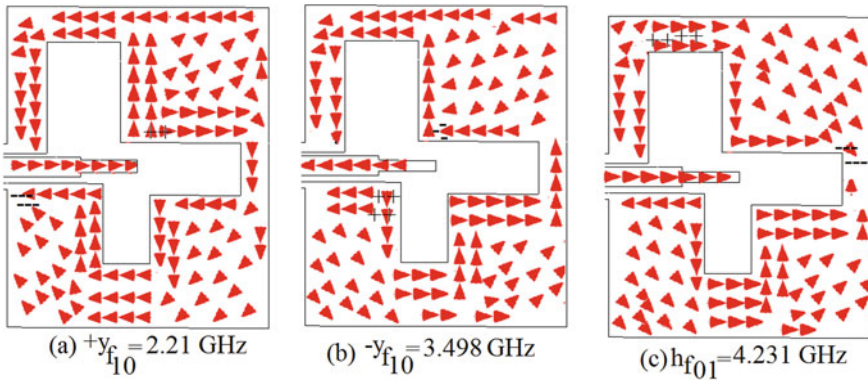


**Fig. 6** Surface current distribution corresponding to the orthogonal modes responsible for enhancement in AR BW **a**  $+yTM_{10}$  **b**  $-yTM_{10}$  **c**  $^hTM_{01}$

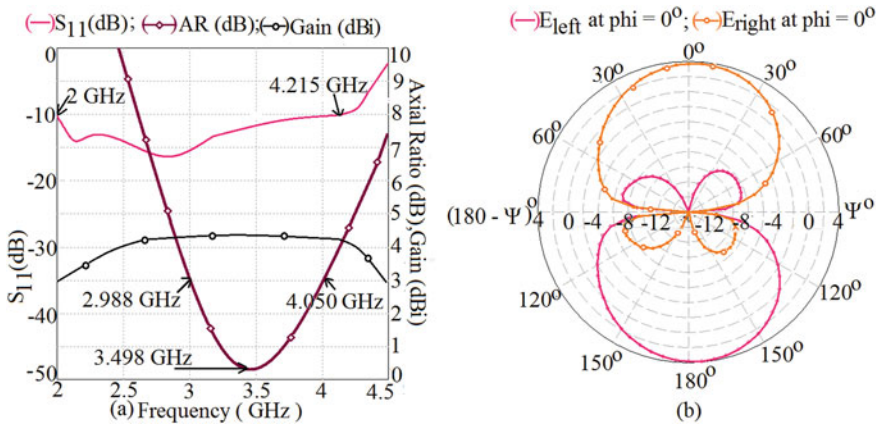


**Fig. 7** Simulated results for optimized geometry for the CPW fed modified helicopter fan-shaped MSA. **a** AR BW superimposed on the VSWR BW, **b** RHCP response along +z-axis and LHCP response along –z-axis

results reported in [27], yield 29.2% of AR BW. The broadside gain 4 dBi is obtained over the complete AR BW. The simulated radiation pattern exhibits RHCP response along the  $+z$ -axis and LHCP response along the  $-z$ -axis.

## 4 Conclusions

The detailed study to bring out the explanation behind wideband CP response of modified helicopter fan-shaped slot MSA using magnetic dipole theory and modal analysis based on the surface current distribution is reported. The length ' $L_3$ ' tunes three orthogonal modes yielding wideband CP response. The antenna configuration yields axial ratio bandwidth of 1.062 GHz (31.1%) and is superimposed on the VSWR bandwidth of 2.215 GHz. The simulated broadside gain over the axial ratio bandwidth is 4 dBi. The simulated radiation pattern exhibits right hand and left hand circular polarization response along the  $+z$ -axis and  $-z$ -axis, respectively. The cross-polarization amplitude for right and left circular polarization is 19 dB down.

## References

1. James JR, Hall PS (1989) Handbook of microstrip antennas, vol 1. Peter Peregrinus, London
2. Lee HF, Chen W (1997) Advances in microstrip and printed antennas. Wiley, New York
3. Balanis CA (1997) Antenna theory, analysis and design. Wiley, New York
4. Gao SS, Luo Q, Zhu F (2014) Circularly polarized antennas, first edn. Wiley, Inc., United Kingdom
5. Heidari AA, Heyrani M, Nakhkash M (2009) A dual-band circularly polarized stub loaded microstrip patch antenna For GPS applications. Progress Electromagn Res 92:195–208
6. Chen W-S, Wu C-K, Wong K-L (1998) Compact circularly polarized microstrip antenna with bent slots. Electron Lett 34(13):1278–1279
7. Nasimuddin N, Qing X, Chen ZN (2010) Slits loaded microstrip antennas for circular polarization. Microwave Optical Technol Lett 52(9):2043–2049
8. Wong KL (2002) Compact and broadband microstrip antennas, 1st edn. Wiley Inc., New York, USA
9. Sharma PC, Gupta KC (1983) Analysis and optimized design of single feed circularly polarized microstrip antennas. IEEE Trans Antennas Propag 31(6):949–955
10. Nayeri P, Lee K-F, Elsherbeni AZ, Yang F (2011) Dual band circularly polarized antennas using stacked patches with asymmetric U-slot. IEEE Antennas Wireless Propag Lett 10:492–495
11. Quzwain K, Ismail A, Sali A (2016) Compact high gain and wideband octagon microstrip yagi antenna. J Electromagn 36(8):524–533
12. Deshmukh AA, Zaveri P (2018) Sequentially rotated gap-coupled variations of plus shape microstrip antennas for dual band circular polarized response. Int J RF Microwave Comput Aided Eng. <https://doi.org/10.1002/mmce.21431>
13. Shi IY, Liu J (2018) A circularly polarized octagon-star-shaped microstrip patch antenna with conical radiation pattern. IEEE Trans Antennas Wave Propag 66(4):2073–2078
14. Jian Y, Wen-Jun L, Cheng Y, Zhu L (2020) Tilted circularly polarized beam microstrip antenna with miniaturized circular sector patch under wideband dual-mode resonance. IEEE Trans Antennas Wave Propag 68(9):6580–6590

15. Reddy VV (2017) Single—feed circularly polarized flared U—fractal boundary microstrip antenna. *IETE J Res.* <https://doi.org/10.1080/03772063.2017.1292862>
16. Wei K, Li JY, Wang L, Xu R, Xing JZ (2017) A new technique to design circularly polarized microstrip antenna by fractal defected ground structure. *IEEE Trans Antennas Propag* 65(7):3721–3725
17. Goudarzi A, Movahhedi M, Honari MM, Saghlatoon H, Mirzavand R (2021) Wideband high-gain circularly polarized resonant cavity antenna with a thin complementary partially reflective surface. *IEEE Trans Antennas Propag* 69(1):532–537
18. Goudarzi A, Movahhedi M, Honari Mousavi MM, Xu R, Li JY, Liu J, Zhou SG, Wei K, Xing ZJ (2018) A simple design of compact dual-wideband square slot antenna with dual-sense circularly polarized radiation for WLAN/Wi-Fi communications. *IEEE Trans Antennas Propag* 66(9):532–537
19. Ullah U, Koziel S (2019) Geometrically simple compact wideband circularly polarized antenna. *IEEE Trans Antennas Propag* 18(6):1179–1183
20. Ullah U, Mabrouk IB, Koziel S (2020) Enhanced performance circularly polarized MIMO antenna with polarization/pattern diversity. *IEEE Access* 8
21. Kaim V, Kanaujia BK, Rambabu K (2021) Quadrilateral spatial diversity circularly polarized MIMO cubic implantable antenna system for biotelemetry. *IEEE Trans Antennas Propag* 69(39):1260–1272
22. Tan W, Shan X, Shen Z (2021) Ultra wideband circularly polarized antenna with shared semicircular patches. *IEEE Trans Antennas Propag* 69(6):3555–3559
23. Rui X, Li J, Qi Y-X, Guangwei Y, Yang J-J (2017) A design of triple-wideband triple-sense circularly polarized square slot antenna. *IEEE Antennas Propag Lett* 16:1763–1766
24. Lin J-F, Zhu L (2021) Low profile high-directivity circularly-polarized differential-fed patch antenna with characteristic modes analysis. *IEEE Trans Antennas Propag* 69(2):723–733
25. Ullah U, Al-Hasan M, Koziel S, Mabrouk IB (2021) A series inclined slot-fed circularly polarized antenna for 5G 28 GHz applications. *IEEE Trans Antennas Propag* 20(3):351–355
26. Wei H, Li C, Liu X, Wen L, Feng T, Jiang W, Gao S (2021) Wideband circularly polarized microstrip patch antenna with multimode resonance. *IEEE Trans Antennas Propag* 20(4):533–537
27. Wang C-J, Chen C-H (2009) CPW-fed stair-shaped slot antennas with circular polarization. *IEEE Trans Antennas Propag* 57(8):2483–2486
28. Chiang MJ, Hung T-F, Bor SS (2010) Dual-band circular slot antenna design for circularly and linearly polarized operations. *Microwave Optical Lett* 52(4):2717–2721
29. Kushwaha N, Kumar R (2016) Design of a wideband high gain antenna using FSS for circularly polarized applications. *Int J Electron Commun.* <https://doi.org/10.1016/j.aeue.2016.05.013>
30. Ramkrishna RVS, Kumar R (2015) A CPW-fed wideband circularly polarized slot antenna with Fss for enhanced gain. *Microwave Optical Lett* 57(5):1199–1204
31. Ding K, Gao C, Yu T, Qu D (2015) CPW-fed C-shaped slot antenna for broadband circularly polarized radiation. *Int J RF Microwave Comput Aided Eng* 25(4): 739–746
32. Li T, Zhang F-S, Gao F, Guo Y-L (2016) CPW-fed circularly polarized square slot antenna with enhanced bandwidth and reduced size for wideband wireless applications. *Progress Electromagn Res C* 65:121–129
33. CST Microwave Studio Suite, Version 2019

# Space-Fed Variations of Compact Microstrip Antennas Using Modified Feed Elements



Adil Parvez, Kshitij Lele, Amit A. Deshmukh, and Venkata APC

**Abstract** Space-fed variations of compact C and H-shape microstrip antennas are proposed for high gain and wideband response. The detailed study is presented using two different feed variations using the proximity feeding. Due to effective illumination of space-fed patches, an optimum response is realized in  $7 \times 7$  array fed using gap-coupled patches. The  $7 \times 7$  space-fed design using C-shape patches yields broadside gain of 14.6 dBi with impedance bandwidth of greater than 2.5 GHz in 4 GHz frequency range. Using H-shape patches, these values are bandwidth more than 2.5 GHz with gain of above 16 dBi. The experimentation has been carried out to validate the simulated results, which shows close agreement.

**Keywords** C-shape microstrip antenna · H-shape microstrip antenna · Ring Shape · Space-fed array · Gap-coupled feeding structure · Proximity feeding

## 1 Introduction

With the rapid developments in the satellite communication and its application in various domains of the wireless communication, requirements for the high gain antennas offering wider bandwidth (BW) has increased [1, 2]. The microstrip antenna (MSA) finds wide usages here due to their numerous advantages [1–3]. Further, the use of compact radiating patch reduces the overall antenna size while designing higher BW and large gain structures [1–3]. The reduction in the patch size offering moderately acceptable values of the cross-polarization level is obtained by employing slot cut technique [3]. Here the slot is embedded on the patch at the maximum current location at the fundamental resonant mode. However, compact slot cut MSAs has poor BW and gain performance. The BW in MSA is increased either by employing thicker substrate in combination with modified feeding structure or by embedding resonant slots inside the patch [4–8]. The gain of the MSA is increased by increasing its aperture area; which is increased by using the parabolic dish [1, 2]. However,

---

A. Parvez · K. Lele · A. A. Deshmukh (✉) · V. APC  
Department of EXTC, SVKM's DJSCE, Mumbai, India

use of dish increases the antenna size. The planar design of high gain antennas is realized by using the microstrip patches by using the reflect array or space-fed arrays [9–16]. In reflect arrays, antenna radiating efficiency is reduced due to presence of feed, which comes in the radiating (receiving) path of electromagnetic waves. Here space-fed array offers better results as the feed antenna is placed below the array elements thereby improving radiating efficiency.

In this paper space-fed designs of compact C-shape and H-shape MSAs are presented using modified feeds, in the 4 GHz frequency range. Two feed configurations, namely, proximity fed rectangular MSA (RMSA) and gap-coupled configuration of RMSAs stacked on proximity fed RMSA are studied. Various spaced fed array (SFA) designs like,  $1 \times 3$ ,  $3 \times 1$ , plus-shaped,  $3 \times 3$ ,  $5 \times 5$  and  $7 \times 7$  are studied. The detailed parametric study for analyzing the gain and BW response in each SFA design is presented. Using lower order SFA, proximity fed RMSA as feed gives optimum response whereas for higher order SFAs gap-coupled stacked design of RMSAs yields optimum response. Here, in C-shape patch,  $7 \times 7$  array yields broadside gain of 14.6 dBi with impedance BW of greater than 2.5 GHz. Using the H-shape MSA in  $7 \times 7$  SFA design, broadside gain of larger than 16 dBi with more than 2.5 GHz of impedance BW is obtained. Thus using SFA configuration and modified feeding configurations, gain and BW of compact C and H-shape MSA has been substantially improved. The low cost FR4 substrate ( $\epsilon_r = 4.3$ ,  $h = 0.16$  cm,  $\tan \delta = 0.02$ ) is used in the present study. The antennas were fed using SMA panel type connector of inner wire diameter 0.12 cm. The gain and BW of the SFA designs were measured in Antenna lab using R & S instruments like, ZVH 8, FSC 6 and SMB 100A. The finite square ground plane of dimension  $40 \times 40$  cm is used in the present study. The antennas discussed in this paper were initially studied using CST software followed by experimentation. The reference wideband horn antennas are used in pattern and gain measurement. The three antenna method is selected in gain measurements.

## 2 Space-Fed C-Shape Microstrip Array Using Modified Feed

The design of space-fed C-shape array fed using proximity fed RMSA is shown in Fig. 1a, b. The C-shape MSA is compact variation of RMSA and thus has lower gain. To improve the same, various SFA designs are presented, like,  $1 \times 3$ ,  $3 \times 1$ , plus shape,  $3 \times 3$ ,  $5 \times 5$  and  $7 \times 7$ . The proposed SFA is designed in 4 GHz band hence the feed RMSA dimensions are calculated such that it operates around this frequency in its  $TM_{10}$  mode. The array patches are compact C-shaped MSAs. The center patch dimensions are  $L = 13.2$  mm and  $W = 16.2$  mm. The slot dimensions of the array patch directly above the feed patch are  $L_1 = 8.6$  mm and  $W_1 = 4.9$  mm and adjacent patch dimensions (outward from the center) are increased by 0.2 mm in length and width. The feed patch dimension is calculated to be  $L_f = 22$  mm,  $W_f =$

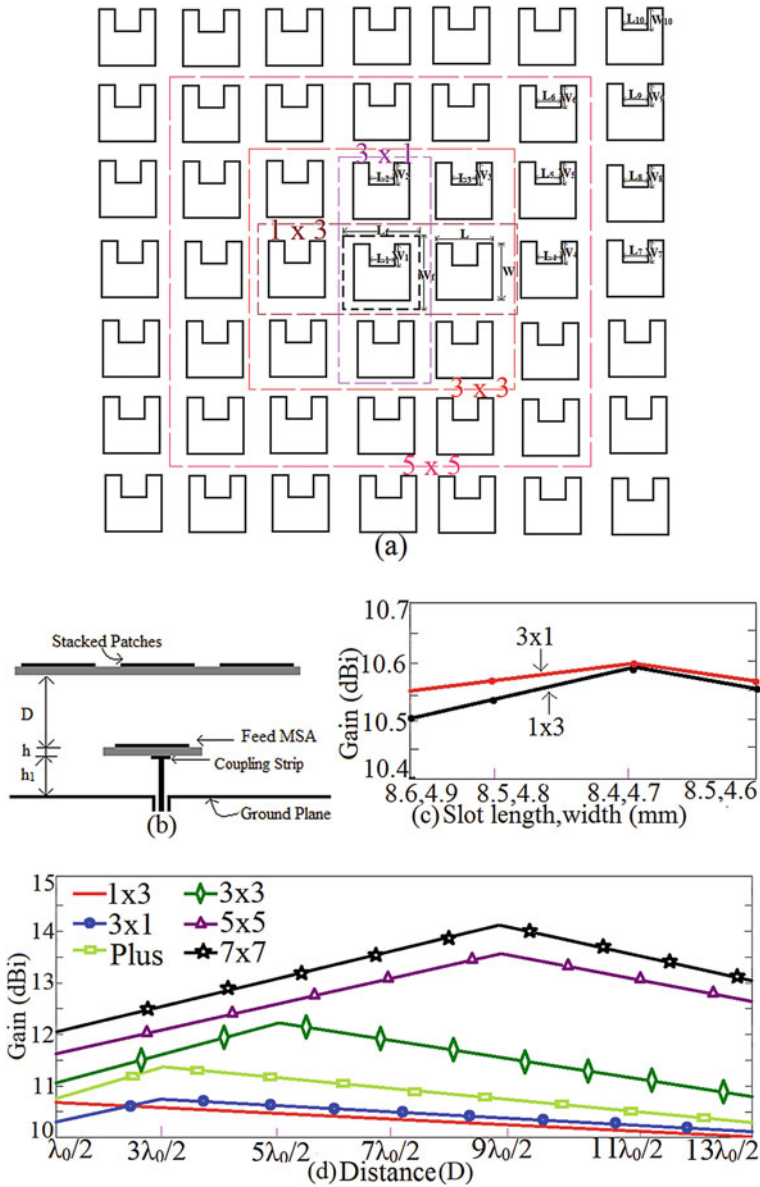


**Fig. 1** a Top and b side views of the SFAs fed using proximity fed RMSA, c gain plots for two variations of SFAs for variation in slot dimensions in C-shape patch, d variation in broadside gain against 'D' for different SFA order

**Table 1** Gain and BW of single proximity c-slot SFA

SFA	Bandwidth, (GHz)	Gain, (dBi)
$1 \times 3$	1.4	10.6
$3 \times 1$	1.43	10.6
Plus	1.38	11.4
$3 \times 3$	1.4	12.2
$5 \times 5$	1.41	13.8
$7 \times 7$	1.4	14.1

26 mm. For optimizing the SFA for each order, two parametric variations are carried out, i.e. variation in slot length on each C-shape patch present away from the center patch and further variation in distance ‘D’ present between the feed and array. After the detuning (slot length variation) the patches away from the center patch, effects of variation in distance ‘D’ on the broadside gain for each SFA have been studied. The plots for these variations are shown in Fig. 1c, d. With increase in SFA order, antenna gain increases but it is obtained for higher ‘D’. The simulated values of the BW and gain realized in each order are shown in Table 1. The optimum results are obtained for  $7 \times 7$  SFA as shown in Fig. 2a–e. Here ‘D’ =  $9\lambda_0/2$  that equals 33.75 cm in 4 GHz band. The BW and gain in  $7 \times 7$  SFA are more than 1.4 GHz and 14 dBi, respectively. The pattern is broadside with cross-polar 15 dB lesser than co-polar.

Amount of increase in the broadside gain with order in SFA is smaller. In the optimum  $7 \times 7$  SFA, separation between fed patch and SFA layer is larger. In order to realize effective illumination of higher order array elements to improve the gain, gap-coupled and stacked design of feeding network is selected as shown in Fig. 2f. Here  $3 \times 3$  gap-coupled array is placed on top of the proximity fed RMSA. The dimensions of stacked gap-coupled RMSA are taken to be 1 mm lesser than fed patch. Using the parametric study, gap-coupled feed network is optimized for gain and BW. Similar to the above, using this feed, SFA of different orders is realized as shown in Fig. 3.

The gain variation for different SFAs against varying ‘D’ is shown in Fig. 4a. In  $1 \times 3$ ,  $3 \times 1$ , plus shape and  $3 \times 3$ , maximum gain is obtained for ‘D’ =  $7\lambda_0/2$ , that equals 26.25 cm, in 4 GHz range. An optimum distance between the feed and array, for the maximum gain in  $5 \times 5$  and  $7 \times 7$  SFA is  $7\lambda_0/2$  and  $11\lambda_0/2$  respectively. The results for all the configurations are summarized in Table 2. The BW is improved using the gap-coupled feed network design, but shows marginal increase in gain in all the designs. The results for  $7 \times 7$  SFA are shown in Figs. 4b, c and 5a–c. The antenna BW has increased by more than 1 GHz in all the configurations using gap-coupled array feed. This is attributed to more number of resonators present in the feed design. The radiation pattern is in the broadside direction with cross-polar levels less than 15 dB observed along broadside direction. The E-plane is aligned along  $\Phi = 0^\circ$ . Antenna gain is close to 15 dBi. In the next section, similar designs of H and ring MSA are studied.

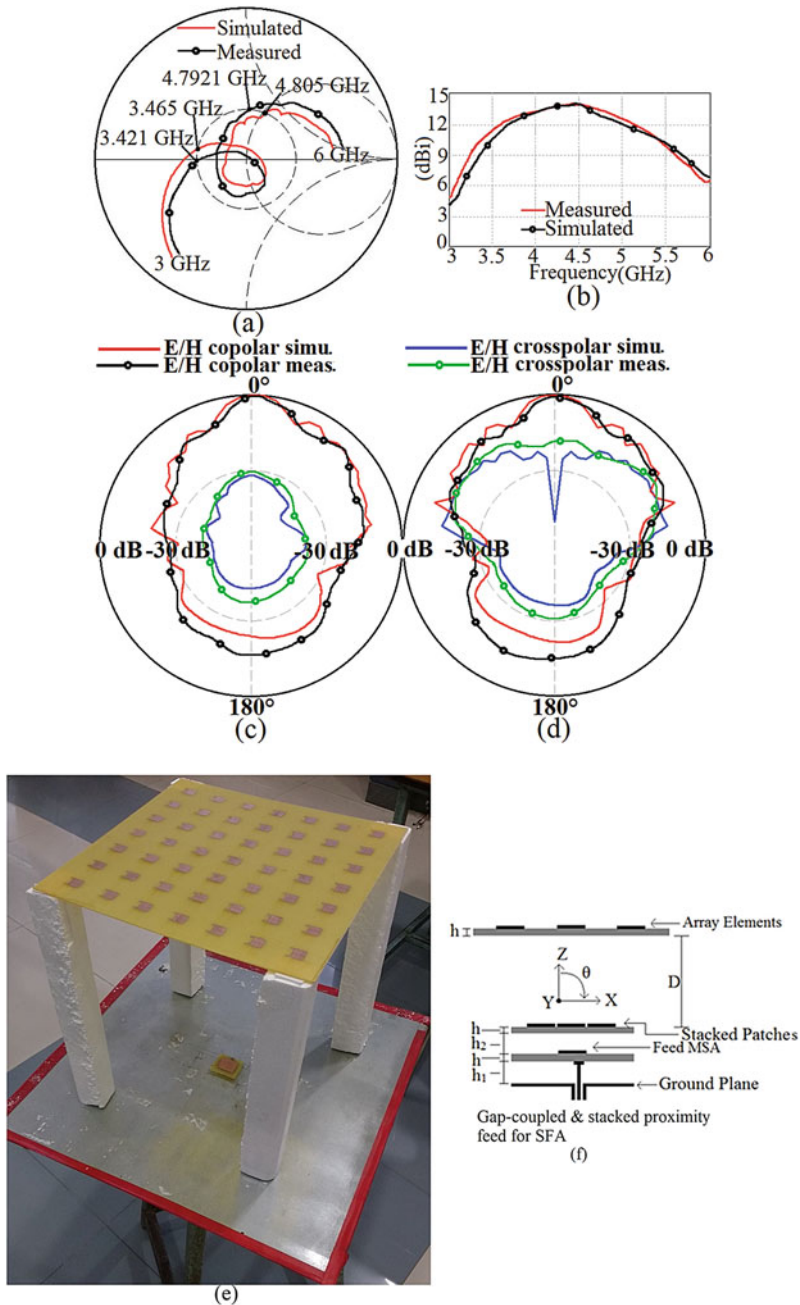


**Fig. 2** a Smith chart, b gain variation over BW, c, d radiation pattern at center frequency of BW, e fabricated prototype for  $7 \times 7$  SFA fed using proximity fed RMSA, f gap-coupled and stacked configuration of RMSA fed using proximity fed RMSA for SFAs



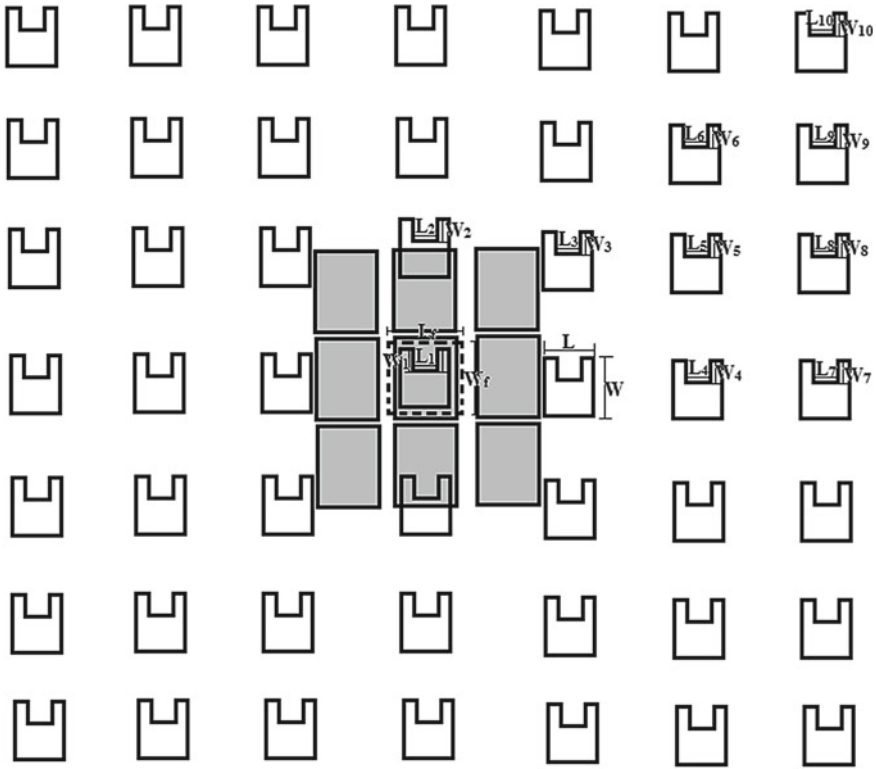
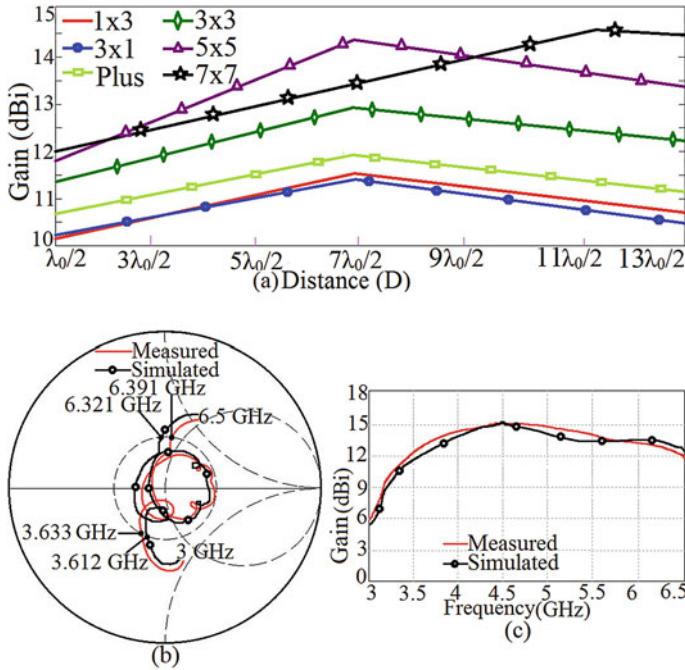


Fig. 3 SFA fed using gap-coupled and stacked RMSA array fed using proximity fed RMSA

### 3 Space-Fed H-Shape Microstrip Array Using Modified Feed

The H-shape MSA SFA fed using the proximity fed RMSA is shown in Fig. 6a. Here different SFAs namely  $1 \times 3$ ,  $3 \times 1$ , plus-shape,  $3 \times 3$ ,  $5 \times 5$ ,  $7 \times 7$ , have been studied. The fed patch parameters are kept as the same as that present in the design with C-shape patches and hence that figure is not given here again. In each SFA variation, detuning of the H-shape MSA frequency is realized by changing the inner slot dimension ( $L_1, W_1, L_2, W_2$ ). Here the top center patch length ‘L’ and width ‘W’ are 13.2 and 16.2 mm, respectively. The center patch has lower slot dimension (i.e. higher frequency) whereas the peripheral patches have larger slot dimension (i.e. lower frequency). The slot dimensions in the patch array present directly above the feed patch, are  $L_1 = 8.6$  mm and  $W_1 = 4.9$  mm and adjacent patch dimensions (outward from the center) are increased by 0.2 mm in slot length and width. For 4 GHz frequency, fed RMSA dimensions are,  $L_f = 22$  and  $W_f = 26$  mm. In each of the variation, detailed parametric study for changing distance ‘D’ between the feed and SFA and slot length of adjoining patches (length detuning) is carried out and the



**Fig. 4** a Gain variation against ‘D’ for SFA using gap-coupled stacked feed, b smith chart and c gain variation over BW for  $7 \times 7$  SFA fed by gap-coupled stacked RMSA feed

**Table 2** Gain and BW using  $3 \times 3$  gap-coupled stacked array feeding C-shape MSA SFA

SFA	BW (GHz)	Gain with single proximity feed (dBi)	Gain with $3 \times 3$ gap coupled feed (dBi)
$1 \times 3$	2.75	10.6	11.7
$3 \times 1$	2.74	10.6	11.2
Plus	2.75	11.36	11.1
$3 \times 3$	2.75	12.25	12.9
$5 \times 5$	2.70	13.85	14.4
$7 \times 7$	2.71	14.1	14.6

gain variations for them are shown in Fig. 6b. The optimum results for all SFAs are summarized in Table 3.

Similar to the C-shape SFA, impedance BW in all the designs is around 1.4 GHz as well as the gain values are comparable. The optimum results in terms of gain and BW are obtained in  $7 \times 7$  design and its results are shown in Figs. 7 and 8. The broadside gain obtained here is above 13 dBi. To improve the gain and BW further, gap-coupled and stacked design of RMSA along with proximity feed is used as the feed element as shown in Fig. 8b. The variation in the broadside gain against ‘D’ is

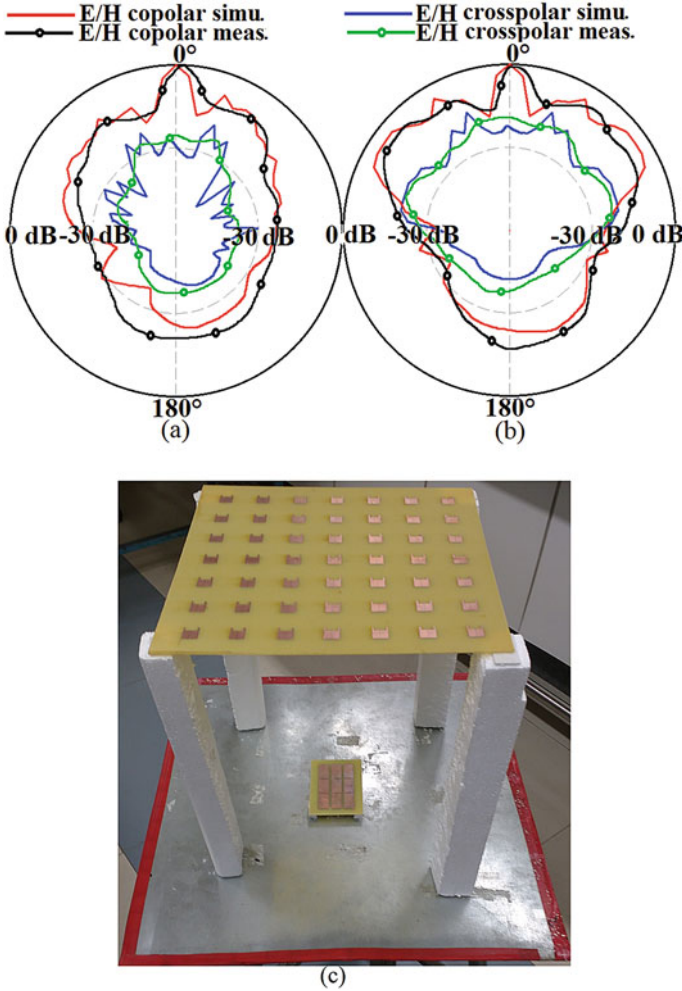


**Fig. 5** a, b Radiation pattern at center frequency of BW and c fabricated prototype for  $7 \times 7$  SFA of C-shape patches fed using gap-coupled and stacked proximity fed RMSA

shown in Fig. 9a. In,  $1 \times 3$ ,  $3 \times 1$  and plus shape, maximum gain is obtained for  $D = 5\lambda_0/2$  and  $7\lambda_0/2$  respectively, that equals 18.75 and 26.25 cm, around 4 GHz.

The results for all the SFA variations are summarized in Table 4. The distance between two patches of SFA is  $0.54\lambda_0$  (4.05 cm) from one center of patch to another center of patch. The dimensions of the array elements are similar to previous H-shaped SFA. Maximum gain is obtained at spacing of  $9\lambda_0/2$  for  $7 \times 7$  SFA. Here the gain of 16.2 dBi and BW of 2.75 GHz is obtained as shown in Fig. 9b–e. The fabricated antenna is shown in Fig. 10.

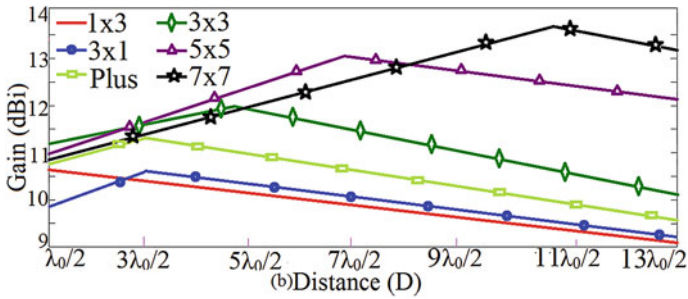
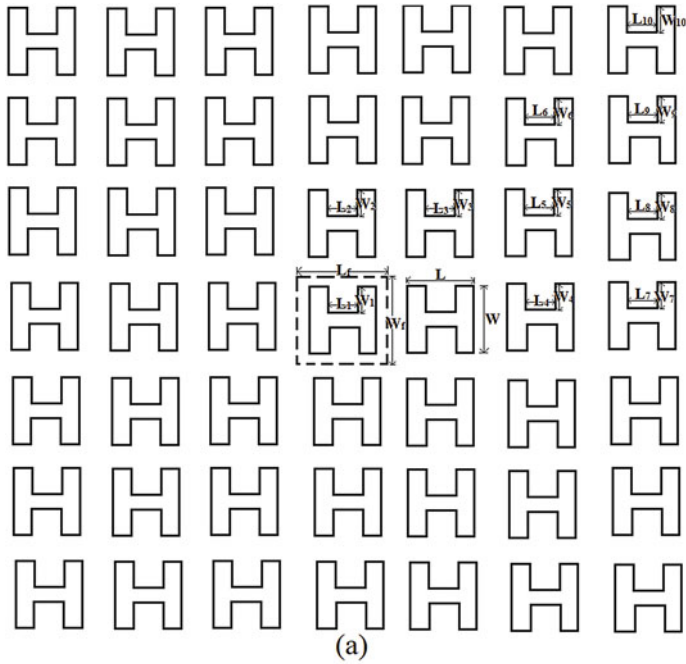


**Fig. 6** a SFA using H-shape MSA fed using proximity fed RMSA and its b variation in gain against distance ‘D’

**Table 3** Gain and BW of single proximity fed H-shape SFA

SFA	Bandwidth, (GHz)	Gain, (dBi)
1 × 3	1.4	10.6
3 × 1	1.42	10.6
Plus shape	1.44	11.3
3 × 3	1.4	11.9
5 × 5	1.38	13.2
7 × 7	1.4	13.5

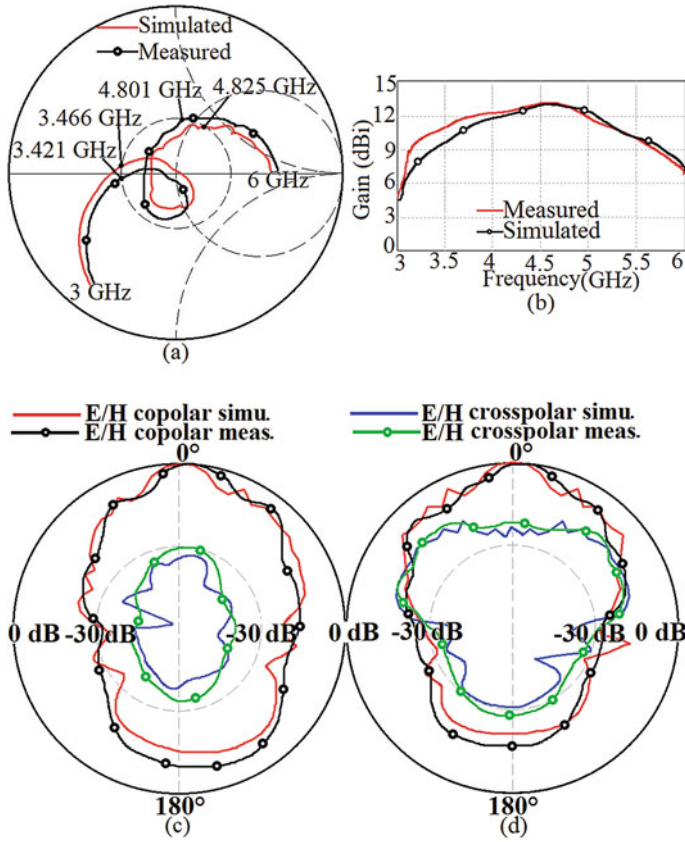
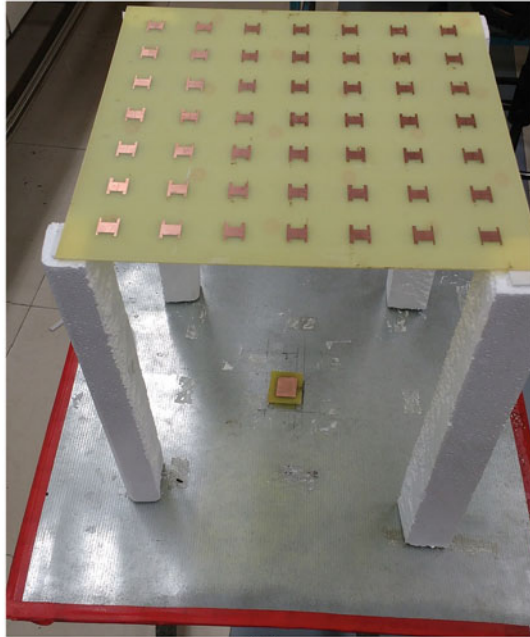


**Fig. 7** a Smith chart, b gain variation over the BW and c, d radiation pattern in E and H-planes for  $7 \times 7$  SFA of H-shape MSA fed using proximity fed RMSA

Similarly, SFA designs using ring shape MSA have been studied using proximity fed RMSA as well as gap-coupled and stacked configuration of RMSA using proximity feed. The detailed gain comparison for two feeds for different array order in SFA are provided in Table 5. The optimum results are obtained in  $7 \times 7$  design. As can be seen that substantial improvement in the broadside gain is obtained using gap-coupled and stacked design. The results for  $7 \times 7$  SFA for ring MSA are shown in Figs. 11 and 12.

### 4 Conclusions

Various SFA designs of compact MSA variations like C-shape, H-shape and ring MSA are presented using modified feeds. Two feed variations namely proximity feed



(a)

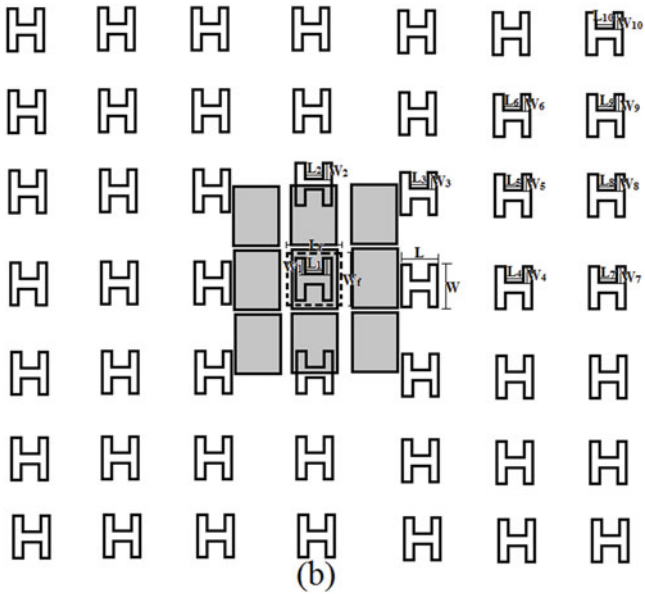


**Fig. 8** **a** Fabricated prototype for  $7 \times 7$  SFA of H-shape MSA fed using proximity fed RMSA, **b** H-shape MSA SFA fed using gap-coupled stacked feed

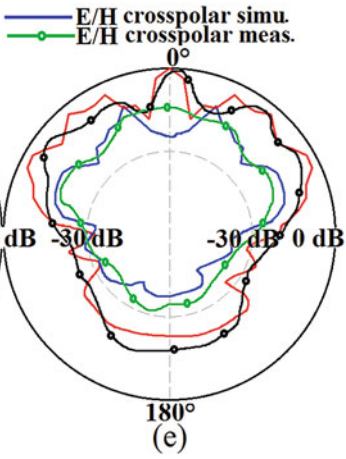
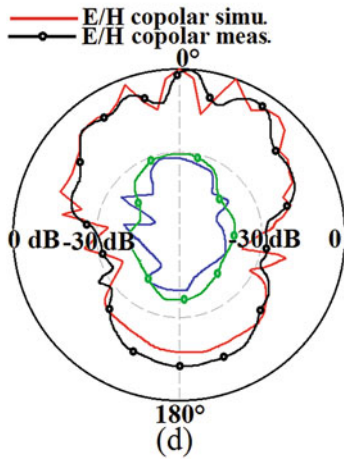
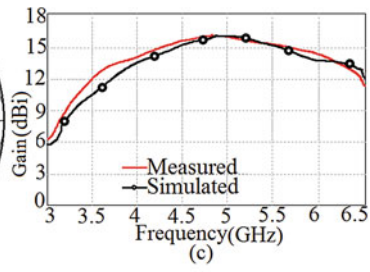
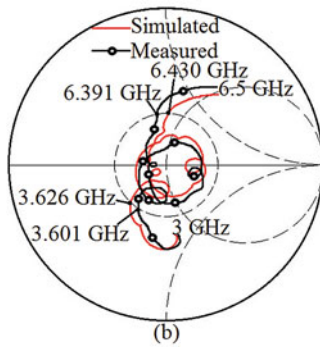
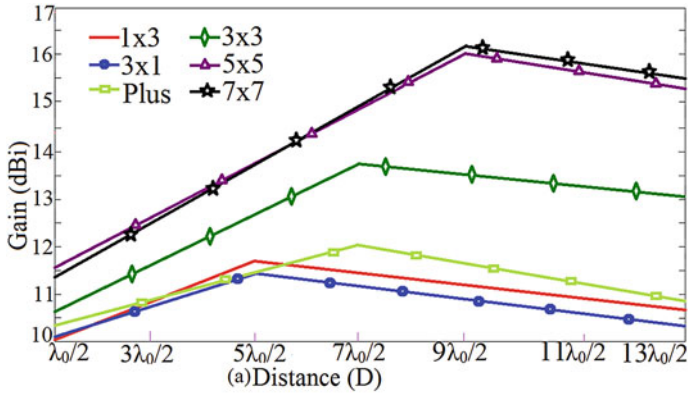


**Fig. 9** a Gain variation against ‘D’, b smith chart, c gain plot and d, e radiation pattern at center frequency of BW for  $7 \times 7$  SFA of H-shape MSA fed using gap-coupled and stacked feed

**Table 4** Gain and BW for H-shape MSA SFA using gap-coupled and stacked feed

SFA	BW, (GHz)	Gain with single proximity feed (dBi)	Gain with 3 × 3 gap coupled feed (dBi)
1 × 3	2.74	10.6	11.67
3 × 1	2.74	10.6	11.31
Plus	2.75	11.34	11.33
3 × 3	2.75	11.94	13.53
5 × 5	2.74	13.2	16.1
7 × 7	2.75	13.54	16.2

**Fig. 10** Fabricated prototype for 7 × 7 SFA of H-shape MSA fed using gap-coupled and stacked feed

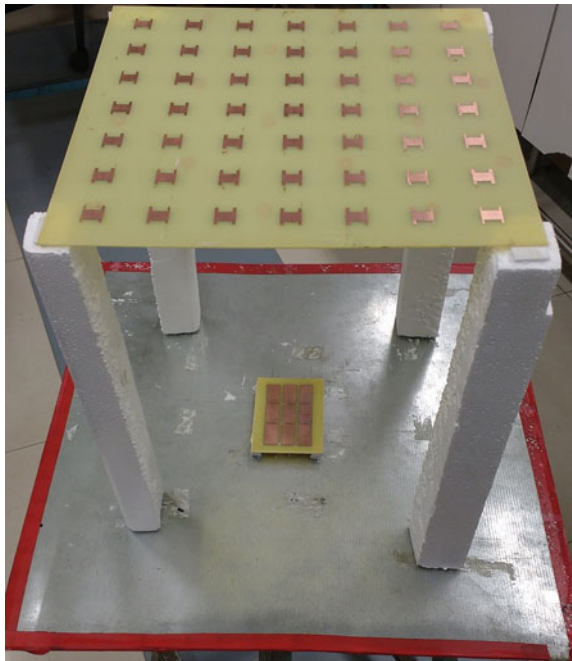


**Table 5** Gain and BW for ring shape MSA SFA using two feed variations

SFA	BW, (GHz)	Gain with single proximity feed (dBi)	Gain with 3 × 3 gap coupled feed (dBi)
1 × 3	2.75	10.15	12.8
3 × 1	2.75	10.14	13.4
Plus shape	2.76	10.63	13.7
3 × 3	2.75	11.05	15.6
5 × 5	2.75	11.55	16.0
7 × 7	2.75	11.66	16.5



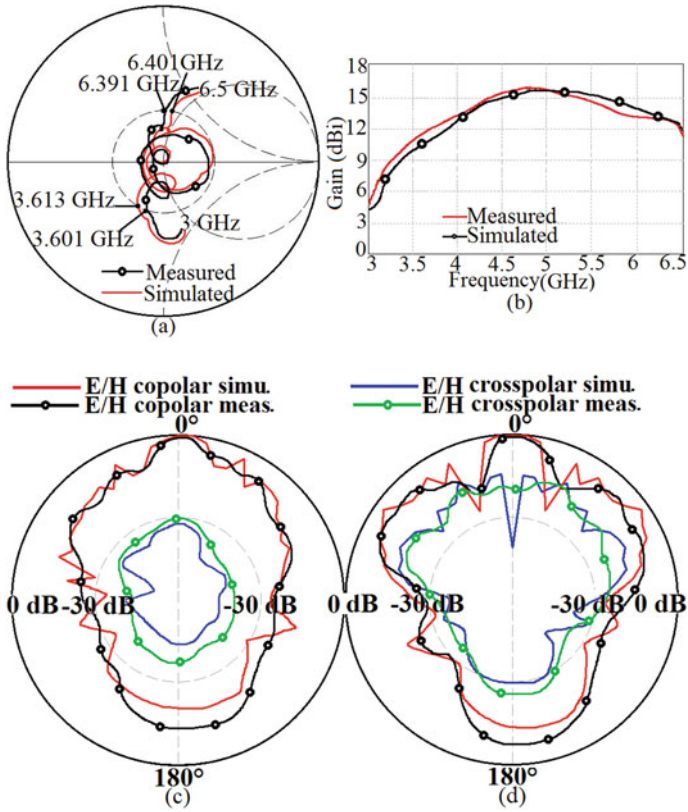
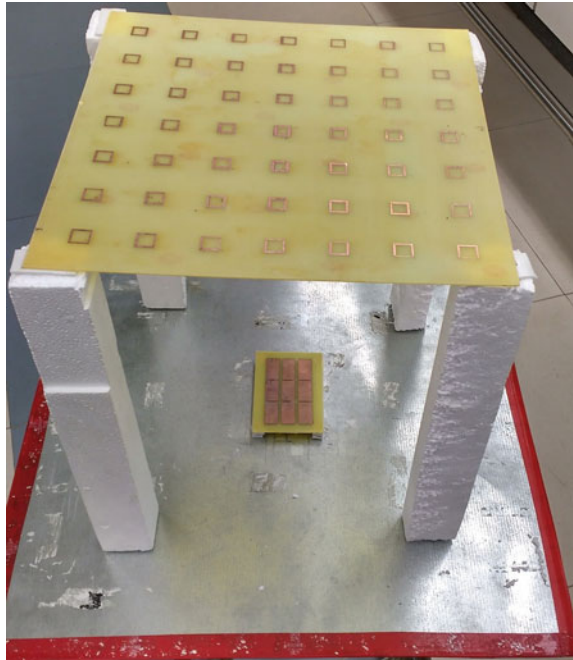


**Fig. 11** a Smith chart, b gain variation over BW, c, d radiation pattern at the center frequency of BW for  $7 \times 7$  SFA of Ring shape MSA fed using gap-coupled and stacked feed

RMSA, gap-coupled and stacked RMSAs using proximity feed RMSA are proposed. The stacked and gap-coupled feed yields uniform excitation of all the SFA elements that yields optimum result in terms of BW and gain. Amongst all the variations, using  $7 \times 7$  H-shape and ring MSA SFA, maximum BW of above 2.5 GHz with gain greater than 16 dBi is obtained.

**Fig. 12** Fabricated prototype of  $7 \times 7$  SFA using Ring shape MSA fed using gap-coupled and stacked feed



## References

1. James JR, Hall PS (1989) Handbook of microstrip antennas, vol I. London Peter Peregrinus
2. Balanis CA (2003) Antenna theory and design, 3rd edn. Artech House, USA
3. Kumar G, Ray KP (2003) Broadband microstrip antennas. Artech House
4. Wong KL (2003) Compact and broadband microstrip antennas, 1st edn. Artech House, USA
5. Ge Y, Esselle KP, Bird TS (2004) A broadband E-shape patch antenna with a microstrip-compatible feed. *Microwave Optical Technol Lett* 42(2):111–112
6. Islam MT, Shakib MN et al (2009) Multi-slotted microstrip patch antenna for wireless communication. *Progress Electromagn Res Lett* 10:11–18
7. Gautam AK, Bishta A, Kanaujia BK (2015) A wideband antenna with defected ground plane for WLAN/WiMAX applications. *Int J Electron Commun* 1–5
8. Neyestanak AA, Kashani FH, Barkeshli K (2007) W-shaped enhanced-bandwidth patch antenna for wireless communication. *Wireless Personal Commun J* 43:1257–1265
9. Simons RN (2000) Suspended patch antennas with electromagnetically coupled inverted microstrip feed for circular polarization. In: *International symposium on antennas and propagation (AP-S) digest, vol 2*, Salt Lake City, UT, USA, pp 992–995
10. Niyomjan G, Huang Y (2006) A suspended microstrip fed slot antenna on high impedance surface structure. In: *First European conference on antennas and propagation, nice*, pp 1–4
11. Chine P, Kumar G (2005) Three dimensional, efficient, directive microstrip antenna array. *IEEE antennas and propagation society international symposium, Washington, USA*, pp 243–246
12. Bhide R, Kumar G (2010) Circularly polarized space-fed microstrip antenna arrays. *Microwave Optical Technol Lett* 52(10):2221–2223
13. Shafai L, Sharma SK, Dameshmand M, Mousari P (2006) Phase shift bandwidth and scan range in microstrip arrays by the element frequency tuning. *IEEE Trans Antenna Propag* 54:1467–1473

14. Mishra PK, Kumar G (2012) Dual polarized circular microstrip space-fed antenna array design with high isolation and broad bandwidth. In: International conference on devices, circuits and systems (ICDCS) 2021, Coimbatore, pp 540–544
15. Bhide R, Kumar G (2010) Equivalence of space-fed microstrip antenna with horn antenna. *Microwave Optical Technol Lett* 52(5):1180–1183
16. Song Q, Zhang XX (1992) Broadband gap-coupled microstrip antenna arrays. In: International symposium on antennas and propagation (AP-S) Digest, Chicago, IL, USA, vol 4, pp 1939–1942

# Rectangular Slot Cut Sectoral Microstrip Antenna for Broadband Response



Venkata A. P. Chavali, Amit A. Deshmukh, and Aarti G. Ambekar

**Abstract** Simple design of a sectoral microstrip antenna with a rectangular slot inserted at its vertex is proposed in this paper. The sectoral antenna behavior is studied by varying the sectoral angle from  $110^{\circ}$  to  $150^{\circ}$ . The sectoral microstrip antenna without the slot realized wideband response due to the space tuning between  $TM_{10}$  and  $TM_{02}$ . A simulated bandwidth of 0.715 GHz (51.5%) is realized in  $120^{\circ}$  sectoral microstrip antenna. Gradual increment in the slot length decreases the frequency of  $TM_{03}$  mode. An optimum bandwidth of 76% with peak gain of 8.12 dBi is realized in  $120^{\circ}$  sectoral microstrip antenna with slot at its vertex due to the space tuning among  $TM_{10}$ ,  $TM_{02}$  and  $TM_{03}$  modes. Simulated results are experimentally verified by fabricating and testing the patch. Broadside radiation patterns are observed at the band start and band stop frequencies of the bandwidth.

**Keywords** Broadband response · Rectangular slot · Sectoral microstrip antenna

## 1 Introduction

Enhancement of the Bandwidth (BW) of the microstrip antenna (MSA) has been the main concern of the researchers over a long time. Simplest technique to achieve wide BW is to adapt multi resonator techniques [1]. Multiple resonances are excited near the fundamental mode frequency by using additional patches in the same plane [2–4] or on the other plane above the fed patch [5–7]. The gain of the antenna is more but due to the addition of parasitic patches, the patch area and volume increases. MSAs using slot cut techniques are relatively simple and wide BW can be realized by cutting slots on a single patch without increasing its area. The surface currents of higher order modes increase with which their frequency decreases near to the fundamental mode frequency. So far so many MSAs with slots of different shapes such as U, E, V and  $\psi$  are reported. The inverted U slot cut MSA reported in [8] realized a wide BW of 68% on relatively thinner substrate. However, the feeding

---

V. A. P. Chavali · A. A. Deshmukh (✉) · A. G. Ambekar  
Department of EXTC Engineering, SVKM's DJSCE, Mumbai, India

arrangement of the antenna is complex. The butterfly shape MSA in [9] has two parallel slots similar to an E-shape MSA realized a BW of 21.5%. But the resonant modes responsible for wider BW are not discussed in the paper. BW enhancement can also be achieved by modifying the shape of a regular shape MSA [10, 11]. Due to the modified shape additional resonances are created which leads to improvement in the BW.

This paper proposes simple configurations of rectangular slot cut sectoral MSA for broadband response. The broadband behavior is explained with the help of surface current distributions. Initially, single sector with  $110^\circ$  sectoral angle for its  $TM_{10}$  mode at 1.2 GHz, is optimized. A wider BW of 0.685 GHz (49.8%) with a peak gain of 8 dBi is realized. This BW is due to the space tuning between  $TM_{10}$  and  $TM_{02}$  modes of the sectoral MSA. Further, a rectangular slot is introduced at the vertex of the sector oriented at half of the sectoral angle. With the gradual increment in the slot length, the higher order  $TM_{03}$  mode frequency reduces. Due to the space tuning between the  $TM_{10}$ ,  $TM_{02}$  and  $TM_{03}$  modes a simulated BW of 1.115 GHz (70.2%) with 8.16 dBi peak gain is realized. This BW is 20.5% greater than the BW of the single sectoral MSA without slot. The broadband behavior of the slot cut sectoral MSA is studied by varying the sectoral angle from  $120^\circ$  to  $150^\circ$ . A maximum impedance BW of 1.195 GHz (73.2%) with a peak gain of 8.12 dBi is realized by  $120^\circ$  slot cut sectoral MSA. The slot cut sectoral MSA is initially simulated and optimized using CST software [12]. The experimental verification is done by testing the fabricated patch using ZVH 8, FSC 6 and SMB 100A on a square ground plane of side 30 cm. The antenna gain is measured using the three-antenna method. A reference wideband horn antenna is used in the measurement of radiation pattern. Broadside radiation pattern across the entire BW is observed. Simulated and measured results are observed to be in good agreement. Through the paper the dimensions are specified in 'cm' and frequency in 'GHz'.

## 2 Rectangular Slot Cut Sectoral MSA

The configuration of proximity fed rectangular slot cut sectoral MSA is shown in Fig. 1a, b. Initially, a single sector of ' $\alpha$ ' =  $110^\circ$  is chosen for its  $TM_{10}$  mode at 1.2 GHz. The sectoral MSA is optimized on suspended FR4 substrate ( $\epsilon_r = 4.3$ ,  $\tan\delta = 0.02$ ,  $h = 0.16$  cm) of total thickness 2.56 cm ( $0.104 \lambda_g$ ). A practically realizable value of air gap ' $h_a$ ' = 2.4 cm is chosen. The radius of the sector ' $R$ ' is calculated using the resonance frequency equation of a rectangular MSA (RMSA) by equating the sector radius equal to length of the RMSA. This is followed by parametric optimization. The value of ' $R$ ' is obtained as 10.3 cm. The sectoral MSA is fed by a square proximity strip of length ' $l_f$ ' = 1.8 located at ' $h_s$ ' = 2, ' $x_f$ ' = 2.6 cm. A simulated BW of 0.685 GHz (49.8%) with a peak gain of 8 dBi is realized. This BW is due to the space tuning between  $TM_{10}$  and  $TM_{02}$  modes of the sectoral MSA. Further, the behavior of the sectoral MSA is studied by varying the sectoral angle from  $120^\circ$  to  $150^\circ$  by keeping its radius constant. The variation in resonant

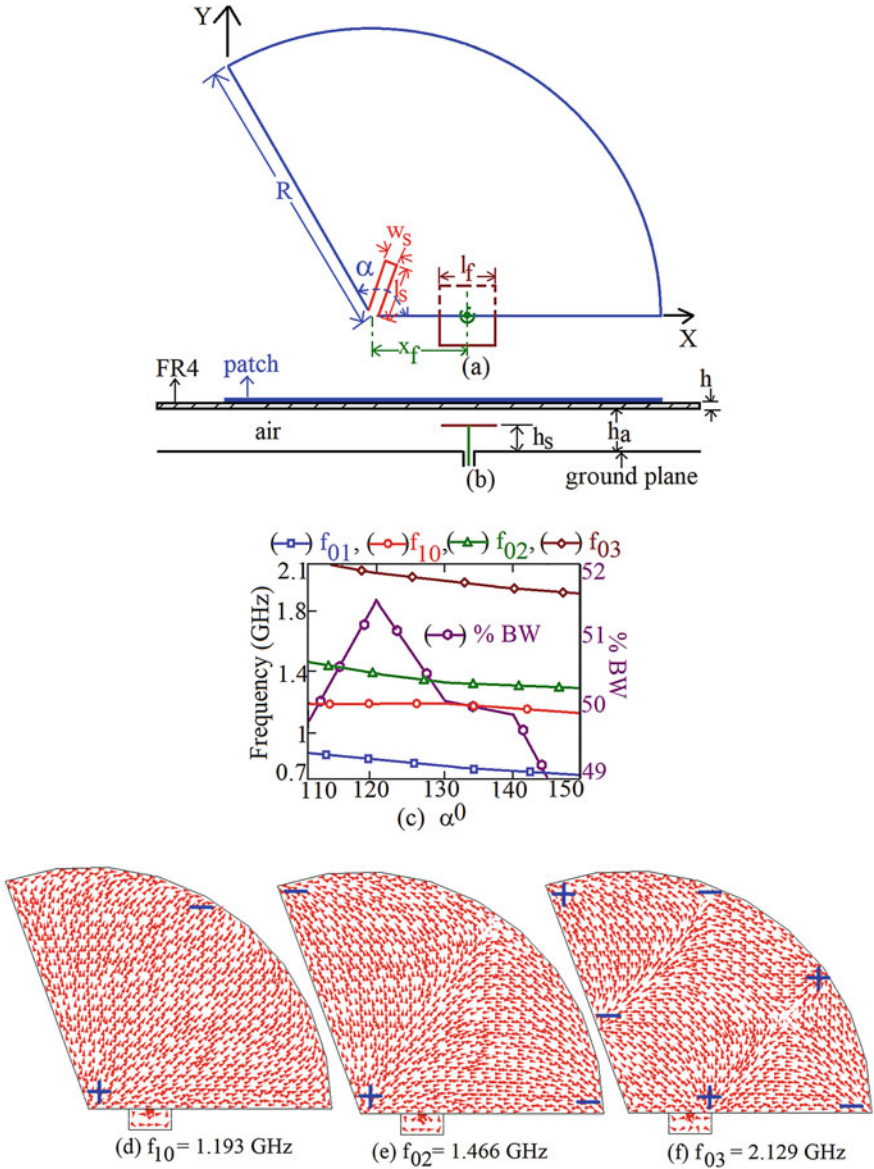


**Fig. 1** a, b Rectangular slot-loaded sectoral MSA, c variation in resonant frequencies and % BW with ' $\alpha$ ', d–f surface current distributions of resonant modes of  $110^\circ$  sectoral MSA

frequencies and % BW with varying sectoral angle is shown in Fig. 1c. The simulated surface current distributions are shown in Fig. 1d–f. It can be observed from Fig. 1c that with the increment in ‘ $\alpha$ ’ the spacing between  $TM_{10}$  and  $TM_{02}$  mode frequencies reduces which is due to the increment in the arc length of the sector. However, due to the impedance tuning the sectoral MSA with  $120^\circ$  sectoral angle realizes a maximum simulated BW of 0.715 GHz (51.5%). With respect to the feed location, excitation of  $TM_{01}$  mode is observed whose frequency reduces with increment in the sectoral angle. Though the higher order  $TM_{03}$  mode is excited in the sector, the frequency of this mode falls outside  $VSWR = 2$  circle.

As discussed earlier, the next higher order mode observed on the sectoral MSA is  $TM_{03}$ . The BW of the sectoral MSA can be further enhanced by reducing the frequency of this mode near to the frequencies of  $TM_{10}$  and  $TM_{02}$  modes. This can be achieved by inserting a slot at the maximum current location of the  $TM_{03}$  mode. As observed from Fig. 1f, the maximum current location of  $TM_{03}$  mode is at the vertex of the sector. Thus, a rectangular slot is cut at the vertex and the length ‘ $l_s$ ’, width ‘ $w_s$ ’ and angle of the slot are parametrically optimized. With the increment in slot length reduction in the frequency of  $TM_{03}$  mode is observed as shown in Fig. 2a. With respect to the position of the slot no significant change is observed in the frequencies of  $TM_{10}$  and  $TM_{02}$  modes. The optimum dimensions of slot are ‘ $l_s$ ’ = 2.4, and ‘ $w_s$ ’ = 0.4 cm. On varying the angle of the slot, optimum BW is observed for ‘ $\alpha/2$ ’ which is equal to  $55^\circ$ . The simulated surface current distributions of slot cut  $110^\circ$  sectoral MSA of various resonant modes are shown in Fig. 2b–d.

A simulated BW of 1.090 GHz (69%) with a peak gain of 8.16 dBi is realized as shown in Fig. 3a. The simulated radiation patterns at band start and band stop frequencies of the BW are shown in Fig. 3b, c where E and H planes are oriented along  $\Phi = 55^\circ$  and  $145^\circ$ , respectively. Broadside patterns are observed with increased cross-polarization which is attributed to the bidirectional variations of the currents of the resonance modes responsible for the BW.

Further, the broadband behavior of the slot cut sectoral MSA is studied by varying the sectoral angle from  $120^\circ$  to  $150^\circ$ . In all the slot cut sectoral MSAs the slot is oriented at an angle ‘ $\alpha/2$ ’. All the antennas are individually optimized and the dimensions of slot cut sectoral MSAs for varying sectoral angle are given in Table 1. It can be seen that the slot length required in optimum configurations of sectoral MSA with  $120^\circ$  to  $150^\circ$  is smaller than that of  $110^\circ$ . This is due to the increased arc length at higher angles in comparison to the arc length at  $110^\circ$  sector. Variation in different parameters such as modal frequencies, frequency ratio, % BW and gain with respect to sectoral angle is shown in Fig. 4a, b. It can be seen that largest simulated BW is realized by the rectangular slot cut sectoral MSA with  $120^\circ$  sectoral angle. Almost constant gain response is observed for the slot cut sectoral MSAs with  $110^\circ$  to  $130^\circ$ . However, reduction in gain is observed due to increased orthogonal currents at higher angles. A simulated BW of 1.195 GHz (73.2%) with peak gain of 8.12 dBi is realized. Further, the simulated results of slot cut sectoral MSAs are experimentally verified by fabricating the patches and conducting the measurements. The simulated and measured results of  $120^\circ$  and  $140^\circ$  slot cut sectoral MSA are shown in Fig. 4c. The rectangular slot cut sectoral MSA with  $120^\circ$  sector realized

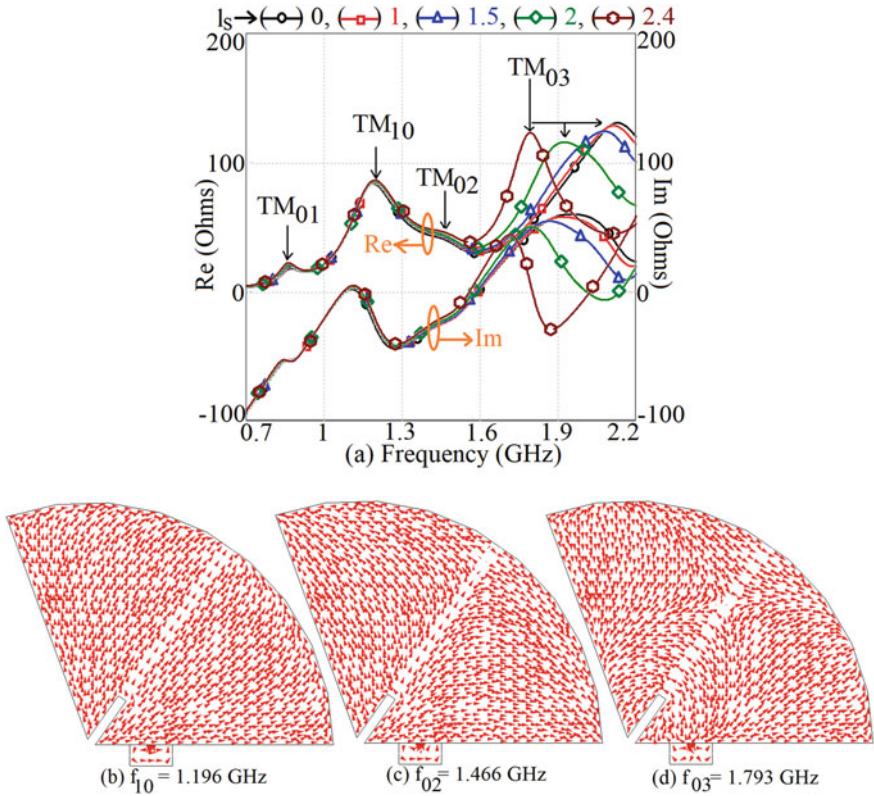


**Fig. 2** a Variation of resonant modes with slot length, b–d simulated surface current distributions at various resonant modes of rectangular slot cut  $110^\circ$  sectoral MSA

a measured BW of 1.237 GHz (76%). Similarly, slot cut sectoral MSA with  $140^\circ$  sector realized simulated and measured BWs of 1.013 GHz (65%) and 1.063 GHz (68%), respectively, with 7.8 dBi peak gain.

The fabricated prototype of rectangular slot cut sectoral MSA with ‘ $\alpha$ ’ =  $140^\circ$  and its simulated and measured radiation patterns observed at band start and band stop frequencies of the BW are shown in Fig. 5a–e. Here, the E and H planes are oriented along  $70^\circ$  and  $160^\circ$ , respectively. Broadside radiation patterns are observed with increased cross-polar component due to the bidirectional current variations.



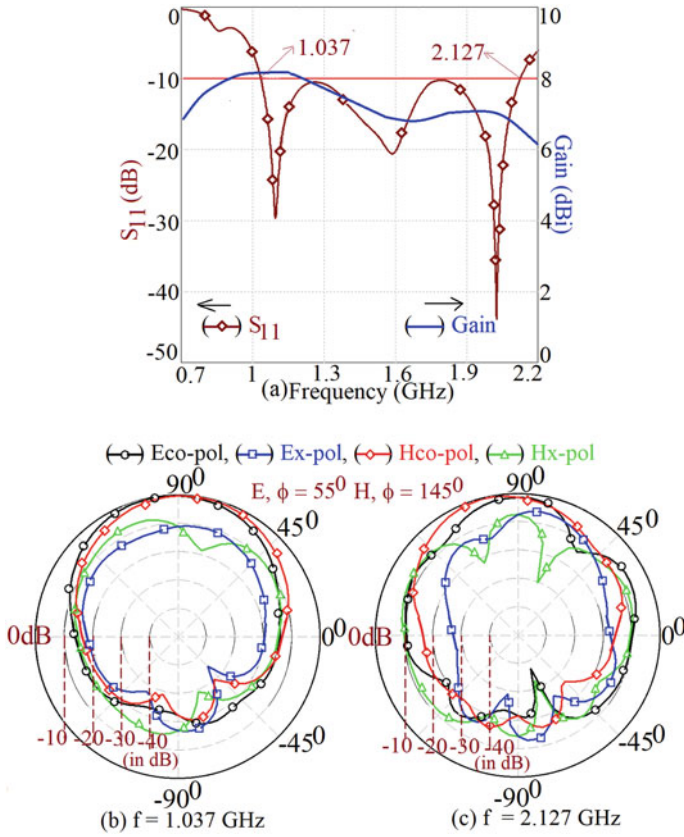


**Fig. 3** Simulated **a**  $S_{11}$  and gain plots, **b, c** radiation patterns nearer to the band start and band stop frequencies of rectangular slot cut  $110^\circ$  sectoral MSA

**Table 1** Dimensions of various parameters for the slot cut sectoral MSA for varying angles

$\alpha$ ( $^\circ$ )	h (cm)	$h_s$ (cm)	R (cm)	$l_s$ (cm)	$w_s$ (cm)	$x_f$ (cm)	$l_f$ (cm)	BW (GHz, %)	Peak Gain (dBi)
110	2.56	2.0	10.3	2.4	0.4	2.6	1.8	1.090, 69%	8.16
120	2.56	2.0	10.3	2.0	0.4	2.6	1.8	1.195, 73.2	8.12
130	2.56	1.8	10.3	2.0	0.4	2.6	2.2	1.048, 66.16	8.18
140	2.56	1.8	10.3	2.0	0.4	2.6	2.2	1.013, 64.66	7.8
150	2.56	1.8	10.3	2.0	0.4	2.1	2.2	0.972, 63	7.38

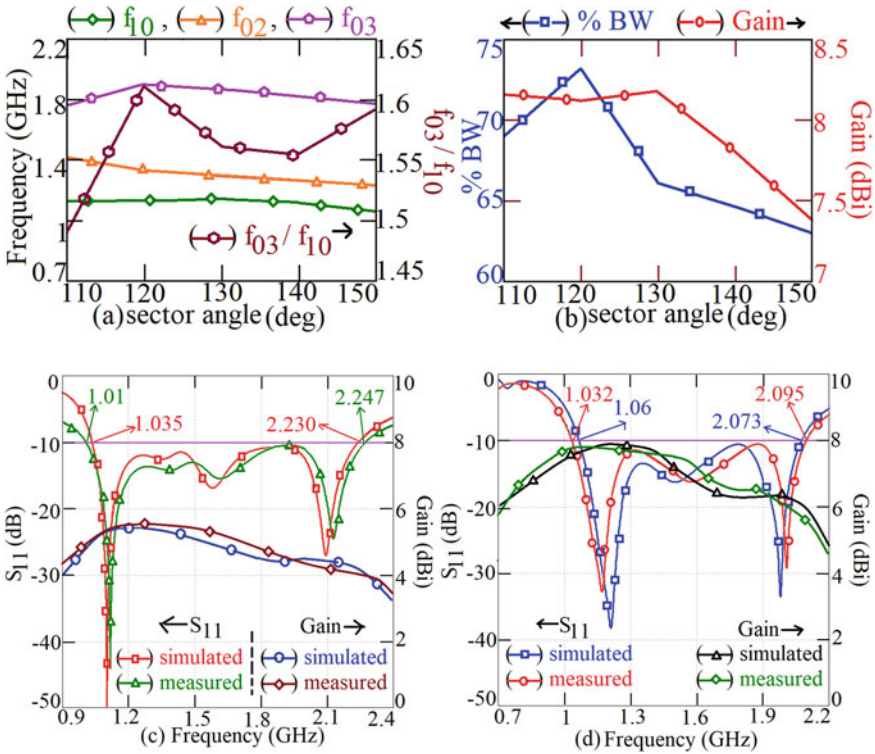
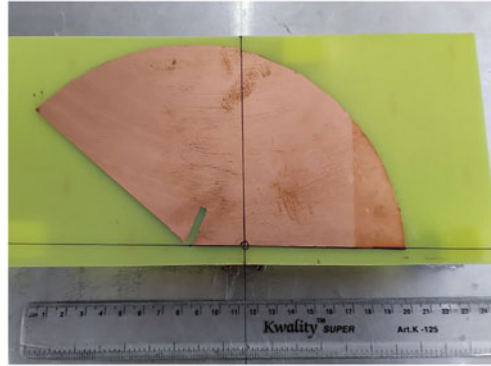


**Fig. 4** Variation in **a** resonant frequencies, frequency ratio, **b** % BW and gain with ‘ $\alpha$ ’ of a slot cut sectoral MSA, and  $S_{11}$  and gain plots of rectangular slot cut sectoral MSA of **c** 120° sector, **d** 140° sector

### 3 Conclusions

Detailed study of a simple rectangular slot cut sectoral MSA is presented in this paper. The resonant modes responsible for broadband behavior are identified through the surface current distributions. The sectoral antenna behavior is studied by varying the sectoral angle from 110° to 150°. The sectoral microstrip antenna without the slot realized wideband response due to the space tuning between  $TM_{10}$  and  $TM_{02}$ . Gradual increment in the slot length decreases the frequency of  $TM_{03}$  mode. An optimum bandwidth of 1.237 GHz (76%) with peak gain of 8.12 dBi is realized in rectangular slot cut 120° sectoral microstrip antenna due to the space tuning among  $TM_{10}$ ,  $TM_{02}$  and  $TM_{03}$  modes. All the antennas exhibited broadside radiation patterns with increased cross-polarization. This elevated cross-polarization is attributed to the bidirectional current variations.



(a)

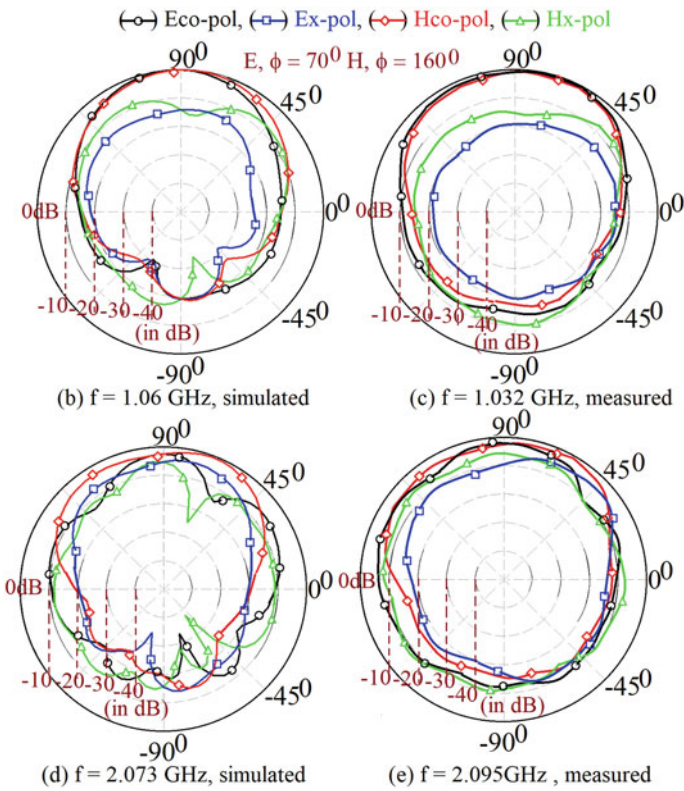


**Fig. 5** a Fabricated prototype, b–e radiation patterns at band start and band stop frequencies of the BW of rectangular slot cut  $140^\circ$  sectoral MSA

## References

1. Kumar G, Ray KP (2003) Broadband microstrip antennas. Artech house
2. Kandwal A, Khah SK (2013) A novel design of gap-coupled sectoral patch antenna. *IEEE Antennas Wirel Propag Lett* 12:674–677
3. Cao Y, Cai Y, Cao W, Xi B, Qian Z, Wu T, Zhu L (2019) Broadband and high-gain microstrip patch antenna loaded with parasitic mushroom-type structure. *IEEE Antennas Wirel Propag Lett* 18(7):1405–1409
4. Chavali V, Deshmukh A, Ambekar A (2020) Modified rectangular microstrip antenna for wide-band response with conical radiation pattern. In: Proceedings of 3rd international conference on communication system, computing and it applications (CSCITA)—2020, Mumbai, India, pp 88–93
5. Katyal A, Basu A (2017) Analysis and optimisation of broadband stacked microstrip antennas using transmission line model. *IET Microwaves Antennas Propag* 11(1):81–91
6. Chopra R, Kumar G (2020) Broadband and high gain multilayer multi resonator elliptical microstrip antenna. *IET Microwaves Antennas Propag* 14(8):821–829
7. Li D, Guo P, Dai Q, Fu Y (2012) Broadband capacitively coupled stacked patch antenna for GNSS applications. *IEEE Antennas Wirel Propag Lett* 11:701–704
8. Radavaram S, Pour M (2018) Wideband radiation reconfigurable microstrip patch antenna loaded with two inverted U-slots. *IEEE Trans Antennas Propag* 67(3):1501–1508
9. Tiwari RN, Singh P, Kanaujia BK (2017) Butter fly shape compact microstrip antenna for wideband applications. *Progress Electromagn Res* 69:45–50
10. Abbaspour M, Hassani HR (2008) Wideband star-shaped microstrip patch antenna. *Progress Electromagn Res* 1:61–68
11. Chavali A, Ambekar A, Kadam A, Deshmukh A, Ray KP (2020) Compact stub loaded modified plus shape microstrip antenna for broadband response. In: ICCCE—2019. Springer, Singapore, pp 111–117
12. CST Microwave Studio, Version 2019

# Analysis and Design of Variations of Planar Inverted F-shape Microstrip Antennas for Wider Bandwidth



Mohil Gala, Amit A. Deshmukh, and Aarti G. Ambekar

**Abstract** Variations of planar inverted F-antennas, widely referred to as PIFA antennas have been reported for the wideband response. In the reported papers, a detailed study highlighting the effects of modification made in the PIFA structure on its resonant modes and impedance at them is not provided. In this paper, a detailed review-based study for different variations of PIFA antennas is presented to put forward the original explanation behind the wideband response achieved. In some of the designs detailed re-designed procedure is presented which helps in the realization of a similar PIFA antenna at a different frequency. Thus, a detailed review-based study supported with a detailed understanding of the wideband response is the main technical contribution in the present paper.

**Keywords** Broadband microstrip antenna · Compact microstrip antenna · Planar inverted F-antenna (PIFA)

## 1 Introduction

With the increasing demands of wireless communication systems and the subsequent developments in the same, the need for compact and wideband antennas that are conformal to the holding surface has increased. Owing to numerous advantages, variations of shorted microstrip antenna (MSA), more commonly referred to as planar inverted F-antenna (PIFA) are widely selected as they offer very larger bandwidth (BW) for smaller patch size [1–4]. The wideband response in PIFA designs is achieved by using either the shorting post or slot cut in the patch or by using a modified feed design [5–8]. However, in the reported work, a thought process behind modifying the PIFA geometry with their effects on the frequencies and impedance levels of the resonant modes of the PIFA patch is not explained in detail. This is essential since it provides a better understanding of the functioning of the shorted patch which further can lead to a design methodology. This paper provides a detailed

---

M. Gala · A. A. Deshmukh (✉) · A. G. Ambekar  
Department of EXTC, SVKM's DJSCE, Mumbai, India

review-based study for different variations of wideband PIFA antennas. It is shown that wideband response is achieved due to the modifications in the frequency and impedance levels at fundamental and higher-order resonant modes of the PIFA patch. Based on this understanding developed, further in some of the PIFA designs, design methodology based on the parametric formulation is presented. The antennas re-designed using them around the given fundamental mode frequency yields a similar wideband response. Thus, an in-depth study to explain the wideband behavior of variations of PIFA antennas is the main technical influence in the present work. The antennas are studied using the IE3D simulation software further by experimentation using ZVH 8, FSC 6, and SMB 100A, in some of the PIFA variations. A ground plane size of  $30 \times 30$  cm is selected in the experimentation and an SMA panel type connector of inner wire diameter 0.12 cm is selected to feed the antennas.

## 2 Analysis of Folded Patch L-slot Cut Shorted MSA

A variation of PIFA antennas, L-slit cut folded patch shorted MSA is revealed in Fig. 1a, b [5]. The structure is fabricated on an air substrate of thickness 0.7 cm. For the reported structure, the inner portion of the L-slot is folded downward and resembles the original L-slot when viewed from the top. The folded inner patch is fed by a shorter co-axial feed which decreases the probe inductance thereby improving the antenna BW considerably. To understand the wideband response in the folded patch feed, its detailed investigation is presented in this paper. The reported configuration is simulated in IE3D. The corresponding smith chart, resonance curve plot is revealed in Fig. 2a, b. Three peaks respectively at 2.27, 5.96 GHz, and 10.424 GHz are observed as per the resonance curve. Because of the optimum spacing between resonant modes at 2.27 and 5.96 GHz, a loop is formed in the smith chart inside  $VSWR = 2$  circles yielding simulated BW from 4.64 to 7.039 GHz. Vector surface current distributions

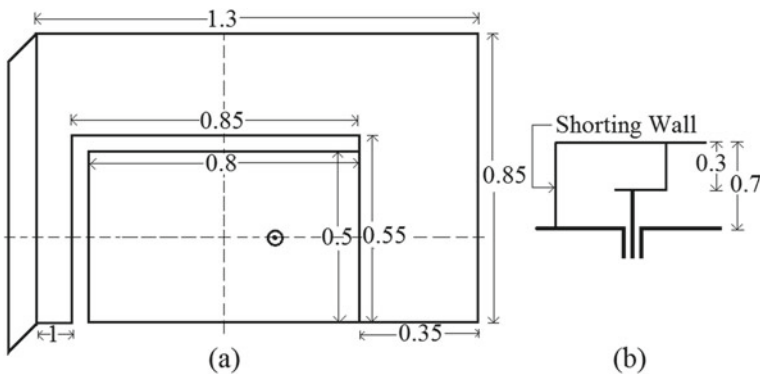


**Fig. 1** a Top and b side views of PIFA embedded with L-shape slot

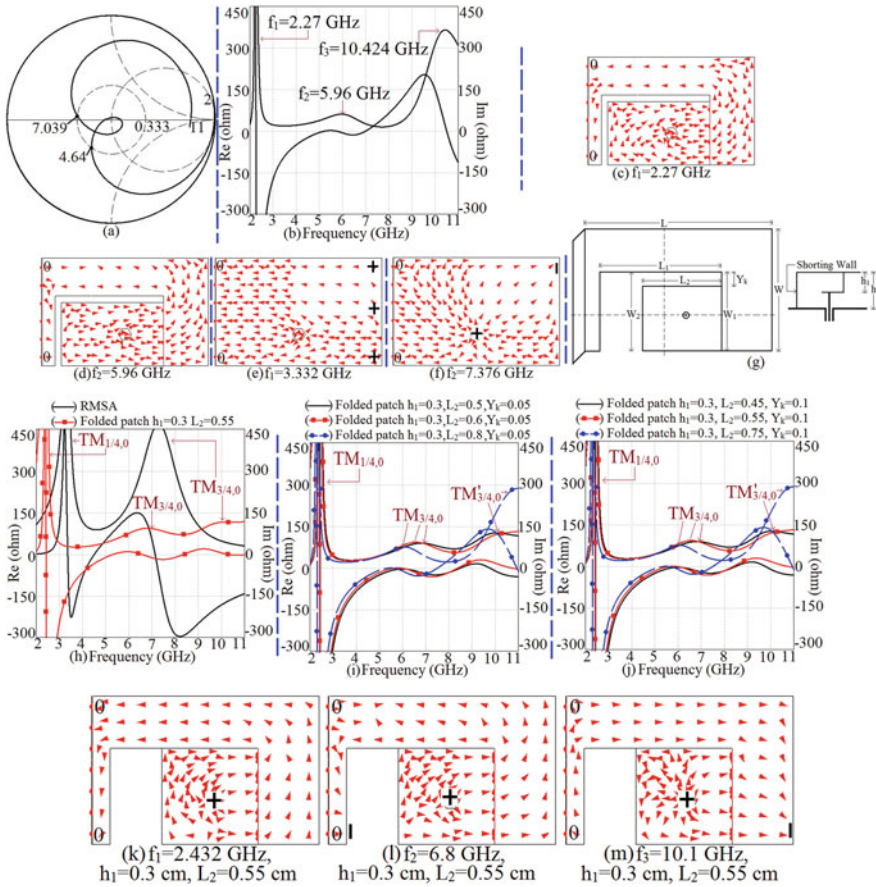


**Fig. 2** a Smith chart, b resonance curve plots and c, d surface current distribution at first two resonant modes for optimum design of PIFA using L-shape folded feed, e, f surface current distribution at first two modes for shorted PIFA design, g schematic of PIFA with slot, and its h-j resonance curve plots and k-m surface current distribution

at the first two resonant peaks are as per Fig. 2c, d, exhibit variations from L-shape feed portion and toward the shorted patch edge. Initially, the structure without any folded inner patch is studied. The shorted RMSA of dimensions  $L = 1.5$  and  $W = 0.85$  cm is fed directly using the coaxial feed of 0.1 cm diameter. The resonance curve plots with the surface current variations for the shorted RMSA are revealed in Fig. 2e, f, h. Two peaks are observed in the resonance curve. With reference to the current distribution observed, two modes are  $TM_{1/4,0}$  and  $TM_{3/4,0}$ .

Inside the shorted RMSA a rectangular slot of length  $L_1$  is cut. That portion of the patch is folded to get the stepped inner patch with length ' $L_2$ ', as shown in Fig. 2g. The folded inner patch dimensions are  $h_1 = 0.3$  cm and  $L_2 = 0.55$  cm and the addition of these two dimensions equals ' $L_1$ '. The inner folded patch is fed with a

coaxial feed. The resonant modes for the folded inner patch are shown in Fig. 2h. The surface current distribution for the resonant modes is shown in Fig. 2k–m. When the slot is embedded followed by the folding of the equivalent patch the current length increases which reduces the mode frequency. Three resonant modes are observed in the resonance curve. The first mode is the fundamental patch  $TM_{1/4,0}$  mode which gets reduced due to the incrementing current path length. Other resonant modes are the  $TM_{3/4,0}$  mode as well as the higher-order  $TM'_{3/4,0}$  which is a degenerated mode.

Inside folded inner patch  $Y_k = 0.05$  cm as seen in Fig. 2g is cut from all the sides to get the L-slot shape from the top. The height  $h_1 = 0.3$  cm is kept constant and the length  $L_2$  is increased in steps as shown from the resonance curve plots in Fig. 2i. With the increase in the length  $L_2$  the current path length increases which reduces the mode frequencies as per the resonance curve plot. The length  $L_2$  is increased to 0.8 cm so that it represents the L-slot from the top as reported in [5]. An impedance BW of 41% as reported in [5] is observed. The patch is further analyzed by doing a complete parametric study. Next, the slot of  $Y_k = 0.1$  cm is cut and the patch length  $L_2$  is increased in steps shown in Fig. 2j. The  $TM_{3/4,0}$  mode frequency reduces as shown in the Figure. Next, the inner folded patch length is varied with inner patch height equal to  $h_1 = 0.4$  cm and  $L_2 = 0.45$  cm, where the total patch length is equal to the slot length  $L_1$ . The vector current variations for this length as per Fig. 3a–c, show presence of  $TM_{1/4,0}$  and higher-order  $TM_{3/4,0}$  modes. The resonance curve plot is shown in Fig. 3d. Further, the slot of  $Y_k = 0.05$  cm is cut and the inner patch length  $L_2$  is varied in steps as shown in Fig. 3d. The frequency at the resonant modes reduces due to the increase in the patch folded length. The slot of  $Y_k = 0.1$  cm is further cut inside the inner folded patch and the inner patch length is increased in steps as shown in Fig. 3e.

With the increase in the inner patch length, the higher-order  $TM_{3/4,0}$  mode frequency reduces as shown in Fig. 3e. For the folded antenna dimensions of  $h_1 = 0.4$  cm,  $L_2 = 0.475$  cm, and  $Y_k = 0.1$  cm, a wide impedance BW of 106% is achieved. The wide impedance bandwidth is a result of the optimal spacing among the 3 modes the  $TM_{1/4,0}$  and  $TM_{3/4,0}$  degenerated modes because of which a loop is formed inside the  $VSWR = 2$  circle yielding a bandwidth from 4.817 to 15.66 GHz as revealed in Fig. 3f. The resonance curve plot for the optimized structure is revealed in Fig. 3e. A wide impedance BW of 106% which is 65% more as compared to the original reported BW of 52% is observed. Fabricated prototype of the optimized MSA is shown in Fig. 3g. Further, based on this optimization process, the parametric formulation is realized for optimized PIFA with an L-shape slot, and the same is presented below, with reference to Fig. 4.

The fundamental mode frequency is calculated using Eq. (1). Further all the antenna parameters are expressed in terms of wavelength and patch dimensions of shorted PIFA without L-shape slot feed and using them, respective dimensions are calculated at given specific frequency. Various antenna dimensions are expressed as;  $h = 0.079\lambda_0$ ,  $h_1 = 0.0452\lambda_0$ ,  $L_1 = 0.09605\lambda_0$ ,  $W_1 = 0.06215\lambda_0$ ,  $L_2 = 0.053675\lambda_0$ ,  $W_2 = 0.05085\lambda_0$ ,  $X_t = 0.0113\lambda_0$ ,  $X_k = 0.04237\lambda_0$ ,  $Y_k = W_1 - W_2$ ,  $X_p = 0.0254\lambda_0$ ,  $W = 0.654L$ . Antennas were re-designed at 1 and 2 GHz and their dimensions are given in Table 1. Re-design antennas yields similar wideband response with BW >



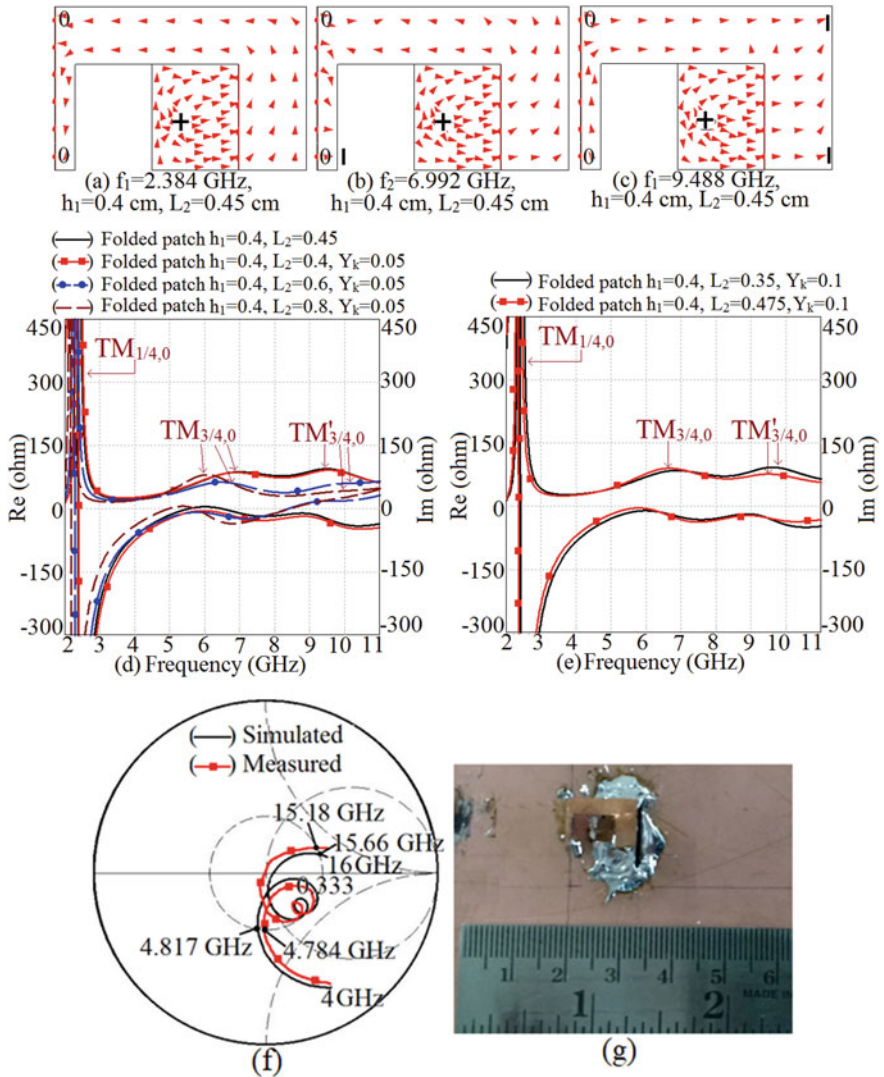


**Fig. 3** a–c Surface current distribution for the folded inner patch for  $h_1 = 0.4$  cm and **d, e** resonance curve plot for different folded inner patch lengths, **f** smith chart and **g** fabricated prototype for optimum design

100%.

$$\lambda_0/4 = L + 1.3h \tag{1}$$

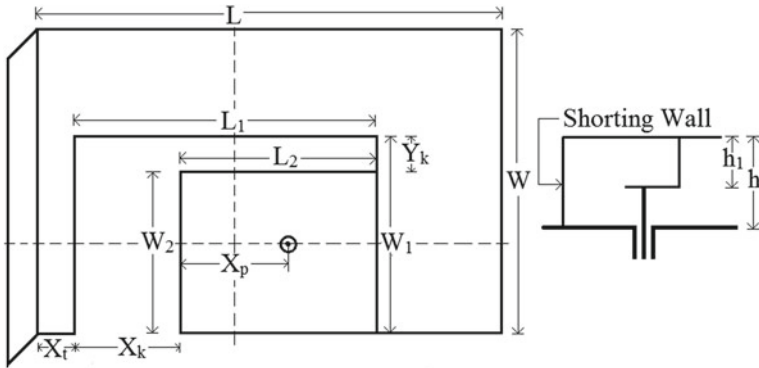


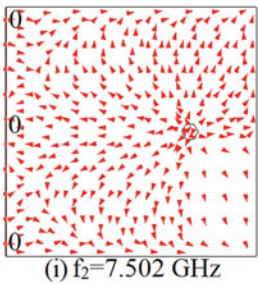
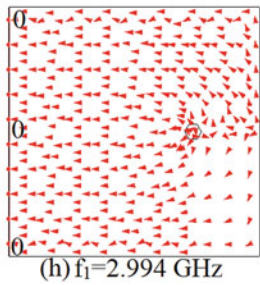
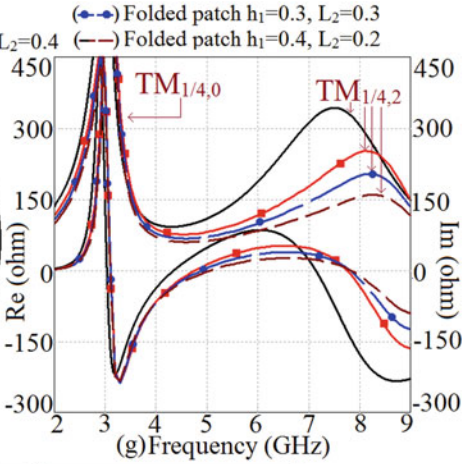
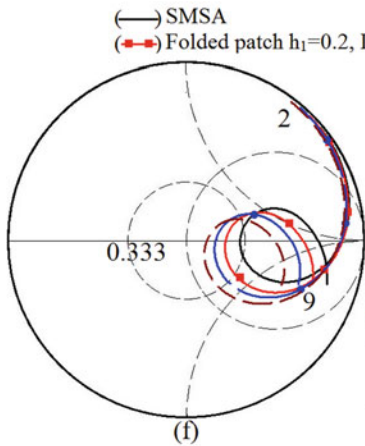
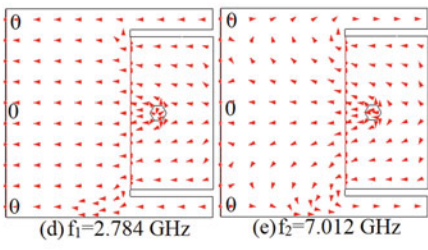
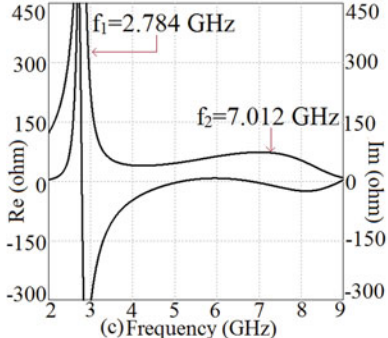
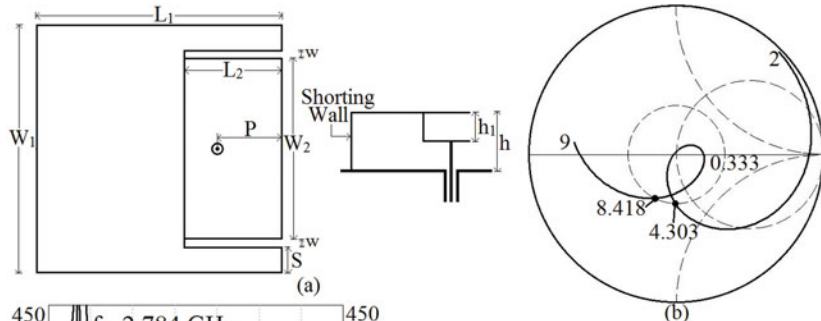
**Fig. 4** a, b Schematic for redesigning of PIFA with L-shape slot feed

**Table 1** Dimensions for re-design PIFA using L-shape slot feed

Parameters	$f_{TM1/4,0} = 1 \text{ GHz}$	$f_{TM1/4,0} = 2 \text{ GHz}$
Length of the patch (L)	4.42 cm	2.21 cm
Width of the patch (W)	2.9 cm	1.44 cm
Height (h)	2.4 cm	1.2 cm
Folded Height ( $h_1$ )	1.4 cm	0.7 cm
Rectangular Slot length ( $L_1$ )	2.9 cm	1.44 cm
Rectangular Slot width ( $W_1$ )	1.9 cm	0.93 cm
Folded patch length ( $L_2$ )	1.55 cm	0.77 cm
Folded width ( $W_2$ )	1.52 cm	0.76 cm
$R_p$	1.5 mm (5, 0)	0.6 mm (2.7, 0)
BW	107.2%	104.2%

### 3 Folded Patch E-shape Cut Shorted MSA

The folded patch feeding technique of widening the impedance BW is applied to the E-shaped patch antenna in [6]. A wide BW of 65% was reported in the folded patch feed E-shaped patch. An in-depth investigation explaining the broadband response in the reported E-slot folded patch structure is presented here. The E-shaped folded patch structure is as per Fig. 5a [6]. Fabrication of MSA is carried on 0.7 cm air-substrate thickness. For the reported structure, the inner portion of the patch is folded downward and it resembles an original E-shape when viewed from the top. The folded inner patch is fed by a shorter co-axial feed probe that decreases the probe inductance, which improves the antenna BW. To understand the wideband response in the folded patch feed E-shaped antenna structure a detailed analysis is presented.



◀**Fig. 5** **a** Shorted E-shape MSA with folded feed, its simulated **b** smith chart and **c** resonance curve plots, its **d**, **e** surface current distribution at observed resonant peaks, **f** smith chart, and **g** resonance curve plots and surface current distribution at **h**  $TM_{1/4,0}$  and **i**  $TM_{1/4,2}$  modes for shorted MSA

The simulation of the reported configuration is done using IE3D. The respective smith chart, as well as resonance curve plot, is as revealed in Fig. 5b, c. Two resonance modes, respectively, at 2.784 and 7.012 GHz as per the resonance plot. Because of the optimal spacing among these resonant modes, a loop is formed in the smith chart inside  $VSWR = 2$  circles, yielding simulated BW from 4.303 to 8.418 GHz. Surface current distributions at the resonant peaks are as per Fig. 5d, e. Uni-directional currents are observed at the first mode whereas those at the second mode are bi-directional over the shorted patch. Initially, the structure without any folded inner patch is studied. The shorted RMSA of dimensions  $L = 1.5$  and  $W = 1.5$  cm is excited directly by the coaxial-feed of 0.1 cm diameter. The smith chart and resonance curve plots for the shorted RMSA are as per Fig. 5f, g. Two peaks are observed in the resonance curve. The surface current distribution for the two resonant modes is as revealed in Fig. 5h, i. Quarter wavelength variations along the patch length are observed at the first peak which corresponds to the shorted fundamental  $TM_{1/4,0}$  mode. For the next resonant peak, current shows a quarter wavelength variation along the patch length with two half wavelength variations along the patch width which corresponds to the shorted  $TM_{1/4,2}$  mode. Inside the shorted RMSA a rectangular slot of length  $L_2$  is cut and folded downwards to get the folded patch feed structure. The folded stepped patch has a length equal to  $L_1$ . The folded height  $h_1$  is varied. The smith chart and the resonance plots for the varying folded height are revealed in Fig. 5f, g. As the folded height is increased the BW increases from 21% for the  $h_1 = 0.2$  cm to 36% for  $h_1 = 0.4$  cm, this is because as the height has increased the distance between the folded patch and the ground plane reduces for which a shorted probe is mandatory which decreases the probe inductance and increases BW. Further, the impedance at the higher-order  $TM_{1/4,2}$  mode also reduces. A slot of width  $w = 0.05$  cm is cut to get the desired E-shape patch and the folded patch length  $L_2$  is increased in steps as shown in the resonance curve plot in Fig. 6c. The current distribution for the variable folded length is revealed in Fig. 6a, b. As the folded patch length  $L_2$  is increased the effective current patch length increases which reduces the frequency of the resonant modes. The reduction in the mode frequency is seen in Fig. 6c. Due to the frequency reduction, the spacing between the modes gets optimized and a loop is shaped inside the  $VSWR = 2$  circle. Thus, the wide impedance BW is achieved because of the coupling between the  $TM_{1/4,0}$  and  $TM_{1/4,2}$ , which results in the broadband response.

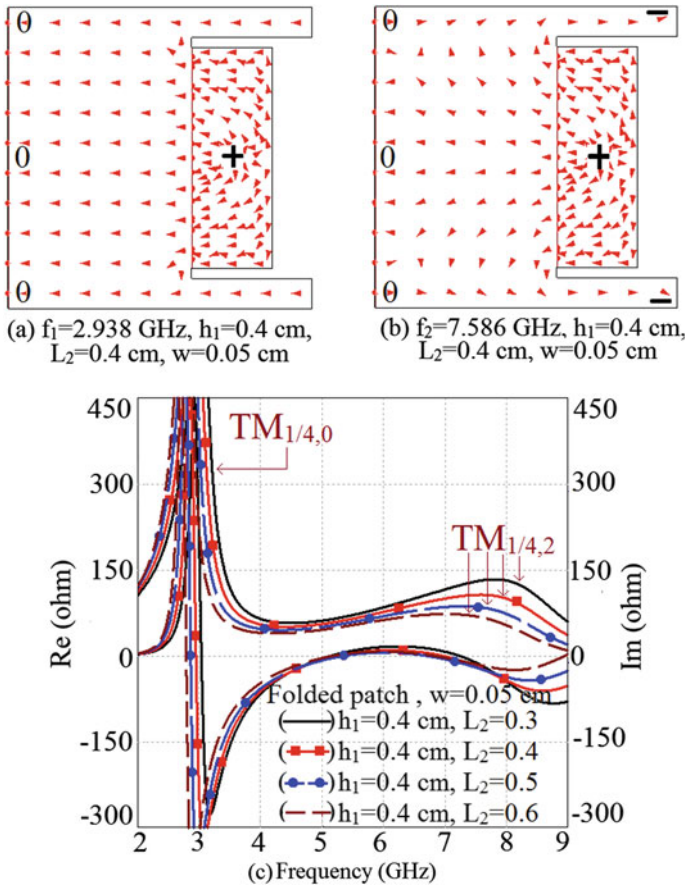
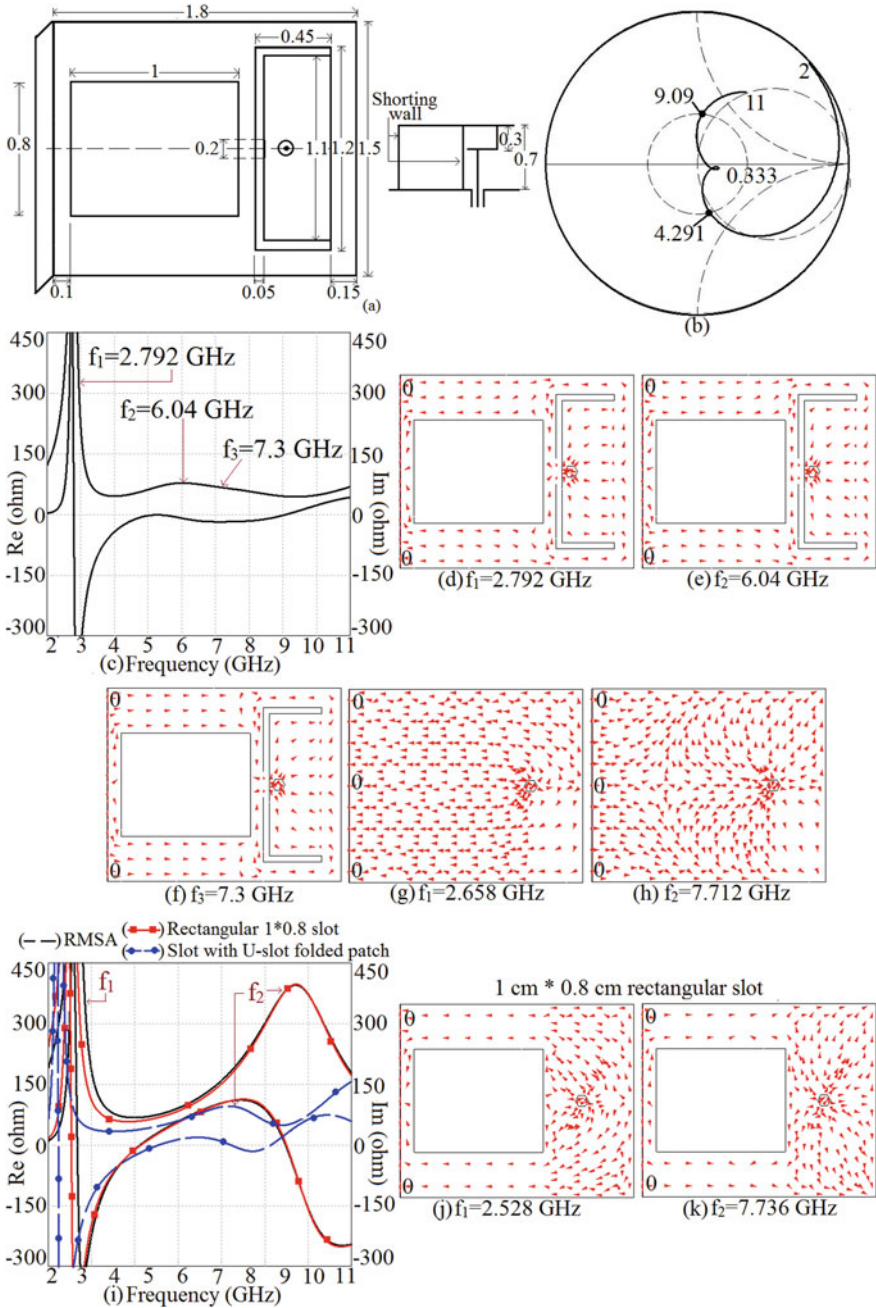


Fig. 6 a, b Surface current distribution for varying folded length and c resonance curve for varying folded length

#### 4 Folded Patch U-slot Cut Shorted MSA with Double Shorting Walls

In [7], a further impedance BW enhancement is achieved with the same overall size and profile as in [5], by introducing an additional shorting wall and a rectangular slot on the upper patch. A BW of 71% is reported compared to the 52% BW reported in [5]. However, in [7], a detailed analysis explaining the wide broadband response due to the rectangular slot and the double shorting walls is not presented. The U-slot folded patch structure with double shorting walls is revealed in Fig. 7a. Fabrication of the structure is carried out on an air-substrate of thickness 0.7 cm. The shorting wall is used for size reduction and also supports the antenna structure. The structure is similar to the structure reported in [5], with an additional rectangular slot



**Fig. 7** a Modified PIFA with rectangular slot and shorting wall, its b smith chart and c resonance curve plots, d–f surface current distribution at observed resonant modes, g, h current distribution for shorted PIFA, i resonance curve plots for varying length, j, k surface current distribution for PIFA with a rectangular slot

and shorting wall for the BW increment. The folded inner patch is fed by a shorter length co-axial feed, which decreases the probe inductance thereby improving the antenna BW substantially. To understand the wideband response in the reported structure a detailed investigation is presented in the paper. Simulation of the reported configuration is carried using IE3D, corresponding smith chart and resonance curve plots are revealed in Fig. 7b, c. Three resonant peaks are observed respectively at 2.792, 6.04, and 7.3 GHz. The optimal spacing between first two resonant modes, yields a loop in the smith chart inside VSWR = 2 circle, resulting in a simulated bandwidth from 4.291 to 9.09 GHz.

The current distributions at the resonant peaks are shown in Fig. 7d–f. A detailed in-depth analysis to study the broadband response in the patch is presented here. Initially, the patch without any slot or the folded inner patch is studied. The shorted RMSA is directly excited using a coaxial feed of 0.1 cm diameter. The surface current distribution and the resonance curve plots for the shorted RMSA are shown in Fig. 7g–i. Two peaks are observed in the resonance curve. The first peak shows quarter wavelength variation along the patch length and is the fundamental  $TM_{1/4,0}$  shorted mode. The next higher-order resonant mode is the combination of the  $TM_{3/4,0}$  and the  $TM_{1/4,2}$  shorted modes. Further inside this shorted patch, the rectangular slot of dimensions  $L_1$  and  $W_1$  as shown in Fig. 8a is cut. The rectangular slot dimensions are varied for the maximum BW and a slot with 1 cm  $\times$  0.8 cm is selected. The current distribution and the resonance curve plot are shown in Figs. 7i–k and 8b, c. Inside this patch, the U-slot folded patch as revealed in Figs. 7a and 8a are introduced with dimensions given.

The current distribution is shown in Fig. 8b, c. The first mode at  $f_1$  corresponds to the shorted  $TM_{1/4,0}$  mode. At next peak  $f_2$  owing to the U-slot cut folded inner patch an open circuit is introduced due to which the  $TM_{1/4,2}$  mode increases and the observed mode is the shorted  $TM_{3/4,0}$  mode and owing to the folded patch feed a shorted feed is essential for reducing the probe inductance as seen from the resonance curve plot in Fig. 7i. The BW increases from 22% for the rectangular slot cut a patch to 63% for the folded patch feed due to the coupling between the resonant modes.

To further enhance the BW an additional shorting wall is introduced into the structure. Shorting wall of width  $w_s$  is introduced as shown in Figs. 7a and 8a. The width of the shorting wall is varied for the BW optimization. The surface current variation is revealed in Fig. 9a–c. The  $f_1$  mode is the shorted  $TM_{1/4,0}$  mode. Due to the additional shorting wall, the  $TM_{3/4,0}$  mode degenerates into two  $TM_{3/4,0}$  with different field distributions at the  $f_2$  and  $f_3$  modes. With an increase in the shorting wall width ' $w_s$ ' the average current path lengths at the modes change which causes the  $TM_{1/4,0}$  mode to increase. An optimum BW is obtained for the shorting wall width of  $w_s = 0.2$  cm. A wide BW of 89% is obtained compared to the reported BW of 71%. Wider bandwidth is the result of optimal spacing between the three resonant modes. Thus, here the PIFA with U-slot folded patch with double shorting walls is discussed an in-depth study explaining the broadband response is presented.

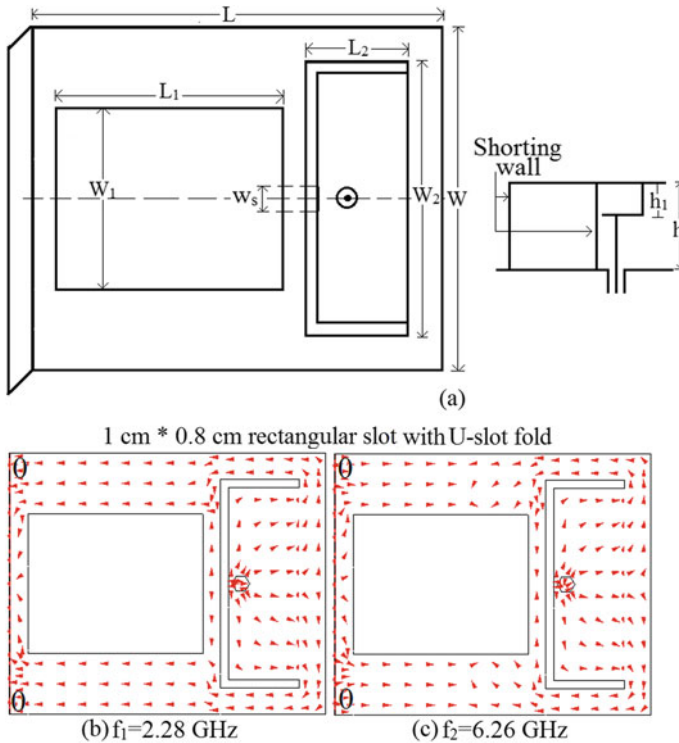


**Fig. 8** a Schematic of Modified PIFA with rectangular slot and shorting wall, its **b, c** surface current distribution at observed resonant modes for a specific length

### 5 Offset Proximity Fed PIFA Antenna

The design of offset proximity fed PIFA antenna is revealed in Fig. 10a [8]. The antenna is fabricated on-air substrate with thickness ‘h’ = 5 mm. It yields a BW of 3.36 GHz (78%). In the reported work, which modes of shorted PIFA yield this BW is not explained. Therefore, step by step study is presented here as per the design evolution as shown in Fig. 10a.

Simulation of the reported configuration is carried in IE3D, corresponding current distributions observed nearer to the realized bandwidth as per Fig. 10b are studied. In first mode, currents exhibit variation along shorted patch length whereas in second mode they are bi-directional over the patch. Therefore, initially, proximity-fed PIFA antenna without offset feed (proximity strip in the middle of patch width) is simulated, and current distribution at observed modes is shown in Fig. 10c, d. In second of this center strip variation, same is placed inside the slot which is cut on the edge of PIFA. For these feed locations, as per the surface current distributions noted,  $TM_{1/4,0}$  and  $TM_{1/4,2}$  modes are present. The further strip is positioned at offset position (similar to that present in optimum design) and surface current distribution at observed resonant



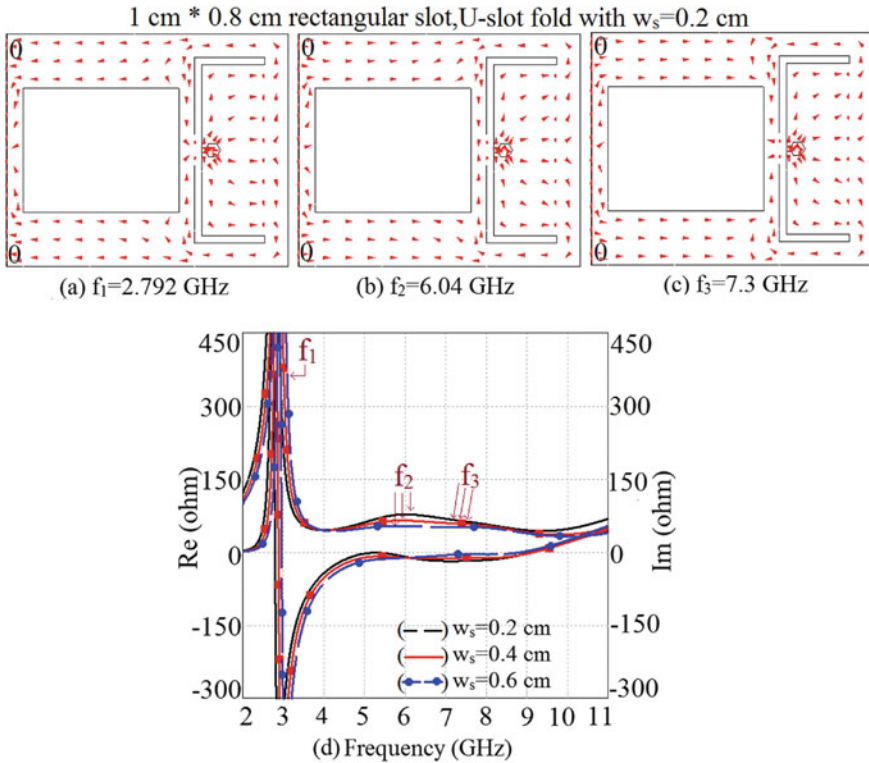


**Fig. 9** a–c Surface current distribution with varying shorting wall width and its **d** resonance curve plot

modes are revealed in Fig. 10e, f. As the strip is next to the offset point,  $TM_{1/4,2}$  mode is not excited, but the  $TM_{1/4,1}$  mode is present. When the strip is placed inside the slot cut on PIFA edge,  $TM_{1/4,0}$  and  $TM_{1/4,1}$  mode along with higher-order mode is observed. The BW is realized around  $f_1$  and  $f_2$  as shown in Fig. 10f, which are  $TM_{1/4,0}$  and  $TM_{1/4,1}$  resonant modes. Thus, wideband response in offset proximity feed PIFA design is owing to  $TM_{1/4,0}$  and  $TM_{1/4,1}$  resonant mode. This detailed explanation with the help of modal current plots is not given in the reported work, which is being presented here.

## 6 Conclusions

The detailed review-based study to provide a detailed explanation for the wideband response in different shorted slot cut variations of compact wideband PIFA antennas is presented. The present study helps in deriving a detailed understanding of the shorted slot cut PIFA antennas as well as designing them with respect to any given

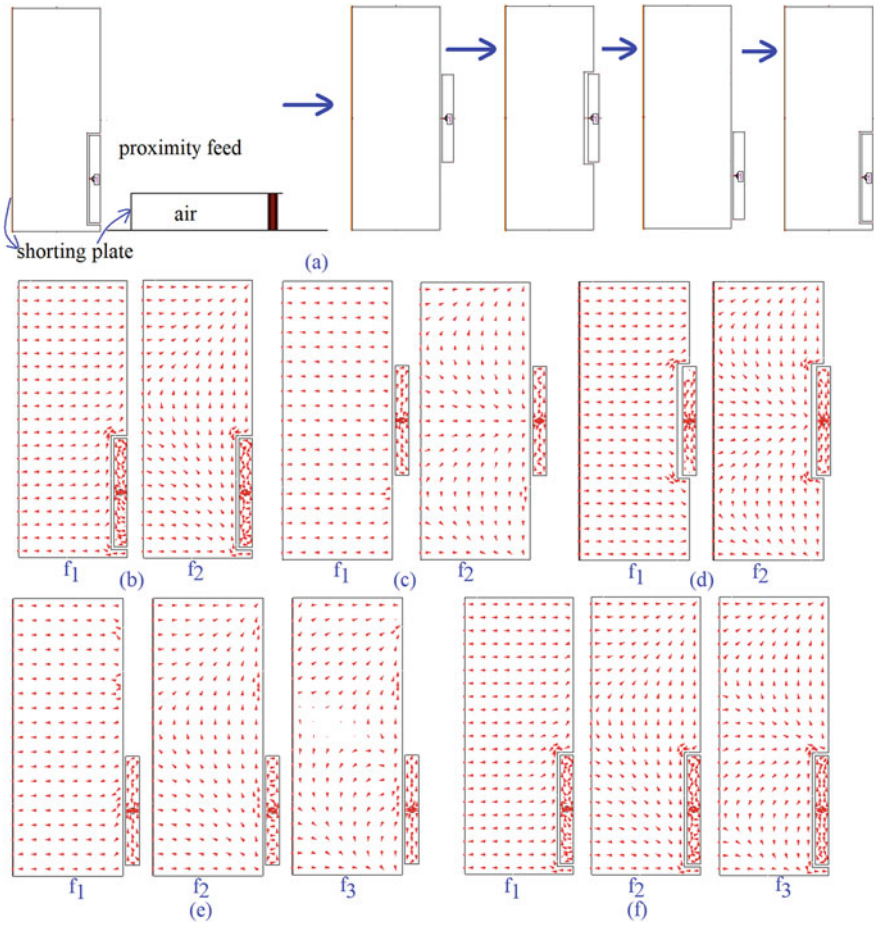


**Fig. 10** a Design and parametric study evolution of offset proximity fed PIFA design, and its b-f surface current distribution at observed resonant modes for various offset feed PIFA variations

frequency as per practical application. This design is procedure is presented for one of the configurations studied in this paper. This kind of detailed work is not reported in the literature for a variety of PIFA designs, and thus this is the novelty in the present study. The radiation pattern in all the designs yields higher cross-polar levels nearly omni-directional pattern because of the shorted patch.

### References

1. Wong KL (2002) Compact and broadband microstrip antennas. Wiley, New York
2. Kumar G, Ray KP (2003) Broadband microstrip antennas, 1st edn. Artech House, USA

3. Garg R, Bhartia P, Bahl I, Ittipiboon A (2001) *Microstrip antenna design handbook*. Artech House, USA
4. Lee HF, Chen W (1997) *Advances in microstrip and printed antennas*. Wiley, New York
5. Chiu CY, Shum KM, Chan CH, Luk K (2003) Bandwidth enhancement technique for quarter-wave patch antennas. *IEEE Antennas Wirel Propag Lett* 2(1):130–132
6. Chiu CY, Wong H, Chan CH (2007) Study of small wideband folded-patch-feed antennas. *IET Microwave Antennas Propag* 1(2):501–505
7. Chiu CY, Chan CH, Luk KM (2004) Study of a small wide-band patch antenna with double shorting walls. *IEEE Antennas Wirel Propag Lett* 3:230–231
8. Chen HD (2008) Broadband designs of coplanar capacitively fed shorted patch antennas. *IET Microwave Antennas Propag* 2(6):574–579

# Analysis and Design of Variations of Compact U-Slot Cut Microstrip Antennas for Wider Bandwidth



Mohil Gala, Amit A. Deshmukh, and A. P. C. Venkata

**Abstract** Designs of compact and wideband microstrip antennas using shorting post or plate and U-slot have been reported. To understand the functioning, this paper presents a detailed review-based study for these shorted and U-slot cut variations of rectangular microstrip antennas. The design formulations are presented in some of the configurations which aid in the re-designing of the similar antennas at given specific resonant frequency.

**Keywords** Compact microstrip antenna · Broadband microstrip antenna · Shorting technique · U-slot · Half U-slot · Resonant length formulation

## 1 Introduction

The requirements for the reduction in the antenna size along with wider bandwidth (BW) lead to the design of shorted slot cut microstrip antenna (MSA) [1–5]. In majority of those reported wideband designs, deep insight into the antenna functioning explaining the resonant modes present and the subsequent design methodology is not given. The present paper provides detailed review-based study for four different variations of U-slot and half U-slot cut MSAs using either shorting post or the shorting plate. The configurations as reported in [3–5] are selected in the present study. The detailed study by analyzing the resonant modes and surface current distribution at those modes, an identification of modes is carried out. Further in each of the designs, resonant length formulation for the shorted patch modes and the design methodology using the same is presented. The shorted slot cut MSAs design using proposed methodology yields similar wideband response. Thus, present study provides systematic study for the different variations of U-slot cut antennas followed by the design procedure, which is not available in the reported papers.

---

M. Gala · A. A. Deshmukh (✉) · A. P. C. Venkata  
Department of EXTC, SVKM's DJSCE, Mumbai, India

## 2 Analysis of Single Shorting Post Loaded Slot Cut MSA

Design of shorting post-loaded U-slot cut rectangular MSA (RMSA) is shown in Fig. 1a [3]. The shorted patch is suspended above the ground plane using foam substrate of thickness 2.8 cm [3]. The positioning of the shorting post converts the patch into a quarter wavelength resonator, whereas a full U-slot is employed to enhance the BW. A simulated BW of 25% around the center frequency of 0.86 GHz is reported. To understand the antenna functioning, shorted MSA is simulated using CST software [6] and their various plots are shown in Fig. 1b, c. The BW is noticed around the second resonant mode frequency. The current distribution at the two

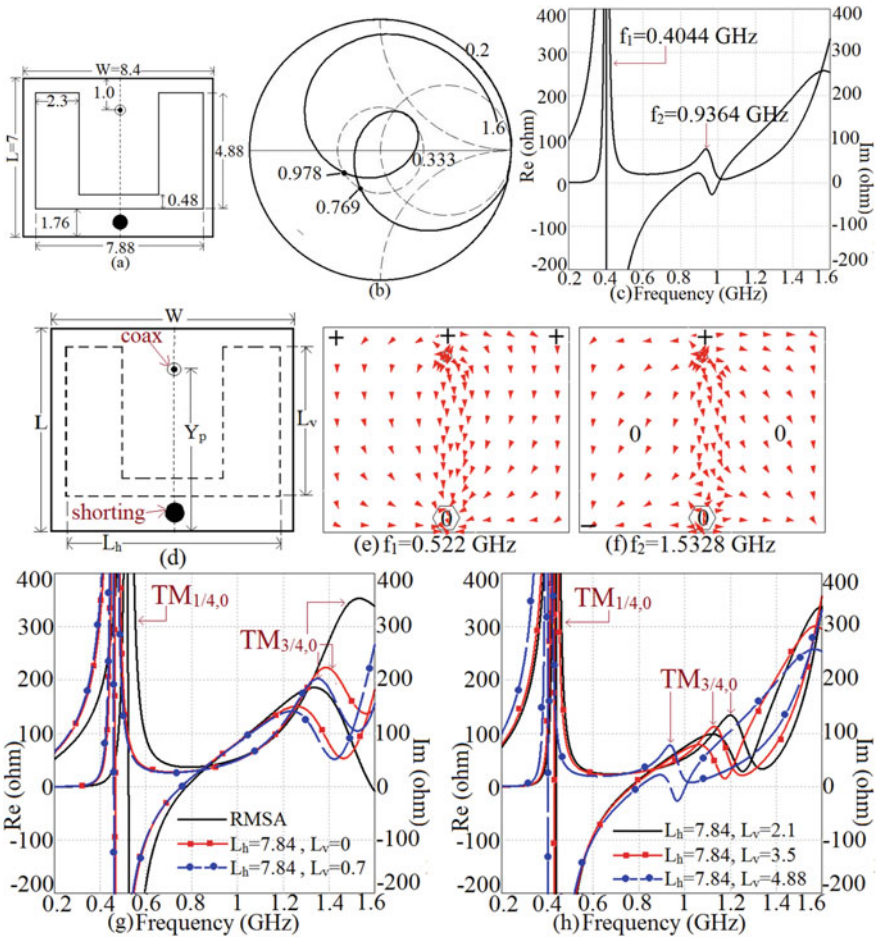


**Fig. 1** a Shorted U-slot cut RMSA, its simulated **b** smith chart and **c** resonance curve plots, **d** schematic of varying length slot cut MSA, **e, f** current distribution at observed resonant modes for the shorted patch, **g, h** resonance curve plots for varying U-slot length

modes was found to be varying along the length of the shorted patch, patch width and around the U-slot.

As per the reported papers, inner U-slot length equals half the wavelength at the slot mode. In the above design, inner U-slot length equals 12.04 cm, which when equated to half the wavelength results in frequency of 1.245 GHz. This value does not match with any of the observed resonant mode frequencies. Further shorted patch and its U-slot cut variation are studied for different slot dimensions and their plots are shown in Fig. 1d–h. Without the U-slot in shorted RMSA,  $TM_{1/4,0}$  and  $TM_{3/4,0}$  modes are observed as they exhibit one and three times the quarter wavelength variations from the open circuit patch edge to the shorting post. With the introduction of U-slot inside the shorted patch, frequencies of two modes reduces, but reduction in  $TM_{3/4,0}$  mode frequency is significant since it exhibits three quarter wavelength variation along shorted length. Further variations in the feed point location optimizes input impedance at modified  $TM_{3/4,0}$  mode to yield wider BW as shown in Fig. 2a, b. With dimensional variations in U-slot, as maximum surface current contribution at  $TM_{1/4,0}$  and  $TM_{3/4,0}$  modes are directed along the length of the shorted patch, an E and H-plane remains along  $\Phi = 90^\circ$  and  $0^\circ$ , respectively. Thus, the wideband response is due to the coupling between the higher order  $TM_{3/4,0}$  and fundamental  $TM_{1/4,0}$  mode.

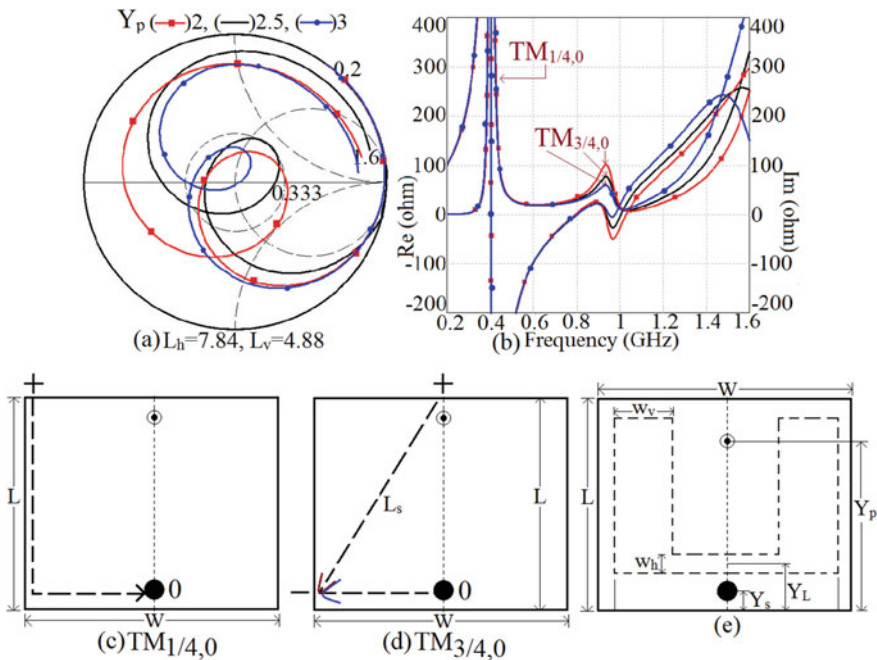


**Fig. 2** a Smith chart and b resonance curve plots for variation in feed point location for shorted U-slot cut RMSA, c, d resonant length estimation at two modes in shorted RMSA, e re-design schematic for shorted U-slot cut RMSA

Next, resonant length formulation and subsequent design procedure are put forward for wideband U-slot cut shorted RMSA as discussed below.

Redesigning Procedure for the U-slot cut shorted post MSA.

First step is finding the  $TM_{1/4,0}$  and  $TM_{3/4,0}$  mode effective length without the slot and later incorporating the U-slot length effects into the same.

(A) *Procedure for the  $TM_{1/4,0}$  mode*

Finding effective resonant length and frequency for the  $TM_{1/4,0}$  mode,

Shorted patch resonant length,

$$L_{\text{eff}} = (L + W/2) + h \quad (1)$$

Frequency equation,

$$f_r = c/\sqrt{\epsilon_r} \left( \sqrt{\left(\frac{m}{L_{\text{eff}}}\right)^2 + \left(\frac{n}{2W_{\text{eff}}}\right)^2} \right) \quad (2)$$

Effect of U-slot length ' $L_h$ ',

$$L_{\text{eh}} = L_{\text{eff}} + \left( L_h \left( \frac{L_h}{2W} \right) \sin\left(\frac{\pi L_h}{5W}\right) \right) \quad (3)$$

Effect of U-slot length ' $L_v$ ',

$$L_e = L_{\text{eh}} + 0.5L_v \quad (4)$$

The frequency calculated using Eq. (2) for  $L_{\text{eff}} = L_e$ ,  $m = 1/4$  and  $n = 0$ , agrees closely with the simulated values against increasing U-slot length, ' $L_h$ ' and ' $L_v$ '.

(B) *Procedure for  $3/4, 0$  mode*

Finding the effective resonant length and frequency for  $TM_{3/4,0}$  mode, further frequency is calculated using Eq. (2) for  $m = 3/4$  and  $n = 0$ . The effects of U-slot dimensions on  $TM_{3/4,0}$  mode frequency are added as specified in Eqs. (6) and (7) and frequency is computed using Eq. (2). Against the increments in the length of the U-slot, calculated frequencies at the two modes matches nearly with the simulated values. Using these formulations, further re-design procedure for shorted U-slot cut RMSA is discussed.

Resonant length at  $3/4,0$  mode,

$$L_{\text{eff}} = \left( W/2 + \left( \sqrt{L^2 + \left( W/2 \right)^2} \right) \right) + h \quad (5)$$

Effect of  $L_h$ ,

$$L_{\text{eh}} = L_{\text{eff}} + \left( \left( \frac{L_h}{4} \right) \left( \frac{L_h}{W} \right) \sin\left(\frac{\pi L_h}{5W}\right) \right) \quad (6)$$

Effect of  $L_v$ ,

$$L_e = L_{eh} + 1.5L_v \quad (7)$$

Next step is to take the ratio of the  $TM_{3/4,0}$  and  $TM_{1/4,0}$  modes. The simulated and the calculated ratio is taken and at the optimized lengths the ratio value of 2.33 is selected for the redesigning. This ratio value is taken as the standard value for redesigning (simulated and calculated ratio values must be within 5%). Further, expressing all the parameters in terms of  $\lambda_0$  and  $L$  for redesigning purpose. Height of the patch  $h = 0.04872\lambda_0$ ; the horizontal slot length is directly calculated as,  $L_h = 0.933 W$ ; distance of the probe from the edge,  $Y_p = 0.1044\lambda_0$ ; distance of the shorting post from the edge,  $Y_s = 0.0087\lambda_0$ ; position of the horizontal slot from the edge,  $Y_1 = 0.03462\lambda_0$ ; width of the Horizontal slot,  $w_h = 0.008\lambda_0$ ; width of the vertical slot,  $w_v = 0.04\lambda_0$ ; Calculating the Patch length by equating the quarter-wavelength to the fundamental mode  $TM_{1/4,0}$  length as given in Eq. (8). Patch width is selected as  $W = 0.833L$ . Once the patch side length for any given redesign is known, the different parameters are calculated from the above and the patch is designed at that frequency. Then from above, the horizontal slot length is calculated and from the formulation equation, the effective horizontal slot length for the  $TM_{1/4,0}$  and the  $TM_{3/4,0}$  is calculated. The effective length of the horizontal slot is taken and the vertical length of the slot is varied in the formulation of the  $TM_{1/4,0}$  and the  $TM_{3/4,0}$  modes which gives the calculated frequencies and then the ratio of the calculated frequencies is taken. The ratio which gives the same value as the above ratio value of approximately 2.33 is noted and the slot length at this ratio is accounted. The above slot length is taken and cut inside the patch. This slot length directly gives the optimized length at which the broadband is achieved. The antenna is redesigned at shorted fundamental mode frequency of 1.5 and 3 GHz and the parameters of the antenna for the same are given in Table 1. Using these parameters similar wideband response is achieved.

Wavelength at desired frequency,

$$\lambda_0/4 = L + W/2 + h, \quad (8)$$

### 3 Analysis of Shorting Plate Loaded Half U-Slot Cut RMSA

Wideband variation of shorted RMSA using half U-slot is displayed in Fig. 3a [4]. The antenna is fabricated on a foam substrate of thickness 1.0 cm [4]. The shorted MSA is fed using a coaxial probe of 0.1 cm in diameter. This design yields BW of 26% at the center frequency of 2.6 GHz. The reported configuration is simulated using CST and its smith chart and its resonance curve are displayed in Fig. 3b, c. The resonance curve exhibits two resonant peaks at 1.16 GHz and 2.792 GHz. The loop is formed inside the  $VSWR = 2$  circle, which yields simulated BW from 2.303 to



**Table 1** Antenna parameters for re-designed single shorted U-slot cut RMSA

Parameters	$f_{TM_{1/4,0}} = 1.5 \text{ GHz}$ (cm)	$f_{TM_{1/4,0}} = 3 \text{ GHz}$
Patch length (L)	2.5	1.5
Patch width (W)	3	1.8
Height	1	0.6
$Y_p$	2.1	1.25
$Y_s$	0.2	0.1
Yl	0.7	0.42
Horizontal slot length ( $L_h$ )	2.8	1.68
Horizontal slot width ( $w_h$ )	0.16	0.1
Vertical slot length ( $L_v$ )	1.8	1.1
Vertical slot width ( $w_v$ )	0.8	0.48

2.986 GHz. The loop is formed due to the optimum spacing between resonant modes at 1.16 and 2.792 GHz. The surface current at the modes is directed along the vertical direction inside the half U-slot cut shorted patch. As per the earlier reported papers on half-slot cut MSA, an inner length of the half U-slot equals quarter wavelength at the slot resonant mode. For the MSA displayed in Fig. 3a, inner half U-slot length equals  $(L_h + (L_v - 0.2))$  4.2 cm, which when equated to half wavelength result the frequency value of 1.785 GHz. This value does not match with any of the observed resonant peaks. Thus, here the quarter wavelength approximation for half U-slot length to determine the slot resonant length does not give closer prediction. To get a detailed insight of the broadband behavior of half U-slot shorted MSA, initially the shorted RMSA without slot is studied. The shorted patch is simulated and its resonance curve plot is displayed in Fig. 3d, e. The resonance curve plot shows two peaks and the surface current distribution at these peaks is shown in Fig. 3f, g. At the first resonant mode, the current shows one quarter wavelength along the length of the patch and no variation along the patch width as it is the  $TM_{1/4,0}$  resonant mode. At the next higher order mode, the current shows quarter wavelength variation across the patch length and half-wavelength variation along the patch width and it is referred as the  $TM_{1/4,1}$  mode. At  $TM_{1/4,0}$  mode, the E-plane is directed along  $\Phi = 90^\circ$ . Due to dominant contribution of currents at  $TM_{1/4,1}$  mode along the patch width, the radiation pattern at this mode is directed along  $\Phi = 0^\circ$ .

Further, inside the shorted RMSA, half U-slot of dimension ' $L_h$ ' and ' $L_v$ ' is cut as shown in Fig. 3j. Initially, the horizontal slot of length ' $L_h$ ' is cut and then the vertical slot of length ' $L_v$ ' is cut. The frequency of  $TM_{1/4,0}$  and the  $TM_{1/4,1}$  mode reduces as the slot is orthogonal to the surface currents at these modes. Further, the vertical slot ' $L_v$ ' is increased. With the increase in ' $L_v$ ' the  $TM_{1/4,0}$  mode frequency reduction is less as the slot is parallel to the surface current at this mode. Due to the half

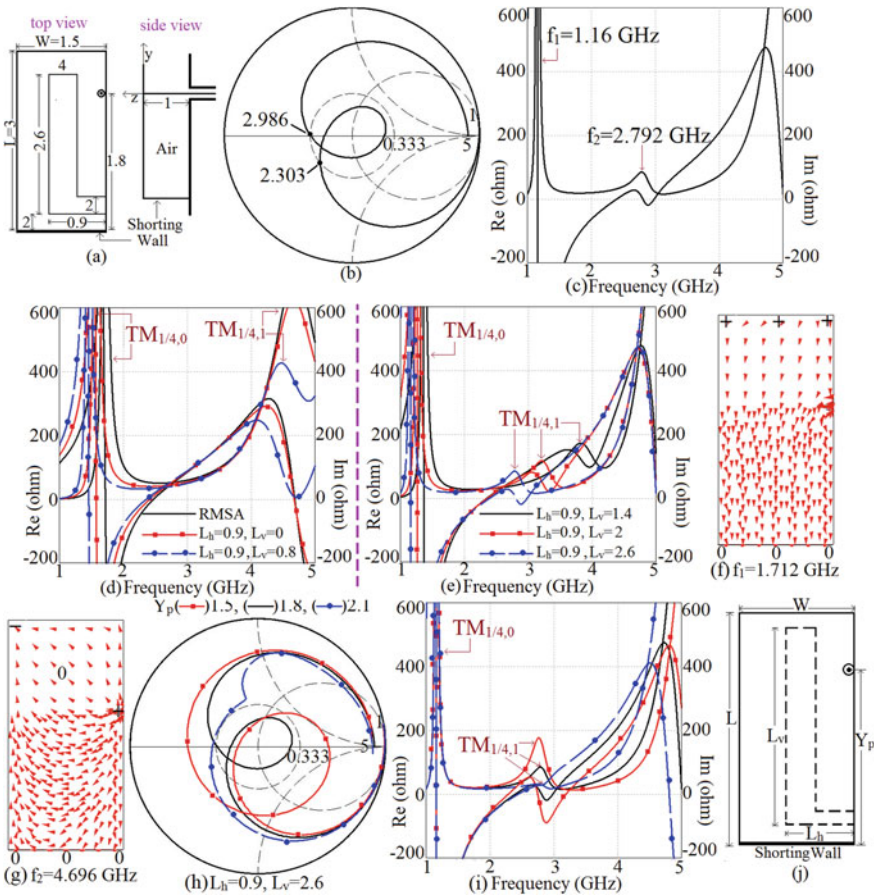


**Fig. 3** a Shorted RMSA with half U-slot, its simulated **b** smith chart, **c** resonance curve plots, **d, e** resonance curve plots against varying slot length, **f, g** surface current distribution at first two resonant modes for shorted RMSA, **h** smith chart and **i** resonance curve plots for varying feed point location for shorted half U-slot cut RMSA, **j** schematic of varying U-slot length shorted RMSA

wavelength variation along the width,  $TM_{1/4,1}$  mode surface currents are orthogonal to the vertical slot length and cause a greater frequency reduction. Due to the increase in the slot dimensions the surface current shows contribution along the shorted patch length. This reorients the E-plane at the  $TM_{1/4,1}$  mode from  $\Phi = 0^\circ$  to  $\Phi = 90^\circ$ . For  $L_h = 0.9$  and  $L_v = 2.6$  cm, smith chart and resonance curve plots for varying feed point locations ( $Y_p$ ) are shown in Fig. 3h, i. As the feed position is increased from 1.5 to 2.1 cm, the input impedance at  $TM_{1/4,0}$  mode remains constant. At the  $TM_{1/4,1}$  mode the maximum field impedance is present inside the Half U-slot. As the coaxial feed is getting placed at the minimum impedance region of the  $TM_{1/4,1}$  mode the input impedance decreases at that mode. Decrease in impedance, shifts the position of the loop formed due to  $TM_{1/4,1}$  mode in the smith chart to move from higher impedance

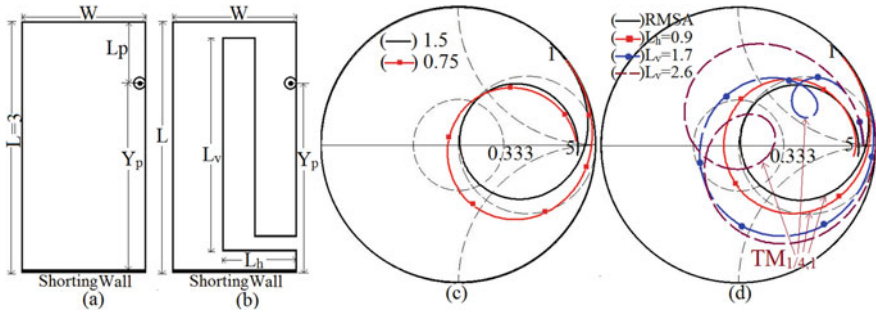


**Fig. 4** **a** Shorted RMSA, **b** shorted half U-slot cut RMSA, smith chart for variation in **c** shorted patch width and **d** dimensions of U-slot for shorted and shorted half U-slot cut RMSA

to lower impedance region. The position of the feed optimized the loop position inside the  $VSWR = 2$  circle for the broad BW. The smith charts for varying shorted patch width (without U-slot) and for increasing U-slot lengths in slot cut shorted MSA as shown in Fig. 4a, b, are displayed in Fig. 4c, d. As seen from Fig. 4a, with a reduction in shorted patch width ( $W$ ), an input impedance locus becomes more capacitive. With the reduction in width, an area of shorted patch reduces which reduces the capacitance formed between the shorted patch and the ground plane. This increases capacitive impedance formed between them which makes an impedance-loci more capacitive. In the optimum half U-slot cut configuration, the position of the coaxial feed optimizes the loop position. Therefore, in the half U-slot cut shorted MSA, with an increase in vertical length of the half U-slot ( $L_v$ ), patch width as seen by the feed reduces, which increases capacitive impedance formed between half U-slot cut shorted MSA and the ground plane. That makes impedance loci more and more capacitive as displayed in Fig. 4c, d. This capacitance actually compensates the longer probe inductance. The loop formed in the impedance loci in Fig. 4c, d is due to modified  $TM_{1/4,1}$  mode that gets optimized inside  $VSWR = 2$  circle with an increase in the length of half U-slot.

**Redesigning Procedure for the Half U-slot cut shorted RMSA.**

First step is finding the  $TM_{1/4,0}$  and  $TM_{1/4,1}$  mode resonant length without the slot,

**(A) Procedure for the  $TM_{1/4,0}$  mode,**

The effective length for the  $TM_{1/4,0}$  mode is calculated using Eq. (9) and frequency by using Eq. (2). The effects of half U-slot are added in Eqs. (10) and (11). Again, the frequency is computed using Eq. (2) for varying U-slot length, which agrees nearly with the simulated data.

Resonant length at  $TM_{1/4,0}$  mode,

$$L_{eff} = L + 1.3h, \tag{9}$$

Effect of  $L_h$  on resonant length,

$$L_{eh} = L_{eff} + \left( L_h \sin\left(\frac{\pi L_h}{4W}\right) \right), \quad (10)$$

Effect of  $L_v$  on resonant length,

$$L_e = L_{eh} + 0.6L_v, \quad (11)$$

(B) *Procedure for  $TM_{1/4,1}$  mode,*

Finding the effective length for the  $TM_{1/4,1}$  mode, with reference to Fig. 4a, resonant length is formulated as given in Eqs. (12) and (13) and frequency is calculated using Eq. (2). Further effects of U-slot length are modeled using Eqs. (14)–(17). The frequency is calculated using Eq. (2) that matches closely with the simulated results. Further using these formulations, re-design procedure for shorted U-slot cut RMSA is discussed.

$$L_{eff} = (L - L_p) + 0.7h, \quad (12)$$

$$W_{eff} = W + L_p + 2(0.7h), \quad (13)$$

$$L_{eh} = L_{eff} + \left( \left(\frac{L_h}{4}\right) \left(\frac{L_h}{W}\right) \sin\left(\frac{\pi L_h}{6W}\right) \right), \quad (14)$$

$$W_{eh} = W_{eff} \quad (15)$$

$$L_e = L_{eh} + \left( L_v \left(\frac{L_v}{L}\right) \right) \quad (16)$$

$$W_e = W_{eh} + \left( L_v \left(\frac{L_v}{L}\right) \right) \quad (17)$$

Next step is to take the ratio of the  $TM_{1/4,1}$  and  $TM_{1/4,0}$  modes. The simulated and the calculated ratio is taken and at the optimized lengths the ratio value of 2.35 is selected for the redesigning. Further, expressing all the parameters in terms of  $\lambda_0$  and  $L$  for redesigning purpose. Height of the patch  $h = 0.05706\lambda_0$ ; the horizontal slot length is directly calculated as,  $L_h = 0.6W$ ; distance of the probe from the edge,  $Y_p = 0.10272\lambda_0$ ; width of the Horizontal slot,  $w_h = 0.0228\lambda_0$ ; width of the vertical slot,  $w_v = 0.02337\lambda_0$ ; Calculating the Patch length by equating the quarter-wavelength to the fundamental mode  $TM_{1/4,0}$  length as given in Eq. (8).

$$\lambda_0/4 = L + 1.3h \quad (18)$$

Patch width is selected as  $W = 0.5L$ . Once the patch side length for any given redesign is known, the different parameters are calculated from the above and the patch is designed at that frequency. Then from above, the horizontal slot length is calculated and from the formulation equation, the effective horizontal slot length

**Table 2** Antenna parameters for re-designed fully shorted half U-slot cut RMSA

Parameters	1 GHz (cm)	3 GHz (cm)
Patch length (L)	5.2	1.7
Patch width (W)	2.6	0.85
Height	1.8	0.55
$Y_p$	3.1	1
$Y_h$	0.5	0.17
Horizontal slot length ( $L_h$ )	1.6	0.51
Horizontal slot width ( $w_h$ )	0.34	0.12
Vertical slot length ( $L_v$ )	4.6	1.4
Vertical slot width ( $w_v$ )	0.7	0.23

for the  $TM_{1/4,0}$  and the  $TM_{1/4,1}$  are calculated. The effective horizontal slot length is taken and the vertical length of the slot is varied in the formulation of the  $TM_{1/4,0}$  and the  $TM_{1/4,1}$  mode, which, gives the calculated frequencies and then the ratio of the calculated frequencies is taken. The ratio which gives the same value as the above ratio value of approximately 2.35 is noted and the slot length at this ratio is accounted. The above slot length is taken and cut inside the patch. This slot length directly gives the optimized length at which the broadband is achieved. The antenna is redesigned at shorted fundamental mode frequency of 1 and 3 GHz and the parameters of the antenna for the same are tabulated in Table 2. Using these parameters similar wideband response is achieved.

#### 4 Analysis of Single Shorting Post Loaded Half U-Slot Cut RMSA

The half U-slot cut RMSA with a single shorting post is displayed in Fig. 5a [3]. The antenna is fabricated on foam substrate of thickness  $h = 2.8$  cm. The shorting post and coaxial feed radius are 0.465 and 0.2 cm. The simulated BW of 19% at a center frequency of 1 GHz is reported. The reported configuration is simulated using CST and its smith chart and resonance curve plot are displayed in Fig. 5b, c. Two peaks in the resonance curve at 0.3596 and 1.0456 GHz are observed. The loop is formed inside the  $VSWR = 2$  circle which results in the simulated BW from 0.92 to 1.107 GHz. The loop is formed due to the optimum coupling between the resonant mode at 0.3592 and 1.0456 GHz. Surface currents at resonant modes are directed along the vertical and horizontal direction inside the slot cut shorted patch. As per reported papers on half U-slot cut MSA, an inner length of U-slot equals quarter wavelength at the slot resonant mode. For MSA shown in Fig. 5a, inner half U-slot length equals  $(L_h + (L_v - 0.48))$  6.04 cm, which when equated to quarter wavelength gives the frequency of 1.241 GHz. This value does not correspond to any

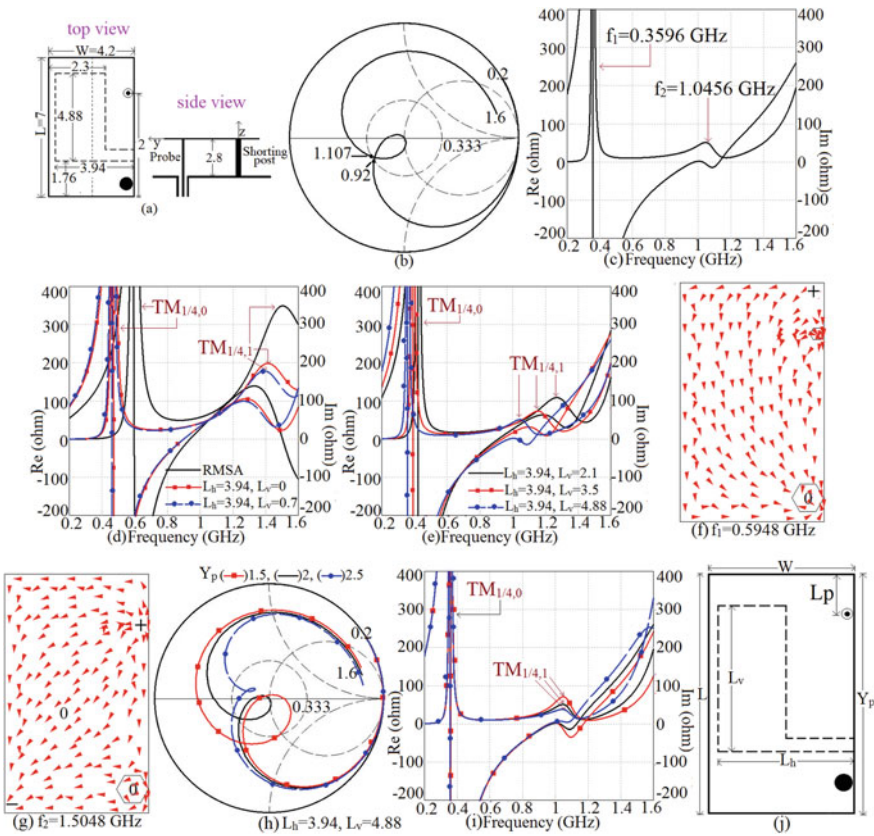


**Fig. 5** a Single shorted RMSA with half U-slot, its simulated **b** smith chart, **c** resonance curve plots, **d**, **e** resonance curve plots against varying slot length, **f**, **g** surface current distribution at first two resonant modes for shorted RMSA, **h** smith chart and **i** resonance curve plots for varying feed point location for shorted half U-slot cut RMSA, **j** schematic of varying half U-slot length single shorted RMSA

of the observed resonant modes. Thus, here quarter wavelength approximation for U-slot length does not give a closer prediction. Initially the shorted RMSA without any slot is studied. The dimensions of the shorted RMSA are  $L = 7.0$  cm and  $W = 4.2$  cm. The shorted patch is simulated and its resonance curve plot is displayed in Fig. 5d. The resonance curve plot shows two peaks and the surface current distribution at these peaks is shown in Fig. 5f, g. The two peaks are due to shorted  $TM_{1/4,0}$  and  $TM_{1/4,1}$  resonant modes. At  $TM_{1/4,0}$  mode, E-plane is directed along  $\Phi = 90^\circ$ . Due to dominant contribution of currents at  $TM_{1/4,1}$  mode along patch width, the pattern at this mode is directed along  $\Phi = 0^\circ$ .

Inside the shorted RMSA, half U-slot of dimension ' $L_h$ ' and ' $L_v$ ' is cut as shown in Fig. 5j. Initially the horizontal slot length ' $L_h$ ' is cut and then the vertical slot length ' $L_v$ ' is embedded. The frequency of  $TM_{1/4,0}$  and the  $TM_{1/4,1}$  mode reduces as the slot

is orthogonal to the surface currents at these modes. Further the vertical slot 'L<sub>v</sub>' is increased. With the increase in 'L<sub>v</sub>' the TM<sub>1/4,0</sub> mode frequency reduction is less as the slot is parallel to the surface current at this mode. Due to the half wavelength variation along the width of the TM<sub>1/4,1</sub> the surface currents are orthogonal to the vertical slot length and cause a greater frequency reduction. Impedance inside half U-slot is higher. Therefore, with increase in value of 'Y<sub>p</sub>', impedance at TM<sub>1/4,1</sub> mode reduces that shifts the loop formed due to same inside VSWR = 2 circle as shown in Fig. 5h, i. Thus, half U-slot in single shorted RMSA tunes spacing between TM<sub>1/4,0</sub> and TM<sub>1/4,1</sub> mode frequencies and feed point optimizes impedance level at same that yields wider BW. Further similar effects in variation in shorted patch width on the probe inductance compensation for thicker substrate as observed in above configuration are observed. Here also increasing half U-slot length reduces effective patch width as seen by coaxial probe that introduces more capacitance which reduces inductive part in the input impedance of the antenna.

Redesigning Procedure for the Half U-slot cut shorted post MSA.

First step is finding the TM<sub>1/4,0</sub> and TM<sub>1/4,1</sub> mode effective length without the slot.

(A) *Procedure for the TM<sub>1/4,0</sub> mode*

The effective resonant length for the TM<sub>1/4,0</sub> mode is obtained using Eq. (19) and frequency is calculated using Eq. (2). Further effects of half U-slot are added as given in Eqs. (20) and (21) and frequency is calculated using Eq. (2). This formulation yields close prediction with the simulated result.

$$L_{\text{eff}} = \left( L + 1.5W + L/2 \right) \quad (19)$$

$$L_{\text{eh}} = L_{\text{eff}} + \left( L_h \sin \left( \frac{\pi L_h}{4W} \right) \right) \quad (20)$$

$$L_e = L_{\text{eh}} + L_v \quad (21)$$

(B) *Procedure for the TM<sub>1/4,1</sub> mode*

The resonant length for shorted patch and further effects of half U-slot are added as given in Eqs. (22)–(27) and frequency is calculated using Eq. (2). This gives closer prediction with the simulated result (Fig. 6).

$$L_{\text{eff}} = L - L_p + h \quad (22)$$

$$W_{\text{eff}} = \left( \sqrt{W^2 + (L - L_p)^2} \right) + 2h \quad (23)$$

Effect of L<sub>h</sub>,

$$L_{\text{eh}} = L_{\text{eff}} + \left( L_h \left( \frac{L_h}{W} \right) \sin \left( \frac{\pi L_h}{6W} \right) \right) \quad (24)$$

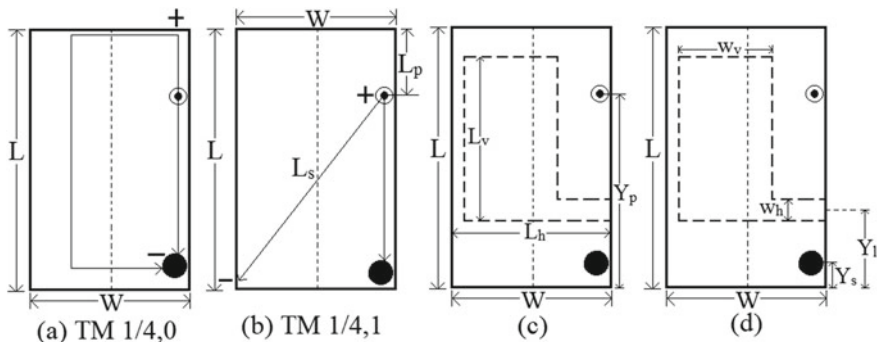


**Fig. 6** a, b Resonant length path at two modes and c, d schematic for re-design MSA

$$W_{eh} = W_{eff} + \left( L_h \left( \frac{L_h}{6W} \right) \sin \left( \frac{\pi L_h}{6W} \right) \right) \quad (25)$$

Effect of  $L_v$ ,

$$L_e = L_{eh} + L_v \quad (26)$$

$$W_e = W_{eh} + \left( L_v \left( \frac{L_v}{L} \right) \right) \quad (27)$$

For the re-designing purpose, the ratio of the  $TM_{1/4,1}/TM_{1/4,0}$  modes is to be taken. The simulated and the calculated frequency ratio is taken and at the optimized lengths the ratio value of 2.94 is selected for the redesigning. Further, expressing all the parameters in terms of  $\lambda_0$  and  $L$  for redesigning purpose. Height of the patch  $h = 0.0555\lambda_0$ ; the horizontal slot length is directly calculated as,  $L_h = 0.938 W$ ; distance of the probe from the edge,  $Y_p = 0.109\lambda_0$ ; distance of the shorting post,  $Y_s = 0.01387\lambda_0$ ; Position of the Horizontal slot from the edge  $Y_1 = 0.03965\lambda_0$ ; width of the Horizontal slot,  $w_h = 0.0095\lambda_0$ ; width of the vertical slot,  $w_v = 0.0456\lambda_0$ ; Calculating the Patch length by equating the quarter-wavelength to the fundamental mode  $TM_{1/4,0}$  length as given in Eq. (28).

$$\lambda_0/4 = \left( L + 1.5W + L/2 \right) \quad (28)$$

Patch width is selected as  $W = 0.6L$ . Once the patch side length for any given redesign is known, the different parameters are calculated from the above and the patch is designed at that frequency. Then from above, the horizontal slot length is calculated and from the formulation equation, the effective horizontal slot length for the  $TM_{1/4,0}$  and the  $TM_{1/4,1}$  is calculated. The effective horizontal slot length is taken and the vertical slot length is varied in the formulations of the  $TM_{1/4,0}$  and the  $TM_{1/4,1}$  modes which gives the calculated frequencies and then the ratio of the calculated frequencies is taken. The ratio which gives the same value as the above ratio value



**Table 3** Antenna parameters for re-designed single shorting post loaded half U-slot cut RMSA

Parameters	1.5 GHz (cm)	2.5 GHz (cm)
Patch length (L)	2.7	1.64
Patch width (W)	1.62	0.98
Height	1.1	0.65
$Y_p$	2.2	1.31
$Y_s$	0.28	0.17
$Y_l$	0.8	0.48
Horizontal slot length ( $L_h$ )	1.52	0.92
Horizontal slot width ( $w_h$ )	0.2	0.12
Vertical slot length ( $L_v$ )	1.2	0.85
Vertical slot width ( $w_v$ )	0.9	0.55

of approximately 2.94 is noted and the slot length at this ratio is accounted. The above slot length is taken and cut inside the patch. This slot length directly gives the optimized length at which the broadband is achieved. The antenna is redesigned at shorted fundamental mode frequency of 1.5 and 3 GHz and antenna parameters for same are given in Table 3. Using these parameters similar wideband response is achieved.

Similar study to analyze the wideband response of fully shorted U-slot cut RMSA has been reported in [5]. Here for the same design as shown in Fig. 7a, resonant length formulation at  $TM_{1/4,0}$  and  $TM_{3/4,0}$  modes and subsequent design methodology is explained.

Procedure for the  $TM_{1/4,0}$  mode: The effective resonant length for the  $TM_{1/4,0}$  mode is given using Eq. (29), whereas the effects of U-slot dimensions are incorporated

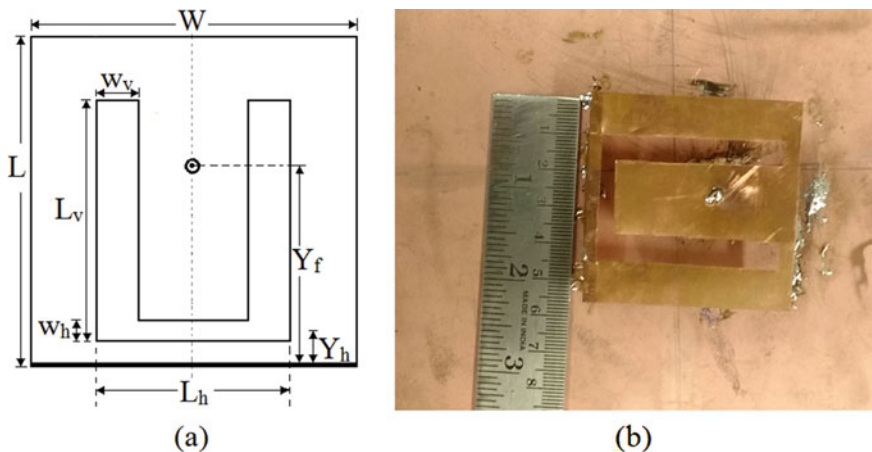


**Fig. 7** a Schematic showing slot parameters and b fabricated prototype for redesigned U-slot cut shorted RMSA

as given in Eqs. (30) and (31). The frequency as calculated using Eq. (2) agrees closely with the simulated data. Further formulation at  $TM_{3/4,0}$  mode is realized using Eqs. (32)–(34). Frequency as calculated using Eq. (2) matches closely with the simulated frequencies. Further using proposed formulation re-designing of similar shorted U-slot cut RMSA is presented at different frequency.

$$L_{\text{eff}} = L + 1.2h \quad (29)$$

$$L_{\text{eh}} = L_{\text{eff}} + \left( L_h \left( \frac{L_h}{W} \right) \sin \left( \frac{\pi L_h}{6W} \right) \right) \quad (30)$$

$$L_e = L_{\text{eh}} + 0.4L_v \quad (31)$$

$$L_{\text{eff}} = L + 1.5h \quad (32)$$

$$L_{\text{eh}} = L_{\text{eff}} + \left( \left( \frac{L_h}{6} \right) \sin \left( \frac{\pi L_h}{6W} \right) \right) \quad (33)$$

$$L_e = L_{\text{eh}} + \left( 2L_v \left( \frac{L_v}{L} \right) \right) \quad (34)$$

For the re-designing purpose, the ratio of  $TM_{3/4,0}/TM_{1/4,0}$  modes is to be taken. The simulated and the calculated frequency ratio is taken and at the optimized lengths the ratio value of 1.9 is selected for the redesigning purpose. Further, expressing all the parameters in terms of  $\lambda_0$  and  $L$  for the redesigning purpose. Height of the patch  $h = 0.05843\lambda_0$ ; the horizontal slot length is directly calculated as,  $L_h = 0.6W$ ; distance of the probe from the edge,  $Y_f = 0.10518\lambda_0$ ; Position of the Horizontal slot from the edge  $Y_h = 0.0175\lambda_0$ ; width of the Horizontal slot,  $w_h = 0.01168\lambda_0$ ; width of the vertical slot,  $w_v = 0.02337\lambda_0$ ; Calculating the Patch length by equating the quarter wavelength to the fundamental mode  $TM_{1/4,0}$  wavelength as given in Eq. (35).

$$\lambda_0/4 = L + 1.2h \quad (35)$$

Patch width is selected as  $W = L$ . Once the patch side length for any given redesign is known, the different parameters are calculated from above and the patch is designed at that frequency. The horizontal slot length is calculated as mentioned above and using the formulation, the effective horizontal slot length for the  $TM_{1/4,0}$  and the  $TM_{3/4,0}$  mode is calculated. The vertical slot length is varied in the formulation of the  $TM_{1/4,0}$  and the  $TM_{3/4,0}$  modes which gives the calculated frequencies and then the ratio of the calculated frequencies is taken. The ratio which gives value of 1.9 is noted and the slot length ' $L_v$ ' at this ratio is accounted. The above slot length is taken and cut inside the patch. This slot length directly gives the optimized broadband response. The antenna is redesigned at shorted fundamental mode frequency of 1 and 3 GHz and antenna parameters for same are given in Table 4. Using these parameters similar wideband response is achieved. The fabricated shorted and U-slot cut antenna for

**Table 4** Antenna parameters for re-designed shorted U-slot loaded RMSA

Parameters	1 GHz (cm)	3 GHz (cm)
Patch length (L)	5.4	1.8
Patch width (W)	5.4	1.8
Height	1.8	0.6
$Y_f$	3.15	1.052
$Y_h$	0.53	0.175
Horizontal slot length ( $L_h$ )	3.3	1.08
Horizontal slot width ( $w_h$ )	0.35	0.12
Vertical slot length ( $L_v$ )	4.6	1.4
Vertical slot width ( $w_v$ )	0.7	0.24

1 GHz frequency is shown in Fig. 7b. Thus, present paper presents a detailed review-based study for wideband antenna obtained using variations of U-slot and shorting technique. This study provides detailed understanding for the functioning of antenna for different shorting conditions. This kind of study is not available in the reported papers.

## 5 Conclusions

The detailed review-based study to provide detailed explanation for the wideband response in different shorting conditions in RMSA and U-slot variations for RMSA is presented. Further based on surface current distribution at respective shorted patch modes, resonant length formulation and design methodology is presented for all shorted U-slot cut RMSA variation. The present study helps in deriving detailed understanding for shorted slot cut antennas as well as designing of them with respect to any given frequency as per practical application. This kind of detailed work is not reported in literature for variety of shorted and slot cut MSA, and thus this is the novelty here.

## References

1. Wong KL (2003) Compact and broadband microstrip antennas, 1st edn. Artech House, USA
2. Kumar G, Ray KP (2003) Broadband microstrip antennas. Artech House
3. Chair R, Mak CL, Lee KF, Luk KM, Kishk AA (2005) Miniature wide-band half U-slot and half E-shaped patch antennas. *IEEE Trans Antennas Propagat* 53(8):1652–2645
4. Mak CL, Chair R, Lee KF, Luk KM, Kishk AA (2003) Half U-slot patch antenna with shorting wall. *Electron Lett* 39(25):1–2

5. Deshmukh AA, Gala M, Agrawal S (2016) U-Slot cut shorted square microstrip antenna. In: Proceedings of ICAECCT—2016, December 2016, Pune, India. <https://doi.org/10.1109/ICAECCT.2016.7942586>
6. CST Microwave Studio, Version 2019

# Microstrip-Line Resonator-Fed Rectangular Microstrip Antenna Using Gap-Coupled Parasitic Semi-circular Shape Patches



Sanjay B. Deshmukh and Amit A. Deshmukh

**Abstract** In this paper, a gap-coupled design of a microstrip-line resonator-fed rectangular microstrip antenna along with a variant of semi-circular patches is proposed. A gap-coupled rectangular microstrip antenna with semi-circular patches is indirectly fed by a pair of  $\lambda/4$  microstrip-line resonators. Enhancement in bandwidth is achieved by coupling resonance introduced by a pair of  $\lambda/4$  microstrip-line resonators and gap-coupled parasitic patches. Design of microstrip-line resonator-fed rectangular microstrip antenna provides a bandwidth of 53 MHz (6.41%) with broadside gain of 5.8 dBi. The optimum response obtained in rectangular microstrip antenna gap-coupled configuration with four semi-circular shape patches in terms of impedance bandwidth and a peak gain is 86 MHz (10.41%) and 7.7 dBi. The proposed design is implemented using  $0.019\lambda_c$  total substrate thickness and the experimental results obtained with the fabricated prototype antenna show a close match with the simulated results.

**Keywords** Microstrip-line resonator · Semi-circular shape · Gap-coupled · High gain · Shorting pin · Rectangular microstrip antenna

## 1 Introduction

In the past few years, rapid development in wireless communication systems demands antennas with higher gain and bandwidth. Microstrip antennas (MSAs) have inherent advantages like low profile, conformal, ease of integration with radio frequency [1]. High gain and bandwidth MSAs are being used in communication systems such as radar, satellite, terrestrial microwave communication system, etc. In the literature, various techniques have been reported for MSA bandwidth enhancement. Many

---

S. B. Deshmukh

Department of EXTC, SVKM's DJSCE, UOM, Mumbai, India

e-mail: [sanjay.deshmukh@djsce.ac.in](mailto:sanjay.deshmukh@djsce.ac.in)

A. A. Deshmukh (✉)

Department of EXTC Engineering, SVKM's DJSCE, Mumbai, India

e-mail: [amit.deshmukh@djsce.ac.in](mailto:amit.deshmukh@djsce.ac.in)

consistent efforts have been made to enhance MSA bandwidth by using various impedance matching and feeding techniques such as aperture coupling feed [2, 3], proximity coupling feed [4], or stacked configurations [5, 6]. However, these techniques use multi-layer substrates that lead to a complex fabrication process. Coupling resonant modes of fed and parasitic patches is another well-known technique to enhance the bandwidth [7]. Bandwidth enhancement in probe-fed MSA cannot carry out beyond  $0.1\lambda_0$  substrate thickness. This is due to an increase in probe inductance that leads to the requirement of an impedance matching network, and excitation of surface wave results in degradation in antenna performance. This drawback can be resolved by using a modified probe with L, T, or hook-shaped feed that decreases inductive components of MSA input impedance [8–10]. Another technique to increase the bandwidth is to employ slots like U, E, psi slots on the radiating patch [11–13]. However, the design of wideband slot cut MSA design is relatively complex than that of gap-coupled configurations. MSA bandwidth enhancement using an electrically thinner substrate is a challenging task. In [14], additional  $\lambda/4$  nonradiating along with radiating patch is used to enhance bandwidth.

In this proposed work, microstrip-line (MS) resonator-fed gap-coupled designs of rectangular microstrip antenna (RMSA) with semi-circular shape are presented. With various combinations of parasitic patches in a configuration such as single RMSA, RMSA gap-coupled with two semi-circular patches along the radiating edge, RMSA gap coupled with two semi-circular patches along nonradiating edge, and RMSA gap coupled with two semi-circular patches each along radiating and nonradiating edges are proposed. Microstrip-line resonator-fed single RMSA yields impedance bandwidth of more than 50 MHz (6.41%) and broadside gain of more than 5.8 dBi. For the configuration RMSA with two semi-circular parasitic patches along radiating edge provides a BW of 75 MHz (9.1%) and peak gain of 7.37 dBi at  $\theta = 20^\circ$ . RMSA with two semi-circular patches long nonradiating patches yields BW of 70 MHz (8.45%) and a peak broadside gain of 6.5 dBi. Further, enhancement in gain and bandwidth is obtained by placing two semi-circular patches along radiating and nonradiating edges of RMSA provides BW of more than 85 MHz (10.4%) and peak gain of 7.7 dBi at  $\theta = 20^\circ$ . The presented gap-coupled MSA structures are optimized in the 700–900 MHz frequency range. The above-specified frequency range is opted for the proposed RMSA gap-coupled configurations as MSA provides narrow BW in these lower frequency bands. For microstrip-line resonator-fed RMSA gap-coupled with semi-circular patches, parametric study and analysis are carried out by varying  $\lambda/4$  resonator length and width, the gap between  $\lambda/4$  resonator and RMSA, and the gap between RMSA and semi-circular shape patches. The dimensions and frequency used in this paper are in millimeters. CST software was used for the optimization of proposed configurations [15]. This simulation study was followed by the experimental validation of proposed configuration parameters—input impedance and radiation pattern. SMA type panel of 0.12 cm inner wire diameter is used to feed proposed. The impedance response is measured using a ZVH-8 vector network analyzer. The antenna pattern measurement is done in an antenna lab using an RF source (SMB 100A) and spectrum analyzer (FSC-6).

## 2 Microstrip-Line Resonator-Fed RMSA Gap-Coupled with Semi-Circular Patches

### 2.1 Microstrip-Line Resonator-Fed RMSA

The basic structure of microstrip-line indirectly fed RMSA is shown in Fig. 1a, b. This configuration is a three-layer structure, consisting of top and bottom FR4 substrate and the middle air layer. Substrate parameters used in this configuration are thickness  $h = 1.6$  mm, dielectric constant  $= 4.3$ , and loss tangent  $\delta = 0.02$ . An FR4 substrate with backed copper acts as a ground plane over which another FR4 is placed with air gap  $'h_a' = 1.6$  mm. On the top of the suspended substrate, a microstrip-line of length  $l_s$  and width  $w_s$  is etched with a pair of  $\lambda/4$  resonators. On this substrate RMSA of length  $L$  and width  $W$  is placed with gap  $g$  from the resonator. Resonator pair has length  $l_r$  and width  $w_r$  with shorting pin of radius  $r$ . The antenna is fed through a microstrip-line using a coaxial probe at a distance of  $X_f$  from the resonator center. RMSA fundamental mode  $TM_{10}$  frequency of 840 MHz is selected and realized using a total substrate thickness of  $0.019\lambda_c$ . A parametric study is carried out to optimize the dimensions of microstrip-line, resonator, and RMSA to resonate RMSA around 840 MHz fundamental frequency.

Optimum response of proposed configuration in terms of bandwidth and gain is 53 MHz (6.41%) and 5.78 dBi and dimensions are as follows:  $L = 120$ ,  $W = 140$ ,  $w_r = 6$  ( $0.016\lambda$ ),  $l_r = 52$  ( $0.25\lambda$ ),  $l_s = 14$ ,  $w_s = 6$ ,  $r = 0.5$ . Figure 1c shows the resonance plot of MS- $\lambda/2$  resonator and MS- $\lambda/2$  resonator-fed RMSA. Two resonance peaks are shown in the resonance plot for MS- $\lambda/2$  resonator-fed RMSA due to coupling of a shorted mode of resonator and RMSA. The parametric study is carried out by varying gap  $g$  between nonradiating  $\lambda/2$  resonator and RMSA with resonator length  $l_r$  and width  $w_r$  value constant. Figure 2a, b shows the effect of variation in coupling

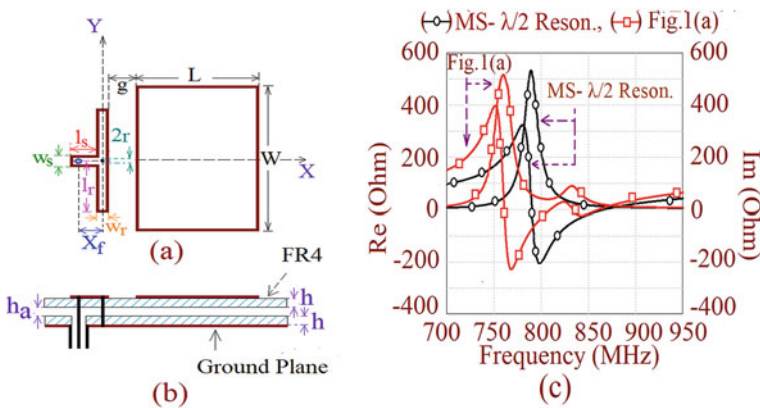


**Fig. 1** a, b Microstrip-line resonator-fed RMSA, c resonance plots of MS-line  $\lambda/2$  resonator and MS-line  $\lambda/2$  resonator-fed RMSA

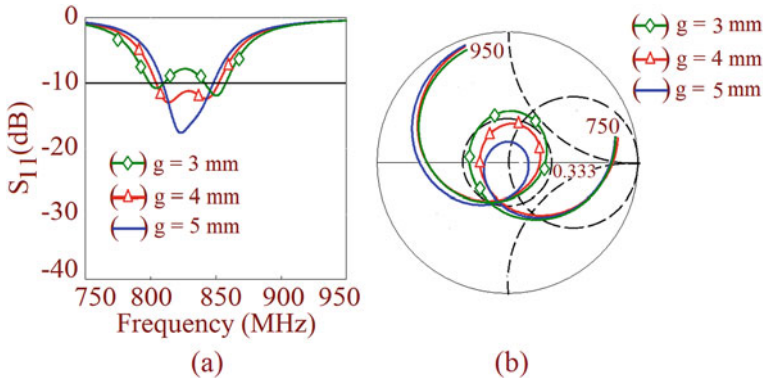
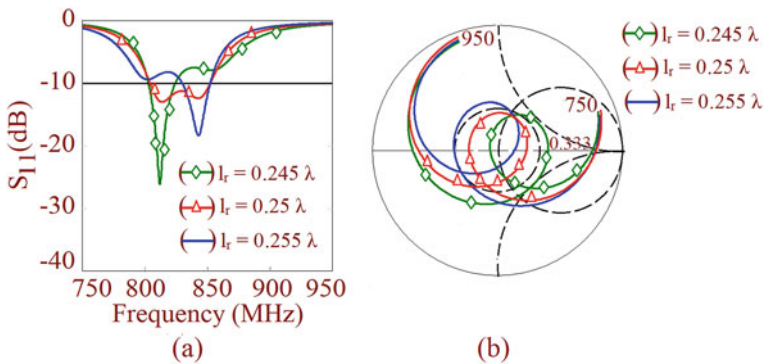


**Fig. 2** **a** Effect of variation in coupling gap  $g$  on the reflection coefficient, **b** effect of variation in coupling gap  $g$  on input impedance ( $w_r = 6, l_r = 52$ )

gap  $g$  on the reflection coefficient and input impedance of the antenna. The size of the loop in the input impedance depends on gap  $g$  between the feed resonator and RMSA. Coupling between resonator feed and RMSA increases with a decrease in the gap between them. An optimum result was obtained for gap  $g = 4$  at which impedance covers the maximum area within VSWR 2 circle.

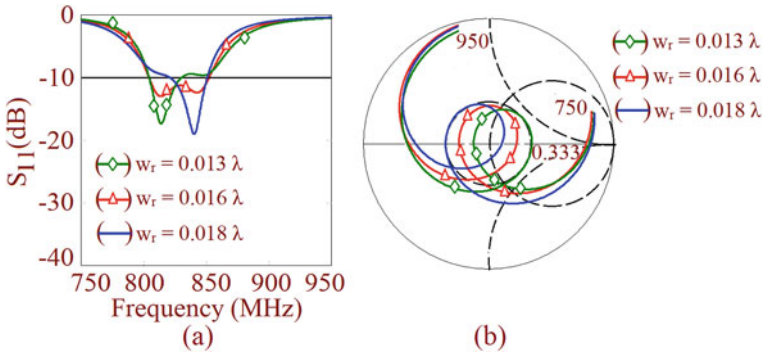
Figure 3a, b depicts the effect of variation in the length of  $\lambda/4$  resonator on the reflection coefficient and input impedance response. The parametric optimization has been carried out by the varying length of  $\lambda/4$  resonator with coupling gap  $g$  and width  $w_r$  value constant. Optimum bandwidth response obtained for resonator length  $l_r = 52$  ( $l_r = 0.25\lambda$ ).

Figure 4a, b represents the effect of variation in the width of  $\lambda/4$  resonator on the reflection coefficient and input impedance response. The parametric variation has been carried for a width of  $\lambda/4$  resonator with coupling gap  $g$  and length  $l_r$  value



**Fig. 3** **a** Effect of variation in the length of  $\lambda/4$  resonator on the reflection coefficient, **b** effect of variation in the length of  $\lambda/4$  resonator on input impedance ( $w_r = 6, g = 4$ )





**Fig. 4** **a** Effect of variation in the width of  $\lambda/4$  resonator on the reflection coefficient, **b** effect of variation in the width of  $\lambda/4$  resonator on input impedance ( $l_r = 52$ ,  $g = 4$ )

constant. For the  $w_r$  value equal to  $0.016\lambda$ , optimum bandwidth response obtained for resonator width  $w_r = 6$  ( $w_r = 0.016\lambda$ ) and entire loop lie within VSWR 2 circle.

In order to enhance bandwidth, two semi-circular patches are placed along radiating and nonradiating edge of RMSA as shown in Fig. 5a, b. Addition of two semi-circular patches couples one more resonant mode to enhance the bandwidth. Optimum simulation for resonator-fed RMSA with two semi-circular patches along radiating and nonradiating patches are 75 MHz (9.1%) and 70 MHz (8.45%), respectively. The simulated gain of these configurations is 7.4 dBi and 6.5 dBi, respectively. As coupling is more along the radiating edge of RMSA as compared to the nonradiating edge, slightly more bandwidth is obtained in radiating edge coupled semi-circular configuration. Figure 6a, b shows simulated return loss and gain plots

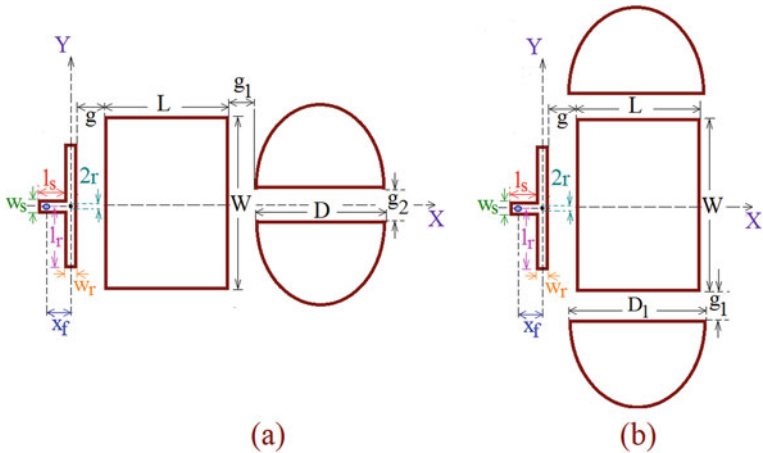


**Fig. 5** **a, b** MS-line  $\lambda/2$  resonator-fed RMSA gap-coupled with two semi-circular patches along radiating and nonradiating edge

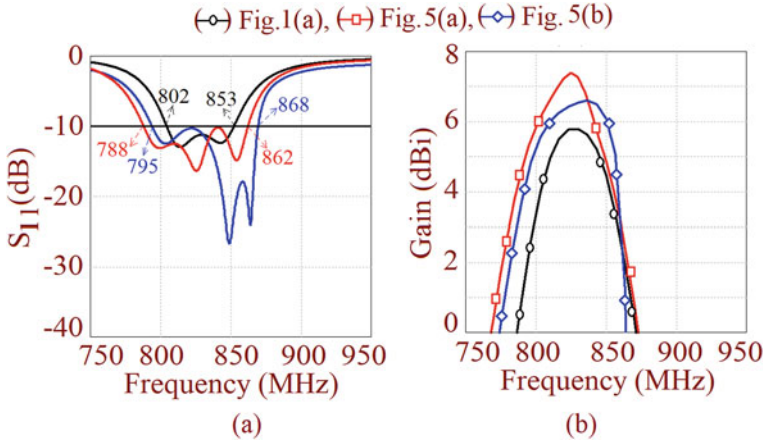


**Fig. 6 a, b** Simulated return loss and gain plots for MS- $\lambda/2$  resonator-fed RMSA, RMSA gap-coupled with two semi-circular patches along radiating and nonradiating edge

for MS- $\lambda/2$  resonator-fed RMSA, and RMSA gap-coupled with two semi-circular patches along radiating and nonradiating edge.

To enhance the bandwidth further, two semi-circular patches are placed along radiating and nonradiating edge of RMSA as shown in Fig. 7a. A parametric study is carried out by varying gap  $g$  between feed resonator and RMSA, gap  $g_1$  between RMSA and semi-circular patches along RMSA radiating edge, gap  $g_2$  and  $g_3$  between patches, diameter  $D$  and  $D_1$  of semi-circular patches. In this configuration, due to asymmetric gap-coupled patches, maximum gain is obtained at  $\theta = 20^\circ$  across the

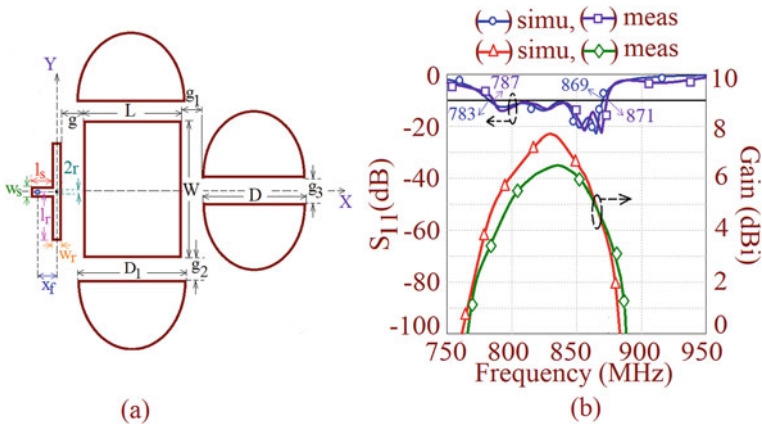


**Fig. 7 a** MS- $\lambda/2$  line resonator-fed RMSA gap-coupled with four semi-circular patches, its **b** gain and return loss plots

entire bandwidth. Figure 7b shows return loss and gain plots of MS- $\lambda/2$  resonator-fed RMSA gap-coupled with four semi-circular patches.

Optimum simulated and measured bandwidth and gain obtained is 86 MHz (10.41%) and 84 MHz (10%), respectively. This configuration provides peak simulated and measured gain of 7.7 and 7 dBi at  $\theta = 20^\circ$ . For the optimized configuration microstrip-line  $\lambda/2$  resonator-fed RMSA with four semi-circular patches, dimensions are  $L = 120$ ,  $W = 140$ ,  $D = 138$ ,  $D_1 = 136$ ,  $g = 2$ ,  $g_1 = 2$ ,  $g_2 = 1.5$ ,  $g_3 = 4$ ,  $x_f = 17$ .

Due to the asymmetrical placement of parasitic patches with respect to feed resonator, gap-coupled patches experience phase delay that pulls the beam maxima from the broadside direction. Hence maximum gain is obtained in direction of  $\theta = 20^\circ$ . Figure 8 shows the simulated and measured radiation pattern at the lower and upper band edge frequency. Figure 8c, d shows tilted beam maxima in the E-plane due to semi-circular patches resonance at the higher frequency which shifts beam maxima. Figure 9 shows a photograph of the fabricated prototype of a microstrip-line  $\lambda/2$  resonator-fed RMSA with four semi-circular patches.

### 3 Conclusions

Three-layer microstrip-line resonator-fed gap-coupled RMSA configurations with semi-circular patches are proposed. The presented configurations use compact pair of  $\lambda/4$  resonator feed and radiating patches on the single substrate to enhance the bandwidth using a thinner substrate. Microstrip resonator dimensions and coupling gap parametric study are presented to figure out the performance of the antenna. The proposed configuration provides reasonably high bandwidth with more than 7 dBi gain using an electrically thinner substrate. The presented configurations can find applications in systems like SCADA, smart grid monitoring systems.

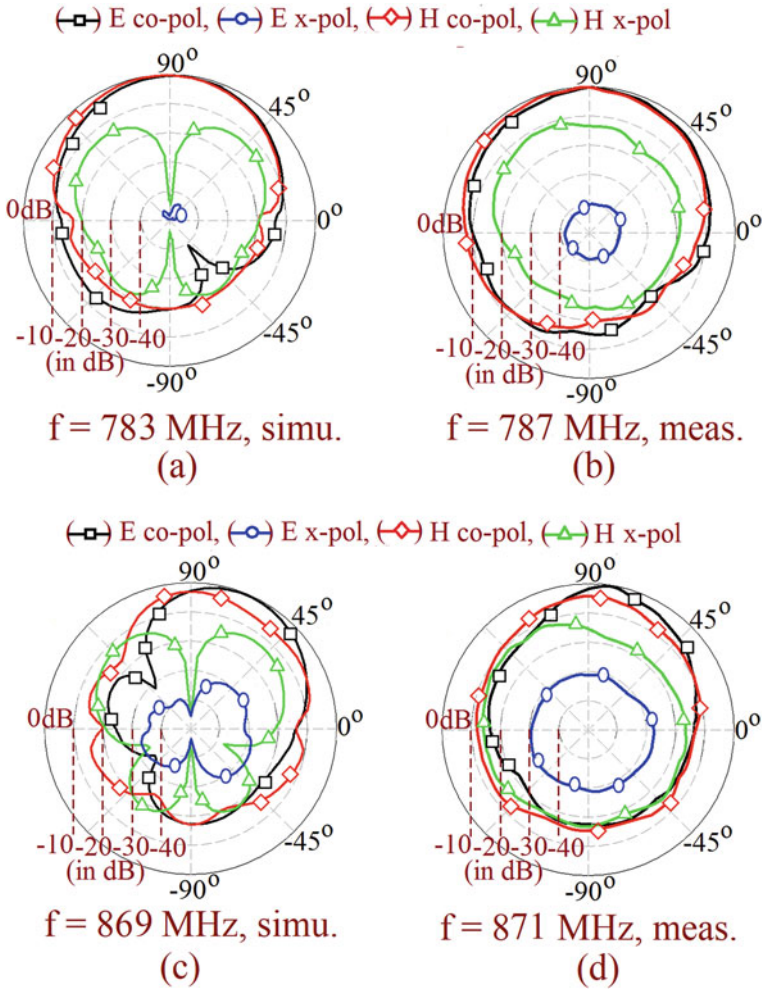


**Fig. 8** a Simulated, b measured radiation pattern at 783 and 787 MHz, c simulated, d measured radiation pattern at 869 and 871 MHz of MS- $\lambda/2$  resonator-fed RMSA gap-coupled with four semi-circular patches configuration

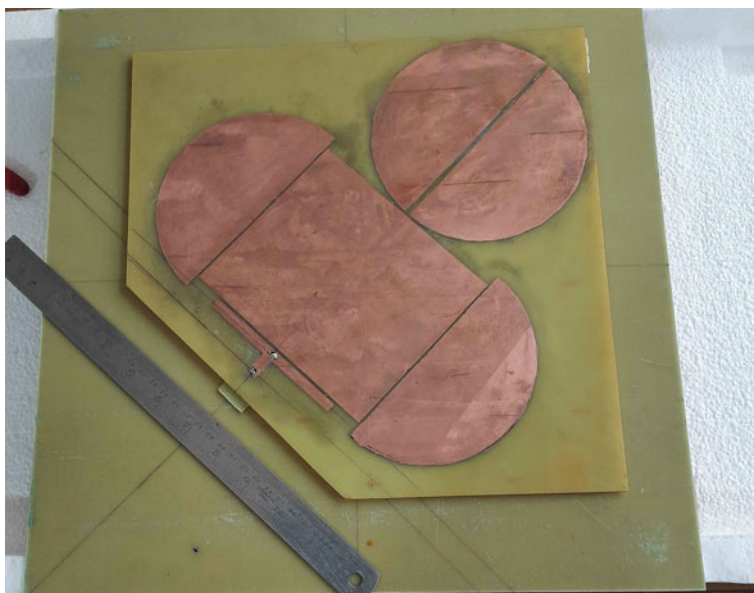


**Fig. 9** Fabricated prototype of microstrip-line  $\lambda/2$  resonator-fed RMSA with four semi-circular patches

## References

1. Kumar G, Ray KP (2003) Broadband microstrip antennas, 1st edn. Artech House, USA
2. Targonski SD, Waterhouse RB, Pozar DM (1998) Design of wide-band aperture-stacked patch microstrip antennas. *IEEE Trans Antennas Propag* 16(9):1245–1251
3. Zhao F, Xiao K, Feng WJ, Chai SL, Mao JJ (2009) Design and manufacture of the wide-band aperture-coupled stacked microstrip antenna. *Prog Electromagn Res* 7:37–50
4. Sun D, Lizhi Y (2010) A broadband impedance matching method for proximity-coupled microstrip antenna. *IEEE Trans Antennas Propag* 58(4):1393–1397
5. Legay H, Shafai L (2004) New stacked microstrip antenna with large bandwidth and high gain. *IEE Proc Microw Antennas Propag* 141(2):199–204
6. Kumar G, Ray KP (2001) Stacked gap-coupled multi-resonator rectangular microstrip antennas. *Proc IEEE/URSI Sympo Antennas Propag* 514–517. <https://doi.org/10.1109/aps.2001.960147>
7. Deshmukh AA, Ray KP (2011) Broadband proximity-fed modified rectangular microstrip antennas. *IEEE Antennas Propag Mag* 53(5):41–56
8. Mak CL, Hong W, Luk KM (2005) High-gain and wide-band single-layer patch antenna for wireless communications. *IEEE Trans Vehicular Technol* 54(1):33–40
9. Mak CL, Lee KF, Luk KM (2000) Broadband patch antenna with a T-shaped probe. *IEE Proc Microw Antennas Propag* 147(2):73–76
10. Kishk AA, Kai FL, Mok WC, Luk KM (2004) A wide-band small size microstrip antenna proximately coupled to a hook shape probe. *IEEE Trans Antennas Propag* 52(1):59–65
11. Ansari JA, Ram RB (2008) Analysis of broad band U-slot microstrip patch antenna. *Microw Opt Technol Lett* 50(4):1069–1073
12. Yang F, Zhang XX, Ye X, Rahmat-Samii Y (2001) Wide-band E-shaped patch antennas for wireless communications. *IEEE Trans Antennas Propag* 49(7):1094–1100
13. Deshmukh AA, Ray KP (2013) Analysis of broadband Psi ( $\Psi$ )-shaped microstrip antenna. *IEEE Antennas Propag Mag* 55(2):107–123

14. Zhang JD, Zhu Lei WuQS, Liu NW, Wu W (2016) A compact microstrip-fed patch antenna with enhanced bandwidth and harmonic suppression. *IEEE Trans Antennas Propag* 64(12):5030–5037
15. CST Microwave Studio, Version 2019

# Microstrip-Line Resonator-Fed Equilateral Triangular Antenna Using Gap-Coupled Parasitic Triangular Shape Patches



Sanjay B. Deshmukh and Amit A. Deshmukh

**Abstract** In this paper, a gap-coupled design of a microstrip-line resonator-fed equilateral triangular microstrip antenna along with a variant of triangular patches is proposed. A pair of  $\lambda/4$  microstrip-line resonators indirectly feeds a gap-coupled equilateral triangular microstrip antenna with triangular patches. Enhancement in bandwidth is achieved by coupling resonance introduced by pair of  $\lambda/4$  microstrip-line resonator and gap-coupled parasitic patches. Design of microstrip-line resonator-fed rectangular microstrip antenna provides a bandwidth of 40 MHz (4.8%) with broadside gain of 5 dBi. An optimum response obtained in an equilateral triangular microstrip antenna gap-coupled configuration with four triangular shape patches in terms of impedance bandwidth and a peak gain is 87 MHz (10.22%) and 6.4 dBi. The proposed design is implemented using  $0.019\lambda_c$  total substrate thickness and the experimental results obtained with the fabricated prototype antenna show a close match with the simulated results.

**Keywords** Microstrip-line resonator · Triangular shape · Gap-coupled · High gain · Shorting pin · Equilateral triangular microstrip antenna

## 1 Introduction

In the recent few years, expeditious development in wireless communication systems requires antennas with higher gain and bandwidth. Microstrip antennas (MSAs) have inherent benefits like low profile, conformal, ease of integration with radio frequency [1]. Many techniques like impedance matching and feeding techniques such as aperture coupling feed [2, 3] and proximity coupling feed [4] have been employed to enhance MSA bandwidth. However, these techniques use multi-layer

---

S. B. Deshmukh

Department of EXTC, SVKM's DJSCE, UOM, Mumbai, India

e-mail: [sanjay.deshmukh@djsce.ac.in](mailto:sanjay.deshmukh@djsce.ac.in)

A. A. Deshmukh (✉)

Department of EXTC Engineering, SVKM's DJSCE, Mumbai, India

e-mail: [amit.deshmukh@djsce.ac.in](mailto:amit.deshmukh@djsce.ac.in)

substrates that require a complex design process. An equilateral triangular microstrip antenna (ETMSA) has a similar performance like a rectangular microstrip antenna (RMSA) with the advantage of small size. The bandwidth of MSA can be enhanced by lowering the dielectric constant of the substrate. Air-suspended ETMSA is used to increase bandwidth [5, 6]. In [7], dielectric superstrate-loaded ETMSA is used to enhance the bandwidth. The bandwidth can be enhanced by incorporating a slot in the MSA. Slots in patches align similar radiation characteristics modes with fundamental mode to get a wideband response. Broadband probe-fed ETMSA is realized by cutting U-slot, which provides 18% impedance bandwidth [8]. In [9], a pair of narrow slots are employed in inset-fed ETMSA for bandwidth enhancement. Wideband designs of TMSA are relatively complex than the gap-coupled MSA designs. Bandwidth improvement in TMSA can be achieved by using shorting wall along the patch edge. Broadband ETMSA with the folded shorting wall is proposed to yield 28% impedance bandwidth and 6.4 dBi broadside gain [10]. A tip truncated V-slot cut ETMSA provides 25% bandwidth by placing shorting wall on opposite edges of the patch [11]. Bandwidth can be enhanced in probe-fed MSA by increasing substrate thickness. Substrate thickness cannot use beyond  $0.1\lambda_0$ . This is due to an increase in probe inductance that leads to the requirement of an impedance matching network, and excitation of surface wave results in degradation in antenna performance. This drawback can be resolved by using a modified probe. Single-layer L-probe-fed TMSA provides 42% bandwidth and peak gain of 6 dBi with a high cross-polar level [12]. A dual L-straplines-fed TMSA is presented in [13] to reduce the cross-polar level and enhance the bandwidth with the drawback of a complex feeding structure. Broadband high gain stacked ETMSA is proposed to obtain 42.2% bandwidth with a peak gain of 10.8 dBi [14]. This structure is high profile and requires a complex design process. MSA bandwidth enhancement using an electrically thinner substrate is a challenging task. In [15], additional  $\lambda/4$  nonradiating along with radiating patch is used to enhance bandwidth.

In this paper, microstrip-line (MS) resonator-fed gap-coupled designs of ETMSA with triangular shape patches are presented. With the various combinations of parasitic patches in a configuration such as single ETMSA, ETMSA gap-coupled with triangular patches along the radiating edge,  $\lambda/2$  nonradiating resonator gap-coupled with ETMSA and two triangular patches, and ETMSA and  $\lambda/2$  nonradiating resonator gap-coupled with two triangular patches are proposed. Microstrip-line resonator-fed single ETMSA yields impedance bandwidth of 40 MHz (4.8%) and broadside gain of 5 dBi. For the configuration ETMSA with two triangular parasitic patches along radiating edge provides a BW of 64 MHz (7.63%) and peak gain of 6 dBi. The configuration  $\lambda/2$  nonradiating resonator gap coupled with ETMSA and two triangular patches provide a BW of 75 MHz (8.75%) and a peak broadside gain of 5.9 dBi. Further, enhancement in gain and bandwidth is obtained by placing two triangular patches along edges of  $\lambda/2$  resonator and ETMSA yields BW of more than 85 MHz (10.11%) and broadside peak gain of 6.4 dBi. Gap-coupled MSA structures presented here are optimized in the 700–900 MHz frequency range. The above-specified frequency range is opted for the proposed ETMSA gap-coupled configurations as MSA provides narrow BW in this frequency band. Initially, parametric study and analysis are carried



out by varying  $\lambda/4$  resonator length and width, the gap between  $\lambda/4$  resonator and ETMSA and the gap between ETMSA and triangular shape patches. CST software was used for the optimization of presented configurations [16]. The dimensions and frequency used in this paper are in millimeters and MHz. This simulation study was followed by experimental validation. SMA type panel of 0.12 cm inner wire diameter is used to feed the antennas. The impedance response is measured using a vector network analyzer ZVH-8, which is used for impedance measurement. The antenna pattern measurement is conducted in an antenna lab using an RF source (SMB 100A) and spectrum analyzer (FSC-6).

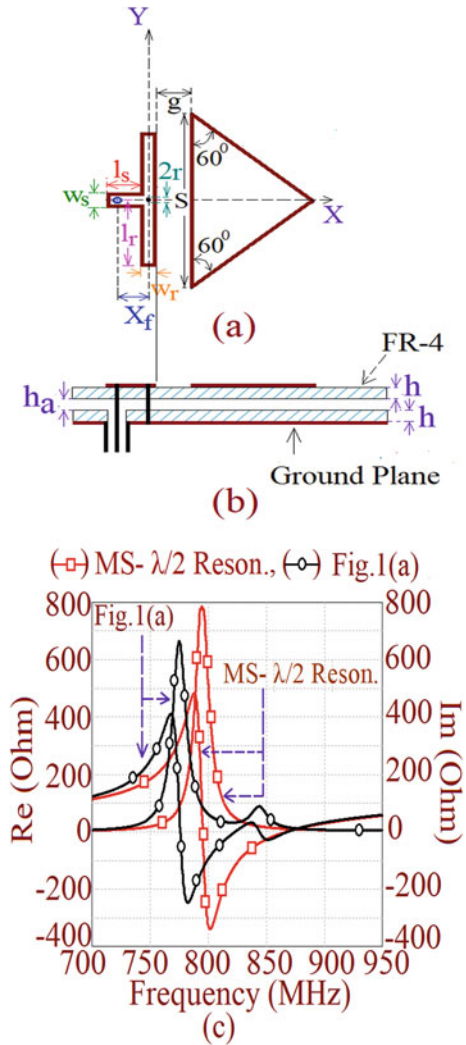
## 2 Microstrip-Line Resonator-Fed ETMSA Gap-Coupled with Triangular Patches

### 2.1 Microstrip-Line Resonator-Fed ETMSA

The basic configuration of microstrip-line indirectly fed ETMSA is shown in Fig. 1a, b. This configuration is a three-layer structure, consisting of the top and bottom layer of FR-4 substrate and the middle air layer. Substrate parameters used in this configuration are as follows: thickness  $h = 1.6$  mm, dielectric constant  $= 4.3$  and loss tangent  $\delta = 0.02$ . An FR4 substrate with backed copper acts as a ground plane over which another FR4 is placed with air gap 'h<sub>a</sub>' = 1.6 mm. On the top of the suspended substrate, a microstrip-line of length  $l_s$  and width  $w_s$  is etched with a pair of  $\lambda/4$  resonators. On this substrate ETMSA of side length 'S' is placed with gap  $g$  from the resonator. Resonator pair has length  $l_r$  and width  $w_r$  with shorting pin of radius  $r$ . An antenna is fed through a microstrip line using a coaxial probe at a distance of  $X_f$  with reference to the resonator. ETMSA fundamental mode  $TM_{10}$  frequency of 840 MHz is selected and realized using a total substrate thickness of  $0.019\lambda_c$ . A parametric study is carried to optimize the dimension of microstrip line, resonator and ETMSA to resonate antenna around 840 MHz fundamental frequency.

The optimum response of the proposed configuration in terms of bandwidth and gain is 40 MHz (4.8%) and 5 dBi, and dimensions are as follows:  $S = 156$ ,  $w_r = 6$  ( $0.016\lambda$ ),  $l_r = 51$  ( $0.25\lambda$ ),  $l_s = 20$ ,  $w_s = 6$ , and  $r = 0.5$ . Figure 1c shows the resonance plot of MS-line  $\lambda/2$  resonator and MS-line  $\lambda/2$  resonator-fed ETMSA. Two resonance peaks are obtained in the resonance plot for MS-line  $\lambda/2$  resonator-fed ETMSA due to the coupling of the shorted mode of a resonator with ETMSA mode. The parametric study is carried out by varying gap  $g$  between nonradiating  $\lambda/2$  resonator and ETMSA with resonator length  $l_r$  and width  $w_r$  value constant. Figure 2a, b shows the effect of variation in coupling gap  $g$  on the reflection coefficient and input impedance of the antenna. The size of the loop in the input impedance depends on gap  $g$  between the feed resonator and ETMSA. Coupling between resonator feed and ETMSA increases with a decrease in the gap between them. The optimum result

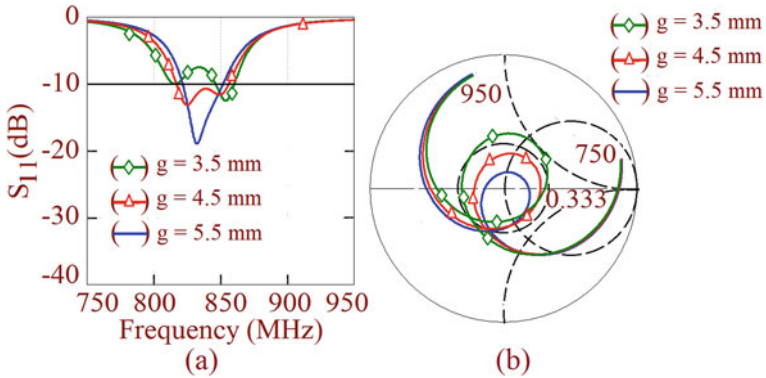
**Fig. 1 a, b** Microstrip-line resonator-fed ETMSA, **c** resonance plot of MS- $\lambda/2$  resonator and MS- $\lambda/2$  resonator-fed ETMSA



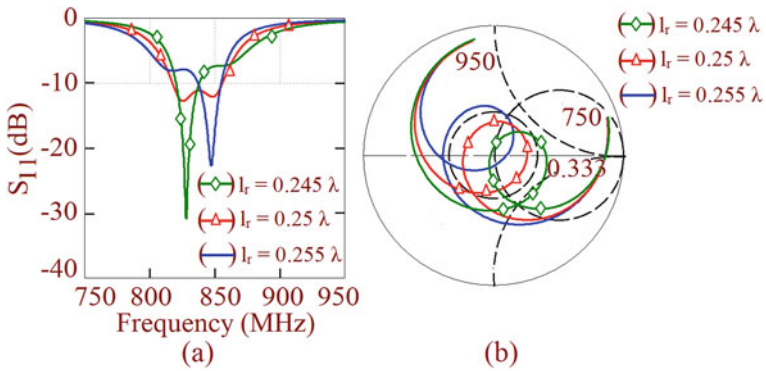
obtained for gap  $g = 4.5$  mm at which impedance covers the maximum area within VSWR 2 circle.

Figure 3a, b depicts the effect of variation in the length of  $\lambda/4$  resonator on the reflection coefficient and input impedance response. The parametric optimization has been carried out by varying the length of  $\lambda/4$  resonator and by keeping the coupling gap  $g$  and width  $w_r$  value constant. The optimum bandwidth response obtained for resonator length  $l_r = 51$  ( $l_r = 0.25\lambda$ ).

Figure 4a, b represents the effect of variation in the width of  $\lambda/4$  resonator on the reflection coefficient and input impedance response. The parametric variation has been carried out for width of  $\lambda/4$  resonator with coupling gap  $g$  and length  $l_r$



**Fig. 2** **a** Effect of variation in coupling gap  $g$  on the reflection coefficient, **b** effect of variation in coupling gap  $g$  on input impedance ( $w_r = 6$ ,  $l_r = 51$ )



**Fig. 3** **a** Effect of variation in the length of  $\lambda/4$  resonator on the reflection coefficient, **b** effect of variation in the length of  $\lambda/4$  resonator on input impedance ( $w_r = 6$ ,  $g = 4.5$ )

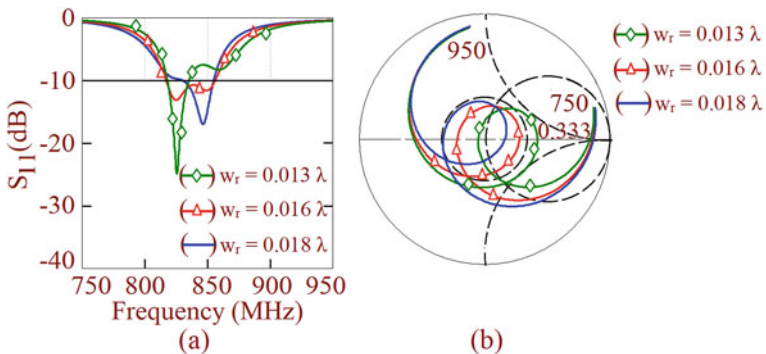


**Fig. 4** **a** Effect of variation in the length of  $\lambda/4$  resonator on the reflection coefficient, **b** effect of variation in the width of  $\lambda/4$  resonator on input impedance ( $l_r = 51$ ,  $g = 4.5$ )

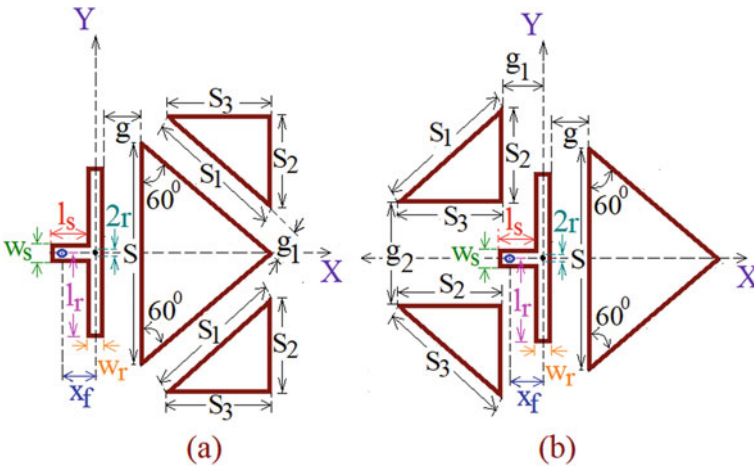
value constant. For the  $w_r$  value equal to  $0.016 \lambda$ , the optimum bandwidth response obtained for resonator width  $w_r = 6$  ( $w_r = 0.016\lambda$ ) and the entire loop lie within VSWR 2 circle.

In order to enhance bandwidth, two triangular patches are placed along ETMSA and  $\lambda/2$  resonator edge as shown in Fig. 5a, b. Addition of triangular patches couples one more resonant mode to enhance the bandwidth. Optimum simulation for resonator-fed ETMSA with two triangular patches along ETMSA and resonator is 64 MHz (7.63%) and 75 MHz (8.75%), respectively. The simulated gain of these configurations is 6 dBi and 5.9 dBi, respectively. As coupling is more along the edge of  $\lambda/2$  resonator as compared to ETMSA edge, slightly more bandwidth is obtained in resonator edge-coupled triangular patches configuration. Figure 6a, b shows simulated return loss and gain plots for MS- $\lambda/2$  resonator-fed ETMSA,  $\lambda/2$  resonator and ETMSA gap-coupled with two triangular patches.

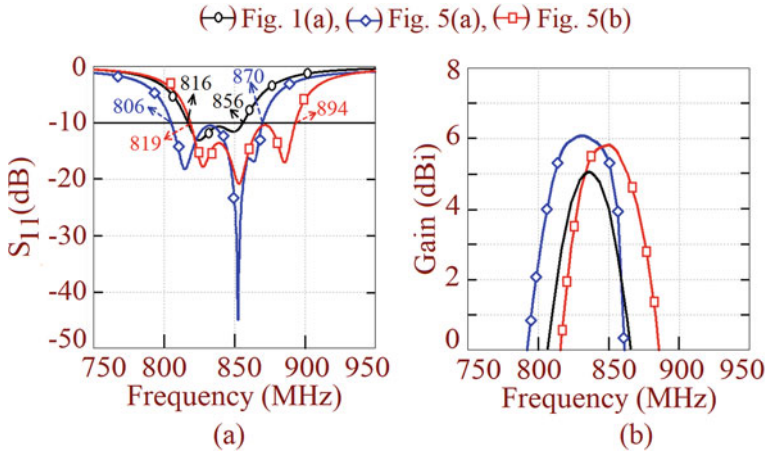
To enhance the bandwidth further, two triangular patches are placed along the edge of ETMSA and resonator as shown in Fig. 7a. A parametric study is carried out by varying gap  $g$  between feed resonator and ETMSA, gap  $g_1$  between ETMSA and triangular patches, gap  $g_2$  and  $g_3$  between triangular patches and resonator.

Figure 7b shows return loss and gain plots of MS- $\lambda/2$  resonator-fed ETMSA gap-coupled with four triangular patches. The optimum simulated and measured bandwidth is 87 MHz (10.22%) and 85 MHz (9.9%), respectively. This configuration provides broadside peak simulated and measured gain of 6.4 and 5.5 dBi. For the optimized configuration microstrip-line  $\lambda/2$  resonator-fed RMSA with four triangular patches, the dimensions are  $S = 156$ ,  $S_1 = 151$ ,  $S_2 = 76$ ,  $S_3 = 131$ ,  $S_4 = 145$ ,  $S_5 = 74$ ,  $S_6 = 126$ ,  $g = 6.5$ ,  $g_1 = 2$ ,  $g_2 = 5$ ,  $g_3 = 12$  and  $X_f = 19$ .

Figure 8 shows the simulated and measured radiation pattern at the lower and upper band edge frequency. Figure 8c, d shows high cross-polar due to excitation



**Fig. 5** a, b MS- $\lambda/2$  resonator-fed ETMSA gap-coupled with two triangular patches along ETMSA and resonator



**Fig. 6 a, b** Simulated return loss and gain plots for MS- $\lambda/2$  resonator-fed ETMSA,  $\lambda/2$  resonator and ETMSA gap-coupled with two triangular patches

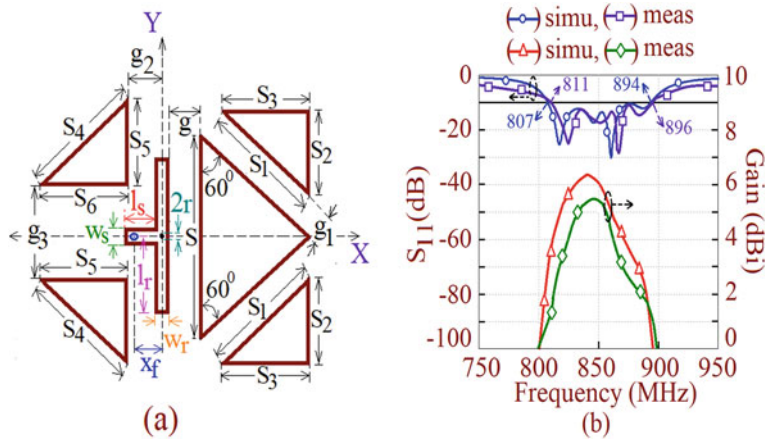


**Fig. 7 a** MS-line  $\lambda/2$  resonator-fed ETMSA gap-coupled with four triangular patches, **b** its gain and return loss plots

of orthogonal mode. Figure 9 shows a photograph of the fabricated prototype of a microstrip-line  $\lambda/2$  resonator-fed ETMSA with four triangular patches.

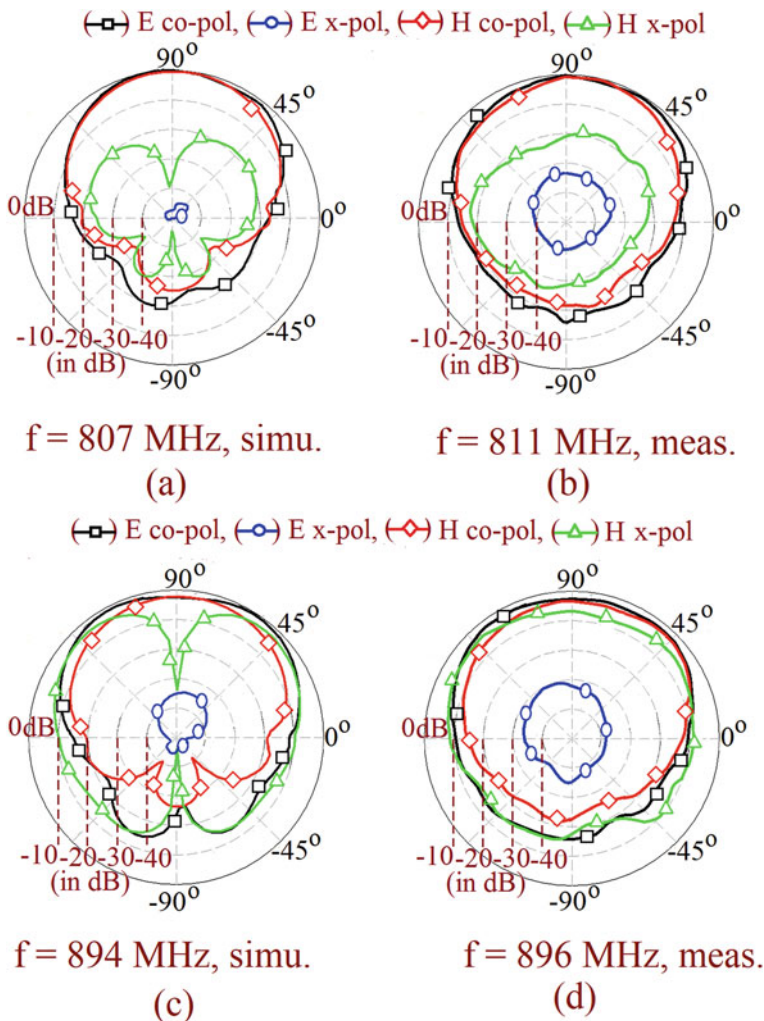


**Fig. 8** **a** Simulated, **b** measured radiation pattern at 807 and 811 MHz, **c** simulated, **d** measured radiation pattern at 894 and 896 MHz of MS- $\lambda/2$  resonator-fed ETMSA gap-coupled with four triangular patches configuration

### 3 Conclusions

Three-layer microstrip-line resonator-fed gap-coupled ETMSA configurations with triangular patches are proposed. The presented configurations use compact pair of  $\lambda/4$  resonator feed and radiating patches on the single substrate to enhance the bandwidth using a thinner substrate. Microstrip resonator dimensions and coupling gap parametric study are presented to figure out the performance of an antenna. The

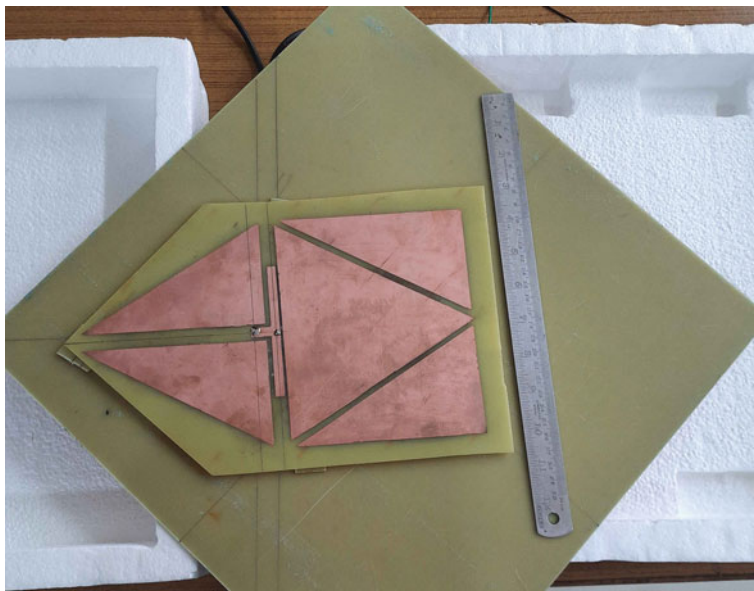


**Fig. 9** Fabricated prototype of MS-line  $\lambda/2$  resonator-fed ETMSA with four triangular patches

proposed configuration provides reasonably high bandwidth with more than 6 dBi gain using an electrically thinner substrate. The presented configurations can find applications in systems like SCADA, Smart Grid monitoring systems.

## References

1. Kumar G, Ray KP (2003) Broadband microstrip antennas, 1st edn. Artech House, USA
2. Yang XH, Shafai L (1995) Characteristics of aperture coupled microstrip antennas with various radiating patches and coupling apertures. *IEEE Trans Antennas Propag* 43(1):72–78
3. Rathi V, Kumar G, Ray KP (1996) Improved coupling for aperture Coupled microstrip antennas. *IEEE Trans Antennas Propag* 44(8):1196–1198
4. Sun D, Dou W, You L, Yan X, Shen R (2011) A broadband proximity-coupled stacked microstrip antenna with cavity-backed configuration. *IEEE Antennas Wirel Propag Lett* 10(4):1055–1058
5. Guha D, Siddiqui JY (2004) Resonant frequency of equilateral triangular microstrip antenna with and without air gap. *IEEE Trans Antennas Propag* 52(8):2174–2178
6. Lee K, Fong L, Kwai M, Dahele JS (1988) Characteristics of the equilateral triangular patch antenna. *IEEE Trans Antennas Propag* 36(11):1510–1518
7. Biswas M, Guha D (2009) Input impedance and resonance characteristics of superstrate-loaded triangular microstrip patch. *IET Microw Antennas Propag* 3(1):92–98
8. Wong KL, Hsu WH (1997) Broadband triangular microstrip antenna with U-shaped slot. *Electron Lett* 33(25):2085–2087
9. Fang S, Tirng W, Kin L, Chiou TW (1998) Bandwidth enhancement of inset-microstripline-fed equilateral-triangular microstrip antenna. *Electron Lett* 34(23):2184–2186
10. Li Y, Chair R, Luk KM, Lee KF (2004) Broadband triangular patch antenna with a folded shorting wall. *IEEE Antennas Wirel Propag Lett* 3(1):189–192

11. Row JS, Liou YY (2006) Broadband short-circuited triangular patch antenna. *IEEE Antennas Trans Propag* 54(7):2137–2141
12. Mak CL, Luk KM, Lee KF (1999) Wideband triangular patch antenna. *IEE Proc—Microw Antennas Propag* 146(2):167–168
13. Chiou SH, Lu JH (2002) Cross-polarization level reduction of broadband triangular patch antenna with dual L-strip lines. *Microw Opt Technol Lett* 33(4):300–303
14. Chopra R, Kumar G (2020) High gain broadband stacked triangular microstrip antennas. *Microw Opt Technol Lett* 62(9):2881–2888
15. Zhang JD, Zhu Lei WuQS, Liu NW, Wu W (2016) A compact microstrip-fed patch antenna with enhanced bandwidth and harmonic suppression. *IEEE Trans Antennas Propag* 64(12):5030–5037
16. CST Microwave Studio, Version 2019



# Designs of Letter Shape Microstrip Antennas for Wideband, Dual-Band, and Circularly Polarized Response



Shefali Pawar, Amit A. Deshmukh, and Aarti G. Ambekar

**Abstract** Compact variation of A-shape microstrip antenna is discussed. To enhance the bandwidth of this compact design, its various gap-coupled multi-resonator variations using compact MSAs like M-shape, N-shape, W-shape, U-shape, and their variations are proposed. The wideband response is attributed to the gap-coupling between fundamental resonant modes among various patches. The gap-coupled variation of A-shape patch with respective M-shape, N-shape, W-shape, and U-shape patches yields wideband response. Here in terms of pattern purity and bandwidth, gap-coupled design of A-shape with M-shape and W-shape patch individually yields optimum response. The gap-coupled variation of A-shape with a combination of M and N-shape patch yields a dual-band CP response. The proposed multi-resonator compact antennas are proposed on suspended FR4 substrate in 800–1200 MHz frequency range and thus will find applications in mobile communication systems in the said frequency band.

**Keywords** Compact microstrip antenna · Broadband microstrip antenna · A-shape · M-shape · N-shape · W-shape · U-shape · Gap-coupled configuration

## 1 Introduction

The microstrip antenna (MSA) in the simplest form consists of a radiating patch on one side of the microwave substrate backed by the ground plane on the other side [1, 2]. To enhance the impedance bandwidth (BW) and gain (radiation efficiency), air suspended variations have been used where the patch fabricated on microwave substrate is suspended above the ground plane using a finite air gap [3, 4]. The suspended design not only utilizes low-cost lossy substrate but also improves the reliability of antenna parameters against the substrate parameter variations [3–5]. The radiating patch in MSA can take any arbitrary shapes, but from a mathematical modeling point of view, regular shape designs have been largely used [1–4]. However,

---

S. Pawar · A. A. Deshmukh (✉) · A. G. Ambekar  
Department of EXTC, SVKM's DJSCE, Mumbai, India

any irregular or modified regular shape can offer some unique design feature that adds to antenna characteristics like, size reduction, multi or wideband response, or circular polarized (CP) response. Recently, designs of A-shape MSAs have been reported [6]. The A-shape patch on thinner substrate offers a multi-band response with reference to its first three resonant modes and offers a tuning feature in the form of stub length and position, which realizes A-shape geometry from the equivalent U-shape one [6]. However, those designs were optimized on a thinner lossy substrate and thus have smaller gain and BW.

In this paper, various gap-coupled designs of compact A-shape MSA using parasitic compact MSAs, like M-shape, W-shape, N-shape, and U-shape patches, are proposed on thicker air suspended FR4 substrate ( $\epsilon_r = 4.3$ ,  $h = 0.16$  cm) for wideband single polarized and wideband response yielding dual-band CP response. The above patch shapes (letter shapes) are chosen as they offer compactness in size due to their modified geometries. Among all the designs, a gap-coupled configuration of A-shape MSA along with M-shape MSAs yields maximum BW. However, the gap-coupled design of A-shape MSA with M-shape and N-shape MSAs yields dual-band CP response occupying inside a wider impedance BW. As the modified patch geometries (letter shape patches) have been used, an overall increase in the total patch size is relatively smaller. The proposed configurations are discussed in the 800–1200 MHz frequency band, thereby making it suitable for mobile communication applications in the 1000 MHz frequency band. The gap-coupled antennas presented in this paper are initially optimized using the IE3D simulations followed by the experimentation using ZVH-8, FSC 6, and SMB 100A. The ground plane size of  $30 \times 30$  cm is selected in the experimentation and an N-type connector of inner wire diameter 0.32 cm is employed to feed the antennas. In the pattern and gain measurement, reference wideband horn antennas were used as the reference antenna. The gain is measured in the lab environment using a three-antenna method, which ensures better accuracy. The required minimum far-field distance is maintained between the reference horn and antenna under test. Thus, novel gap-coupled configurations of compact letter shape MSA for wideband and dual-band CP response, requiring smaller overall patch size is the new technical contribution in the proposed work.

## 2 Wideband Gap-Coupled Letter Shape MSAs

The gap-coupled design of A-shape MSA with parasitic M-shape MSA is shown in Fig. 1e, f. The gap-coupled design is studied on a total substrate thickness of 2.96 cm, i.e. air gap of 2.8 cm. The A-shape MSA is a variation of U-shape patch and surface current distribution at the first two resonant modes in two patches is shown in Fig. 1a–d. The variation in surface currents is orthogonal across two modes and thus they offer dual-polarization across them. The tuning of the first frequency ( $f_{10}$ ) is realized by changing the stub position in the A-shape patch. The proposed gap-coupled variations are presented with reference to the fundamental  $TM_{10}$  mode in the fed and parasitic patches, in all the designs. In each configuration, a parametric study is carried out

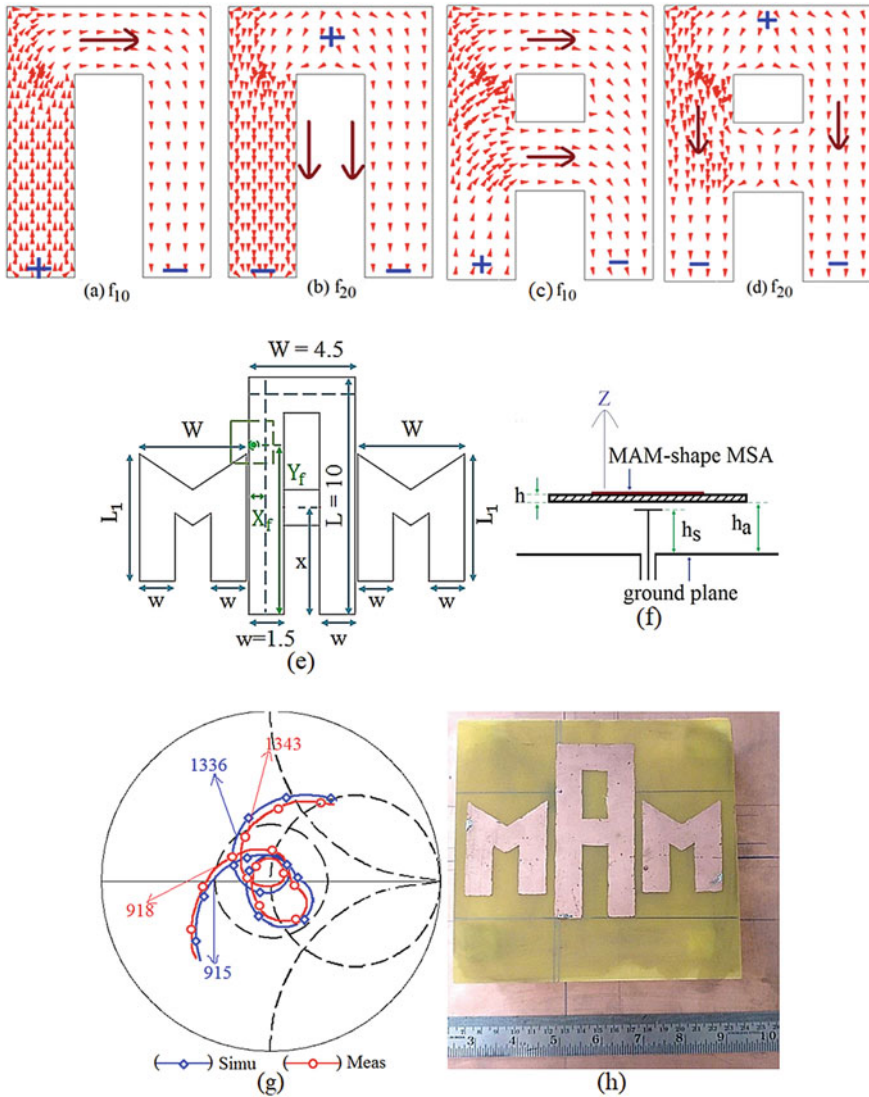


**Fig. 1** a–d Surface current distribution for U-shape and A-shape MSAs, e, f gap-coupled MAM shape MSA its g input impedance plots h fabricated prototype

for the variation in parasitic patch dimensions, proximity strip parameters, i.e. its dimension and position below the patch, which lead to the optimum result in gap-coupled design. In all the parasitic patches, their total length along the respective patch dimension equals half the wavelength. The optimum result in A-shape MSA gap-coupled with M-shape patches is obtained for  $x = 45$  mm,  $g = 3$  mm and for feed-point  $(X_f, Y_f) = (2.5, 72.5)$ . The proximity feed patch dimension is  $18 \times 18$  mm.

The simulated and measured input impedance plot and the fabricated prototype of the MSA are shown in Fig. 1g, h. The simulated BW is from 915 to 1336 MHz (421 MHz) and the measured bandwidth is from 918 to 1343 MHz (425 MHz). The radiation pattern at three frequencies over the BW is shown in Fig. 2a–f. The pattern is in the broadside direction with E and H-planes aligned along  $\Phi = 0^\circ$  and  $90^\circ$ , respectively. The peak broadside antenna gain is 8 dBi.

In the next configuration, A-shape MSA is gap-coupled on each lateral side with W-shaped MSA as shown in Fig. 2g. The optimized configuration is obtained for  $x = 49$  mm,  $g = 5$  mm and for the feed-point at  $(X_f, Y_f) = (2.5, 72.5)$ . The proximity feed patch dimension is  $18 \times 18$  mm and the configuration is shown in Fig. 2g.

The simulated and measured input impedance plot and the fabricated prototype of the MSA are shown in Fig. 2h, i. The simulated BW is from 924 to 1346 MHz (422 MHz) and the measured BW is from 904 to 1355 MHz (451 MHz). The radiation pattern at three frequencies over the BW (band start, center, and bands top) is shown in Fig. 3a–f. The pattern is in the broadside direction with E and H-planes aligned along  $\Phi = 0^\circ$  and  $90^\circ$ , respectively. The peak antenna gain in the broadside direction is around 8 dBi.

In another gap-coupled design, A-shape MSA is gap-coupled on each lateral side with two N-shape MSAs. The optimized configuration in this design is obtained for  $x = 45$  mm,  $g = 7$  mm and for the feed-point  $(X_f, Y_f) = (7.5, 67.5)$ . The proximity feed patch dimension is  $18 \times 18$  mm and the configuration is shown in Fig. 4a. The simulated and measured input impedance plot and the fabricated prototype of the MSA are shown in Fig. 4b, c. The simulated BW of configuration is from 940 to 1290 MHz (350 MHz) and the measured BW is from 912 to 1320 MHz (408 MHz). The pattern shows broadside radiation but due to N-shape patches, higher cross-polarization levels are observed over the BW. The design of A-shape MSA gap-coupled with M-shape and N-shape MSA is shown in Fig. 4d. For the same proximity feed parameters as present in the N-A-N design optimum response is realized. The input impedance plots and the fabricated prototype for the optimum design are shown in Fig. 4e, f. The simulated BW is from 893 to 1303 MHz (410 MHz) and the measured BW is from 870 to 1310 MHz (440 MHz).

This design shows dual-band CP response over a frequency range from 958 to 978 MHz (20 MHz) and 1270 to 1284 MHz (14 MHz) for an axial ratio less than 3 dB. Over the impedance and axial ratio BW, antenna gain is larger than 5 dBi. Thus, in comparison to previous gap-coupled designs, a combination of M and N-shape MSA yields a dual-band CP response. The design of gap-coupled A-shape MSA with U-shape MSAs is shown in Fig. 5a. The optimized configuration is obtained for  $x = 41$  mm,  $g = 3$  mm and for  $(X_f, Y_f) = (7.5, 72.5)$ . The proximity feed strip dimension is  $19 \times 19$  mm. The input impedance plot and the fabricated prototype are shown in Fig. 5b, c. The simulated BW is from 1093 to 1330 MHz (237 MHz) and the measured BW is from 1070 to 1345 MHz (275 MHz). The antenna yields a broadside pattern across the BW with a peak gain of larger than 7 dBi.

In the next configuration, A-shape MSA is gap-coupled on each lateral side with inverted U-shape MSA. The optimized configuration of this proposed MSA is obtained for  $x = 45$  mm,  $g = 5$  mm and for feed-point  $(X_f, Y_f) = (2.5, 67.5)$ .

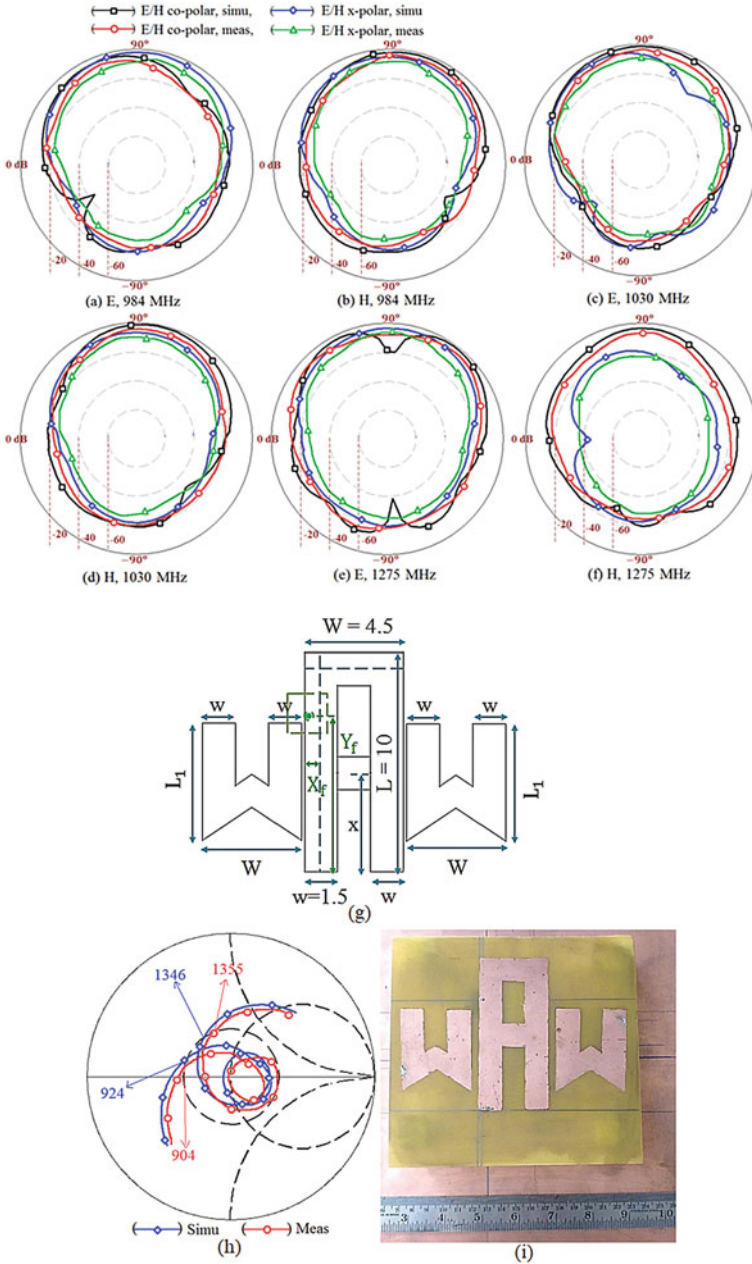


**Fig. 2** a–f Radiation pattern nearer to band start, center, and bandstop frequencies for gap-coupled MAM shape MSAs, g gap-coupled W-shape MSA with A-shape and its h smith chart, and i fabricated prototype

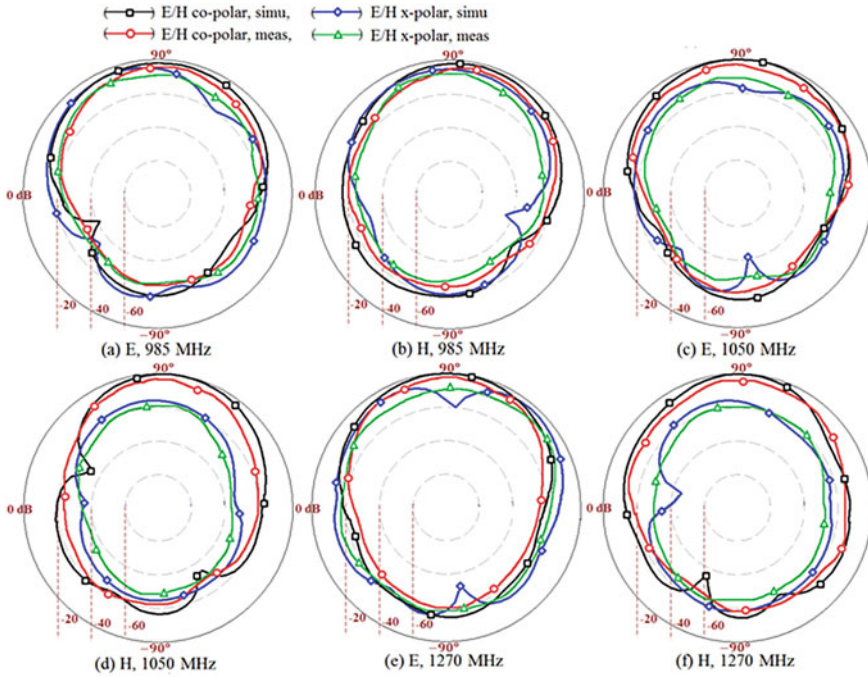


**Fig. 3** a–f Radiation pattern over the BW for gap-coupled WAW shape MSAs

The proximity feed patch dimension is  $18 \times 18$  mm and the configuration is shown in Fig. 6a. The simulated and measured input impedance plot and the fabricated prototype of the MSA are shown in Fig. 6b, c. The simulated BW is from 1040 to 1411 MHz (371 MHz) and the measured BW is from 1021 to 1415 MHz (395 MHz). The antenna yields a broadside pattern across the BW with a peak gain of larger than 6 dBi.

In the next configuration, A-shape MSA is gap-coupled on each lateral side with an A-shaped MSA of the same dimensions as the fed patch. The optimized configuration of this proposed MSA is obtained for  $x = 49$  mm,  $g = 1$  mm and for feed-point  $(X_f, Y_f) = (2.5, 72.5)$ . The proximity feed patch dimension is  $18 \times 18$  mm and the configuration is shown in Fig. 7a. The simulated and measured input impedance plot and the fabricated prototype of the MSA are shown in Fig. 7b, c. The simulated BW is from 896 to 1176 MHz (280 MHz) and the measured BW is from 910 to 1195 MHz (285 MHz). The radiation pattern is in the broadside direction with an average gain of above 5 dBi over the complete BW. Thus, among all the gap-coupled configurations, the design of M-shape patches with A-shape MSA yields optimum results in terms of BW and pattern characteristics. However, for providing the frequency agility, the design of A-shape MSA with M-shape and N-shape patches provides optimum results.

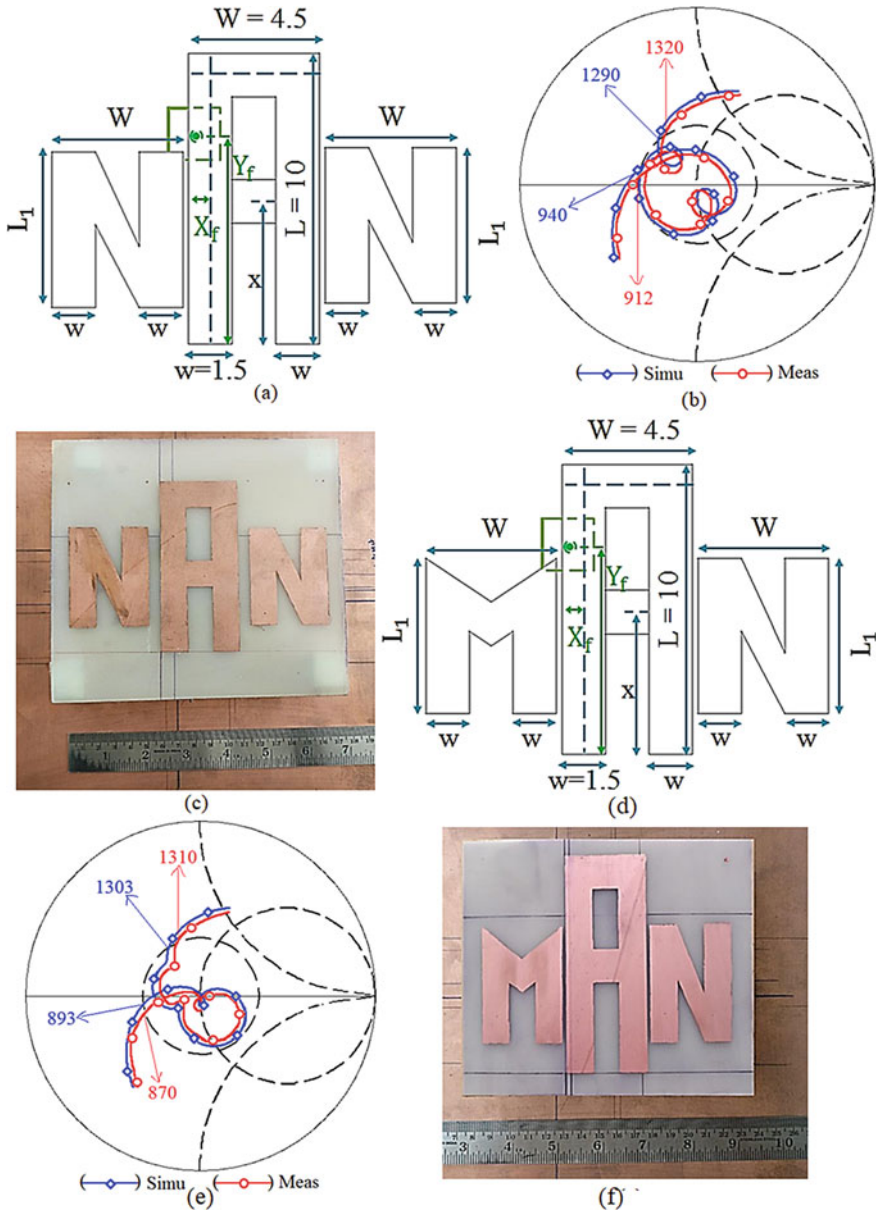


**Fig. 4** a Gap-coupled design of N-A-N MSAs, its b input impedance plots, c fabricated prototype, d gap-coupled design of M-A-N MSAs, its e input impedance plots, and f fabricated prototype

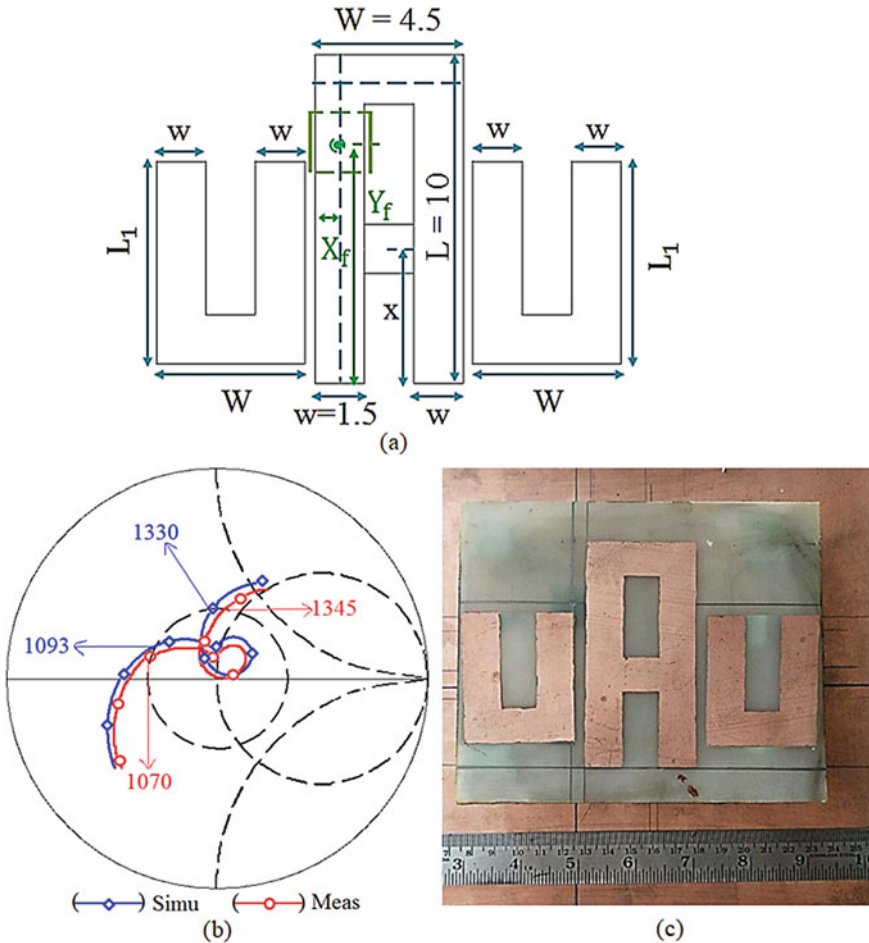


**Fig. 5** a Gap-coupled design of U-A-U MSAs, its b input impedance plots and c fabricated prototype

### 3 Conclusions

Various designs of A-shape MSAs gap-coupled with compact M-shape, N-shape, W-shape, U-shape, and inverted U-shape patches are proposed for a wideband response on a thicker substrate using proximity feed. Among all the designs, a configuration of A-shape MSA with M-shape patches yields optimum BW and gain, whereas from a frequency and polarization agility point of view, the design of A-shape MSA with M-shape and N-shape patches provides optimum results. The proposed configurations can find applications in mobile communication systems in 800–1200 MHz frequency bands.



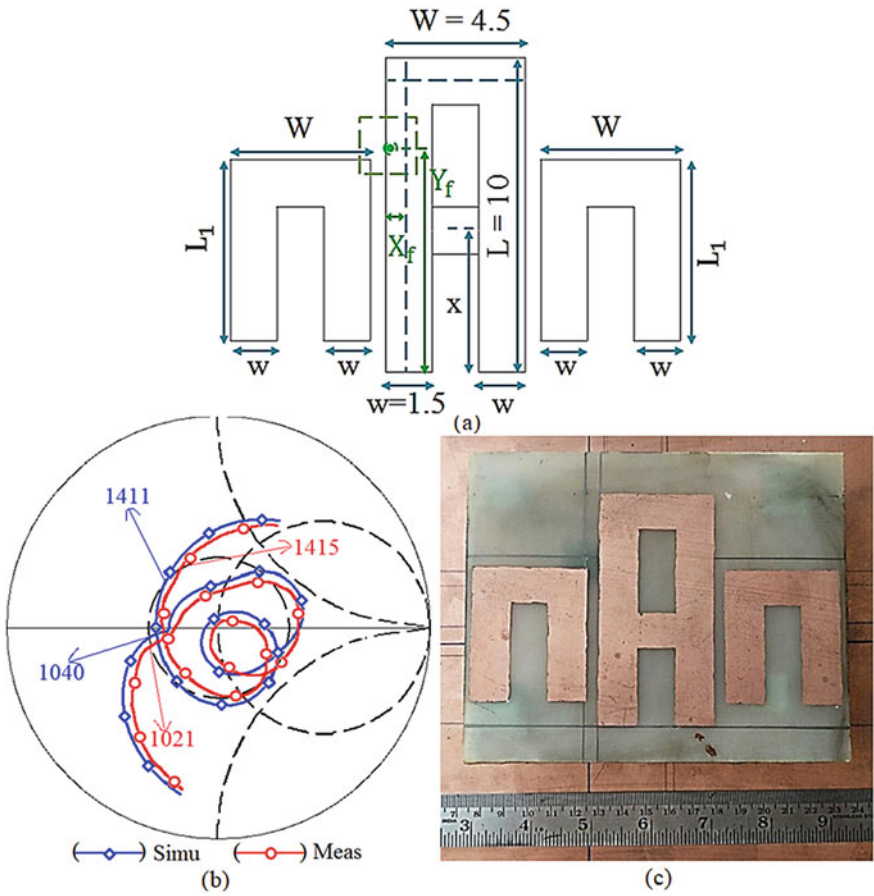


**Fig. 6** a Gap-coupled design of U-A-U MSAs using inverted parasitic patches, its b input impedance plots and c fabricated prototype

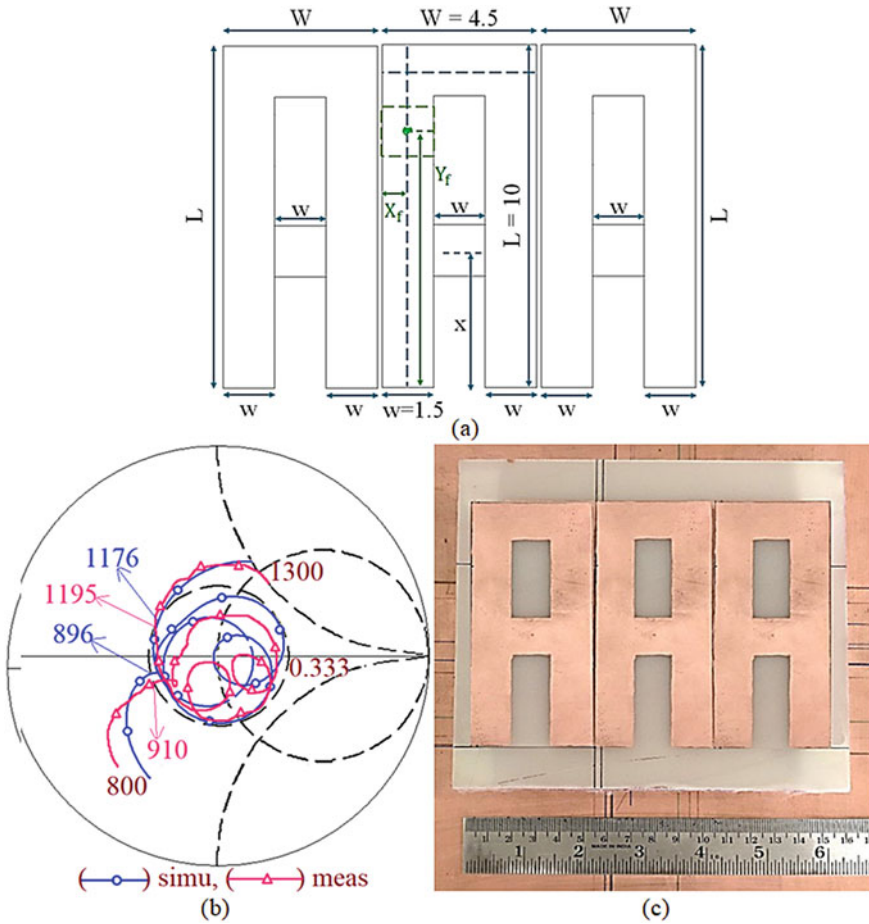


**Fig. 7** a Gap-coupled design of A-A-A MSAs, its b input impedance plots and c fabricated prototype

## References

1. Garg R, Bhartia P, Bahl I, Ittipiboon A (2001) Microstrip antenna design handbook. Artech House, USA
2. Lee HF, Chen W (1997) Advances in microstrip and printed antennas. Wiley, New York
3. Wong KL (2002) Compact and broadband microstrip antennas. Wiley, New York
4. Kumar G, Ray KP (2003) Broadband microstrip antennas, 1st edn. Artech House, USA
5. Deshmukh AA, Kumar G (2001) Reliability of suspended rectangular microstrip antenna. In: Proceedings of international conference on quality, reliability and control, Bombay, India, Dec. 26–28
6. Deshmukh AA, Pawar S, Ray KP (2017) Novel designs of A-Shape microstrip antennas for multi-Band dual polarized response. In: Proceedings of ICAC3—2017, Mumbai, India, pp 1–6. <https://doi.org/10.1109/ICAC3.2017.8318743>

# Analysis of Broadband Circularly Polarized Half E-Shape Microstrip Antenna



Venkata A. P. Chavali, Amit A. Deshmukh, and Aarti G. Ambekar

**Abstract** Analysis of a broadband circularly polarized half E-shape microstrip antenna is presented in this paper. The resonant modes responsible for broadband as well as circular polarization are identified with the help of surface current distributions. With respect to the offset feed location  $TM_{01}$ ,  $TM_{10}$  and  $TM_{11}$  modes get excited in the rectangular microstrip antenna. With the increasing slot length, reduction in  $TM_{01}$  and  $TM_{11}$  mode frequencies is observed which yields coupling between  $TM_{10}$  and  $TM_{11}$  modes. The surface currents of the two modes at the maximum slot length are directed horizontally, resulting in a linearly polarized broadband response. The introduction of shorting bar in the slot orients the  $TM_{11}$  mode current in a vertical direction, creating orthogonal currents resulting in CP response. When simulated an impedance bandwidth of 36% and axial ratio bandwidth of 6.6% with 8.73 dBi peak gain is observed. Detailed analysis revealed that CP realization can be possible by re-optimizing half E-shape MSA without inserting shorting bar. Optimization of the slot length realized similar results as that of the half E-shape MSA with shorting bar.

**Keywords** Broadband response · Circular polarization · Half E-shape microstrip antenna · Offset feed

## 1 Introduction

Broadband response of microstrip antenna (MSA) can be achieved by adopting techniques such as gap coupling [1–5], using stacked configurations [6–8], modifying the shape of regular MSAs [9, 10] and using slot cut techniques [11–13]. In most broadband antennas, single polarization of the antenna is maintained over the entire bandwidth (BW). But in applications like mobile phone communication, the antenna should be able to receive a signal from any direction to avoid the loss of the signal. In such scenarios antenna with either circular polarization (CP) or elliptical polarization is preferred. CP can be realized by creating time and space orthogonality of

---

V. A. P. Chavali · A. A. Deshmukh (✉) · A. G. Ambekar  
Department of EXTC Engineering, SVKM's DJSCE, Mumbai, India

the patch modes. The coplanar CP antenna reported in [14] realized an impedance BW of 27% and axial ratio (AR) BW of 16%. But the design of the feed network is complex. The low-profile broadband CP antenna with wide beamwidth in [15] achieved a relatively wide impedance BW of 72.5% and an AR BW of 54%. But the orthogonal modes resulting in CP and the resonant modes responsible for such a wider BW are not discussed in the paper. Also, to realize CP, two Wilkinson power dividers and one  $180^\circ$  phase-shifted feeding network are employed which makes the configuration complex. Similarly, the antennas reported in [16, 17] employed multiresonator techniques along with complex feed arrangement, with which the complexity and size of the antenna increases. In [18], a compact half E-shape MSA for circular polarization is reported. Initially, a half E-shape MSA with offset feed is realized in which two resonant modes whose surface currents are aligned in the same direction are excited resulting in a linearly polarized antenna. With the insertion of the shorting bar surface currents at the higher frequency get reoriented in the vertical direction, resulting in the reduction of AR below 3 dB. An impedance BW of 35% and AR BW of 5.3% are reported to be achieved. Though the configuration is simple compared to the other reported CP antennas, a detailed discussion about the modes responsible for the achieved impedance BW and AR BW is not presented. Thus, analysis of the reported CP half E-shape MSA is carried out to understand the modes responsible for the wide impedance BW and AR BW. Resonant modes are identified through surface current distributions. With respect to the offset feed location,  $TM_{01}$  and  $TM_{11}$  modes get excited in the rectangular microstrip antenna. With the increasing slot length, reduction in  $TM_{01}$ ,  $TM_{11}$  mode frequencies and increment in the  $TM_{10}$  mode impedance are observed, which yields optimum coupling between  $TM_{10}$  and  $TM_{11}$  modes. The introduction of shorting bar in the slot orients the  $TM_{11}$  mode current in a vertical direction creating orthogonal currents resulting in CP response. Also, a detailed analysis of the resonant modes and surface current distributions revealed that the insertion of the shorting bar is not necessary to realize broadband CP response. By optimizing the length of the half E-slot, a simulated  $S_{11}$  BW of 0.855 GHz (36.6%), AR BW of 0.17 GHz (6.8%) with a peak gain of 8.6 dBi is realized which is the same as that realized in half E-shape MSA with shorting bar. All the simulations are carried out using CST software [19]. Throughout the paper, all the dimensions are specified in centimeters and frequency in GHz.

## 2 Analysis of Circularly Polarized Half E-shape MSA

The reported circularly polarized half E-shape MSA is shown in Fig. 1a, b. The antenna is designed on a Rogers Duroid 5880 substrate ( $\epsilon_r = 2.33$ ,  $h = 0.157$ ,  $\tan \delta = 0.001$ ) placed above a foam layer of thickness 1 cm. The dimensions of the reported antenna are  $L = 4.9$ ,  $W = 5.5$ ,  $L_s = 4.3$ ,  $W_s = 1.2$ ,  $P_s = 1.1$ ,  $l = 1.2$ ,  $W_b = 2.5$ ,  $y_f = 1.1$ ,  $x_f = 0.22$  cm. The reported surface current distributions of the half E-shape MSA with shorting bar at two frequencies are shown in Fig. 1c, d. Due to the orthogonality in the surface currents and their equal magnitudes, CP response

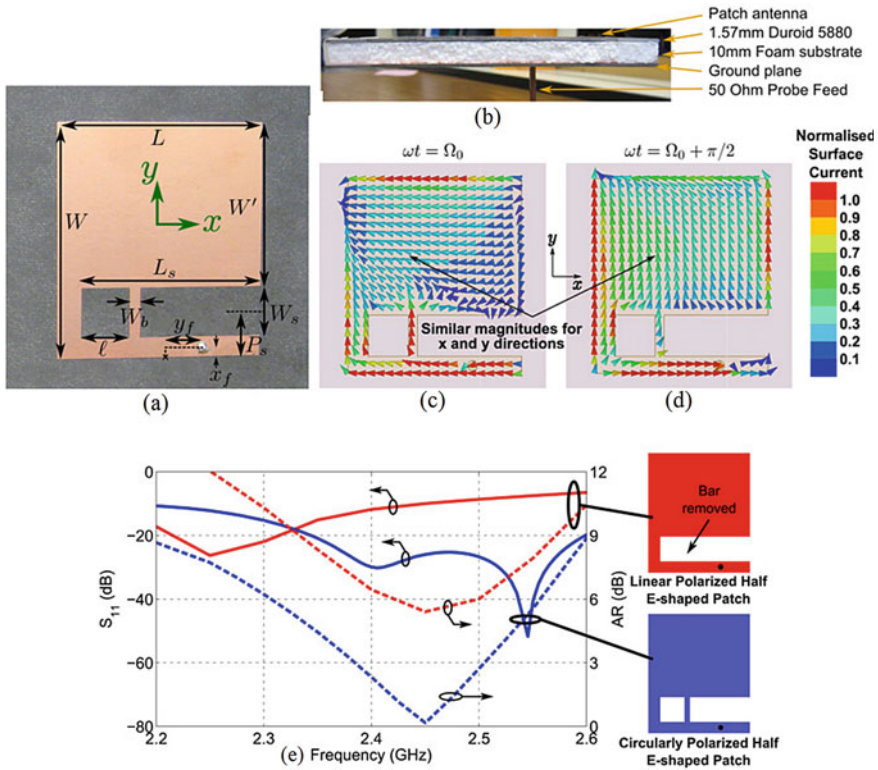


**Fig. 1** a, b Circularly polarized half E-shape MSA, c, d surface current distributions, and e  $S_{11}$  and AR plots of half E-shape MSA without and with shorting bar [18]

is realized with an AR BW of 5.3%. In the MSA without a bar, this orthogonality is not achieved due to the orientation of surface currents in the same direction. The comparison of half E-shape MSA with and without shorting bar in terms of the reflection coefficient ( $S_{11}$ ) and AR is shown in Fig. 1e. An impedance BW of 35% and AR BW of 5.3% is reported to be achieved by the half E-shape MSA with shorting bar, whereas impedance BW of 18% with increased AR value is observed without the shorting bar. Though the antenna is compact and realized good AR BW, the modal explanation responsible for the wider impedance BW and the AR BW is not provided. In order to understand the modal behavior of the reported half E-shape MSA, the antenna is simulated using CST.

Initially, on simulating the RMSA with the reported dimensions, two resonant modes are observed from the resonant peak plot, which are identified as  $TM_{01}$  and  $TM_{11}$  through the surface current distributions. With the gradual increment in slot length, ' $L_s$ ' the resonant frequency of  $TM_{01}$  and  $TM_{11}$  mode decreases as shown in Fig. 2a, b. Also, the impedance of  $TM_{10}$  mode increases and coupling with the  $TM_{11}$  mode takes place. The surface current distributions for the reported slot length  $L_s =$

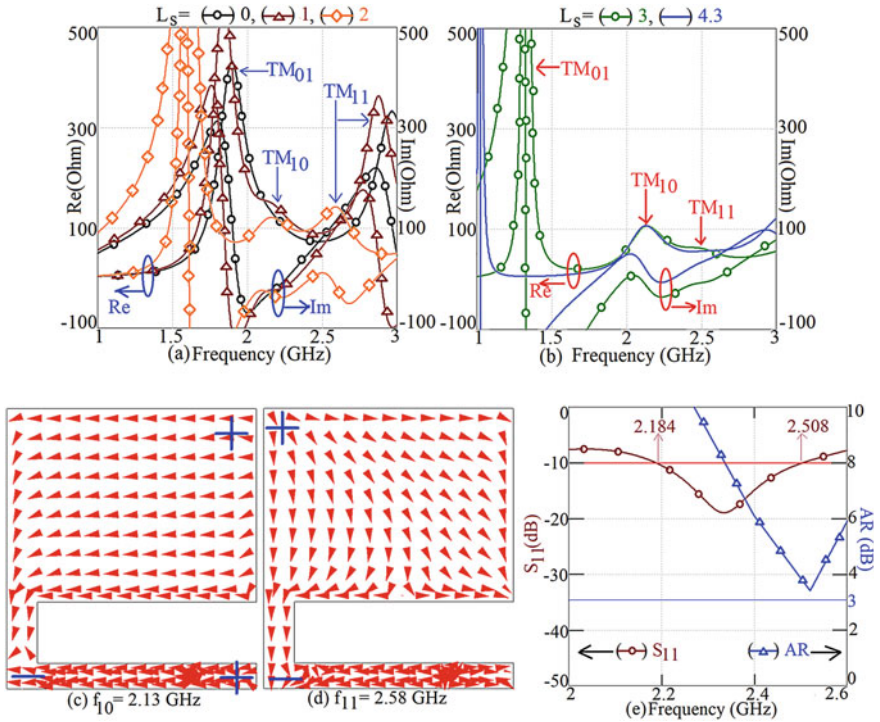


**Fig. 2** Simulated **a, b** resonant frequency plots for varying slot length, **c, d** surface current distributions, and **e**  $S_{11}$  and AR plots of half E-shape MSA without bar

4.3 cm is shown in Fig. 2c, d. From the resonance frequency plot and surface current distributions, it can be seen that the  $TM_{11}$  mode of the patch is weakly excited at the maximum slot length and also surface currents at this mode are mostly oriented in the horizontal direction as that of  $TM_{10}$  mode. Due to the coupling of  $TM_{10}$  and weakly excited  $TM_{11}$  modes, a simulated  $S_{11}$  BW of 0.324 GHz (13.8%) is realized, and due to the horizontally oriented surface currents, increased value of AR is observed as shown in Fig. 2e. Next, a shorting bar as per the given dimensions in the reported paper is inserted in the half E-shape MSA. The simulated resonance frequency plot of half E-shape MSA without bar and with bar and surface current distributions with bar are shown in Fig. 3a–c. It is observed that with the insertion of the shorting bar in the half E-shape MSA, the impedance of  $TM_{11}$  mode increases, and optimum coupling between  $TM_{10}$  and  $TM_{11}$  mode takes place. The surface currents at  $TM_{11}$  mode get oriented in the vertical direction, as shown in Fig. 3c.

Thus, with the introduction of the shorting bar, orthogonality between the surface currents of  $TM_{10}$  and  $TM_{11}$  modes is created, which is the necessary condition to realize CP. Due to this orthogonality, the AR value decreases below 3 dB. Hence, a simulated  $S_{11}$  BW of 0.86 GHz (36.75%) and AR BW of 0.166 GHz (6.7%) with a peak gain of 8.72 dBi is realized as shown in Fig. 3d. These values are slightly larger

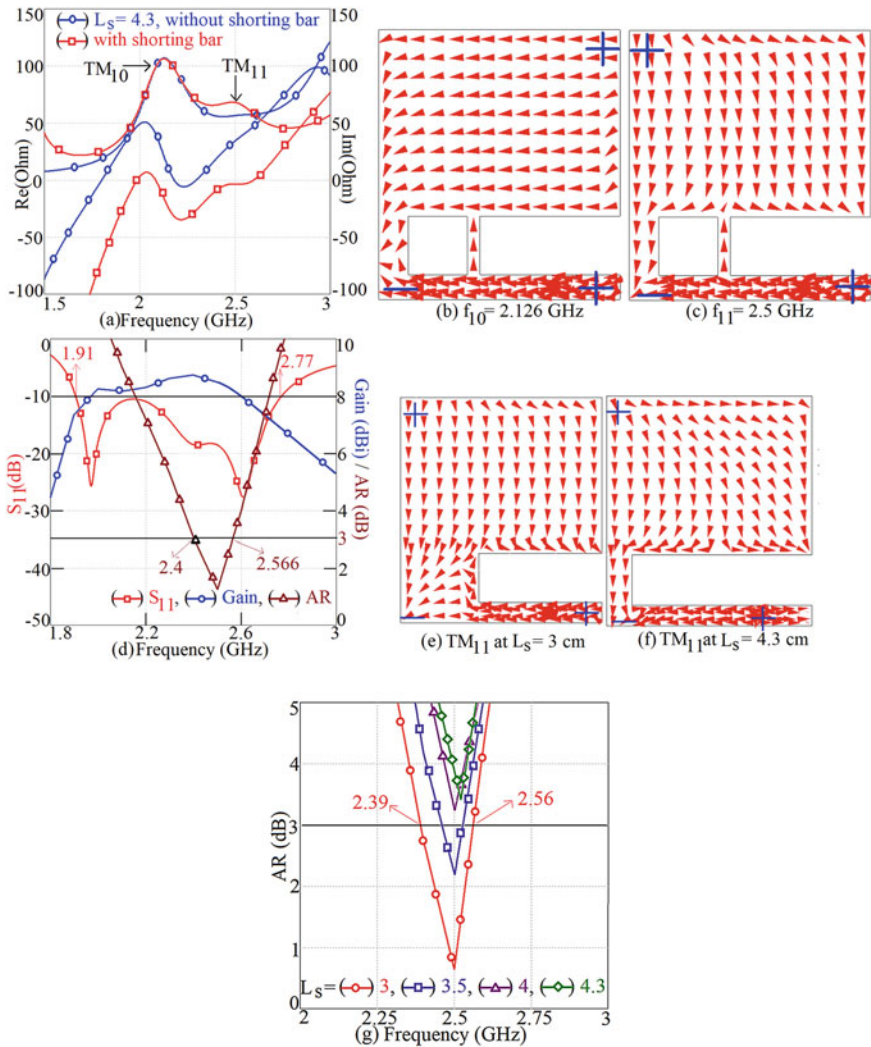


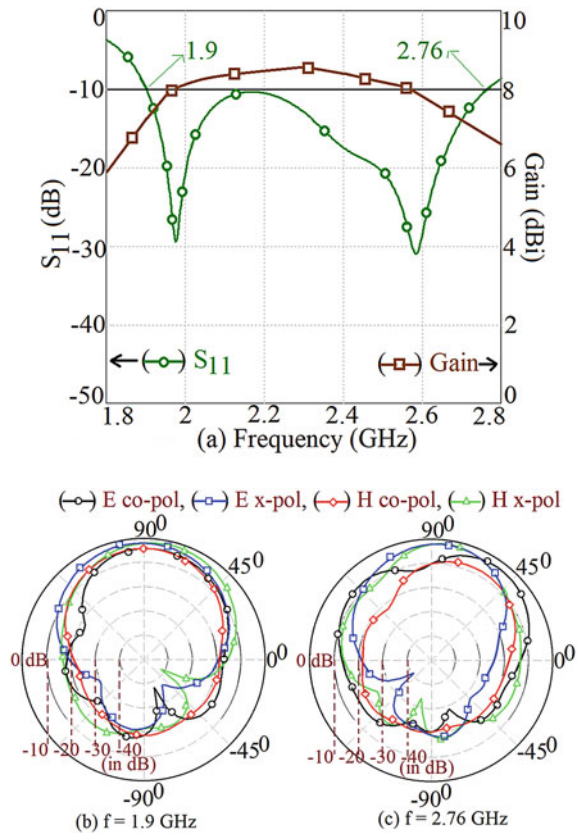
**Fig. 3** Simulated **a** resonance frequency plots without and with shorting bar, **b, c** surface current distributions and, **d**  $S_{11}$  and AR plots of half E-shape MSA with shorting bar, and **e, f** surface current distributions, **g** AR plots for  $L_s$  variation of half E-shape MSA without shorting bar

than the reported values. The difference in the results is attributed to the variation in substrate parameters. Further, the reported half E-shape MSA without shorting bar is analyzed for CP response. The surface current distributions and AR values are observed by varying the E-slot length. The simulated surface current distributions of  $TM_{11}$  mode at  $L_s = 3$  and  $L_s = 4.3$  cm are shown in Fig. 3e, f. It can be seen that the orientation of surface currents at  $L_s = 3$  cm is in the vertical direction whereas the horizontal component of currents is present at  $L_s = 4.3$  cm due to the re-orientation

of surface currents at a larger length of the slot along the horizontal direction. These vertical currents at  $L_s = 3$  cm are orthogonal to that of the surface currents of  $TM_{10}$  mode, realizing CP response yielding an AR BW of 0.17 GHz (6.8%). Also, due to impedance tuning of  $TM_{10}$  and  $TM_{11}$  resonant modes,  $S_{11}$  BW of 0.855 GHz (36.6%) with 8.6 dBi peak gain is realized. The optimum results are shown in Figs. 3g and 4a. These  $S_{11}$  and AR BWs are the same as that of the  $S_{11}$  and AR BWs realized in the reported half E-shape MSA with shorting bar.

The simulated radiation patterns at band start and band stop frequencies of  $S_{11}$  plot of half E-shape MSA without shorting bar are shown in Fig. 4b, c. Broadside radiation patterns are observed at band start and band stop frequencies of  $S_{11}$  BW.

**Fig. 4** a  $S_{11}$  and gain plots, b radiation patterns at band start and stop frequencies of half E-shape MSA without shorting bar





### 3 Conclusions

Analysis of a circularly polarized half E-shape MSA is presented. Modal behavior of the antenna is understood by studying the surface current distributions at the resonant peaks observed in the resonance frequency plot. With the increment in slot length, the frequency of  $TM_{01}$  and  $TM_{11}$  modes reduces and the impedance of  $TM_{10}$  mode increases. At the maximum slot length due to the weak excitation of  $TM_{11}$  mode, a narrow  $S_{11}$  BW is observed. Also, due to the orientation of surface currents in the horizontal direction at both  $TM_{10}$  and  $TM_{11}$  modes, the AR value greater than 3 dB is observed which results in linear polarization. In order to increase the  $S_{11}$  BW and re-orient the surface currents of  $TM_{11}$  mode in a vertical direction shorting bar is introduced in the slot. A simulated  $S_{11}$  BW of 0.86 GHz (36.75%) and AR BW of 0.166 GHz (6.7%) with a peak gain of 8.72 dBi is realized due to optimum coupling between  $TM_{10}$  and  $TM_{11}$  resonant modes. However, from the detailed analysis of the half E-shape MSA, it is understood that a similar broadband CP response can be realized without the shorting bar by optimizing the slot length. At slot length of 3 cm, due to orthogonality between  $TM_{10}$  and  $TM_{11}$  mode currents and space tuning between them, a simulated  $S_{11}$  BW of 0.855 GHz (36.6%), AR BW of 0.17 GHz (6.8%) with a peak gain of 8.6 dBi is realized which is same as that realized in half E-shape MSA with shorting bar. Radiation patterns near the band start and band stop frequencies exhibited broadside patterns.

### References

1. Kumar G, Ray KP (2003) Broadband microstrip antennas. Artech house
2. Wong KL (2003) Compact and broadband microstrip antennas, 1st edn. Artech House, USA
3. Yoo J, Son HW (2020) A simple compact wideband microstrip antenna consisting of three staggered patches. *IEEE Antennas Wirel Propag Lett* 19(12):2038–2042
4. Qian JF, Chen FC, Chu QX, Xue Q, Lancaster MJ (2018) A novel electric and magnetic gap-coupled broadband patch antenna with improved selectivity and its application in MIMO system. *IEEE Trans Antennas Propag* 66(10):5625–5629
5. Cao Y, Cai Y, Cao W, Xi B, Qian Z, Wu T, Zhu L (2019) Broadband and high-gain microstrip patch antenna loaded with parasitic mushroom-type structure. *IEEE Antennas Wirel Propag Lett* 18(7):1405–1409
6. Chopra R, Kumar G (2020) High gain broadband stacked triangular microstrip antennas. *Microwave Opt Technol Lett* 62(9):2881–2888
7. Chopra R, Kumar G (2020) Broadband and high gain multilayer multi resonator elliptical microstrip antenna. *IET Microwaves Antennas Propag* vol. 14, no. 8, (2020), 821–829.
8. Li D, Guo P, Dai Q, Fu Y (2012) Broadband capacitively coupled stacked patch antenna for GNSS applications. *IEEE Antennas Wirel Propag Lett* 11:701–704
9. Abbaspour M, Hassani HR (2008) Wideband star-shaped microstrip patch antenna. *Progress Electromagn Res* 1:61–68
10. Mondal K, Shaw A, Sarkar PP (2017) Inverted question mark broadband high gain microstrip patch antenna for ISM band 5.8 GHz/WLAN/WIFI/X-band applications. *Microwave Opt Technol Lett* 59(4): 866–869
11. Lu HX, Liu F, Su M, Liu YA (2018) Design and analysis of wideband U-slot patch antenna with U-shaped parasitic elements. *Int J RF Microwave Comput Aided Eng* 28(2):1–11

12. Tiwari RN, Singh P, Kanaujia BK (2017) Butterfly shape compact microstrip antenna for wideband applications. *Progress Electromagn Res* 69:45–50
13. Chen Y, Yang S, Nie Z (2010) Bandwidth enhancement method for low profile E-shaped microstrip patch antennas. *IEEE Trans Antennas Propag* 58(7):2442–2447
14. Fu S, Kong Q, Fang S, Wang Z (2014) Broadband circularly polarized microstrip antenna with coplanar parasitic ring slot patch for L-band satellite system application. *IEEE Antennas Wirel Propag Lett* 13:943–946
15. Wang L, Weng Z, Jiao YC, Zhang W, Zhang C (2018) A low-profile broadband circularly polarized microstrip antenna with wide beamwidth. *IEEE Antennas Wireless Propag Lett* 17(7):1213–1217
16. Ding K, Gao C, Qu D, Yin Q (2017) Compact broadband circularly polarized antenna with parasitic patches. *IEEE Trans Antennas Propag* 65(9):4854–4857
17. Feng G, Chen L, Wang X, Xue X, Shi X (2017) Broadband circularly polarized crossed bowtie dipole antenna loaded with parasitic elements. *IEEE Antennas Wirel Propag Lett* 17(1):114–117
18. Kovitz JM, Rajagopalan H, Rahmat SY (2016) Circularly polarised half E-shaped patch antenna: a compact and fabrication-friendly design. *IET Microwaves Antennas Propag* 10(9):932–938
19. CST Microwave Studio, Version 2019

# Modal Analysis of Penta Band-Notched Elliptical Planar UWB Antenna



Ameya A. Kadam and Amit A. Deshmukh

**Abstract** An elliptical-shaped penta band-notched ultra-wideband antenna is investigated. The antenna realizes five notches at frequency bands 2.4–2.6, 3.3–3.75, 3.9–4.2, 5.15–5.85, and 7.9–8.4 GHz, while yielding UWB performance from 2.15 to 12.5 GHz. To investigate the realization of the notch bands, the modal analysis of the antenna is performed. The consequence of U-shaped and inverted U-shaped slots incorporated in the patch on the resonant modes is examined with aid of simulated current distribution. It is experiential that the addition of inverted U-shaped slot increases the input impedance of  $TM_{21}$  mode, while that of U-shaped slot increases the input impedance of  $TM_{20}$  mode giving notches. The U-shaped patch in the elliptical patch incorporated near the feedline surges the input impedance of  $TM_{30}$  mode to yield the notch characteristic.

**Keywords** Ultra-wideband antenna · Modal analysis · Band notch response · U-shaped slot loaded antenna

## 1 Introduction

Ultra-wideband (UWB) communication systems have achieved popularity and consideration subsequently 2002 due to their wideband (3.1–10.6 GHz), planar, compacted, and less power consumption. The UWB antennas with different patch shapes as rectangular, hexagonal, triangular, and their altered variations are used commonly [1–6]. However, key design problem in UWB systems is potential interference from prevailing parallel communication systems, like WLAN operating in 2.4–2.484, 5.15–5.35, 5.725–5.825 GHz bands, Wi-MAX 3.3–3.7 GHz band, C-band satellite communication 3.9–4.2 GHz, and X-band satellite frequency 7.8–8.45 GHz. By incorporating band-reject filters, these interferences can be minimized. But the usage of filters surges the involvedness and also the cost of the system. Therefore, to

---

A. A. Kadam · A. A. Deshmukh (✉)  
EXTC Department, SVKM's Dwarkadas J Sanghvi College of Engineering, Vile-Parle, Mumbai, India

minimize the interferences causing due to mentioned systems to UWB, the implementation of these antennas with notched frequency bands is desirable. The general technique to realize notch band is to include different kinds of slots on the radiating structure [6–10]. Other techniques to get band-notched characteristics are incorporation of split ring resonator or its complement form slot [11], parasitic elements in the vicinity of structure [12], implementing electromagnetic bandgap (EBG) structure [13]. Also, numerous other techniques have been grasped to generate a multiple band notch in refs [14, 15]. However, thorough clarification about the influences of amendments in geometry of radiating structure that consequences in notch responses in terms of patch or ground plane resonant modes is not given.

In this paper, the reported penta band notch elliptical monopole antenna with UWB response is scrutinized in detail [15]. To realize notch bands, the U-shaped slots in the patch are incorporated. But the paper does not explain the consequence of slots on the resonant modes of the elliptical patch. The novelty of this paper is the scrutiny of placement of slots to get notch response by perturbing the resonant modes present at those frequencies. To get more perception about the modes, the vector current distributions on the patch at the resonant modes are analyzed.

## 2 Elliptical Monopole with U-shaped and Inverted U-shaped Slots

The geometrical structure of the reported penta band-notched antenna with U-shaped and inverted U-shaped slots in the elliptical patch is depicted in Fig. 1a [15].

The antenna was fabricated on FR-4 substrate with a dielectric permittivity of 4.4, loss tangent of 0.02, 1.6 mm thickness, and is excited by the characteristic impedance of  $50 \Omega$  microstrip feedline with width of 3 mm. The antenna structure is a planar elliptical-shaped patch incorporated with U-shaped slots. The optimized antenna dimensions are:  $L_{h1} = 19$ ,  $L_{v1} = 9.5$ ,  $L_{h2} = 12$ ,  $L_{v2} = 7.2$ ,  $L_{h3} = 8$ ,  $L_{v3} = 5$ ,  $L_{h4} = 4$ ,  $L_{v4} = 9.8$ ,  $L_{h5} = 1$ ,  $L_{v5} = 5.4$  mm. The ground plane of size 14 by 34 mm<sup>2</sup> and 0.5 mm is lower than the radiating patch. The simulated plots of resonance curve and  $S_{11}$  of the antenna are depicted in Fig. 1b. The notch within frequency bands of 2.4–2.6, 3.3–3.75, 3.9–4.2, 5.15–5.85, and 7.9–8.4 GHz is obtained along with UWB response from 2.15 to 11 GHz with  $S_{11} < -10$  dB.

## 3 Analysis of Antenna

To understand the functioning of the antenna and the effects of U-shaped slots, an analysis of antenna was carried out. The incorporation of slots in the elliptical patch in a sequential manner is depicted in Fig. 2a–f. Using CST2019, the antenna without any slot is simulated initially. The identification of resonant modes is carried

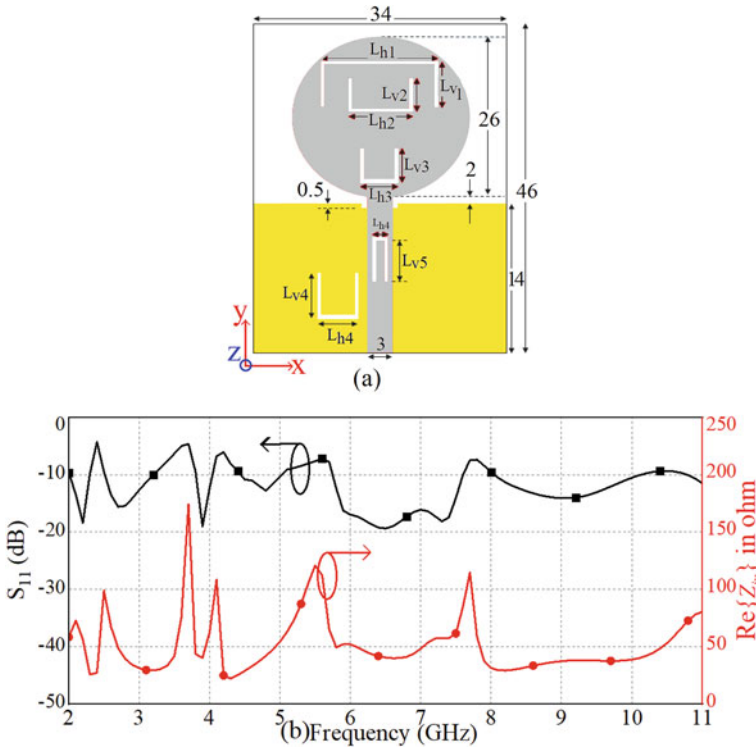


**Fig. 1** a Reported structure of band-notched UWB antenna, b simulated plots of reflection coefficient ( $S_{11}$ ) and real part of input impedance ( $Z_{in}$ ) [15]

out. The fundamental and subsequent higher modes in elliptical monopole patch are analogous to that of circular microstrip patch besides exhibit multiples of half-wavelength variations. The simulated plots of resonance curve and  $S_{11}$  of antenna without slots are depicted in Fig. 3a.

It is perceived that antenna structure without slots is capable of yielding UWB response from 2.2 to 10.4 GHz. The input impedance varies within the range of 40–82  $\Omega$  signifying a good match within this band. At various resonant modes, the observed vector current distributions are depicted in Fig. 3b–e.

Furthermore, the analysis of the effect on resonance curve and  $S_{11}$  due to insertion of upper U-shaped slot depicted in Fig. 2b is carried out. Initially, the effect of adding only horizontal section of inverted U-shaped slots is evaluated. The slot length  $L_{h1}$  is varied while upholding width of the slot  $W_s = 0.5$  mm. It is noticed that as the slot length  $L_{h1}$  is varied, the  $Z_{in}$  corresponding to  $TM_{21}$  mode gets increased slightly as depicted in Fig. 4a. To surge the impedance at  $TM_{20}$  mode pointedly for band notch realization, the vertical slots are introduced with slot length  $L_{v1}$ . As slot length  $L_{v1}$  increases, the impedance of  $TM_{21}$  mode increases significantly and surges beyond 110  $\Omega$  ensuing in notch within ISM band. The tuning of the notch frequency can be

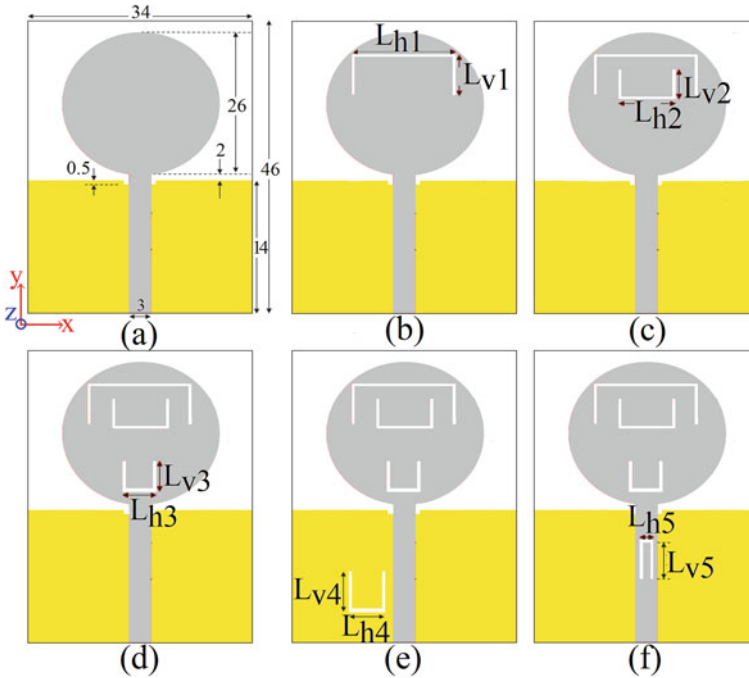


**Fig. 2** Evolution of antenna: **a** Elliptical monopole antenna without slots, **b** with first U-shape slot for notch at ISM, **c** with second U-shape slot for notch at Wi-MAX, **d** with third U-shape slot for notch at WLAN, **e** with fourth U-shape slot for notch at C-band, **f** with fifth U-shape slot for notch at X-band

done by varying slot length  $L_{v1}$ , which is depicted in Fig. 4b. Hence, by optimizing the dimensions of the inverted U-shaped slot incorporated in the upper portion of elliptical patch, the band notch can be realized in ISM band.

Next, the investigation of  $S_{11}$  and resonance curve due to the presence of U-shaped slot with horizontal dimensions  $L_{h2}$  and vertical dimension  $L_{v2}$  shown in Fig. 2c is carried out. The width of the slot  $W_s = 0.5$  mm is set aside constant. As the vertical slot length  $L_{v2}$  is varied, the impedance corresponding to  $TM_{20}$  mode gets increased as represented in Fig. 5a. As slot length  $L_{v2}$  increases, the impedance of  $TM_{20}$  mode surges significantly and increases beyond  $120 \Omega$  resulting in the formation of notch. The tuning of notch frequency can be obtained by varying slot length  $L_{v2}$  as shown in Fig. 5a. Hence, by optimizing the dimensions  $L_{h2}$ ,  $L_{v2}$  of the U-shaped slot incorporated in elliptical patch the band notch can be realized in Wi-MAX band. The antenna structure is further analyzed for inclusion of U-shaped slots in the patch near the feedline. As the vertical slot dimension  $L_{v3}$  is increased, the impedance corresponding to resonant mode  $TM_{30}$  increases. This increase in impedance leads to the formation of band notch within WLAN band as depicted in Fig. 5b. Hence, by optimizing the dimensions  $L_{h3}$ ,  $L_{v3}$  of the U-shaped slot incorporated near the feedline the band notch can be realized in WLAN band.

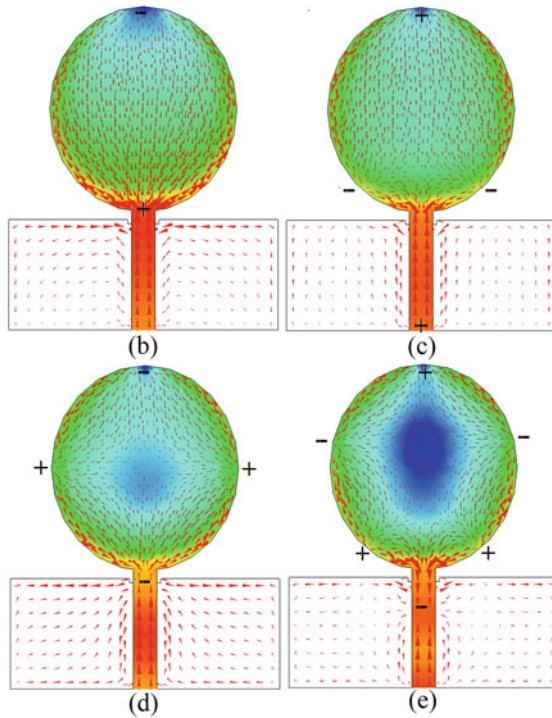
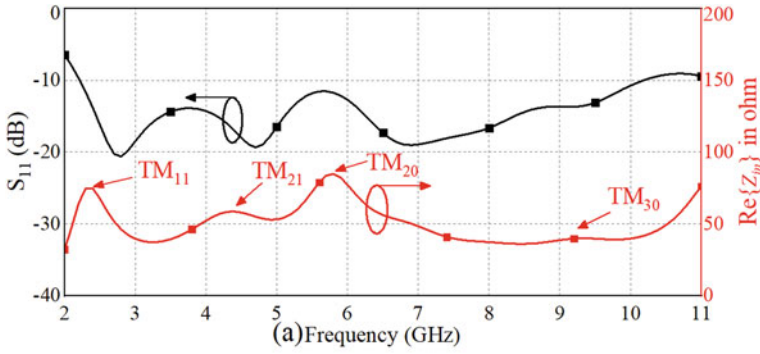


**Fig. 3** **a** Simulated plots of  $S_{11}$ , resonance curve for the monopole antenna without slots, **b–e** Current distributions at resonant modes **b**  $f_{TM11} = 2.34$  GHz, **c**  $f_{TM21} = 4.39$  GHz, **d**  $f_{TM20} = 5.78$  GHz, **e**  $f_{TM30} = 9.28$  GHz

Later, the addition of U-shaped slot in the ground plane and inverted U-shaped slotline resonator gives two notch bands in C-band and X-bands, respectively. The inverted-shaped slot acts as a resonator at 7.9 GHz. It acts as a parallel resonance circuit, which restricts the energy of the corresponding frequency to travel in the radiating structure at the resonance frequency. The U-shaped slot incorporated in

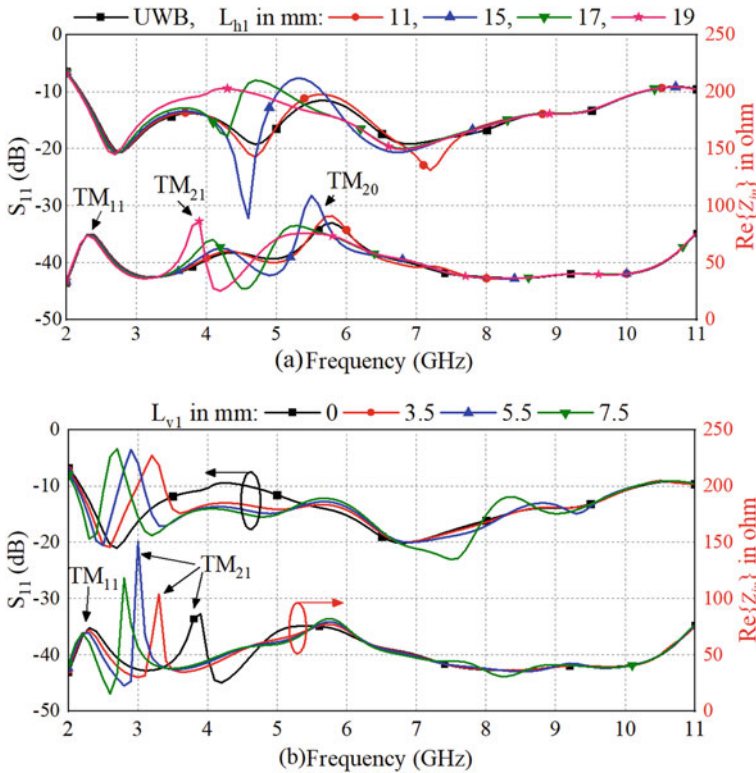


**Fig. 4** Simulated plots of  $S_{11}$  and resonance curve for **a** various values of  $L_{h1}$ , **b** various values of  $L_{v1}$  for constant  $L_{h1} = 19$  mm

ground plane and in the vicinity of feedline also acts as resonating structure near about 4.2 GHz.

The scalar and vector current distributions at various notched frequency are shown in Fig. 6a–e. The size of the arrow indicates the amount of surface current density. The color nomograph mentioned in Fig. 5 also indicates intensity of the surface current density. The condensed current distribution around the upper inverted U-shaped slot has been observed at 2.4 GHz. This structure significantly perturbs the current distribution of  $TM_{11}$  mode as the structure is placed orthogonal to the current at this mode. This results in notch characteristics in ISM band. Also, the condensed current distributions are observed around the U-shaped slots incorporated in the elliptical patch at respective notch frequencies.

The input impedance of the reported antenna is investigated for the band-notched characteristic. Figure 7a shows the phase and magnitude of the simulated input impedance. It can be seen from Fig. 7 that in the 3.7 GHz WiMAX band, 4.2 GHz C-band, 5.5 GHz WLAN band, and 7.8 GHz X-band, the magnitude of the impedance is a significantly high value, and the phase of the same is changing from positive to a



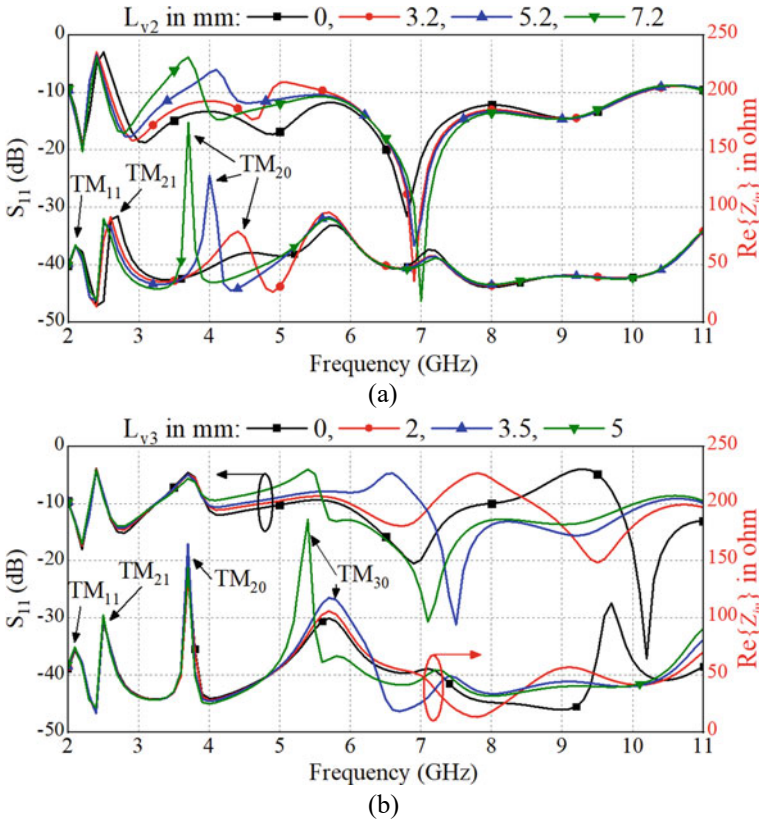


**Fig. 5** Plots of simulated  $S_{11}$  and resonance curve for numerous values of **a** vertical slot length  $L_{v2}$  for fixed value of  $L_{h2} = 12$ , **b** vertical slot lengths  $L_{v3}$  for fixed value of  $L_{h3} = 8$  mm

negative. It means that the antenna exhibits parallel resonance in these bands. While in the 2.4 GHz ISM band, the magnitude of impedance equals nearly zero ohm, and the phase of impedance is changing from negative to positive, which proves that the antenna has series resonance characteristics within ISM band. The equivalent LC circuit model of the penta band-notched antenna is depicted in Fig. 7b.

## 4 Conclusions

A planar profile, printed penta band-notched elliptical-shaped UWB monopole antenna with U-shaped and inverted U-shaped slots, is investigated in detail. To investigate the notch bands' formation, the modal analysis of the antenna is accomplished. The effect of slots and their dimensions on the resonant modes are analyzed with aid of current distributions and resonance curves. The inverted U-shaped slot

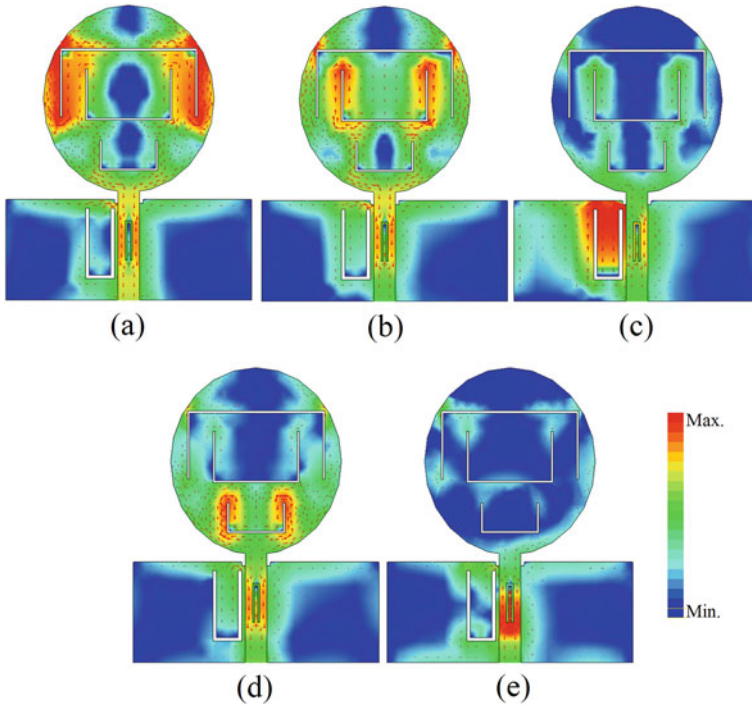


**Fig. 6** Current distribution at notched frequencies for monopole antenna **a** 2.4, **b** 3.7, **c** 4.2, **d** 5.7, and **e** 7.8 GHz

surges the input impedance of  $TM_{21}$  mode whereas larger U-shaped slots increase that of  $TM_{20}$  mode, which produces band notch response. The increment in the overall length of the slots decreases the resonant frequency conforming to these modes. Also, the reported antenna behavior in the notched band is analyzed in terms of resonant circuits.

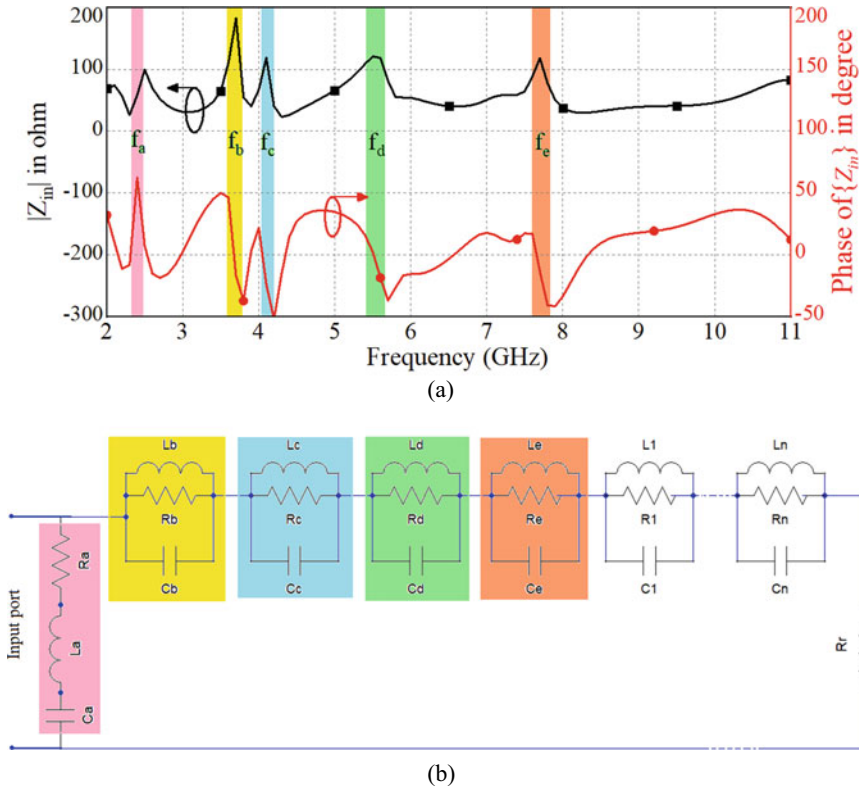


**Fig. 7** a The magnitude and phase of the simulated input impedance, b the equivalent LC model of the penta band-notched antenna

## References

1. FCC report and order for part 15 acceptance of ultra-wideband (UWB) systems from 3.1–10.6 GHz. Washington DC. (2002)
2. Ray KP, Thakur SS, Deshmukh RA (2012) UWB printed Sectoral monopole antenna with dual polarization. *Microw Opt Technol Lett* 54:2066–2070
3. Ray KP (2008) Design aspect of printed monopole antenna for ultrawide band applications. *Int J Antennas Propag* 1–8
4. Ray KP, Ranga Y (2006) Printed rectangular monopole antennas. *IEEE Antenna Propag Soc Int Symp* 1693–1696
5. Liu Y, Hong T (2010) A novel monopole antenna for ultra-wide band application. *Microw Opt Technol Lett* 52(12):2694–2696
6. Azim R, Islam MT, Misran N (2013) Printed circular disc compact planar antenna for UWB applications. *Telecommun Syst* 52(2):1171–1177
7. Sarkar M, Daniel A, Dwari S (2013) Compact printed monopole antenna for ultra-wideband application with dual band notched characteristic. *Microw Opt Technol Lett* 55:2595–2600
8. Hammache B, Messai A, Messaoudene I, Denidni TA (2019) A compact ultra-wideband antenna with three C-shaped slots for notched band characteristics. *Microw Opt Technol Lett* 61(1):275–279

9. Nguyen DT, Hyun D (2012) Very compact printed triple band-notched UWB antenna with quarter-wavelength slots. *IEEE Antenn Wirel Propag Lett* 11:411–414
10. Saha C, Natani P, Shaik LA, Siddiqui JY, Antar Y (2017) Square/hexagonal split ring resonator loaded exponentially tapered slot ultra-wideband (UWB) antenna with frequency notch characteristics. *Microw Opt Technol Lett* 59(6):1241–1245
11. Islam MT, Azim R, Mobashsher AT (2012) Triple band-notched planar UWB antenna using parasitic strips. *Prog Electromagn Res* 129:161–179
12. Li T, Li GH, Liang CH (2012) Design of compact UWB band-notched antenna by means of electromagnetic-bandgap structures. *Electron Lett* 48:608–609
13. Deshmukh AA, Mohadikar PV (2017) Modified rectangular shape patch antennas for ultra-wide band and notch characteristics response. *Microw Opt Technol Lett* 59:1524–1529
14. Haroon S, Alimgeer KS, Khalid N, Tariq B, Shafique F, Khan SA (2015) A low profile UWB antenna with triple band suppression characteristics. *Wirel Personal Commun* 82(1):495–507
15. Devireddy SR, Govardhani I (2020) A Penta band notched elliptical planar monopole antenna for UWB applications. *Progress Electromag Res M* 93:53–66

# Sectoral Microstrip Antenna for Dual-Polarized Broadband Response



Aarti G. Ambekar, Amit A. Deshmukh, and Venkata A. P. Chavali

**Abstract** A sectoral microstrip antenna is proposed for a dual-polarized broadband response. The variations in sectoral angle optimize the spacing between fundamental mode  $TM_{10}$  and higher-order mode  $TM_{20}$ , yielding a bandwidth of more than 175 MHz (>20%). The proximity-fed air suspended configuration yields a broadside radiation pattern over the bandwidth with again more than 7.5 dBi. The orthogonal current distributions across  $TM_{10}$  and  $TM_{20}$  modes yield dual polarization. The bandwidth of specific polarization is overseen by the sectoral angle and feed position in a sectoral patch.

**Keywords** Sectoral microstrip antenna · Dual polarization · Proximity feeding · Broadband Response

## 1 Introduction

In recent years, due to development in wireless communication systems, the demand for dual-polarized antennas has been increased. Many applications prefer antennas, with dual polarization and broader bandwidth (BW), for proper utilization available frequency spectrum. Due to miniaturization, microstrip antennas (MSAs) are the best candidates for the realization of dual-polarized broadband response due to their small profile and ease of integration [1–4]. Many techniques like the use of multiple stack patches [5], loading schemes using slots or stubs [6, 7], complex feeding techniques [8] have been used for the realization of dual-polarized broadband response. Overlapped parasitic patches are used in Ref. [9] for the realization of dual-polarized wideband response, lack in giving an in-depth explanation of the effect of parasitic patches on the realization of said response. In spite of fabricating on a thicker substrate, BW realized is less in Ref. [10]. Reconfigurable techniques used in Ref. [11] for the realization of polarization agile broadband response increase the complexity of structure due to the use of extra biasing circuits.

---

A. G. Ambekar · A. A. Deshmukh (✉) · V. A. P. Chavali  
Department of EXTC, SVKM's DJSCE, UOM, Mumbai, India

In this paper, a proximity-fed air suspended design of sectoral microstrip antenna (S-MSA), which is a variation of circular MSA (CMSA), is proposed for a dual-polarized broadband response. Optimal spacing between  $TM_{10}$  and  $TM_{20}$  yields a broadband response with bandwidth (BW) more than 175 MHz ( $>20\%$ ). A broadside radiation pattern is observed across the bandwidth with a gain of more than 7.5 dBi. Due to  $TM_{10}$  mode at lower frequencies of BW, E-plane is directed along  $\Phi = 90^\circ$ , whereas because of  $TM_{20}$  mode toward higher frequencies of BW, E-plane is directed along  $\Phi = 0^\circ$ , which realizes dual polarization. Furthermore, with variations of the sectoral angle and proximity feed position, tuning of the dual-polarized BW is realized. Thus, without using any extra patch, slot, or stub, broader BW with polarization agility is realized using a single S-MSA only by varying sectoral angle and proximity feed positions. These all are technical contributions of the present work. The proposed configuration is first analyzed using CST Microwave Studio [12]. A proximity feeding technique using an N-type connector is selected for exciting the antenna. High-frequency instruments, namely, ZVH—8, FSC 6, and SMB—100A, are used in the experimental verification. A three-antenna gain measurement method is used for gain measurement. A good agreement is observed between the simulated and measured results.

## 2 Proximity-Fed Sectoral Microstrip Antenna

Proximity-fed S-MSA with varying sectoral angle ' $\theta^\circ$ ' and radius ' $r$ ' is as per Fig. 1a. The units for the patch dimensions and frequencies referred to in the paper are in 'cm' and 'MHz', respectively. The proposed structure is fabricated on FR4 substrate

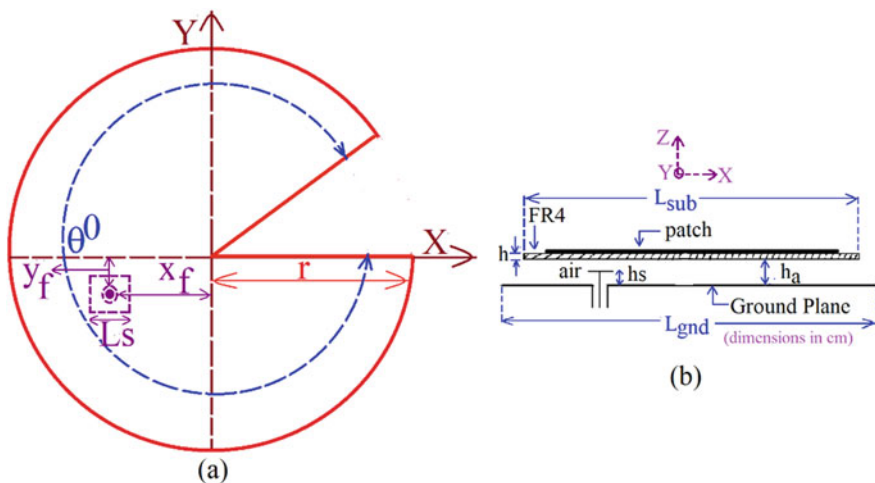


**Fig. 1** a Top view and b side view of the proposed sectoral MSA

( $\epsilon_r = 4.3$ ,  $h = 0.16$  cm) and it is suspended in air at a height of ' $h_a$ ' = 2.8 cm above the ground plane. The sector radius is calculated as ' $r$ ' = 0.7 cm for the frequency range of 950 MHz, which is equivalent to  $TM_{11}$  mode frequency of CMSA.

Initially, the S-MSA is simulated for the angle ' $\theta$ ' =  $345^\circ$ , and ' $x_f, y_f$ ' = -49, -1.8 with ' $L_s$ ' = 1.4 cm and ' $h_s$ ' = 2.7 cm. The corresponding resonance curve is revealed in Fig. 2a. Two peaks are observed, respectively, at ' $f_1$ ' = 710 MHz and ' $f_2$ ' = 892 MHz. For identifications of modes surface, current distributions observed at respective peaks are as shown in Fig. 2b-c. '+' and '-' signs in the current plots indicate field polarities. For the first peak, half-wavelength variation is observed along the perimeter that corresponds to  $TM_{10}$  mode, which is a fundamental mode of S-MSA, while for the second peak, two half-wavelength variations are observed along the second peak, which corresponds to  $TM_{20}$  mode. As per the current distributions, the current maxima among the modes are orthogonal, which may lead to a dual-polarized response. Broader bandwidth is a result of optimal spacing between consecutive modes. Owing to the current variations and geometry of S-MSA, the

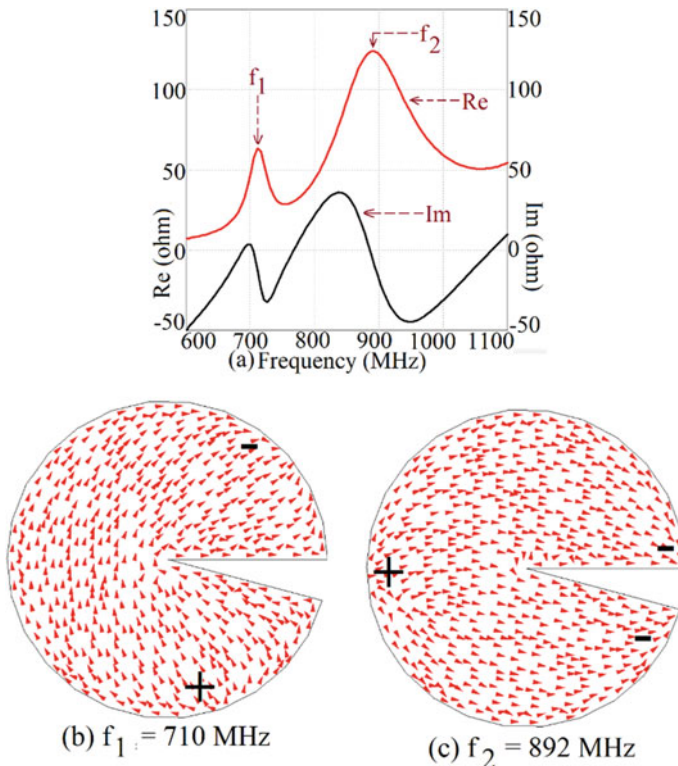
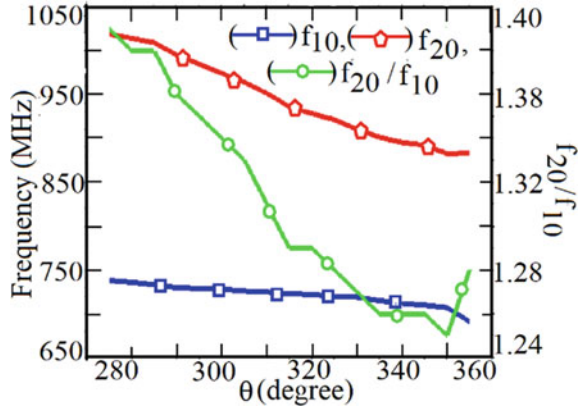


**Fig. 2** a Resonance curve for  $\theta = 345^\circ$  and b-c surface current distributions at two peaks observed for  $\theta = 345^\circ$  of proposed S-MSA

**Fig. 3** Frequency ' $f_{10}$ ', ' $f_{20}$ ' and ratio ' $f_{20}/f_{10}$ ' plots for ' $\theta$ ' variations of the proposed S-MSA



sectoral angle will affect corresponding modal frequencies. For observing it, parametric is carried with respect to sectoral angle ' $\theta$ ' variations. The respective observed frequencies ' $f_{10}$ ', ' $f_{20}$ ' and their ratio plots are as shown in Fig. 3. With increasing ' $\theta$ ', the corresponding values of modal frequencies and ratios are decreasing, optimizing the spacing between them. So, for higher values of ' $\theta$ ', a broadband response is realized.

As the tuning of  $TM_{10}$  and  $TM_{20}$  mode is realized by varying sectoral angle ' $\theta$ ', tuning of horizontal and vertical polarization can be also done by ' $\theta$ ' variation. Hence, for observing the effect of sectoral angle on polarization, axial ratio (AR) is monitored for different values of ' $\theta$ '. The corresponding 'AR' plots are shown in Fig. 4a–d. With a decrementing value of ' $\theta$ ', AR is increasing till  $290^\circ$ , while from  $280^\circ$  onwards, it is again decrementing. Orthogonal surface current distributions across  $TM_{10}$  and  $TM_{20}$ , yield dual polarization. A close spacing with equal contribution of orthogonal current distributions across the modes yields circular polarization (CP), same is observed for ' $\theta = 350^\circ$ ', showing AR below 3 dB, as shown in Fig. 3a. Thus, CP is realized for ' $\theta = 350^\circ$ '. The reflection coefficient ( $S_{11}$ ), AR and gain for the optimized CP response at  $350^\circ$  are shown in Fig. 5a. The simulated impedance BW observed is 127 MHz while its measured value is 126 MHz. Due to closer spacing between  $TM_{10}$  and  $TM_{20}$  modes, AR BW is very less, simulated is 10 MHz while measured is 6 MHz. Radiation patterns observed at a center frequency of CP response are shown in Fig. 5b–c, indicating a difference between cross and co-polar levels less than 3 dB across broadside direction.

As the tuning of  $TM_{10}$  and  $TM_{20}$  modes is realized by varying sectoral angle ' $\theta$ ', tuning of horizontal and vertical polarization BW is obtained by ' $\theta$ ' variation. Also, the selection of proximity feed location decides the different amount of coupling between  $TM_{10}$  and  $TM_{20}$  modes, which will affect the bandwidth of that particular mode. For getting this polarization bandwidth tuning, S-MSA is simulated for ' $\theta = 335^\circ$ ', for four different proximity feed positions. The observed smith charts for four different feed positions are revealed in Fig. 6a. The variations in loop size for different feed positions for  $TM_{10}$  and  $TM_{20}$  indicate that the feed position is affecting



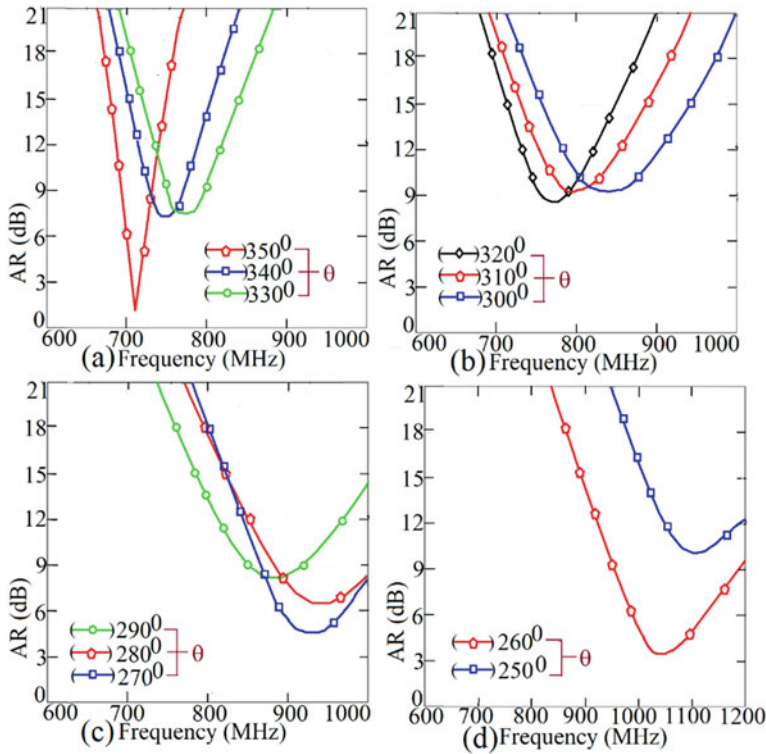


**Fig. 4** a–d Axial ratio (AR) plots for different values of ‘ $\theta$ ’ for the proposed S-MSA

the bandwidth of the modes. For monitoring, the bandwidth with respect to horizontal and vertical polarization, simulated  $S_{11}$  and gain plots are observed for two different feed locations, respectively, at ‘ $x_f, y_f$ ’ = – 49, –1.8 cm and –4.4, –1.8 cm as shown in Fig. 6b. It yields simulated impedance bandwidth of 167 MHz (21%) and 158 MHz (20%) for the respective feed positions. For lower frequency range due to  $TM_{10}$  mode, E-plane is along  $\Phi = 90^\circ$  yielding vertical polarization (VP), while for higher frequency values due to  $TM_{20}$  mode, E-plane is along  $\Phi = 0^\circ$  yielding horizontal polarization (HP).

For the feed position, ‘ $x_f, y_f$ ’ = –4.9, –1.8 cm, till the frequency 766 MHz, polarization is vertical (VP) while above it, the polarization is horizontal (HP). Similarly for the feed position, ‘ $x_f, y_f$ ’ = –4.4, –1.8 cm, till the frequency 786 MHz, vertical polarization is realized while above its polarization is horizontal. So over 48% of VSWR bandwidth, polarization is vertical while for 52%, polarization is horizontal for ‘ $x, y_f$ ’ = –4.8, –1.8 cm while for ‘ $x_f, y_f$ ’ = –4.4, –1.8 cm, over 67% of VSWR bandwidth polarization is vertical and for 33%. Thus, by varying the proximity feed position, polarization BW tuning can be realized.

The optimum dual-polarized broadband response is realized for ‘ $\theta$ ’ =  $335^\circ$  with proximity feed position at ‘ $x_f, y_f$ ’ = –5.4, –1.8. The  $S_{11}$ , gain and AR BW plots are

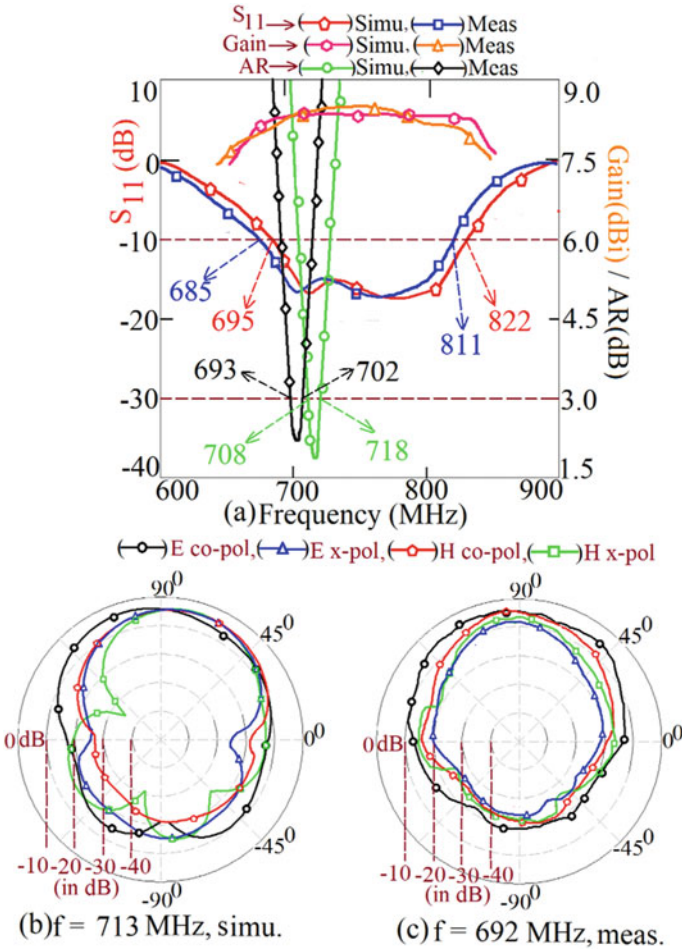


**Fig. 5** a  $S_{11}$ , AR and gain plots and b radiation pattern at a center frequency of CP response at  $\theta = 350^\circ$  for the proposed S-MSA

revealed in Fig. 7a. The radiation patterns observed near band start and band stop frequencies are shown in Fig. 7b–e. The simulated VSWR BW is 184 MHz (24%) while the measured value is 183 MHz (23%). The reflection coefficient for the desired frequency range is below  $-10$  dB. The simulated gain is 8 dBi while its measured value is 7.5 dBi in the broadside direction. For band start frequencies, E-plane is aligned along  $\Phi = 90^\circ$  while for band stop frequencies, E-plane is aligned along  $\Phi = 0^\circ$ . Thus, the proposed work explains the functioning of S-MSA for realizing dual-polarized broadband response in terms of patch resonant modes. The variations in sectoral angle affect the type of polarization. Sectoral angle along with proximity feed position variation tunes the polarization BW also. These all are innovative technical contributions provided by this work.

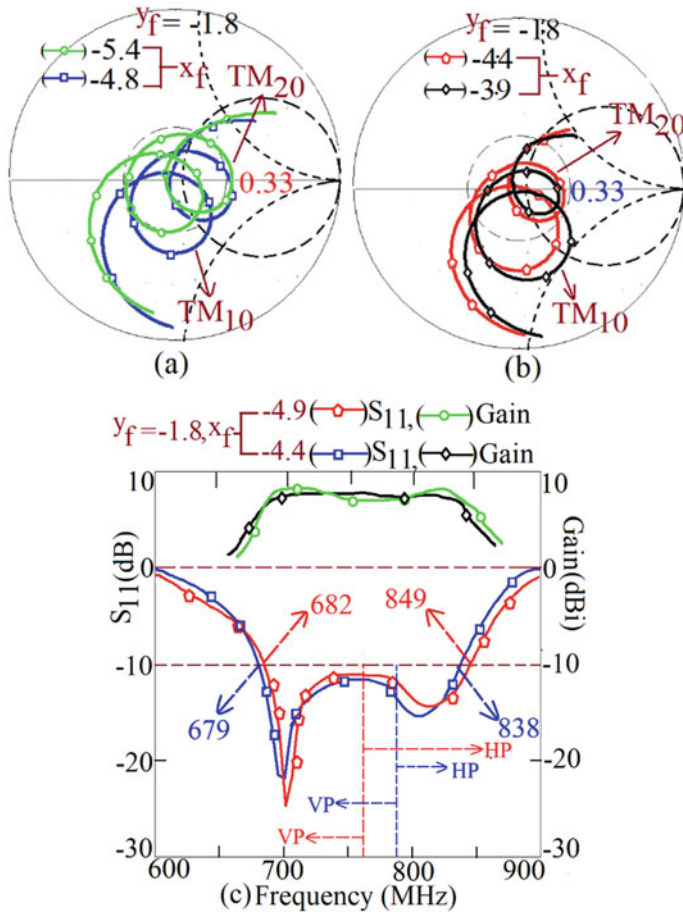


**Fig. 6** a Smith charts and b  $S_{11}$ , and gain plots for different feed positions at ' $\theta$ ' = 335° for the proposed S-MSA

### 3 Conclusions

An innovative approach using sectoral MSA is proposed for the realization of dual-polarized broadband response. The proposed work gives a clear insight into antenna functioning in terms of patch resonant modes for the realization of the said response. The sectoral angle variations affect the spacing between TM<sub>10</sub> and TM<sub>20</sub> modes of S-MSA, which realizes broadband response. Due to orthogonal current variations across the respective modes, dual polarization is realized. For optimum dual-polarized broadband response, VSWR BW of around 185 MHz (23%) is realized with broadside gain around 7.5dBi. The bandwidth of individual polarization is tuned by adjusting the sectoral angle and proximity feed position with variable BW ratio changing from 48 to 52% and 67 to 33%, respectively.

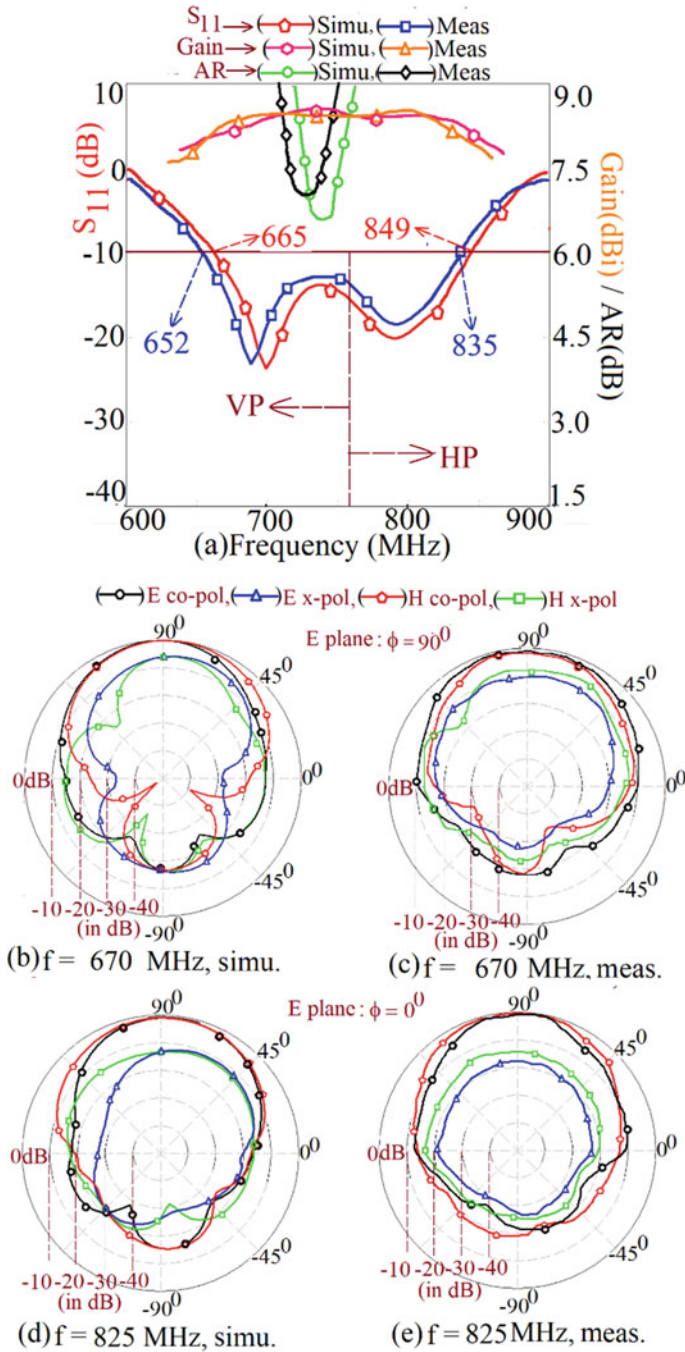


**Fig. 7** a  $S_{11}$ , gain and AR plots, radiation patterns at **b** and **c** band start frequency and **d** and **e** band stop frequency at  $\theta = 335^{\circ}$  for the proposed S-MSA

## References

1. Wong KL (2002) Compact and broadband microstrip antennas. John Wiley and Sons, New York
2. Kumar G, Ray KP (2003) Broadband microstrip antennas, 1st edn. Artech House, USA
3. Garg R, Bhartia P et al (2001) Microstrip antenna design handbook, 1st edn. Artech House
4. Bahal IJ, Bhatia B (1980) Microstrip antenna, 1st edn. Artec House
5. Zhao F, Zhang W, Han LG, Yang R (2018) A wideband dual-polarized patch antenna fed with the aperture-coupled microstrip. *Electromagnetics* 38(1):58–69
6. Wong K-L, Hao CT, Tzung WC (2002) Broadband dual-polarized aperture-coupled patch antennas with modified H-shaped coupling slots. *IEEE Trans Antenn Propag*, 50, 188–191
7. Deshmukh AA, Pawar S, Ambekar AG, Kamble P, Ray KP (2017) Compact Y-shape antenna for dual polarized wideband response. *IEEE Appl Electromag Conf (AEMC)* 1–2
8. Ryu KS, Kishk AA (2008) Wideband dual-polarized microstrip patch excited by hook shaped probes. *IEEE Trans Antenn Propag* 56(12):3645–3649
9. Rambabu K, Alam M, Bornemann J, Stuchly MA (2004) Compact wideband dual-polarized microstrip patch antenna. *IEEE Antenn Propag Soc Symp*, C.A, USA. 2:1955–1958
10. Gao SC, Li LW, Leong MS, Yeo TS (2001) A novel dual-polarized, wide-band microstrip patch antenna with aperture coupling. *IEEE antennas and propagation society international symposium. digest. Held in conjunction with: USNC/URSI National Radio Science Meeting*, Boston, MA, USA 4:78–81
11. Babakhani B, Sharma S (2015) Wideband frequency tunable concentric circular microstrip patch antenna with simultaneous polarization reconfiguration. *IEEE Antennas Propag Mag* 57(2):203–216
12. CST Microwave Studio, Version 2019

# Stub Loaded A-Shape Microstrip Antenna for Dual Polarized Multiband Response



Aarti Gajanan Ambekar, Amit A. Deshmukh, and Venkata A. P. Chavali

**Abstract** For dual polarized multiband response an innovative design of an A-shape microstrip antenna is projected. By modifying geometry of traditional U-shape antenna, A-shape geometry is realized. An externally connected stub positioned on the A-shape antenna edge adjusts the impedance of higher order modes  $TM_{20}$ ,  $TM_{30}$ , and  $TM_{40}$  modes with respect to the  $TM_{10}$  mode that yields multiband response. On a thinner substrate, the configuration displays bandwidth of  $>1.5\%$  and broadside gain across each band. The orthogonal current variations across the  $TM_{10}$ ,  $TM_{20}$ ,  $TM_{30}$ , and  $TM_{40}$  modes realize polarization diversity.

**Keywords** A-shape antenna · Multiband response · Frequency diversity · Polarization diversity

## 1 Introduction

From the last few years, to satisfy the need for modern wireless communication systems demand for the dual polarized (DP) multiband antenna is increased. Because of ease of integration and low profile microstrip antennas (MSAs) is one of the best candidates meant for the recognition of dual polarized multiband response. Modified patch geometry with loading schemes like slots or stubs can be used in the realization of multiband dual polarized response [1–4]. The loading scheme using slot is used as it provides compactness [5, 6], while for the frequency or polarization tuning stubs are preferred [7]. Due to multiple patch parameters, the multiband design reported in [8] is complex while the dual band configuration reported in [9] using U-shape feed does not provide a detailed explanation for the selection of modified feed. The use of artificial magnetic conductors increases the cost of configuration reported in [10]. In the dual band design using two rectangular slots and shorting pins [11], an in-depth explanation about consequence of slots, on the antenna resonant modes that

---

A. G. Ambekar · A. A. Deshmukh (✉) · V. A. P. Chavali  
Department of EXTC, SVKM's DJSCE, UOM, Mumbai, India

yield multiple frequencies is not discussed. Reconfigurable design reported in [12] makes the integration complex due to the use of biasing circuits of active devices.

In the present manuscript, an innovative design of A-shape MSA for DP multi-band response is projected on thinner substrate. The A-shape MSA is realized from U-shape MSA by introduction of stub sideways the length of U-shape MSA. Position and dimension of stub tunes higher order mode  $TM_{20}$  and  $TM_{30}$  mode with respect to the fundamental mode  $TM_{10}$  mode frequencies to comprehend multiband response. Across consecutive resonant modes orthogonal current distribution yields dual polarization. Further for yielding polarization diversity and tuning of  $TM_{40}$  mode, an external stub is connected on the top edge of the A-shape patch. The optimum response covering four frequency bands with center frequencies as 976, 1199, 1416, and 1780 MHz with BW more than 1.5% realizing frequency ratio of 1:1.28:1.58:1.87 is achieved. In all the bands the antenna offers a broadside radiation pattern. With these characteristics, the proposed antenna could be a promising solution for wireless applications which need polarization and frequency diversity. Thus, an in-depth explanation for the realization of quadruple response offering DP by analyzing the higher order resonant mode excitement in A-shape MSA shows innovativeness of the contemporary work. Thus, the anticipated configuration is modest in execution and offers BW of more than 1.5% with a smaller frequency ratio. The proposed configurations are first analyzed using CST Microwave Studio [13]. Coaxial feeding technique using SMA type connector is selected for exciting the antenna. High frequency instruments, namely, ZVH—8, FSC 6, and SMB –100 A are used for testing. A decent matching is observed amongst the simulated and measured results.

## 2 A-Shape Microstrip Antenna

An A-shape MSA excited with coaxially feeding is as revealed in Fig. 1a. Throughout the paper the patch dimensions are in ‘cm’ and frequencies are in ‘MHz’. The projected MSA is fabricated on thinner FR4 substrate ( $\epsilon_r = 4.3$ ,  $h = 0.16$  cm). U-shape MSA is modified for realizing A-shape MSA. The dimensions for the U-shape MSA for 1000 MHz frequency range are ‘L’ = 6.0, ‘W’ = 4.5, and ‘w’ = 1.5 cm as shown below, while for A-shape MSA the ‘stub1’ dimensions are ‘ls’ = 1.5, and ‘d’ = 2.7 cm. Both of these MSAs are simulated for ‘ $x_f, y_f$ ’ = –1.4, 4.5 cm, the corresponding resonant plots are as shown in Fig. 1b. For the A-shape MSA, the surface current distributions are as publicized in Fig. 2a–c. Depending on integer multiples of half-wavelength variations of current along the length, identified modes are  $TM_{10}$ ,  $TM_{20}$ , and  $TM_{30}$ , respectively. As detected from the current distributions, the maximum current between the consequent modes is orthogonal, which is good sign of realization of DP response.

Owing to the direct path length for half-wavelength variations, formed due to stub position, the frequency of  $TM_{10}$  is increased while  $TM_{20}$  and  $TM_{30}$  mode frequencies are remaining constant for the A-shape MSA compared to the U-shape as given away

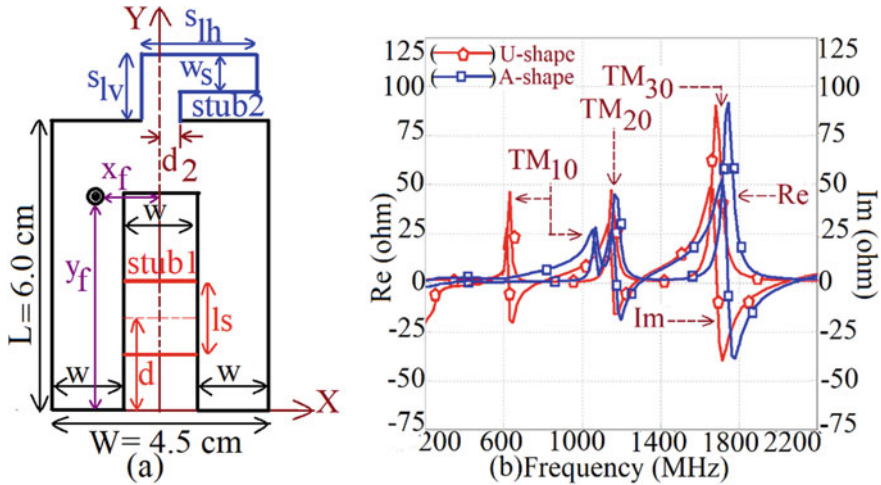


**Fig. 1** a Geometry of the proposed A-shape MSA, b resonance curve plot for U-shape and A-shape MSA

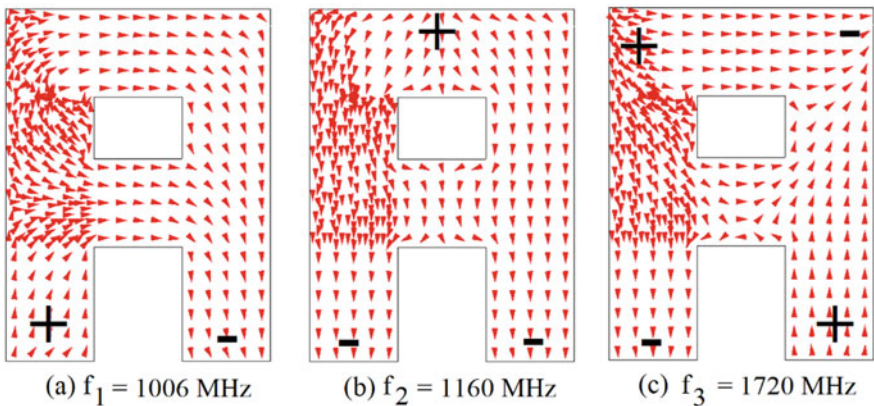


**Fig. 2** a–c Vector surface current distributions at three peaks of the A-shape MSA for dual polarized multiband response

in Fig. 1b. For witnessing the effect of this stub, on the individual modal frequencies, and realization of probable dual polarized multiband response, parametric is carried with respective to ‘stub1’ position ‘d’. The corresponding resonance graph is as publicized in Fig. 3a. It is detected from the resonance graph that, as ‘d’ varies from 2.7 to 1.9 cm,  $TM_{10}$  mode frequency is increasing, which is qualified to a reduction in active resonant length as surface currents follow the extent laterally the ‘stub1’, joining dual arms of U-shape MSA. But for realization optimized multiband dual polarized response proper tuning of  $TM_{20}$  and  $TM_{30}$  mode is required.



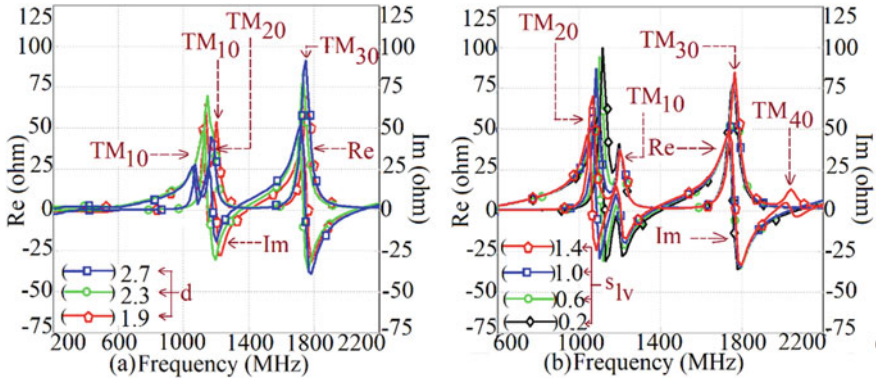


**Fig. 3** Resonance plots for variations of **a** ‘stub 1’ position ‘d’ and **b** ‘stub 2’ vertical length ‘s<sub>1v</sub>’ of A-shape MSA

### 3 Stub Loaded A-Shape MSA

To realize optimized DP multiband response optimization of the higher order modes TM<sub>20</sub>, TM<sub>30</sub> is mandatory with regard to the fundamental TM<sub>10</sub> mode. Slots at minimum field or stub at maximum field position are the mostly used loading schemes for yielding the same. For the A-shape geometry, the stub technique is selected. The maximum field position of TM<sub>20</sub> mode is exactly in the middle of the top edge portion of the A-shape patch as exposed in Fig. 2b. Hence a ‘stub 2’ with overall length ‘s<sub>1h</sub> + s<sub>1v</sub>’ and width ‘w<sub>s</sub>’ is positioned at ‘d<sub>2</sub>’ as given away in Fig. 1a for optimizing the TM<sub>20</sub> mode.

For observing the effect of this stub on corresponding mode frequencies, a parametric is supported out for the distinction in ‘s<sub>1v</sub>’, ‘s<sub>1h</sub>’ with ‘w<sub>s</sub>’ = 0.8 cm. Corresponding resonance plots are as shown in Figs. 3b, 4a. With incrementing value of ‘s<sub>1v</sub>’, Due to placement of stub at maximum field position TM<sub>20</sub> mode frequency is

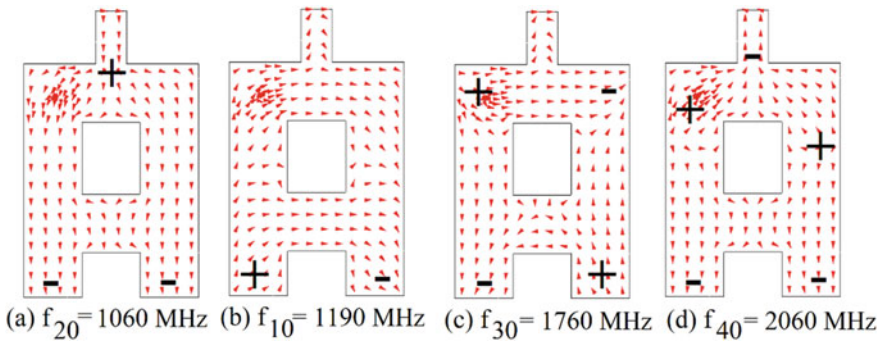


**Fig. 4** **a-d** Vector surface current distributions for ‘s<sub>1v</sub>’ = 1.4 cm of the A-shape MSA

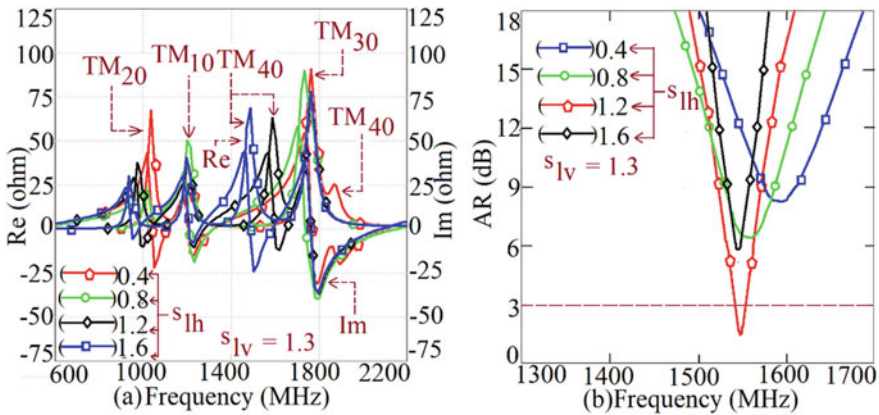


**Fig. 5** a Resonance plots and b AR plots for variations of ‘s<sub>lh</sub>’ for the A-shape MSA

coming down while TM<sub>10</sub> and TM<sub>30</sub> modes are unaffected due to situation of stub at their lowest field position. For ‘s<sub>lv</sub>’ = 1.4 cm, one more peak is observed next to TM<sub>30</sub> mode that corresponds to the next higher order mode TM<sub>40</sub>. As per the surface current distributions given away in Fig. 4d, ‘stub2’ is exactly at the maximum field of TM<sub>40</sub> mode, hence its frequency is decreasing with incrementing stub length. For retentive firmness of the MSA ‘s<sub>lv</sub>’ = 1.3 cm is kept constant. Further parametric is continued with respect to ‘s<sub>lh</sub>’ variations, corresponding resonance plots are as given away in Fig. 5a.

As shown in Fig. 5a, with incrementing value of ‘s<sub>lh</sub>’, TM<sub>20</sub> and TM<sub>40</sub> mode frequencies are further reducing, while TM<sub>10</sub> and TM<sub>30</sub> mode frequencies are remaining unaffected. For monitoring the polarization change, simulated axial ratio (AR) plots are observed for different values of ‘s<sub>lh</sub>’ as shown in Fig. 5b. For ‘s<sub>lh</sub>’ = 0.8 cm, AR below 3 dB attributed realization of circular polarized response. This is due to the close spacing between TM<sub>30</sub> and TM<sub>40</sub> mode with an identical influence of the orthogonal surface currents across the modes. TM<sub>40</sub> mode frequency is further coming down below TM<sub>30</sub> mode, with a further incrementing value of ‘s<sub>lh</sub>’.

Optimal DP multiband response is detected meant for ‘s<sub>lv</sub>’ = 1.3 cm, ‘s<sub>lh</sub>’ = 1.6 cm, and ‘ws’ = 0.8 cm. This anticipated A-shape MSA is fabricated on a thinner FR4 substrate. Simulated and measured reflection coefficients (S<sub>11</sub>) plots are as given away in Fig. 6a. The simulated and measured radiation pattern plots detected at middle frequencies of each of the four bands are as shown in Figs. 7a–d and 8a–d.

The S<sub>11</sub> for the desired frequency bands is < -10 dB. The replicated center frequencies are ‘f<sub>1</sub>’ = 986, ‘f<sub>2</sub>’ = 1208, ‘f<sub>3</sub>’ = 1489, ‘f<sub>4</sub>’ = 1794 MHz and corresponding measured values are ‘f<sub>1</sub>’ = 976, ‘f<sub>2</sub>’ = 1199, ‘f<sub>3</sub>’ = 1416, ‘f<sub>4</sub>’ = 1780 MHz. The simulated BWs are 20 MHz (2%), 25 MHz (2.1%), 32 MHz (2.2%), 34 MHz (1.9%), while corresponding measured values are 19 MHz (1.9%), 24 MHz (2%), 31 MHz (2.1%), and 33 MHz (1.85%), respectively, at each band. Owing to maximum current contributions laterally in horizontal directions, the E-plane for TM<sub>10</sub> and TM<sub>30</sub> is

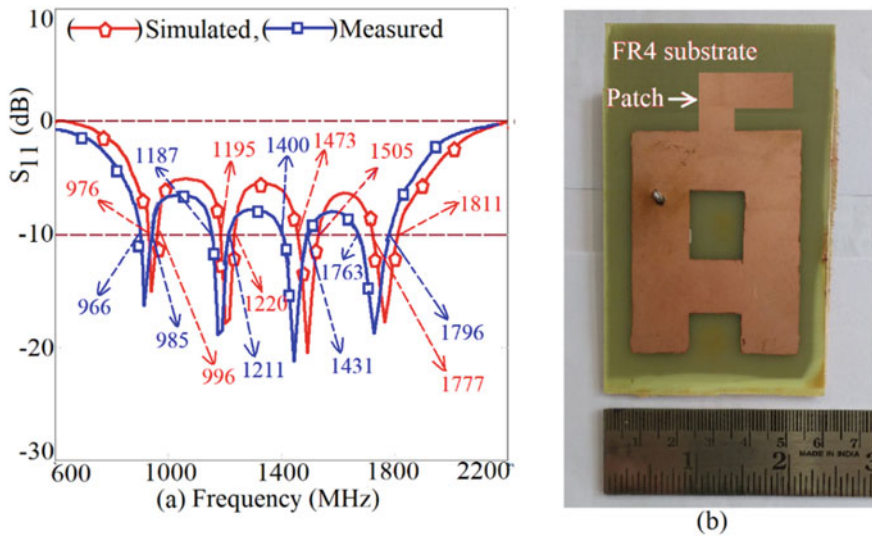


**Fig. 6** **a** Reflection coefficient ( $S_{11}$ ) plot and **b** Fabricated prototype for the A-shape MSA

focused laterally at  $\Phi = 0^\circ$  while for  $TM_{20}$  and  $TM_{40}$  as the maximum current influence is laterally in vertical direction E-plane is directed along with  $\Phi = 90^\circ$  yielding dual polarization. As the configuration is invented on thinner FR4 substrate, hence gain realized is almost near to zero, which can be improved by fabricating it on a thicker substrate or substrate with smaller  $\epsilon_r$ . The fabricated prototype is as shown in Fig. 5b.

## 4 Conclusions

A simple coaxially fed innovative stub loaded A-shape MSA for the DP multiband response is presented. The anticipated work makes available in-depth clarification for the antenna employed in relations of the patch resonant modes. Tuning of  $TM_{20}$ ,  $TM_{30}$ , and  $TM_{40}$  mode frequency with respect to  $TM_{10}$  mode is the result of stub connected in the A-shape patch. This produces DP multiband response with BW  $> 1.5\%$  across each band. The stub length changes the spacing between respective modal frequencies and also tunes polarization between consecutive bands yielding frequency as well as polarization diversity. The proposed design with the single stub shows broadside radiation patterns across the BW.

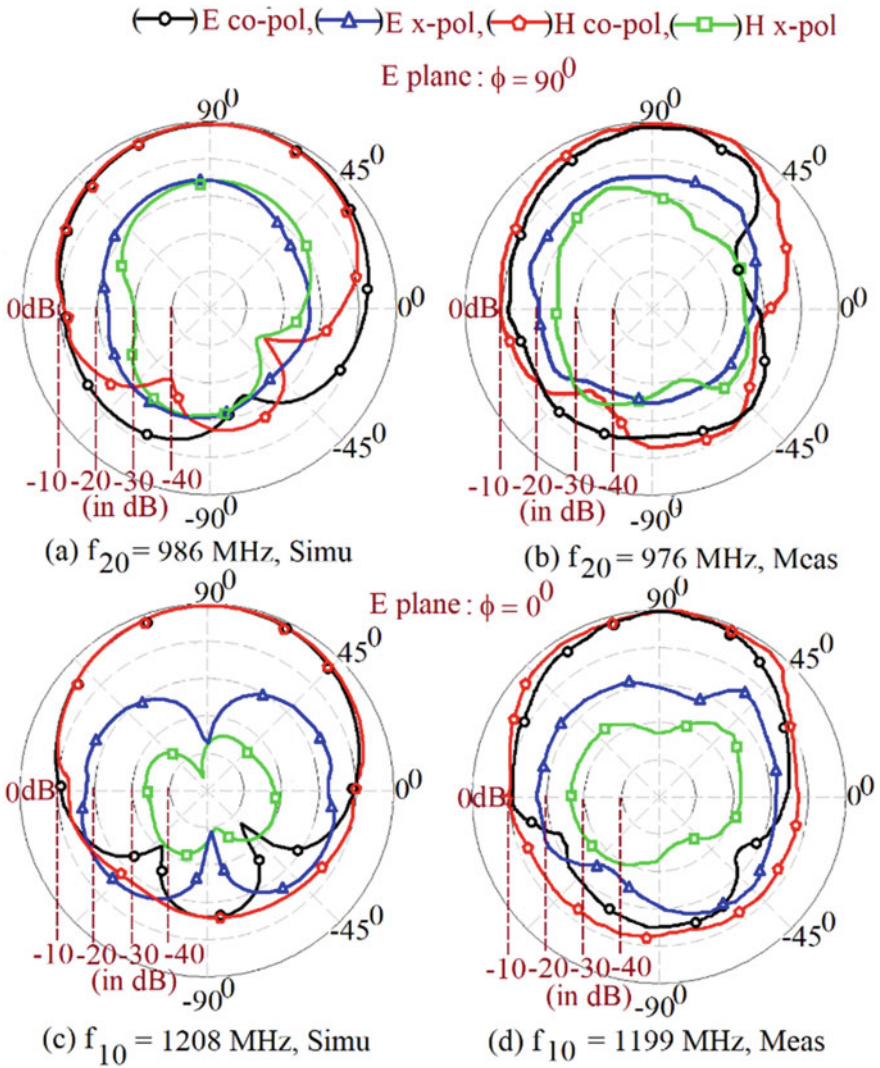


**Fig. 7** a–d Simulated and measured radiation patterns of  $TM_{20}$  and  $TM_{10}$  mode for the A-shape MSA

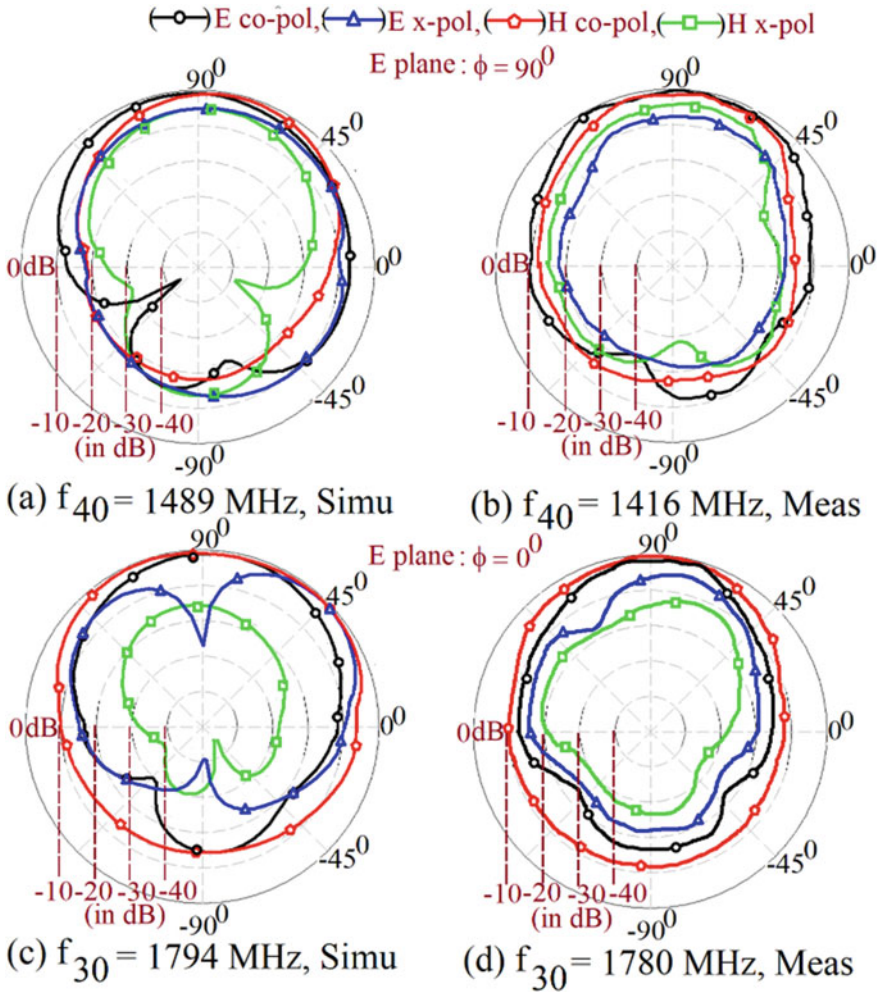


**Fig. 8** a–d Simulated and measured radiation patterns of  $TM_{40}$  and  $TM_{30}$  mode for the A-shape MSA

## References

1. Garg R, Bhartia P et al (2001) Microstrip antenna design handbook, 1st edn. Artech House
2. Bahal IJ, Bhatia B (1980) Microstrip antenna, 1st edn. Artec House
3. Kumar G, Ray KP (2003) Broadband microstrip antennas, 1st edn. Artech House, USA
4. Wong KL (2002) Compact and broadband microstrip antennas. John Wiley and Sons, New York
5. Shynu SV, Augustin G, Aanandan CK, Mohanan P, Vasudevan K (2006) C-shaped slot loaded reconfigurable microstrip antenna. Electron Lett 42(6):316–317
6. Liu S, Qi SS, Wu W, Fang DG (2014) Single layer single patch four band asymmetrical U-slot patch antenna. IEEE Trans Antennas Propag 62(9):4895–4899

7. Trong NN, Hall L, Fumeaux CA (2015) frequency and polarization reconfigurable stub loaded microstrip patch antenna. *IEEE Trans Antennas Propag* 63(11):5235–5240
8. Falade OP, Rehman MU, Gao Y, Chen X, Parini CG (2012) Single feed stacked patch circular polarized antenna for triple band GPS receivers. *IEEE Trans Antennas Propag* 60(10):4479–4484
9. Mobashsher AT, Islam MT, Misran N (2010) A novel high-gain dual-band antenna for RFID reader applications. *IEEE Antennas Wirel Propag Lett* 9:653–656
10. Ghosh A, Kumar V, Sen G, Das S (2018) Gain enhancement of triple-band patch antenna by using triple-band artificial magnetic conductor. *IET Microw Antennas Propag* 12(8):1400–1406
11. Tung HC, Wong KL (2001) A shorted microstrip antenna for 2.4/5.2GHz dual-band operation. *Microw Opt Technol Lett* 30(6):401–402
12. Tekin I, Knox M (2012) Reconfigurable microstrip patch antenna for WLAN software defined radio applications. *Microw Opt Technol Lett* 54:644–649
13. CST Microwave Studio, Version 2019

# Space Fed Rectangular Microstrip Antenna Arrays



Adil Parvez, Amit A. Deshmukh, A. P. C. Venkata, and Tushar Sawant

**Abstract** Using the rectangular microstrip antennas, various space fed array designs are proposed for high gain and broadband response in 4 GHz frequency range. A detailed study is presented using different feed variations like the proximity feeding and gap-coupled resonators. Due to the effective illumination of the peripheral space fed patches, an optimum response is realized in  $7 \times 7$  array fed using the proximity fed gap-coupled rectangular patches. This design yields broadside peak gain of 18.2 dBi with an impedance bandwidth of 2.75 GHz. The feed design of E-shape MSA with stacked and gap-coupled rectangular patches exciting the  $7 \times 7$  patch arrays yields broadside peak gain of 17.6 dBi with impedance bandwidth of 2.31 GHz. The E-shape feed simplifies the fabrication complexities in the feeding patch. The experimentation has been carried out to validate the simulation, which shows close agreement.

**Keywords** Space fed array · Rectangular microstrip antenna · E-shape microstrip antenna · Gap-coupled stacked feed · Proximity feeding

## 1 Introduction

With the developments in the wireless communication systems, requirement of the high gain and wider bandwidth (BW) antennas has increased [1, 2]. Due to the numerous advantages, microstrip antenna (MSA) finds wide usages here [1–3]. Earlier days, MSAs were considered to be narrow BW devices, but over the last two–three decades, many techniques have been reported that enhance the antenna BW. The BW is increased using thicker substrate, using modified feeding structure, by embedding the resonant slots inside the patch [3–6]. The antenna gain is increased by increasing its aperture area, which is increased by using the parabolic dish [1, 2]. However, space fed array configurations prove to be the efficient solution amongst

---

A. Parvez · A. A. Deshmukh (✉) · A. P. C. Venkata · T. Sawant  
Department of EXTC, SVKM's DJSCE, Mumbai, India

all as the structure is planar, removes the effects of blocking efficiency present in other array designs [7–10].

In this paper, space fed array designs of rectangular MSA (RMSA) fed using various modified feedings are presented for wideband and high gain response in 4 GHz frequency range. Two feed configurations proximity fed RMSA and gap-coupled RMSAs stacked on proximity fed RMSA are studied for gain and BW enhancement. Using each feed, spaced fed array (SFA) of order like,  $1 \times 3$ ,  $3 \times 1$ , plus shaped,  $3 \times 3$ ,  $5 \times 5$  and  $7 \times 7$ , is studied. In each design, parametric study for analyzing the gain and BW response is carried out. For lower order SFAs, proximity fed RMSA as feed gives optimum response whereas for higher order SFAs gap-coupled stacked design of RMSAs yields optimum response. Further to simplify the feed design, E-shape MSA in place of proximity feed RMSA is studied for exciting the stacked gap-coupled RMSAs as well as space fed elements. In both the feeding network,  $7 \times 7$  SFA yields optimum gain and BW of above 17.5 dBi and 2 GHz, respectively. The low cost FR4 substrate ( $\epsilon_r = 4.3$ ,  $h = 0.16$  cm,  $\tan \delta = 0.02$ ) is used to fabricate the fed and SFA elements. The SMA panel type connector is selected to feed the antennas. A finite square ground plane of dimension  $40 \times 40$  cm is used in the present study. The antennas discussed in this paper were initially studied using IE3D software followed by the experimentation. The experimental verification for the proposed SFAs is carried out in the antenna lab using R & S instruments like, ZVH-8, FSC 6, and SMB 100A. A reference wideband horn antennas are used in the pattern and gain measurement. A three-antenna method is used for the gain measurements.

## 2 Space Fed RMSA Arrays

The main focus of the study presented in this paper is in realizing higher gain wider BW designs employing RMSAs. In an array, BW is decided by the feed element whereas the gain is decided by the effective placement of the array elements around the fed patch. Thus initially the designs of space fed arrays consisting of rectangular patches, fed using proximity fed RMSA are discussed as shown in Fig. 1a. The SFA is proposed in 4 GHz frequency range. For this frequency, proximity fed RMSA dimensions are selected such that  $f_{TM10} = 4$  GHz. On glass epoxy substrate ( $\epsilon_r = 4.3$ ,  $h = 1.6$  mm) which is suspended above the ground plane with ' $h_1$ ' = 4.8 mm, RMSA dimensions are length ' $L_f$ ' = 22 and width ' $W_f$ ' = 26 mm. A proximity feeding copper strip of dimension  $3.5 \times 3.5$  mm is placed at a height of 4.8 mm above the ground plane and below the fed RMSA. In this space fed array, proximity fed RMSA excites an array of rectangular patches which are fabricated on glass epoxy substrate and are kept at height ( $D$ ) = ' $n\lambda_o/2$ ', above the fed RMSA. Here ' $n$ ' is an integer and ' $\lambda_o$ ' is the free space wavelength at 4 GHz. In addition to the distance ' $D$ ', gain is also a function of the length variation over the space fed patches. This is also referred to as the length detuning. This progressive detuning in length exists in the patches which are away from the central rectangular patch which is placed directly on top of the proximity fed RMSA. In each configuration, a parametric study has been carried



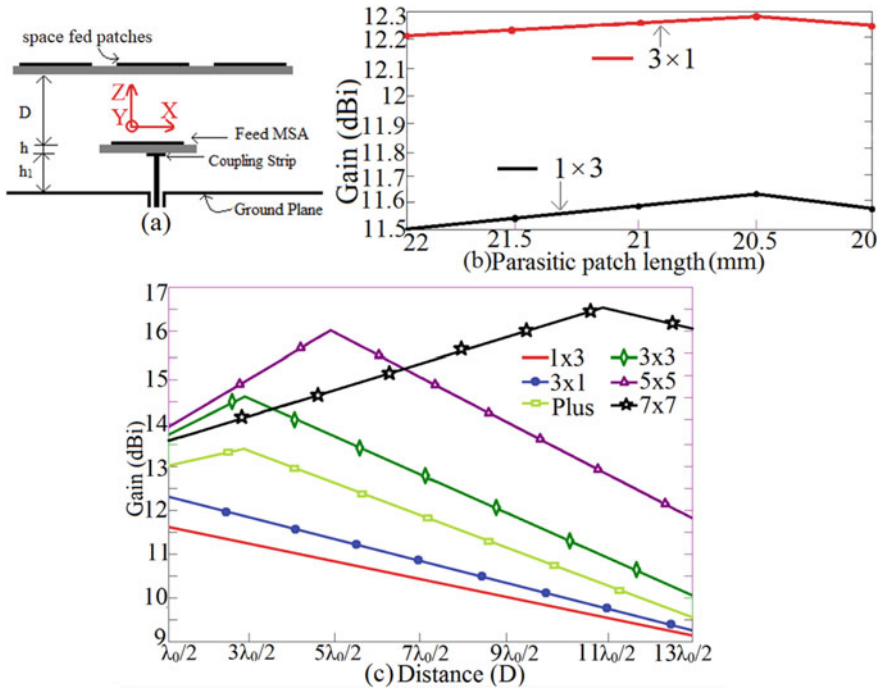


**Fig. 1** a Side view SFA fed using proximity fed RMSA, its gain variation against b detuned patch length and c distance between fed patch and space fed layer

out for the detuning in patch length to optimize for the gain as shown in Fig. 1b, for  $1 \times 3$  and  $3 \times 1$  SFAs. Thus the dimension of the center top patch is kept the same as the bottom fed patch. That of the adjacent patch is selected as  $L_1 = 20.5$  mm and next patches (outwards from the center) length are reduced by 0.5 mm for the desired length detuning. Similar tapering in length is applied to the diagonal patches in the higher order SFAs. Various SFAs, namely,  $1 \times 3$ ,  $3 \times 1$ , plus shape,  $3 \times 3$ ,  $5 \times 5$ ,  $7 \times 7$ , have been studied as shown in Fig. 2. Further in different SFAs, parametric study for varying distances 'D' is carried out and the broadside gain plots for them are shown in Fig. 1c. It is noted that for lower order SFAs, maximum gain is obtained for lower 'D' whereas for higher order  $7 \times 7$  SFA, an optimum gain is obtained for larger 'D'. With an increase in the SFA order, a higher distance is needed for the effective illumination of the peripheral array elements with reference to the incident electromagnetic energy. The results for each SFAs are given in Table 1. Among various SFAs, BW changes due to the changes in the mutual coupling among various patches with the distance variation. In terms of the VSWR BW, optimum results are obtained in lower order,  $1 \times 3$  and  $3 \times 1$  space fed arrays, whereas in terms of the gain and BW both, optimum results are obtained in  $7 \times 7$  SFA. Various results for  $7 \times 7$  SFA are shown in Fig. 3a–d. In  $7 \times 7$  SFA, simulated BW is 1.3 GHz (30.6%) whereas the measured BW is 1.315 GHz (31.14%), respectively. The pattern is in the

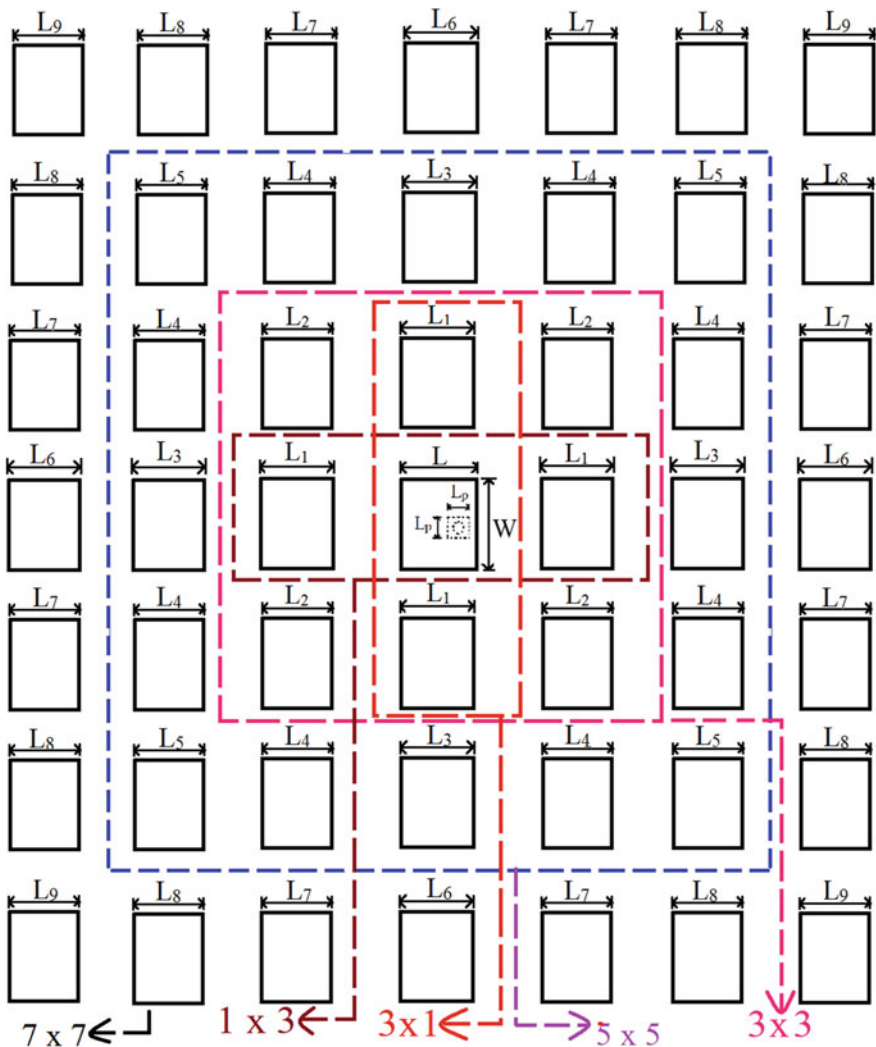
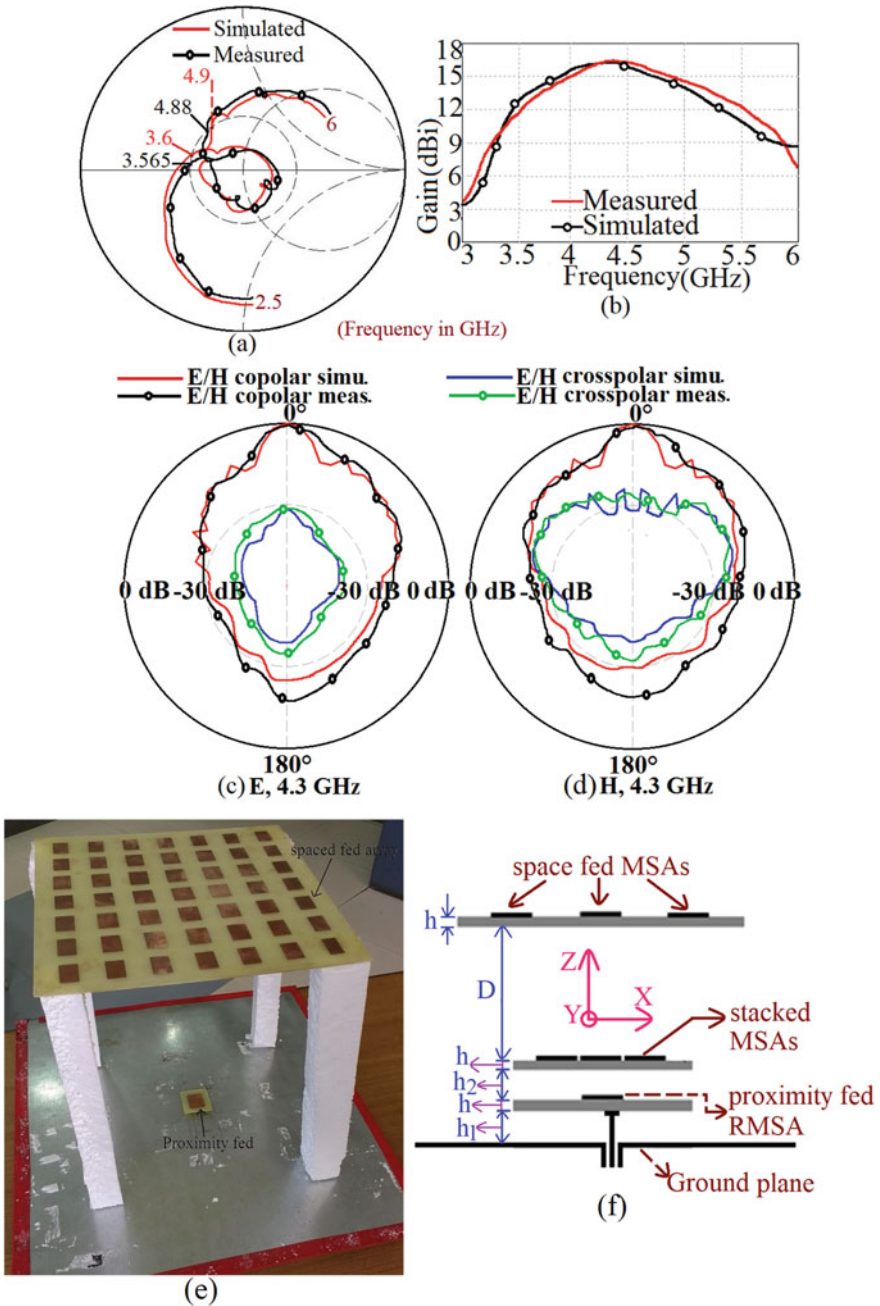


Fig. 2 SFA variations fed using proximity fed RMSA

Table 1 Gain and BW of single proximity fed SFA

SFA	BW (GHz)	Gain (dBi)
1 × 3	1.65	11.6
3 × 1	1.51	12.3
Plus shape	1.15	13.3
3 × 3	1.1	14.6
5 × 5	1.32	16.0
7 × 7	1.3	16.5



**Fig. 3** a Smith chart, b gain variation over BW, c, d radiation pattern at center frequency of BW, and e fabricated prototype of proximity fed RMSA feeding 7 × 7 space fed array f side view of SFA fed by gap-coupled stacked designs of RMSAs fed using proximity fed RMSA

broadside direction with cross polar (XP) levels less than 10 dB as compared with the co-polar (CoP) levels observed in the broadside direction. The E- and H-planes are directed along  $\Phi = 0^\circ$  and  $90^\circ$ , respectively. Simulated and measured peak antenna gain is above 16 dBi. The fabricated design of  $7 \times 7$  SFA is shown in Fig. 3e. As seen from Table 1, an increase in gain from  $3 \times 3$  to  $7 \times 7$  space fed array is only by 2 dBi. For larger increase in total aperture this gain increment is marginal.

In the present design, only a single proximity feed patch is exciting all the space fed elements. Due to this effective illumination of the peripheral elements in larger order space fed arrays is not realized, which results in smaller increase in the gain. To realize the effective illumination of the peripheral space fed elements, modified feeding system is considered as discussed in the following sections.

To realize an optimum excitation of the peripheral elements, multiple patches are needed to feed the SFA elements. For this first the gap-coupled configuration of rectangular patches which were or stacked on to the fed proximity fed RMSA is considered in the feed design as shown in Fig. 3f. Initially in the stacked layer, plus shape variation of gap-coupled rectangular patches is considered, in which parasitic rectangular patches are gap-coupled to the central stacked patch along the two coordinate axis. The RMSA dimensions in the stacked gap-coupled layer are optimized for getting the maximum BW. In the optimum feed design, stacked layer is kept at height ( $h_2$ ) of 4 mm above proximity fed RMSA. The length and width of RMSAs in the stacked layer are 14 and 26 mm, respectively. An air gap between two patches along x-axis is 12 mm whereas that along y-axis it is 1 mm. Various configurations like,  $1 \times 3$ ,  $3 \times 1$ , Plus shape,  $3 \times 3$ ,  $5 \times 5$ ,  $7 \times 7$ , have been studied and optimized for the gain and BW as shown in Fig. 4.

The SFA element dimensions are selected in the similar manner to that selected in the previous array design. The simulated BW gain observed in broadside direction using this modified feed for  $3 \times 3$  to  $7 \times 7$  space fed arrays is given in Table 2. In all the variations impedance BW is around 3.1 GHz. In higher order arrays gain is increased by nearly 0.5 dBi. Thus in comparison to a single proximity feed patch, plus shape feed design yields nearly twice the impedance BW with gain increase by 0.5 dBi. The results for  $7 \times 7$  space fed array are shown in Fig. 5a–e. For the  $7 \times 7$  array, simulated and measured BW is 3.142 GHz (68.6%) and 3.174 GHz (69.8%), respectively. Radiation pattern for the same is in the broadside direction with cross polar levels less than 15 dB as compared with the co-polar levels. The E- and H-planes are aligned along  $\Phi = 0^\circ$  and  $90^\circ$ , respectively. The simulated and measured peak antenna gain is greater than 16.5 dBi. Thus in comparison with single proximity feed, improvement in BW is observed rather than the gain. Instead of plus shape design in stacked gap-coupled layer,  $3 \times 3$  array of rectangular patches is further considered for the effective illumination of peripheral elements in the higher order designs, as discussed below and shown in Fig. 5f. Here, a design of  $3 \times 3$  SFA is shown.

The side view of this configuration is similar to that shown in Fig. 3f with only difference is the gap-coupled  $3 \times 3$  RMSA array is present in the stacked layer. The use of gap-coupled  $3 \times 3$  RMSAs will increase the overall aperture of the feed area, which will help in the effective illumination of the peripheral space fed patches that

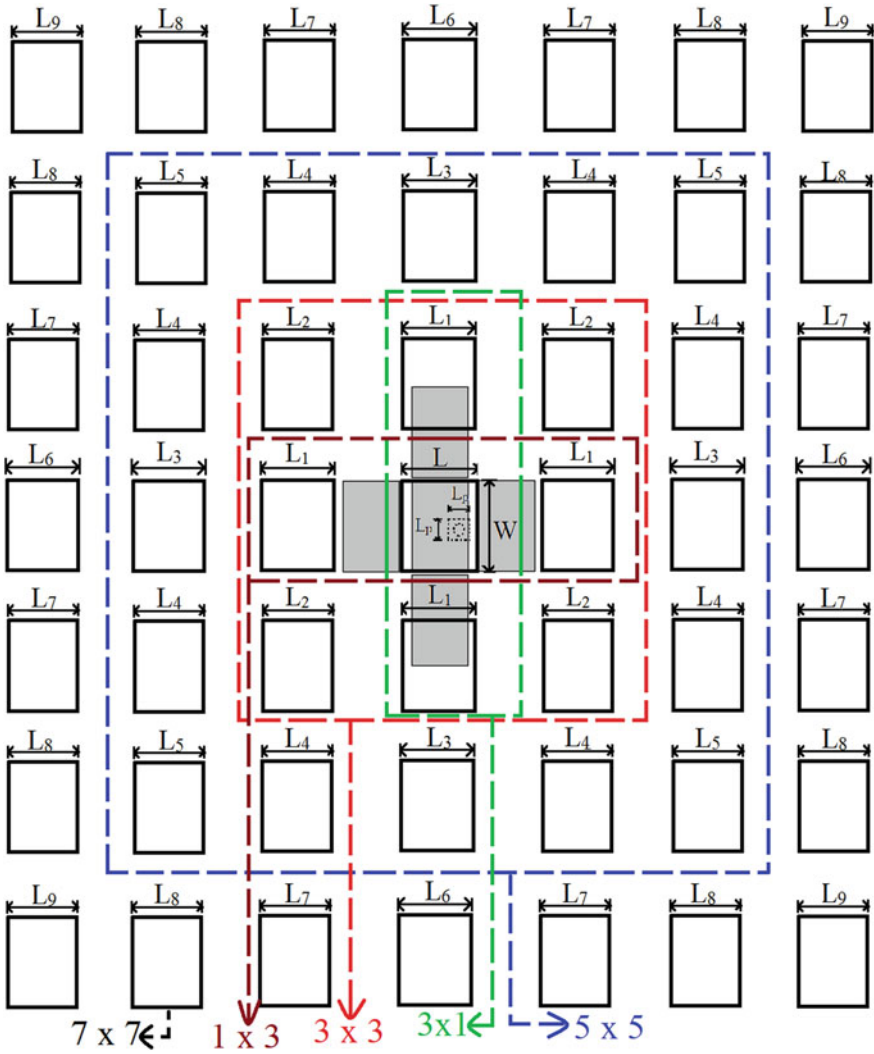


**Fig. 4** SFA variations fed by gap-coupled and stacked RMSAs fed using proximity fed RMSA

**Table 2** Gain and BW for space fed arrays fed using plus shape design of RMSAs

SFA designs	BW plus shape feed (GHz)	Gain, proximity fed RMSA (dBi)	Gain, plus shape stacked RMSA (dBi)
3 × 3	3.11	14.6	14.7
5 × 5	3.1	16.0	16.5
7 × 7	3.142	16.5	16.9

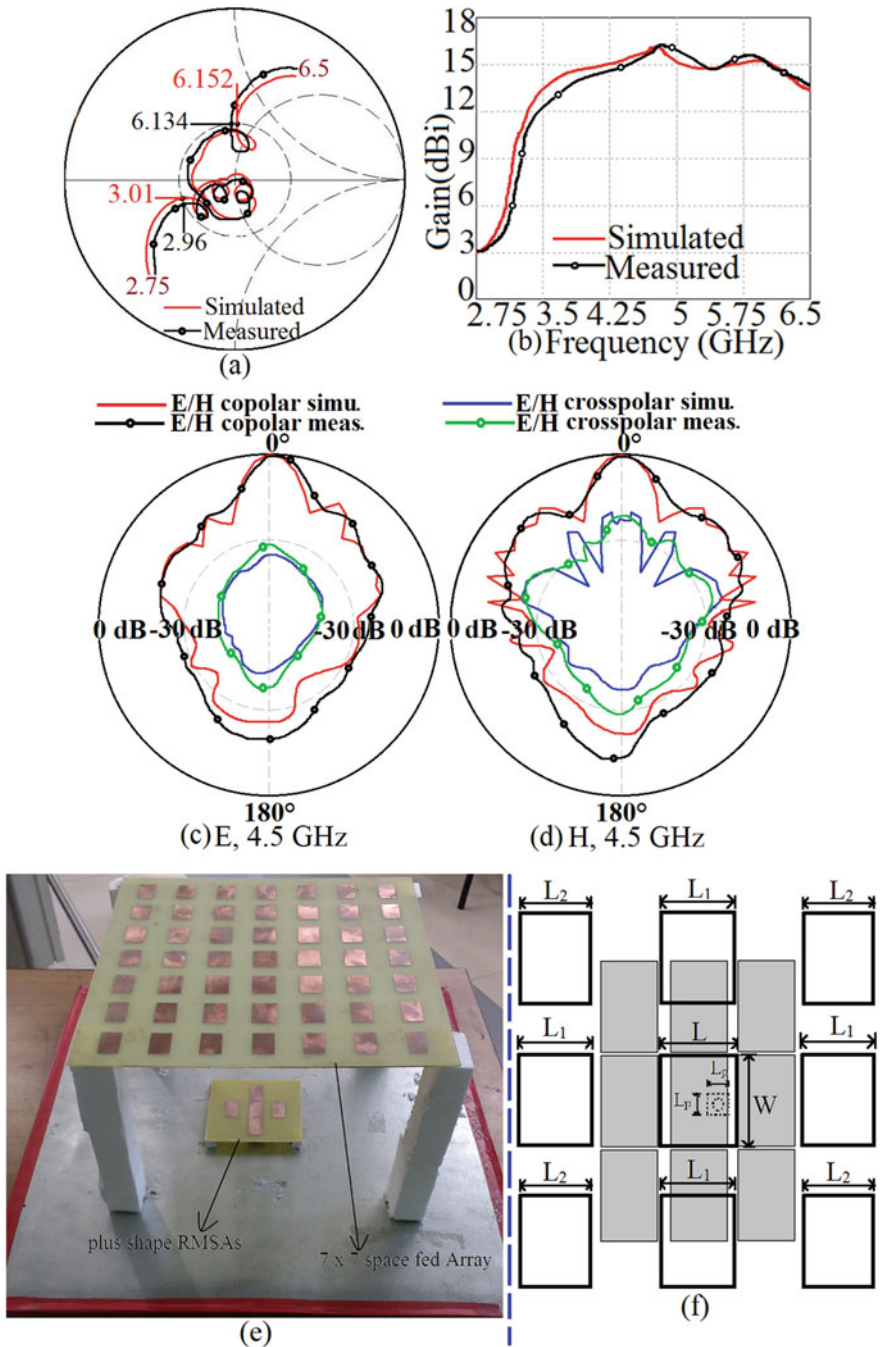
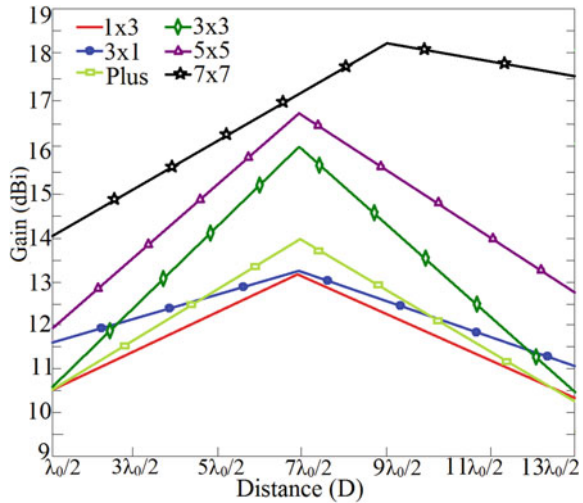


**Fig. 5** a Smith chart, b gain variation over BW, c, d radiation pattern at center frequency of BW, and e fabricated prototype of plus shape design of RMSAs feeding 7 × 7 SFA, f 3 × 3 SFA design feeding using 3 × 3 stacked gap-coupled proximity fed RMSAs

**Fig. 6** Variation in broadside gain for different order of SFAs fed using  $3 \times 3$  stacked gap-coupled proximity fed RMSAs



will increase the broadside gain. Various dimensions in the  $3 \times 3$  feed design are optimized using the parametric study to achieve the maximum BW. In  $3 \times 3$  RMSA array in the feed, separation between the two glass epoxy substrate layer ‘h<sub>2</sub>’ is same as that present in the plus shape feed design. The length and width of stacked RMSAs in  $3 \times 3$  array are 13.75 mm and 26 mm, respectively. Since more number of patches are present in the stacked layer, a smaller air gap of 3 and 0.5 mm between the patches along x and y-axes, respectively, is needed. Similar to the previous designs, various SFA variations are realized. In each of the variations, a detailed parametric study is carried out for the variation in distance ‘D’ in between the fed RMSAs and space fed RMSAs and the gain plots for them are shown in Fig. 6.

As seen from the gain plot, maximum gain for the array order till  $5 \times 5$ , is obtained for ‘D’ =  $7\lambda_0/2$ . A higher value of ‘D’ even for smaller arrays is attributed to the use of  $3 \times 3$  stacked gap-coupled layer in the feed design which offers higher illumination of the space fed patches. Therefore even for smaller order space fed arrays, higher distance is needed. The table of comparison between the impedance BW with the realized gain against various feeding arrangements is provided in Table 3. The simulated impedance BW for various space fed arrays is around 2.7 GHz. As the BW is governed by the feed network, the reduction in the same is attributed to the close placement of the resonant modes across various gap-coupled stacked RMSAs in the  $3 \times 3$  feed layer. In terms of gain enhancement, till the plus shape space fed arrays, smaller increase in gain is noted. But for higher order arrays, increase in the gain is by nearly 2 dBi. The results for  $7 \times 7$  space fed array using  $3 \times 3$  stacked and gap-coupled RMSA feed are given in Figs. 7 and 8a. The impedance BW obtained using simulation and measurement are 2.8 GHz (56%) and 2.79 GHz (55.5%), respectively. The pattern and gain measurement setup is shown below in Fig. 8b.

**Table 3** Gain and BW of SFAs using  $3 \times 3$  gap-coupled and stacked feed design of RMSA fed using proximity feed RMSA

SFA design	BW (GHz)	Gain, proximity fed RMSA (dBi)	Gain, plus shape stacked RMSA (dBi)	Gain, $3 \times 3$ Array of stacked RMSA feed (dBi)
$1 \times 3$	2.74	11.6	12	13.3
$3 \times 1$	2.75	12.3	12.6	13.3
Plus shape	2.7	13.3	13.5	14
$3 \times 3$	2.68	14.6	14.7	16
$5 \times 5$	2.7	16.0	16.5	17
$7 \times 7$	2.75	16.5	16.7	18.2

The measurements for all the optimum designs are carried out inside the Antenna Lab. The high frequency instruments, namely, ZVH-8, SMB 100A, and FSC 6 have been used in impedance, pattern, and gain measurements. The finite square ground plane of side length 50 cm has been used in simulation and measurements.

Thus using modified feed designs, impedance BW and gain in higher order space fed arrays is improved. For lower order arrays, i.e., till  $3 \times 3$  array design, simple proximity fed RMSA design offers optimum BW and gain results with lower values of 'D'. But in higher order designs, for higher gain,  $3 \times 3$  array network of feed is the optimum. Further it is noticed in the proximity feed design discussed in the above configurations that from practical implementation point of view, realizing proximity feed at a height of 4.8 mm is difficult. To overcome this problem, modified feed design with E-shape patch in the bottom feed layer is considered as shown in Fig. 9a, b. The  $3 \times 3$  array of gap-coupled RMSAs is placed on top of the coaxially fed broadband E-shaped MSA, to realize the multi-layer stacked microstrip feed network. The wideband design of E-shape MSA offers increased BW due to coupling between its fundamental and second-order orthogonal modes. Again the optimization process and design details for E-shape MSA are not discussed here since they are widely reported in the available literature.

The  $3 \times 3$  RMSA gap-coupled design is considered in the stacked layer since it gives optimum gain with higher order space fed arrays. In the feed layer, suspended configuration is used in which E-shaped patch is fabricated on glass epoxy substrate ( $h = 1.6$  mm) which is suspended in air at a height of  $h_1 = 4$  mm. This realizes total substrate thickness of 5.6 mm ( $0.075\lambda_0$ ) for the feed patch. The dimensions of optimized E-shaped MSA are length 'L' = 24 mm, width 'W' = 26 mm, slot length 'S<sub>1</sub>' = 16 mm, slot width 'S<sub>w</sub>' = 2 mm. The  $3 \times 3$  stacked RMSA array, fabricated on glass epoxy substrate, is placed over the fed E-shape patch at a height of 'h<sub>2</sub>' = 4 mm. The dimensions of the stacked  $3 \times 3$  RMSA are length = 14 mm and width = 26 mm. By placing RMSA elements at distance 'D' on top of stacked feed network various SFA configurations namely,  $1 \times 3$ ,  $3 \times 1$ , Plus shape,  $3 \times 3$ ,  $5 \times 5$  and  $7 \times 7$  arrays are realized as shown in Figs. 9b and 10.

A parametric study for varying distances between the feed and space fed array elements is carried out and gain plots for same are shown in Fig. 9c. Till  $3 \times 3$  array



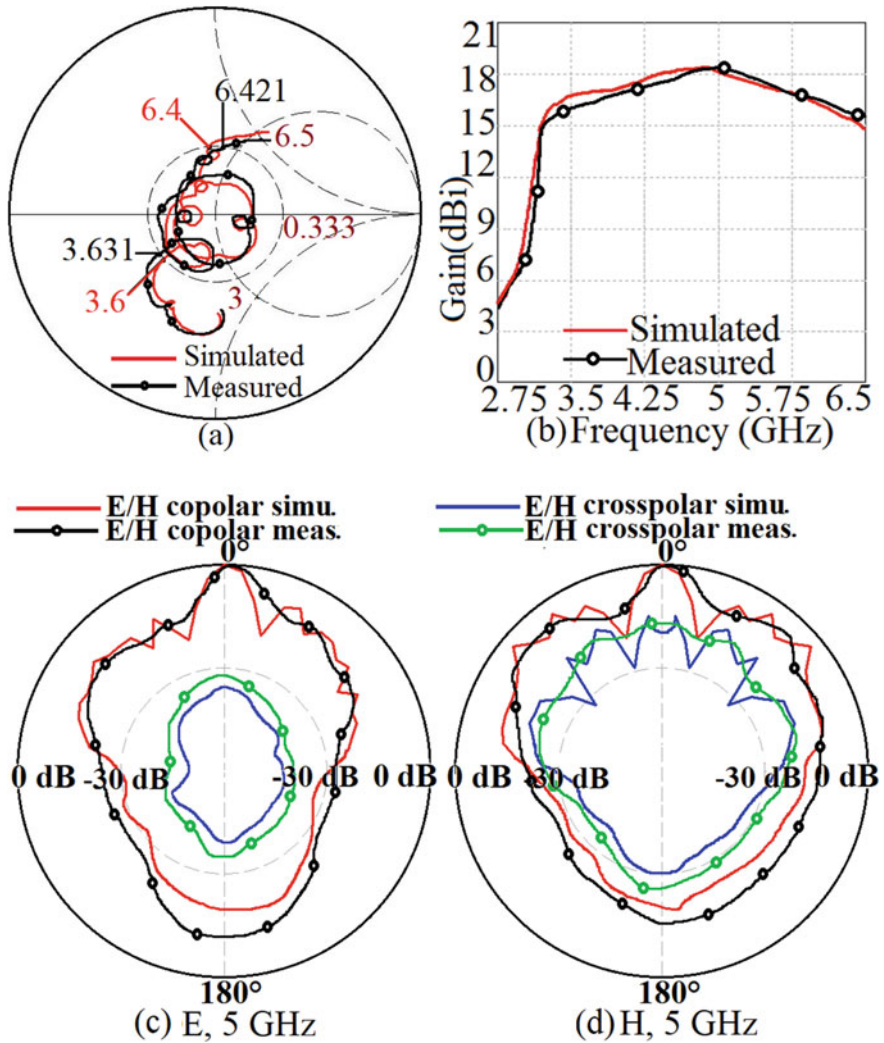
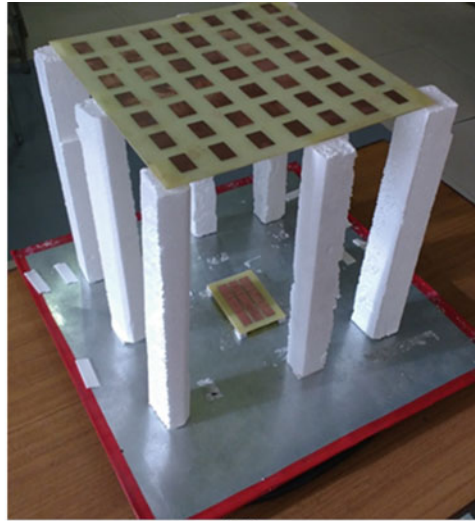


**Fig. 7** a Smith chart and b broadside gain variation over the BW and c, d radiation pattern at center frequency of VSWR BW for  $7 \times 7$  SFA design fed by  $3 \times 3$  stacked and gap-coupled configuration of RMSAs

design, maximum gain is observed for ' $3\lambda_0/2$ ' distance whereas in  $5 \times 5$  array, gain of above 15 dBi is obtained for separation of ' $3\lambda_0/2$ ' between the feed and space fed elements. The BW and gain values for this SFA variation are given in Table 4. A maximum gain is obtained in  $7 \times 7$  design for the spacing of ' $11\lambda_0/2$ '. Here the observed broadside gain is larger than 17 dBi. The results for  $7 \times 7$  SFA are shown in Fig. 11. The simulated BW in  $7 \times 7$  array is 2.249 GHz (55.2%) whereas the BW as obtained using measurement is 2.222 GHz (54.85%). The simulated and



(a)

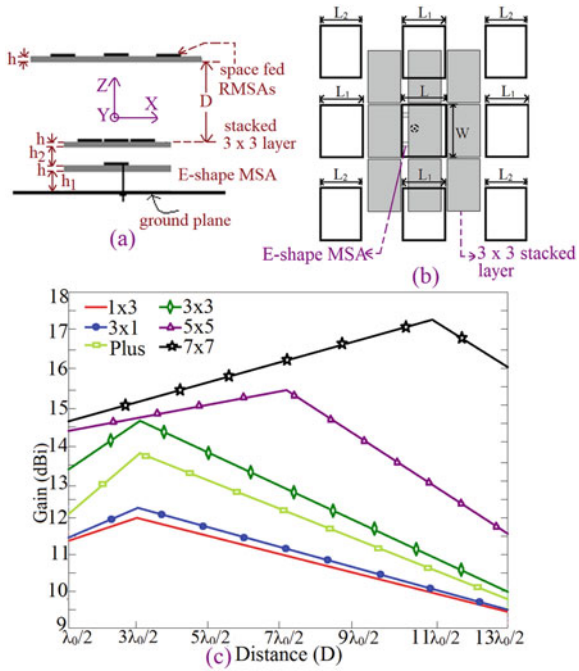


(b)

**Fig. 8** **a** Fabricated prototype of  $7 \times 7$  SFA design fed by  $3 \times 3$  stacked and gap-coupled configuration of RMSAs and **b** radiation pattern and gain measurement setup

measured antenna gain is close to 18 dBi with average gain of above 15 dBi over most of the impedance BW. The radiation pattern is in the broadside direction with cross polar component less than 15 dB as compared with co-polar component. In comparison with respect to the proximity fed RSA design in  $3 \times 3$  stacked gap-coupled RMSAs, design using E-shape MSA feed offers marginally smaller values of the BW and gain. But use of E-shape MSA in feed layer simplifies the fabrication process.

**Fig. 9** a, b SFA fed using feed combination of stacked RMSAs and E-shape MSA and c gain variations against distance 'D' for different space fed variations



### 3 Conclusions

In the proposed work, various feeding techniques have been explored in the feed layer of the SFA of rectangular patches. In the lower order arrays, simple proximity fed RMSA as the feed element offers optimum results in terms of VSWR BW and gain. Using stacked and gap-coupled modified feed designs, larger spacing between the space fed elements and the feed layer is needed, which also increases the antenna size. Hence for the lower order arrays simple proximity feed RMSA is preferred. For realizing higher gain, higher order in SFA is needed. Here to achieve effective illumination of the peripheral elements,  $3 \times 3$  gap-coupled stacked design placed on proximity fed RMSA or E-shape MSA offers optimum gain and BW. From the fabrication simplicity, coaxially feed E-shape MSA can be used, which offers BW of above 2 GHz with peak broadside gain of nearly 18 dBi. There have been different SFA designs reported in the literature but design with the proposed modified feed networks for better aperture illumination is not presented and compared. Thus novelty in the present work lies in presenting detailed study for different feeding networks using simple multi-resonator gap-coupled and stacked variations for feeding the SFA elements to achieve a higher gain.

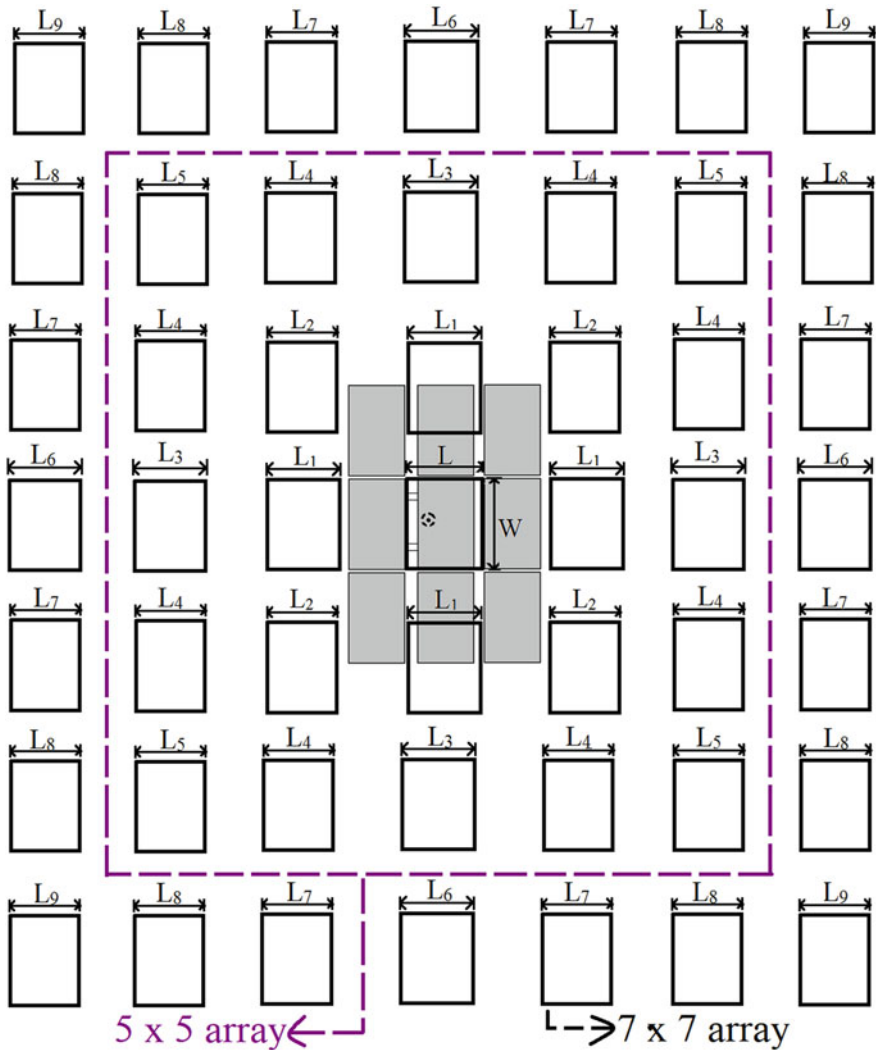


**Fig. 10**  $5 \times 5$  and  $7 \times 7$  SFA fed using combination of stacked RMSAs placed on top of coaxially E-shape MSA

**Table 4** Gain and BW of E-shape fed SFAs

SFA	Simulated BW (GHz)	Gain (dBi)
$1 \times 3$	2.27	12
$3 \times 1$	2.29	12.4
Plus shape	2.31	13.8
$3 \times 3$	2.28	14.6
$5 \times 5$	2.30	15.4
$7 \times 7$	2.31	17.6

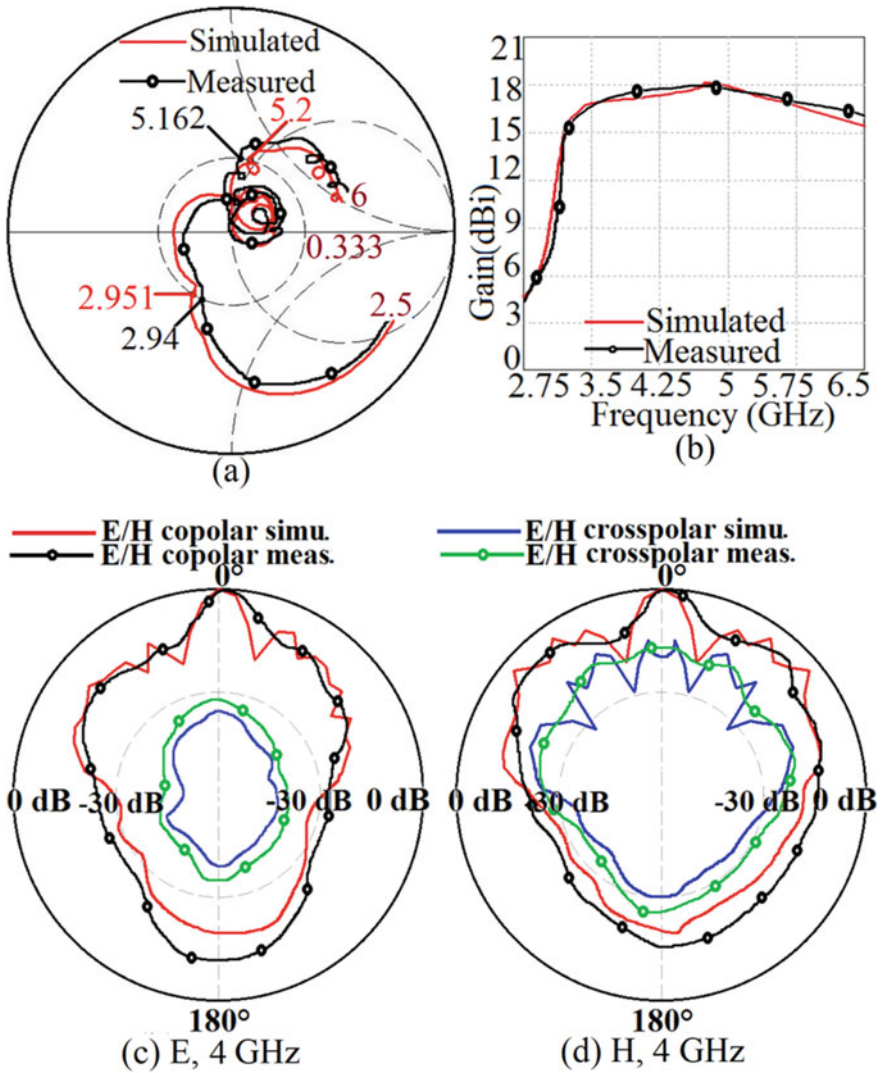


**Fig. 11** a Smith chart, b gain variation over BW and c, d radiation pattern at center frequency of VSWR BW for  $7 \times 7$  SFA fed using combination of stacked RMSAs placed on top of coaxially E-shape MSA

**References**

1. James JR, Hall PS. Handbook of microstrip antennas, vol I. Peter Peregrinus, London
2. Balanis CA (2003) Antenna theory and design, 3rd edn. Artech House
3. Kumar G, Ray KP (2003) Broadband microstrip antennas. Artech House
4. Wong KL (2003) Compact and broadband microstrip antennas, 1st edn. Artech House

5. Neyestanak AA, Kashani FH, Barkeshli K (2007) W-shaped enhanced-bandwidth patch antenna for wireless communication. *Wirel Pers Commun J* 43:1257–1265
6. Islam MT, Shakib MN et al (2009) Multi-slotted microstrip patch antenna for wireless communication. *Prog Electromagn Res Lett* 10:11–18
7. Chine P, Kumar G (2005) Three dimensional, efficient, directive microstrip antenna array. In: *IEEE antennas and propagation society international symposium, Washington, USA*, pp 243–246
8. Bhide R, Kumar G (2010) Circularly polarized space-fed microstrip antenna arrays. *Microw Opt Technol Lett* 52(10):2221–2223
9. Shafai L, Sharma SK, Dameshmand M, Mousari P (2006) Phase shift bandwidth and scan range in microstrip arrays by the element frequency tuning. *IEEE Trans Antenna Propag* 54:1467–1473
10. Mishra PK, Kumar G (2012) Dual polarized circular microstrip space-fed antenna array design with high isolation and broad bandwidth. In: *International conference on devices, circuits and systems (ICDCS) 2012, Coimbatore*, pp 540–544

# Space-Fed Variations of Circularly Polarized Microstrip Antennas Using Modified Feed Elements



Kshitij Lele, Adil Parvez, Amit A. Deshmukh, and A. G. Ambekar

**Abstract** A novel circularly polarized space-fed array antenna using single patch feed and gap-coupled feeding structures has been proposed. Using an array of gap-coupled patches as the feed element ensures a uniform excitation of the higher order space-fed arrays elements that increases their gain by 2 dBi. To increase the gain further, suspended configurations for both the feeding structures have been proposed, which improves the gain characteristics.

**Keywords** Circularly polarized microstrip antenna · Space-fed array antenna · Gap-coupled feeding structure · Suspended microstrip antenna

## 1 Introduction

With rapid advancements in satellite communication, requirements for high gain antennas have increased. High gain antennas are usually realized by using parabolic reflectors or by using an array of printed microstrip patches. However, parabolic reflectors have curved surfaces and are larger in size and printed arrays have the disadvantage of the feed-network losses and high cross-polar radiation, resulting from the feeding network that limits their gain [1]. Microstrip reflects arrays (MRAs) or space-fed arrays (SFAs) provide an alternative to these technologies. MRAs consist of an array of microstrip patches fed by a microstrip feeding element. The array is placed at a distance of ' $n\lambda_0/2$ ' from the fed-patch. The fed-patch illuminates the array of microstrip patches which in turn re-radiate a high gain signal in the opposite direction. SFAs have comparatively higher gain as compared to MRAs as they use a superstrate for the array and hence there is no blockage of radiation due to the fed-patch. In SFAs, the distance between the fed-patch and the center patch is shorter than that between the fed-patch and the non-centered patches. Hence, to compensate for the phase difference, the length of the non-centered patches is reduced so as to detune

---

K. Lele · A. Parvez · A. A. Deshmukh (✉) · A. G. Ambekar  
Department of EXTC, SVKM's DJSCE, Mumbai, India

their frequency from that of the center patch, thus yielding a uniform planar phase-front [2, 3]. Nowadays, most applications require antennas to be circularly polarized so that the performance of the antenna does not depend on its orientation. Circularly polarized SFAs can be obtained by feeding a square patch at two orthogonal locations along its principal axes with a two-branch coupler [4, 5]. Alternatively, a nearly square microstrip patch can be fed at an appropriate position along the diagonal to excite two orthogonal modes. However, in the case of SFAs, a single microstrip patch is insufficient to ensure uniform excitation of higher order arrays [6].

In this paper, a circularly polarized SFA with a single patch and a gap-coupled array feeding structure is proposed. First, a circularly polarized non-suspended nearly square patch is designed by feeding it along the diagonal to excite two orthogonal modes. This patch is then used as a feeding element for a circularly polarized SFA. A parametric study for varying distances between the fed-patch and the array is done for  $1 \times 1$ ,  $1 \times 3$ ,  $3 \times 1$ , plus-shaped,  $3 \times 3$ , and  $5 \times 5$  configurations. The simulated results for all optimum configurations have been tabulated. Simulated and measured results of the  $5 \times 5$  configuration which yields an axial-ratio bandwidth (ARBW) of 50 MHz and a gain of 13 dBi have been presented. In order to ensure that all the patches of higher order arrays are excited uniformly, the single microstrip patch feed is replaced by a  $3 \times 3$  array of gap-coupled circularly polarized patches [7–10]. Results for various configurations for the gap-coupled array feed, like  $1 \times 3$ ,  $3 \times 1$ , plus-shaped,  $3 \times 3$  have been presented. It is observed that the  $3 \times 3$  gap-coupled feeding structure increases the gain of around 2 dBi as compared to the single patch feed. The simulated and measured results for the  $5 \times 5$  array configuration which yields an ARBW of 124 MHz and a gain of 15.1 dBi have been presented. Next, in order to increase the gain even further, a two-layer air suspended configuration is proposed [10–13] for both, the single patch and gap-coupled array feeding structure. A parametric study for varying distances between the fed-patch and the array is also presented for the suspended single patch feed configurations ranging from  $1 \times 1$  to  $7 \times 7$ . The simulated and measured results of the  $5 \times 5$  configuration having a gain of 16 dBi and an ARBW of 121 MHz have been presented. Similar to the non-suspended configuration, an array of suspended gap-coupled patches are also used as the feed element. The results for  $1 \times 3$ ,  $3 \times 1$ , plus-shaped,  $3 \times 3$  gap-coupled array feeding structures have been presented. This feeding structure is then used in various SFA configurations like  $1 \times 3$ ,  $3 \times 1$ , plus-shaped,  $3 \times 3$ ,  $5 \times 5$ , and  $7 \times 7$ , and a parametric study for varying distances between the fed-patch and the array is done. The simulated and measured results for the  $5 \times 5$  configuration with an ARBW of 40 MHz and a gain of 16.9 dBi have been presented. The proposed SFAs are first simulated using IE3D software on Taconic substrate ( $\epsilon_r = 3.2$ ,  $h = 1.6$  mm,  $\tan \delta = 0.001$ ). The antenna is fed using SMA panel type connector. The measured impedance response is obtained using ‘ZVH-8’, whereas the radiation pattern and broadside co-polar gain is measured inside the antenna lab using ‘FSC 6’ and ‘SMB 100A’.



## 2 Non-suspended SFA with Single Patch and Gap-Coupled Array Feeding Structure

Proposed SFAs are designed to operate in the 4 GHz frequency band and hence the dimensions ( $L = 19$  mm and  $W = 19.7$  mm) of the diagonally fed nearly square MSA (SMSA) are chosen such that  $f_{TM10} = 4$  GHz. This patch is then used as a feeding element for  $1 \times 1$ ,  $1 \times 3$ ,  $3 \times 1$ , plus-shape,  $3 \times 3$ , and  $5 \times 5$  SFA configurations. The top and side view of the  $5 \times 5$  SFA configuration is shown in Fig. 1a, b.

The center patch of the array has the same dimensions as that of the feed element. However, the distance between the fed-patch and the center patch is less as compared to the distance between the fed-patch and the adjacent patches of the array. Hence, the length and the width of the non-centered array patches are reduced to compensate for the phase difference. A parametric study for varying distance 'D' in between the fed-patch and array elements is carried out and results for the same are tabulated in Table 1. For all the optimum configurations, gain, AR, and VSWR BW are given in Tables 3 and 4. The simulated and measured results for  $5 \times 5$  SFA are shown in Fig. 2a. The simulated and measured BW of  $5 \times 5$  SFA is 167 and 160 MHz, respectively.

The radiation pattern for  $5 \times 5$  SFA is in the broadside direction with an equal level for co- and cross-polar radiation. The gain increment obtained for higher order arrays using a single patch feed is lower. For higher order SFAs, it is not possible to uniformly excite the patches that are present towards the corners of the array. Hence, the gain of the feed element itself is increased by using a gap-coupled patches array. The center patch of this array is co-axially fed along the diagonal of the patch and the adjacent patches are placed along the radiating as well as non-radiating edges of the center patch. Different gap-coupled feed array configurations have been studied and their results are tabulated in Table 5. It can be seen that a  $3 \times 3$  gap-coupled design yields the optimum result. This design is selected further as feed for various SFAs and a parametric study for variation in gain against 'D' is further carried out and the same is presented in Table 2. Various antenna results for various order SFAs using the non-suspended gap-coupled  $3 \times 3$  feed, are given in Tables 3 and 4. The simulated and measured BW for  $5 \times 5$  SFA is 174 and 154 MHz, respectively. Due to the use of gap-coupled patch feed, broadside gain is above 15 dBi, which is 2 dBi higher as compared with similar SFA using a single patch feed. The multiple loops in the impedance locus are attributed to multiple resonances present in SFA fed using gap-coupled patches. The radiation pattern for  $5 \times 5$  SFA is in the broadside direction with an equal level for co- and cross-polar radiation (Fig. 3).

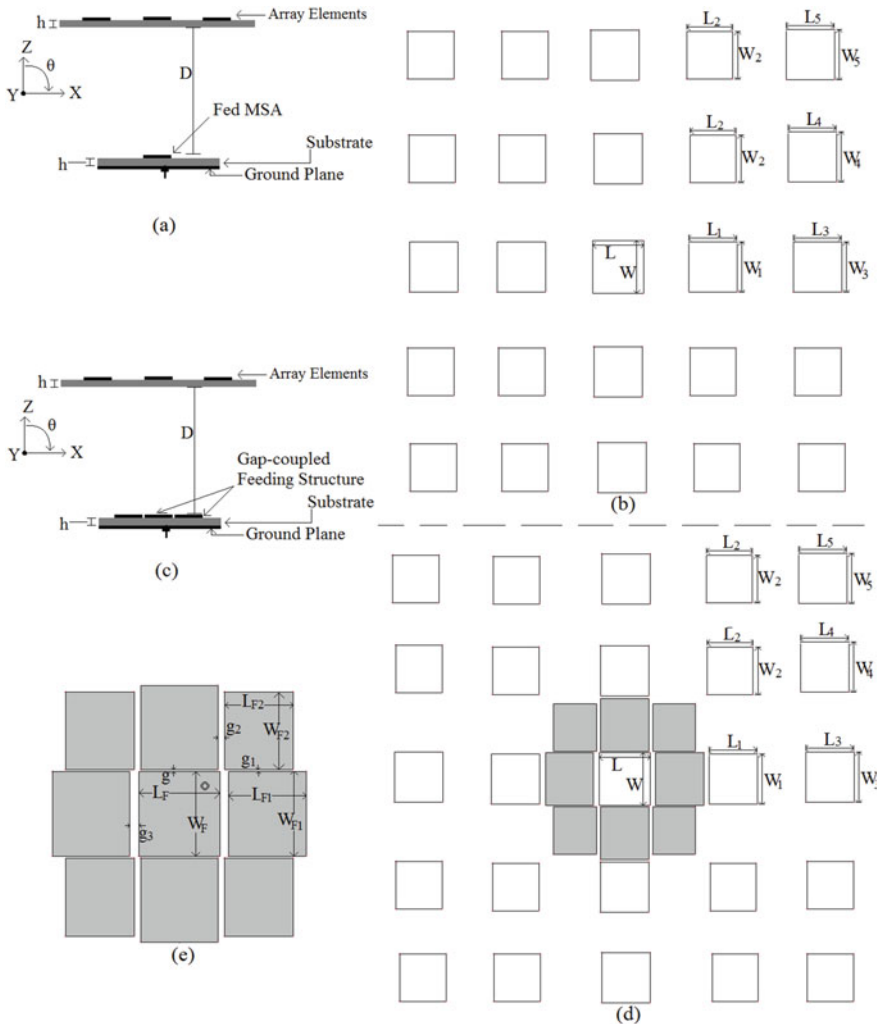


**Fig. 1** a Side view and b top view of the non-suspended single patch feed  $5 \times 5$  SFA configuration, c side view and d top view of the non-suspended gap-coupled feed  $5 \times 5$  SFA configuration, and e top view of the  $3 \times 3$  array of the gap-coupled feeding element

### 3 Suspended SFA with Single Patch and Gap-Coupled Feed Elements

To further increase the gain of the proposed SFA configurations, the fed-patch is suspended in the air to increase the overall substrate thickness and thus its radiation efficiency. First, a circularly polarized nearly SMSA having dimensions  $L_{S1} = 23$  mm and  $L_{S2} = 25$  mm is designed on a Taconic substrate which is suspended in the air

**Table 1** Gain variation against ‘D’ for various non-suspended single patch feed SFAs

SFA	$D = \lambda/2$	$D = 3\lambda/2$	$D = 5\lambda/2$	$D = 7\lambda/2$
$1 \times 1$	7.9 (dBi)	8.2 (dBi)	7.1 (dBi)	–
$1 \times 3$	8.9	9.2	8.2	–
$3 \times 1$	9	9.25	8.5	–
Plus-shaped	10.2	10.75	10	–
$3 \times 3$	10.7	11.8	11.25	–
$5 \times 5$	–	11.75	13	12.6 (dBi)

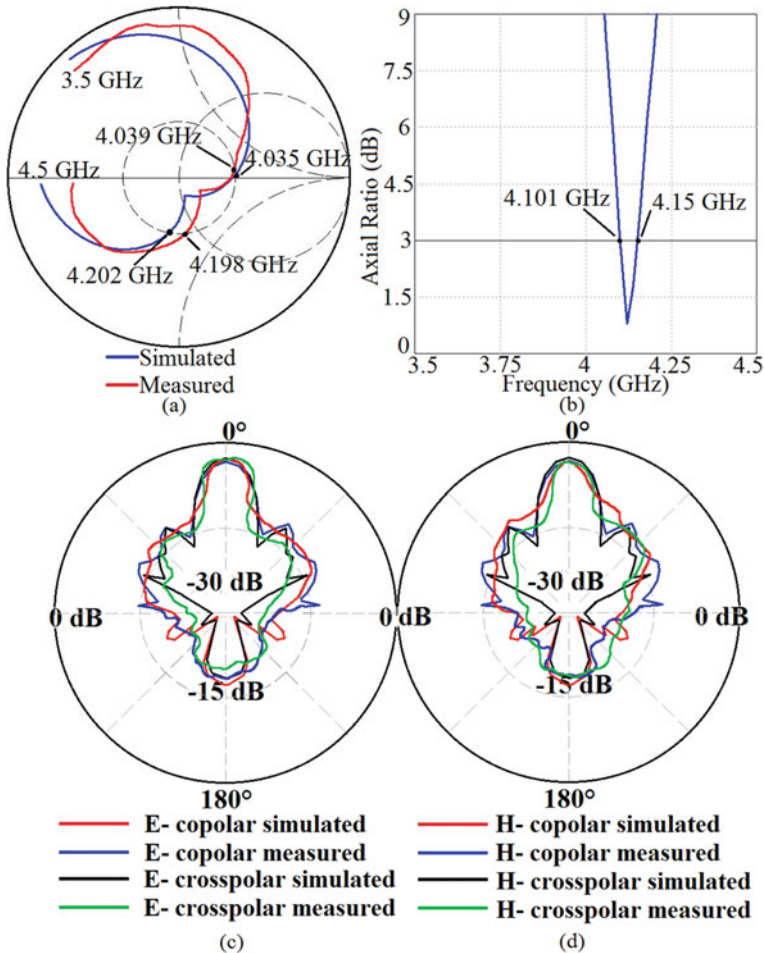


**Fig. 2** a Input impedance plots, b simulated AR BW plot and radiation pattern plots in c E- and d H-planes for  $5 \times 5$  SFA fed using non-suspended single patch feed

**Table 2** Gain variation against 'D' for SFAs using non-suspended gap-coupled patch feed

SFA	$\lambda/2$	$3\lambda/2$	$5\lambda/2$
$1 \times 1$	11.1 (dBi)	11.5 (dBi)	10.8 (dBi)
$1 \times 3$	12	12.3	11.6
$3 \times 1$	11.6	12	11.3
Plus-shaped	12.8	13.2	12.6
$3 \times 3$	13.1	14.1	13.6
$5 \times 5$	14.8	15.1	14.2

**Table 3** Antenna parameters for various SFAs using different feeds

SFA	$1 \times 1$		$1 \times 3$		$3 \times 1$	
	Single patch feed	Gap-coupled feed	Single patch feed	Gap-coupled feed	Single patch feed	Gap-coupled feed
VSWR BW (MHz)	149	181	135	145	180	195
AR BW (MHz)	41	113	40	120	41	115
Gain (dBi)	8.2	11.5	9.2	12.3	9.25	12

**Table 4** Antenna parameters for various higher order SFAs using different feeds

SFA	Plus-shaped		$3 \times 3$		$5 \times 5$	
	Single patch feed	Gap-coupled feed	Single patch feed	Gap-coupled feed	Single patch feed	Gap-coupled feed
VSWR BW (MHz)	150	166	146	190	167	174
AR BW (MHz)	40.4	110	41	112	50	124
Gain (dBi)	10.75	13.1	11.8	14	13	15.1

**Table 5** Antenna parameters for various gap-coupled feed design

Gap-coupled feed design	VSWR BW (MHz)	AR BW (MHz)	Gain (dBi)
$1 \times 3$	102	80	7.1
$3 \times 1$	110	74	6.8
Plus-shaped	172	95	9.6
$3 \times 3$	155	120	9.75

using a thickness of 1.6 mm. Using suspended single patch as the feed,  $1 \times 1$ ,  $1 \times 3$ ,  $3 \times 1$ , plus-shaped,  $3 \times 3$ ,  $5 \times 5$ , and  $7 \times 7$  SFAs have been studied. The top and side views of the  $5 \times 5$  SFA configuration are shown in Fig. 4a, b. A parametric

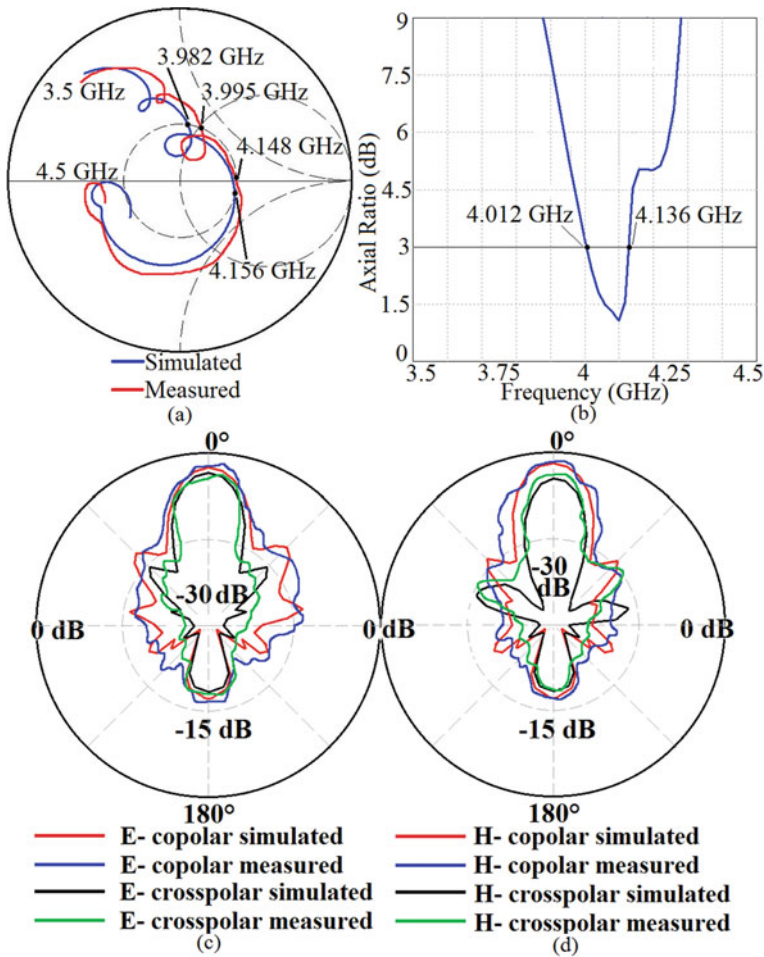


**Fig. 3** a Input impedance plot, b AR BW plot, and radiation pattern plots in c E and d H-planes for  $5 \times 5$  SFA using the non-suspended gap-coupled feed

study for varying distance ‘D’ between the fed-patch and the array is carried out and their results are tabulated in Table 6. For the optimum distance ‘D’ in each configuration, AR BW, VSWR BW, and the gain have been presented in Tables 8 and 9. The simulated and measured input impedance plot and the radiation pattern in the E- and H-planes for the  $5 \times 5$  SFA using single patch fed, are shown in Fig. 5a and c, d, respectively. Due to a single patch, excitation of higher order SFAs is not optimum and thus the gap-coupled design for the feed antenna in suspended variation is explored here as shown in Fig. 4c–e (Table 7).

As  $3 \times 3$  gap-coupled array gives the optimum result as given in Table 10, similar to the non-suspended configuration,  $3 \times 3$  gap-coupled arrays are used as the feed element to ensure that all the patches of the higher order arrays are excited uniformly.

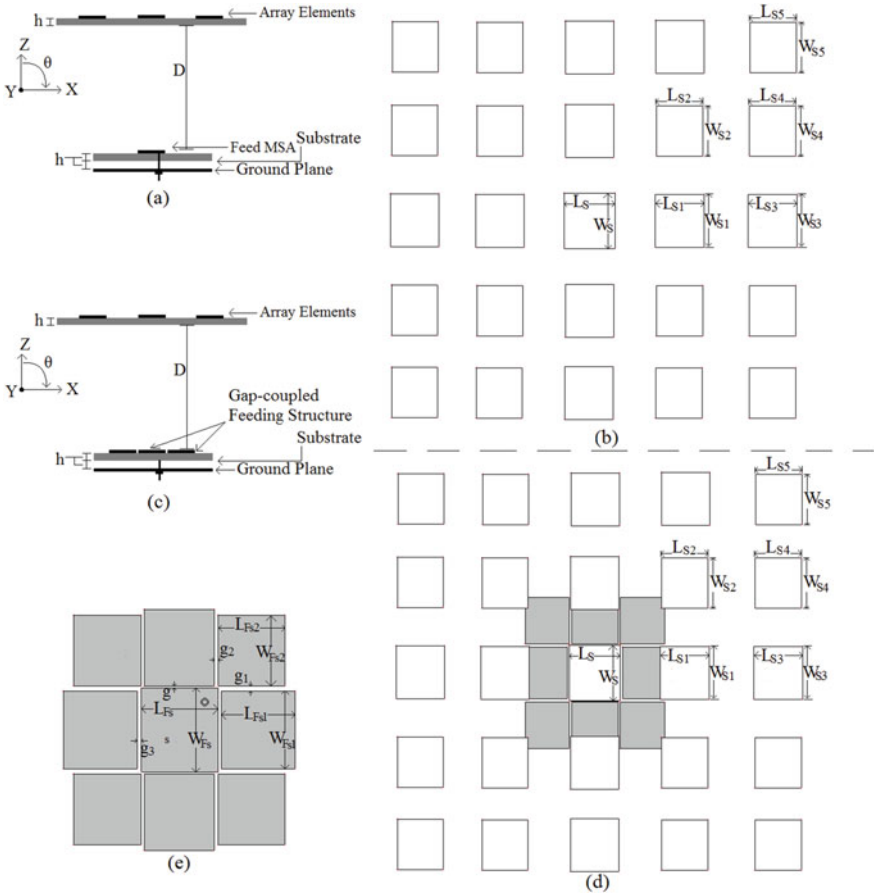


**Fig. 4** a Side and b top views of the suspended single patch feed  $5 \times 5$  SFA, c side and d top views of suspended gap-coupled feed  $5 \times 5$  SFA, and e top view of  $3 \times 3$  gap-coupled array feed

**Table 6** Gain variation against ‘D’ for various SFAs using suspended single patch feed

SFA	$\lambda/2$	$3\lambda/2$	$5\lambda/2$	$7\lambda/2$	$9\lambda/2$	$11\lambda/2$
$1 \times 1$	9.7 (dBi)	10 (dBi)	9.3 (dBi)	–	–	–
$1 \times 3$	11.1	11.5	11	–	–	–
$3 \times 1$	11	11.6	10.9	–	–	–
Plus-shaped	12.8	13.2	12.5	–	–	–
$3 \times 3$	13.7	14.6	13.6	–	–	–
$5 \times 5$	–	15.3	15.7	16 (dBi)	15.4 (dBi)	–
$7 \times 7$	–	–	15.9	16.1	16.5	16.25 (dBi)

**Table 7** Gain variation against ‘D’ for various SFAs using a suspended gap-coupled feed

SFA	$\lambda/2$	$3\lambda/2$	$5\lambda/2$	$7\lambda/2$	$9\lambda/2$	$11\lambda/2$
$1 \times 1$	11.9 (dBi)	12.3 (dBi)	11.6 (dBi)	–	–	–
$1 \times 3$	12.9	13.3	12.6	–	–	–
$3 \times 1$	12.5	13	12.3	–	–	–
Plus-shaped	13.8	14.25	13.5	–	–	–
$3 \times 3$	–	14.6	14.9	14.3 (dBi)	–	–
$5 \times 5$	–	–	16.5	16.9	16.4 (dBi)	–
$7 \times 7$	–	–	17.1	17.6	17.9	17.2 (dBi)

**Table 8** Antenna parameters for various SFAs using different suspended feeds

SFA	$1 \times 1$		$1 \times 3$		$3 \times 1$	
	Single patch feed	Gap-coupled feed	Single patch feed	Gap-coupled feed	Single patch feed	Gap-coupled feed
VSWR BW (MHz)	476	453	468	479	480	492
AR BW (MHz)	92	45	98	35	90	41
Gain (dBi)	10	12.3	11.5	13.3	11.6	13

**Table 9** Antenna parameters for various higher order SFAs using different suspended feeds

SFA	Plus-shaped		$3 \times 3$		$5 \times 5$		$7 \times 7$	
	Single patch feed	Gap-coupled feed	Single patch feed	Gap-coupled feed	Single patch feed	Gap-coupled feed	Single patch feed	Gap-coupled feed
VSWR BW (MHz)	412	443	420	456	454	449	430	445
AR BW (MHz)	89	40	80	35	121	40	85	52
Gain (dBi)	13.2	14.25	14.6	14.9	16	16.9	16.5	17.9

The  $3 \times 3$  gap-coupled array, shown in Fig. 4e, is then used as the feed element for various SFA configurations, like  $1 \times 1$ ,  $1 \times 3$ ,  $3 \times 1$ , plus-shaped,  $3 \times 3$ ,  $5 \times 5$ , and  $7 \times 7$ . The simulated and measured input impedance plot of the  $5 \times 5$  SFA having a gap-coupled feeding structure, is shown in Fig. 6a. The radiation pattern plots in the E- and H-plane for this configuration are shown in Fig. 6c, d. Using the gap-coupled suspended feed,  $5 \times 5$  SFA yields a gain of nearly 17 dBi whereas  $7 \times 7$  SFA realizes 18 dBi of gain. Thus gap-coupled suspended design optimizes radiation efficiency and gives an optimum value of AR BW and gain. The fabricated prototype

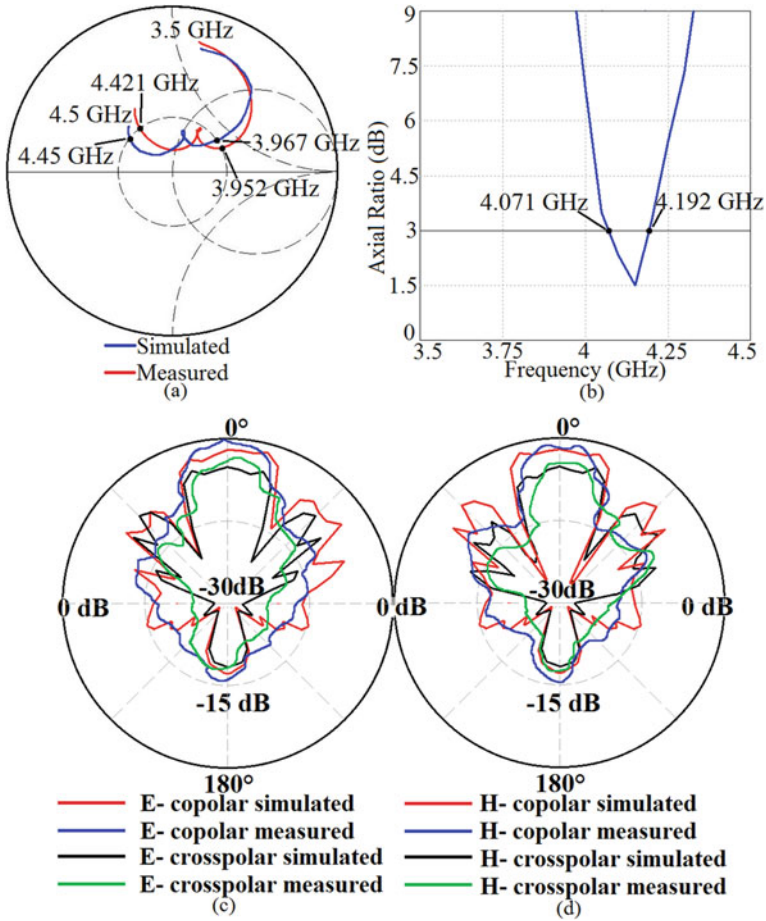


**Fig. 5** a Input impedance plot, b simulated AR BW plots and radiation pattern in the c E- and d H-planes for  $5 \times 5$  SFA fed using air suspended  $3 \times 3$  array

**Table 10** Antenna parameters for various suspended gap-coupled feed design

Suspended gap-coupled feed design	VSWR BW (MHz)	AR BW (MHz)	Gain (dBi)
$1 \times 3$	245	26	7.3
$3 \times 1$	255	20	7.1
Plus-shaped	260	52	9.25
$3 \times 3$	560	40	10.4



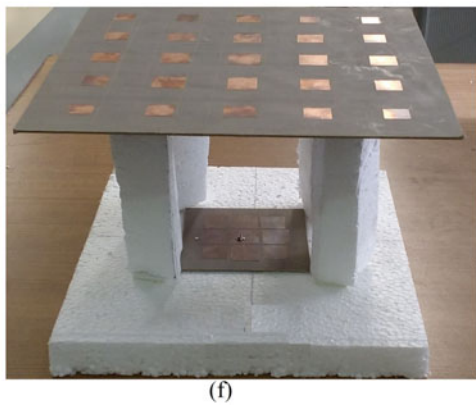
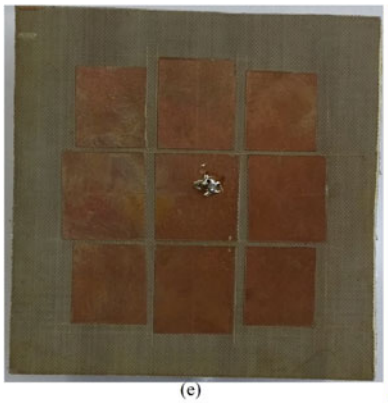
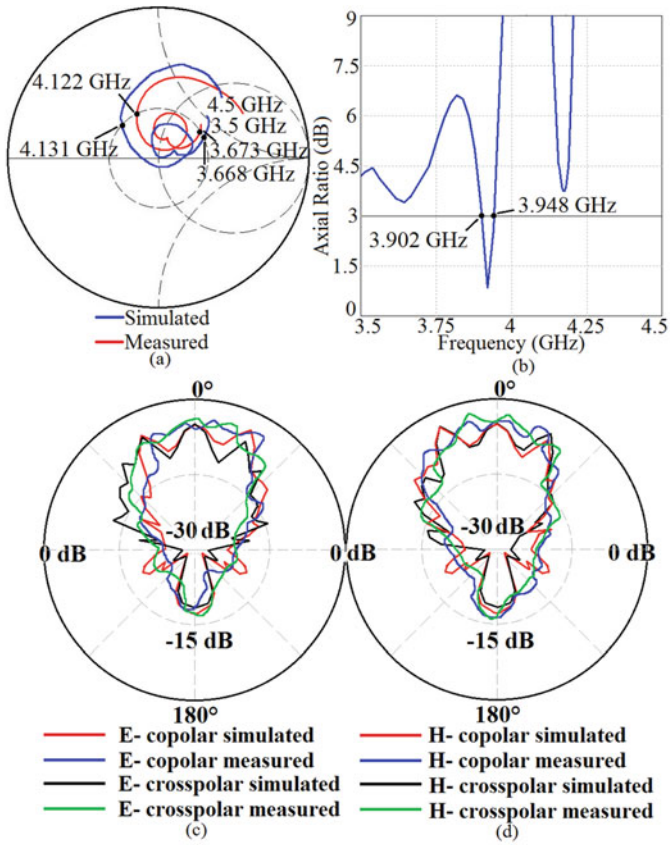


**Fig. 6** a Input impedance plot, b simulated AR BW plot, and radiation pattern plots in the c E- and d H-plane of the 5 × 5 SFA, fabricated prototype of e feed gap-coupled 3 × 3 array and its f 5 × 5 SFA variation

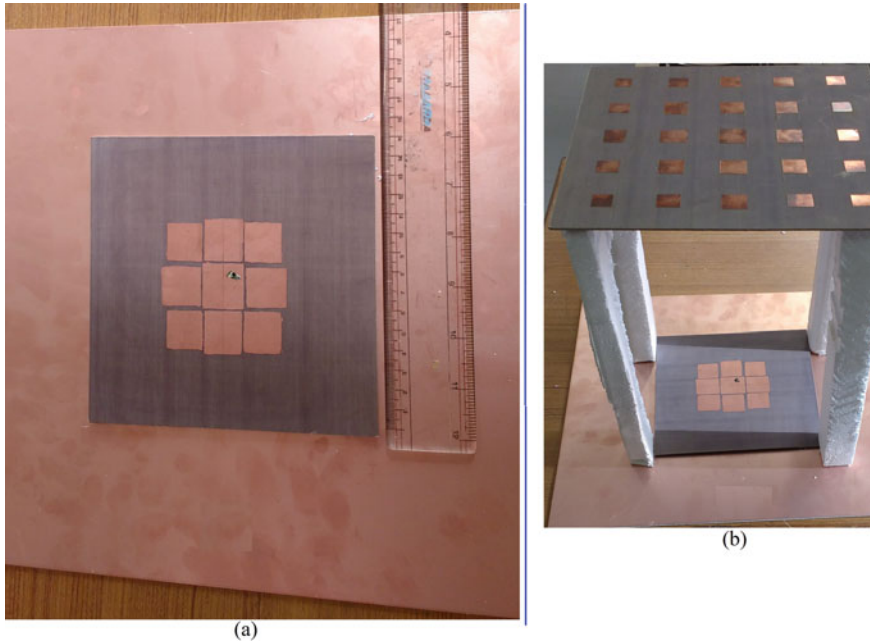


**Fig. 7** Fabricated prototype of **a** feed gap-coupled  $3 \times 3$  array and its **b**  $5 \times 5$  SFA variation

of the gap-coupled feeding structure and the  $5 \times 5$  SFA for the non-suspended and suspended configurations are shown in Figs. 6e, f and 7a, b. Thus, present paper discusses the various configuration of higher order SFA using modified gap-coupled feed patches. The use of gap-coupled feed patches realizes efficient excitation of perimeter elements that realizes maximum gain and AR BW. These kinds of modified feed SFA are not reported in the literature for circular polarized design, and thus this is the novelty in the proposed study.

## 4 Conclusions

Circularly polarized SFAs using a single patch and gap-coupled array feed are presented. The non-suspended  $5 \times 5$  SFAs yield gain of around 13 and 15 dBi for the single patch and the gap-coupled array feed, respectively. The suspended single patch fed  $5 \times 5$  SFA yields a gain of 16 dBi whereas the use of a gap-coupled array as the feed element here yields a gain of nearly 18 dBi.

## References

1. Chine P, Kumar G (2005) Three dimensional, efficient, directive microstrip antenna array. In: IEEE Antennas and propagation society international symposium, Washington, USA, pp 243–246
2. Bhide R, Kumar G (2010) Equivalence of space-fed microstrip antenna with horn antenna. *Microw Opt Technol Lett* 52(5):1180–1183
3. Shafai L, Dameshmand SK, Dameshmand M, Mousari P (2006) Phase shift bandwidth and scan range in microstrip arrays by the element frequency tuning. *IEEE Trans Antenna Propag* 54:1467–1473
4. Bhide R, Kumar G (2010) Circularly polarized space-fed microstrip antenna arrays. *Microw Opt Technol Lett* 52(10):2221–2223
5. Kumar G, Ray KP (2003) Broadband microstrip antennas. Artech House
6. Mishra PK, Kumar G (2012) Dual polarized circular microstrip space-fed antenna array design with high isolation and broad bandwidth. In: International conference on devices, circuits, and systems (ICDCS), Coimbatore, pp 540–544
7. Aanandan CK, Mohanan P, Nair KG (1990) Broad-band gap coupled microstrip antenna. *IEEE Trans Antennas Propag* 38(10):1581–1586
8. Song Q, Zhang, X-X (1992) Broadband gap-coupled microstrip antenna arrays. In: International symposium on antennas and propagation (AP-S) digest, Chicago, IL, USA, vol 4, pp 1939–1942
9. Song Q, Zhang X-X (1995) A study on wideband gap-coupled microstrip antenna arrays. *IEEE Trans Antennas and Propag* 43(3):313–317
10. Simons RN (2000) Suspended patch antennas with electromagnetically coupled inverted microstrip feed for circular polarization In: International symposium on antennas and propagation (AP-S) digest, Salt Lake City, UT, USA, vol 2, pp 992–995
11. Wójcik D, Surma M (2012) Low cost dual-polarized suspended microstrip antenna array for 5.8 GHz point-to-point links. In: Proceedings of 22nd international conference Radioelektronika, Brno, Czech Republic, pp 1–4
12. Lau NU, Sloan R (2003) Broadband millimeter-wave suspended microstrip antenna array. In: International symposium on antennas and propagation (AP-S) digest, Columbus, OH, USA, vol 1, pp 288–291
13. Niyomjan G, Huang Y (2006) A suspended microstrip fed slot antenna on high impedance surface structure. In: First European conference on antennas and propagation, Nice, pp 1–4

# Analysis of Multiple Shorting Posts Loaded Square Microstrip Antenna for Circular Polarized Response



Amit A. Deshmukh, A. P. C. Venkata, Aarti G. Ambekar, and Tushar Sawant

**Abstract** Detailed study to explain the circular polarized response in multiple shorting posts loaded square microstrip antenna is presented in this paper. The resonant modes present in each design leading to the final configuration, i.e., modes in square patch against four shorting post loaded design and further against final multiple shorting post loaded design are discussed in detail. The loading of additional shorting posts placed in the shorted patch center point, degenerates and tunes the inter spacing between orthogonal  $TM_{20dv}$  and  $TM_{20dh}$  resonant modes that yields circular polarized response offering axial ratio bandwidth of 52 MHz in 2450 MHz frequency band. This detailed study for the resonant modes present in the shorted patch is not given in the reported paper, and thus the original explanation for the circular polarized response in multiple shorting posts loaded square microstrip antenna is the main technical contribution in the proposed work.

**Keywords** Square microstrip antenna · Circular polarized microstrip antenna · Shorting post

## 1 Introduction

The microstrip antenna (MSA) due to their several advantages finds maximum applications in modern day wireless communication systems [1, 2]. One of the main features of MSA for which they are preferred over other antenna variations is the generation of circular polarized (CP) response using single radiating patch. Over the last three–four decades, several techniques have been reported to realize CP response, which include methods like single feed design using power divider circuit, single feed design employing narrow slot in the patch, modified shapes of the radiating patch, use of resonant slots like U-slot or pair of rectangular slots [3–10]. To reduce the size of MSA, technique of shorting post has been employed, where it converts the conventional half wavelength resonator into a compact quarter wavelength resonator,

---

A. A. Deshmukh (✉) · A. P. C. Venkata · A. G. Ambekar · T. Sawant  
Department of EXTC, SVKM's DJSCE, Mumbai, India

which reduces the patch size by 50% or more. In the literature, method of shorting post has been employed to yield CP response [11]. In the configuration reported in [11], multiple shorting post placed at different places in the square MSA (SMSA) are selected. The shorting post are used for compact design and placement of same changes the boundary condition in the patch and thus the resonant modes present in the design. This is because shorting post forces the field to go to zero value at a given shorting point whereas in un-shortened patch, depending upon the excited mode, zero field condition exist along the dimensions of patch. Thus in [11], which of the shorted patch modes which are responsible for realizing the reported CP response is not clearly explained. Also, the modes in shorted patch against SMSA are not clearly highlighted.

In this paper, detailed analysis to study the CP response in multiple shorting posts loaded SMSA fed using coaxial feed is presented. The antenna response is analyzed using CST software [12] where the response of the optimum configuration against the original SMSA and diagonally shorted SMSA using four shorting posts are analyzed for the resonant modes present. The placement of four shorting posts towards the diagonal vertex point in the square patch alters the resonant modes present. This leads to the diagonal variation in the resonant fields. Further, with the addition of additional shorting post in the patch center, second order diagonal mode degenerates into orthogonal resonant modes. An optimum spacing between them obtained using centrally placed shorting posts yields optimum CP response. Here, a CP AR BW of 52 MHz (1.07%) is achieved with a peak broadside gain of above 4 dBi. In comparison with the un-shortened patch, this AR BW is realized at a much higher frequency (nearly by 900 MHz) and thus against the equivalent SMSA design in the same frequency range offering CP response, the shorted configuration is not a compact design. Thus, the present paper puts forward a detailed parametric analysis to explain the resonant mode-based explanation for the CP response in multiple shorting posts loaded square patch. This kind of explanation with respect to the shorted resonant modes present is not provided in [11]. Further, the present study also concludes that in comparison with the un-shortened patch at the same frequency of AR BW achieved, shorted configuration needs higher patch size, thus not leading to a compact design, as which is generally obtained using the shorted patches.

## 2 Analysis of Multiple Shorting Post Loaded SMSA

A configuration of multiple shorting post loaded SMSA fed using coaxial feed fabricated on microwave dielectric substrate of parameters,  $h = 0.25$  cm,  $\epsilon_r = 3.0$ ,  $\tan \delta = 0.02$  is shown in Fig. 1a. The diagonal shorting post are loaded at a distance 'd' from each other, whereas the distance between centrally placed shorting post is 'd<sub>1</sub>'. This design for the feed point shown yields simulated and measured AR BW of 2436–2452 MHz and 2444–2460 MHz, respectively, with right hand CP (RHCP) response [11]. Generally, as per the reported literature on compact MSAs, shorting post are used to realize compact designs and thus in [11], a clear understanding for

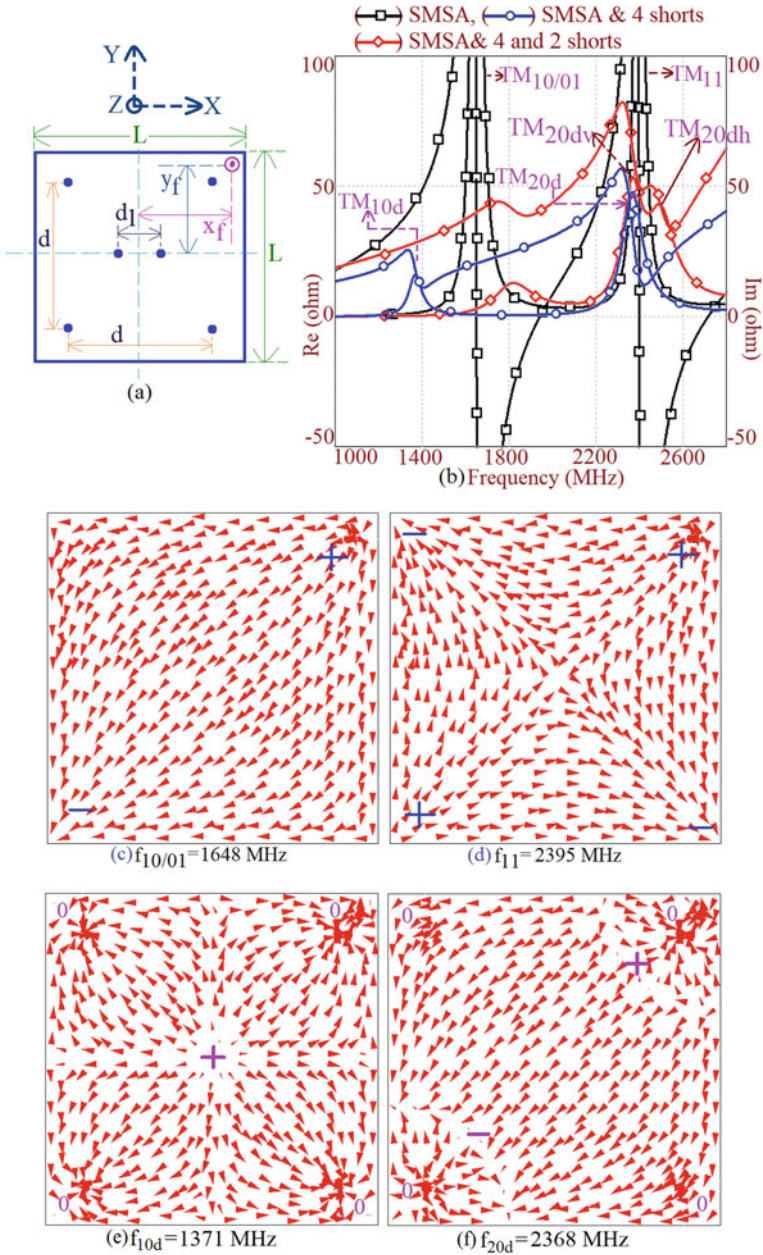


**Fig. 1** **a** Multiple shorting post loaded SMSA, its **b** resonance curve plots for different shorted variations, surface current distribution at observed resonant modes for **c, d** SMSA and **e, f** SMSA with diagonally placed shorting posts

the modes present in the shorted patch that gives this CP response is not explained. Therefore, the reported configuration is analyzed using CST software and the resonance curve plots for the optimum design, equivalent SMSA, and that using four diagonally placed shorting post SMSA design, are shown in Fig. 1b. The surface current distribution at the observed resonant modes for SMSA and four shorting posts loaded SMSA is also shown in Fig. 1c–f. In SMSA for the feed point shown, ( $x_f = 2.2$  and  $y_f = 2.2$  cm), two resonant modes are excited.

By observing their surface current distributions and comparing them with the resonant mode distributions of SMSA, they are identified as  $TM_{10/01}$  and  $TM_{11}$ . Since the square patch is present,  $TM_{10}$  and  $TM_{01}$  mode frequencies are nearly the same and thus they lead to a single peak in the resonance curve plot. Hence the same is identified as  $TM_{10/01}$  in the plot. As noted from the surface current and resonance curve plots, fundamental mode frequency of equivalent SMSA is 1648 MHz which is at least 800 MHz lower than the frequency range where the CP response is observed, i.e., with reference to the reported results. When the shorting post are loaded at the diagonal corners, one resonant peak is observed at a frequency below the  $TM_{10/01}$  mode frequency of SMSA and one is observed nearer to the  $TM_{11}$  mode frequency. With reference to the current distributions observed, here diagonal variations in currents are noted. At the first mode, field is maximum in the center of SMSA whereas it goes to zero value nearer to the four shorting posts. Thus, with reference to the diagonal points, fields vary from ‘0’ to ‘+’ in the patch center and further to ‘0’ towards the diagonal point. Due to this variation, this mode is referred to as  $TM_{10d}$ . When the boundary conditions across the patch edges are similar, i.e., either open circuit or short circuit, the resonant modes in the microstrip patch are always integer multiples of the half wavelength variation. And thus, at the next peak, a two half wavelength variation, i.e., two sections of the quarter wavelength variation plus one section of the half wavelength variation, are observed along the diagonal axis. At the orthogonal diagonal axis, the field passes through its null value around the shorting post as observed. The resonance curve plots for the final configuration, i.e., with the addition of two shorting posts in the patch center and the surface current distribution at the observed resonant modes for the same are shown in Figs. 1b and 2a–c.

At the first resonant peak, the field/current shows variation with reference to the both shorting points, i.e., with reference to patch corners and the center. Due to the addition of this centrally placed shorting posts, the effective surface current length for the half wavelength variation reduces that increase its frequency as shown in Fig. 1b. Nearer to the higher frequency peaks, the degenerated modes are observed. With reference to the shorting post position, half wavelength variation along the vertical and horizontal directions and with a quarter wavelength variation with reference to the corner points shorting posts are observed. Thus here, earlier  $TM_{20d}$  mode has degenerated into two orthogonal modes in the vertical and horizontal directions and thus they are referred to as  $TM_{20dv}$  and  $TM_{20dh}$ . This degeneration is the result of placement of two additional shorting post in the patch center with a spacing in between them. To analyze the effects of these centrally placed shorting posts, parametric study for variation in distance ‘ $d_1$ ’ between them is carried out and the resonance curve and AR BW plots for the same are shown in Fig. 2d, e. With an

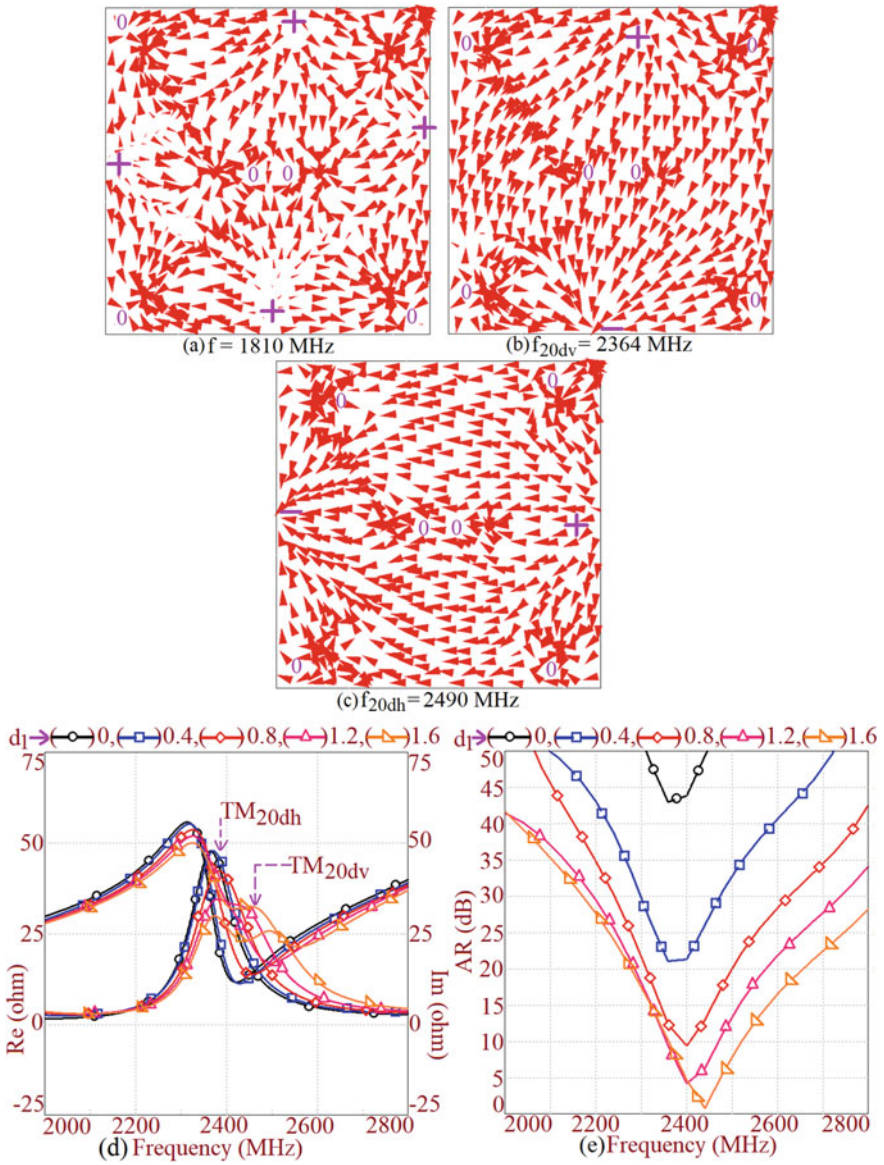


**Fig. 2** a–c Surface current distribution at observed resonant modes for multiple shorting post loaded SMSA and its **d** resonance curve and **e** axial ratio plots for variation in ‘ $d_1$ ’



increase in the distance ' $d_1$ ', resonant length at  $TM_{20dv}$  mode is not modified since the shorting posts are placed at the minimum field location of the same. Therefore, its frequency remains unchanged. However, with an increase in distance ' $d_1$ ', effective half wavelength length at  $TM_{20dh}$  mode reduces since two shorting positions are created with an increased spacing between the two posts. This increases  $TM_{20dh}$  mode frequency. Further, interspacing between them yields optimum CP response as shown in Fig. 2e. For ' $d_1$ ' = 1.6 cm, shorted SMSA shows AR BW of 52 MHz center around 2435 MHz with a broadside peak gain of above 4 dBi as shown in Fig. 3f. The time-varying surface current distribution at the center frequency of AR BW is shown in Fig. 3a–d. The surface currents are rotating in the counterclockwise direction thereby giving right hand CP (RHCP) response, as shown in Fig. 3e as well.

Thus, it is concluded from the present analysis that the fundamental mode frequency of un-shortened SMSA is much lower than the frequency at which CP response is obtained. Thus, in equivalence, reported multiple shorted SMSA CP design is not a compact configuration. The position of diagonally placed shorting posts leads to mode distributions along the diagonal axis, and degeneration of the same using centrally placed shorting post yields CP characteristics. By observing the current distribution at the degenerated and original shorted modes, it is clear that the second order mode frequency ( $TM_{20d}$ ) of the multiple shorting post loaded SMSA contributes to the CP response. Thus, in comparison to the SMSA offering CP response around its fundamental mode, reported shorted CP design will require larger patch size. Thus, in the present work, based upon various shorted configurations, an original explanation for the resonant mode identification of the antenna and subsequent generation of the CP response with respect to the modes present, is put forward. This kind of detailed study based on the shorted patch modes is not presented in the original paper in [11].

### 3 Conclusions

Analysis to study the CP response in multiple shorting posts loaded SMSA is presented in this paper. The placement of shorting posts leads to a diagonal field (current) distribution of the resonant modes in shorted patch, and degeneration of its second order mode using centrally placed shorting posts leads to CP characteristics. Thus in comparison, CP response in shorted configuration is achieved at much higher frequency than the fundamental mode frequency of equivalent un-shortened SMSA. Therefore, although a shorting technique is used, reported shorted CP design is not a compact design. In comparison, CP SMSA design without shorting post operating at its fundamental mode in the 2435 MHz frequency band will yield nearly same AR BW but with much smaller patch size.

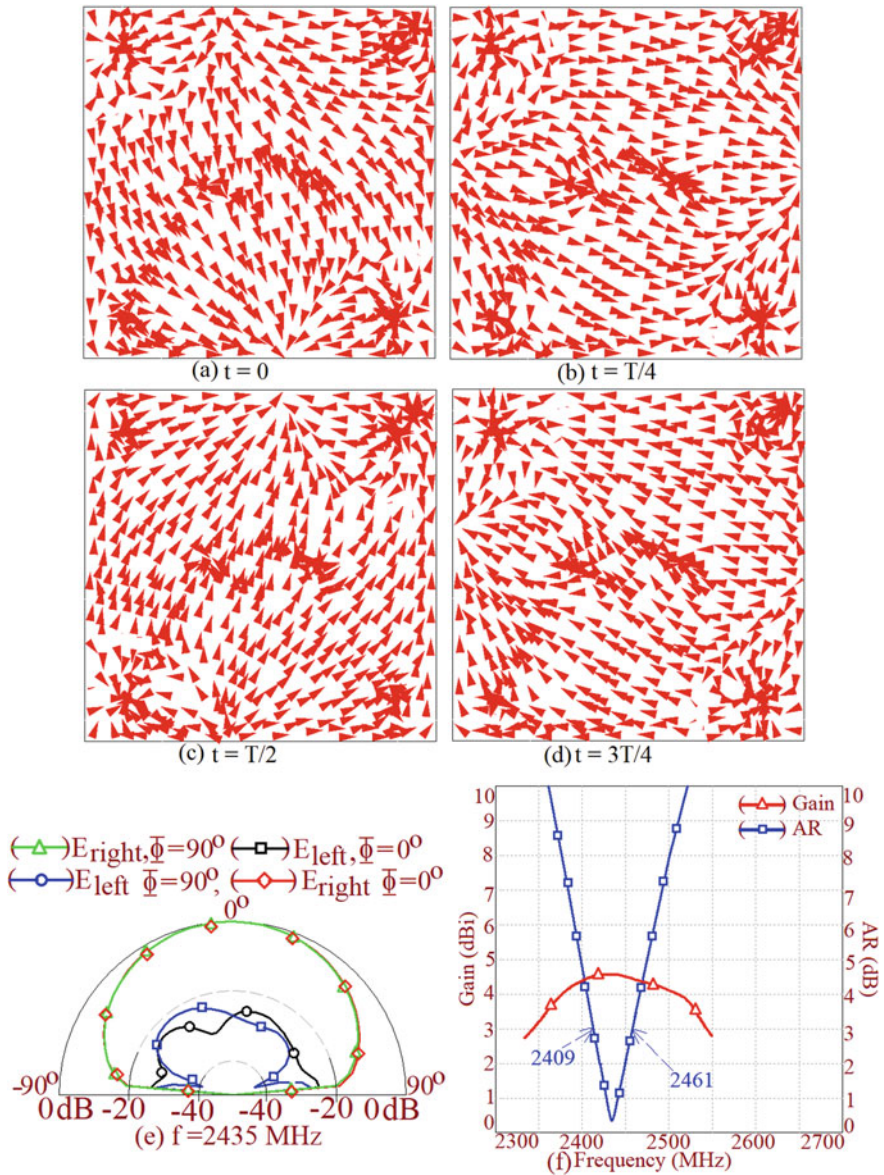


**Fig. 3** a–d Time-varying surface current distribution at the center frequency of AR BW, e simulated polarization and f broadside gain and AR BW plots for multiple shorting posts loaded SMSA

## References

1. James JR, Hall PS (1989) Handbook of microstrip antennas, vol I. Peter Peregrinus, London
2. Guha D, Antar YM (2011) Microstrip and printed antennas—new trends, techniques and applications. Wiley
3. Kumar G, Ray KP (2003) Broadband microstrip antennas. Artech House
4. Wong KL (2002) Compact and broadband microstrip antennas. Wiley, New York
5. Ding K, Gao C, Qu D, Yin Q (2017) Compact broadband circularly polarized antenna with parasitic patches. *IEEE Trans Antennas Propag* 65(9):4854–4857
6. Kovitz JM, Rajagopalan H, Rahmat SY (2016) Circularly polarised half E-shaped patch antenna: a compact and fabrication-friendly design. *IET Microw Antennas Propag* 10(9):932–938
7. Yu J, Lu W-J, Cheng Y, Zhu L (2020) Tilted circularly polarized beam microstrip antenna with miniaturized circular sector patch under wideband dual-mode resonance. *IEEE Trans Antennas Propag* 68(9):6580–6590
8. Li D, Guo P, Dai Q, Fu Y (2012) Broadband capacitively coupled stacked patch antenna for GNSS applications. *IEEE Antennas Wirel Propag Lett* 11:701–704
9. Fu S, Kong Q, Fang S, Wang Z (2014) Broadband circularly polarized microstrip antenna with coplanar parasitic ring slot patch for L-band satellite system application. *IEEE Antennas Wirel Propag Lett* 13:943–946
10. Wang L, Weng Z, Jiao YC, Zhang W, Zhang C (2018) A low-profile broadband circularly polarized microstrip antenna with wide beamwidth. *IEEE Antennas Wirel Propag Lett* 17(7):1213–1217
11. Zhang X, Zhu L, Liu N-W (2017) Pin-loaded circularly-polarized patch antennas with wide 3-dB axial ratio beamwidth. *IEEE Trans Antennas Propag* 65(2):521–528
12. CST Microwave Studio, Version 2019

# Design of UWB Rectangular Microstrip Antenna with Defected Ground Structure to Detect Breast Cancer



A. Sudhakar, M. V. Nageswara Rao, and Telagarapu Prabhakar

**Abstract** This paper presents a microstrip UWB antenna to detect breast cancer tumors based on microwave imaging system. The lower frequency range guarantees acceptable depth of penetration, whereas higher frequency range guarantees better picture resolution. As a result, based on the lower and higher frequencies of the UWB bands, both deeply buried and tiny tumors may be identified. The suggested antenna is planned on FR-4 substrate having a size of 12 mm × 20 mm with thickness of 1.6 mm and relative permittivity ( $\epsilon_r$ ) of 4.4 which gives frequency range from 4.33 to 9.11 GHz with frequency rejection from 4.58 to 5.93 GHz. To overcome electromagnetic obstruction (EMI) between UWB frameworks and Wireless Local Area Networks (WLANs) in view of IEEE 802.11a standard for Ultra-WideBand (UWB) correspondence, the suggested antenna comprises of a rectangular patch and combinations of rectangular and inverted T slot on ground plane. The outline parameters and the execution of the suggested antenna are investigated by utilizing HFSS. The suggested antenna shows a decent omni directional radiation pattern with highest gain of 8.98 dB at 4.48 GHz.

**Keywords** UWB (Ultra-Wide Band) Antenna · Rectangular shape · Breast cancer · SAR (Specific Absorption Rate) · Microstrip feeding

---

A. Sudhakar (✉) · M. V. Nageswara Rao · T. Prabhakar  
GMR Institute of Technology, Rajam, Srikakulam, Andhra Pradesh, India  
e-mail: [sudhakar.a@gmrit.edu.in](mailto:sudhakar.a@gmrit.edu.in)

M. V. Nageswara Rao  
e-mail: [nageswararao.mv@gmrit.edu.in](mailto:nageswararao.mv@gmrit.edu.in)

T. Prabhakar  
e-mail: [prabhakar.t@gmrit.edu.in](mailto:prabhakar.t@gmrit.edu.in)

## 1 Introduction

Breast cancer is currently the frequent cancer in India, according to data from the PBCR (Population-Based Cancer Registry) website. It is critical to notice breast cancer at a premature stage so that treatment can be simple and successful. Breast cancer detection tools include mammography, ultrasound, tomography, and MRI. Mammography has been shown to be painful in young women, but ultrasound may be the ideal substitute for it as it is also more cost efficient. The major disadvantage of ultrasonography is its low quality, which has certain negative consequences due to ionized radiation. Microwave imaging technologies can be a good replacement for the methods mentioned above since they are safer, more readily available, and can be used for early stage diagnosis. Monthly scans of healthy volunteers using a clinical prototype are discussed in [1]. Microwave imaging techniques are based on differences in dielectric characteristics between malignant tumor tissues and healthy tissues. The differences between the electric and magnetic fields are critical for determining the position and volume of malignant tissue, among other things. Identification of tumors within breast phantoms using multi-static radar is explained in [2]. Calibration procedure is demonstrated in [3]. A survey of radar systems is presented in [4]. A novel breast cancer detection approach that combines thermography and high-frequency excitation methods is discussed in [5]. A T-Shaped slotted rectangular patch antenna for ISM band usage at 2.45 GHz is recommended in [6]. It has been demonstrated in [7] that UWB microwave imaging surpasses X-ray mammography. An antenna [8] is constructed on a low-cost RT-Rogers 5880 (lossy) substrate with horizontal narrow slots on the radiating element and a ground plane.

An implanted Coplanar Waveguide (CPW)-fed antenna is described in [9]. A micro strip antenna at 2.45 GHz is presented in [10]. Confocal imaging for cancer screening is demonstrated [11] utilizing a monopole slot antenna array with a  $4 \times 4$  matrix. Two different tumor phantoms with 10 mm spacing are resolved using measured data. An overview of concepts and electromagnetic techniques for microwave breast imaging is provided in [12]. A novel breast model system based on a UWB antenna for detecting tumor malignancy is described in [13]. Using a side slotted Vivaldi antenna, the ISM band, which is used for breast phantom measurement, is clustered around 2.4 GHz [14]. A tiny slotted UWB antenna is depicted in [15].

The antenna [16] was designed to meet the UWB standards by adding a few rectangular slots on a rectangular patch. For transmitting and receiving the UWB signal, two types of horn antennas are presented in [17]. A breast tumor detecting antenna is proposed in [18]. A unique design of an ultra-wideband circular microstrip patch antenna operating in the authorized FCC spectrum for the detection of breast tumors is recommended in [19]. A rectangular microstrip antenna is recommended in [20]. A three-layered stacked aperture coupled microstrip antenna (SACMPA) with a faulty ground structure is depicted in [21].

In this paper, etching off some of the conducting material from the ground in the forms of rectangle and inverted T discovered an antenna appropriate for UWB

applications spanning from 4.33 to 9.11 GHz with WLAN notch frequency ranging from 4.58 to 5.93 GHz. The problem of supplying a broad bandwidth in a small package is handled by etching the structure and using a defective ground structure. The proposed antenna is designed to detect breast cancer tumors in the UWB band. The article is organized as follows: the second portion covers the antenna’s design and construction, and the third portion provides simulated and measured results for antenna parameters. Finally, in the fourth portion, the conclusion is delivered.

## 2 Materials and Methods

The fundamental concept of this antenna is executed with a defective ground structure to improve bandwidth and reduce size. The ground is slotted with a rectangle and inverted shaped T slot. The substrate material is FR4 to give improved efficiency and a wider band range and the substrate is distributed across a surface area of  $12 \times 20 \times 1.6 \text{ mm}^3$ , giving it a compact appearance. A bidirectional pattern is created, which lowers power loss and results in minimum return loss. To achieve impedance matching, the microstrip feeding method is utilized.

The initial design consists of rectangular-shaped patch of dimensions  $20 \text{ mm} \times 12 \text{ mm}$  printed on FR-4 substrate of 1.6 mm thickness with fully copper coated ground. To make this antenna to operate in the ultra-wideband, it is fed with microstrip line of width 2.8 mm and length of 5 mm. The ground is etched with rectangular and inverted T shapes to increase the bandwidth and also to introduce WLAN notch properties. The proposed antenna structure is shown in Fig. 1.

The front aspect of the manufactured antenna is shown in Fig. 2. At a frequency of 4.48 GHz, the overall dimensions produced by this design are  $0.29\lambda$ ,  $0.179\lambda$ , and  $0.023\lambda$ . As a result, the antenna has reduced dimensions and is more practical

**Fig. 1** Proposed antenna structure

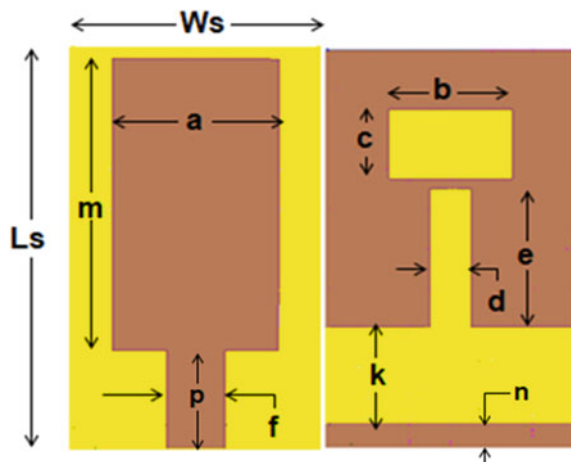


**Fig. 2** Proto type antenna **a** front view **b** rear view

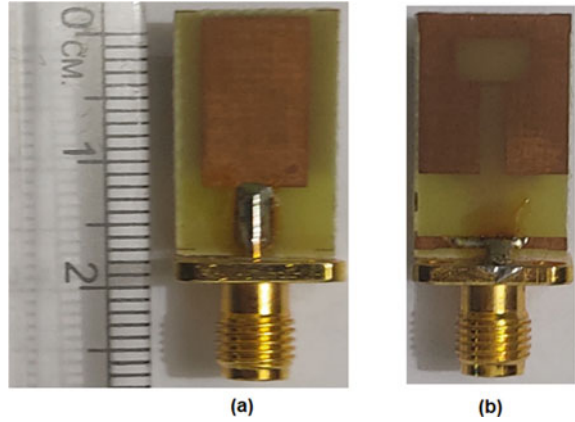


**Table 1** Dimensions of recommended antenna

Parameter	Description	Size (mm)
Ws	Substrate width	12
Ls	Substrate length	20
a	Patch width	8
b	Rectangular slot width	6
c	Rectangular slot length	3.5
d	Width of vertical arm of T slot	2
e	Length of vertical arm of T slot	7
f	Width of microstrip line	2.8
k	Width of horizontal arm of T slot	4.5
m	Patch length	10
n	Thickness of bottom ground	1.25
p	Length of microstrip line	5

for detecting breast cancer tumors. Table 1 shows the dimensions of the suggested antenna and subsequently the antenna performance characteristics are simulated and measured.

### 3 Results and Discussion

The recommended FR4-based UWB antenna with WLAN notch properties is operating in the frequency range from 4.33 to 9.11 GHz with a stop band from 4.58 to 5.93 GHz. The same has been simulated using HFSS software. The simulated and measured S11 plot is depicted in Fig. 3. The reflection coefficient is the measure of how well the device or the line are matched and the power reflected from the

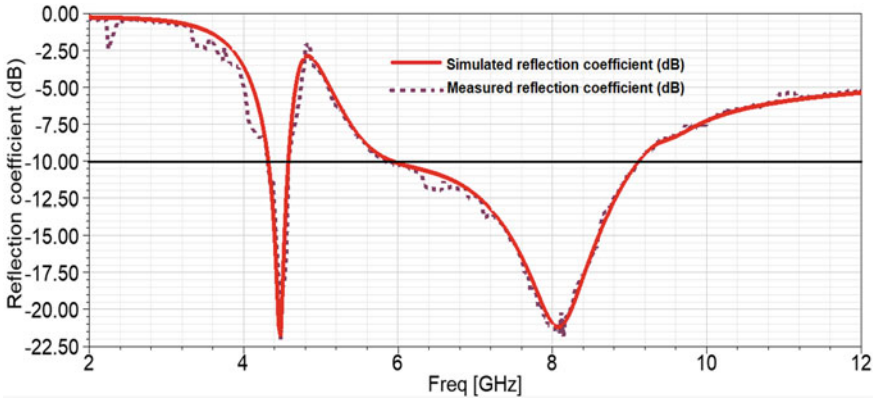


Fig. 3 S11 parameters versus frequency

antenna, at 4.48 GHz the reflection coefficient is found to be  $-21.78$  dB. The fabricated antenna is tested, and the obtained return loss at the operating frequency is found to be  $-21.78$  dB at 4.48 GHz and  $-21.29$  dB at 8.04 GHz.

The specific absorption rate (SAR) is the measure of amount of energy absorbed by the human body when exposed to a radio frequency (RF) electromagnetic field. The average SAR value for a human body is 1.6 W/kg. Figure 4a depicts the antenna’s simulated SAR pattern and Fig. 4b shows the surface current distribution at 4.48 GHz. The patch of the antenna has a homogeneous distribution of deep blue that indicates 0% SAR value, making it most appropriate for on-body applications.

Figure 5a depicts the gain performance of the FR4 UWB antenna. The graph results demonstrate that the recommended UWB antenna has a peak gain of 8.98 dB,

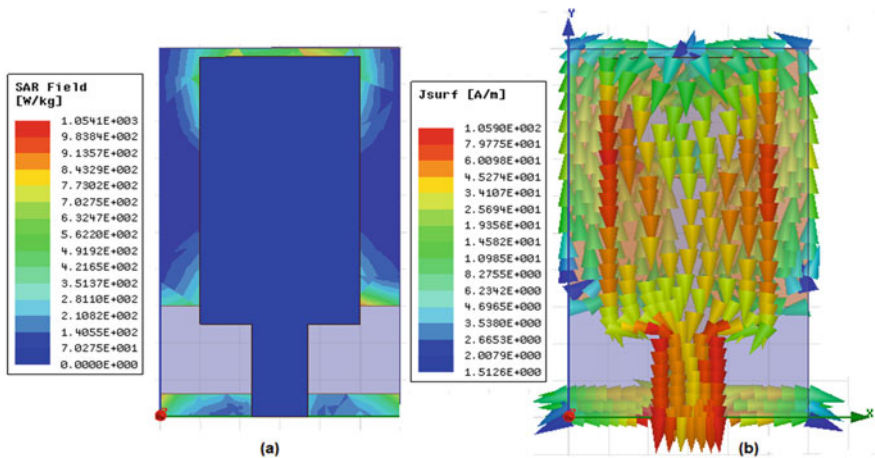


Fig. 4 Simulated a SAR pattern b surface current distribution at 4.48 GHz



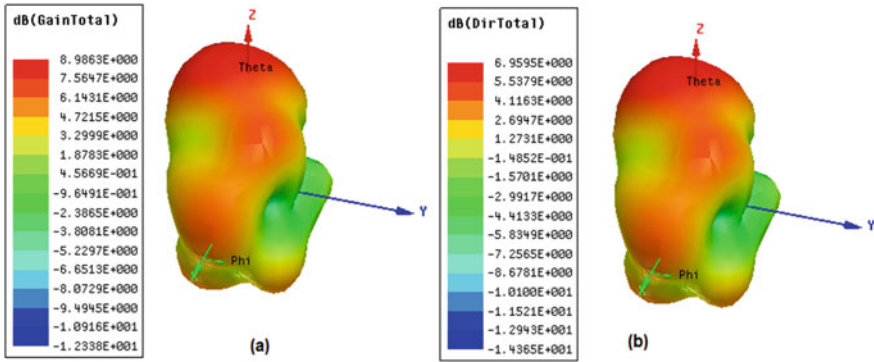


Fig. 5 Simulated a 3D gain b directivity at 4.48 GHz

making it more appropriate for biomedical applications. The gain plot as a function of direction is bidirectional, indicating that it can transmit and receive electromagnetic energy. The concentration of radiated radiation in a single direction is referred to as directivity. Figure 5b depicts the directivity of the proposed UWB antenna.

Figure 6 depicts the far-field radiation patterns at  $0^\circ$  and  $90^\circ$  of both azimuth and elevation plane. The term gain refers to the combination of antenna directivity and electrical efficiency.

The obtained directivity for this antenna is 6.95 dB. The power reflected from the antenna is defined by the VSWR. Figure 7 shows that the VSWR is 1.02 at a resonant frequency of 4.48 GHz. As a consequence, impedance matching has improved and more power is sent to the antenna. Figure 8a depicts the E-field, 3-D radiation pattern of this antenna. Figure 8b depicts the proposed antenna's H-field 3-D radiation pattern.

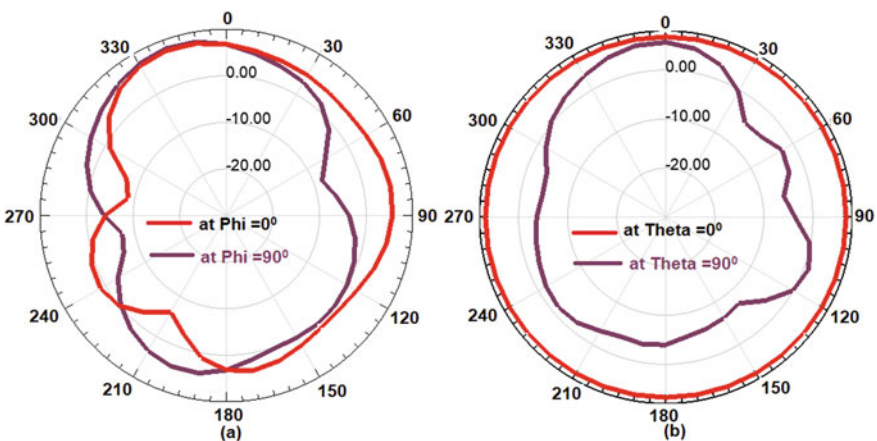


Fig. 6 a E-field pattern b H-field pattern at 4.48 GHz

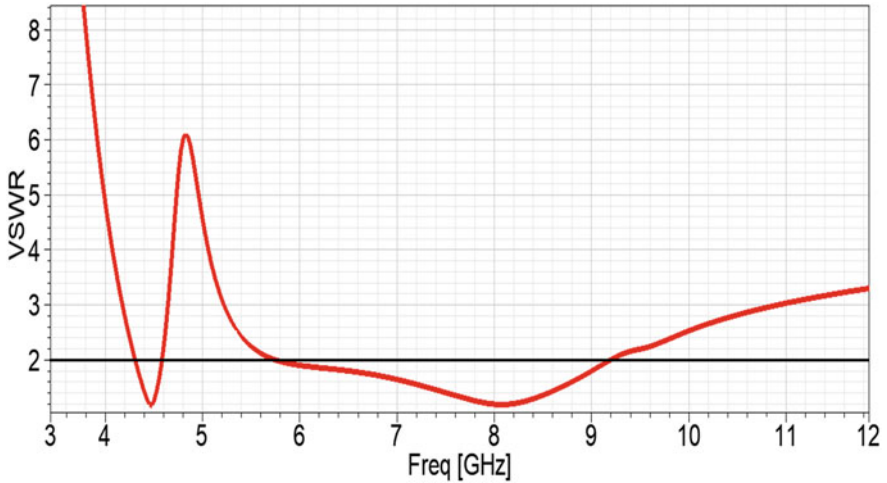


Fig. 7 VSWR versus frequency

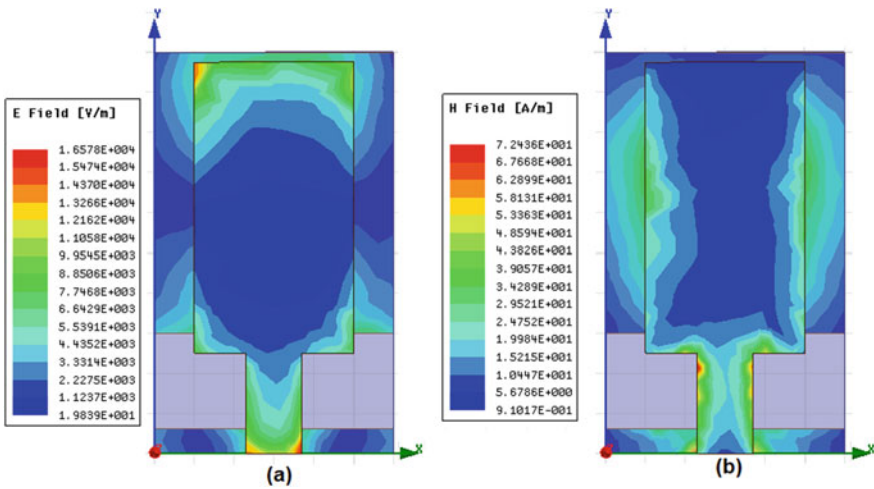


Fig. 8 At 4.48 GHz **a** E-field distribution **b** H-field distribution

### 4 Conclusion

The rectangular-shaped ground is slotted with rectangular and inverted T-shaped slot to provide enhanced bandwidth and WLAN notch characteristics. The proposed antenna operates in UWB range of 4.33–9.11 GHz. WLAN notch properties are introduced to avoid the interference in view of IEEE 802.11a standards. The defected

ground structure offers satisfactory bandwidth of 0.25 GHz at resonant frequency of 4.48 GHz and minimum SAR required for the antenna to be concerned in the bio-medical applications. The maximum gain is 8.98 dB at 4.48 GHz.

## References

1. Porter E, Coates M, Popovic M (2016) An early clinical study of time-domain microwave radar for breast health monitoring. *IEEE Trans Biomed Eng* 63(3):530–539
2. Byrne D, Sarafianou M, Craddock IJ (2017) Compound radar approach for breast imaging. *IEEE Trans Biomed Eng* 64(1):40–51
3. Kwon S, Lee S (2017) In-place calibration with single measurement in time-domain microwave breast imaging. *IEEE Antennas Wirel Propag Lett* 16:206–209
4. Pisa S, Pittella E, Piuze E (2016) A survey of radar systems for medical applications. *IEEE A&E Syst Mag Part II of II*:64–81
5. Rahmatinia S, Fahimi B (2017) Magneto-thermal modeling of biological tissues: a step toward breast cancer detection. *IEEE Trans Magn* 53(6):1–4
6. Gupta HK, Sharma R, Thakre VV (2017) Breast cancer detection by T-shaped slotted planner antenna. *Ind J Sci Technol* 10(8):1–7
7. Aydin A, Aydin EA (2017) Evaluation of limestone layer's effect for UWB microwave imaging of breast models using neural network. *Tech J* 11:50–54
8. Susila JJ, Fathima HR (2017) A slot loaded rectangular microstrip patch antenna for breast cancer detection. *Int Res J Eng Technol* 4(4):3394–3397
9. Shanmuganatham T, Kumar SA (2014) Design of an implantable CPW fed dual dipole antenna for dual band biomedical applications. *Int J Biomed Eng Technol* 14(1): 46–59
10. Hamsagayathi P, Sampath P, Gunavathi M, Kavitha D (2016) Design of slotted rectangular patch array antenna for biomedical applications. *Int Res J Eng Technol* 3(1):114–120
11. Song H, Kubota S, Xiao X, Kikkawa T (2016) Design of UWB antennas for breast cancer detection. In: *Proceedings of international conference on electromagnetics in advanced applications*, pp 321–322
12. Mahmud MZ, Islam MT, Misran N, Almutairi AF, Cho M (2018) Ultra-wideband (UWB) antenna sensor based microwave breast imaging: a review. *Sensors (Basel)* 18(9):1–15
13. Amdaouch I, Aghzout O, Naghar A, Alejos AV, Falcone F (2018) Breast tumor detection system based on a compact UWB antenna design. *Prog Electromagn Res M* 64:123–133
14. Jayapriya C, Jeyanthi KMA (2018) Design of an ultra-wideband antenna for breast cancer detection. *Int J Eng Technol* 7(3):471–475
15. Amdaouch I, Aghzout O, Naghar A, Alejos AV, Falcone F (2019) Design of UWB compact slotted monopole antenna for breast cancer detection. *Adv Electromagn* 8(5):1–6
16. Rahayu Y, Waruwu I (2019) Early detection of breast cancer using ultra wide band slot antenna. *Sinergi* 23(2):115–122
17. Vijayarveswari V, Jusoh M, Sabapathy T, Aliana R, Khatun S, Ahmad ZA, Osman MN (2017) Performance verification on UWB antennas for breast cancer detection. In: *Proceedings of international conference on emerging electronic solutions for IoT*, pp 1–4
18. Srinivasan D, Gopalakrishnan M (2020) Design of compact UWB antenna for the detection of breast cancer tumor. *Int J Adv Sci Technol* 29(3):5945–5956
19. Fatimi AE, Bri S, Saadi A (2019) UWB antenna with circular patch for early breast cancer detection. *Telkomnika* 17(5):2370–2377
20. Venkateshkumar U, Yamunadevi S, Yogitha U, Ponraj S (2021) A compact UWB antenna design for breast cancer detection. *J Phys: Conf Ser* 1–7
21. Kaur G, Kaur A (2020) Breast tissue tumor detection using “S” parameter analysis with an UWB stacked aperture coupled microstrip patch antenna having a “+” shaped defected ground structure. *Int J Microw Wirel Technol* 12(7):635–651

# **Networking & Signal Processing**

# Mode Selection Criterion Using Statistics for Direct Link Communication in Next Generation



Pallavi Sapkale and Uttam Kolekar

**Abstract** Direct link communication is an underlying promising method for next generation which helps to transfer data between two devices without involvement of evolved node base station (eNB). Device to device (D2D) means direct link communication supports more data rate, less latency, and minimizes the energy consumption due to its short range communication. Device-to-device (D2D) communication supports a more accurate scheme for improving the quality of service criteria for next generation networks. Furthermore, to obtain the better result of D2D communication, multiple methods need to highlight and mode selection is one of them. This work explains the mode selection (MS) criterion using degree of freedom (DoF) in statistics for next generation cellular networks. We analyzed the better statistics for the D2D users according to their mode selections. Graphical results show that our proposed work performs significantly better than conventional schemes for delay and better throughput.

**Keywords** Direct link communication · 5G · Statistics · Mode selection

## 1 Introduction

The recent progress in cellular networks developed with speedy growth and more reliable communications, due to modern frequency resource allocations [1]. With the huge demand of mobile data for next generation cellular networks, researchers proposed various techniques to handle such expanded network traffic. Furthermore, in cellular networks, direct link communication as a new technique is developed for the next generation to support the large network traffic [2]. In cellular networks,

---

P. Sapkale (✉)

D.J. Sanghavi College of Engineering, Vileparle, Mumbai, India

RAIT Nerul, Navi Mumbai, India

U. Kolekar

APSCOE, Thane, Mumbai, India

direct link communication is a modern scheme which supports direct communication between two nearby mobile users without the involvement of an evolved base station (eNB). The Device-to-Device (D2D) communication will minimize the energy consumption and delay because of small transmission distance [3, 4]. Most recently, various researchers accept that D2D Communications will be an important aspect of the next generation networks. Even though direct link technology serves a lot of advantages in network communication, on the other hand, it faces a lot of difficulties that should be taken into attention. In order to expand the network performance with direct link communication, various issues have to be handled. The main challenges in direct link communications are mode selection, resource management, link interference, energy consumption, and location discovery.

### ***1.1 Mode Selection***

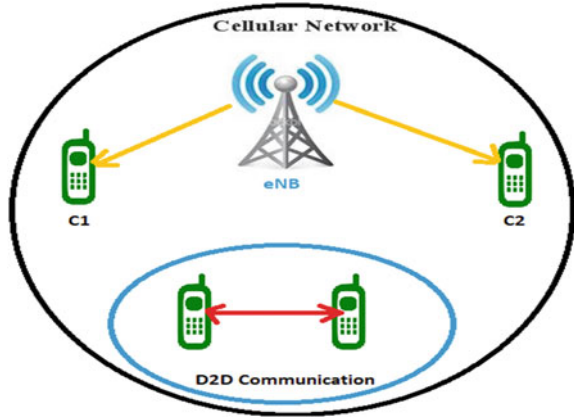
Mode selection is the process which can provide connectivity towards Device-to-Device (D2D) mode or a cellular mode (CM) [5]. This procedure can select whether the D2D link is permitted to underlay or overlay. Selection procedure is a mandatory choice because once in a while D2D connectivity is worse than cellular. Mode selection is mainly subdivided into two parts: static and dynamic. Static is stable while dynamic changes with time. Devise challenges regarding mode selection can be listed below. One is, decided time for mode switching and, at the same period, which type of quantifying signals are needed. For better performance, such signals are minimal. Finally, what type of calculations are used for the users? It could be location path or Signal-to-Noise ratio (SNR) [6]. In this paper, we focused on mode selection in direct link communication using degrees of freedom. A plenty of advent work in direct link communication focused on cellular coverage and throughput gain [7]. Pricing models for direct link has been discussed in [8]. Recently, improvement of spectrum efficiency and energy efficiency was highlighted in [9].

### ***1.2 Direct Link Communication in Cellular Network***

Figure 1 depicts the traditional direct link communication in cellular networks [10]. In cellular networks, a geographical area is based on an evolved base station (eNB) and it supports the network connectivity to all nodes. In direct link communication, devices communicate to each other partially or without dependency on base station.

In this paper, our aim is to improve the performance during direct link communication in terms of power consumption, while gaining maximum system throughput and guaranteeing for high Quality of Service (QoS) requirements. To do so, we proposed a mode selection criterion using Degrees-of-freedom (DoF) for Device-to-Device Communication in next generation cellular network. The main features of the work are as follows:

**Fig. 1** Direct link communication in cellular network [11]



- We analyze the issues that appear when mode selection techniques are used for selecting a traditional network or device-centric network to improve the performance of direct link communications in the next generation.
- We formulate the statistics as a mode selection-based method which improves the performance in direct link communication in the form of high SNR and better throughput, and the degree of freedom is mainly designed by the system configuration.
- We implement a modified analysis of the proposed statistical method based on mode selection method and the traditional-based mode selection method.
- Simulation results show the analysis of the proposed work and present work. It is seen that the devised mode selection method has fine results.

This workflow is as follows. Section 2 described the proposed system. In Sect. 2.3, we explained the statistics-based mode selection algorithm. In Sect. 3, we calculate and compare results of proposed statistics mode selection and existing method. Finally, conclusions are drawn in the last section.

## 2 Proposed System Model

Figure 2 shows user equipment (UE1) communicates to UE2 either via the cellular mode or using a D2D mode. D2D communication is a direct link between two devices without involvement of eNB [11]. Hence, comparing to conventional cellular network, direct link network serves for more energy efficiency, high throughput, and less delay because of the short distance between two devices. This communication is more flexible and increases the network performances during mode selection. Direct link communication is mainly classified into three parts. First one is direct link control, which supports control of networks and provides better connectivity. Second one is direct link coverage which provides the range of networks like in, out,

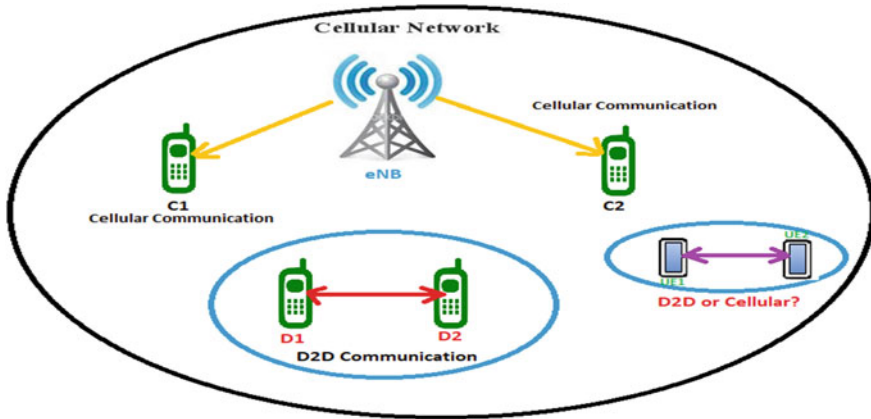


Fig. 2 UE1 communicates to UE2 with cellular mode or D2D mode [11]

and partial range. Last one is direct link communication mode in which a device user is able to share similar resource blocks with other users, it could be cellular user or device user [4]. We used a single cell network in which Device-to-Device (D2D) communication is active with the partial connectivity of the base station (eNB). Both users within the cell can communicate using one of two possible modes, as illustrated in Fig. 2 as cellular mode and direct link mode. When devices are not in the connecting area and want to communicate with the device, then they select a device as a relay node. It is also called multi-hop.

### 2.1 System Calculation and Assumptions

We assume a cell with one base station and different users like cellular as well as D2D users which is indicated in Fig. 2. Here, we consider every user having an antenna denoted with  $U_a$ , and eNB also having its own antenna which denotes  $B_a$ . But,  $B_a$  is always greater than  $U_a$ . Users can communicate with relay in the same cell or neighbor cell via base station which is known as traditional communication means cellular mode otherwise direct communication means direct link mode. We assume that users are randomly distributed in area A. And according to the homogeneous Poisson process  $\varphi$  of intensity  $\lambda_i$ , where A is subset of  $M^2$  which is a fix set of users place, and  $\varphi(A)$  indicates the users number of Poisson's in set A. Here, cell is having radius  $r$  and total area is  $\pi r^2$ . Also consider that the eNB is situated at centered (Table 1).

There are three main possibilities shown in Fig. 2 from which users are either, first is cellular users, second is already in D2D, and third one is dependent on mode selection criteria like cellular mode or direct link mode. Here, we assume N is network in cell so cellular network users are  $N_C$  and direct link users are  $N_D$ . Similar assumption



**Table 1** Assumptions for proposed system

Assumption	Number	Details
Cell	One	With one base station
Users	Two	Cellular and D2D
Antenna	One user ( $U_a$ ) and base station $B_a$	–
Area	Randomly distributed ( $A$ ), [ $A \subset M^2$ ]	

is used in [12]. So, the total number of users in one set is the addition of all three possibilities. We used two different slots for the calculation.

$$N_C = \{(C_1, eNB), (C_2, eNB) \dots (C_{N_C}, eNB), (D_1, DN_{D+1}), (D_2, DN_{D+2}) \dots (DN_D, D_2, ND)\} \quad (1)$$

And for proposed mode selection is from device 1 (UE1) to device 2 (UE2), i.e. (UE1, eNB), (UE2, eNB). Similarly for eNB to C1 and C2.

And for device-centric,

$$N_D = \{(C_1, eNB), (C_2, eNB) \dots (C_{N_C}, eNB), (D_1, DN_{D+1}), (D_2, DN_{D+2}), \dots, (DN_D, D_2, ND)\} \quad (2)$$

And the proposed mode selection is from device 1 (UE1) to device 2 (UE2), i.e. (UE1, UE2) and vice versa.

Degree of Freedom for the proposed direct link users can select the possible modes.

## 2.2 Mode Selection with Degree of Freedom in Statistics

When a proposed pair of direct link communication connects with cellular mode or direct link mode, then one pair is formed from source (s) to destination (d). Here, we consider (s, d) is a pair for communication. And also consider,  $C_l$ ,  $D_m$ , and  $U_n$  indicate the cellular user  $l$ , D2D user  $m$ , and proposed mode selection  $n$ , respectively. For the proposed system communication pair, during the cellular communication, it required two slots like uplink and downlink; while during the device-to-device communication, it needed a single slot. Selection is based on the better performance of the system; if the performance of cellular network is maximum, then it chooses the cellular network, and if the performance of direct link communication is better, then it goes for direct link [If  $\eta_C > \eta_D =$  cellular and if  $\eta_C < \eta_D =$  D2D]. Such selection is difficult for the general system; hence, in proposed work, we calculate the selection on the basis of probability conditions.

$$\text{a. } (N_C, N_D, B_a, U_a) = (N_C, 0, B_a, U_a) \quad (3)$$

$$\text{b. } (N_C, N_D, B_a, U_a) = (1, N_D, B_a, U_a) \quad (4)$$

$$\text{c. } (N_C, N_D, B_a, U_a) = (1, 1, B_a, U_a) \quad (5)$$

These conditions indicate the number of users and its type in the present network. For condition a.

$$\eta c = 0.5 \min[B_a - \sum_{m=1}^{N_C} d_{Cm}^{eNB} 2U_a] \quad (6)$$

$$\eta D = \min[B_a - \sum_{m=1}^{N_C} d_{Cm}^{eNB} U_a - \nu c] \quad (7)$$

where  $\nu c$  is maximum network connection from the antenna.

For condition b.

$$\eta c = \min\{\max[B_a - \sum_{m=1}^{N_D} d_{Dm}^{DND+m}, \frac{U_a - \nu D}{2}], U_a - \nu D\} \quad (8)$$

$$\eta D = U_a - \nu D \quad (9)$$

For condition c.

$$\eta c = \min[B_a - \frac{d_{Cm}^{eNB} - d_{UE1}^{UE2}}{2} U_a - d_{UE1}^{UE2}] \quad (10)$$

$$\eta D = U_a - [\max d_{Cm}^{eNB}, d_{UE1}^{UE2}] \quad (11)$$

### 3 Result

In this section, we discussed how proposed methods are more effective than conventional methods by analyzing the performance parameters in the form of energy efficiency and better throughput. Here, for simulation, we consider ten users in a single cell. The experiment of proposed work is done in MATLAB. The performance of this work is employed for better parameters such as energy consumption and better output. For better connectivity during direct link communication, delay should be less. Here, we consider how much time is taken to transmit the packets from UE1 to UE2.

$$Delay = \frac{L_B}{R} \tag{12}$$

where  $L_B$  is packet length in bits and  $R$  is link bandwidth.

Here, we adapted methods for the evaluation like mode selection scheme for LTE A, mode selection method using graph based, and also consider mode selection methods for interference. Figure 3 shows the results for proposed work with direct link communication analysis for a single cell using ten users. The analysis is based on mode selection criteria. Here, blue hexagon is for macro base station and dark green is for small cells. The white circle and red circle represent the user position in the macro and, the white represents the user is in conventional mode and red indicates communication is in direct link mode. Figure 4 shows the comparison between existing methods and proposed methods for delay.

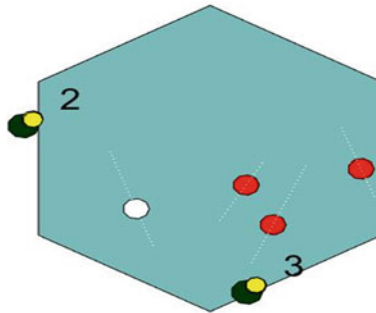


Fig. 3 Single cell topology for ten users

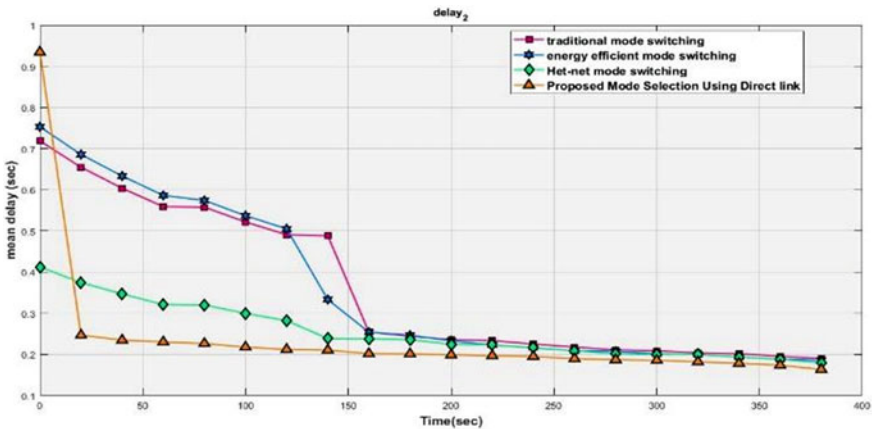


Fig. 4 Comparison of delay between existing methods and proposed

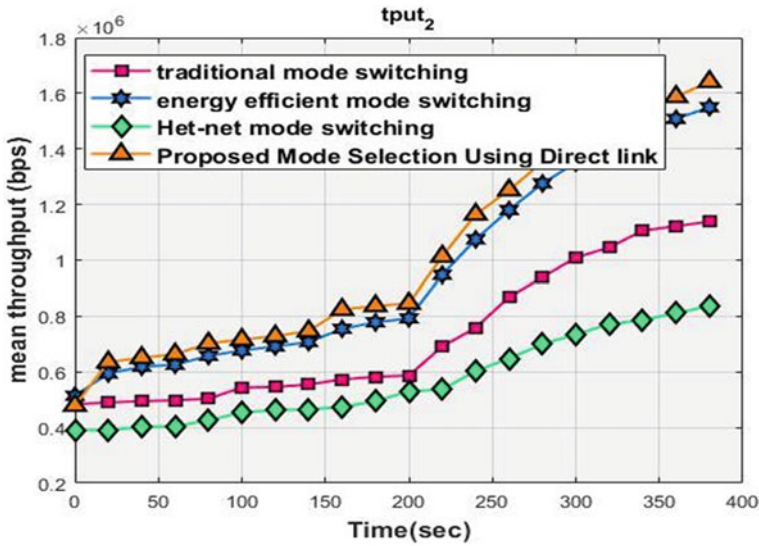


Fig. 5 Maximum throughput with proposed method

Table 2 Comparative analysis of proposed method with existing methods

Users	Metrics	Traditional mode switching	Energy efficient mode switching	Het-Net mode switching	Proposed mode selection using direct link
10	Delay (s)	0.185	0.182	0.168	0.159
	Throughput (bps)	1,128,542	1,490,120	835,392.1	1,681,432

Simulation time for the system is 400 s., and during the simulation, the proposed system gives minimum delay with respect to time. And in Fig. 5, maximum throughput occurs with change in time.

Table 2 shows the comparative analysis of proposed mode selection method with existing methods, and proposed method delay is 0.159 s which is less than all existing systems. Also the throughput of the proposed method is 1,681,432 bps better than existing one.

### 4 Conclusion

We devise a new approach scheme for direct link communication using mode selection. The scheme integrates a statistics mode selection in cellular networks. Here, the performance of the system is better with energy consumption as well as throughput.

The degree of freedom in statistics is adapted for selecting the mode for direct link communication or in cellular mode. Here, the statistics depend on the conditions and selects the better option. Compared to existing work, devised work gives less energy consumption and maximal throughput.

## References

1. Federico et al (2018) Distributed mode and power selection for non-orthogonal D2D communications: a stochastic approach. *IEEE Trans Cogn Commun Netw* 4(2):232–243
2. Militano L, Araniti G, Condoluci M, Farris I, Iera A (2015) Device-to-device communications for 5G internet of things. *EAI Endorsed Trans Internet Things* 15(1)
3. Gandotra P, Jha RK, Jain S (2017) A survey on device-to-device (D2D) communication: architecture and security issues. *J Netw Comput Appl* 78:9–29. ISSN 1084-8045. <https://doi.org/10.1016/j.jnca.2016.11.002>
4. Hussein HH, Elsayed HA, Abd El-kader SM (2020) Intensive benchmarking of D2D communication over 5G cellular networks: prototype, integrated features, challenges, and main applications. *Wirel Netw* 26:3183–3202. <https://doi.org/10.1007/s11276-019-02131-2>
5. Pallavi V, Sapkale, Uttam D, Kolekar, " Modified Naïve Bayes Classifier for Mode Switching and Mobility Management Using Cellular Networks" ,Springer Nature 2020, *Wireless Personal Communications* <https://doi.org/10.1007/s11277-020-07794-1>.
6. Phunchongharn P, Hossain E et al (2013) Resource allocation for device to device communications underlying LTE-advanced networks. *IEEE Wirel Commun* 20(4):91–100
7. Golrezaei N, Mansourifard P, Molisch AF, Dimakis AG (2014) Base-station assisted device-to-device communications for high-throughput wireless video networks. *IEEE Trans Wirel Commun* 13(7):3665–3676
8. Tehrani MN, Uysal M, Yanikomeroglu H (2014) Device-to-device communication in 5G cellular networks: challenges, solutions, and future directions. *IEEE Commun Mag* 52(5):86–92
9. Gandotra P, Jha RK (2019) Energy-efficient device-to-device communication using adaptive resource-block allocation. *Int J Commun Syst* 2019:e3922. <https://doi.org/10.1002/dac.3922>
10. Safdar GA et al (2016) Interference mitigation in D2D communication underlying LTE-A network. *IEEE Access* 4:7967–7987. <https://doi.org/10.1109/ACCESS.2016.2621115>
11. Li Y, Song W, Su Z, Huang L, Gao Z (2018) A distributed mode selection approach based on evolutionary game for device-to-device communications. *IEEE Access* 6:60045–60058. <https://doi.org/10.1109/ACCESS.2018.2874815>
12. Liu Z, Peng T, Xiang S, Wang W (2012) Mode selection for device-to-device communication under LTE-advanced networks. In: *Proceedings of IEEE international conference on communications (ICC)*, Ottawa, Canada, June 2012, pp 5563–5567

# Impact of 5G Technology on Indian Industries



C. A. Sathiyamoorthy, V. Sivasankaran, V. Venkataramanan,  
Mohd Faisal Mohd Sadique, and Soumyaprakash Dashmohapatra

**Abstract** Internet penetration rate in India is reported to be 50% by 2020. This is an increase of 1036% compared with the internet penetration rate in 2008. The introduction of fifth-generation cellular technology in India is set to increase the penetration rate. With widespread availability, 5G technology will enable the high speed of data transfer. High-speed internet industries such as agriculture, healthcare and IoT are expected to experience digital transformation as they become available everywhere. Reforms in defense technologies are possible with new technology. Furthermore, in the era of smart devices, the availability of 5G will play a vital role in enhancing the functionality of smart devices, which will lead to digital transformation in various industries.

**Keywords** 5G · Internet penetration · Agriculture · Healthcare · IoT

## 1 Introduction

Alexander Graham Bell invented the telephone to communicate through speech. This invention came as a result of his attempt to improve the performance of the telegraph that was capable of sending and receiving only one message at a time. This invention made it possible for more data to be transferred at a particular instant.

---

C. A. Sathiyamoorthy (✉)

Department of Electronics & Communications, CMS College of Engineering, Namakkal, Tamil Nadu, India

V. Sivasankaran

School of EEE, VIT Bhopal University, Bhopal, Madhyapradesh, India

V. Venkataramanan

Department of Electronics & Telecommunications, Dwarkadas J. Sanghvi College of Engineering, Mumbai, Maharashtra, India

M. F. M. Sadique · S. Dashmohapatra

Department of Information Technology, Dwarkadas J. Sanghvi College of Engineering, Mumbai, Maharashtra, India

After this historical invention, this domain has seen a lot of changes. Every change that comes tries to improve upon its predecessor. Mobile wireless communication was a revolutionary change in this field as it improved connectivity. Using this technology people living in different countries and continents could connect in a matter of seconds. Improvements are still being made to various parameters such as latency, data-carrying capacity and speed of mobile wireless communication networks to optimize its performance. These modifications have been classified into mobile wireless generations. Currently, four generations of communication networks are in use.

First-generation (1G) networks were first implemented in 1980 in Tokyo, Japan. The configuration of the network is capable of sending only voice calls. The speed of the network is about 2.4 kilobytes per second (kbps). Techniques such as Frequency Division Multiple Access (FDMA) multiplexing and circuit switching were used for efficient transmission of speech signals. It was succeeded by the second-generation (2G) network, which had a speed of about 14–64 (kbps) and was digitally encrypted. This network is capable of providing text messaging service. It used some techniques such as Time Division Multiple Access (TDMA) multiplexing and circuit switching. It improved the quality of communication by using a narrow band digital network. Third-generation network 3G is launched in 2002 with the aim of providing multimedia communications. Network speeds are approximately 384 kbps to 2 Mbps (Megabytes per second). 3G networks used Code Division Multiple Access (CDMA) multiplexing and used the communication spectrum more effectively in comparison to previous generation networks to facilitate a high quality of audio, voice and data transmission and data transfer. There was a significant increase in the speed and efficiency of data transfer, and facilities for multimedia support were developed. The fourth-generation (4G) network used increased bandwidth to deliver amazing speeds. The speed of the network is about 200 Mbps. It had the ability to provide internet on the go. Besides high speed and increased performance, it is more secure compared with previous generations of networks [1]. The fifth-generation (5G) network is expected to be a game changer. At speeds of up to 1 Gbps (Gigabits per second), its performance overloads the previous generation networks, making them outdated and obsolete. Overall generations of network are explained in Fig. 1.

In this paper, we discuss the impact of 5G on various industries. Section 2 provides a brief overview of 5G networks. Section 3 discusses how 5G will affect the Indian

**Fig. 1** Generations of network [2]



economy. Section 4 describes the application phenomena of 5G, following Sect. 5 discusses the impact of 5G on the healthcare, IoT and agricultural sectors.

## 2 5G Cellular Network

5G mobile networks will reduce the cost of cellular plans worldwide. By combining core, radio access and cloud technologies, these networks can be implemented in various use cases, can handle large amounts of data traffic and are compatible with devices that require different functional requirements. 5G is expected to embrace and support special application events in sectors such as manufacturing, energy, utilities, healthcare, pharmaceuticals, transportation and logistics [3]. It uses the concept of flat Internet Protocol (IP) so that different Radio Access Network (RANs) can be easily upgraded to a single nanocore network. The flat IP concept makes 5G compatible with all kinds of technologies. Nanotechnology is used as a security mechanism in the network. Symbolic names are assigned to all devices in a flat IP configuration, which differs from the normal step by identifying individual devices by their respective IP addresses. The flat IP architecture of 5G has the following benefits:

- Decreases the amount of money spent on operations as well as the capital required to be invested in the network by reducing the number of network components on the data path.
- Highly adaptable as it tries to make changes to its infrastructure according to the emerging needs of the application.
- Reduces the latency of the system [4].
- The radio access and core networks are developed independently thereby making the network more flexible and easy to develop. This flexible network can then be used to develop applications in both mobile as well as the normal IP address networks.

### Architecture of the network

The main objective of the architecture is to achieve the data receiver without any error or delay. Otherwise, the purpose of the new generation network will be completely in vain [5, 6]. Architecture includes the following technologies:

- i. *Cloud computing*: It enables us to access resources anytime, anywhere. It uses the World Wide Web (WWW) to store information. The cloud contains various servers such as database server, streaming server, web server. All of these servers are connected together to create one big cloud. These big clouds consist of small clouds of General Packet Radio Service (GPRS)), Enhanced Data for Global Evolution (EDGE). On the 5G network, the cloud is the central storage area where all the information is stored. Therefore, users can access the content without the need for internet access. Another advantage of cloud computing



is that developers can easily add any extensions or applications on the cloud, making life much easier for the user.

Cloud computing provides the following services:

- *Software*: Cloud computing provides Software as a service (SAAS) where numerous services are provided on the cloud platform. A good example of this is the Gmail, Google Drive service provided as part of the Google Cloud Platform suite.
- *Platform*: Cloud computing provides platform as a service (PAAS) where cloud can be used to deploy applications on the Internet. Example: Amazon Web Services, such as Google Cloud Platform.
- *Infrastructure*: *Cloud computing provides Infrastructure as a service (IAAS). These act as the backbone of the applications. They provide storage space on the cloud. Example: Amazon S3.*

Using these services of the cloud 5G satisfies all the requirements of the customer.

- ii. *MIMO*: Multiple Input Multiple Output (MIMO) enables the user to send and receive data over the channel. The channel used by the user uses to send data is also used by him/her to receive data. According to a survey, a person generates about 1.7 MB of data per second [7]. Larger data require multiple transfer channels. This causes a lot of data traffic on the network, causes congestion and slows down the speed of the entire network. 5G uses MIMO technology [8] so the network will not be slow as this technology will reuse the same channel for sending and receiving data.
- iii. *Use of Macrocells*: The structure of a cell in any network is a hexagon. Whenever a user moves from one cell to another, mobile devices stop their communication with the network of the previous cell and search for a network in the next cell. All of this happens in a matter of seconds, and the search consumes more power. It is therefore used to avoid the use of these macrocells. In the case of macrocells, their size is large, the number of handoffs decreases and thereby saving power. Figure 2 demonstrates the 5G macro cell structure.

## Features of 5G

5G is the upcoming revolution of mobile technology. The features and their application are beyond the belief of a normal human being. With high speed, this is enough to match the cell phone usage.

With a large collection of innovative features, now your smartphone will be on par with the laptop. You can use a broadband internet connection; other notable features that appeal to people include high gaming options, wide multimedia options, ubiquitous connectivity, zero latency, fast response time and high-quality sound, and the ability to convert HD video to another cell phone without compromising audio and video quality [2]. Figure 3 is about features of 5G, it is shown below.

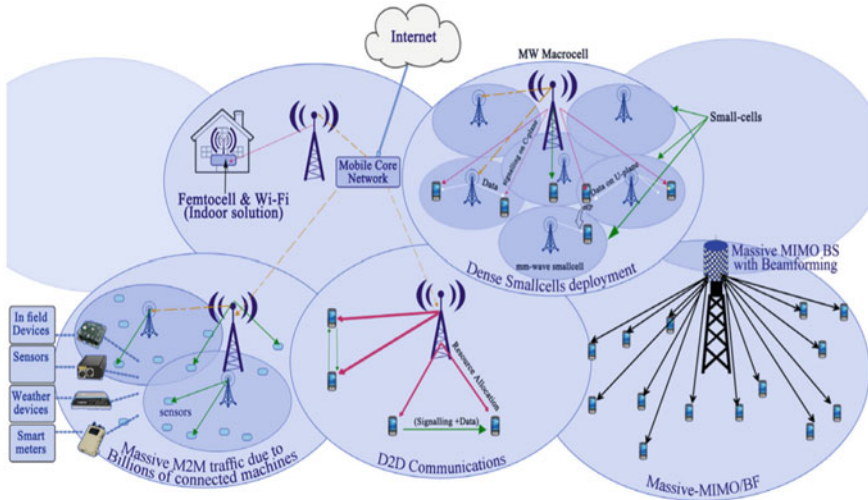


Fig. 2 Use of macro cell structure in 5G architecture [9]

Fig. 3 Features of 5G



**Constraints of Broadband Technology**

• **Fixed broadband**

- Despite having high-distance wireless modems/WiFi hotspots, standard broadband still does not provide the level of mobility that today’s consumers want.
- Fixed broadband deployment is not only Capex serious, it takes longer to deploy. This may delay the deadline for Telcos to go to market.
- India still has wireline broadband penetration. Therefore, standard broadband operation does not match the size/modules provided by the services.

**Table 1** Comparison of 4G and 5G [10]

Comparison	4G	5G
Technology	LTE, WiMAX	MIMO, mmwaves
Bandwidth	100 MHz	300 GHz
Access system	CDMA	BDMA
Applications	TV and mobile applications, smart devices	Medical procedures, smart agriculture, robots

- **4G LTE**

- Higher latency values in 4G prevent it from being used for industrial and work critical applications.
- In view of data hungry applications, rich content and billions of connected devices, the 4G network will not be able to handle the data speed expected in the future.
- 4G uses complex modulation techniques that allow the battery to drain faster with other factors such as coverage gaps and better data rates (compared to 2G/3G).

- **5G**

- 5G's data speed is anticipated around 10 Gbps. With such speeds, 5G will biggest user experience and revolutionize the mobility content available online.
- 5G network is designed for <1 ms latency. Therefore, the 5G major technology testing industries in conjunction with IoT are automotive, medical and manufacturing.
- 5G technology will move the mobile to the cloud based on the processing abilities of the handsets. Therefore, handsets are expected to have longer battery life than before.
- Provides services based on 5G network segmentation in a software-defined Networking (SDN)/Network Function Virtualization (NFV) environment, through which operators allocate network resources (slices) according to customer needs.
- 5G is anticipated to practice higher frequency bands (30–300 GHz), which will offer better performance, bandwidth scaling and lower interference [3].

Table 1 shows the comparison between 4 and 5G based on multiple factors such as the technology used, bandwidth, type of access system and applications.

### 3 Impact on Indian Economy

5G is set to be the future of wireless networking. This marks the beginning of a new era in communication. This will increase the bandwidth and increase the download speed exponentially, while at the same time significantly reducing the delay (time delay between an action and response). On a 5G network, the delay can be less than

a millisecond, which is 100 times better than 4G. Self-driving cars and the Internet of Things (IoT)—a network of connected devices that allow data to be collected and exchanged, for example, smart homes—are close enough to thank 5G development. 5G is believed to make the most drastic impact on the global economy compared with previous versions of cellular technology. Network operators are expected to spend 800 \$ billion on 5G networks between 2020 and 2025. The contribution by 5G in the global gross domestic product is expected to be 2.2 trillion by the year. Furthermore, 22 million jobs would be created in telecom sector by the year 2035 [11]. When the full economic benefits of 5G are realized around the world, 5G mobile technology can create trillions of products and services, from retail to education, transportation, entertainment and everything in between. As per I.H.S. Market study, 5G technology will have an impact on global GDP (between 2020 and 2035), equivalent to adding one economy to India's size in the current global economy. The value chain associated with 5G technology is \$3.5 trillion (in dollars today) production, and it will create 22 million new jobs. It added that the technology will help grow many economic sectors by providing 5G-enabled services. Most importantly, 5G-enabled services could create huge jobs in India and other countries. So it is going mainstream in 2021 [12].

Although the initial market penetration is estimated to be less after the rollout of 5G services for a few years, the rate of penetration is forecasted to rise increasingly to reach over 90% by the year 2040 as shown in Fig. 4.

mmWave spectrum plays a key role in enabling high-speed and ultra-low-latency features required by many 5G applications. India is benefiting significantly from mmWave 5G. For the period 2025–2040, it is estimated that mmWave 5G will provide \$150 billion in additional GDP to India. The manufacturing sector will see the biggest impact, accounting for about a fifth. With an impact of nearly \$4 billion, the healthcare sector is also benefiting greatly from mmWave 5G [13]. The economic impact of mmWave 5G is explained in Fig. 5.

## **4 Use Cases of 5G**

### ***4.1 Reliable Low Latency Communication***

Reliable low latency communication is required when the processes that are carried out require high accuracy with respect to time. The communication must be reliable as any disturbance in the network can be fatal for the stakeholders involved. This type of communication is generally required in healthcare where the medical procedures are carried out remotely. Vehicle to vehicle communication, autonomous driving and industrial robotics are some other use cases where the requirement of reliability is critical.

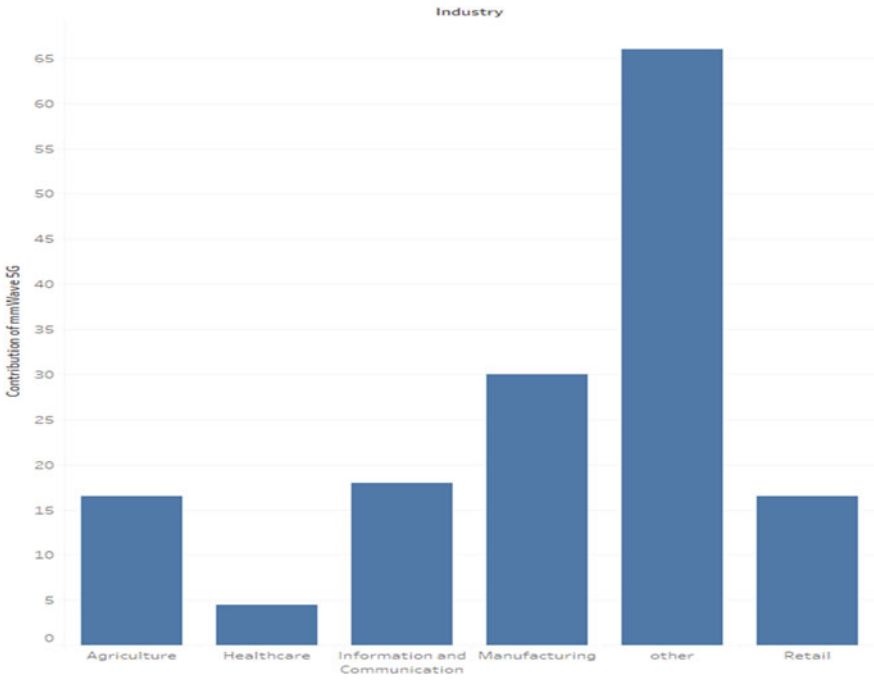


Fig. 4 Industry-wise contribution of mmWave 5G in India

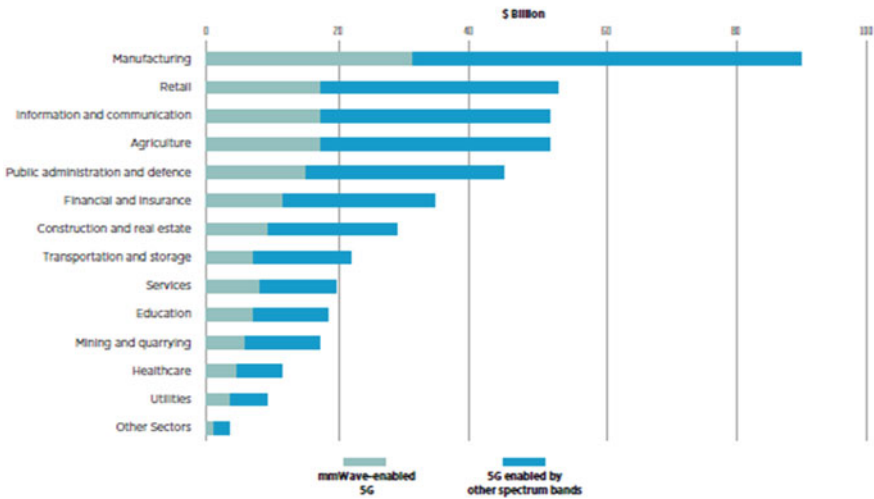


Fig. 5 5G and mmWave: economic impact in India by sector (2023–2040) [13]

## 4.2 *Machine to Machine Communication*

Machine to Machine Communication can be also considered as communication involved in the Internet of Things (IoT). With this type of communication, there is a potential to revolutionize industries by using advanced technologies that can work without any human intervention. This type of communication can be used in industries like agriculture and manufacturing.

## 4.3 *Enhanced Mobile Broadband (eMBB)*

With enhanced mobile broadband, an internet experience similar to a fixed broadband experience is possible. It would enable 360 video streaming, live augmented reality (AR) and virtual reality (VR) applications [14]. Major attributes that are associated with eMBB are higher user mobility, higher capacity and enhanced connectivity.

# 5 Impact on Indian Industries

## 5.1 *Healthcare*

With the number of patients increasing day by day, it is not possible for doctors to attend to all the patients in person. Moreover, the amount of doctors operating in rural areas is less as compared with the doctors operating in urban areas. 4G has already brought a lot of significant changes to the field of medicine. One significant change it brought that patients and doctors can communicate from their respective homes. This was very beneficial in today's dire times where people are noting venturing out more often due to the COVID-19 pandemic as well as it provides improved healthcare to the rural population. 5G networks having a higher data transfer rate and low latency aim to outperform 4G networks in this field.

In the field of healthcare, 5G can have the following use cases:

1. **Precision Medicine:** In precision medicine, medicine is prescribed according to the genetics of the patient, i.e. it is customized according to the needs of the patient. Making use of Artificial Intelligence (AI) algorithms we can make specific recommendations for the patients. Making use of such high-speed technologies people can quickly send data such as their blood sugar, cholesterol level to the doctor thereby saving a lot of money and time.
2. **Telemedicine:** With the help of telemedicine doctors living in cities can get connected very easily to people living in rural areas. This is highly beneficial for the people living in villages where the healthcare facilities are subpar. They also save a lot of money and time as they get treated remotely. Moreover, this

also enables the doctor to get connected to patients from faraway areas thereby increasing his profitability.

3. **Training using augmented or virtual reality:** AR and VR tools can be used to train surgeons or residents. These technologies provide a real-time hologram of the organ, which can be further dissected to see the internal areas of the organ. This is a very useful tool as the surgeons or residents can see and learn everything in a visual manner.

## 5.2 *Internet of Things*

The high speed of 5G networks makes them capable of harnessing the power of the computationally intensive AI algorithms using IoT devices. Some use cases are:

1. **Improving Big Data Processing:** 5G networks make use of the MIMO technology so as to reduce network congestion and traffic. By using a 5G intelligent IoT, huge amount of data can be easily processed in an optimized way. AI algorithms make sure that all the data transfer occurs in the best possible way while 5G makes sure that the speed of the entire system does not decrease. Moreover, the AI algorithms are capable of identifying any patterns that occurring in this huge volume of data thereby enabling huge businesses to make smarter decisions.
2. **Intelligent Networking:** In Intelligent networks, the AI algorithms decide the path the packet will take across the network. This is highly beneficial for the entire network as it reduces the time taken by the packet to reach its destination as well as maximizes the throughput of the network.
3. **Smart Transportation System:** By combining 5G with IoT-smart vehicles has become a possibility now. Cars now have an improved access to the internet. They come along with a lot of applications such as maps, music which are integrated with them. Besides entertainment, there are also a lot of safety features that have been incorporated. Sensors are placed on the rear so that the car does not crash into someone behind it. In terms of traffic management, sensors are fitted to traffic lights, which provide data that help the users to take routes, which will reduce their journey time.

## 5.3 *Agriculture*

The current generation of the cellular network does not provide high-speed data, especially in remote areas. Therefore, the current generation fails to meet the requirement of smart agriculture as the agricultural IoT devices require reliable and high-speed connections to track changes in real time. For farms with low internet connectivity, multiple high-cost devices such as MIMO, network slicing devices and small cells are required to maintain reliable connectivity. This makes smart farming unaffordable for most farmers. With the availability of 5G, transforming traditional farming

to smart farming would be more accessible to a larger number of farmers in India given the reduction in cost for the setting up network in the farm. Low-cost devices and low energy consumption and low-cost devices further optimize the cost [15].

Real-time monitoring of the farm is possible when stable internet connectivity is available. With help of wireless sensors factors such as humidity, moisture and temperature can be tracked. Using the values of these factors, automotive actions can be initiated to make the required changes. Irrigation can be automated by using soil moisture sensors. Sensors like DHT11 and LDR can collect information about the humidity, temperature and light intensity [16]. These data can be used to predict weather conditions. With smart devices, real-time monitoring of farms with large areas would be possible with 5G. Fire detection, intrusion detection and crop disease can be automated by using devices with image processing capabilities. With low energy consumption that would be enabled by the 5G technology, the life time of the smart IoT devices would also get longer. Figure 6 shows an example of an intelligent farm assistant with multiple functionalities that can be used for smart farming with the support of 5G.

Farms operating on a larger scale can upload data collected from various IoT sensors onto the cloud. These data can be used for decision-making through real-time analytics. Yield prediction, fertilizer recommendation and pesticide recommendation are some of the possible applications possible through data science. Figure 7 shows operations that are enabled by 5G for providing decision support using the data collected through sensors.

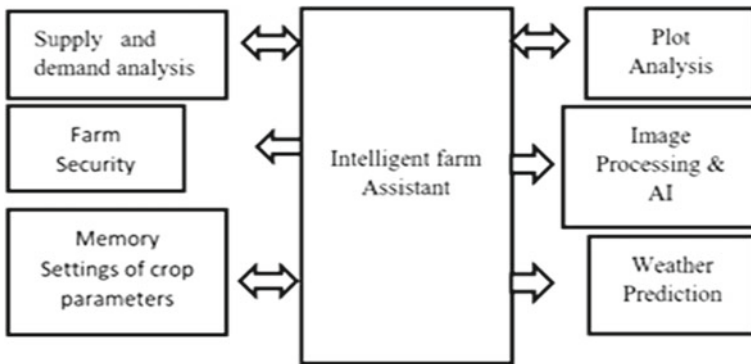


Fig. 6 Example of an intelligent farm assistant

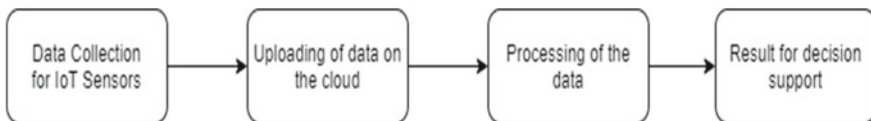


Fig. 7 Operations enabled by 5G for decision support



With the growing population to reach up to 10 billion in the year 2050, smart farming with 5G support would play a crucial role in meeting the increasing demand for farm produce. According to a UN report, a 70% increase in food production worldwide would be possible by using technologically advanced methods.

## **6 Challenges with 5G**

Although 5G technology is vital for digital transformation for multiple industries and contributing to the economic growth of India, there are several major difficulties in setting up 5G technology before it is available to all.

### **6.1 Low ARPU in India**

The monthly average revenue per user (ARPU) in India is one of the lowest among the countries with similar GDP. It was recorded to be 2.3 \$ a month for the year 2019 [17]. Furthermore, the debt on telecom operators in India is on some of the highest levels compared with other countries. These factors reduce the capacity of the telecom operator to make heavy investments in new technologies. Shared infrastructure for operation can be used to reduce the overall infrastructure cost incurred by a single telecom operator. Spectrum cost should be minimized by the policy-makers to increase the financial feasibility of 5G technology in India.

### **6.2 Compatible Devices**

As of 2020, 4G subscribers account for 81% of the total mobile users in India [18]. This number has drastically increased over the past years with the availability of low-cost internet. The Indian Smartphone market registered a year over the year growth rate of 42% in October 2020 [19]. Although the number of smartphone users is rising dramatically in India, the Indian smartphone market is highly price sensitive. For widespread acceptability of 5G, smartphones supporting 5G would be required to be sold at penetrative pricing for mass adoption and the migration of users from the existing 4G devices to 5G devices would be essential [20, 21].

### **6.3 Infrastructure Requirements**

Apart from the cost that is involved in installing the equipment required for 5G technology, the space required by the massive MIMO equipment is another important

factor that needs to be considered by the telecom companies. Apart from the spectrum requirements, other technical requirements include small cells and RAN cell towers, edge-computing capabilities, and security infrastructure [22]. A widespread fiber-optic network is required before the commercial release of 5G services.

## 7 Conclusion

The ever-increasing demand for the internet can be fulfilled in the future with the new generation of cellular technology. Furthermore, in the era of smart devices, machine learning and artificial intelligence reliable, high speed and energy-efficient network technology are necessary to make the digital transformation feasible in different industries. The transformation of agriculture, healthcare, IoT and other industries would be a driving factor for the economy of the country and the world at large. By overcoming the challenges of the infrastructure requirement with cost optimization and support of the government, the promising functionalities proposed by the 5G technology can be utilized by different industries and normal internet users.

## References

1. Eluyode OS, Akomolafe DT (2013) Comparative study of biological and artificial neural networks. *Euro J Appl Eng Sci Res* 2(1):36–46
2. 5G technology: an overview [Online]. <https://medium.com/@nagasanjayvijayan/5g-technology-an-overview-275cfb61cfd3>
3. 5G: the catalyst to digital revolution in India. Deloitte Analysis
4. Venkataramanan V, Kannan V (2017) Bit Error rate analysis of LTE physical layer with different channel models. *Int J Commun Antenna Propag (IRECAP)* 7(7):641
5. Guilhaume-Chaillet A, Munier C, Michaud M (2004) Microprocessor packaging strategy: reliability of various flip chip BGA packages on different printed circuit boards. In: 5th international conference on thermal and mechanical simulation and experiments in micro-electronics and micro-systems, EuroSimE. IEEE, pp 322–327
6. Mapare V, Shinde S, Latpate M, Kadam KP (2013) Employment of artificial neural network in manipulating design constraints of rectangular micro strip patch antenna. *Int J Recent Technol Eng (IJRTE)* 2(1). ISSN: 2277-3878
7. How much data is created every day [Online]. <https://techjury.net/blog/how-much-data-is-created-every-day/gref>
8. Venkataramanan V, Lakshmi S (2018) A case study of various wireless network simulation tools. *Int J Commun Netw Inf Secur (IJCNIS)* 10(2):389–396
9. Millimetre wave frequency band as a candidate spectrum for 5G network architecture: a survey—scientific figure on ResearchGate. [https://www.researchgate.net/figure/5G-network-architecture-comprises-macro-cells-MW-band-small-cells-mm-wave-band\\_fig14\\_329160131](https://www.researchgate.net/figure/5G-network-architecture-comprises-macro-cells-MW-band-small-cells-mm-wave-band_fig14_329160131)
10. Manikandan A, Venkataramanan V, Kavitha M, Parvathi S (2012) Performance analysis of LTE physical layer based on release 8&9 through simulink environment. *Int J Adv Technol Eng Res (IJATER)* 2(6):92–97
11. Adoption of 5G will boost the job creation by telecom sector [Online]. <https://telecom.economictimes.indiatimes.com/tele-talk/adoption-of-5g-will-boost-the-job-creation-by-telecom-sector/4078>

12. What is 5G and why it is important for India [Online]. <https://www.boomlive.in/fact-file/explained-what-is-5g-and-why-it-is-important-for-indias-economy-8982?infiniteScroll=1>
13. The impacts of mmWAVE 5G in India, GSMA intelligence, based on data from the UN, IMF and OECD, 2020 [Online]. <https://data.gsmainelligence.com/research/research/research-2020/the-impacts-of-mmwave-5g-in-india>
14. Venkataramanan V, Lakshmi S (2019) Hardware co simulation of LTE physical layer for mobile network applications. *Futur Gener Comput Syst* 99:124–133
15. Tang Y, Dananjayan S, Hou C, Guo Q, Luo S, He Y (2021) A survey on the 5G network and its impact on agriculture: challenges and opportunities. *Comput Electron Agric* 180:105895. ISSN 0168-1699. <https://doi.org/10.1016/j.compag.2020.105>
16. Doshi J, Patel T, Bharti SK (2019) Smart farming using IoT, a solution for optimally monitoring farming conditions. *Procedia Comput Sci* 160:746–751. ISSN 1877-0509. <https://doi.org/10.1016/j.procs.2019.11.016>
17. Forecast of smartphone users in India [Online]. <https://www.statista.com/statistics/467163/forecast-of-smartphone-users-in-india/>
18. Mobile-users-are-on-4g-phones-survey [Online]. <https://telecom.economictimes.indiatimes.com/news/81-of-indian-mobile-users-are-on-4g-phones-survey/74608766>
19. India's smart markets's YoY growth [Online]. <https://www.idc.com/getdoc.jsp?containerId=prAP47181020#:~:text=NEW%20DELHI%2C%20December%2017th%2C%202020,October%20shipping%2021%20million%20units>.
20. GSMA-5G-moves-from-hype-to-reality. International [Online]. <https://www.gsma.com/newsroom/press-release/gsma-5g-moves-from-hype-to-reality-but-4g-still-king/>
21. Tabassum R, Ahmed S (2020) Xiaomi invades the smartphone market in India. *Decision* 47:215–228. <https://doi.org/10.1007/s40622-020-00242-w>
22. 5G network infrastructure [Online]. <https://www.sdxcentral.com/5g/definitions/5g-network-infrastructure/>
23. Doubling farmers income [Online]. [https://niti.gov.in/writereaddata/files/document\\_publication/DOUBLING%20FARMERS%20INCOME.pdf](https://niti.gov.in/writereaddata/files/document_publication/DOUBLING%20FARMERS%20INCOME.pdf)
24. Accelerating India's future with 5G [Online]. <https://www.thehindubusinessline.com/opinion/accelerating-indias-future-with-5g/article9577944.ece>
25. Mobile average revenue per user by country [Online]. <https://www.statista.com/statistics/668966/mobile-average-revenue-per-user-by-country/>
26. mmWave 5G in India [Online]. <https://www.gsma.com/spectrum/wp-content/uploads/2020/11/mmWave-5G-in-India.pdf>

# Remote ECG Monitoring System Using IoT and Machine Learning



Bhavya Sekhani, Dishay Shah, and Vishaka Kelkar

**Abstract** This paper details the development of a remote ECG monitoring system to bridge the gap that currently exists between the health care industry and the use of modern technology. A compact ECG monitor has been developed using an ECG sensor and microcontroller ESP8266. The patient can connect the three probes at a strategic location on their arm or chest, and the ECG data and graph will be updated directly on the cloud platform. R-peaks in the ECG data are detected using the Hamilton Detection algorithm. These data are further analyzed and classified by Machine Learning algorithms such as convolution neural network (CNN). We achieved an accuracy of 96.6% and 98.86% on the test and training set, respectively, that proved the reliability of the system. Using this system, accurate deductions regarding the patients' health can be made by the doctor.

**Keywords** Electrocardiogram · Internet of Things (IoT) · Machine Learning (ML) · NodeMCU

## 1 Introduction

During these difficult times of COVID-19, the need and importance of remote health monitoring have increased tremendously. There is a severe lack of availability of doctors and regular health check-ups for parameters like oxygen level, pulse rate, and ECG values have become extremely important in order to ensure a healthy lifestyle [1]. Internet of Things is a new-age technology that uses a sensor-based network that is powered by Microcontrollers, and it can be used to transform the existing healthcare solutions.

---

B. Sekhani (✉) · D. Shah · V. Kelkar  
Department of Electronics and Telecommunication, Dwarkdas J. Sanghvi College of Engineering,  
Mumbai, India

V. Kelkar  
e-mail: [vishaka.kelkar@djsce.ac.in](mailto:vishaka.kelkar@djsce.ac.in)

IoT uses sensors to detect an extensive range of physical entities ranging from the moisture content in the soil to the air pressure of the car tire. It has enabled high-level connectivity between these devices. It has changed the healthcare industry, increasing efficiency, lowering costs, and putting the focus back on better patient care. Meanwhile, it continues to grow from building blocks of automation and machine-to-machine communication to the smallest sensors [2].

Fitness trackers, blood glucose monitors, and other wearables have gained a lot of importance. Consumers have also been receptive of the new technologies since it makes their life easier. There are currently 3.7 million medical devices currently in use, and the number is increasing exponentially. Physicians, doctors, and medical staff also support IoT in healthcare as it leads to effective management of patients, equipment, and staff. It also reduces the task load on doctors and reduces the overall treatment cost [3].

A remote ECG monitor powered by microcontrollers has been developed with an aim to make 'healthcare at home', easy. The data are recorded, saved, and processed using machine learning algorithms to detect any anomaly that might occur. The doctor can also access past and real-time health-related data of the patient remotely.

## 2 Literature Review

A smart healthcare system using Raspberry-Pi was developed to monitor patient health. The parameters being monitored were temperature, body movement and heart rate, blood pressure, and ECG. Smart sensors were connected to a cloud server where the data were stored. The Raspberry-Pi acted like a server and would automatically update the data on the website. The project, however, does not use Machine Learning algorithms, which is extremely important in analyzing the information accurately, thus predicting the potential cardiovascular problems the patient might be having [4].

A portable health monitoring system was proposed to provide a low-cost, wireless system, which allows the patient to monitor several health parameters remotely and quickly. The proposed machine learning algorithm provides the best accuracy than other Machine Learning approaches with minimum time complexity. Future studies consist of implementation of such a system with parallel processing with high-dimensional data using Hadoop or cloud environment [5].

The proposed system is that the data from the sensor network are collected and processed by the microcontroller. Health monitoring system, health state prediction system, and emergency alert system are the three major sectors of the proposal. The data stored in the database are tested using the KNN classifier, which classifies various states of the person's health. However, K-nearest neighbor algorithm has certain limitations such as the training set is large and takes a lot of space. For every test data, the distance should be computed between test data and all the training data. Thus, a lot of time may be needed for the testing process [6].

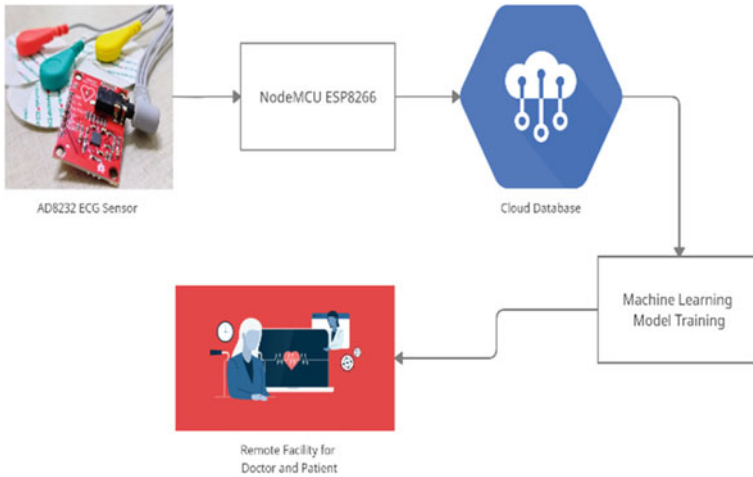


**Fig. 1** The remote ECG monitoring system mainly consisted of three sections. The microcontroller is used to collect the ECG data and graph and store it directly to a cloud database. The Machine Learning algorithms are used to analyze the same and present the results to both the patient and doctor

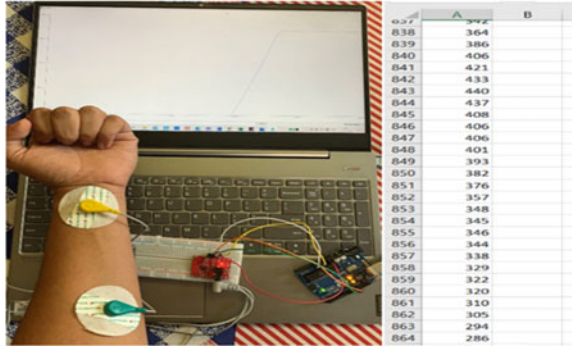
A new framework based on cloud and IoT-based health care applications for analysis and monitoring of serious diseases, specifically diabetes. UCI Repository dataset and medical sensors are used to generate medical data of people suffering from diabetes. A new classification algorithm has been proposed called Fuzzy Rule-based Neural Classifier for detection of disease and its severity. Real health records from various hospitals were used for this training. In this, direction could be the introduction of an effective security mechanism using novel cryptographic algorithms for providing better security to the medical data on cloud databases [7] (Fig. 1).

### 3 Methodology

#### 3.1 ECG Detection

The ECG sensor, AD8232 was connected to the Arduino and its three connecting nodes are placed at three strategic locations on the arm or chest (as shown in Fig. 2). The ECG graph is visualized using the serial plotter and serial monitor. Using the Teraterm software, the entire data are collected directly in the form of a CSV file (as shown in Fig. 2). This file can be now used for the Machine Learning stage.

**Fig. 2** ECG detection using Arduino Uno and Arduino IDE



### 3.2 Cloud Capability

On the udibots platform, the data get publish periodically and one can select the duration, span, type of graph, and frequency of the data required accordingly. We also could now achieve much higher levels of security as only the doctor or authorized personnel can access the patients' medical records in real time (Fig. 3).

The automated alert system, where certain family members, hospital staff, and your doctor will be receiving an alert as soon as an anomaly is observed in the patient's heart rate. The cloud platform has also analyzed machine learning much

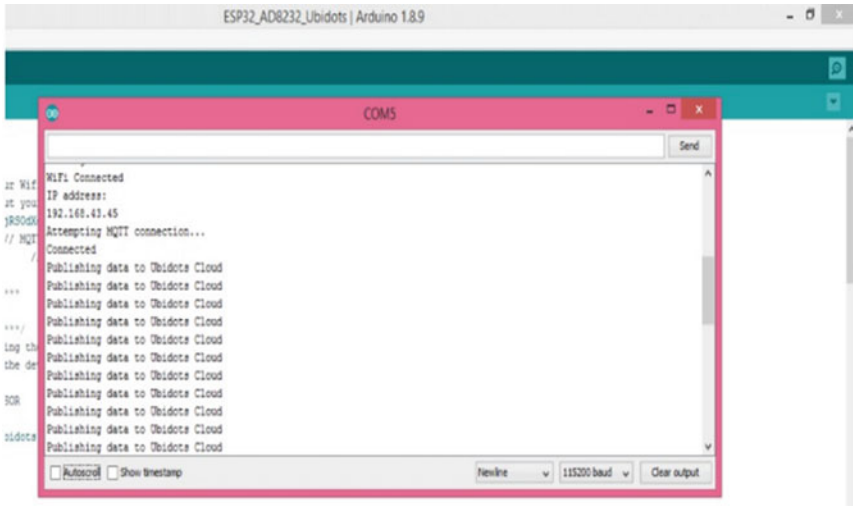


**Fig. 3** Enabling cloud function gave the entire process a more real-time experience. The AD8232 sensor was connected and powered by the NodeMCU. After entering the WifiSSID code and password, we use services like PubSub and MQTT communication protocol to publish the ECG data directly to the Udibits cloud platform



**Fig. 4** (As observed in Fig. 4), the ECG graph with P, Q, R, S, T points is plotted directly on cloud. This allows the doctor to observe the graph and make accurate deductions regarding the patients’ health. You can also observe the dashboard, which can help the patient and doctor to design and adjust it in a way convenient to them

easier as it can be directly done on the cloud platform, thus also increasing the real-time experience (Fig. 4).

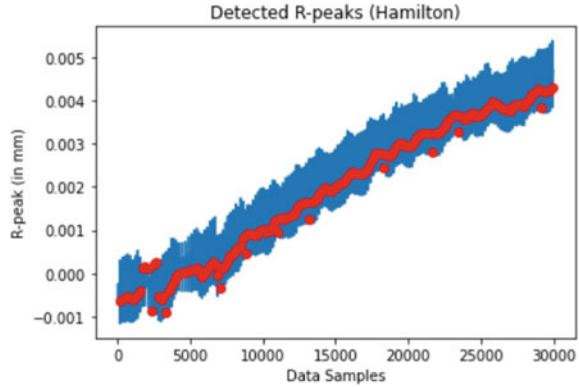
### 3.3 R-Peak Detection Algorithms

We have implemented six different algorithms to detect the R-Peaks from the ECG readings and compared the outputs obtained from these methods to determine the most efficient and accurate method. The six methods we used are Christov, Pan Tompkins, Engzee, 2 average, SWT Detector, and Hamilton. We then compared the outputs obtained from these algorithms to determine the most efficient and accurate method. Hamilton detection was found to be the most efficient algorithm.

The dataset we used comprised of several subjects. Each subject performed five different tasks for 2 min. These tasks were, sitting, taking a math test on a tablet, walking on a treadmill, running on a treadmill, and using a bike (Fig. 5).



**Fig. 5** Detected R-peaks using Hamilton detection algorithm



### 3.4 Machine Learning

In the final machine learning stage, we worked on classifying the patients’ heart-beat into five classes using Convolution Neural Networks (CNN). The five different classes are as follows: 1. Class 0 (N): Normal; 2. Class 1 (S): Super Ventricular Premature beat; 3. Class 2 (V): Premature Ventricular Contraction; 4. Class 3 (F): Fusion of ventricular beat; 5. Class 4 (Q): unclassified beat.

We used the MIT-BIH Arrhythmia data set.

- Number of samples: 109,446
- Number of categories: 5
- Sampling frequency: 125 Hz
- Classes: [‘N’: 0 ‘S’: 1 ‘V’: 2 ‘F’: 3 ‘Q’: 4].

The data represented are highly skewed (as observed in Fig. 6) and need to be cleaned before machine learning algorithms can be applied to it.

**Fig. 6** Over-sampled dataset

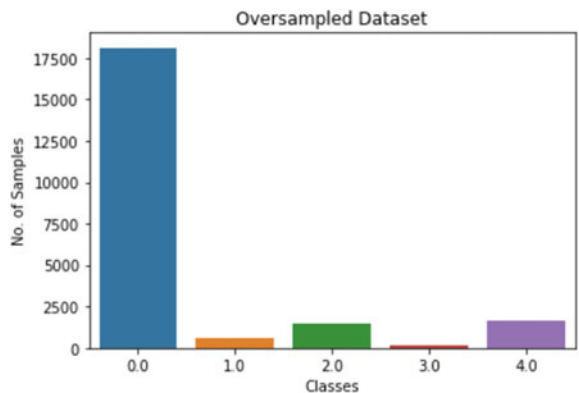
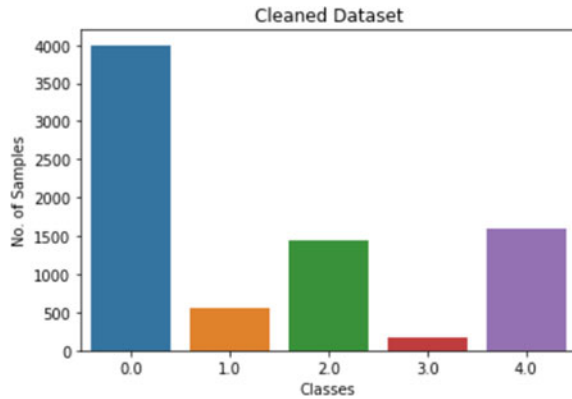


**Fig. 7** The following graph shows the new under-sampled data frame. The x-axis shows the output (column 187), and the y axis shows the count of samples belonging to each class



The graph above shows that the data are imbalanced. More than 80% of the data have been classified in Class 0. To obtain accurate and precise predictions, the data must be balanced. We performed under-sampling to reduce the number of rows of Class 0 as compared with the other classes (Fig. 7).

### 3.5 Model Training

For building this machine-learning model, we imported the TensorFlow (Keras) library on Python. Using the Scikit learn library, we split the data into a training set (90%) and a test set (10%), respectively. We have built a sequential model consisting of three 1D convolution layers, one max-pooling layer, one dropout layer, one flatten layer, and finally three dense layers. We used the ReLU (Rectified Linear Units) Activation Function in the convolution layer and the first two dense layers. In the last dense layer, we used the Softmax Activation Function. We compiled the model using Adam optimizer. We finally fit this model into the dataset and trained it for 10 epochs.

## 4 Results and Discussion

The model plateaus after performing more than 10 epochs. Hence, we concluded that 10 epochs were sufficient to determine the accuracy of our training set (Figs. 8, 9 and 10).

Certain insights obtained from graph: 1. Class 0, 2, 4 that are majority are well predicted (above 90%); 2. Class 1 and 3 that are minority are 80% correctly predicted.

On applying our machine learning model to the test set, we obtained an accuracy of 96.6%, which proved that the system was reliable and accurate.

**Fig. 8** The figure above shows the loss curve for the training set. The x-axis denotes the number of epochs while the y-axis denotes the loss

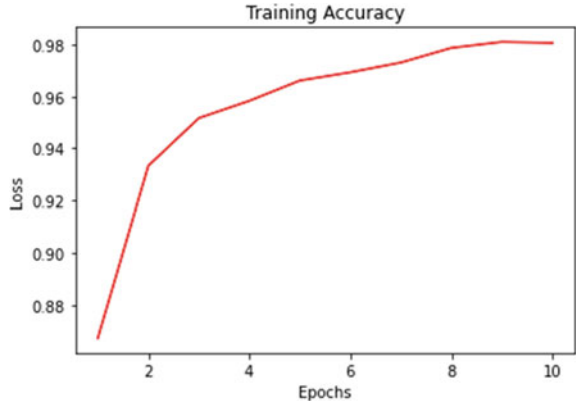


**Fig. 9** The figure presents the training accuracy graph of our model. We obtained an accuracy of 98.86% on the training set after performing 10 Epochs

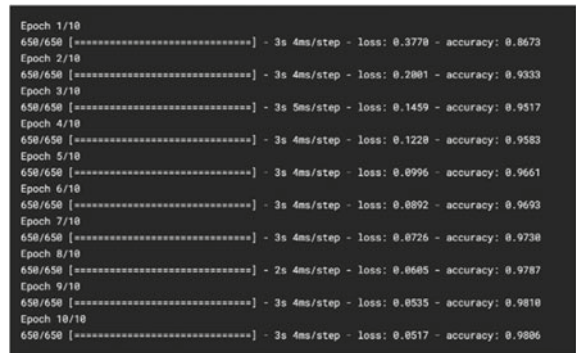
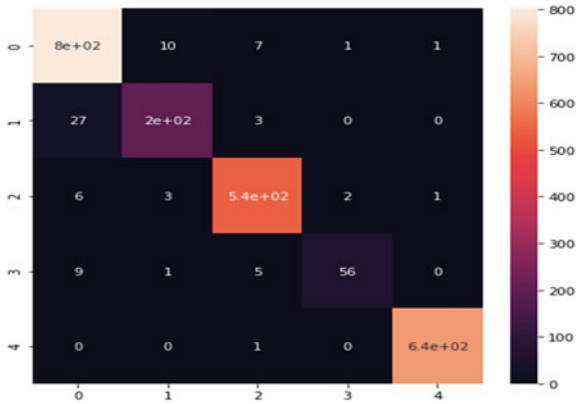


**Fig. 10** Given above is the Heat Map for the training set. This gives us the number of correct and incorrect predictions made by the training model for each class. Referring to the figure given below, we can see that for class 3, there are 56 true positives and 15(9 + 1 + 5) false positives



## 5 Conclusion

A remote ECG monitoring system can be useful to the health care industry as well as the general public. It ensures the health and safety of individuals and healthcare workers. It also helps save time, money and reduces effort. The system developed is compact, robust, and low cost and can help transform the health care industry in rural and urban areas likewise. Especially during the difficult time of COVID-19 pandemic, such a system can be extremely useful and crucial.

The future medical devices will be able to detect the wearers' psychological and physiological parameters, and regulations will be possible according to the data that have been collected. The devices could also pay more attention to the emotional state of the individual as well.

## References

1. Bhagat RB et al (2020) The COVID-19, migration, and livelihood in India: challenges and policy issues. *Migr Lett* 17(5):705–718
2. Carnaz G, Nogueira VB (2016) An overview of IoT and healthcare
3. Lee BM, Ouyang J (2014) Intelligent healthcare service by using collaborations between IoT personal health devices. *Int J Bio-Sci Bio-Technol* 6(1):155–164
4. Naik S, Sudarshan E (2019) Smart healthcare monitoring system using raspberry Pi on IoT platform. *ARPJ Eng Appl Sci* 14(4):872–876
5. Yadav SS, Jadhav SM (2019) Machine learning algorithms for disease prediction using IoT environment. *Int J Eng Adv Technol* 8(6):4303–4307
6. Priyadharsan DMJ et al (2019) Patient health monitoring using IoT with machine learning
7. Kumar PM et al (2018) Cloud and IoT based disease prediction and diagnosis system for healthcare using Fuzzy neural classifier. *Futur Gener Comput Syst* 86:527–534

# Cognitive Radio Networks: Path Toward Advanced Spectrum Sensing—A Survey



Pradnya Kamble and Alam N. Shaikh

**Abstract** Cognitive radio network has gained a lot of popularity in the era of wireless communication to overcome an issue of scarce bandwidth. Cognitive radio network (CRN) has opened with tremendous research areas toward the spectrum sensing and sharing. In this paper, we will see the different techniques used for the detection of primary user's (PU) activity and assign the spectrum to secondary user (SU) if the spectrum is unutilized by the primary user without interfering the primary user and utilized the spectrum efficiently. This paper is an attempt to through light on the primary idea of research work, which is going in the field of cognitive radio networks in wireless communication.

**Keywords** Cognitive radio networks · Spectrum sensing · Narrow band spectrum sensing · Wideband spectrum sensing

## 1 Introduction

Insufficient utilization of radio spectrum because of a fixed spectrum allocation and access techniques had resulted in a scare bandwidth problem as per the FCC Federal Communications Commission it has reported only 6% portion of the expensive radio spectrum is properly utilized, and remaining spectrum yes underutilized [1]. To solve this spectrum, scarcity problem intelligent communication technology is introduced is called as dynamic spectrum access (DSA) as an answer to the existing wireless technology, it allows unlicensed users to access the licensed spectrum band opportunistically without creating interference to the licensed users [2].

---

*Present Address:*

P. Kamble (✉)

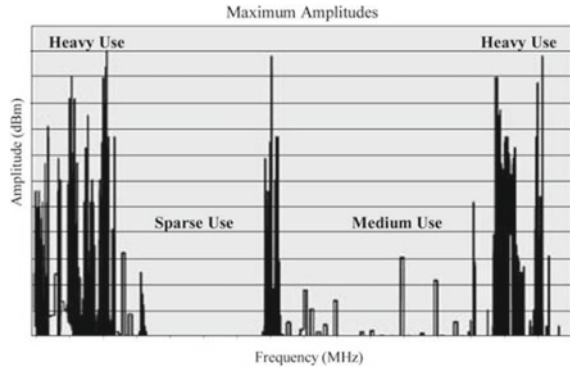
Department of Electronics and Telecommunication Engineering, K. J. Somaiya Institute of Engineering and Information Technology, Sion, Mumbai 400022, India

e-mail: [pkamble@somaiya.edu](mailto:pkamble@somaiya.edu)

A. N. Shaikh

Vasantdada Patil Pratishthan's College of Engineering, Sion, Mumbai 400022, India

**Fig. 1** Spectrum utilization  
[2]



Cognitive radio networks sense the environment and accordingly it changes their transmitter parameters such as frequency, modulation, frame structure. The work focuses on conventional spectrum sensing schemes named as energy detection matched filter detection and cyclostationary feature detection.

The key performance indicators of spectrum sensing techniques are addressed in terms of probability of primary user detection alarm (Pd) probability of miss detection (Pm), probability of false alarm (Pf) [3].

Figure 1 shows the utilization of spectrum over a large geographical area. The use of spectrum is more in some part of the spectrum while a large amount of spectrum is UN utilized as per the Federal Communications [1, 2].

A cross-layer design approach is more specifically used. To enhance the spectrum efficiency, spectrum sensing and spectrum sharing are used in cooperative manner, with respect to dynamic nature of underlying spectrum management, spectrum mobility functions along with transport routing medium access and physical layer functionalities are considered [2].

## 2 Working of Cognitive Radio Network

Joseph Mithola introduced a new technology named cognitive radio network (CRN), a CRN is a smart software-defined radio, which senses radio environment and detects unoccupied channels, and as per the requirement, it changes its transmitter or receiver parameters such as bandwidth, modulation, transmit power, operating frequency [3]. Cognitive radio network mainly has two types of users, primary users (PUs) and secondary users (SUs), licensed users are called as primary users those who have received license from government, non-licensed users are called as secondary users. Secondary users can access the available empty radio spectrum bands only if there is no primary user activity, secondary user must reconfigure their transmitter parameters for accessing the licensed channel, once the primary user activity is

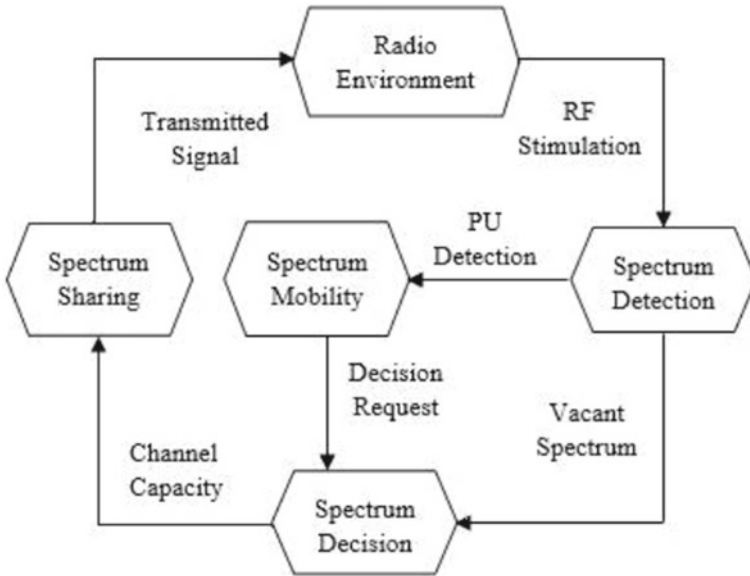


Fig. 2 Working of cognitive radio network [2]

detected, secondary user must leave channel immediately. Figure 2 shows the working of cognitive radio networks [3].

- **Spectrum Detection:** Cognitive radio network senses the radio environment and detects the available free spectrum band, which can be assigned to the secondary user.
- **Spectrum Decision:** Once the detection activity is over, available free bands need to be assigned to the secondary users based on the requirements of the secondary user.
- **Spectrum Sharing:** Spectrum band sharing is performed, a spectrum scheduling is performed between primary users and secondary users.
- **Spectrum Mobility:** Once the primary user activity is detected, secondary user must leave the spectrum and can perform handoff procedure to do any other free spectrum.

### 3 Features of Cognitive Radio

The next-generation technology enables the dynamic access of spectrum in an efficient manner. The important features of cognitive radio networks are as follows.

### **3.1 Cognitive Capability**

Cognitive capability is the ability of the radio technology to cognize the information from its RF environment, along with simple observing the power in a few frequency bands, its spatial and temporal variations are acquired to avoid interference to other users. Vacant spaces in the spectrum can be identified, and befitting operating parameters can be selected.

### **3.2 Reconfigurability**

Reconfigure ability facilitates the radio to dynamically adapt according to the radio environment for the transmission and reception of the information on pool of frequencies [2, 4].

## **4 Spectrum White Space or Hole**

The main aim of cognitive radio network is to get the best obtainable spectrum using the features of cognitive radio, white spaces are spread over a wideband of spectrum. Frequency spectrum is assigned to licensed users called as primary users; an important task is to share the licensed spectrum without interfering the other licensed users. Unutilized spectrum is called as white space or a spectrum hole, once the primary user activity is detected, the cognitive user must vacate the spectrum and move to another white space. CR models themselves changing their characteristics such as modulation type transmission power to abate the interference. Figure 3 shows the spectrum holes [5].

## **5 Spectrum Sharing Methodologies**

Cognitive radio network operates in two access modes, (1) overlay model and (2) underlay model, overlay cognitive radio network access opportunistically, divide spaces whereas underlay cognitive radio network access the grey spaces of radio spectrum under SINR limitations. Hybrid cognitive radio networks are formed by combining the underlay and overlay models. Figure 4 shows the overlay and underlay models [3, 5].



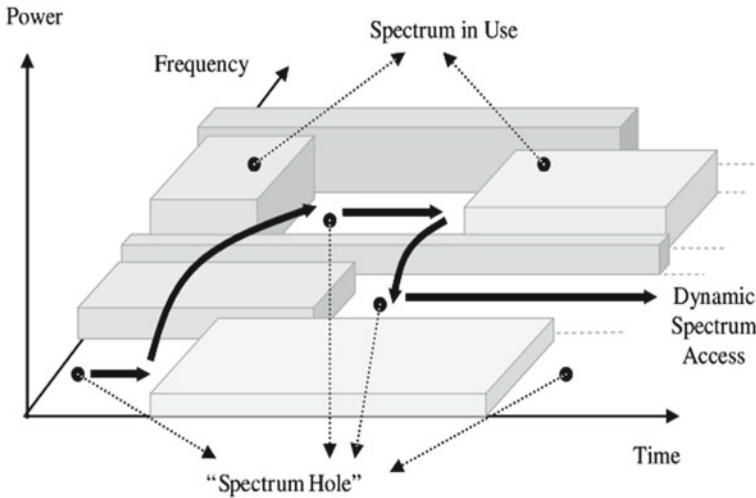


Fig. 3 Spectrum hole [2]

### 5.1 Overlay Model

In overlay approach as shown in Fig. 4a, the SU needs complete information about the PU’s signal and parameters. The main advantage of this scheme is that SUs can transmit the data at any power (without interfere to PUs). The SUs can make use of the PUs’ related information to remove the interference caused by PUs, using the approach like dirty power coding. SU can also help relay part to the PU’s final destination, and this supports to cancel the interference of PU [5].

### 5.2 Underlay Model

In underlay approach as shown in Fig. 4b, the SU can coexist with the PU as long as the SU transmits the data below a predefined interference threshold/interference temperature, the SU can spread its signal over a wide frequency band and can transmit the data below the noise floor of the PUs. The main feature of this paradigm is that it does not need to execute spectrum sensing process. Indeed, the SUs can transmit the data even in poor network conditions, where spectrum is being accessed all time by PUs. However, the SU must limit its transmission power to achieve certain interference threshold. Therefore, a SU is forced to bind its data transmission over small coverage. This paradigm can be more adequate because a wide range of spectrum is accessed by SUs. Complexity is the main disadvantage of this scheme, which may lead to difficulties in hardware implementation in CR networks [5].

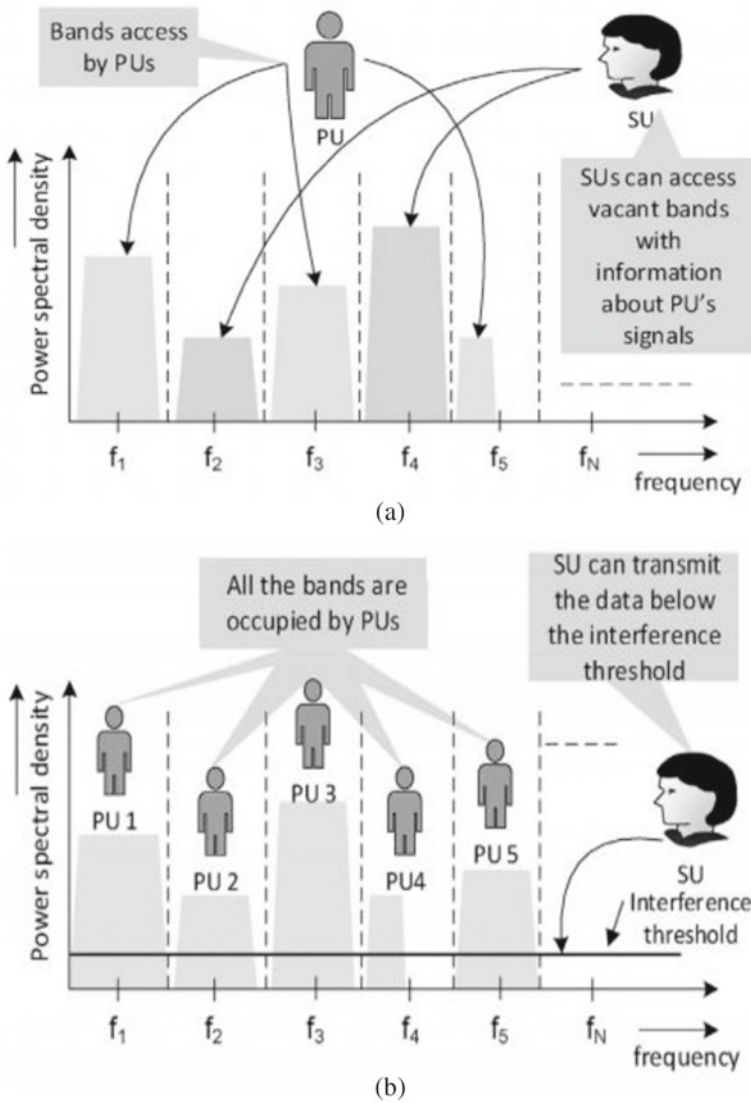


Fig. 4 a Overlay model and b underlay model [5]

## 6 Spectrum Sensing Methodologies

Extensive research is going on spectrum sensing techniques for cognitive radio networks while detecting the vacant spaces, significant challenges are faced because spectrum holes change over frequencies' locations and time. Spectrum sensing techniques are mainly classified into two categories, narrowband spectrum sensing and

wideband spectrum sensing. Narrowband spectrum sensing gets the status of single spectrum at a particular time whereas wideband spectrum sensing gets the status of wide frequency band, generally, the bandwidth of wideband exceeds the coherent bandwidth of the channel [4, 6]. Spectrum sensing methodologies can be broadly classified as conventional spectrum sensing techniques and advanced spectrum sensing techniques [7].

## **6.1 Conventional Spectrum Sensing Techniques**

In cognitive radio networks, secondary user must guarantee the availability of free spectrum. Two important designing parameters are considered, first activity of primary user before transmission of day and threshold value information to ensure and occupancy of spectrum. Various sensing schemes ... are defined [5, 8].

### **6.1.1 Energy Detection-Based Sensing Scheme**

In this detection scheme, receiver does not need to get any information related to primary user, certain threshold value is used to check the presence of primary user. This system is less complex in terms of implementation and computation. Threshold value is defined to decide between two hypotheses, to identify whether primary user is present or not, and the detection probability (Pd) false alarm (Pf) is used to calculate the performance of energy detection-based spectrum sensing method [4, 7].

A low Pd value would result in missing the presence of the primary user with high probability, which increases the interference to the primary user, a high Pf value would result in low spectrum utilization since false alarms increase the number of missed opportunities. The shadowing and the multi-path fading factors are considered for the energy detector. In this case, while Pf is independent of C, when the amplitude gain of the channel varies due to the shadowing/fading, Pd gives the probability of the detection conditioned on instantaneous SNR as follows [4].

### **6.1.2 Cyclostationary Feature-Based Sensing Scheme**

Modulated signal has some periodic nature, which can be considered in terms of pilots, cyclic prefixes, and preamble for synchronization purposes. Cyclic correlation function is used instead of power spectral density, as noise does not get correlated, noise and signal can be differentiated; it can be used to identify the periodicity to detect the random signal, i.e., noise. Cyclostationary feature-based sensing scheme especially best performs in low SNR conditions mobile application compared with energy detection-based sensing scheme. The limitation of cyclostationary feature-based sensing scheme is it takes more time to sense, consumes more power, and has complex processing [4, 7].

### **6.1.3 Matched Filter Detection Scheme**

When the secondary user has prior information of primary user signal, it is said to be optimal detection, which performs correlations between primary signals and detected signal, based on which it sets the correlation threshold. Matched filter acquires pre knowledge of primary users for detection, this scheme limits the performance.

### **6.1.4 Covariance-Based Spectrum Sensing Scheme**

It uses the correlation of received signals at various time periods unlike energy detection correlation of noise at different time periods will be zero advantage of covariance-based spectrum sensing is that it overcomes the noise occurred due to uncertainty. A covariance matrix-based spectrum sensing analysis can be used to receive considerable performance gain. The ability to overcome noise effect caused by uncertainty is remarkable. The advantage of covariance-based spectrum sensing scheme is that threshold value does not depend on SNR, which can overcome noise effect caused by uncertainty.

## ***6.2 Advanced Spectrum Sensing Techniques***

Conventional spectrum sensing schemes handle single frequency band but to identify multiple frequency bands the cooperation of secondary users is needed it also reduces the sensing time. Despite good results incorporation of secondary users, few problems faced like malicious secondary users reduce reliability also they affect the Corporation gain, few advanced spectrum sensing schemes are incorporated to overcome the problems of conventional spectrum sensing schemes [4, 7].

### **6.2.1 Wideband Compressive Spectrum Sensing Scheme**

When the signal bandwidth is greater than coherence bandwidth, this scheme is applied. On the basis of sampling frequency, there exist two types of approaches to realize wide-band spectrum sensing named as Nyquist-based and sub-Nyquist-based sampling. Based on sampling frequency, there are two categories in wideband spectrum sensing schemes named Nyquist-based sampling and sub-Nyquist-based sampling, which are used to identify the used and unused spectrum with sampling rate.

At first, it is assumed that wideband sensing is advantageous to sample desired spectrum by simple Nyquist sampling rate reduces the influences of malicious users. The drawbacks of this scheme are high sensing time, high computational complexity, and high sampling rates. The sub-Nyquist wideband spectrum sensing scheme over-

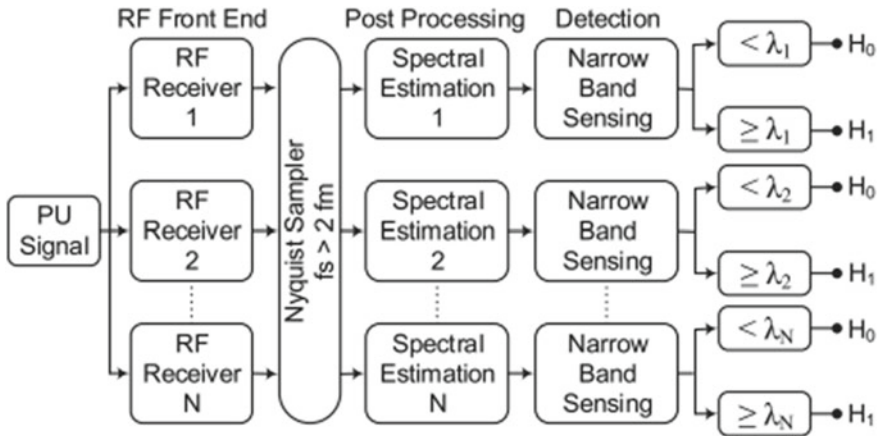


Fig. 5 Nyquist-based wideband spectrum sensing [5]

comes these limitations. Compressive sensing is proposed to identify the activity of primary user over a wide spectrum band and results a statistical characterization of the primary user signals in the band.

### Nyquist-Based Wideband Spectrum Sensing

In this frequency spectrum, sampling plays an important role. It follows the Shannon’s sampling theorem. Sampling rate is greater than the double of maximum frequency of signal ( $f_s > 2 f_m$ ). It is accurate, and cost-effective complexity is involved and requires high sampling rate (Fig. 5).

### Sub-Nyquist Wideband Spectrum Sensing

It is used to identify the spectrum spaces over a wideband, the sampling rate of sub-Nyquist sensing is less than Nyquist rate. Signals can be reconstructed using compressed sensing [5].

The limitations such as high sampling rate and system complexity involved in Nyquist-based sensing scheme are filtered by sub-Nyquist sampling-based scheme, which is the foundation for hardware implementation. This scheme is used to detect spectrum holes. Sampling rate of sub-Nyquist rate is less than the Nyquist rate. Compressed sensing scheme is used to reconstruct the signal. Implementation of compressive sensing in CR networks is explained in Fig. 6. The process is explained in four stages. In the first stage, to glean some observations, a sub-Nyquist sampler is essential. In the second, reconstruction of signal is functioned from the samples taken for observation. In the third, frequency band localization is performed to examine

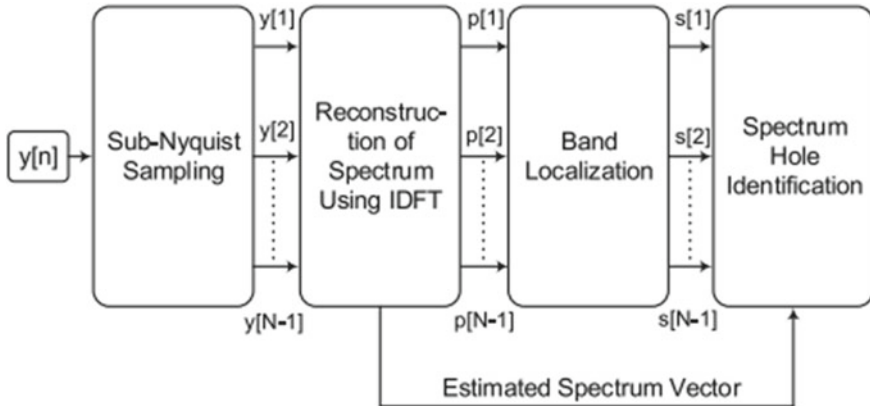


**Fig. 6** Sub-Nyquist band spectrum sensing [5]

sub-bands. In the fourth stage, spectrum hole identification is done to take final decisions in this sensing scheme.

### 6.2.2 Adaptive Compressive Spectrum Sensing

This scheme uses compressed samples to recover the wideband spectrum. It is used to remove signal acquisition; it also simplifies the threshold value to execute the spectrum sensing.

Sparsity removal is not required while sensing the wideband by using an appropriate number of measurements from consecutive time slots in adaptive compressive sensing scheme. It aims to detect and reconstruct it perfectly the original signal [4, 5].

## 7 Applications and Future Scope

Wireless network offers a great advantage for many applications. It is a key technology to establish a heterogeneous wireless network, cognitive radio networks support future multimedia applications like machine-to-machine communication, military applications, public safety applications, vehicular ad hoc networks. A customized spectrum sensing scheme can be designed for real-time scenario. Advanced spectrum sensing is aimed to improve the spectrum sensing in cognitive radio networks. Hybrid models can be incorporated to upgrade the performance of spectrum sensing. Artificial intelligence machine learning and deep learning are widely used in hybrid models. Synthetic data generation adversarial networking (GAN) makes cooperative spectrum sensing intelligent. In cooperative spectrum

sensing scheme, supervised and unsupervised learning classification is used. Adaptive threshold determination is a new scheme proposed in the field of spectrum sensing in cognitive radio networks to reduce the total error probability [9, 10].

## 8 Conclusion

In this paper, we have provided a brief review of working of cognitive radio networks, cognitive radio network functionality, concept of spectrum hole, spectrum sharing in cognitive radio networks, and spectrum sensing techniques in cognitive radio networks from conventional spectrum sensing techniques to the advanced spectrum sensing techniques. This paper is an attempt to brief about different spectrum sensing schemes in cognitive radio networks.

## References

1. Spectrum policy task force report. Federal Commun. Commission, Washington, DC, USA. Tech. Rep. 02-155 (2002)
2. Akyildiz IF, Lee W-Y, Vuran MC, Mohanty S (2006) NeXt generation/dynamic spectrum access/cognitive radio wireless networks: a survey. *Elsevier Comput Netw* 50(13):2127–2159
3. Kaur R, Buttar AS, Anand J (2018) Methods of hybrid cognitive radio network: a survey. In: *Proceedings of the 2nd international conference on electronics, communication and aerospace technology (ICECA 2018)*. IEEE conference record # 42487. IEEE Xplore. ISBN 978-1-5386-0965-1
4. Verma M, Baghel A (2020) An Article on prediction algorithm in cognitive radio networks using spectrum sensing. In: *2020 international conference on computer communication and informatics (ICCCI-2020)*, 22–24 Jan 2020, Coimbatore, India
5. Ali A, Hamouda W (2016) Advances on spectrum sensing for cognitive radio networks: theory and applications. *IEEE Commun Surv Tutor* 19(2). Second Quarter
6. Cai P, Zhang Y (2020) Intelligent cognitive spectrum collaboration convergence of spectrum sensing spectrum access and coding technology. *Intell Convergent Netw* 2020(1):79–98
7. Gupta MS, Kumar K (2019) Progression on spectrum sensing for cognitive radio networks: a survey classification & future research issues. *Springer J Netw Comput Appl* 143(2019):47–7
8. Venkateshkumar U, Ramakrishnan S (2020) Detection of spectrum hole from n-number of primary users using machine learning algorithms. *IET J Eng* 2020(5):175–188. eISSN 2051–3305
9. Wilzeck A, Dimitrov E, Tissen A (2011) Applications of cognitive radio systems for industrial wireless automation, CogART '11, 26–29 Oct, Barcelona, Spain
10. Qin Z, Li GY (2020) Pathway to intelligent radio. *IEEE Wirel Commun*

# Pattern Classification for Remote Sensing Images Using Back Propagation Network



Telagarapu Prabhakar, S. Sri Durga Kameswari, and A. Sudhakar

**Abstract** The technique of assigning land cover pattern classifications to pixels is known as image categorization. It may divide pictures into groups such as forest, urban, agricultural, and others. A large picture dataset with 21 land-use types is used to evaluate the methods in this study. In addition to standard techniques, there are comparisons to be made. Texture characteristics are extracted from remote sensing pictures using DWT at two degrees of decomposition. The UC-Mercedes dataset is used to explain the findings. At the approximation sub-band, 72 features are extracted at the second level of decomposition using DWT and other feature extraction methods. The data are classified using the supervised Back Propagation (BPN) approach, and the results with the highest accuracy are determined.

**Keywords** Remote sensing images · Preprocessing · Texture feature extraction · Classification · Back propagation (BPN)

## 1 Introduction

Remote sensing is a way of gathering information about various items all around the world without directly interacting with them. It is a method of gathering and analyzing non-instant geographic data to extract information about features and objects on the Earth's surface, oceans, and atmosphere. The existing Earth monitoring technologies (e.g., multi/hyper spectral [1], synthetic aperture radar, and so on) generate an increasing number of various types of aerial or satellite pictures with varying resolutions (spatial resolution, spectral resolution, and temporal resolution). This demands the use of intelligent earth observation via remote sensing pictures, which enables intelligent detection and categorization of Land use and Land Cover (LULC) conditions from airborne or space platforms. The goal of remote sensing image scene classification, a prominent issue in aerial and satellite image analysis, is to categorize scene pictures into a discrete set of significant LULC classes depending on their

---

T. Prabhakar (✉) · S. S. D. Kameswari · A. Sudhakar  
GMR Institute of Technology, Rajam, Srikakulam, Andhra Pradesh, India  
e-mail: [prabhakar.t@gmrit.edu.in](mailto:prabhakar.t@gmrit.edu.in)

© The Author(s), under exclusive license to Springer Nature Singapore Pte Ltd. 2022  
H. Vasudevan et al. (eds.), *Proceedings of International Conference on Wireless Communication*, Lecture Notes on Data Engineering and Communications Technologies 92, [https://doi.org/10.1007/978-981-16-6601-8\\_25](https://doi.org/10.1007/978-981-16-6601-8_25)

271

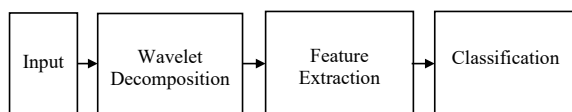


contents. Due to the importance of remote sensing image scene classification in a wide range of applications, such as natural hazards detection [2, 3], LULC determination, geospatial object detection, geographic image retrieval, vegetation mapping, environmental monitoring, and urban planning, significant efforts have been made in developing various methods for the task over the past decades. Low-level features or hand-crafted features were utilized in early scene categorization algorithms, with the goal of creating distinguishing human-engineering attributes locally or globally, such as shape, color, texture, and spatial information. In scene classification, representative features such as the scale invariant feature transform (SIFT), color histogram (CH), local binary pattern (LBP), Gabor filters, grey level co-occurrence matrix (GLCM), and histogram of oriented gradients (HOG) or their mixes are frequently employed. While these low-level characteristics work well on photos with uniform texture or spatial arrangements, they are restricted in their capacity to differentiate images with more difficult and complicated situations. This is since human engagement in feature design has a substantial impact on the efficacy of scene picture representation capability. Mid-level feature techniques, in contrast to low-level feature-based approaches, aim to calculate a holistic picture representation based on local visual characteristics such as SIFT, color histogram, or LBP of local image patches. The standard approach for generating mid-level features in remote sensing pictures is to first extract local characteristics of image patches and then encode them. Because of its simplicity and efficiency, the well-known bag-of-visual-words model is the most common mid-level approach and has been widely used for remote sensing picture scene categorization [4–6].

## 2 Methodology

Figure 1 shows the block diagram of Classification of Remote Sensing Images with the GLCM- and PCA-based features. The images acquired from UC Merced Land Use Dataset. This is a 21-class land-use image dataset meant for research purposes. There are 100 images for each image measures  $256 \times 256$  pixels of the following 21 classes: (1) Agricultural, (2) airplane, (3) baseball diamond, (4) beach, (5) buildings, (6) chaparral, (7) dense residential, (8) forest, (9) freeway, (10) golf course, (11) harbor, (12) intersection, (13) medium residential, (14) mobile home park, (15) overpass, (16) parking lot, (17) river, (18) runway, (19) sparse residential, (20) storage tanks, and (21) tennis court. This study used remote-sensed photos from the public source UC MERCEDES, with each class including 100 images, retrieved 72 texture characteristics in all directions after applying 2D Haar to the images, and computed

**Fig. 1** Classification of remote sensing. Images with wavelet and texture-based features



mean and range for each of them. BPN classification is utilized for the images on which wavelet transform and texture features are performed.

**Wavelet Decomposition**

Figure 2 shows two-level wavelet decomposition features. To denoise the pictures, a 2D Haar wavelet is used to each one. Mother wavelet is another name for Haar Wavelet. Wavelet is used for a limited amount of time. Wavelet is becoming more widely used in image processing and feature extraction. Wavelet transforms provide the advantages of multi-resolution and space-frequency localization. Because of the wavelet decomposition, layers of approximated and detailed coefficients are produced. A wavelet transform is a method for multi-resolution analysis and to analyze the signal in various frequency bands using this multi-resolution technique. The time–frequency representation is provided by the wavelet transform. It is not uncommon for a certain spectral component to be of special interest at any one time. The wavelet and resolution levels were used to apply the 2D-DWT to the remote sensed pictures, producing detail coefficient matrices and one approximation coefficient matrix. The high pass filter at each level provides fine details, whereas the low pass filter linked with the scaling function produces crude approximations. The high pass filter at each level provides fine details, whereas the low pass filter linked with the scaling function produces crude approximations.

**Texture Feature Extraction and Feature Selection**

This technique extracts the GLCM features and feeds them to the classifier. (1) Statistical Features are among the GLCM Features [7], (SF) (2) Matrices of Spatial Gray Level Dependence (SGLDM), (3) Statistics on grey level differences (GLDS), (4) Matrix of Gray Tone Differences in the Neighborhood (NGTDM), (5) Matrix of statistical features (SFM), (6) Texture energy measurement laws (LTEM), (7) Fractal texture dimension analysis (FDTA), (8) Fourier Power Spectrum (Fourier Power Spectra) (FPS), (9) Parameters for the shape, and (10) GRLLM (Gray Level

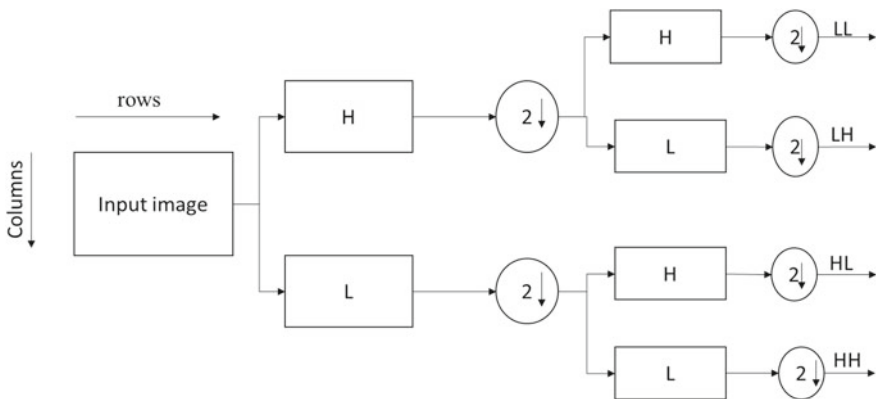


**Fig. 2** Two-level wavelet decomposition features

Run Length Matrix). After extracting GLCM texture features, must decrease the feature set using principal component analysis to get optimum features. As a result, the performance of the optimum features classifier may improve. PCA is defined as “an orthogonal linear transformation that transfers data to a new coordinate system such that the greatest variance by any projection of the data lies on the first coordinate (first principal component), the second greatest variance lies on the second coordinate (second principal component), and so on” (second principal component). PCA is a technique for reducing data dimensionality without sacrificing too much information, used in signal processing and picture compression, as well as machine learning. These optimum characteristics serve as an input vector for classifying remote sensing images [8].

### **Classification**

The BPN Supervised Classifier was utilized in this case. Back propagation algorithms have been commonly used for the training of artificial neural network. In this process, we used four hidden neurons and weights between the processing units are iteratively adjusted so that the overall error measure is minimized. BPN Classifier is an example of instance-based learning in which the training dataset is saved, and a classification for a new unclassified record may be determined by comparing it to the most similar records in the training set. This technique has been used to a wide range of applications, including data mining, statistical pattern identification, and image processing. Handwriting recognition and satellite pictures are examples of successful uses [9, 10].

## **3 Results and Discussion**

This article examines the texture feature extraction and classification method, which was trained on 50 remote sensing pictures per class and evaluated on 50 remote sensing images per class. Remote Sensed pictures are used to extract texture characteristics, used remote sensed pictures from the public source UC MERCEDES for this research, with each class including 100 images. After applying 2D Haar to the pictures, extracted 72 texture features in all directions and calculated the mean and range for all of them. Next utilized principal component analysis to choose the top 10 characteristics. Based on BPN classification, it is categorized in different classes using these optimum characteristics. For the pictures on which wavelet transform and BPN classification is used. Figure 3 shows the database of various classes.

### **2D Wavelet Decomposition**

#### **Preprocessing**

#### **Texture Feature Extraction**

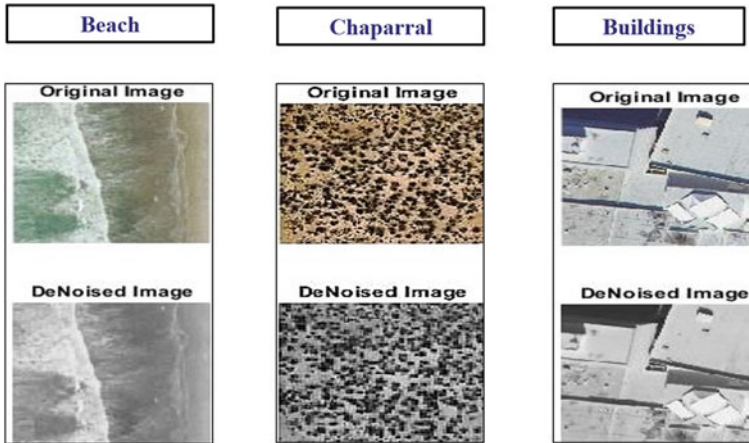
Figure 4 shows wavelet decomposition (tree level), and Fig. 5 shows denoised images. The GLCM features were extracted from with and without wavelet. Following feature



Fig. 3 Database of various classes



Fig. 4 Wavelet decomposition (tree level)



**Fig. 5** Denoised images

extraction, these features were provided to the best feature selection technique, which was utilized in this case to improve classification performance. From agriculture images, it is observed that there is a variation in Mean values of  $M\_entropy$ ,  $R\_entropy$ , low gray level run emphasis, and standard deviation of  $R\_ASM$ ,  $M\_difference$ ,  $R\_entropy$  for before and after applying wavelet to the images. From airplane images, it is observed that there is a variation in  $R\_entropy$ , low gray level run emphasis, and standard deviation of  $R\_ASM$ ,  $R\_SUM$ ,  $R\_entropy$  for before and after applying wavelet to the images. From Baseball Diamond images, it is observed that there is a variation in  $M\_contrast$ ,  $M\_difference$ ,  $R\_ASM$ ,  $R\_sum$  variance,  $R\_entropy$ ,  $R\_information$ , short-run low gray-level emphasis, and standard deviation of  $M\_contrast$ ,  $M\_difference$  for before and after applying wavelet to the images. Observed almost no change in some features like complexity, area, run length features radial sum, etc. From Beach images, it is observed that there is a variation in Mean values of  $M\_contrast$ ,  $M\_difference$ ,  $R\_ASM$ ,  $R\_sum$  variance,  $R\_entropy$ ,  $R\_information$ , short-run low gray-level emphasis, and standard deviation of  $M\_contrast$ ,  $M\_difference$ ,  $R\_sum$  variance,  $R\_ASM$ ,  $R\_information$  for before and after applying wavelet to the images. Figures 6 and 7 show GLCM-based Texture Feature Extraction of mean and standard deviation values of all features. Observed almost no change in some features like complexity, mean, texture related features, radial sum, etc. From buildings images, it is observed that there is a variation in Mean values of  $M\_contrast$ ,  $M\_difference$ ,  $R\_ASM$ ,  $R\_sum$  variance,  $R\_entropy$ ,  $R\_information$ , short-run low gray-level emphasis, and it is observed that there is a great variation in standard deviation values of before and after applying wavelet to the building's images in the feature perimeter. Observed almost no change in all features like complexity,  $M\_contrast$ ,  $R\_ASM$ , area, texture kernel features, radial sum. From Chaparral images, it is observed that there is a great variation in Mean values of before and after applying wavelet to the Chaparral image features  $R\_entropy$ . Observed

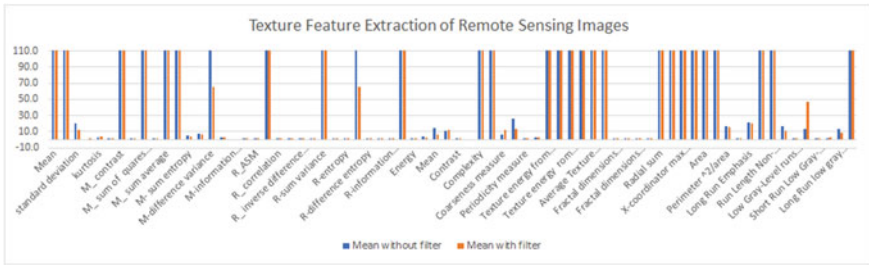


Fig.6 GLCM-based texture feature extraction of mean values of all features

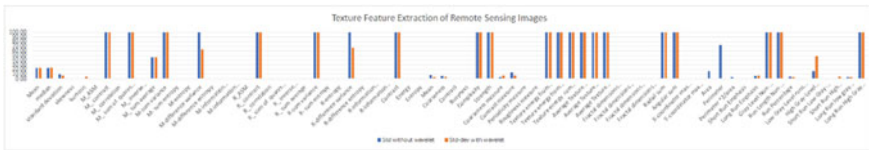


Fig. 7 GLCM-based texture feature extraction of standard deviation values of all features

almost no change in remaining features. It is observed that there is a great variation in standard deviation values of before and after applying wavelet to the Chaparral images in the features R\_ASM, R\_SUM, R\_entropy. Observed almost no change in some features like complexity, strength, radial sum, etc. From Dense Residential images, it is observed that there is a great variation in Mean values of before and after applying wavelet to the Dense Residential images features low gray level run emphasis. Observed almost no change in remaining features. It is observed that there is a great variation in standard deviation values of before and after applying wavelet to the Dense Residential image's features area, perimeter, R\_entropy. Observed almost no change in some features like complexity, texture kernel features, radial sum, etc. From Forest images, it is observed that there is great variation in Mean values of before and after applying wavelet to the Forest image features M\_difference, R\_ASM, R-sum variance, R\_entropy. Observed almost no change in remaining features. It is observed that there is a great variation in standard deviation values of before and after applying wavelet to the Forest image features M\_contrast, M-difference, run length features. Observed almost no change in some features like complexity, strength, radial sum, etc. From the Freeway images, it is observed that there is a great variation in Mean values of before and after applying wavelet to the Freeway image features low gray level run emphasis. Observed almost no change in remaining features. It is observed that there is a great variation in standard deviation values of before and after applying wavelet to the Freeway image features M\_contrast, perimeter. Observed almost no change in some features like complexity, M\_sum of squares, area, radial sum, etc. From the Golf court images, it is observed that there is a great variation in Mean values of before and after applying wavelet to the Golf court image features M\_contrast, M\_difference, R\_ASM, R-sum variance,

R\_entropy, R\_information. Observed almost no change in remaining features. It is observed that there is a great variation in standard deviation values of before and after applying wavelet to the Golf court image features M\_contrast, M-difference, short-run low gray-level emphasis. Observed almost no change in some features like complexity, strength, area, radial sum, etc. From the Harbor images, it is observed that there is a great variation in Mean values of before and after applying wavelet to the Harbor image features coarseness, low gray level run emphasis, perimeter, short-run low gray-level emphasis. Observed almost no change in remaining features. It is observed that there is a great variation in standard deviation values of before and after applying wavelet to the Harbor image features low gray level run emphasis, short run gray level emphasis. Observed almost no change in some features like complexity, M\_contrast, M\_sum of squares, radial sum, etc. From the Intersection images, it is observed that there is a less variation in Mean values of before and after applying wavelet to the Intersection image features coarseness, low gray level run emphasis, perimeter. Observed almost no change in remaining features. From the results of GLCM texture feature extraction, it is observed that there is a great variation in standard deviation values of before and after applying wavelet to the Intersection image features low gray level run emphasis. Observed almost no change in some features like M\_contrast, M\_sum of squares, texture kernel features, etc. From the Medium Residential images, it is observed that there is a great variation in Mean values of before and after applying wavelet to the Medium Residential image features low gray level run emphasis. Observed almost no change in remaining features. From the results of GLCM texture feature extraction, it is observed that there is a great variation in standard deviation values of before and after applying wavelet to the Medium Residential image features low gray level run emphasis. Observed almost no change in almost all features. From the Mobile Home Park images, it is observed that there is a little variation in Mean values of before and after applying wavelet to the Mobile Home Park image features coarseness, low gray level run emphasis. Observed almost no change in remaining features. From the results of GLCM texture feature extraction, it is observed that there is a great variation in standard deviation values of before and after applying wavelet to the Mobile Home Park image features R\_sum of squares (variance). Observed almost no change in most of the features in this class. From the Overpass images, it is observed that there is a great variation in Mean values of before and after applying wavelet to the Overpass image features low gray level run emphasis. Observed almost no change in remaining features. From the results of GLCM texture feature extraction, it is observed that there is a great variation in standard deviation values of before and after applying wavelet to the Overpass image features low gray level run emphasis, area. Observed almost no change in most of the features. From the Parking lot images, it is observed that there are fewer variations in Mean values of before and after applying wavelet to the Parking lot image features standard deviation, coarseness,  $\text{perimeter}^2/\text{area}$ , low gray level run emphasis. Observed almost no change in remaining features. From the results of GLCM texture feature extraction, it is observed that there is a great variation in standard deviation values of before and after applying wavelet to the Parking Lot image features low gray level run emphasis, area. Observed almost no change in most of the

features. From the River images, it is observed that there is a great variation in Mean values of before and after applying wavelet to the river image features  $M\_difference$ ,  $R\_ASM$ ,  $R\_sum$  variance,  $R\_entropy$ , low gray level run emphasis. Observed almost no change in remaining features. From the results of GLCM texture feature extraction, it is observed that there is a great variation in standard deviation values of before and after applying wavelet to the River image features  $M\_contrast$ ,  $M\_difference$ ,  $R\_ASM$ ,  $R\_sum$  variance,  $R\_entropy$ ,  $R\_information$ . Observed almost no change in some features like  $m\_sum$  of squares, textural kernel-related features, complexity, etc. From the Runway images, it is observed that there are fewer variations in Mean values of before and after applying wavelet to the Runway image features short-run low gray-level emphasis. Observed almost no change in remaining features. From the results of GLCM texture feature extraction, it is observed that there is a great variation in standard deviation values of before and after applying wavelet to the Runway image features short-run low gray-level emphasis, area. Observed almost no change in most of the features. From the Sparse Residential images, it is observed that there are fewer variations in Mean values of before and after applying wavelet to the Sparse Residential image's features  $R\_entropy$ , low gray level run emphasis. Observed almost no change in remaining features. From the results of GLCM texture feature extraction, it is observed that there is a great variation in standard deviation values of before and after applying wavelet to the Sparse Residential image features  $M\_contrast$ ,  $M\_difference$ ,  $R\_ASM$ ,  $R\_sum$  variance,  $R\_entropy$ ,  $R\_information$ . Observed almost no change in some features like  $m\_sum$  of squares, textural kernel related features, complexity, etc.

**Classification**

Features of with filter, without filter, with feature selection, and without feature selection are given to BPN classifier, and calculated performance metrics like accuracy, sensitivity, specificity. Table 1 listed the performance metrics of Back Propagation Network (BPN) classification.

$$Accuracy = \frac{TP + TN}{TP + TN + FP + FN} \tag{1}$$

$$Sensitivity = \frac{TP}{TP + FN} \tag{2}$$

**Table 1** Performance of back propagation network (BPN) classification

	Without wavelet and without feature selection (%)	Without wavelet and feature selection (%)	With wavelet and without feature selection (%)	With wavelet and with feature selection (%)
Accuracy	75	70	75	85
Sensitivity	90	60	70	87.7
Specificity	70	60	80	92.7



$$\text{Specificity} = \frac{TN}{TN + FP} \quad (3)$$

## 4 Conclusion

The database for this paper includes a truth image collection of 21 land-use classifications. The texture characteristics of the multiple class pictures are extracted using textural feature analysis, and the best features are utilized in the BPN classifier to describe the multiple classes, texture feature extraction with wavelet decomposition and BPN classification is the technique presented here. On the 2100 pictures, the suggested system is used. Other techniques are outperformed by the suggested methods. The suggested method's accuracy, sensitivity, specificity is 85, 87.7, 92.7%, respectively.

## References

1. Cheng G, Han J, Lu X (2017) Remote sensing image scene classification: benchmark and state of the art. *Proc IEEE* 105(10):1865–1883
2. Nogueira K, Penatti OAB, Dos Santos JA (2017) Towards better exploiting convolutional neural networks for remote sensing scene classification. *Pattern Recogn* 61:539–556
3. Nijhawan R et al (2019) A futuristic deep learning framework approach for land use-land cover classification using remote sensing imagery. In: *Advanced computing and communication technologies*. Springer, Singapore, pp 87–96
4. Tong X-Y et al (2018) Learning transferable deep models for land-use classification with high-resolution remote sensing images. Preprint at [arXiv:1807.05713](https://arxiv.org/abs/1807.05713)
5. Carranza-García M, García-Gutiérrez J, Riquelme JC (2019) A framework for evaluating land use and land cover classification using convolutional neural networks. *Remote Sens* 11(3):274
6. Xu L et al (2020) Multi-structure joint decision-making approach for land use classification of high-resolution remote sensing images based on CNNs. *IEEE Access* 8:42848–42863
7. Haralick RM, Shanmugan K, Dinstein I (1973) Textural features for image classification. *IEEE Trans Syst Man Cybern* 3(6):610–621
8. Huang H, Xu K (2019) Combing triple-part features of convolutional neural networks for scene classification in remote sensing. *Remote Sens* 11(14):1687
9. Jin B et al (2019) Object-oriented method combined with deep convolutional neural networks for land-use-type classification of remote sensing images. *J Indian Soc Remote Sens* 47(6):951–965
10. Telegarapu P (2011) Closed planar shape classification using nonlinear alignment. In: *2011 IEEE recent advanced in intelligent computational systems*

# Design of Spectral and Energy Efficient Network in Massive MIMO System



Suresh Dannana and Gottapu Sasibhushana Rao

**Abstract** Developments in 5G communication attract a more number of wireless application users. This will lead to increase high data traffic (voice, video, text). The present wireless network cannot support such demand. Since spectrum is scarce, spectrum efficiency should be improved to support such a huge demand for data traffic. Massive MIMO is a promising technology, it improves spectrum efficiency. However, size of hardware, digital signal processing techniques, and more number of antennas at base station consume more power. It leads to poor energy efficiency of wireless network. Network operators are putting in efforts to improve energy efficiency, in addition to that making these networks greener. This paper discusses the impact of increase in more number of antennas at base station, multiple number of user equipment on SE-EE trade-off. In addition, this paper discusses how the energy efficiency of wireless network can be improved by serving multiple UEs while simultaneously increasing the number of antennas at base station.

**Keywords** Spectral efficiency · Energy efficiency · Massive MIMO · Data traffic · Base station

## 1 Introduction

Current wireless networks are designed with massive MIMO technology to meet the demand of high data rates. These massive MIMO networks have capability of improving the spectral efficiency (SE) and energy efficiency (EE). Massive MIMO is consisting an array of more than hundred antennas having multiuser data transmission capability. All these antennas are spatially connected with user equipment (UEs). The spectral efficiency is improved with multiplexing gain. On the other hand, this improvement can be obtained by deploying more hardware [1, 2] (A/D converters,

---

S. Dannana (✉)  
GMR Institute of Technology, Rajam, Andhra Pradesh, India

G. S. Rao  
AU College of Engineering (A), Andhra University, Visakhapatnam, Andhra Pradesh, India

D/A converters), signal processing techniques (channel coding and modulation) and infrastructure (backhaul), in turn, increase the circuit power (CP) per each base station. This circuit power model is characterized by poor energy efficiency. This work is motivated by green radio communication [3, 4] and is a new research area, which deals the issues between technology and environment. In massive MIMO technology, more number of antennas are placed to ensure reliable communication between base station and user equipment. Massive MIMO can reduce the multipath fading effects, interference from other cells. The EE [1] is defined as the number of bits transferred per Joule of energy. The energy consumption in massive MIMO is of two types. One is transmission power consumption and second one is circuit power consumption [5, 6]. Transmission power consumption is extremely low in massive MIMO networks. On the other hand, circuit power consumption is high, due to size of hardware is more in massive MIMO. Circuit power will be increased due to increase in number of antennas [7] at base station. This will lead to decrease in energy efficiency.

To design good communication system maximum, Spectral Efficiency (SE) is the key factor, which depends on channel capacity. Spectral Efficiency is an average number of bits per each sample that can be reliably transmitted over the communication channel. Communication channel is a major source of noise. SE can be dependent on Signal to Interference Noise Ratio (SINR) as well as encoding/decoding schemes. Massive MIMO is using simple receive combine schemes such as Minimum mean square (MMSE), Maximal Ratio Combining (MRC), Zero Forcing (ZF). The MMSE receive combine technique maximizes not only instantaneous signal to interference noise ratio (SINR) but also minimizes the mean square error (MSE) in the data detection. At low SNR, MRC can achieve the same array gain as in the case of a single-user system. In ZF, the SINR can be made as high as desired by increasing the transmit power. Zero forcing is having more computational complexity compared with MRC, because it requires pseudoinverse of matrix. ZF performs as MMSE at high SNR, and at low SNR, MRC is performed as MMSE combine scheme. This paper focuses on the trade-off [8–10] between SE and EE as a function of multiple antennas at base station and number of user equipment. This paper explains, takes the base station antenna powers as well as user equipment powers in to account to compute the energy efficiency. Previous works are taken only transmitted powers. Here realistic power consumption model is considered to know the SE-EE trade-off.

This paper organizes in the following manner. System model and trade-off between SE and EE are discussed in Sects. 2 and 3, respectively. Simulation results are explained in Sect. 4. Section 5 comprises the conclusion of this paper.

## 2 System Model

In this paper, two cell wireless model is considered with massive MIMO systems at base station antenna. Consider Up Link (UL) model of wireless communication [11] is shown in Fig. 1. The channel  $h$  establishes connection between base station

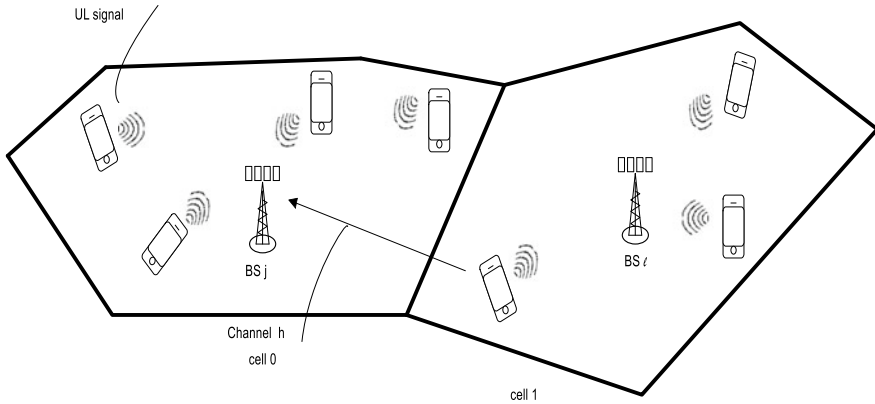


**Fig. 1** Two cell model

and user equipment. Assume that there is no co-operation between base stations in cellular system.

Consider fast fading channel model, to estimate the channel by using MMSE channel estimation scheme. In massive MIMO system, consider a base station with  $M$  number of antennas and  $K$  number of user equipment’s with one antenna. Assume  $M \gg K \gg 1$ .

The received UL signal  $y_j$  at base station  $j$  can be modeled as

$$y_j = \sum_{l=1}^L \sum_{k=1}^{k_l} h_{lk}^j x_{lk} + w_j \tag{1}$$

where,  $w_j$  is Gaussian noise with mean of zero and variance  $\sigma_{UL}^2$ . The uplink transmitted signal from UE  $k$  cell in cell  $l$  is denoted by  $x_{lk}$  and  $h_{lk}^j$  is channel gain between UE  $k$  in cell  $l$  and BS in cell  $j$ .

(i) Coherence Block structure

In coherence block structure [7], all UEs send their pilot sequences simultaneously followed by UL and DL data [12]. Consider a transmission model where time–frequency resources consist  $T_c$  coherence time, and bandwidth is  $B_c$  Hz. The coherence block model is shown in Fig. 2. This coherence block consists  $\tau_c = B_c T_c$  number complex-valued transmission symbols for both data and pilot signaling.

Each coherence block is operated in TDD mode. Coherence block contains  $\tau_p$  UL pilot signals  $\tau_u$  Data signals and  $\tau_d$  DL data signals. Here  $\tau_c = \tau_p + \tau_u + \tau_d$ , the fraction of UL and DL data can be selected based on the network traffic characteristics, while  $\tau_p$  is a design parameter.

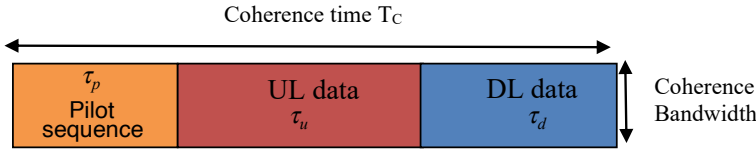


Fig. 2 Uplink coherence block

### 3 Trade-Off Between SE and EE

The energy efficiency of wireless network is defined as spectral efficiency [8, 9] obtained per one unit of power expended (in Joules). Generally, by increasing number of antennas at base station in massive MIMO can enhance the SE. It can be happened by deploying more hardware, signal processing techniques, and large infrastructure. In turn, all these can increase the circuit power and hence EE is reduced. Hence, there is a trade-off between SE and EE. However, at particular values of antennas at base station and number of user equipment, there is a chance to get maximum EE without sacrificing SE.

In this paper, SE-EE trade-off is discussed for up-link massive MIMO system. Certain methods such as multiplexing and increasing number of antennas at each base station are considered to get the trade-off. Once the number of antennas is fixed, other parameters such as transmitted power required to send signals, number of end users, number of pilot signals to get SE-EE trade-off.

The energy efficiency is defined as follows

$$\eta = \frac{SE}{PC} = \frac{SE}{ETP + CP} \tag{2}$$

where, ETP is effective transmit power, and CP is circuit power required for control signaling.

(i) Impact of increase in antennas at base station

To understand the impact of multiple base station antennas on trade-off between SE and EE, consider network model as shown in Fig. 1 under the assumption of  $M$  number of base station antennas and  $K = 1$  number of users in each cell. Consider MRC combine scheme at the receiver. Then, from channel capacity of wireless network, the spectral efficiency  $\zeta$  is defined as

$$\zeta = \log_2 \left( 1 + \frac{P_u}{\sigma_{UL}^2} (M - 1) \beta \right) \tag{3}$$

where,  $p_u$  is up link transmit power,  $\sigma_{UL}^2$  is noise power, and  $\beta$  is channel gain of active UE. To evaluate impact of multiple BS antennas on energy efficiency consider

a power consumption model with circuit power (CP) as  $P_f$  and  $ETP = \frac{P_u}{\mu_{PA}}, P_{BA}$  is power consumed by circuit components of base station antennas. Where  $\mu_{PA}$  is power amplifier efficiency.

$$\eta = \frac{\zeta}{PC} = \frac{\log_2\left(1 + \frac{P_u}{\sigma_{UL}^2}(M - 1)\beta\right)}{\frac{P}{\mu_{PA}} + P_f + MP_{BA}} \tag{4}$$

From Eq. (3), transmitted power  $p$  can be

$$p = \frac{(2^\zeta - 1)\sigma_{UL}^2}{(M - 1)\beta} \tag{5}$$

Therefore, energy efficiency is

$$\eta = \frac{\zeta}{PC} = \frac{\zeta}{\frac{(2^\zeta - 1)\sigma_{UL}^2}{(M - 1)\mu_{PA}\beta} + P_f + MP_{BA}}$$

$$\eta = \frac{\zeta}{PC} = \frac{\zeta}{\frac{(2^\zeta - 1)C_0}{(M - 1)} + P_f + MP_{BA}} \tag{6}$$

where,

$$C_0 = \frac{\sigma_{UL}^2}{\mu_{PA}\beta}$$

From Eq. (6), it is observing that trade-off between SE and EE is monotonic decreasing function. An increased SE always comes at the cost of a decreased EE.

To get the optimal point of EE and SE take the derivative of Eq. (6) with respect to  $\zeta$  and equate it to zero.

$$\zeta^* = \frac{W\left(\frac{(M - 1)}{C_0 e}(P_f + MP_{BA}) - \frac{1}{e}\right)}{\log_e 2} \tag{7}$$

Therefore, the optimum EE can be

$$\eta^* = \frac{(M - 1)e^{-W\left(\frac{(M - 1)}{C_0 e}(P_f + MP_{BA}) - \frac{1}{e}\right) - 1}}{C_0 \log_e 2} \tag{8}$$

Equations (7) and (8) provide  $\zeta^*$ , and  $\eta^*$  in closed form, hence it can be analyzed, how both are affected by system parameters. Since  $W(y)$  is an increasing function hence  $SE^*$  increases not only with  $M$  (number of base station antennas) but also with

powers  $P_f$  and  $P_{BA}$ . From Eq. (8), it can be observed that optimum EE decreases with increasing of  $P_f$ ,  $P_{BA}$  and number of base station antennas ( $M$ ).

(ii) Impact of increase in User Equipment at cell

To understand the impact of number of User Equipment (UE), consider a network model with SDMA transmission technique,  $K$  number of users in each cell and  $M$  number of base station antennas. Consider relative inter-cell interference coefficient as  $\beta'$ .

The spectral efficiency SE is

$$\zeta = \log_2 \left( 1 + \frac{M-1}{(K-1) + K\beta' + \frac{\sigma_{UL}^2}{p\beta}} \right) \quad (11)$$

where,  $p$  is transmit power,  $\beta$  is channel gain of active UE, and  $\sigma_{UL}^2$  is variance of noise.

The corresponding energy efficiency can be

$$\eta = \frac{K\zeta}{K \left( \frac{M-1}{2^{SE}-1} - K\beta' + 1 - K \right)^{-1} C' + CP} \quad (12)$$

where,  $C' = \frac{\sigma_{UL}^2}{\mu_{PA}\beta}$ , the circuit power  $CP = P_f + MP_{BA} + KP_{UE}$ ,  $P_{UE}$  is power required by each single antenna. To get the optimal point of EE and SE take the derivative of Eq. (12) with respect to SE and equate it to zero.

The optimum energy efficiency can be obtained as

$$\eta^* = \frac{1}{\left( 1 - \left( \frac{2^{\zeta^*}-1}{M-1} \right) (K\beta' - 1 + K) \right)^{-2} \frac{C' \log_e 2}{M-1} 2^{\zeta^*}} \quad (13)$$

Equation (13) shows the impact of multiple UE's and inter-cell interference on SE-EE trade-off. As inter-cell interference and number of UE's increase, the degradation of EE for a given SE is observed from Eq. (13).

## 4 Results

Trade-off between Spectral Efficiency (SE) and Energy Efficiency (EE) is shown in Fig. 3. Impact of fixed power is illustrated in Fig. 3. Here uplink of Wiener model is considered, with assumption of number of User Equipment (UE) ( $K$ ) is one and no interference signal from other cells. Trade-off is observed for number of base station antennas  $M = 15$ , power amplifier efficiency  $\mu_{PA} = 0.4$ , fixed powers

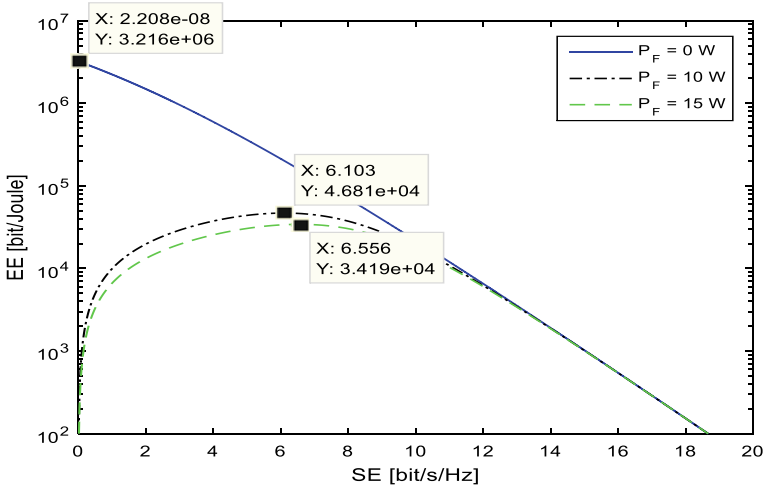


**Fig. 3** SE-EE trade-off at different values of fixed power  $P_f$

$P_f \in \{0, 10, 15\}$  Watts and base station antenna power  $P_{BA} = 0$  Watt. From Fig. 3, it is observed that if  $P_f = 0$ , there is a monotonic decreasing trade-off between EE and SE. If  $P_f > 0$ , then energy efficiency is unimodal function that increases for values of SE such that  $\frac{(2^S-1)C_0}{(M-1)} < P_f$  and decreases to zero as  $\frac{\zeta}{(2^S-1)}$  for larger values of SE. As  $P_f$  is increasing, it can be observed that SE-EE curve becomes flatter. From Fig. 3, it is observed that for  $P_f = 10$ W, at SE = 6.103 bit/s/Hz maximum EE is observed, later it is decreased to zero. Similar observation is made for  $P_f = 15$ W, maximum EE is obtained for SE = 6.556 bit/s/Hz.

Trade-off between Spectral Efficiency (SE) and Energy Efficiency (EE) is shown in Fig. 4, by considering similar conditions of Fig. 3, except  $CP = P_f + M P_{BA}$ . The SE-EE trade-off is unimodal function of  $M$ . Figure 4 is observed at different number of base station antennas such as  $M = 2, 20, 150$ , respectively. From Eq. (11), energy efficiency is linearly decreasing function of number of base station antennas as it increases the more hardware and, thus higher circuit power.

Table 1 illustrates the SE-EE trade-off for different values of  $M$ . From Table 1, it is observed that highest EE is achieved for  $M = 20$  as  $1.949 \times 10^4$  bit/Joule. For  $M = 150$ , EE value 6497 bit/Joule is achieved. Increasing number of antennas monotonically improves the SE, which even grows without bound as  $M$  tends to infinite, but the positive effect on EE is vanished.

Figure 5 shows the EE vs SE with number of UE's  $K = \{5, 15, 40\}$  and strength of inter-cell interference  $\beta'$  as  $-3$  dB. To get this result, considered  $M = 15$ ,  $\mu_{PA} = 0.35$ ,  $P_{fa} = 8$ W,  $P_{BA} = 0.9$ W and  $P_{UE} = 0.45$ W. The SE-EE trade-off curve is unimodal function of  $K$  and  $\beta'$  (since inter-cell interference is function of  $\beta'$ ). SE is slowly increasing function of  $M$  but each additional UE increases the power consumption. Therefore, the degradation in EE for a given SE increases as  $K$  and  $\beta'$  increases.



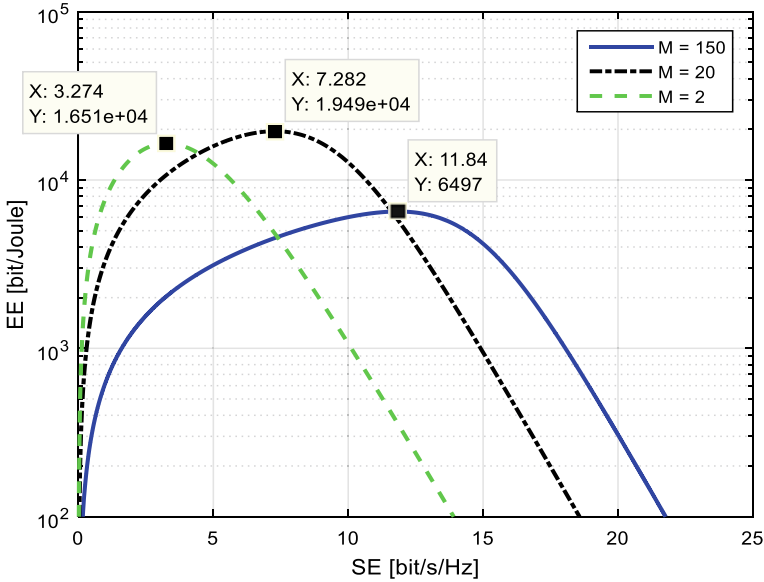


Fig. 4 SE-EE trade-off for different values of base station antennas

Table 1 Impact of number of base station antennas on SE-EE trade-off

S. No.	SE (bit/s/Hz)	EE (bit/Joule)		
		M = 2	20	150
1	0	0	0	0
2	2	$1.37 \times 10^4$	6668	1278
3	3	$1.64 \times 10^4$	$1.007 \times 10^4$	1920
4	7	4827	$1.949 \times 10^4$	4464
5	10	1012	$1.27 \times 10^4$	6044
6	12	338	6497	6497
7	16	0	516	2858

Table 2 illustrates the impact of number of users on SE-EE trade-off. With considering setup maximum EE as 2.709 bits/Joule is achieved at  $K = 15$ . For  $K = 40$ , it is observed from Table 2 that EE value  $2.257 \times 10^4$  bits/Joule is observed. As number of UE's increases, the relative strength of inter-cell interference and hardware increases, which, in turn, decreases the EE.

Figure 6 shows the impact of ratio  $M/K$  on SE-EE trade-off by taking  $K = 10$ . By adding the proportional number of base station antennas to counteract the increased interference, more EE can be achieved. But this ratio would increase the power consumption. So optimal pair  $(M, K)$  is required to attain maximum EE.

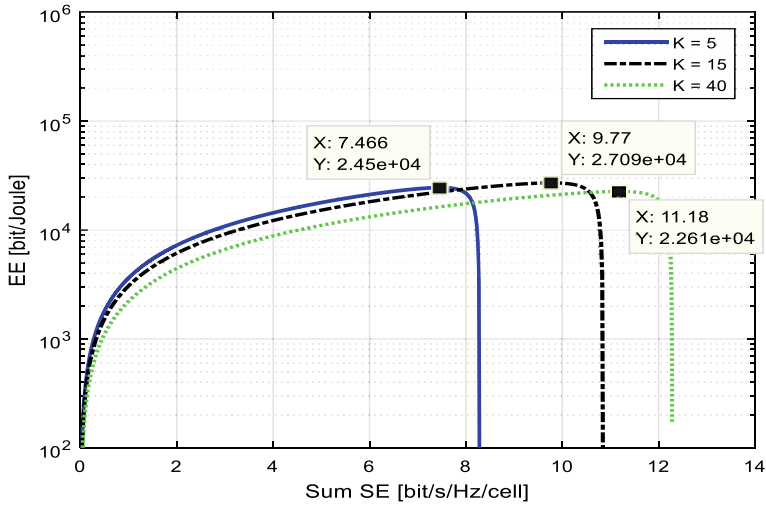


Fig. 5 SE-EE trade-off for different values of users

Table 2 Impact of number of users on SE-EE trade-off

S. No.	SE (bit/s/Hz/cell)	EE (bit/Joule)		
		$K = 2$	$K = 15$	$K = 40$
1	0	0	0	0
2	2	7336	6310	4367
3	4	$1.44 \times 10^4$	$1.21 \times 10^4$	8986
4	6	$2.13 \times 10^4$	$2.139 \times 10^4$	$1.334 \times 10^4$
5	7	$2.45 \times 10^4$	$2.10 \times 10^4$	$1.551 \times 10^4$
6	9	0	$2.709 \times 10^4$	$1.949 \times 10^4$
7	14	0	0	$2.257 \times 10^4$

Table 3 shows the SE-EE values at different  $M/K$  ratios. From Table 3, it is observed that at  $M/K = 3$ , maximum EE is attained as  $4.196 \times 10^4$ . For  $M/K = 9$ ,  $E$  value  $3.236 \times 10^4$  is observed.

### 5 Conclusion

In this paper, trade-off between SE and EE in massive MIMO network is discussed. Spectral efficiency can be increased by deploying more antennas at base station and increase in UEs. To place more antennas at base station, large number of A/D, D/A converters, power amplifiers, coding and decoders, channel estimators are required. It leads to more power consumption. Hence, it reduces the energy efficiency. In

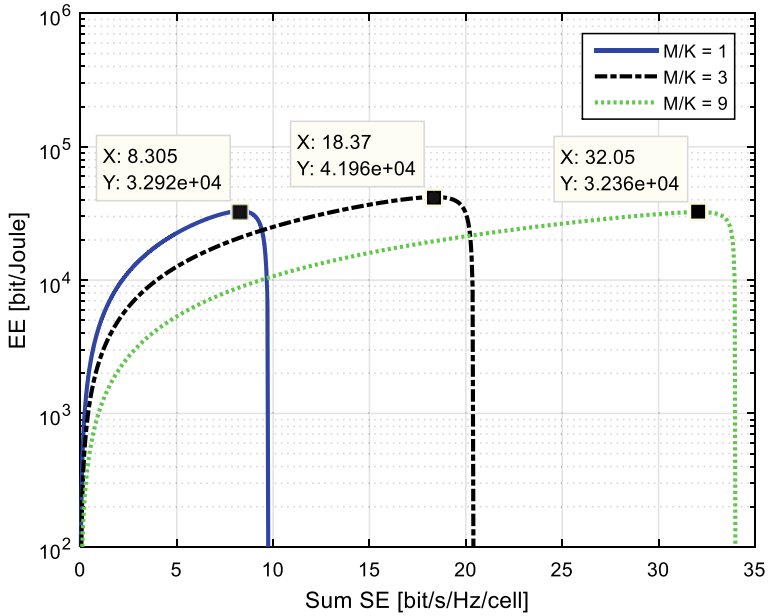


Fig. 6 SE-EE trade-off for different values of base station antenna-UE ratio

Table 3 Impact of number of base station antennas-UE ratio on SE-EE trade-off

S. No.	SE	EE		
		M/K = 1	M/K = 3	M/K = 9
1	0	0	0	0
2	5	$2.252 \times 10^4$	$1.305 \times 10^4$	5440
3	8	$3.25 \times 10^4$	$2.06 \times 10^4$	8604
4	10	0	$2.49 \times 10^4$	$1.07 \times 10^4$
5	15	0	$3.685 \times 10^4$	$1.6 \times 10^4$
6	18	0	$4.196 \times 10^4$	$1.91 \times 10^4$
7	25	0	0	$2.66 \times 10^4$
8	32	0	0	$3.236 \times 10^4$

this paper, the impact of multiple antennas at base station, and increase in user equipment,  $M/K$  ratio on SE-EE trade-off are discussed. When antennas at base station are increased, it is observed that the highest EE is achieved for  $M = 20$  as  $1.949 \times 10^4$  bit/Joule, whereas EE 6497 bit/Joule is achieved for  $M = 15$ . With considering setup, impact of number of UE's is observed as maximum EE as 2.709 bits/Joule at  $K = 15$  and for  $K = 40$ , EE value  $2.257 \times 10^4$  bits/Joule is achieved. Impact of  $M/K$  ratio on SE-EE trade-off is observed as for  $K = 10$ , by increasing the base station antennas in balanced manner, energy efficiency can be improved. At

$M/K = 3$ , maximum EE is attained as  $4.196 \times 10^4$  while at  $M/K = 9$ , EE value  $3.236 \times 10^4$  is observed. Finally, this paper concludes that by deploying more hardware and properly balancing profits and expenses, SE-EE trade-off can be obtained.

## References

1. Bashar M, Cumanan K, Burr AG, Ngo HQ, Larsson EG, Xiao P (2019) Energy efficiency of the cell-free massive MIMO uplink with optimal uniform quantization. *IEEE Trans Green Commun Netw* 3(4):971–987
2. Zhang Y, Zhou M, Qiao X, Cao H, Yang L (2019) On the performance of cell-free massive MIMO with low-resolution ADCs. *IEEE Access* 7:117968–117977
3. Ngo HQ, Le-Nam T, Duong TQ, Matthaiou M, Erik Larsson G (2017) On the total energy efficiency of cell-free massive MIMO. *IEEE Trans Green Commun Netw* 2(1):25–39
4. Kumar R, Gurugubelli J (2011) How green the LTE technology can be. In: *Proceedings in Wireless VITAE*
5. Ha D, Lee K, Kang J (2013) Energy efficiency analysis with circuit power consumption in massive MIMO systems. In: *Proceedings of IEEE international symposium on personal, indoor and mobile radio communication (PIMRC)*
6. Cui S, Goldsmith A, Bahai A (2004) Energy-efficiency of MIMO and cooperative MIMO techniques in sensor networks. *IEEE J Sel Areas Commun* 22(6):1089–1098
7. Rusek F, Persson D, Lau BK, Larsson EG, Marzetta TL, Edfors O, Tufvesson F (2013) In: *Scaling up MIMO: opportunities and challenges with very large arrays*. *IEEE Signal Process Mag* 30(1), 40–60
8. Björnson E, Sanguinetti L, Hoydis J, Debbah M (2014) Designing multi-user MIMO for energy efficiency: when is massive MIMO the answer. In: *IEEE wireless communications and networking conference (WCNC)*, pp 242–247
9. Björnson E, Larsson EG, Debbah M (2015) Massive MIMO for maximal spectral efficiency: how many users and pilots should be allocated? *IEEE Trans Wirel Commun* 15(2):1293–1308
10. Chen Y, Zhang S, Xu S, Li GY (2011) Fundamental trade-offs on Green wireless networks. *IEEE Commun Mag* 49(6):30–37
11. Jose J, Ashikhmin A, Marzetta TL (2011) Pilot contamination and precoding in multi-cell TDD systems. *IEEE Trans Wirel Commun* 10(8):2640–2651
12. Hoydis J, Brink ST, Debbah M (2013) Massive MIMO in the UL/DL of cellular networks: how many antennas do we need? *IEEE J Sel Areas Commun* 31(2):160–171

# Autonomous Pesticide Spraying Robot Using SVM



S. Sri Durga Kameswari, Telagarapu Prabhakar, and K. Krishna Kishore

**Abstract** Nowadays, agricultural automation is one of the major drifts. Without effective utilization of agricultural land, it is crucial to ensure growth in food production in our country. This project aims to increase the productivity of crops (which are small and complex in farming) using several machine learning techniques, which diminishes the manual labor apparently. This autonomous farming bot detects its path automatically through (support vector machine) SVM image classifier under supervised learning technique. After image classification, it predicts the way and sprinkles water/spray pesticides followed by regular health indication. Plant health indication is done by an application named Plantix where Web-Camera sends continuous pictures, which are captured during the movement. Here, core processor used is Raspberry Pi 3 model b. Raspberry Pi sends commands to motor driver after path prediction by Pi-Camera. Thereafter, motor driver controls DC motors according to the commands from R-Pi.

**Keywords** Pi-camera · Plantix · Raspberry Pi · SVM · Web-camera

## 1 Introduction

As agriculture is the backbone of our country and there is an enormous need to maintain agricultural sustainability, we should concentrate more on the development of the technologies used in agriculture. Nearly 70% of us depend only on agriculture. The total grain production in India per year is 275 million tonnes. It is the primary occupation for most of the people. It is difficult to monitor the field every time. Smart Farming is the next rising technology where farmers can monitor the plants from anywhere. This smart farming uses modern deployments, which yields high quality and quantity of agricultural products. This project aims to help the farmers by reducing their work through continuous monitoring of fields autonomously; at the same time, it sprinkles the water and sprays the pesticides. When the autonomous robot identifies

---

S. S. D. Kameswari (✉) · T. Prabhakar · K. K. Kishore  
GMR Institute of Technology, Rajam, Srikakulam, Andhra Pradesh, India  
e-mail: [durgakameswari.s@gmr.it.edu.in](mailto:durgakameswari.s@gmr.it.edu.in)

© The Author(s), under exclusive license to Springer Nature Singapore Pte Ltd. 2022  
H. Vasudevan et al. (eds.), *Proceedings of International Conference on Wireless Communication*, Lecture Notes on Data Engineering and Communications Technologies 92, [https://doi.org/10.1007/978-981-16-6601-8\\_27](https://doi.org/10.1007/978-981-16-6601-8_27)

293

the diseased plant, it sends the snaps of that plant to an application called Plantix and that application will process the data and indicates several preventive measures to farmer. We use image classification and object detection principles to detect obstacles through Pi-Camera to avoid collision. Pi-Camera detects the road through supervised machine learning and follows the path and if any obstacle arises, it compares all the training models and predicts the path such that it moves autonomously. The autonomous robot notices the surroundings of the crop and discovers the infected plants using image processing, and the complete data of the septic plant will be taken at the early stage from the developed application. So, the productivity of the crop can be increased to an extreme level.

As earth comprises the mixture of gases and some are harmful to humans. When you are spraying the pesticides, it is harmful to your health and most of the farmers won't have prior knowledge about the detrimental effects. Moreover, vegetable fields and under-sized plants can't be efficiently monitored due to a lot of complexities in spraying pesticides to them. So, this whole technology can be imbibed through Agri-bots. Agri-bot is a robot designed to do multiple tasks at a time like ploughing the field, sowing the seeds, sprinkling water, and spraying pesticides. Farmers can have access to GPS, soil scanning, data management, and internet of things, which diminishes a lot of labor done by a farmer.

## 2 Literature Survey

Autonomous navigation system had been developed a decade ago. But the rage toward the topic is never falling down. In the past decade, there has been a push toward automation in horticulture industry. But spraying pesticides on vegetable crops is intricate. A large number of research have been carried out in order to develop and implement strategies for recognizing crop rows using image processing techniques based on Hough transform. In 1992 a feature extraction approach has been developed in digital image processing, image analysis, and computer vision that has long been widely used to recognize geometric features such as lines and curves [1]. Methods based on least squares fitting: The term "least squares" refers to a solution that minimizes the sum of the squares of the errors in the solutions to each individual equation (least squares) [2]. The technique includes picture segmentation, row skeleton extraction, straight-line extraction, vanishing point detection, and crop row recovery. However, this technique places a high premium on region skeletons, which can be difficult to remove in some cases, particularly in pictures with a strong weed pressure. Additionally, this technique was computationally intensive [3]. In the year 2015, researchers have analyzed the geometry of field landscape using stereo pictures in order to detect crop rows. Later in his career, he created a stereo image processing method for detecting and tracking ground objects.

### 3 Proposed Methodology

In this project, we made an attempt to reduce the complexities faced by farmers by creating an autonomous vehicle, which is able to indicate plant health along with sprinkling water/spraying pesticides to the entire field. Each and every plant's condition is visible to the farmer through the applications like Raspi-Cam Remote and preventive measures, biological control, and chemical control through Plantix [4]. Autonomous navigation is the current trend, which uses machine learning or deep learning models, and it generally comprises of capturing images through camera, annotation of the captured images using annotator, pre-processing, training model, and prediction of the path [5] (Figs. 1 and 2).

Pi-Camera is used here to capture the images and compare with the trained datasets of crops and path for the navigation of the robot (Fig. 3).

This can be achieved by using an image classifier called SVM, and we train that SVM algorithm with an immense number of images, and further, it attains a mathematical classification with which a robot can assess the path by avoiding obstacles and drive accordingly (Fig. 4).

This algorithm analyzes the images and creates hyper-plane such that obstacles will be at support vector points [6] where hyper-plane refers to the maximum margin from the two classes (say lane boundaries and obstacles in autonomous navigation).

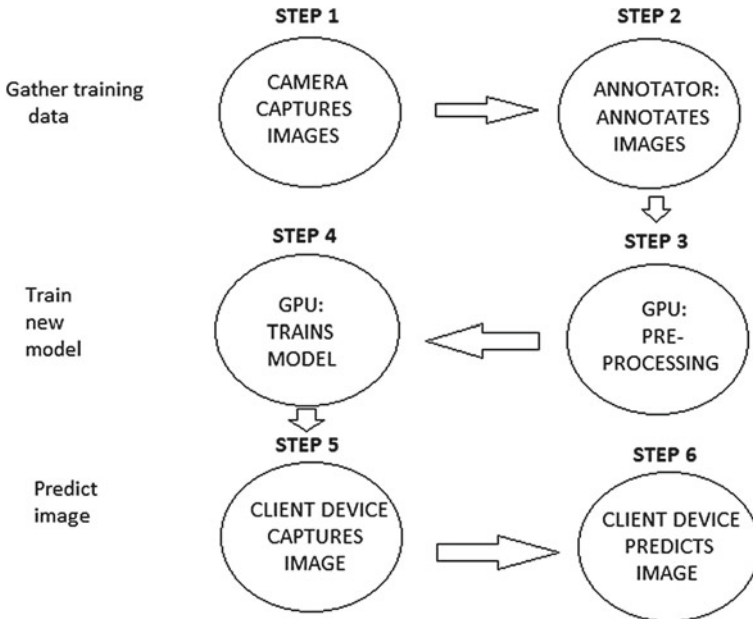
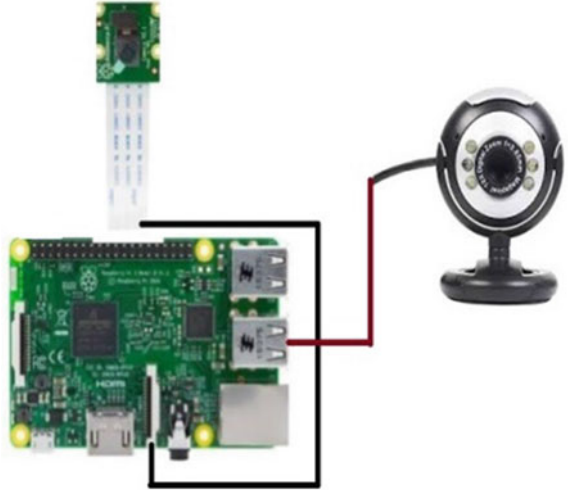


Fig. 1 Workflow for giving autonomy to robot

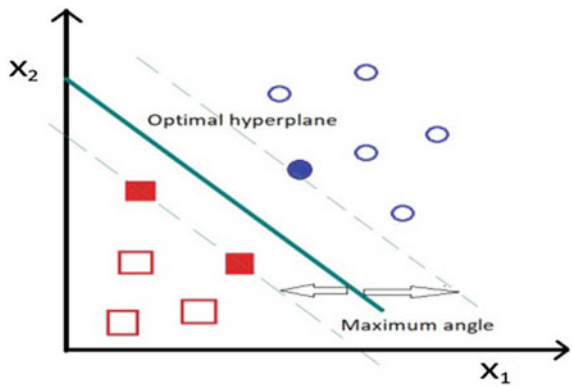
**Fig. 2** Vision-based system



**Fig. 3** Crop rows image in dataset



**Fig. 4** SVM image classifier with optimal hyper-plane





The robot’s job is to remain within the solid line limits while avoiding all obstacles in its route. The virtual robot is unaware of its surroundings. It gathers information about the surroundings online and utilizes support vector machines to find a collision-free route.

To utilize the SVM for route planning, the whole environment detected by the robot is split into two classes of datasets, and the SVM is used to find the hyperplane with the greatest margin between the two classes of datasets. This hyper-plane illustrates a path that is devoid of collisions. Figure 5 illustrates the conventions used to present the simulation results [7, 8].

After prediction of path through classification of crops from path using SVM, Raspberry Pi sends commands to motor driver to drive the motors accordingly [9] (Fig. 6). Raspberry Pi and motor driver connections are given in Fig. 7.

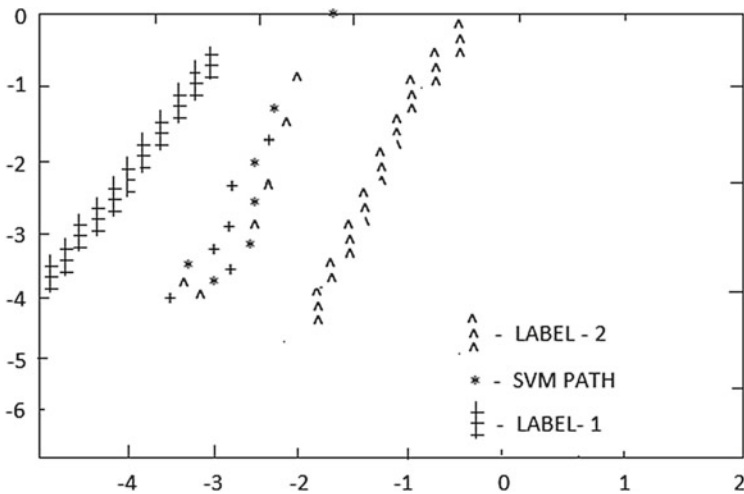


Fig. 5 SVM path detection simulation



Fig. 6 Different crops classification with path

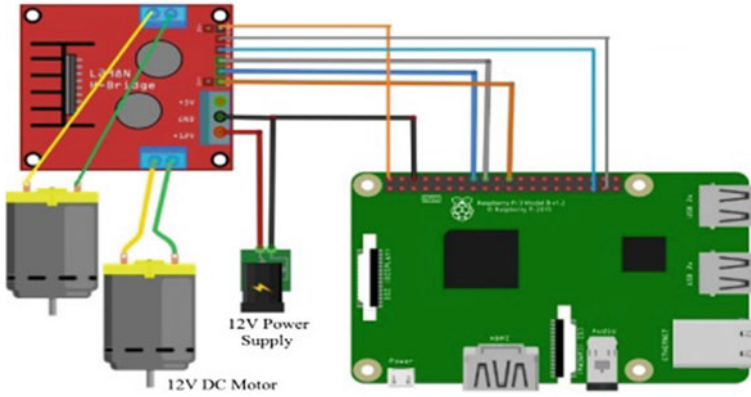


Fig. 7 Engine network

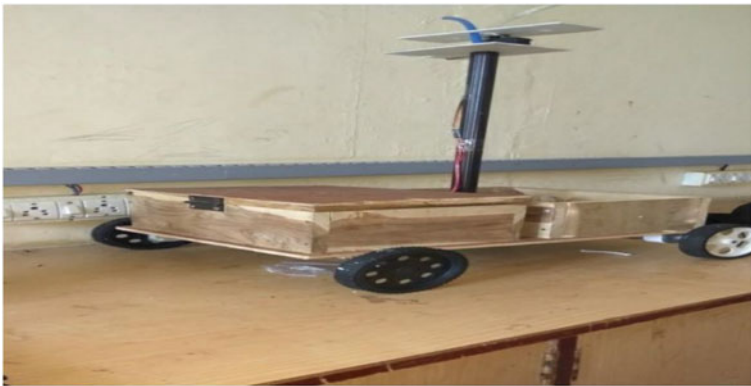


Fig. 8 Developed prototype

Along with autonomous driving, it sprinkles water and pesticides as well. For this, we are using vacuum pump motors to suck the water/pesticides such that it spits through small nozzles, which are connected to the pipes (blue and white) as shown in Fig. 8.

## 4 Components' Description

### Raspberry Pi

The Raspberry Pi is a low-cost, credit card-sized computer that is a powerful small gadget and allows individuals of all ages to explore computers and learn to write in

languages such as Scratch and Python. It has 64 bit Quad core working at a frequency of 1.2 GHz ARM processor, a family of CPU based on RISC (Reduced Instruction Set Computer). It has 40 GPIO headers (General Purpose Input Output) pins specifically, 27 GPIO header (General Purpose Input Output) pins specifically, 27 GPIO pins that consist of SPI, I2C, UART pins, two 5 v power supply pins, two 3.3 v power supply pins. It has BCM4313 inbuilt Wi-Fi and Bluetooth module and inbuilt 1 GB RAM. It works simply by installing Raspbian operating system.

### Pi Camera

The Raspberry Pi Foundation has officially launched their latest official camera board in the form of the Raspberry Pi Camera v2. The Raspberry Pi Camera Module v2 is a custom-designed add-on board for Raspberry Pi that incorporates a high-quality 8 megapixel Sony IMX219 image sensor and a fixed focus lens. Now, the Raspberry Pi Zero has a camera connection. With the newly released Raspberry Pi Zero Camera Adapter, one can now attach a Raspberry Pi camera to their Zero. This software enables the displaying of static images with dimensions of up to  $3280 \times 2464$  pixels and video of up to 1080p30, 720p60, and  $640 \times 480$ p90. It uses the unique CSI interface that was particularly developed for camera connection.

### L298N Motor Driver

The L298N motor driver is used to power high-current loads such as motors. The L298N motor controller is configured as an H-bridge, which is advantageous when regulating the direction of rotation of a DC motor. The advantage of an H-bridge is that it allows for the provision of a separate power source for the motor. Remove the +12 v jumper if you are not utilizing +12 v power. When you connect the +12 v jumper, the onboard voltage regulator is activated, and you may now source +5 v from the +5 v port. The microcontroller is linked through enabling pins and input pins up to +5 v. The external power supply is linked to the +12 v through a common ground shared with the +5 v. Indeed, this pin may receive voltages ranging from +7 to +35 v.

### DC Motors

A motor is a device that transforms electrical energy into mechanical energy. A DC motor is a type of rotatory electrical equipment that converts direct current electrical energy to mechanical energy. It operates on the following fundamental principle: “Whenever a current-carrying conductor is put in a magnetic field, it is subjected to a mechanical force.” A direct current motor is made up of permanent magnets on the outside and a rotating armature on the inside. Permanent magnets are stationary, referred to as stators, while the armature spins, referred to as rotors.

### Vacuum Pump

A vacuum pump is a device that removes gas molecules from a sealed volume in order to leave behind a partial vacuum. Vacuum pumps are combined with chambers and operational procedures into a wide variety of vacuum systems. Sometimes more than one pump will be used in a single application.

	Variance	Skewness	Curtosis	Entropy	Class
0	3.62160	8.6661	-2.8073	-0.44699	0
1	4.54590	8.1674	-2.4586	-1.46210	0
2	3.86600	-2.6383	1.9242	0.10645	0
3	3.45660	9.5228	-4.0112	-3.59440	0
4	0.32924	-4.4552	4.5718	-0.98880	0

**Fig. 9** The crop row dataset has 1372 rows and 5 columns

## 5 Software Requirements

SVM needs the installation of a number of libraries. Due to the fact that we are using Python, implementing SVMs will be a little bit simpler. Calculating the margin between the decision border and the support vectors and optimizing this margin requires sophisticated mathematics. We will instead look into how SVM is implemented in Python using the Scikit-Learn package.

### Implementing SVM with Scikit-Learn

Our objective is to estimate whether or not a crop row has a route based on four properties of the note, namely, the skewness of the wavelet converted picture, the image's variance, the image's entropy, and the image's kurtosis. This is a binary classification issue, and we will solve it using the SVM method. The remainder of the section is devoted to typical machine learning procedures (Fig. 9).

## 6 Results

The developed model is tested for various conditions, and the sample images of the working are displayed in Fig. 10. The model is able to distinguish the paths effectively and sprinkles water on plants accordingly.



**Fig. 10** a Autonomous robot sprinkling water with crop detection using SVM linear image classifier. b Autonomous robot sprinkling water with lane detection. c Autonomous robot sprinkling water

## 7 Conclusion

This paper examined the concept of Agri-bot and its application to the identification of crop rows. The study resulted in the development of an autonomous robot capable of recognizing obstacles using non-probabilistic linear binary classification. This navigation system was built using a support vector machine classifier. This system was examined both offline and online. Finally, it was determined that the constructed system was more accurate and less expensive than the bulk of the mentioned works. Additionally, its processing frequency exceeded that of similar works. Finally, it was feasible to demonstrate the system's effective behavior in an actual navigation circuit.

## References

1. Rovira-Más F, Zhang Q, Reid JF, Will JD (2005) Hough-transform-based vision algorithm for crop row detection of an automated agricultural vehicle. *Proc Inst Mech Eng Part D J Automob Eng* 219(8):999–1010. <https://doi.org/10.1243/095440705X34667>
2. Billingsley J, Schoenfisch M (1995) Vision-guidance of agricultural vehicles. *Auton Robot* 2:65–76
3. Pla F, Sanchiz JM, Marchant JA, Brivot R (1997) Building perspective models to guide a row crop navigation vehicle. *Image Vis Comput* 15:465–473
4. Romeo J, Pajares G, Montalvo M, Guerrero JM, Guijarro M, Ribeiro A (2012) Crop row detection in maize fields inspired on the human visual perception. *Sci World J* 2012:10 p. <https://doi.org/10.1100/2012/484390>. Article ID 484390
5. Sainz-Costa N, Ribeiro A, Burgos-Artizzu XP, Guijarro M, Pajares G (2011) Mapping wide row crops with video sequences acquired from a tractor moving at treatment speed. *Sensors* 11:7095–7109. <https://doi.org/10.3390/s110707095>
6. Velmurugan K, Mathumitha B, Merylen Jenow B, Thamizh Oviyam R (2019) Automated vehicle: autonomous driving using SVM algorithm in supervised learning. *Int J Eng Res Technol (IJERT) RTICCT* 7(Issue 01)
7. Tellaeche A, Burgos-Artizzu X, Pajares G, Ribeiro A, Fernández-Quintanilla C (2008) A new vision-based approach to differential spraying in precision agriculture. *Comput Electron Agric* 60(2):144–155
8. Fontaine V, Crowe TG (2006) Development of line-detection algorithms for local positioning in densely seeded crops. *Can Biosyst Eng* 48:7.19–7.29

9. Jones G, Gée C, Truchetet F (2009) Modelling agronomic images for weed detection and comparison of crop/weed discrimination algorithm performance. *Precision Agric* 10:1–15. <https://doi.org/10.1007/s11119-008-9086-9>

# Applications of AI Techniques like Machine Learning Methods and Deep Learning Models (ANNs) in Emerging Areas: A Review



Pranav H. Panicker, Amit A. Deshmukh, and Sunil H. Karamchandani

**Abstract** In today's world, we come across numerous advancements in various fields of technology. In key areas, such as communication networks, microstrip antennas, signal and image processing (like speech and character recognition), Internet of things and embedded systems etc., there have been major breakthroughs aided and made possible through the use of artificial intelligence techniques such as machine learning and deep learning models (primarily including artificial neural networks). Some important developments propelled by the use of these techniques and its applications in the respective fields is what has been analysed in this paper.

**Keywords** Machine learning · Communication networks · Internet of things · Artificial neural networks · Speech recognition · Dynamic time warping · Microstrip antenna

## 1 Introduction

Important developments in various areas of technology today are aided by the use of Artificial Intelligence (AI) techniques, such as Machine learning (ML) and specific deep learning techniques like Artificial neural networks (ANNs) and their applications in the respective fields is relevant to be studied. Most of the modern emerging trends, such as next-generation communication networks, Internet of Things (IoT) and its corresponding embedded systems, antennas, signal and image processing, speech and character recognition, etc., are all boosted and developed further using AI. Looking into select few applications in such areas is helpful and gives a better understanding of how great the impact of different AI techniques has been in this modern era.

---

P. H. Panicker (✉)

Electrical Engineering, IIT Tirupati, Tirupati, Andhra Pradesh 517506, India

A. A. Deshmukh · S. H. Karamchandani

EXTC Department, SVKM's DJSCE, Mumbai, Maharashtra, India

## 2 Applications in Certain Fields

### 2.1 *In Communication Networks and 5G Evolution*

For wireless communication network systems, ML methods are really useful and versatile as they are helpful in a vast set of different aspects pertaining to these wireless networks. For example, communication networks can use machine learning approaches to take use of big data analytics and observation-based decision making to create more efficient, independent and intelligent networks. Specifically, deeper ML techniques like reinforcement learning are as such utilised for aspects like independent decision-making. Along with this, a quite logical ML application is to use intelligent and predictive data analytics to improve situational awareness and overall network operations [1]. In this context, ML will enable the wireless network to parse through massive amounts of data generated from a variety of sources, ranging from wireless channel measurements and sensor readings to drones and surveillance images, in order to create a comprehensive operational map of the network's massive number of devices [2]. This map can then be used to enhance numerous services across the wireless network, such as fault monitoring and user tracking. Similarly, much like the aid provided by ML, ANNs are proposed for major applications in the wireless communication domains. They can be used for a variety of reasons, such as for predictions, inferences and intelligent and predictive analytics. ANNs in wireless networks can also be used to enable self-organising network operations by implementing ANN-based ML at the network's edge as well as across its multiple components [3].

ML is also a really promising AI method designed to support modern radio terminals, such as smart 5G mobile terminals [4] and 5G networks, which rely on the support of ML techniques, because they require huge amounts of data to accurately forecast actions, for which ML is really helpful. This acts as a perfect support for 5G, because it can carry more data at a faster rate than current networks [5]. The ML techniques also help the network in this scenario to autonomously gain access to the most valuable spectral bands with the help of sophisticated spectral efficiency learning and inference, in order to control the transmission power [4]. And also, by integrating ML into 5G technology, mobile devices will be able to construct dynamically adaptable clusters, based on learnt data and intelligent base stations will be able to make decisions for themselves. Due to this, network applications could become more efficient, have lower latency and be more reliable as a result. A large number of users are expected to be connected to several thousands of network nodes in such modern communication networks. By providing quick, flexible, adaptable and intelligent control, neural networks can help enhance the development of this new telecommunication infrastructure [6].



## 2.2 *Application in Internet of Things (IoT)*

The internet of things, or IoT, is a network of interconnected computing devices, mechanical and digital machinery that enables network data transfer without the need for human-to-human or human-to-computer interaction. One of the most crucial goals of IoT is to improve the quality of life for humans by reducing the physical interaction between humans and the devices. Thus, we see that techniques involving ANNs can be used to predict and analyse the user's behaviour to provide advanced information for the IoT devices. However, using ANNs for IoT has its own drawbacks. The practical deployment of an IoT system faces a number of obstacles [7], which include aspects like data analytics, computation, transmission capabilities, connectivity issues, end-to-end latency and security [8]. Another problem is that with the IoT, both energy and computing resources are limited. As a result, the energy and computational costs of training ANNs should be weighed against the accuracy requirement of a specific ANN-based learning method [3]. The higher the needed accuracy, the more computational and energy resources are required.

This is where the implementation of the big-little approach for IoT systems [9] is quite helpful in providing a solution as it works on the concept of taking a large trained neural network for a certain classification problem, and using it to distil a smaller neural network that only classifies a well-chosen subset of the output space. This smaller neural network is best suited for execution locally on embedded devices; whether or not the input is additionally transferred to the Cloud for evaluation with the larger neural network depends on the application's needs (Fig. 1).

This representation of the big-little neural network, depicts how the little neural network shown, is able to group just select output classes while being processing with less power from CPU. The findings obtained through the testing carried out in [9] suggest that prioritising a certain class can reduce the number of calculations required to get the same performance after classification. This can improve the overall network respond faster while retaining the same level of accuracy.

## 2.3 *Applications in Microstrip Antennas*

In telecommunications, a microstrip antenna (MSA) is the one that is produced on a printed circuit board (PCB) using photolithographic processes and it is similar to an internal antenna (as required in the system on chip integration). Microwave frequencies are where they are most commonly employed as at lower frequencies (<500 MHz) their size becomes larger. These antennas have grown in popularity in recent years as a result of their thin planar design, which may be accommodated into the surfaces of consumer goods, aeroplanes missiles, etc., and also due to their ease of manufacture by utilising printed circuit methods.

In the subject of communication, neural network modelling has been widely employed as a computational method to solve a variety of practical problems. In

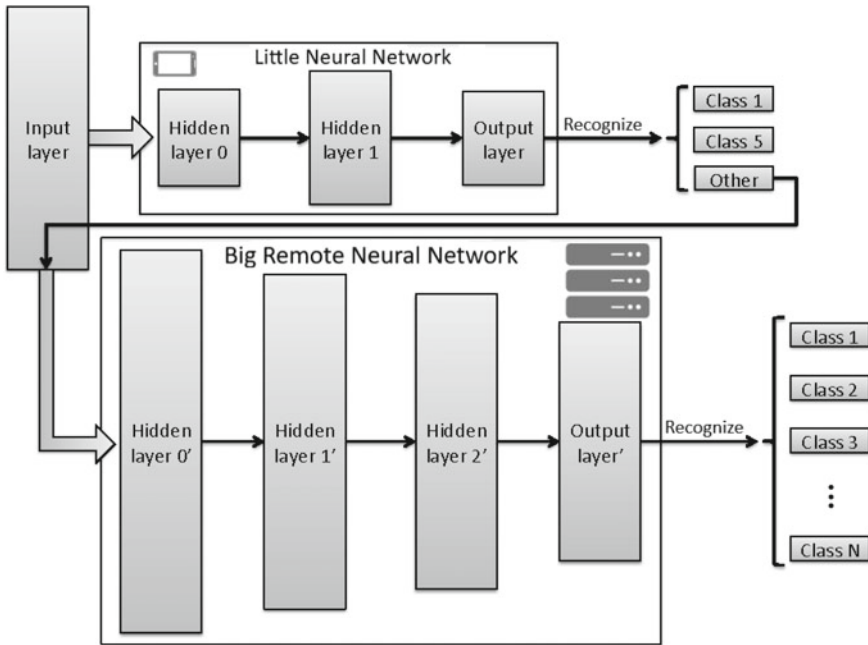


**Fig. 1** A diagrammatic representation of the big-little network, which allows reduced usage of the CPU system for its execution [9]

the context of MSAs, the ANN models for certain MSAs like the rectangular MSA (RMSA) and equilateral triangular MSA (ETMSA), have been found to provide a really accurate prediction of patch dimensions for a broad range of frequencies as well as substrate thickness [10, 11] (Fig. 2).

The above provided model is based on the supervised network. It gets trained via input and target data. With the aid of target data, the ANN learns from the input data and transforms it into the desired output. This particular model displays input neurons, that represent dielectric constant ( $\epsilon_r$ ), RMSA resonant frequency ( $f_r$ ),

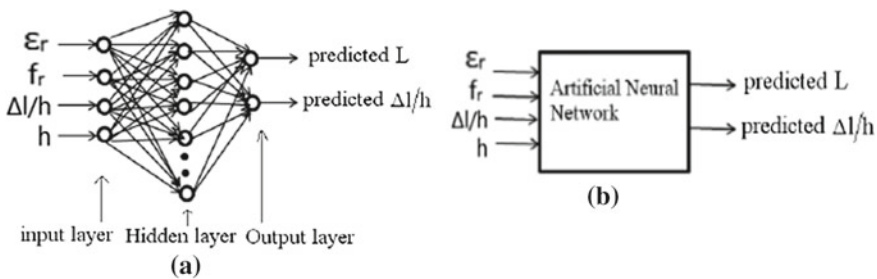


**Fig. 2** a, b ANN Model representation of the RMSA (coaxially suspended) [14]

thickness of the air substrate ( $h$ ) on which the RMSA is present and ' $\Delta l/h$ ', where ' $\Delta l$ ' is the fringing field length extension. The equations to calculate ' $\Delta l$ ', patch width ' $W$ ' using patch length ' $L$ ', and ' $f_r$ ' are provided in [12, 13]. Using the data from input neurons at different resonant frequencies, the patch side length ' $L$ ' and ' $\Delta l/h$ ' can be predicted. For the predicted values, the experiment conducted in [10] is able to show how the model is useful in aiding to design RMSA for different substrates on any frequency. That depicts the importance of the predictive ability of ANNs as we can see in this case for MSAs.

## 2.4 *Speech and Character Recognition*

**Speech Recognition:** Human-to-human communication relies heavily on speech. As a result, users have evolved to expect spoken computer interfaces. We still require sophisticated languages that are difficult to learn and utilise in order to communicate with robots in the modern era. automatic speech recognition (ASR) is quite helpful remedy in this case. It is a computer science and computational linguistics multi-disciplinary topic that develops approaches and technology that allow computers to recognise and translate spoken language into text.

Hidden Markov Models (HMMs) [14] are some important ML models used in developing several speech recognition systems. Because a voice signal can be considered as a piecewise stationary signal or a short-time stationary signal, HMMs are utilised in speech recognition. Speech can be approximated as a stationary process for a small-time frame. For many stochastic applications, speech can be thought of as a Markov model. Also, HMMs are used to provide effective frameworks for designing time-varying spectral vector sequences [15]. Due to this, these models are found in practically all current large vocabulary continuous speech recognition (LVCSR) systems.

Apart from the usage of HMMs, Dynamic Time Warping (DTW), is another special type of algorithm that is highly useful and impactful in speech processing. It helps with recognising the compatibility of sound [16] and this method is used to compare the similarity of a pattern across time frames. It is a sound-based algorithm that determines the best warping path among two datasets and outputs the path warping values as well as the distance between them. The warping path is the separation between two patterns when compared; the narrower the warping path, the more similar the two patterns are.

n	1	1	2	1	2	1	1	0
r	1	1	2	1	2	0	0	1
e	2	2	1	2	1	2	2	2
t	1	1	2	0	2	1	1	1
t	1	1	2	0	2	1	1	1
a	2	2	0	2	0	2	2	2
p	0	0	2	1	2	1	1	1
	p	p	a	t	a	r	r	n

**Fig. 3** A cost matrix diagram to show the DTW to compare 2 words (the reference word on the vertical axis and speech input word on Y-axis), with a particular warping path indicated

Words when spoken by different people can have different time periods or structures as compared to the original word when analysed by a recognition device (or application), such as in the diagram given above (where the reference word is “PATTERN”, but the input word is “PPATARRN”). DTW solves this issue by correctly arranging words and determining the shortest distance between the two words [17]. The purpose of DTW is to use dynamic programming (DP) to find the optimum mapping with the shortest distance (which is realised by formulating a program code for it). Because both  $x$  and  $y$  are usually vectors of time series, we need to compress or expand in time to obtain the optimal mapping, the approach is termed “time warping.”

For this particular method, looking at Fig. 3, the values in each position indicate the relation ( $d[I][J]$ ) between the corresponding row and column letters. So, if the particular row and column letters are different consonants, then the value at that position is 1. Similarly, the value will be 2 for a vowel and consonant pair, and 0 if the letters are same. To find the optimum distance, for each step we will take the distance (value) between each of the points in question and add it by the shortest distance we’ve determined so far. This gives us the best distance between two sequences up to that point. The formula becomes

$$\text{Table}[I][J] = d(I, J) + \min(\text{Table}[I - 1][J], \text{Table}[I - 1][J - 1], \text{Table}[I][J - 1]) \quad (1)$$

$I, J$  are the indexes of the present position (labelled from 0 till the end on the respective axes). Initially the value of “Table” will be 0, but moving along the different warping paths will provide different final values. The lowest possible value results in getting the best match. This ultimately helps us determine the shortest and most

optimum distance through the matrix which helps in providing the best possible match for the word via the speech recognition application which utilises this method. This is how dynamic time warping can be very helpful as a technique to help build such AI-based speech recognition devices/applications.

**Character Recognition:** Character identification is a fascinating subject that falls within the Pattern Recognition umbrella. Many neural networks have been designed to recognise handwritten characters, whether letters or digits, automatically. The advantage of neural networks over other pattern recognition systems is that they give the designer a lot of flexibility [18], allowing expert knowledge to be incorporated into the architecture to reduce the number of parameters set by training by examples.

Following are some ANNs which have been used for character recognition.

- Multilayer neural networks such as Backpropagation neural networks.
- Neocognitron.

The pattern of connection from one layer to the next is localised in back-propagation neural networks, despite the fact that there are numerous hidden layers. Similarly, neocognitron contains numerous hidden layers, and training for such applications is done layer by layer.

## 2.5 Other Miscellaneous Applications

Neural networks are capable of learning, adapting to changes, and simulating human thought processes with a minimal human input. They could be extremely beneficial to today's computer-integrated manufacturing systems as well as future intelligent manufacturing systems [19]. Traditional rule-based decision support systems [20] are becoming obsolete as advanced production systems become more complex and dynamic. In all facets of manufacturing operations, neural network technology is gaining traction. Apart from this, ANNs are useful for various other applications as well because there are several characteristics/attributes that make them quite effective. The table provided below depicts some of the key attributes of ANNs and the specific areas where their applications come in handy.

While discussing the different areas where ML and other techniques like ANNs are applied extensively, we can also refer to certain data which represents the expected increase in adoption/implementation of some of these emerging trends in a collection of surveyed companies in 2025 (compared to the same data from 2018) (Table 1).

These chart values give a clear indication of the upward rise and growth in the implementation of these mentioned modern technologies within the different sectors that the surveyed companies belong in. And this is helpful in understanding the importance and relevance of these technologies that are supported by AI methods, as they are expected to fuel future growth in a variety of industries, as well as boost demand for new job types and skill sets. As such, this is just one of the various several

**Table 1** Some applications of ANNs that are based on their most distinctive attributes

Attribute	Description	Application example
Adaptive learning	Neural networks model complex and non-linear relationships and algorithms, and improve on their existing knowledge	They exhibit Adaptive learning in different aspects such as for improving accuracy in predictive analysis and pattern recognition and by adapting to the most optimal model and changing inputs while training
Self-organisation	The ability to gather and classify large volumes of data makes neural networks uniquely suited for organising the complicated visual problems posed by medical image analysis	Self-organizing neural networks (SONNs) help create maps of input data and are used for classification and visualisation of higher dimensional data in lower dimension
Real-time operation	Neural networks can help in forming a large array of algorithms, that are capable to help shape up the design of devices which require quick and simple responses in real time	ANNs help in developing driverless vehicles that have the ability to recognise and respond to their surroundings in real time, allowing them to safely navigate. Another example of its real-time operation is in designing of AI-based drones for navigation
Fault tolerance	It is the property that allows an ANNs to operate suitably in the event of one or more components being lost. They enable the systems with fault to immediately replace faulty components with backups	It is a highly useful attribute especially necessary for systems requiring security, data protection, data integrity, etc.
Prognosis/forecasting	Some multi-layer ANNs contain hidden layers of nodes, and through the various input–outputs of this nodes, they are able to analyse and predict outcomes	On time series data, such as weather data, ANNs can be utilised to create predictions

methods using certain simplified data to showcase the rise of AI and its impact on the industries of today and in general on the entire world (Fig. 4).

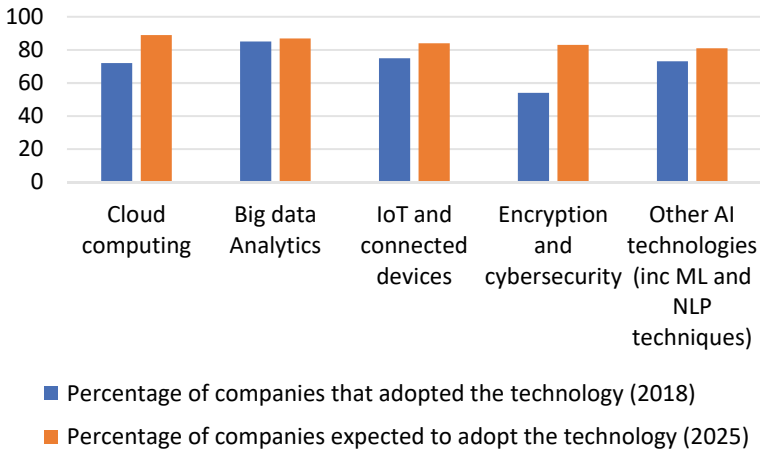


**Fig. 4** Percentage comparison of the emerging trends being adopted in companies surveyed in 2018 versus its expected values in 2025 ( Source—Future of Jobs Survey 2020, World Economic Forum)

### 3 Conclusions

In this paper, we have gone through some key areas such as next-generation communication networks, IoT, microstrip antennas, speech recognition, etc., wherein modern AI techniques such as machine learning applications and deep learning Artificial neural network methods. For some of the aspects such as in IoT or speech recognition, etc., we have looked into techniques like Big-little neural networks, HMMs, Dynamic Time Warping and others as well. Some of the key characteristics/attributes of ANNs and their uses are also put forward to give some added insight into their modern-day resourcefulness. Also, we have analysed some data with regards to a few miscellaneous applications of AI techniques to showcase how here has been positive growth in their implementation in several surveyed companies of different industries.

### References

1. Bi S, Zhang R, Ding Z, Cui S (2015) Wireless communications in the era of big data. *IEEE Commun Mag* 53(10):190–199
2. Ferber J (1999) *Multi-agent systems: an introduction to distributed artificial intelligence*, vol 1. Addison-Wesley, Reading
3. Chen M, Challita U, Saad W, Yin C, Debbah M (2017) Artificial neural networks-based machine learning for wireless networks: a tutorial. <https://doi.org/10.1109/COMST.2019.2926625>
4. Jiang C, Zhang H, Ren Y, Han Z, Chen K-C, Hanzo L (2017) Machine learning paradigms for next-generation wireless networks. *IEEE Wirel Commun* 24(2):98–105. <https://doi.org/10.1109/MWC.2016.1500356WC>

5. Abdellah A, Koucheryavy A (2020) Survey on artificial intelligence techniques in 5G networks. *J Inf Technol Telecommun SPbSUT, Russia* 8(1):1–10
6. Park Y-K, Lee C (1995) Applications of neural networks in high-speed communication networks. *IEEE Commun Mag* 33(10):68–74. <https://doi.org/10.1109/35.466222>
7. Al-Fuqaha A, Guisani M, Mohammadi M, Aledhari M, Ayyash M (2015) Internet of things: a survey on enabling technologies, protocols, and applications. *IEEE Commun Surv Tutor* 17(4):2347–2376
8. Hu Y, Sanjab A, Saad W (2019) Dynamic psychological game theory for secure internet of battlefield things (IoBT) systems. *IEEE Internet Things J* 6(2):3712–3726
9. Coninck E, Verbelen T, Vankeirsbilck B, Bohez S, Simoens P, Demeester P, Dhoedt B (2016) Distributed neural networks for internet of things: the big-little approach. 170:484–492. [https://doi.org/10.1007/978-3-319-47075-7\\_52](https://doi.org/10.1007/978-3-319-47075-7_52)
10. Deshmukh AA, Kulkarni SD, Venkata APC, Phatak NV (2015) Artificial neural network model for suspended rectangular microstrip antennas. In: *Proceedings of ICAC3—2015, Mumbai, India*
11. Deshmukh AA, Kulkarni SD, Venkata APC, Nagarbowdi SB (2015) Artificial neural network model for suspended equilateral triangular microstrip antennas. In: *Proceedings of ICCICT—2015, Mumbai, India*
12. Wong K-L (2004) *Compact and broadband microstrip antennas*, vol 168. Wiley
13. Kumar G, Ray KP (2003) *Broadband microstrip antennas*. Artech House
14. Kouemou GL, Dymarski P (2011) History and theoretical basics of hidden Markov models. In: *Hidden Markov models, theory and applications*, vol 1
15. Gales M, Young S (2007) The application of hidden Markov models in speech recognition. *Found Trends Signal Process* 1(3):195–304. <https://doi.org/10.1561/2000000004>
16. Permanasari Y, Harahap EH, Ali EP (2019) Speech recognition using dynamic time warping (DTW). *J Phys Conf Ser* 1366(1). IOP Publishing
17. Paliwal K (1982) A modification over Sakoe and Chiba's dynamic time warping algorithm for isolated word recognition. *Signal Process* 4:329–333
18. Guyon I (1991) Applications of neural networks to character recognition. *Int J Pattern Recogn Artif Intell* 5(01n02):353–382
19. Zhang H-C, Huang SH (1995) Applications of neural networks in manufacturing: a state-of-the-art survey. *Int J Prod Res* 33(3):705–728. <https://doi.org/10.1080/00207549508930175>
20. Udo GJ (1992) Neural networks applications in manufacturing processes. *Comput Ind Eng* 23(Issues 1–4):97–100. ISSN: 0360-8352



# **Embedded Systems and Internet of Things (IoT)**

# Detection and Monitoring of Harmful Gases in Air Using a Microcontroller and Android App



Nidhi Patel, Yuti Bhavsar, Sakshi Mundra, Vraj Dharia, and Rahul Taware

**Abstract** Air pollution is mainly due to industries, garbage burning, and emission from vehicles. And in metropolitan cities like Mumbai there are ample number of industries. Not only industries but also tons of vehicles. So, the quality of air is not good. The main concern is to monitor air pollution and take measures. This project is aimed at developing an IOT device which uses sensors which are interfaced with NodeMCU and ADS1115 and then the output is notified on the mobile application. The gas sensors used in this device are MQ135 (gives us the Air Quality Index) and MQ7 (measures the concentration of Carbon Monoxide coal gas). The sensors will monitor the air quality, the readings will be recorded by the NodeMCU and the data will be provided to us on the mobile application and on Thingspeak.

**Keywords** Air pollution · Gas sensors · Arduino · Filter · Particulate matter · Air quality index · PPM · IOT · Mobile application

## 1 Introduction

The air we inhale gives a major impact on our health, thus keeping up to pure air is essential for nutrition. Air quality is a major concern. From indoor air contamination to outdoor, all are inconvenient to our well-being. It is very much dangerous for kids to inhale toxic air. Not only kids but it is harmful for everyone. The problem is seriously amplified in the metropolitan cities due to the presence of ample amounts of industries, vehicles, etc. The different sources of indoor air contamination incorporate the consumption of ovens, incense sticks, and so on. Additionally, the fundamental contributing sources to outdoor contamination may incorporate vehicle fumes exhaust, flames, and industrial gases through chimneys. The significant air poisons comprise ozone, particular matter, carbon monoxide (CO), nitrogen dioxide (NO<sub>2</sub>) and sulfur dioxide (SO<sub>2</sub>) and a large group of chemicals known as volatile organic compounds (VOCs). Out of these toxic gases, the effect of carbon monoxide gas

---

N. Patel · Y. Bhavsar · S. Mundra (✉) · V. Dharia · R. Taware  
Department of EXTC, DJSCOE, Vile-Parle (W), Mumbai 400 056, India

is intense and deadly. The sources of carbon monoxide are burning of fossil fuels, unvented kerosene, gas space heaters leaking chimneys and furnaces, gas stoves and particular sorts of paints likewise produce carbon monoxide. Due to emission of toxic gases from various sources such as industries, vehicles, etc., it is difficult for everyone to inhale pure air and also it leads to premature deaths. Immediate action to improve air quality will be easy to implement once the concentration is measured [1].

## 2 Harmful Gases

Some of the major pollutants are Ozone, Particulate Matter, Carbon monoxide, Ammonia gas, etc.

### I. Ozone

Ozone protects us from harmful ultraviolet rays but only when it is present in the Earth's stratosphere. Otherwise, ground-level ozone is very much harmful. Some of the causes of ozone are emission from vehicles, power plants, and other fossil fuel burning facilities. It is a major component of smog which causes coughing, chest tightness or pain, decreases lung function and worsen asthma and other chronic lung diseases and also harms the lining of the lungs, makes lungs more susceptible to infection, and potentially damages them permanently.

### II. Particulate Matter

Particulate matter (PM) refers to small particles, both solid and liquid, which will enter the lungs and cause respiratory problems. Particles that are between 2.5 and 10  $\mu\text{m}$  (smaller than the width of a person's hair), called PM10, arise from crushing and grinding activities and mud on roads. PM but 2.5  $\mu\text{m}$ , called PM2.5, can only be seen through a microscope. The cause of PM2.5 is mainly combustion like forest fires, emission from cars, etc. Additionally, ammonia from fertilized fields and manure can combine with industrial emissions to form PM2.5. It is very important to avoid inhalation of PM2.5 as it can penetrate deep into the lungs, enter the bloodstream. So, in this project a filtered mask is designed such that it can help blocking particles which are less than size 2.5.

### III. Carbon Monoxide (CO)

Carbon monoxide gas is formed when the carbon is not burnt completely. It is a colorless and odorless gas. The major causes of CO pollution are emission from vehicles, forest fires, emission from chimneys and wood burning stoves. In cold weather, CO gas is found in higher concentration as combustion usually remains incomplete due to cold weather and as a result of which gas is trapped closer to the ground. It is very dangerous for people who are already suffering from cardiovascular disease because CO decreases the amount of oxygen reaching our body's organs

causing more chest pain. It results in dizziness, blurred vision, and confusion when the concentration is high. Extremely high concentration of CO gas can be fatal.

#### IV. Ammonia (NH<sub>3</sub>)

Ammonia is a colorless gas with suffocating odor which consists of hydrogen and oxygen atoms. It is highly irritating gas. It is naturally produced in the human body and also it is present in air, water, soil, plants, animals, etc. Risk from this gas depends on the duration of exposure, amount and route of exposure. It can result in blindness, lung damage or death when the concentration is very much high. Also exposure to higher concentrations can result in irritation, immediate burning of eyes, nose, throat and can cause other respiratory diseases [2].

### 3 System Configuration







#### 3.1 Working Principle

The table explains the Air Quality Index ranges. If the AQI is in the range 0–50 ppm, then the Air quality is good and it is safe. If the AQI is in the range 51–100 ppm, then concentration of pollutants, dust, toxic gases is moderate in air and there might be minor breathing discomfort to sensitive people. If the AQI is in the range 101–200 ppm, then concentration of pollutants, dust, toxic gases is moderately high in air and there might be severe breathing problems to people with lungs, asthma, and heart diseases. If the AQI is in the range 201–300 ppm, then concentration of pollutants, dust, toxic gases is high in air and there will be breathing problems to most people on prolonged exposure. If the AQI is in the range 301–400 ppm, then concentration of pollutants, dust, toxic gases is moderately high in air and it will result in respiratory illness on prolonged exposure. If the AQI is in the range 401–500 ppm, then concentration of pollutants, dust, toxic gases is very much high in air and this will affect healthy people and will seriously impact those people who are already suffering from various diseases (Fig. 1).

The working principle is such that sensor MQ7 will measure the concentration of CO in air and sensor MQ135 will measure the Air Quality Index. Now, the output of the sensors will be given to NodeMCU. The output data will be displayed using an Android app. The output will also be displayed on the Thingspeak platform where users can visualize data by looking at the graphs plotted [4].

#### 3.2 Block Diagram

We are using a NodeMCU microcontroller as our main chip to receive input from the sensors MQ135 and MQ7. Microcontroller is driven by a 12v Dc power supply.

AQI	Remark	Color Code
0-50	Good	
51-100	Satisfactory	
101-200	Moderate	
201-300	Poor	
301-400	Very Poor	
401-500	Severe	

**Fig. 1** Air quality index [3]

Also, NodeMCU has only 1 analog pin, so to increase the number of analog pins, we are using ADS1115. ADS1115 is a 16-bit Analog to Digital converter using which multiple analog sensors can be interfaced with NodeMCU. It is a I2C supported device [5]. Sensor MQ135 connected to NodeMCU will measure the AQI and sensor MQ7 which is connected to ADS1115 will measure the concentration of Carbon Monoxide in air. Each sensor requires Vcc and ground supply which is given from the controller device. After measuring, the output is given to NodeMCU where analog output of sensor MQ135 is converted into PPM and analog output of sensor MQ7 is converted into  $\mu\text{g}/\text{m}^3$ . This data is printed on thingspeak where a graph of values is displayed. Also, we can plot different widgets and visualizations using thingspeak platform. It will also be displayed on the Android app (Fig. 2).

### 3.3 Circuit Diagram

See Fig. 3.

#### Circuit Diagram Explanation

##### Components used and their main function in project

1. **Microcontroller (NodeMCU ESP8266):** Processing the collected data
2. **Analog to Digital Converter (ADS1115):** Converts analog output of sensor into digital signal.
3. **Sensors (MQ135, MQ7):** Collecting data (presence of gas and its amount present)

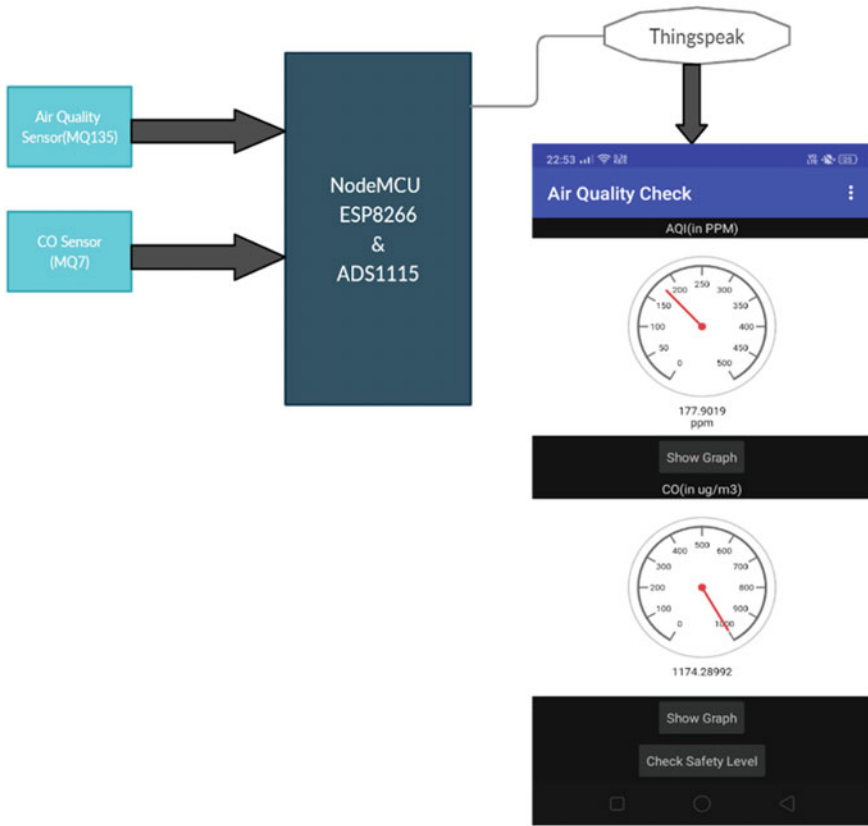


Fig. 2 Functional block diagram

- 4. **Breadboard:** to assemble the circuit.
- 5. **Wires:** To connect the components.
- 6. **USB cable:** Programs and provides power to NodeMCU.

**Explanation**

- 1. The components are set up on a breadboard as shown, where a VCC and Ground bus is created for all components in general (VCC = 5 V).
- 2. The gas sensors used, MQ135 (measures air quality) and MQ7 (monitors Carbon Monoxide) interact with the environment and provide an analog output.
- 3. As NodeMCU contains a single analog input pin, an analog to digital converter (ADS1115) is used to convert the analog output given by one of the sensors into a digital signal.
- 4. NodeMCU can be considered as the heart of this project; as it collects the data provided by sensors, processes it, i.e., converts this data into a number which we can understand (ppm) and allows to further pass the processed data to the application through which it could be consumed by the users [6].

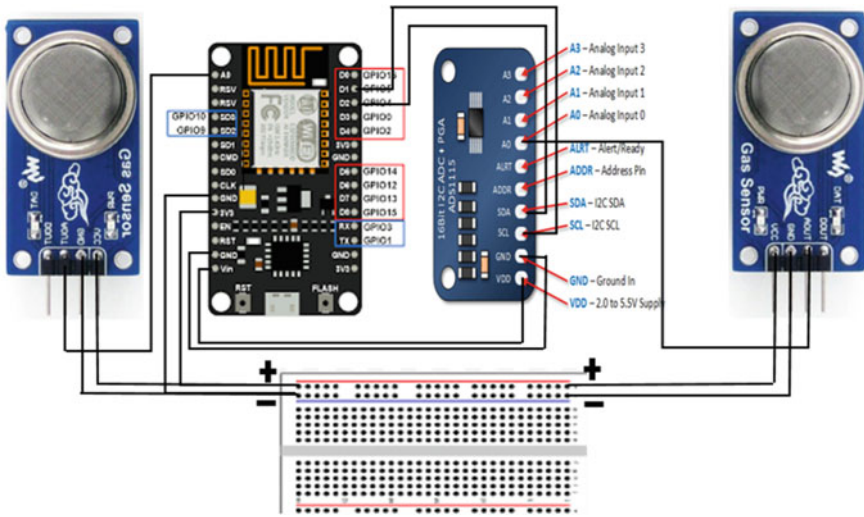


Fig. 3 Layout of the circuit

5. NodeMCU is programmed by Arduino IDE which is operated in serial monitor mode.
6. Further, the application would indicate about the air quality in the vicinity (Fig. 4).

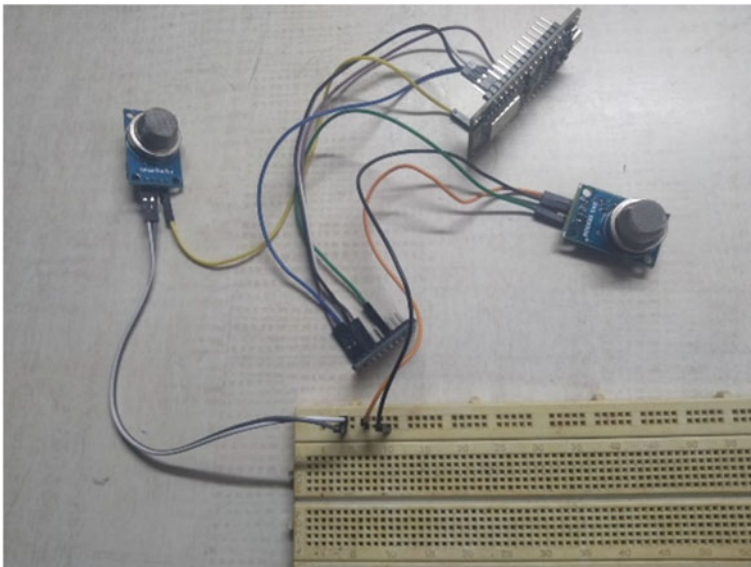


Fig. 4 Working experimental setup

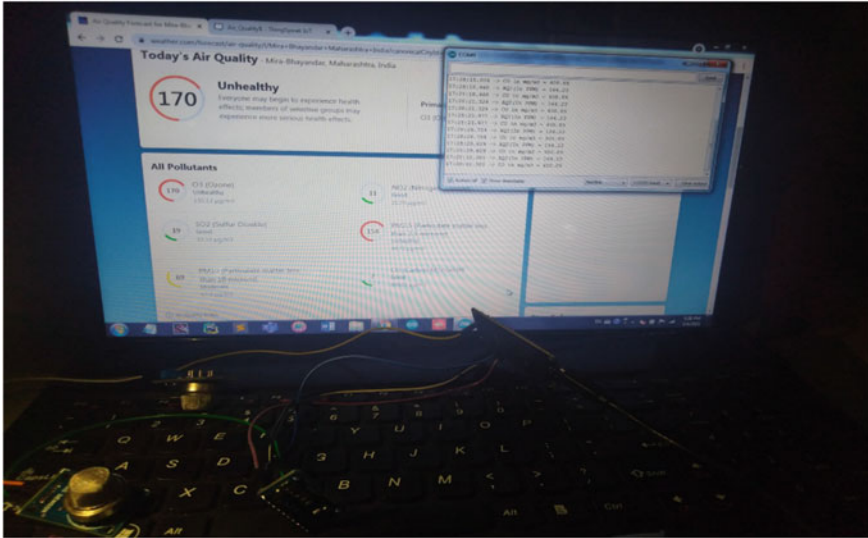


Fig. 5 Experimental setup

## 4 Output

As shown in the figure below, we compared our output with the standard values. And it was observed that the standard value of AQI at Mira-Bhayander was 170 ppm and our value was around 164.23 ppm (Figs. 5 and 6).

## 5 Android Application

Android app is designed using MIT App Inventor. It is very much easy to build an app using MIT App Inventor because here instead of writing code, we just have to drag and drop the inbuilt blocks on the screen. It becomes very much easy to build complex applications [7]. For the user interface, there are a wide range of built-in blocks available like Button, CheckBox, Datepicker, Image, Label, ListPicker, switch, and many more. The following components are used to build our Application:

- Label: To display titles like Air Quality Index, Carbon Monoxide, etc.
- Button: To add buttons for navigating to different screens.
- Webviewer: To show the output of Thingspeak on Android Application.

In our application 4 screens are added. Home screen is to display the output in the Gauge widget and buttons like ‘show graph’, ‘check safety levels’ are added on the home page. As soon as the user clicks on the button ‘check safety levels’, another page with safety level values is opened. If the user wants to analyze the output he/she



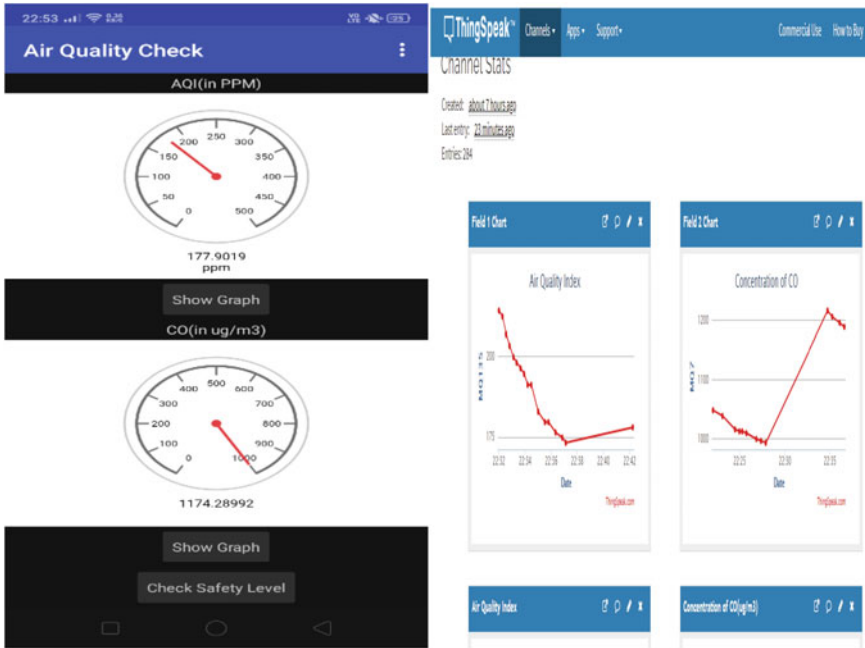


Fig. 6 Output on application and ThingSpeak

can see the graphs by clicking on the ‘show graph’ button. The logic of navigating to different screens and coming back to the homepage on pressing the back button is added using different built in blocks.

## 6 Comparison of Actual AQI with Results of Device

Actual AQI	AQI shown on device	Location	Time
53	49.8	Miraroad (E)	19:48
42	43.3	Bhayandar (E)	22:48
48	47.2	Bhayandar (E)	9:12
45	47	Borivali (W)	14:05

## 7 Conclusion and Applications

Hence, using gas sensors and all the calculations mentioned, we are able to get analog voltage which is used to get the Air Quality Index in PPM. Also, we have selected sensor MQ7 to get the concentration of CO because as mentioned earlier CO is one the most harmful gas and, using MQ135, we get the general AQI. Concentration of CO with more precision is obtained using MQ7.

The graph of these values is also obtained using Thingspeak platform. Along the graph, other widgets like gauge meter are also added in the Thingspeak channel.

The output is also obtained on the Android Application which is designed using MIT App Inventor.

The device made is low cost, advanced, real time, and unique. This would allow one to reduce the amount of toxic gases and other harmful particles that they inhale. Hence, this would provide a regular check of harmful gases in the surroundings and guide about the usage of filters in masks accordingly [8].

This device can also be useful at household level; i.e. to detect gases methane which is generated in houses due to gas stoves to a major extent. This would help to detect and monitor excessive presence of harmful gas like methane inside homes. On a broader scale, this device can also be of industrial use to detect leakages of harmful gases. This leakage could be sensed by rise in the levels of such gases in the industry/in the surrounding devices which can prevent major destruction and lives of people. This data is generally not available to a common man, since data provided by the government includes a vast range of areas, whereas here, one can monitor their surroundings and then decide the usage of different filters in the worn mask [9] (As wearing masks is of great importance in this pandemic).

## References

1. [https://app.cpebccr.com/AQI\\_India/](https://app.cpebccr.com/AQI_India/)
2. Tragos EZ, Angelakis V, Fragkiadakis A, Gundlegard D, Nechifor CS, Oikonomou G, Gavras A (2014) Enabling reliable and secure IoT-based smart city applications. In: 2014 IEEE international conference on pervasive computing and communication workshops (PERCOM WORKSHOPS). IEEE, pp 111–116
3. Shah J, Mishra B (2016) IoT enabled environmental monitoring system for smart cities. In: 2016 international conference on internet of things and applications (IOTA). IEEE, pp 383–388
4. Pasha S (2016) ThingSpeak based sensing and monitoring system for IoT with Matlab analysis. *Int J New Technol Res* 2(6)
5. Khan R, Khan SU, Zaheer R, Khan S (2012) Future internet: the internet of things architecture, possible applications and key challenges. In: 2012 10th international conference on frontiers of information technology. IEEE, pp 257–260
6. Ranjan M, Rai Kumar R (2009) Understanding parts per million in real time air quality index. *J Math Adv Sci* 23–29
7. Kumar NS, Vuayalakshmi B, Prarthana RJ, Shankar A (2016) IOT based smart garbage alert system using Arduino UNO. In: 2016 IEEE region 10 conference (TENCON). IEEE, pp 1028–1034

8. Karamchandani S, Gonsalves A, Gupta D, Pervasive monitoring of carbon monoxide and methane using air quality prediction. In: 2016 3rd international conference on computing for sustainable global development (INDIACom)
9. Jha RK, Air quality sensing and reporting system using IoT. In: 2020 second international conference on inventive research in computing applications (ICIRCA)

# Telecom Customer Churn Prediction



Mehul Bhargava, Shruti Singh, Jaya Sharma, and D. Franklin Vinod

**Abstract** In the Telecommunication Industry, customers have the option of selecting from numerous telecom companies, and can easily move from one service provider to another. In this extremely competitive market, telecom companies experience an average of 10–20% annual churn rate which is considerably high. It costs noticeably more to acquire a new customer than to hold a current customer. Thus, retaining high profitable customers is a crucial business aim. Because of the direct impact on the revenues of the companies, they are looking for a means to predict customers who are expected to leave. In this research, we have examined data of customers of a telecom company, made predictive models to recognize customers at high risk of churn, and identify the prime reasons for customer churn. Churn prediction will understand the actions and behavior of customers which will predict the customers who are likely to churn and the causes for churn.

**Keywords** Telecom · Machine learning · Customer churn prediction · Data

## 1 Introduction

Machine learning is one of the applications of Artificial Intelligence (AI) which allows a system to learn and improve without being explicitly programmed. Machine learning itself has a wide range of applications like prediction, detection, classification, translation, and recognition. In Machine learning, prediction refers to applying various algorithms to a dataset and predicting the trends. For instance, predicting heart failure, predicting bitcoin price, and predicting diabetes, etc. Classification algorithms classify the dataset into two or more classes. For example, classifying mails as Spam and Non-Spam, classifying if a student will be admitted or not, etc. Prediction of the customers is highly used in the Telecommunication Industry to predict the customers who are likely to churn and classify them as Churners or Non-Churners. Every year Telecom companies face a significant number of customers

---

M. Bhargava (✉) · S. Singh · J. Sharma · D. Franklin Vinod  
Department of Computer Science and Engineering, SRM Institute of Science and Technology,  
Modinagar 201204, Uttar Pradesh, India

© The Author(s), under exclusive license to Springer Nature Singapore Pte Ltd. 2022  
H. Vasudevan et al. (eds.), *Proceedings of International Conference on Wireless Communication*, Lecture Notes on Data Engineering and Communications Technologies 92, [https://doi.org/10.1007/978-981-16-6601-8\\_30](https://doi.org/10.1007/978-981-16-6601-8_30)

325

leaving or discarding their services, as a result, they need a system that can predict the customer churn. Customer Churn Prediction also helps them to increase their annual revenue, decrease the loss of customers and it will also help them to find and improve the area where their services are lacking [1].

Telecom companies generally provide services like calling, messaging, and internet data. Customers can use these services in two ways, either postpaid or prepaid. Prepaid means customers pay for the services in advance and then use them. In this model, when customers want to stop the services or switch to another operator, they usually inform the service provider to halt the services and it is directly a case of churn. Postpaid customers pay annually or monthly after using the services. In this model, customers stop using the services or switch to another operator without informing the current service provider. In this case, it gets difficult for us to identify customer churn. Customer churn prediction is more crucial and laborious for prepaid customers [2]. This system is based on the Indian and other Southeast Asian markets (prepaid services).

Churn can be defined in two ways Revenue-based Churn and Usage-based Churn. In Revenue-based Churn, customers who have not used any revenue-generating services like internet data, SMS and outgoing calls over a given period of time. For instance, in rural areas old-aged parents only receive calls from their children and they don't use any other service. In Usage-based Churn, customers who have not used any outgoing or incoming services such as calling and messaging over a period of time [3]. For instance, a customer who has stopped using any of the services provided by the telecom operator. In our system, we have used a usage-based definition to define churn.

## 2 Related Work

A lot of Telecom companies today are using various predictive models to overcome the problem of customer churn. The improvement and advancement of these models takes place regularly to make it much better and to add new functionalities. Some of the existing systems that were examined and studies are described below.

Kavitha et al. [4] proposed this model to predict customer churn in the telecom industry using various machine learning techniques. In this model, they have used Random Forest, Logistic Regression, and XGBoost. The dataset they have used was already trained and tested, which helped them to achieve more accuracy. They processed the data in an efficient way including Data Filtering, Noise Removal, and Feature Selection. After processing data, they applied machine learning techniques and found that the Random Forest algorithm gives the maximum accuracy than XGBoost and Logistic Regression. Also, Random Forest is the best suitable for classification and handling nonlinear data efficiently. But this model lacks in the visualization of data as well as the final results and it also used a dataset that was already trained and tested which lowers down this model's effectiveness.

Labhsetwar [5] suggested a model for predicting customer churn in the Telecom Industry using Machine Learning techniques, namely Logistic Regression, AdaBoost Classifier, Naïve Bayes Classifier, XGB Classifier, SGD Classifier, Support Vector Machine, and Extra Tree Classifier. His research suggested that the Extra Trees Classifier, Support Vector Machine, and AdaBoost Classifier have the best churn prediction modeling performance. The research also gives a visualization of results. This model fails to handle class imbalance as the churn rate is typically low.

Balasubramanian and Selvarani [6] put forward a model by mainly using Data Mining techniques for predicting customer churn in telecom systems. They used a customer-level dataset and processed it by performing data acquisition, preparation, derived variable finally data extraction [7]. The models being constructed are Decision Tree and Neural Networks, and it was concluded that Decision Tree surpasses Neural Networks and is easy to construct. The model is not effective and doesn't perform a proper analysis and it doesn't suggest ways to reduce the churn rate [8].

### 3 Proposed System

We have used a dataset which is loaded as a CSV file and certain data manipulation and other operations are being performed on data. After this, training and testing will take place for different models with and without Principal Component Analysis (PCA). In the end, a model with the highest accuracy is selected for customer churn prediction and factors of churn are also concluded [9]. We have also given some recommendations to maintain annual revenue, increase business in the telecom industry, and keep customers always happy and satisfied with the services [10].

#### 3.1 Dataset Specification

The dataset is customer-level information of a leading telecom company, it is two-dimensional data with the shape (99,999, 226) which means 99,999 rows and 226 columns. The data of customers is provided for a span of 4 months that are June, July, August, and September, where Good Phase is June, Action phase is in the month of July and August, and Churn phase is the month of September. This dataset will be explored, understood, cleaned, prepared, Exploratory Data Analysis will be performed on it and finally trained and tested before modeling. A data dictionary is also there which contains meanings of abbreviations. For example: NUM (Number), MOBILE\_NUMBER (Customer phone number), 2G (2G network), REC (recharge), T2O (telecom operator to another operator), etc. Sample outputted customer historical data in Jupyter Notebook using Python programming language is shown in Fig. 1.

	mobile_number	circle_id	loc_og_t2o_mou	std_og_t2o_mou	loc_ic_t2o_mou	last_date_of_month_6	last_ds
0	7000842753	109	0.0	0.0	0.0	6/30/2014	
1	7001865778	109	0.0	0.0	0.0	6/30/2014	
2	7001625959	109	0.0	0.0	0.0	6/30/2014	
3	7001204172	109	0.0	0.0	0.0	6/30/2014	
4	7000142493	109	0.0	0.0	0.0	6/30/2014	

Fig. 1 Outputted dataset

### 3.2 Data Understanding and Cleaning

In data understanding, we have checked the shape of data, statistics of missing columns, missing value analysis and column significance. Cleaning included removal of columns with no variance (skewness), missing value imputations, remove insignificant columns, removing columns with very high percentage of missing values.

### 3.3 Exploratory Data Analysis

In this system, EDA is used for deriving new features: Univariate Analysis, Bivariate Analysis, Multi-Collinearity Analysis, and Outlier detection and treatment. Understanding the data and behavior of customers in an efficient way by visualizing it using Bar charts, Pair plots, and Heat maps. One of the Bar charts and Pair plots are shown in the Fig. 2 and Fig. 3, respectively.

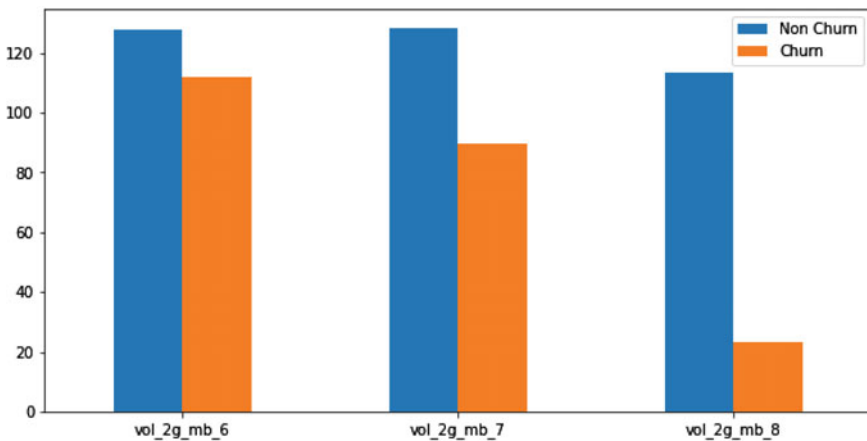


Fig. 2 Bar chart

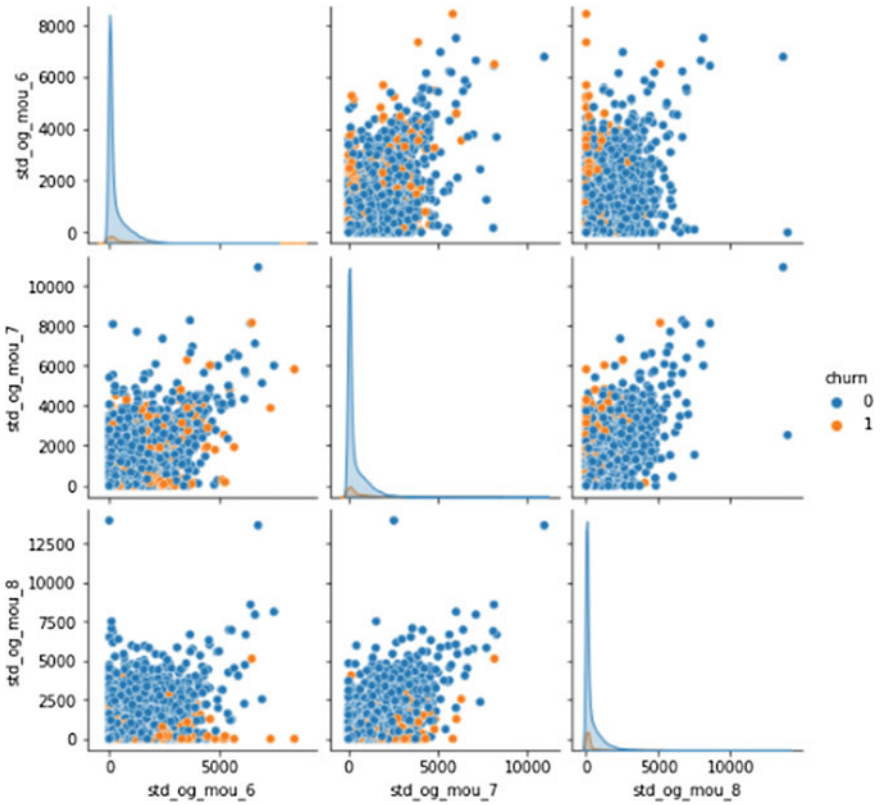


Fig. 3 Pair plot

### 3.4 Algorithms

The following Machine Learning algorithms have been used: Logistic Regression, Random Forest, Support Vector Machine (SVM) and Gaussian Naive Bayes Classifier. These are Supervised Learning algorithms. Customer Churn Prediction is a classification problem, where we will classify customers as Churners or Non-Churners, this is the reason we have used the above-mentioned algorithms as they perform efficiently in classification problems. Principal Component Analysis (PCA) is used to reduce dimensionality as the dataset is too large. Hyperparameter tuning is also used to tackle overfitting in models.



### 3.5 Data Modeling

Data Modeling is subdivided into various segments, like splitting the data into test and train, handling the imbalances inferred from EDA, performing data standardization, performing Principal Component Analysis (PCA), and then trying various algorithms (Logistic Regression, Random Forest, Support Vector Machine (SVM) and Gaussian Naive Bayes Classifier) on the dataset to come up with a final model with good accuracy. This will lead to predict the customers who are likely to churn. Now, for predicting the reasons for churn we have again trained and tested these Machine Learning models without implementing Principal Component Analysis (PCA).

## 4 Working

The Architectural Design is shown in the Fig. 4 which shows the overview of the System used to predict customer churn.

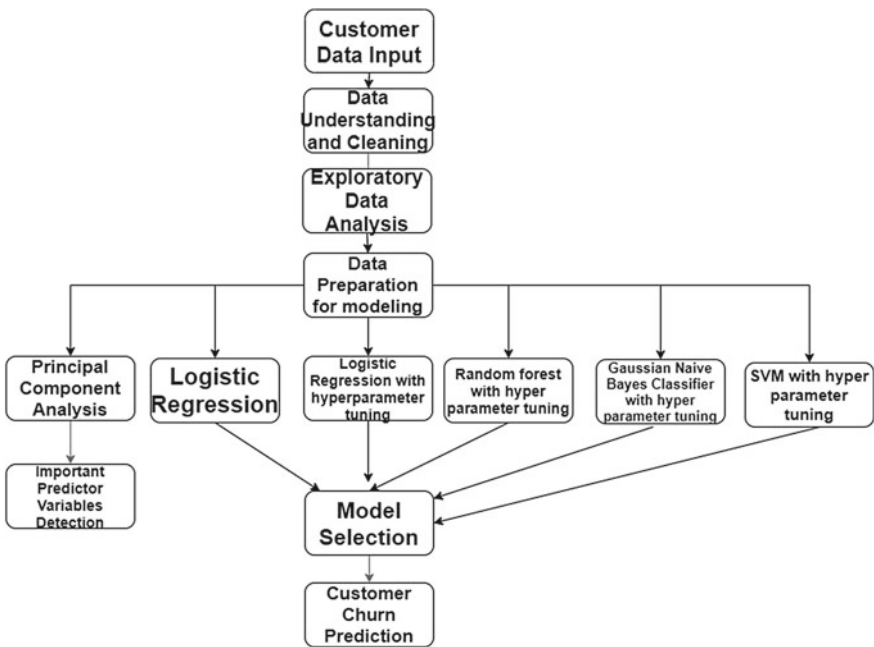


Fig. 4 Architectural design of the system

## ***4.1 Data Preparation***

The system reads the customer data input as a CSV file, then data understanding and cleaning takes place. Understanding includes checking the shape of data, statistics of missing columns, missing value analysis, and column significance. Cleaning included removal of columns with no variance (skewness), missing value imputations, remove insignificant columns, removing columns with a very high percentage of missing values.

## ***4.2 Exploratory Data Analysis (EDA)***

This includes summarizing the main characteristics of data sets and also visualizing them using Bar Charts, Pair Plots, and Heat Maps. In this System, Exploratory Data Analysis performs Univariate Analysis, Bivariate Analysis, Multi-Collinearity Analysis, and Outlier detection and treatment. Further, preparation of data for modeling starts with class imbalance handling. Since our dataset is large, Principal Component Analysis is used which reduces dimensionality for a better understanding of customer data.

## ***4.3 Training and Testing***

Once the data is prepared for modeling, different models (Logistic Regression without Hyperparameter tuning, Logistic Regression with Hyperparameter tuning, Gaussian Naive Bayes Classifier with Hyperparameter tuning, Random forest with Hyperparameter tuning, Support Vector Machine with Hyperparameter tuning) are trained and tested to predict churn, after which the best model will be selected and finally give the list of customers likely to churn. After this, the Logistic Regression model and Random Forest model are again implemented without Principal Component Analysis to predict the crucial reasons for customer churn. Finally, based on our observations best models are selected for prediction based on their accuracy. We have also suggested and recommended some ways to reduce the churn rate.

## ***4.4 Model Selection***

Based on our observations best models are selected for prediction depending on their accuracy. The accuracy is calculated by Confusion Matrix which are shown in Table 1 and Table 2 for Logistic Regression with PCA and Random Forest without PCA

**Table 1** Confusion matrix of logistic regression with PCA

	Precision	Recall	f1-score	Support
0	0.98	0.81	0.89	8307
1	0.27	0.83	0.41	694
Accuracy			0.82	9001
Macro avg	0.63	0.82	0.65	9001
Weighted avg	0.93	0.82	0.85	9001

**Table 2** Confusion matrix of random forest without PCA

	Precision	Recall	f1-score	Support
0	0.98	0.93	0.95	8307
1	0.46	0.73	0.57	694
Accuracy			0.91	9001
Macro avg	0.72	0.83	0.76	9001
Weighted avg	0.94	0.91	0.92	9001

respectively. We have also suggested and recommended some ways to reduce the churn rate.

## 5 Results and Analysis

After experimenting on the models, we have observed the results obtained by performing the models after implementing Principal Component Analysis (PCA) and it is inferred that the best model for prediction based on Accuracy, Recall, AUCROC Precision-Recall Curves (PCA) is Logistic Regression with PCA. Also, the Best Model for Feature Selection Based on Accuracy, Recall, AUC-ROC Precision Recall Curves (Non-PCA) is Random Forest. The Confusion Matrix for Logistic Regression with PCA and Random Forest without PCA are shown in the Table 1 and Table 2 respectively.

We recommend the following strategies to the companies to improve business, increase annual revenue, and reduce the chances of customer churn: If the users haven't recharged in the Good Phase, then the company should provide them with some offers and incentivize them to recharge during the Action Phase (month of July and August). If we see a drop in Minutes of Usage in the Action Phase then provide free (additional) Local and STD minutes on a minimum recharge amount. Provide Free (additional) Operator to other Operator minutes during non-peak hours (10 PM in the night to 6 AM in the next morning) or better termed as Night Pack against a minimum recharge amount in the Action Phase. Provide Free (additional) Facebook data in the Action phase to the probable Churners.

## 6 Conclusion

This paper demonstrates several models that are used to predict customer churn and two of them are selected as the most effective and efficient ones. Based on our observations, it can be concluded that the Logistic Regression model is the best for identifying the customers about to churn and the Random Forest model is best for finding the reasons for churn. Some important features like roaming, STD, and local calls both incoming and outgoing are good indicators of customer churn and the companies need to pay attention to these to decrease the churn rate. Comparing with the other models, this model will be very helpful for the Telecom Companies to predict customer churn with accuracy and efficiency and will fulfil their needs that lead to business improvement. While this model is eminent in predicting the customer churn in Telecom Industry, there may be some parts where it can be improved further. We can apply Lazy learning approaches to have better customer churn prediction.

## References

1. Babu S, Ananthanarayanan NR (2014) A review on customer churn prediction in telecommunication using data mining techniques. *Int J Sci Eng Res (IJSER)* 04:2347–3878
2. Bagul N, Berad P, Surana P, Khachane C (2021) Retail customer churn analysis using rfm model and k-means clustering. *Int J Eng Res Technol (IJERT)* 10:349–354
3. Varun E, Ravikumar P (2020) Churn prediction in telecom industry using social network analysis. *Int J Eng Res Technol (IJERT)* 08:121–124
4. Kavitha V, Mohan Kumar SV, Hemant Kumar G, Harish M (2020) Churn prediction of customer in telecom industry using machine learning algorithms. *Int J Eng Res Technol (IJERT)* 09:181–184
5. Labhsetwar SR (2020) Predictive analysis of customer churn in telecom industry using supervised learning. *ICTACT J Soft Comput* 10:2054–2060
6. Balasubramanian M, Selvarani M (2014) Churn prediction in mobile telecom system using data mining techniques. *Int J Sci Res Publ* 04:2250–3153
7. Mehruz Reza Md, Nahar S, Akter T (2018) Segmentation of mobile customers using data mining techniques. *Int J Eng Res Technol (IJERT)* 07:251–255
8. Chandana S, Varun E, Vineetha G, Kumar P (2018) Analysis of telecom customer churn prediction by building decision tree. *Int J Eng Res Technol (IJERT)* 06:1–6
9. Saini N, Monika, Garg K (2017) Churn prediction in telecommunication industry using decision tree. *Int J Eng Res Technol (IJERT)* 06, 439–447
10. Sharma RR, Sachdeva R (2017) Review on prediction of churn customer behavior. *Int J Eng Res Technol (IJERT)* 06:257–261

# Delve into the Realms with 3D Forms: Visualization System Aid Design in an IOT-Driven World



Aamir Khambaty, Drumil Joshi, Fawzan Sayed, Keagan Pinto, and Sunil Karamchandani

**Abstract** Since its inception, Augmented Reality (AR) has shown immense promise in several applications. This project aims to amalgamate computer vision and AR techniques to create a platform that has applications in several industries like retail, gaming, cosmetics, electronics manufacturing, etc. The project implements steps like object detection—where the model detects and describes pertinent features from the input image. Oriented FAST and Rotated BRIEF (ORB) is the algorithm chosen for the same, due to its robustness. ORB is an open-source algorithm developed at OpenCV Labs. Additionally, the project also implements Feature matching in order to determine the spatial orientation of the target object in the camera feature. The algorithm selected for this is FLANN (Fast Approximate Nearest Neighbor Search Library). Moreover, this project uses Raspberry-Pi which provides excellent computing abilities and a high-definition camera can be mounted onto it. This camera is the input feed through which the image fed to the model can be augmented on an object.

**Keywords** Augmented reality · ORB · FLANN · OpenCV · Raspberry-Pi · IoT

## 1 Introduction

Computer vision is one of the rapidly advancing fields in the domain of machine learning and artificial intelligence. Computer vision enables smart devices such as computers and robots to interpret, analyze, and process digital images and videos. Computer visions employ mathematical tools used in image processing techniques to perform operations over digital images and videos. Computer vision offers a plethora of applications such as object detection and identification, object tracking, facial recognition, medical diagnosis, movement analysis, augmented reality, classification of objects, and many more. In this project, we are using computer vision for Augmented Reality (AR). AR is an enhanced version of the real physical world

---

A. Khambaty (✉) · D. Joshi · F. Sayed · K. Pinto · S. Karamchandani  
Dwarkanadas J. Sanghvi College of Engineering, Mumbai, India

that is achieved through the use of digital visual elements, sound, or other sensory stimuli delivered via technology. AR uses the existing real-world environment and puts virtual information on top of it to enhance the experience. For example, in the furniture business, AR enables customers to place a virtual piece of furniture in their room with the help of their camera before purchasing it. AR extends its application to multiple fields such as healthcare, shopping, cosmetics, and many more [1]. In this project, we are using the techniques of feature mapping and detection of computer vision to augment virtual objects in a real environment with the help of cameras and the Raspberry Pi computer.

## 2 Literature Survey

AR is a promising field with exciting innovations being made every day. Karczmarek et al. carried out feature extraction to obtain information about both local and global properties of an object using chain code-based local descriptor and extended it to facial recognition [2]. Zhu et al. used deep reinforcement learning to develop a target-driven visual navigation framework, where it was possible to take actions and interact with objects [3]. Souhail Guennouni et al. proposed a real-time system to detect multiple objects using the OpenCV library. Mukherjee et al. proposed a comparative experimental study of image feature detectors and descriptors by performing a comprehensive review of a large number of popular feature detectors developed in the last three decades [1]. The study made several contributions to the development of a generic comparison of feature detectors and descriptors. Ethan Rublee et al. proposed that ORB is a more efficient alternative to SIFT or SURF; they achieved this by demonstrating that ORB is two orders of magnitude faster than SIFT while performing as well in many situations [4].

## 3 Methodology

In this research, we implemented knowledge of AR in computer vision. Research of AR in computer vision is of the hour and implementing it from scratch with help of Python and OpenCV makes it more robust. We have divided the whole research into four major portions: Data Acquisition System from Raspberry Pi, Feature Detection, Feature Matching, and 3D Projection of Augmented Image as shown below in the flowchart (Fig. 1).



Fig. 1 Flowchart

### 3.1 Data Acquisition System Using Raspberry Pi

The Raspberry Pi is one small Linux computer board built and developed in the United Kingdom. The latest in a line of these computers is the Raspberry Pi 4 Model B that is implemented in our research work. Corresponding to its low cost, modular design, and high processing power, it becomes an ideal Iot device and various other applications such as image processing, machine learning, etc. Modularity is achieved because it comes with the latest hardware and software capabilities such as HDMI, USB-C, Wi-Fi, and high-definition camera support. It comes with a 1.5 GHz CPU and 8 GB Ram which gives it enough power to process image processing applications in context to our research. As Python is the primary programming language that supports OpenCV library for image processing, and with the support of the Raspberry Pi camera module, it becomes an independent tool suitable for our research. OpenCV is an open-source Python library, used for computer vision in artificial intelligence, machine learning, face recognition, etc. In OpenCV, CV is a concise form of computer vision, which is defined as a study field that helps computers to understand the content of digital images such as photos and videos (Fig. 2).



Fig. 2 Raspberry Pi with camera

### 3.2 Feature Detection

To augment any graphic on the image, we want to look for interesting regions in an image that means to features of the image [2]. The smallest detail in any algorithm for computer vision projects is called Features. Gradient changes, edges, corners, lines, and angles in the image define the look and contrast of the image [2]. Descriptors is a common term we will come across while working with algorithms related to feature detection [3]. We will use the properties of the detected features found such as what kind of calculation was done, the number of spokes, the angle of the lines, the placement of the text, the use of fonts, all of these become adjectives in real life. In our research, features are vectors that have information about the elements in which they are stored. This information can be gradient angle, number, limit, intensity pixels values, etc. [4]. Although there are many algorithms available in the OpenCV platform for feature detection and descriptor computing such as SIFT, SURF, and others, the reason here we have chosen the ORB algorithm for our research is that ORB is a free algorithm developed in OpenCV Labs. It consists of Oriented FAST and Rotated BRIEF and is a better option as compared to the patented algorithms such as SIFT and SURF. FAST is used to find the element and BRIEF is used to find the meanings of that element. As a whole, ORB performs excellent in experimenting the things. Hence, by this process, we do feature detection (Fig. 3).



Fig. 3 Feature detection



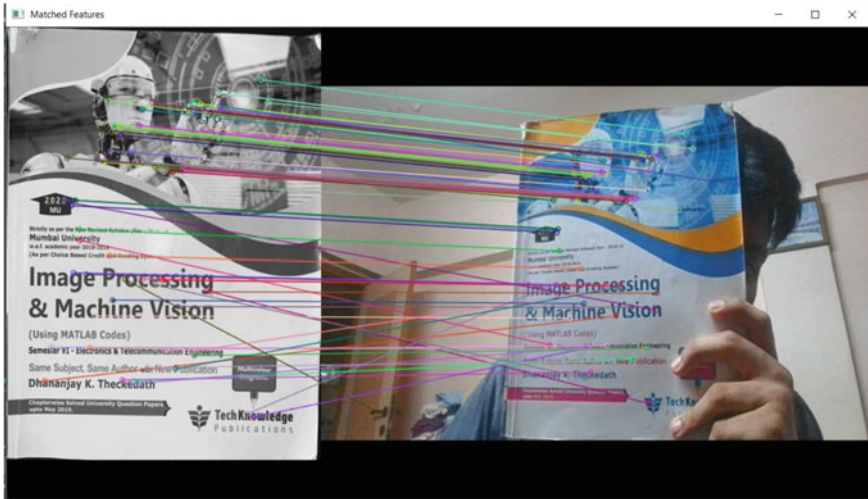


Fig. 4 Feature matching in normal orientation

### 3.3 Feature Matching

Feature matching is the process of comparing the features of the input image and the image to be found. We use it for object tracking in this project [5]. Feature-based object tracking is where the features of the input image and the target image are continuously compared to detect and compute the motion of the target object in the real world. This concept is implemented using the FLANN-based Matcher. Fast Library for Approximate Nearest Neighbors, or FLANN, is a collection of very powerful algorithms that are highly optimized for nearest neighbor searches. The advantage of this method is that it is highly effective for large databases and fast real-time computing. Index parameters and search parameters as recommended in OpenCV documentation is used as parameters to make the FLANN searcher. The built function is then used to generate a list of all the good matches, using the descriptors of the input frames from the video and the descriptors of the image to be found. This is how we get the feature matched output showing if the target image is in the frame of the camera (Figs. 4, 5, and 6).

### 3.4 3D Projection of Augmented Image

This is the final step of the entire process, where we will be projecting the image to be augmented (augment image for future reference) onto the input images from the camera. We first note down the source keypoints from the input image and then find the destination keypoints after the feature matching step. We have a set a threshold

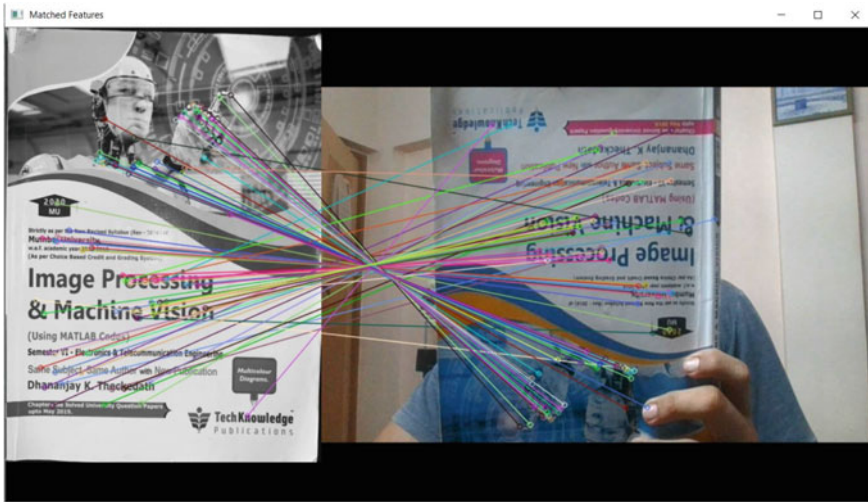


Fig. 5 Feature matching in inverted orientation

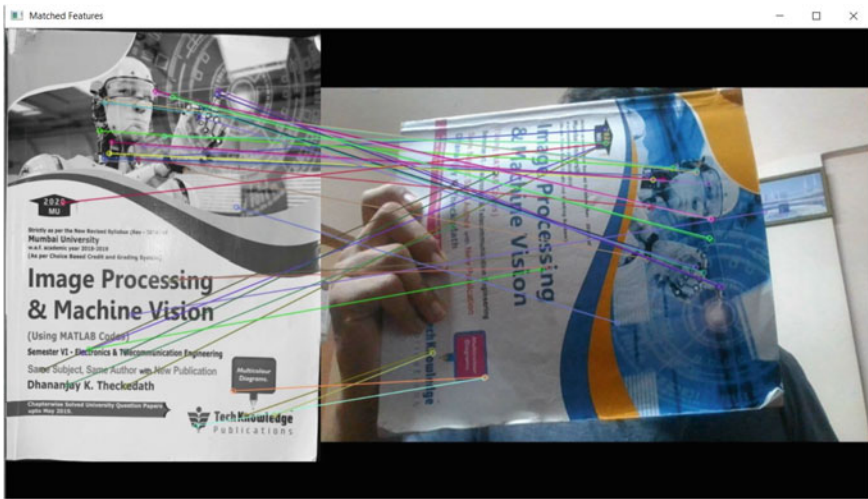


Fig. 6 Feature matching in right turned orientation

of at least ten matches for us to declare that the target object is in the frame. A homographic matrix is then found for the image. This basically helps in setting the augmented image in the right 2D plane in the image as the target object won't always be parallel to the camera and will need to be warped in a certain direction. A perspective transform is applied to map the key points of the target image on the input image. This creates the warped target image which can now be placed on the input image. The area where the warped target image sits on the input image is finally filled with back

color and that part of the image is added with the warped augment image, giving us the final desired output of the input image containing the augment image in place of the target image.

### 4 Results and Conclusion

We have successfully implemented 3D Image Augmentation. The process employed by us has shown itself to be very efficient and easy to implement. The camera module was sufficient enough with respect to clarity, producing above par results. Feature detection and feature matching were done effectively and worked in even the most extreme case scenarios. The results obtained on the output are of exceptional quality. 3D Augmenting of Image was hence successfully performed (Figs. 7, 8, and 9).

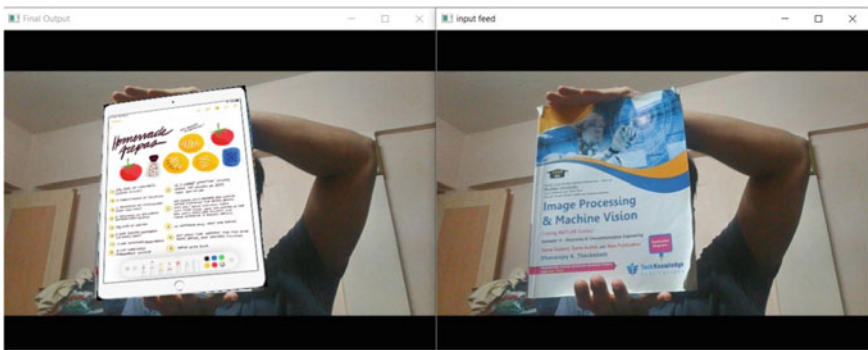


Fig. 7 Image augmenting in normal orientation

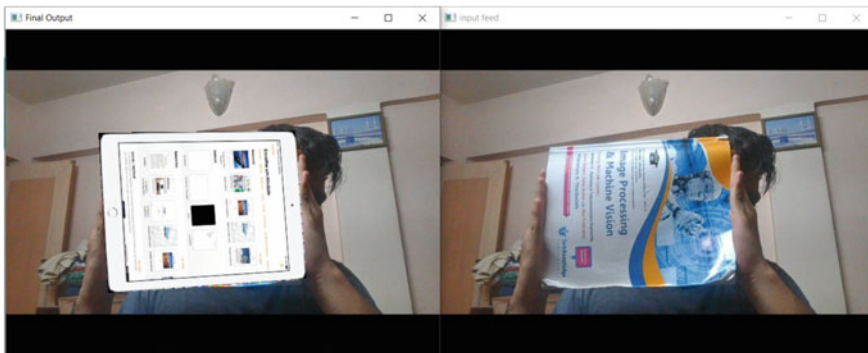
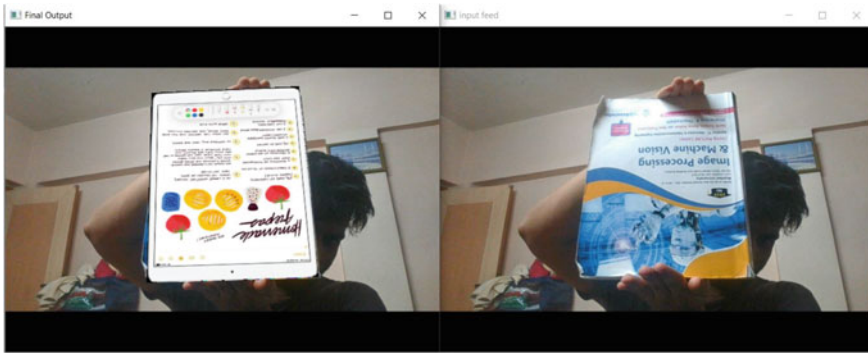


Fig. 8 Image augmenting in sideways orientation



**Fig. 9** Image augmenting in inverted orientation

## 5 Enhancing Retail Experience

### 5.1 Medical Field

Doctors could use augmented reality as a visualization and training aid for surgery. It is possible to collect 3D datasets for file the patient in realtime uses similar sensations magnetic resonance imaging (MRI), ultrasound imaging, or computed tomography scans (CT). These are data sets can be provided and physically integrated time from the point of view of the real patient. Visible commands can be a reminder for a young surgeon of the necessary steps, without the need to look away from the patient just look at the manual.

### 5.2 Enhancing Retail Experience

AR can be extensively used in retail establishments where the customers shopping experienced is enhanced. For example, while purchasing or renting furniture online, the user could directly place a virtual model of that chair or table he is interested in directly in his room before actually purchasing it. This is very useful today given the pandemic scenario where we are completely refraining ourselves from going physically to stores and purchasing everything online.

### 5.3 Annotation and Visualization

AR can be used to describe things related to public or private areas in details. Requests for public use details will consider availability of public information to be used. For

example, portable display like smartphone can provide information about content on library shelves when the user moves around the library in real time. User can identify the parts of the engine model and the AR program will display the name of the identified part. Similarly, AR can provide a list of items available on grocery store. Either way, these definitions could be linked to private notes as well. For example, one can make list of reminders and paste a window containing this list in this field of vision.

## 5.4 Education and Training

AR applications can supplement a standard curriculum. Things such as text, images, video, and audio can be focused on real-time viewing of the reader of nature. Teaching materials such as textbooks, postcards, and more readings may contain embedded text “Tags” that produce more student information in multimedia format, when scanned AR device. AR technology also allows learning about remote interaction, where students as well teachers who are not in the same body. The site can share a virtual standard unpopular virtual learning environment objects and learning materials, and engage and another within the area.

## References

1. Mukherjee D, Wu QMJ, Wang G (2015) A comparative experimental study of image feature detectors and descriptors. *Mach Vis Appl* 26:443–466. <https://doi.org/10.1007/s00138-015-0679-9>
2. Karczmarek P, Kiersztyn A, Pedrycz W, Dolecki M (2017) An application of chain code-based local descriptor and its extension to face recognition. *Pattern Recogn* 65:26–34. <https://doi.org/10.1016/j.patcog.2016.12.008>
3. Zhu Y, Mottaghi R, Kolve E, Lim JJ, Gupta A, Li FF, Farhadi A (2017) Target-driven visual navigation in indoor scenes using deep reinforcement learning. In: *Proceedings of international conference on robotics and automation (ICRA 17)*. IEEE Press, pp 3357–3364. <https://doi.org/10.1109/ICRA.2017.7989381>
4. Rublee E, Rabaud V, Konolige K, Bradski G (2011) ORB: an efficient alternative to SIFT or SURF. In: *Proceedings of international conference on computer vision (ICCV 11)*. IEEE Press, pp 2564–2571. <https://doi.org/10.1109/ICCV.2011.6126544>
5. Ma Y, Wang J, Xu H, Zhang S, Mei X, Ma J (2017) Robust image feature matching via progressive sparse spatial consensus. *IEEE Access* 5:24568–24579. <https://doi.org/10.1109/ACCESS.2017.2768078>

# Autonomous Parking System Perception and Control Simulations on ROS-Gazebo



Sunil Karamchandani, Saurabh Pednekar, Atharva Pusalkar, Shivani Bhattacharjee, and Disha Issrani

**Abstract** Autonomous systems are being developed in the automotive industry as an aid for the driver in terms of safety and comfort. Automated parking technology is one such key aspect in the domain. It provides the driver with quick and safe parking without any manual inputs. This paper discusses the method of parking scene recognition, perception, path tracking, and control of the vehicle for autonomous parking systems. Simulations based on control of the car while parking mode are also demonstrated.

**Keywords** Autonomous parking · Perception · SLAM · Control · ROS · Gazebo

## 1 Introduction

With the constant increase in the number of electric vehicles, the world is rapidly going in the direction of automating day-to-day automotive processes. Automated parking assistance is in such an area which is being started to be implemented in vehicles in recent times. Autonomous parking aids the driver in parking vehicles safely and instantly without manual help. As an added advantage to safety and comfort, autonomous parking helps in efficient use of the available parking space which provides tremendous help taking into consideration the exponential increase in the number of vehicles in the world.

In earlier days, the research on automated parking systems was based on ultrasonic sensing technologies for perception. In recent times, visual sensing methodologies like cameras and LiDARs are widely used for perception purposes. This is due to the development of machine vision algorithms and image processing methods. These methods provide the necessary accuracy along with time efficiency.

This paper is organized as follows:

First, the perception and SLAM algorithm methods are discussed. To begin, the data is collected from odometry sensing units consisting of cameras, LiDAR, and

---

S. Karamchandani · S. Pednekar (✉) · A. Pusalkar · S. Bhattacharjee · D. Issrani  
Dwarkanadas Jivanlal Sanghvi College of Engineering, No. U-15, J.V.P.D. Scheme, Bhaktivedanta Swami Rd, Opp. Cooper Hospital, Vile Parle, Mumbai, Maharashtra 400056, India

vehicle inertial measurement unit (IMU) to determine the path and vehicle orientation. The simultaneous location and mapping (SLAM) algorithm plans a parking trajectory of the vehicle based on the parking scene and the vehicle orientation.

Second, based on the trajectory a control mechanism is established which independently controls all the four wheels and steering at a fixed vehicle velocity. The wheel rpm is controlled by the motor controller input to the motors whereas a steering actuator based on servomechanism actuates the steering for path adjustments.

Third, the control mechanisms for automatic parking controllers were simulated on robot operating system (ROS) and Gazebo to determine the dynamics of the model.

## 2 Perception and SLAM Algorithms

Perception techniques for autonomous parking processes can be realized with the help of placing parking in a way such that the vehicle length and width along with a marginal extra amount of space for vehicle movement during the process and a buffer for error correction. Perception setup consists of two stereo rolling shutter cameras which can transmit raw data to the general processing unit (GPU) over ethernet. A pipeline-based pose estimation from images can be achieved with the help of a previous structural information of the object, i.e., parking cones. The sub-modules of pipeline, viz., object detection, keypoint regression, and pose estimation are run as nodes using ROS [7–9].

The object detection in the pipeline is in the form of You Look Only Once (YOLOv2).

YOLOv2 can be trained for detecting parking cones which act as points to plan a path for vehicle movement trajectory. Bounding box method for detecting cones can be used for detecting by feeding prior information of height and width of the cone and could be recalculated by anchor boxes used by YOLOv2 as shown in Fig. 1 [1].

YOLOv2 was chosen for its robustness and fast performance for relatively large images. For 3D detection of the traffic cones, the pipeline leverages feature matching using the semi-global matching algorithm (Hirschmüller et al. 2007) (Fig. 2). Using the computed disparity and depth for each pixel of the left image, the 3D point of the center of the cone patch is determined [1].

To leverage the cone positions, the system uses a landmark-based SLAM algorithm called fastSLAM 2.0. This is due to the fact that the SLAM pipeline must run in real time and easily tunable. The fastSLAM approach also runs in  $N \log(N)$  time complexity with accuracy proportional to the number of particles. The proposed pipeline runs at 25 Hz with two redundant sources of cone positions and one odometry source. The landmarks are then fed to a rule-based path planner that generates a trajectory to follow based on the relative positions of the traffic cones. The motion primitives for the planning algorithm are determined using the car dimensions and minimum parking space required [5].

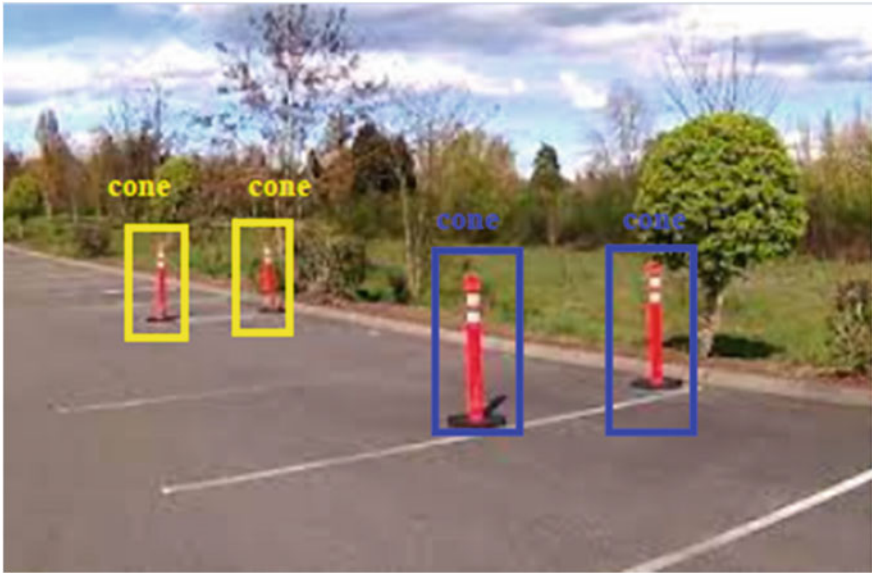


Fig. 1 Parking cone detection using YOLOv2

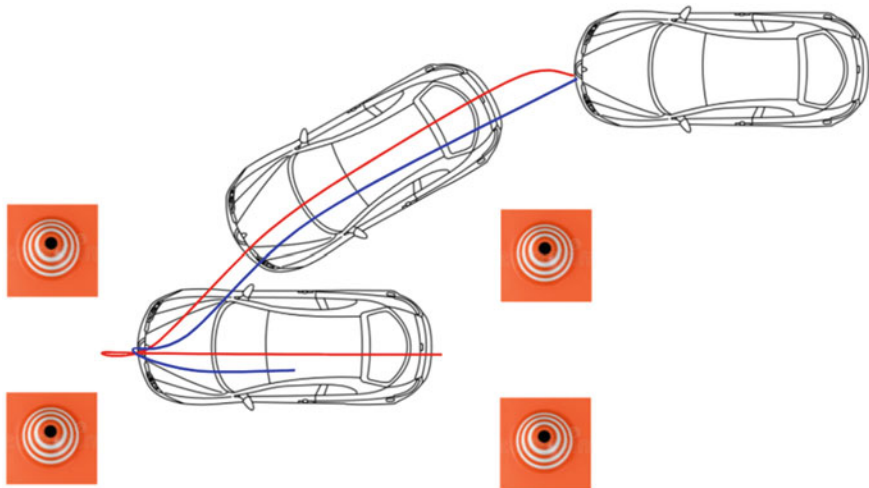


Fig. 2 Path generated from SLAM landmarks and odometry

### 3 Vehicle Dynamic Control

Pure pursuit is a tracking calculation that works by figuring the radius of curvature that will move a vehicle from its present situation to some objective position. The



calculation picks an objective position that is some distance in front of the vehicle on the way. The straight speed is expected to be consistent, and thus you can change the direct speed of the vehicle anytime. The calculation at that point pushes the look-forward point on the way dependent on the current situation of the vehicle until the last mark of the way. Considerations can be made that this vehicle continuously pursues a point before it (Fig. 3). This calculation expects optimal conditions such as no skidding or tire slip and ideal reaction from actuators [2].

The virtual curvature for the control to reach the desired point can be given by

$$R = \frac{2\sin(\theta)}{L_a} \tag{1}$$

where  $R$  = radius of curvature,  $\theta$  = pure pursuit angle, and  $L_a$  = look ahead distance.

From the equation, the required steering angle can be computed by using Ackerman geometry and double track model [3]. The equation for the steer angle is given by

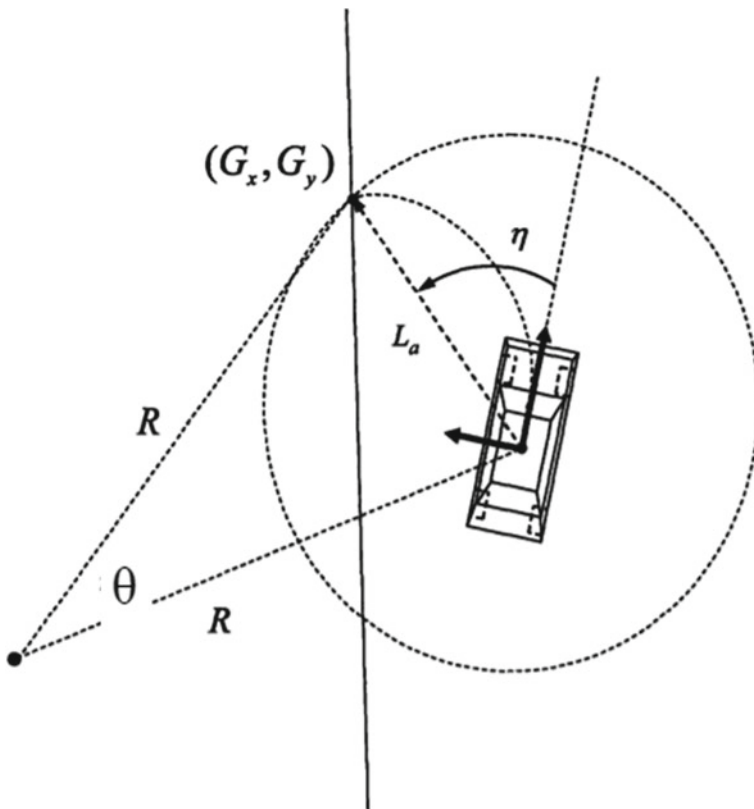


Fig. 3 Desired point using pure pursuit

$$\phi = \tan^{-1} \frac{2Lb\sin(\theta)}{La - Lt\omega\sin|\theta|} \tag{2}$$

where  $\phi$  = steer angle,  $Lb$  = wheelbase, and  $Lt\omega$  = track width.

Now, the next position for center of gravity by assuming small angles can be calculated by

$$dy = vx(\beta + \psi) \tag{3}$$

where  $\beta$  = tire slip angle and  $\psi$  = yaw movement (Fig. 4).

The pure pursuit angle can be decomposed as  $\theta_a$  and  $\theta_b$  as shown in Fig. 5, therefore the radius of curvature for pure pursuit can be calculated assuming small angles by.

Therefore  $\theta_a = y_d - y/La$  and  $\theta_b = -\beta - \psi$

$$R = 2 \left( \frac{y_d - y}{La^2} - \frac{\psi + \beta}{La} \right) \tag{4}$$

where  $y_d$  is the required location of car's center of mass. Now, the linearized control equation can be written as

$$\phi_d = 2Lb \left( \frac{y_d - y}{La^2} - \frac{\psi}{La} \right) \tag{5}$$

where  $\phi_d$  is the required steer angle value (Fig. 6).

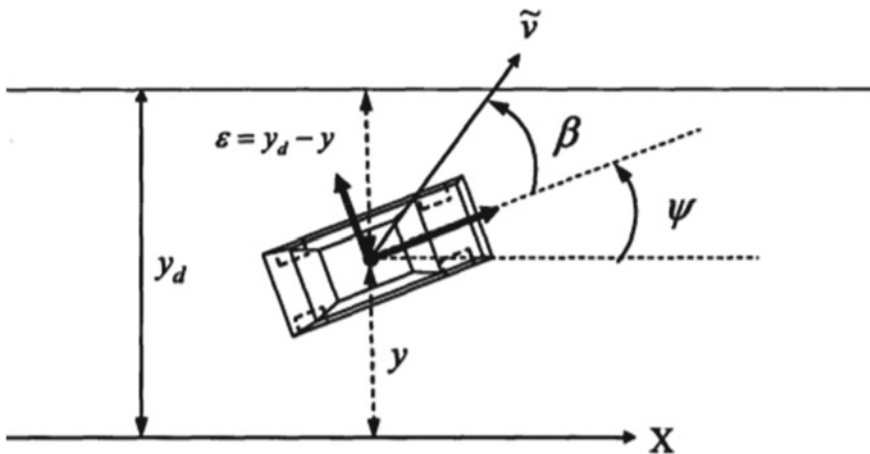


Fig. 4 Pure pursuit line following

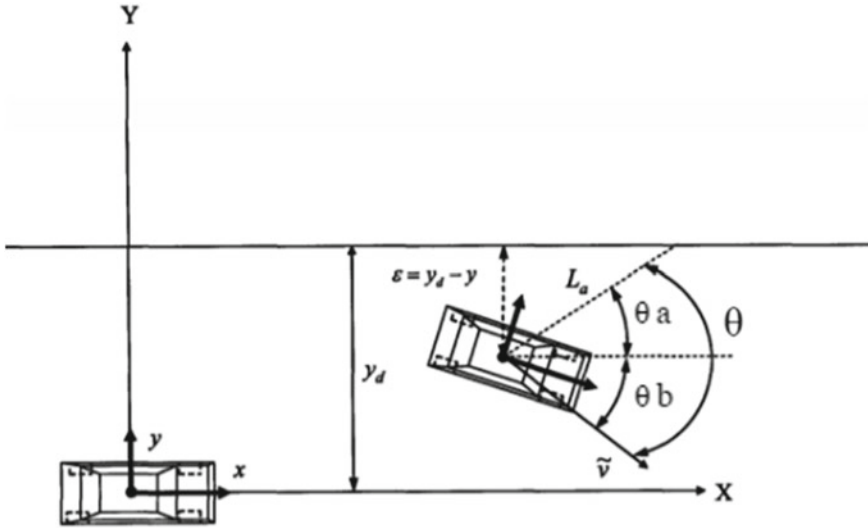


Fig. 5 Pure pursuit angle decomposition

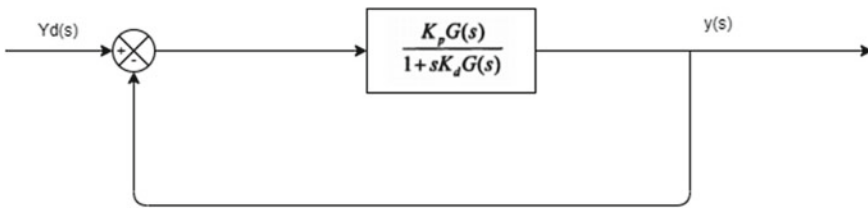


Fig. 6 The figure depicts the control system flow of the steer angle controller

Considering the controller as a proportional derivative type for simplicity and the proportional and derivative gains can be give as.

$$K_p = \frac{2Lb}{La^2} \text{ and } K_d = \frac{2Lb}{La \cdot vx} \tag{6}$$

and transfer function as  $G(s) = \frac{v^2}{s^2 Lb}$  where  $V$  is forward velocity of the car [4].

### 4 Simulation Analysis on ROS-Gazebo

Simulations were done to analyze the outdoor environment stimulus of the designed control mechanism. A real environment was created with parking cones placed on the side of the road. Sensory robot independent plugins *gazebo\_ros\_imu*,

**Table 1** Car parameters considered for Gazebo robot

Wheelbase	2.5 mts
Car length	4.5 mts
Track width	1.5 mts
Car width	1.8 mts
Maximum steer angle	35 deg

**Fig. 7** Isometric view of successfully parked vehicle using control algorithm on Gazebo

*gazebo\_ros\_depth-camera, gazebo\_ros\_camera\_utils*. URDF robot model of general car was created with following specifications (Table 1 and Figs. 7, 8):

URDF robots were spawned and the ROS nodes were simulated simultaneously in gazebo. Data from perception cameras is firstly used to estimate the amount of available area for parking and based on the maneuver and size of the car the spot is finalized for parking. Secondly, the path trajectory is generated and the car follows it by the described control mechanism [10].

## 5 Conclusion

As of now various autonomous parking methods have been implemented in cars like Audi A8, Tesla model S, Ford expedition, etc. With an increasing demand for electric cars, fully autonomous driving systems can be implemented. In this paper, perception and SLAM methods like YOLOv2 and FAST SLAM 2.0 were discussed which provide required accuracy and speed for detection. Further better anchor boxes for

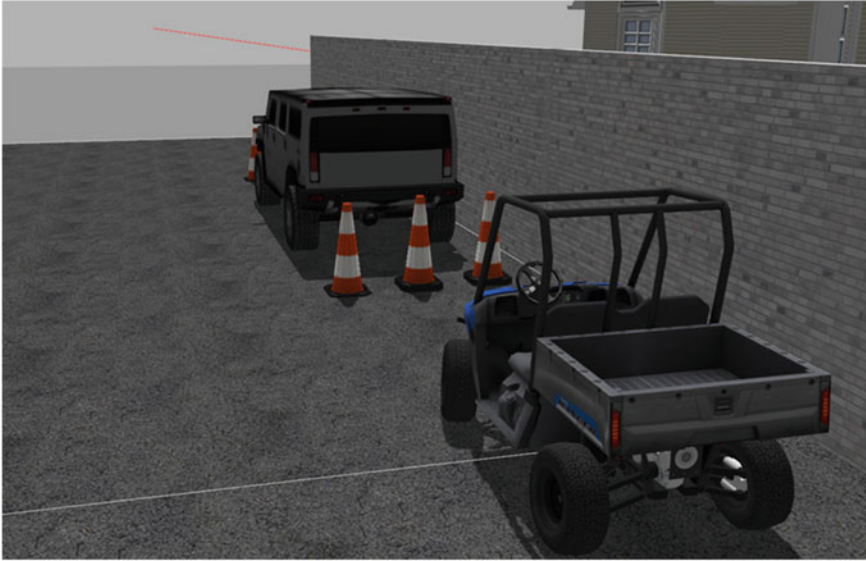


**Fig. 8** Rear view of successfully parked vehicle using control algorithm on Gazebo

YOLOv2 can be obtained with more training of the dataset thus increasing generalizing ability. Pure pursuit control method using Ackerman steering geometry was used for designing the control. However, it was noticed that extreme maneuvers resulted in substandard vehicle performance due to the fact that position of each wheel at instance was neglected.

## References

1. Redmon J, Farhadi A (2016) YOLO9000: better, faster, stronger. [arXiv:1612.08242](https://arxiv.org/abs/1612.08242)
2. Campbell SF (2007) Steering control of an autonomous ground vehicle with application to the DARPA urban challenge, pp 85–110
3. Zhao J-S, Liu X, Feng Z-J, Dai JS (2013) Design of an Ackermann-type steering mechanism
4. Coulter RC (1992) Implementation of the Pure Pursuit path tracking algorithm. The Robotics Institute Carnegie Mellon University
5. Shin DH (1990) High performance tracking of explicit path by roadworthy mobile robots. Doctoral Thesis, Dept. of Civil Engineering, CMU
6. Hecker S, Dai D, Van Gool L (2018) End-to-end learning of driving models with surround-view cameras and route planners. In: European conference on computer vision (ECCV)
7. Levinson J, Askeland J, Thrun S, et al. (2011) Towards fully autonomous driving: systems and algorithms. In: IEEE intelligent vehicles symposium (IV)
8. Valada A, Vertens J, Dhall A, Burgard W (2017) Adapnet: Adaptive semantic segmentation in adverse environmental conditions. In: Robotics and automation (ICRA), 2017 IEEE international conference. IEEE

9. Hirschmuller H (2008) Stereo processing by semiglobal matching and mutual information. *IEEE Trans Pattern Anal Mach Intell* 30(2):328–341. <https://doi.org/10.1109/TPAMI.2007.1166>
10. Koenig N, Howard A (2004) Design and use paradigms for Gazebo, an open-source multi-robot simulator. In: 2004 IEEE/RSJ international conference on intelligent robots and systems (IROS) (IEEE Cat. No.04CH37566), vol 3, pp 2149–2154. <https://doi.org/10.1109/IROS.2004.1389727>

# Bus Monitoring System Using Raspberry Pi



Tushar Sawant and Krupansh Shah

**Abstract** Today the world is suffering from global pandemic, and maintaining a social distance is a must. COVID-19 has changed the perception of the whole world. Public Transport Company has been developing the system for displaying the position of the passenger vehicle for convenience of the customers. However, those systems only indicate the position of the vehicle but not show the availability of seats in the vehicle. People will waste time waiting for the next passenger vehicle and cannot manage the time of travel or activities correctly. If customers know both position of the passenger vehicle and vacancy of seats, people can use the time to do other activities before the passenger vehicle arrives. So, in this project, we are going to help those people by letting them know the situation of bus whether it is crowded or empty or moderate by notifying the passenger count on their phone through an application and later on they can decide whether to take this bus or wait for the next arrival. So, in this project, the passenger information system is designed by using image processing technique. Raspberry Pi can be connected with Raspberry Pi 4 in the bus for detecting the object on the bus and sending the data to the server via 4G communication. This system uses open-source computer vision (open CV) real-time object detection to analyze and process the data and then calculate the count of the passenger by using the maximum face detection data.

**Keywords** Open Cv · Raspberry Pi · Raspberry camera · Solenoid valve · Android

---

T. Sawant (✉)

EXTC Dept., Dwarkadas J. Sanghvi College of Engineering, VileParle, Mumbai, India  
e-mail: [Tushar.Sawant2@djsce.ac.in](mailto:Tushar.Sawant2@djsce.ac.in)

K. Shah

Mechatronics Dept., Mukesh Patel School of Technology Management and Engineering,  
VileParle, Mumbai, India

## 1 Introduction

Public transport are getting awfully crowded, and with increasing demand we need to find the balance between space and resources allocated to meet the needs of the population. BEST is the second-largest mass transport system in Mumbai after the suburban train network and ferries 30 lakh commuters daily. To ease the travel of commuters, we propose an idea of an app called “Bustrack.” None of the current applications in the market like M-Tracker provide the exact time in which the bus will reach the user and they just show the tentative time of arrival of the bus but with bus track the customer can see the exact location of the bus and how much time it will take to reach the user. I have developed this app using Flutter. Some of the BEST buses arrive so late that the commuters have to wait on the bus station for hours, which time they could have used to do more productive work. In order to prevent the overcrowding of the bus, I have developed a pneumatic door system. When the number of people surpasses maximum limit the door closes and won't open until the number of people in the bus does not come down from the maximum limit. We have used a V2 camera to monitor the number of people currently traveling on the bus and this data collected is sent to the Raspberry Pi which processes the data and gives the number of people currently traveling [1]. If the number of individuals surpasses the maximum limit the door will not open until the number of people on the bus does not become lower than the maximum limit.

Also in this pandemic maintaining social distance is the only solution we have right now. This is also one of the reasons to propose this idea so that commuters can travel without breaking social distancing norms and also save abundant time by not standing at the bus station for hours and instead do something more productive [3].

## 2 Methodology

The public detector for the bus will help us to tell the number of passengers traveling in the bus and vacant seats available. It uses a Raspberry Pi camera that captures the image within the bus. A GPS module will be used in the bus as well as it will help to track the live location of the bus. Firstly, the image will be captured by the camera and that image will be communicated to a Raspberry Pi. Raspberry Pi is used as a microcontroller. The microcontroller will communicate with the camera and GPS module is used to extract the image and the parameters (Fig. 1).

The microcontroller will act as a transferring device that will only capture the image from the camera and upload it on the server. The microcontroller will upload this image on a server where all the data including the live location using the GPS module will be uploaded. The image sent on the server will be processed by open-source computer vision (Open CV) real-time object source detection to analyze and detect the number of faces inside the bus at that moment which will hence give the number of people inside the bus. That information will be used to find out the number



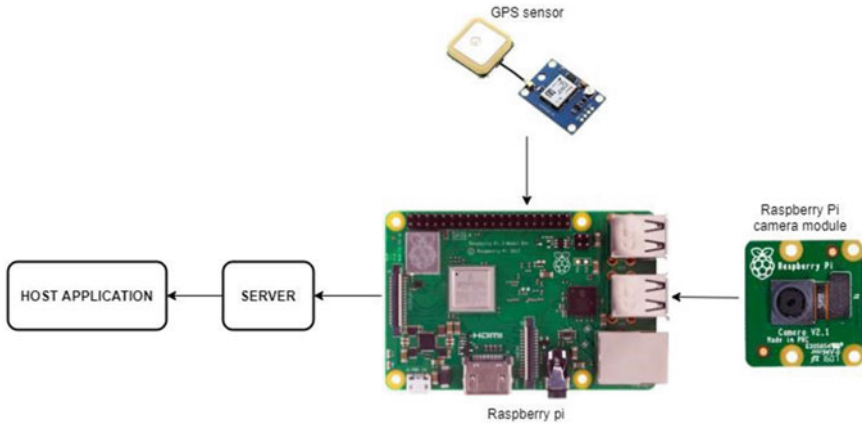


Fig. 1 a Block diagram of the system

of empty seats available in the bus. The information which is collected will now be sent to the server through Internet.

The server will then use the application to convey to the user the number of people in the bus and also will use the GPS module to track the exact location of the bus. The server will get data from all buses and will provide information on the application regarding which buses do have seats available and which do not. It will also display which bus will have available seats which is nearest to the location of the user and is going in the direction the user wants to reach.

We have created an Android application using Flutter. Flutter is an open-source UI software development kit used to develop cross-platform applications for Android, Linux, iOS, Mac, Windows, and Google. Android Studio is the official *integrated development environment* (IDE) for *Google's Android operating system* built on *JetBrains' IntelliJ IDEA* software and designed specifically for *Android development*. It is available for download on *Windows-*, *macOS-*, and *Linux-*based operating systems or as a subscription-based service.

### 3 System Working

Firstly, the camera captures a video footage which is directly fed to the processor which is the Raspberry Pi. The Raspberry Pi compares them with the dataset loaded in the SD card. We have used the fer2013 dataset here as it is the best dataset for image detection and processing. Thus, when we write the code we train the dataset and test it for predicting the outcome for a test image. On comparing the continuous feed from the camera with the dataset and code there are rectangles formed around faces of individuals depicting that there are these many people currently traveling on the bus [2]. Thus, this process is continuously repeated until the ordinance key is

pressed and we exit from the output screen. The Raspberry Pi uses Python to create frames to check person's presence on the seat. If the person is sitting in the bus can be captured by Raspberry Pi camera and count will be incremented or decremented depends on the number of frames generated by Raspberry Pi [5]. The bus monitoring system helps passengers to identify the frequency of the bus, the expected time, and how many passengers are traveling inside the bus. After every stop, the count of the passengers will be updated, so passenger comes to know that which bus will be helpful for him to reach their destination.

## 4 Flowchart

To understand the functioning of the model the flowchart is shown in Fig. 2.

In this the camera will capture the image and send it to central monitoring system. The sensors are placed to check GPS coordinates of the bus which will be updated from server side every time when new coordinates will be available. The camera will count number of passengers traveling in the bus using Raspberry Pi frames and update the count on the server [4].

Once count of passengers in the bus is available on the server it will be updated on the app. The passengers will be using Android application called "Bucker," which will help the user to track the live location of the bus by the help of a map and also show how much time the bus will take to reach the user, so the user can leave for the bus stop accordingly (Fig. 3).

We designed the user login page where it asks the person using the app to login with their credentials and if they are a first time user then they are asked to sign up with their name, email ID, and password. All this data are directly stored into a database. If the user is a driver then they have to sign in with the credentials already provided to them and all the drivers' data has been stored into a database so as to trace their location when they login from that very minute.

Next, the user will be redirected to the home page where the user can search the bus with the help of a bus digit UI code by which the bus is identified by the people. Supposedly if the user enters 84 and if that number bus exists in our database the user will be redirected to a map or else message will be shown that the particular bus number does not exist.

Next, if user has entered a valid bus number, then the user will be able to see the current location of the bus and their own location, and it will precisely show them how much time the bus will take to reach the user's current location. Thus, making it very convenient for the user as he/she doesn't have to waste any time by standing at the bus station for hours.

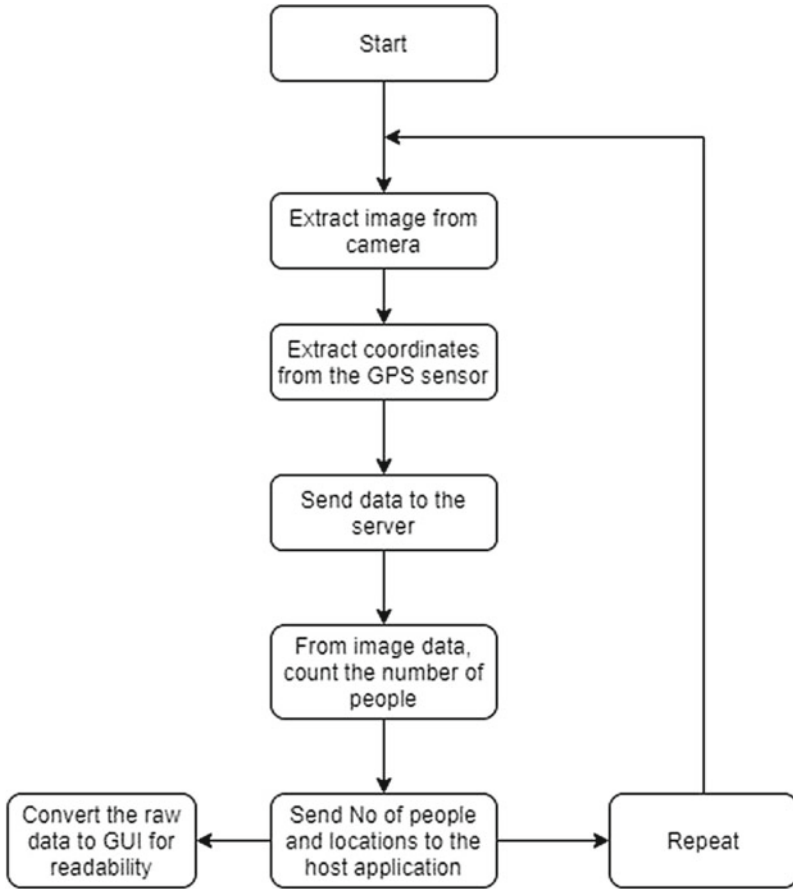


Fig. 2 Flowchart of the detection of the images

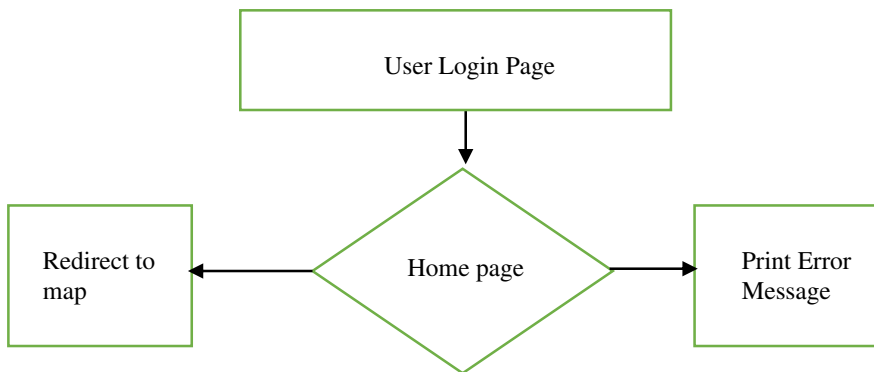


Fig. 3 Flowchart of the Android application page

## 5 Result and Analysis

The camera which is installed on bus will capture the images of the people sitting in the bus. These images will be communicated to Raspberry Pi used as a microcontroller. The microcontroller will extract the image and transfer and upload it on the server. The microcontroller will upload this image on a server where all the data including the live location using the GPS module will be uploaded. The image sent on the server will be processed by open-source computer vision (Open CV) real-time object source detection to analyze and detect the number of faces inside the bus at that moment which will hence give the number of people inside the bus. That information will be used to find out the number of empty seats available in the bus. The information which is collected will now be sent to the server through Internet.

Figure 4 shows the Raspberry Pi, camera, and bus model with passenger's images. The Raspberry Pi camera will continually scan passenger faces and update the number of passengers in the bus on the server.

Figure 5 shows the detection of the faces using V2 camera of Raspberry Pi. The Python code will create frame which will update the passenger count on the server (Fig. 6).

In the above figure, the camera is placed at a distance of 2 m and result is obtained which shows detection of the passenger faces with the help of the frames. The output is obtained with live tracking of the images and updating the value as GPS position changes (Fig. 7).

Figure 7 shows application interface, where it is showing driver and rider login. The driver login directs to the next page which will ask driver bus number and path to follow. If rider login is used then the rider will select location and search for buses running on that route. Once rider selects the bus number, then respective bus expected time, number of passengers traveling inside bus, and the available seats inside bus. Using BUSTRACK application the user gets option to see the available buses and there corresponding stop location which will help to identify the buses running on that route with number of passengers traveling inside the bus.

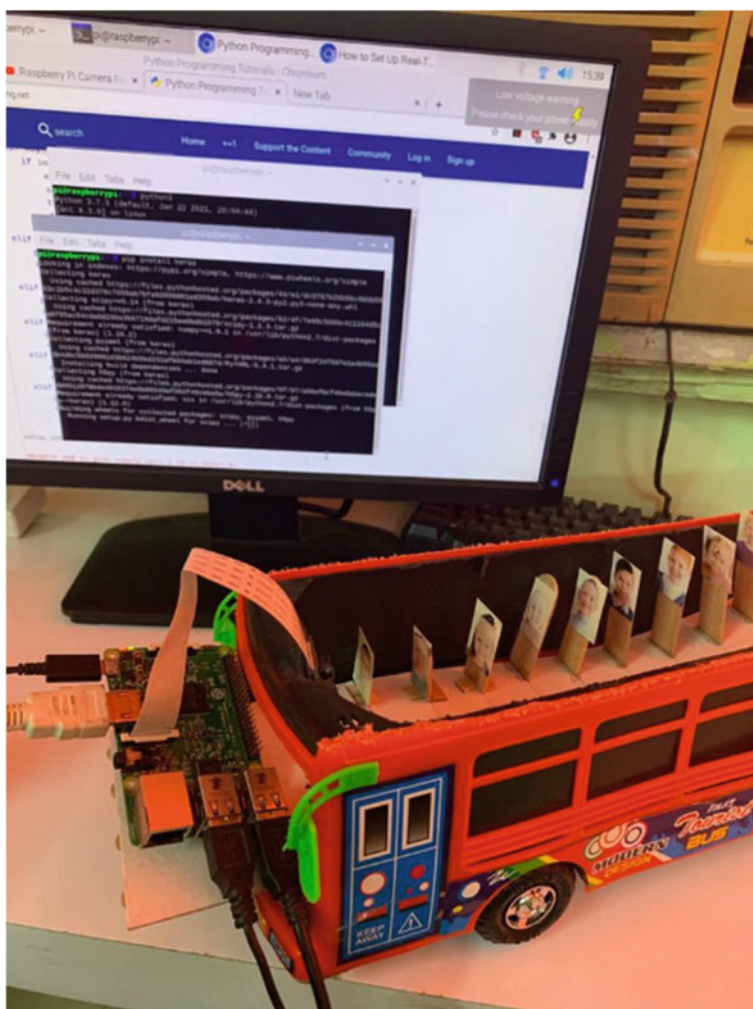


Fig. 4 Bus prototype

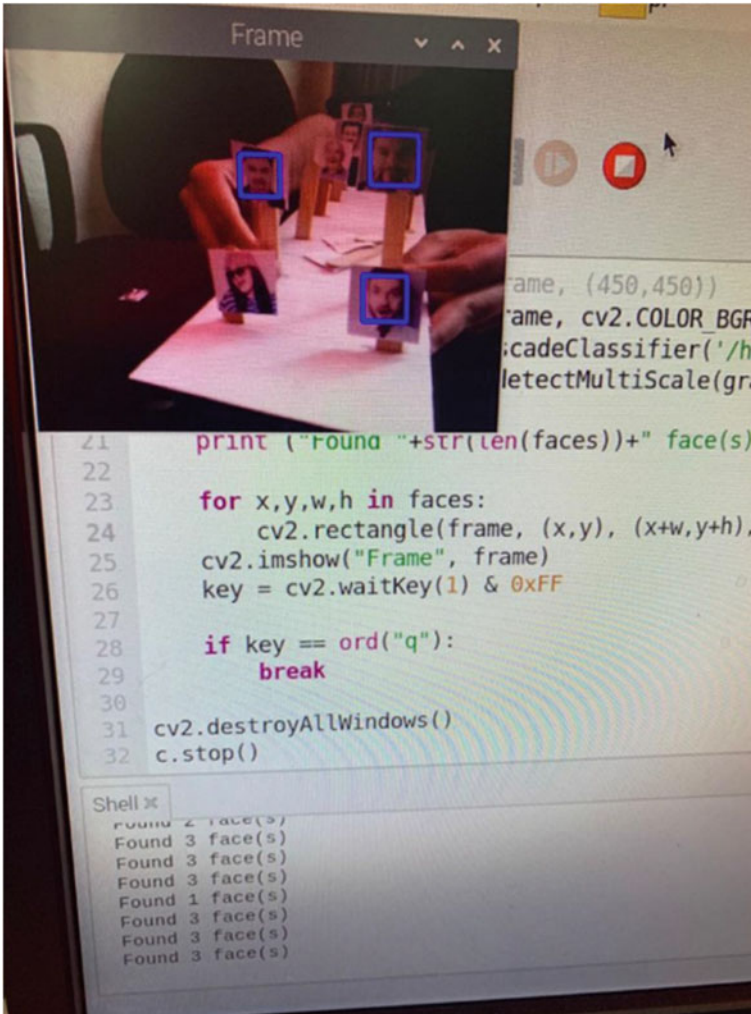


Fig. 5 Detection of the passengers using R-PI camera

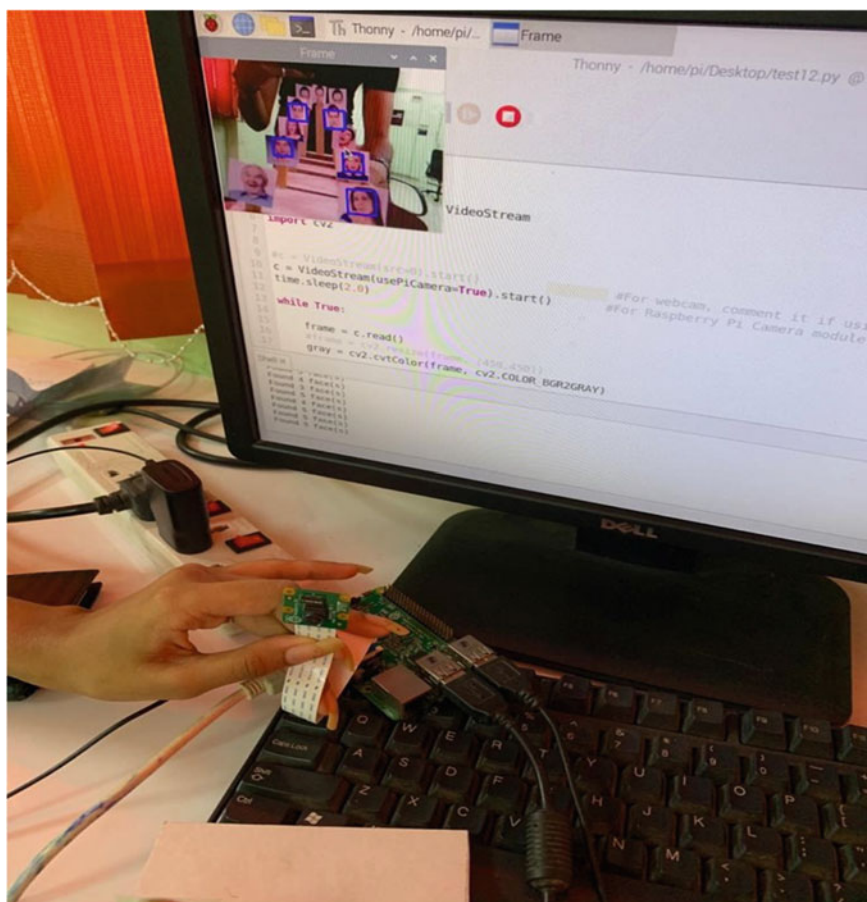
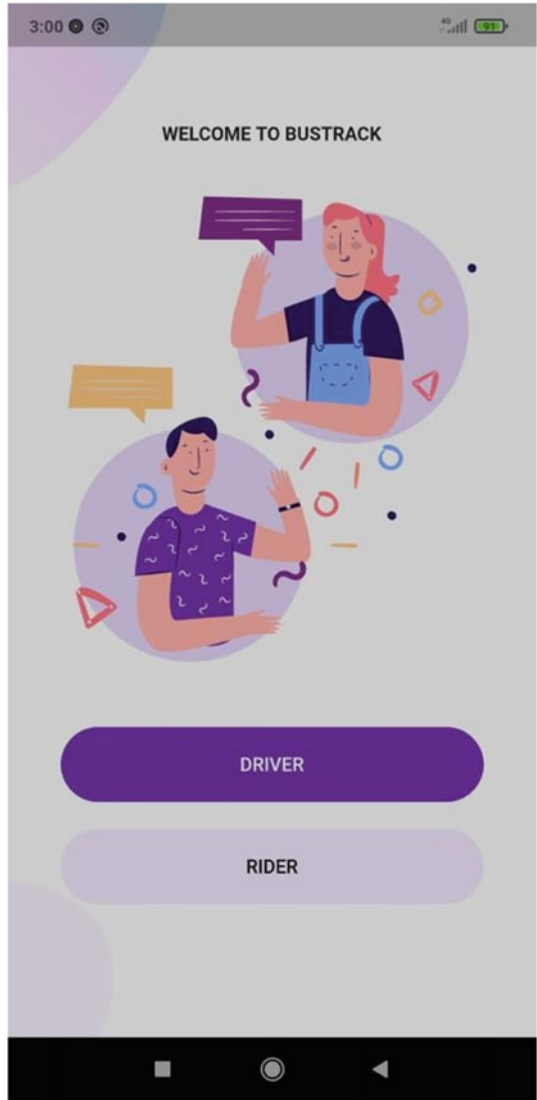


Fig. 6 Prototype with output

**Fig. 7** Application graphical user interface





## 6 Conclusions

A new transport system can be developed on the basis of this project which can be implemented in Mumbai as the numbers of passengers are increasing day by day. This system also gives the count of number of passengers traveling in the bus. The implementation of this project will make the life of the common people using public transport much comfortable. The passenger can plan his travel schedule effectively and in turn save time by avoiding the waiting for the bus which can be utilized in a productive manner. The comfort and ease will attract more people to use public transport which will increase the revenue of the government. Due to ease and comfort many people will avoid their own transport and opt for public transport which will reduce the traffic on the road.

## References

1. Manlise CO, Martinez Jr JM, Belnzo JL, Perz CK, Postreo MKTA (2015) Real-time integrated CTV using face and pedestrian detection image processing algorithm for automatic traffic light transitions. School of Electrical, Electronics and Computer Engineering, Mapua Institute of Technology
2. Sharma H, Saurv S, Singh S, Sain AK, Sain R (2015) Analyzing impact of image scaling algorithms on Viola-Jones face detection framework. Advanced Electronics System, Academy of Scientific and Industrial Research, CSIR-Central Electronics Research Institute
3. Luh G-C (2014) Face detection using combination of skin color pixel detection and Viola-Jones face detector. Department of Mechanical Engineering, Tatung University
4. Viola P, Jones M (2001) Rapid object detection using a boosted cascade of simple features. Mitsubishi Electric Research Labs, Compaq Cambridge Research Lab
5. Sredhar K, Panl B (2012) Enhancement of images using morphological transformations. Int J Comput Sci Inf Technol (IJCSIT) 4(1):3–50

# Author Index

## A

Ambekar, Aarti Gajanan, 3, 29, 65, 75, 129,  
139, 157, 167, 193, 207

## B

Bhargava, Mehul, 325  
Bhattacharjee, Shivani, 345  
Bhavsar, Yuti, 315

## C

Chavali, Venkata A. P., 3, 49, 65, 91, 139,  
157, 167, 177, 207

## D

Dannana, Suresh, 281  
Dashmohapatra, Soumyaprakash, 235  
Deshmukh, Amit A., 3, 21, 29, 39, 49, 65,  
75, 91, 109, 119, 129, 139, 147, 157,  
167, 177, 193, 207, 303  
Deshmukh, Sanjay B., 109, 119  
Dharia, Vraj, 315

## F

Franklin Vinod, D., 325

## G

Gala, Mohil, 75, 91

## I

Issrani, Disha, 345

## J

Joshi, Drumil, 335

## K

Kadam, Ameya A., 147  
Kadam, Poonam A., 21  
Kamble, Pradnya, 259  
Kameswari, S. Sri Durga, 271, 293  
Karamchandani, Sunil, 335, 345  
Karamchandani, Sunil H., 303  
Kelkar, Vishaka, 249  
Khambaty, Aamir, 335  
Kishore, K. Krishna, 293  
Kolekar, Uttam, 225

## L

Lele, Kshitij, 49, 193

## M

Mundra, Sakshi, 315

## N

Nageswara Rao, M. V., 215

## O

Odhekar, Anuja, 39

## P

Panicker, Pranav H., 303

© The Editor(s) (if applicable) and The Author(s), under exclusive license  
to Springer Nature Singapore Pte Ltd. 2022

H. Vasudevan et al. (eds.), *Proceedings of International Conference on Wireless  
Communication*, Lecture Notes on Data Engineering and Communications  
Technologies 92, <https://doi.org/10.1007/978-981-16-6601-8>

Parvez, Adil, [49](#), [177](#), [193](#)  
Patel, Nidhi, [315](#)  
Pawar, Shefali, [129](#)  
Pednekar, Saurabh, [345](#)  
Pinto, Keagan, [335](#)  
Prabhakar, Telagarapu, [215](#), [271](#), [293](#)  
Pusalkar, Atharva, [345](#)

**R**

Rajasekar, B., [13](#)  
Rao, Gottapu Sasibhushana, [281](#)

**S**

Sadique, Mohd Faisal Mohd, [235](#)  
Sapkale, Pallavi, [225](#)  
Sathiyamoorthy, C. A., [235](#)  
Sawant, Tushar, [29](#), [177](#), [207](#), [355](#)

Sayed, Fawzan, [335](#)  
Sekhani, Bhavya, [249](#)  
Shah, Dishay, [249](#)  
Shah, Krupansh, [355](#)  
Shaikh, Alam N., [259](#)  
Sharma, Jaya, [325](#)  
Singh, Shruti, [325](#)  
Sivasankaran, V., [235](#)  
Sreenivasa Rao, B. M. S., [13](#)  
Sudhakar, A., [215](#), [271](#)

**T**

Taware, Rahul, [315](#)

**V**

Venkataramanan, V., [235](#)